Steam Turbine Rotor Reliability—Task Details

EPRI

EPRI NP-923
Project 502
Interim Reports
November 1978

Keywords:
Rotor Lifetime
Boresonic Exam
Rotor Metallography
CrMoV Forgings
Retired Rotors
STRAP

Prepared by
Battelle, Columbus Laboratories,
Southwest Research Institute,
and
Westinghouse Electric Corporation

ELECTRIC POWER RESEARCH INSTITUTE

Steam Turbine Rotor Reliability — Task Details

NP-923
Research Project 502

Interim Reports, November 1978

Prepared by

BATTELLE, COLUMBUS LABORATORIES
505 King Avenue
Columbus, Ohio 43201

SOUTHWEST RESEARCH INSTITUTE
P.O. Drawer 28510
San Antonio, Texas 78284

WESTINGHOUSE ELECTRIC CORPORATION
Research and Development Center
1310 Beulah Road
Pittsburgh, Pennsylvania 15235

WESTINGHOUSE ELECTRIC CORPORATION
Lester Branch
P.O. Box 9175
Philadelphia, Pennsylvania 19113

Principal Investigators
S. D. Brown, Battelle, Columbus Laboratories
G. A. Clarke, Westinghouse
T. S. Cook, Southwest Research Institute
J. W. Cunningham, Westinghouse
J. R. Fox, Battelle, Columbus Laboratories
M. J. Golis, Battelle, Columbus Laboratories
L. D. Kramer, Westinghouse
H. G. Pennick, Southwest Research Institute
T. T. Shih, Westinghouse
R. J. Warren, Battelle, Columbus Laboratories
C. H. Wells, Southwest Research Institute

Prepared for

Electric Power Research Institute
3412 Hillview Avenue
Palo Alto, California 94304

EPRI Project Manager
F. E. Gelhaus
Nuclear Power Division

EPRI PERSPECTIVE

PROJECT DESCRIPTION

Turbine rotors are highly reliable components, with major failures occurring only once in several thousand turbine-years of operation. However, the costs of even infrequent failures are significant to the whole industry and are much larger than the direct costs of replacing a failed rotor. Following an intensive review of the Gallatin Unit-2 rotor burst and several earlier events, it was concluded that the phenomena involved were not necessarily unique and could be of generic concern to the utility industry. This led to RP502, a project on the reliability of steam turbine rotors. This project is one of 10 research efforts currently funded by EPRI that relate directly to various aspects of steam turbine performance. There are nearly 30 other active projects whose results are to some degree related to the reliability of steam turbines.

PROJECT OBJECTIVES

The primary goal of this project is to develop a rotor lifetime prediction system that will permit utilities to perform or confirm the analyses on which run/retire decisions are based. These analyses are best performed using actual operating history and inspection data. However, the code system also can be employed in a parameter survey mode to determine the sensitivity of the run/retire decisions to the completeness of the stress and fracture analysis models and to the uncertainties in the data on flaws, duty cycles, and properties. Since inspection data represent essential input for valid analyses, another project objective has been to evaluate the state of the art of the nondestructive inspection systems and processes used in rotor bore examinations.

CONCLUSIONS AND RECOMMENDATIONS

The status of the project at this interim point is as follows. A computer code system, the Steam Turbine Rotor Analysis Program (STRAP), is completed, and the code is available from the EPRI Code Center. While the fracture mechanics routine represents the state of the art, the data base does not adequately represent the linkup within clustered defects that is caused by crack growth across the ligaments,

especially under the combined effects of creep and low-cycle fatigue. The model for the change induced in material toughness by aging embrittlement is also subject to improvement because the data available so far is limited. Both effects are key aspects of the lifetime analysis. Two contractors (Commercial Machine Works and Westinghouse Electric Corp.) have used the data obtained in assessing current nondestructive evaluation (NDE) systems in this project to improve their procedures. An important further step will be to verify the inspection techniques against flaws near the bore surface and for radially oriented fatigue cracks of various sizes. Improved discrimination in flaw sizing is an essential requirement for a definitive lifetime prediction system. In addition to the Gallatin rotor, two retired rotors were used for testing inspection systems and methods and for providing specimens for material properties measurements. Both rotors were taken out of service by the utilities that provided them, on the basis of recommendations by the turbine manufacturers. On destructive examination, both were found to have only small, relatively widely spaced flaws. For one rotor, the calculations strongly suggested that the flaws were benign. The other rotor was found to exhibit significant temper embrittlement. This condition decreases the critical flaw size by a factor of about 4. Both rotors were indicated to be Class C. The existence of embrittlement in only one of the project rotors indicates a wide variation in the probability of embrittlement within the range of the Class C designation. These results highlight the ambiguities still present in both the present NDE data and the generic properties data which are used as the basis for run/retire decisions. Extension of the NDE work to additional rotors with a larger population of flaws (including significant, nonbenign flaws) is needed to provide more generally applicable correlations. Advanced inspection techniques with better capability for flaw imaging and sizing are under development for other applications and are scheduled to be adapted for use on turbines.

The research effort to date provides an improved interim tool for guiding run/retire decisions. It also provides a foundation for future work aimed at producing a more rigorous basis for such decisions with fewer areas of ambiguity.

The project effort is scheduled to continue with the cooperation of the turbine facility of American Electric Power Service Corporation (AEP), which is providing the project with extensive facilities for rotor inspection and with a selection of retired rotors. A related supporting effort sponsored by AEP is contracted with Southwest Research Institute for development of TREES, an improved boresonic inspection system. The output from the TREES minicomputer will be used directly as input

to the STRAP calculations. Battelle, Columbus Laboratories (BCL) will continue to focus on improved bore inspection system hardware and techniques. BCL will also adapt imaging methods and advanced signal-processing techniques that have been developed on other NDE projects to the steam turbine rotor inspection process.

Floyd E. Gelhaus, Program Manager
Nuclear Power Division

Blank Page

ABSTRACT

The overall project objective is to establish and confirm by test the viability of a steam turbine rotor component lifetime prediction system that is based on finite element thermo-elastic stress analysis and fracture mechanics, and that uses details of field NDE inspection results as input to the calculations. The purpose is to provide U.S. utility personnel with an improved understanding of, and the analytical software capable of performing or confirming, rotor lifetime (run/retire) analysis. The effort to date has been composed of four tasks (contracts):

Task 1 - Lifetime Prediction Analysis System
Southwest Research Institute

Task 2 - Nondestructive Evaluation
Battelle, Columbus Laboratories

Task 3 - Destructive Tests
and
Task 4 - Material Mechanical Properties Measurements
Westinghouse Electric Corporation, Research and Development Laboratory in conjunction with the Steam Turbine Division

The automated Steam Turbine Rotor Analysis Program (STRAP) has been developed to facilitate the prediction of rotor lifetime given the duty cycle of the turbine and the results of ultrasonic examination from the rotor bore. STRAP consists in part of a preprocessor code that generates the boundary conditions and finite element mesh for transient and steady-state temperature and stress analysis employing the ANSYS general-purpose structural analysis code. A postprocessor contains fracture toughness, stress-rupture, yield strength, and fatigue crack growth rate data for air-melted 1 Cr-Mo-V forgings, on the basis of which the local stress and temperature values are screened to determine the critical crack size, the initial crack size that could grow to critical size within a specified number of hours or cycles, and the minimum area fraction of defects that could link up to result in a significant crack. A boresonic data reduction code allows rapid sorting of indicated flaw sizes and locations to determine the regions of greatest defect density.

This report combines four separate task reports that detail the project research since January 1976. Each report is self-contained, with its own summary, contents, and references. Also available is a project summary report (EPRI NP-923-SY), which presents highlights of the research results.

CONTENTS

SUMMARY

Task 1: Lifetime Prediction Analysis System

The automated Steam Turbine Rotor Analysis Program (STRAP) has been developed to facilitate the run/retire decision for a rotor. STRAP consists in part of a preprocessor code that, given certain duty cycle and rotor geometry parameters, generates the finite element mesh and the boundary conditions for transient and steady-state temperature and stress analyses that are performed by the ANSYS general-purpose structural analysis code. A postprocessor contains fracture toughness, stress-rupture, yield strength, and fatigue crack growth rate data for air-melted 1 Cr-Mo-V forgings; on the basis of these material properties, the local stress and temperature values are screened to determine the critical crack size, the initial crack size that could grow to critical size within a specified number of hours or cycles, and the minimum area fraction of defects that could link up to result in a significant crack. The program is designed to evaluate the results of a boresonic inspection, assess the significance of the detected flaws, and estimate the remaining life on the basis of those flaws.

The lifetime prediction code is still under development; the analytical models and material property data base used in the program are not complete. These deficiencies are the targets of the continuing RP502 effort. For example, there is currently no way to assess the probability of temper embrittlement of an individual rotor short of determining the fracture appearance transition temperature, which has been found to be highly variable. No suitable crack growth algorithm has been developed for temperatures in the creep range, and an unequivocal interpretation of the TVA Gallatin rotor burst event in terms of measured mechanical properties is still being sought.

In spite of the limitations of the current version of STRAP, it has provided a means of making conservative predictions of the remaining life of a steam turbine rotor. Five rotors have been examined during this program, and the stress and temperature distributions for each are discussed. The results of the fracture analysis of the rotors are also presented.

In addition to the application of STRAP to specific rotors, the code itself is described in some detail. This discussion includes the geometry and heat transfer modeling, the duty-cycle description requirements, and the material data base used. The methods of evaluating the fracture characteristics, both for an isolated flaw and for clusters, are presented, and the limitations of the current code are pointed out.

Task 2: Nondestructive Evaluation

This task is aimed at determining the effectiveness of nondestructive means of assessing the presence of objectionable discontinuities within the volume of steam turbine rotors. The results of field and laboratory studies conducted primarily in 1977 resulted in a state-of-the-art report on boresonic examination (EPRI NP-744), and these are discussed, along with additional technical findings. The general results suggest that significant improvements can be made in the technologies associated with rotor examination, particularly when the NDE results are to be used as the data base for making failure predictions founded on fracture mechanics concepts. Numerous areas of concern are identified, particularly those associated with data gathering (transducers and mechanical positioners) and informational displays (test data formats and completeness).

It is desirable that inspection groups prove their system's capabilities through performance demonstration before conducting an investigation. The following tentative acceptance criteria are proposed for rotor inspection systems.

- System sensitivity and reliability. Each system should be able to detect a single 1/16-inch flat-bottom hole (FBH) in the region from 1/8 to 1-1/2 inch from the bore surface. This should be demonstrated by passing the near-bore transducer system through a calibration block containing several such FBHs. The normal routine scanning parameters should be used. To qualify, the system must detect all the holes in 9 out of 10 tries.

- System resolution. Each system should be able to resolve the presence of three 1/16-inch side-drilled holes (SDHs) spaced 3/16 inch apart and arranged in various patterns. If automatic recording equipment is used, the three holes must be seen distinctly on the chart.

- System coverage. Each system should be incremented in either the z or the theta direction so that a 1/16-inch FBH 1/4 inch from the bore surface is detected on three consecutive scans.

- Shear wave system sensitivity. Each system should be able to detect a 1/32-inch SDH in the region from 1/4 to 1-1/2 inches from the bore surface.

- Shear wave system resolution. Each system should be able to resolve the presence of three 1/16-inch SDH spaced 3/16 inch apart and arranged in various patterns.

- Shear wave system coverage. Each system should be incremented so that a 1/16-inch FBH 1/4 inch from the bore surface is detected on three consecutive scans.

- Data report format. Data reports generated by the rotor inspection should be in reasonable agreement so that later inspections can be compared with earlier ones. The most complete way would be to supply the owner a tabulated list of each detected indication including its exact location, maximum signal amplitude, equivalent FBH size, and comments on whether it is a single indication, part of a cluster, or a cloud indication.

Task 3: Destructive Tests

The object was to destructively section retired turbine rotors that had been boresonically inspected in order to determine the metallurgical and flaw structure existing at the time of retirement and to determine the degree of correspondence between the actual flaws and the NDE results.

Two retired IP-LP rotors, Joppa 3 and Buck 6, manufactured in the early 1950s were cut up in performing this task. Small pieces cut from selected near-bore regions of the rotors were subjected to C-scan and radiography and were progressively polished at small intervals through flawed areas. The flaws revealed were quantified with respect to location, area and volume fraction, size, and nearest neighbor distance. Location and size were compared with boresonic results.

Although no metallurgical anomalies were found, both rotors contained a large number of small flaws, generally confirming the results of the commercial boresonic inspections. However, because of the small size and close spacing of the flaws and uncertainties in position arising from boresonic techniques and cutting, a one-to-one correlation between a specific boresonic indication of location and size and a specific dissected flaw was rarely possible.

In spite of the large number of flaws, the area fraction and the volume fraction of flaws in both rotors, averaged over dimensions considered critical by modeling, were less than 0.01. Inspection of low-cycle fatigue specimen fractures from the Joppa 3 rotor disclosed that subcritical cracks generated under high cyclic stresses in laboratory tests made large deviations from the expected fracture plane in order to follow the path of least resistance established by the flaws in spite of their low volume fraction.

The general conclusion is that existing NDE boresonic techniques, while probably adequate for large flaws, do not provide a good representation of detailed flaw structure in rotors with small, closely spaced flaws, such as Joppa 3 and Buck 6.

Task 4: Material Mechanical Properties Measurements

An extensive evaluation of the mechanical properties of two 1950-vintage air-cast Cr-Mo-V steel rotor forgings was conducted. The rotors investigated were the TVA Gallatin Station No. 2 IP-LP rotor that burst in June 1974 and the Electric Energy Inc. Joppa Station No. 3 IP-LP rotor that was retired after 17 years of service. Tensile, Charpy, impact, fracture toughness, fatigue crack growth, and low-cycle fatigue data were developed for both rotor materials under a wide variety of loading conditions. Creep and blunt-notch fatigue crack initiation tests were also conducted with the Gallatin material.

In addition to the mechanical testing, detailed fractographic examination of broken test specimens was undertaken to both characterize and identify the controlling fracture mechanisms. The fractographic features associated with various testing conditions were compared with the fractographic evaluation of the Gallatin rotor burst. A brief summary of the Gallatin rotor failure is also included. With regard to the mechanical testing of the Gallatin material, it was found that the mechanical properties were similar to other 1950-vintage rotors. The only test that showed any evidence of intergranular cracking similar to that found in the Gallatin rotor was a low-cycle fatigue test conducted with a 23-hour dwell time at a nominal strain range of 2.98% of 800^{o}F (427^{o}C). A biaxial state of stress had no effect on the initiation of fatigue cracks in blunt-notched CT specimens when tested at 800^{o}F with a 1-hour dwell period. This result, as well as the absence of any intergranular cracking at the initiation site, suggests that a creep phenomenon did not play a dominant role in the initiation of cracks in these specimens.

An evaluation of peak low dwell time effects on cyclic loading revealed a threefold increase in fatigue crack growth rate with an increase in dwell time from 15 minutes to 22-2/3 hours at 800^{o}F. Again, it was noticed that fatigue cracking was transgranular.

The mechanical properties of the Joppa No. 3 rotor were found to be uniform throughout the axial and radial extent of the rotor. These properties were also found to be similar to the properties of other 1950-vintage Cr-Mo-V rotors. The uniformity of the Charpy impact properties suggests that the Joppa rotor saw little if any

in-service degradation. The fatigue crack growth rate of the Joppa rotor was found to be similar to those of the Gallatin rotor and two other retired Westinghouse rotors. A three-dimensional surface representing log da/dN - log T - log ν was found to describe the interaction of temperature and frequency of the fatigue crack growth rate for this material.

A complete toughness-versus-temperature curve was developed for the Joppa material by using K_{Ic} and J_{Ic} techniques. A good agreement was found between the estimated value of toughness based on the Begley-Logsdon correlation method and actual test results.

The large low-cycle fatigue specimens showed a classic example of the linkup process between defects. It was observed that in an approximately constant stress field, the linkup process occurred in a three-dimensional pattern, with the crack front searching out defects on various nearby planes.

The Buck-6 rotor material exhibited significant temper embrittlement. These data are currently being analyzed and will be presented and compared with corresponding Joppa 3 and Gallatin results in a special supplementary report to be issued in January 1979.

Steam Turbine Rotor Reliability - Task Details

Task 1. Lifetime Prediction Analysis System

Prepared by

SOUTHWEST RESEARCH INSTITUTE
P. O. Drawer 28510
San Antonio, Texas 78284

Principal Investigators

T. S. Cook
H. G. Pennick
C. H. Wells

Blank Page

CONTENTS

Blank Page

ILLUSTRATIONS

TABLES

SUMMARY

An automated Steam Turbine Rotor Analysis Program (STRAP) has been developed to facilitate the run-retire decision for a rotor. STRAP consists in part of a preprocessor code that, given certain duty cycle and rotor geometry parameters, generates the finite element mesh and the boundary conditions for transient and steady state temperature and stress analyses which are performed by the ANSYS general purpose structural analysis code. A postprocessor contains fracture toughness, stress-rupture, yield strength and fatigue crack growth rate data for air-melted 1 Cr-Mo-V forgings; on the basis of these material properties, the local stress and temperature values are screened to determine the critical crack size, the initial crack size that could grow to critical size within a specified number of hours or cycles, and the minimum area fraction of defects which could link up to result in a significant crack. The program is designed to evaluate the results of a boresonic inspection, assess the significance of the detected flaws, and estimate the remaining life based on those flaws.

The life prediction code is still under development, as the analytical models and material property data base used in the program are not complete. These deficiencies are the targets of the continuing RP502 effort. For example, there are currently no means to assess the probability of temper embrittlement of an individual rotor short of determining the fracture appearance transition temperature, which has been found to be highly variable. No suitable crack growth algorithm has been developed for temperatures in the creep range, and an unequivocal interpretation of the TVA Gallatin rotor burst event in terms of measured mechanical properties is still being sought.

In spite of the limitations of the current version of STRAP, it has provided a means for making conservative predictions of the remaining life of a steam turbine rotor. Five rotors have been examined during this program, and the stress and temperature distributions for each of these rotors are discussed. The results of the fracture analysis of the rotors are also presented.

In addition to the application of STRAP to specific rotors, the code itself is described in some detail. This discussion includes the geometry and heat transfer modelling, the duty cycle description requirements, and the material data base used. The methods of evaluating the fracture characteristics, both for the isolated flaw and for clusters, are presented. The limitations of the current code are pointed out as they arise.

Section 1

INTRODUCTION

The origin of the RP502 project was the catastrophic fracture in June 1974 of the TVA Gallatin Plant Unit No. 2 IP rotor. Following a review of this event, it was concluded that the conditions which led to the burst were not necessarily confined to this particular rotor. It was suspected that the Cr-Mo-V rotors manufactured in the 1950's by the air melt technique presented a generic problem. In particular, these older rotors appeared to be deficient in some material properties when compared to rotors produced by modern manufacturing techniques. In view of the large potential interest in the life assessment of this class of older steam turbine rotors, a program was undertaken to develop a life prediction system for these units.

Objectives of Task I of the RP502 Program

Overall, the goal of the RP502 program was to increase the reliability of steam turbine rotors by advancing in-service nondestructive evaluation techniques and interpreting the significance of these results in an analytic lifetime prediction system. Task I involved the development of the life prediction system for 1950 vintage rotors manufactured from air melted chrome-molybdenum-vanadium steel. Other tasks of the RP502 program involved the development of material property data for this steel for inclusion in the code and the evaluation of available boresonic inspection systems that would supply the detected flaw data for the prediction system.

The specific objective of Task I was to develop a comprehensive analytical system that could, with a relatively small number of operator inputs, evaluate the risk of failure of a steam turbine during continuing operation. For a given rotor geometry and operating cycle, the system would determine the transient and steady state temperature and stress distributions in the rotor. Based on typical materials data, the system would then determine critical and initial crack sizes for the cycle and the desired life. The results of this analysis would then be compared to the results of a boresonic inspection and the significance of the inspection results determined.

In developing the analysis system, one goal was to keep operator input to a minimum. This objective conflicts with the desired flexibility to describe a wide range of rotors, as a code capable of modelling a number of geometries would require a large number of input parameters. This was resolved by keeping the input simple at the risk of some loss in generality. However, as more experience is gained in dealing with a number of different rotors, the code may be expanded to handle those features commonly encountered but not yet included.

It should also be pointed out that the present code is designed to utilize the results of a boresonic inspection. Since the boresonic inspection achieves its maximum resolution near the bore, the model of the rotor was designed to be compatible with this. That is, not only is the finite element mesh more refined at the bore, but great detail in the modelling of the features at the periphery is not required. Instead, engineering judgement is used to provide simple models of blade loading, seals, etc. at the periphery of the rotor. These simple models provide satisfactory results in the neighborhood of the bore, but might have to be refined for detailed calculations at the blade root.

The postprocessor, which contains the fracture analysis code, was intended to encompass all fracture modes likely to occur in the rotor. A number of modes are included, but the lack of a definitive explanation of the Gallatin burst, the recent discovery of temper embrittlement in a rotor, and the lack of a creep crack growth model have resulted in the current code being limited in its fracture analysis. As will be discussed, the latter two problems are currently being addressed and as better models and materials data becomes available, it will be incorporated into the analysis system.

Summary of Accomplishments

The current status of the RP502 project is summarized in Figure 1-1. The analytical system, STRAP, consists of a geometry and heat transfer preprocessor (PPMESH) and a fracture analysis postprocessor (FRAC) written for a general purpose structural analysis computer code (ANSYS). The preprocessor accepts the principal dimensions of the rotor, blade weights, interstage seal configuration, and end conditions such as steam or water shaft seals. The operator must specify the history of rotor speed, steam inlet and outlet temperature and pressure, and shaft seal fluid temperature.

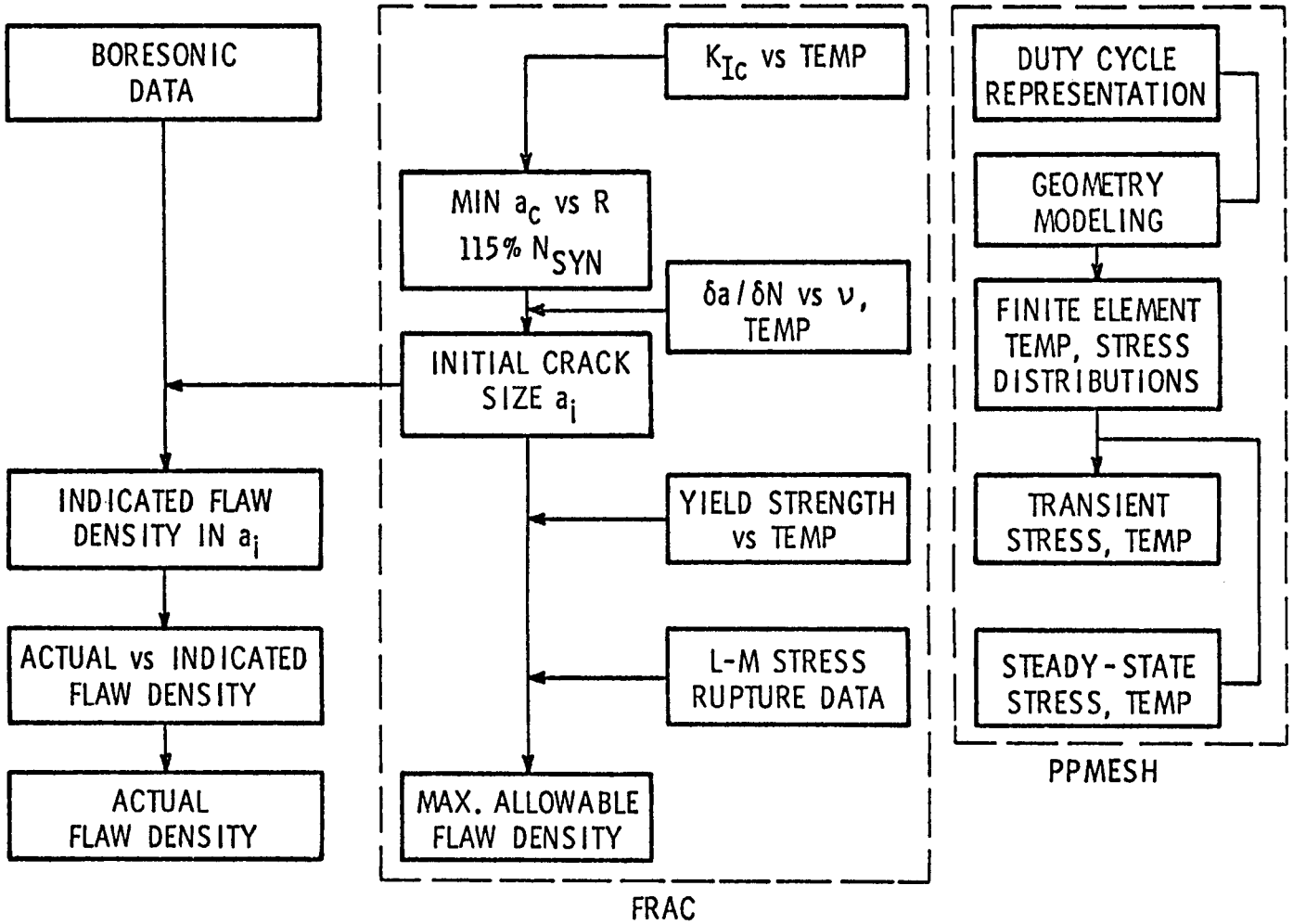

FIGURE 1-1. STEAM TURBINE ROTOR ANALYSIS PROGRAM (STRAP)

The preprocessor then generates the finite element model of the rotor, calculates blade loads, steam leakage flow and heat transfer coefficients, and manages the transient temperature distribution analysis by the ANSYS code. Then the combined thermal and centrifugal stress distribution is calculated at a sufficient number of time steps to determine the peak transient and steady state values of stress at the centroid of each element. These values are stored for fracture analysis.

As shown in Figure 1-1, FRAC contains data on Cr-Mo-V steel to evaluate several possible fracture modes. Brittle fracture is evaluated by K_{IC} vs temperature properties; as will be explained in a subsequent section, ductile fracture is evaluated through the yield properties. Low cycle fatigue crack growth data as a function of temperature and frequency is contained within the code, as is stress rupture data based on the Larsen-Miller parameter. It should be noted, however, that the code does not contain provision for stress corrosion cracking or cracking in bending or torsion. Methods are contained for predicting the growth and criticality of isolated flaws of various shapes as well as three-dimensional distributions of flaws. With the exception of an algorithm for creep crack growth, the postprocessor contains sufficiently conservative data on 1 Cr-Mo-V steel to allow run-retire decisions for most situations if the flaw geometry is known.

Future Activities

While the current versions of the codes PPMESH and FRAC are complete and will allow a decision to be made regarding continued service of a given rotor, there are a number of improvements that could be made to the codes. One problem arises because the automated analysis sytem represents a compromise between generality and the cost and complexity of use, and so it will not handle some rotor configurations currently in service. For example, it does not allow the modeling of a variable thickness disk or large diameter changes between sections of an integral rotor. Similarly, the code does not provide the means to include shrunk-on disks in the analysis. It should be emphasized that these constraints arise due to the automation of the mesh generation. The preprocessor can be modified to accept virtually any geometry, but at the cost of increased complexity of input and operation.

Another modification of the code that could be incorporated in future work would allow cracking at the periphery of the rotor to be studied. PPMESH was designed to utilize the results of a boresonic inspection,and so the mesh generation provides maximum accuracy in the near bore region. In order to model adequately the periphery of the rotor, changes in the mesh generation would be required.

Any changes in geometry modelling involve tradeoffs, but they are, in principle, straightforward. Other areas involve improvements to current fracture mechanics models and are, therefore, considerably more complex. For example, the interaction between a crack and a rotor bore or between two inclusions can involve elastic-plastic fracture mechanics; the development of new elastic-plastic models will be part of the RP502 continuation activity.

The two major unresolved problems in describing the fracture properties of Cr-Mo-V rotors are the temper embrittlement and creep crack growth. Recent test results have shown an increase in Fracture Appearance Transition Temperature (FATT) of 300°F for one rotor. It is not known whether the probability of such embrittlement can be predicted from the available history of a forging or whether metallographic or fracture tests will have to be performed on coupons from the rotor. In either case, the fracture toughness data base used in FRAC may have to be modified. The other problem is the variability of creep crack growth rate, which requires the acquisition of a data base and the development of a crack growth algorithm. Both problems are being addressed as part of the continuation of RP502.

Section 2

DUTY CYCLE ANALYSIS

In the following sections, reference is made to rotors manufactured by two companies, General Electric and Westinghouse. During the development of STRAP, examples of both companies' rotors were used to guide the geometric and heat transfer modelling contained in the codes. Since the approach to rotor design taken by the two companies is not the same, the preprocessor requires that the operator specify which of the two companies manufactured the rotor being analyzed. If the rotor has been produced by another manufacturer, then it must still be classified as a General Electric or Westinghouse rotor. It is expected, however, that eventually the geometric modelling will be expanded to include rotors made by other companies, under their own classification.

Program Logic

The overall flow of the RP502 Steam Turbine Rotor Analysis lifetime prediction system is shown in Figure 2-1. This figure shows the relationships between the preprocessor, PPMESH, the structural analysis code, ANSYS, and the fracture analysis code, FRAC, and indicates the general steps in the analysis. The first step in the analysis is the specification of the geometry and duty cycle of the rotor; PPMESH uses this information to generate the finite element mesh and prepare for the entry into the ANSYS heat transfer analysis (HTA). Following this analysis, PPMESH initiates the stress analysis. Once this second analysis is complete, the maximum stresses can be determined. Finally, in a subsequent operation, FRAC performs the fracture analysis. Separation of FRAC into a distinct unit was done for economic reasons. It is not cost effective to combine FRAC with the much more expensive structural analysis.

Duty Cycle Description

Three steps in the turbogenerator startup procedure have been identified as significant from a lifetime standpoint: the prewarming of the rotor prior to roll-off, the acceleration of the rotor from roll-off

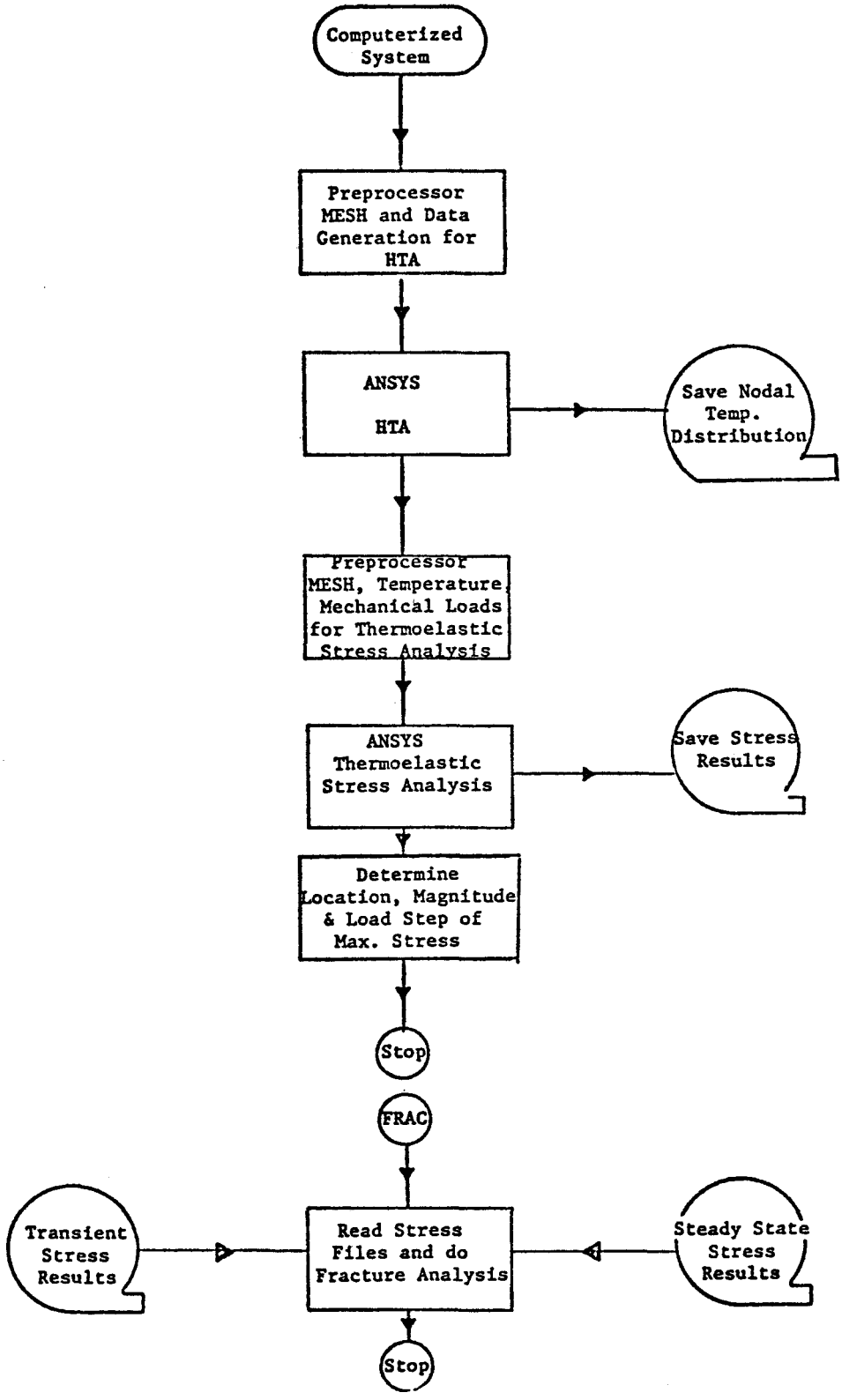

FIGURE 2-1. FLOW CHART OF RP502 STEAM TURBINE ROTOR ANALYSIS PROGRAM

to synchronous speed, no load, and the interval from synchronous speed, no load, to the attainment of steady state inlet steam temperature. During the last step, i.e. the loading of the unit, the steam pressure at each stage is generally found to be proportional to turbogenerator load. Cooling of the inlet steam during the first two steps by heat loss to the rotor and casing cannot be determined since the steam flow rate during warmup is not available; neglect of this cooling tends to make calculations of transient stress conservative.

Since a completely detailed description of the boundary conditions would be a formidable task, the heat transfer and stress analysis preprocessor developed in this program does not attempt to model every portion of the rotor surface with a high degree of precision. Rather, the approach taken is to apply engineering judgment so that a minimum amount of detail regarding the geometry and duty cycle of the rotor must be specified by the user. This simplifies operator input to the analysis and, while sacrificing some details, provides a conservative analysis of the rotor.

The only information regarding operation of the turbine required for the heat transfer analysis consists of the description of the duty cycle of the unit. The required variables, expressed as functions of time, are:

1. RPM
2. Cooling steam temperature
3. Inlet and outlet steam pressure
4. Fraction of maximum load
5. Inlet and outlet steam temperature

While a detailed discussion of the modeling used in the analysis is given in References (1) and (2), a description of some of the features of the model will be included here. The pressure-time history is specified as the inlet and outlet pressure before and during roll-off, at synchronous speed/no load, and at maximum load. Prior to roll-off, the pressure drop along the rotor is assumed to be zero. However, this results in zero mass flow (eq. 2-1) which, in turn, results in computational problems in those heat transfer coefficients, e.g. eq. 2-3, which contain the mass flow in the denominator. Thus, the outlet pressure must be input as slightly less than the inlet pressure; a convenient value of pressure drop is 0.25 psia. Following roll-off, as the rotor is brought up to operating speed, the pressure drop is assumed constant. After synchronous speed is attained, the stage pressures at maximum load are scaled to give

the pressure distribution at any level of turbogenerator load. On the basis of detailed information obtained from the TVA Gallatin and Electric Energy, Inc., Joppa plants, a linear relationship exists between the inlet and extraction point pressures and the load; this is shown in Figure 2-2. For the Gallatin No. 2 IP rotor the pressure drop along the rotor length was approximately linear, while for the Joppa No. 3 IP-LP rotor, on the basis of limited information, a negative exponential best fit the data. It was subsequently found, however, that the temperature distribution was not particularly sensitive to which function was used to describe the pressure drop along the rotor. Moreover, the use of the same pressure drop distribution function for both the General Electric and Westinghouse rotors simplified the input to the computer code, and so a linear pressure drop along the turbine was assumed for all rotors. Thus the Seward and Buck rotors, which were analyzed after the Joppa rotor, had the linear pressure drop distribution function.

The steam temperature conditions are input at six time intervals (or in the case of the seal cooling steam, seven times) during the loading cycle. The temperatures at intermediate times are obtained by interpolation of these values. The inlet and outlet steam temperatures define the temperature drop along the rotor. On the basis of limited operating data, this temperature drop was assumed to be linear along General Electric rotors, while a sine-squared function was used to describe the drop along the Westinghouse rotors. The cooling steam temperature is used to determine the temperature of the steam seals, and the RPM-time history is used in the calculation of the heat transfer coefficients for rotor elements that are treated as rotating disks or cylinders.

The thermal distributions are obtained through the computation of heat transfer coefficients; no temperature boundary conditions are applied to the rotor. Five heat transfer coefficients are used to describe the various surfaces and are detailed in the next section.

Heat Transfer Coefficients

Since the transient metal surface temperature may differ from that of the bulk steam by 100°F or more, all thermal boundary conditions used in ANSYS are obtained through the use of heat transfer coefficients. Those coefficients are computed by PPMESH, and in keeping with the objective of the analysis, it is intended that these coefficients should realistically

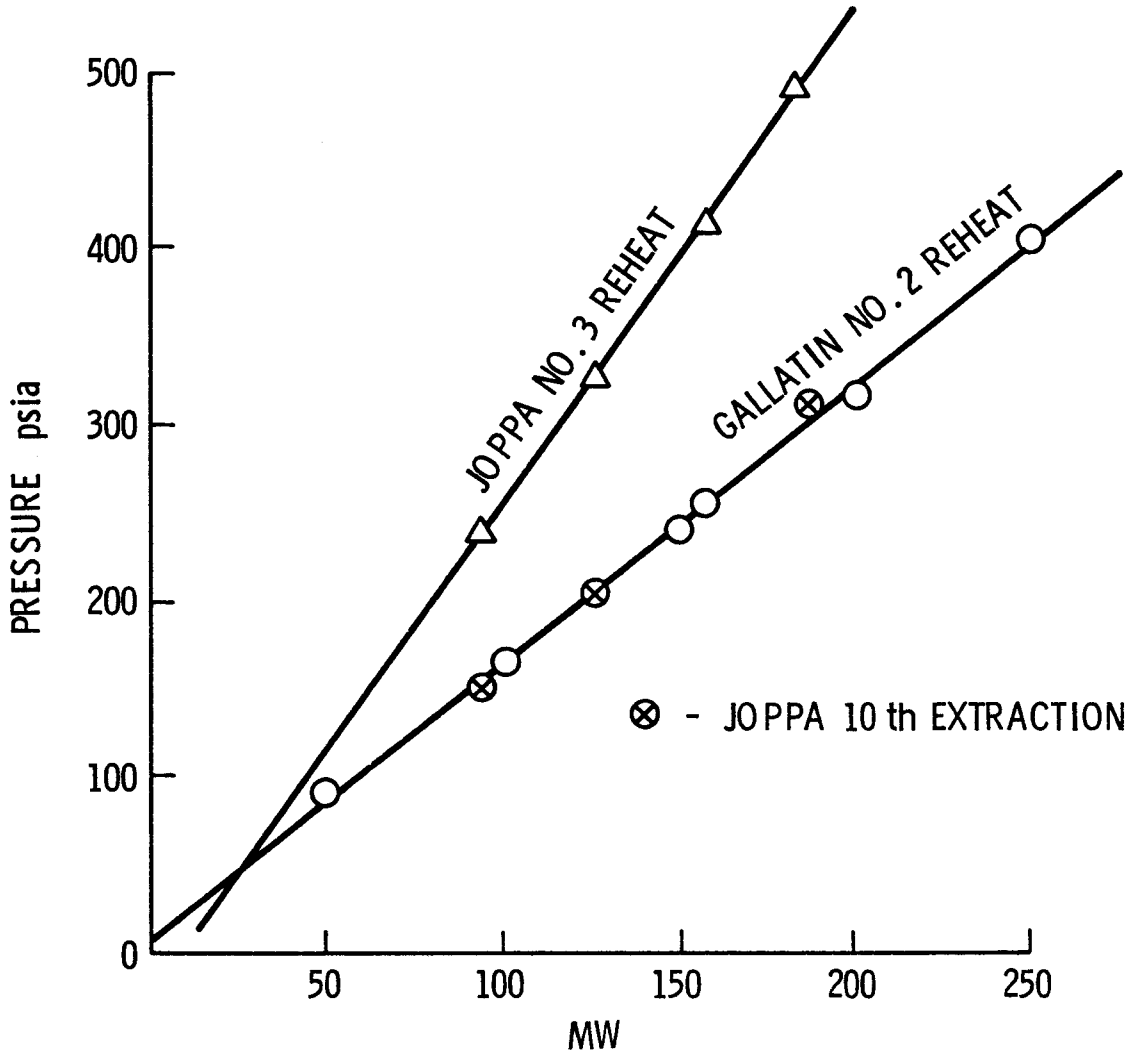

FIGURE 2-2. ILLUSTRATION OF LINEARITY BETWEEN STAGE PRESSURE AND LOAD

represent the actual rotor conditions without requiring excessive detail at the periphery. It is assumed that for the Westinghouse and General Electric rotors, 50 to 75 percent, respectively, of the pressure drop for each stage takes place across the labyrinth seals. This pressure drop is used in computing the seal leakage flow by Martin's formula (3),

$$\frac{\dot{M}}{A} = 18,000 \left(\frac{P_1}{V_1}\right)^{1/2} \left(\frac{1 - \left(\frac{P_2}{P_1}\right)^2}{N - \log_e \frac{P_2}{P_1}} \right)^{1/2} \qquad (2\text{-}1)$$

where

$\dot{M}$ = Leakage flow, lb_m/hr

A = Leakage area, ft^2

P_1 = Pressure upstream of the seal, lb/ft^2

P_2 = Pressure downstream of the seal, lb/ft^2

V_1 = Initial specific volume of steam, ft^3/lb

N = Number of seal teeth

It should be noted that differences in seal design have been observed between the General Electric and the Westinghouse rotors. Generally, the Westinghouse rotors have the same seal at each stage of the rotor; this geometry is built into the computer code and requires no input from the user. For most General Electric rotors, the seal geometry, i.e., the number of teeth, is different at each stage. The user must specify the number of seal teeth in this case; this one geometry is then applied to all seals in the rotor. Experience with the program has shown that the temperature distribution is only slightly perturbed by changing the seal geometry. However, to be conservative, the number of teeth specified should reflect the minimum use in that particular rotor.

Once the mass flow is known, the heat transfer coefficient is computed from (4)

$$h = 0.98 \left(\frac{K}{2\delta}\right) \left(\frac{\dot{M}}{A} \frac{2\delta}{\mu}\right)^{0.6} \left(\frac{W_s}{\delta}\right)^{-0.58} \qquad (2\text{-}2)$$

where

K = Steam conductivity, btu/sec ft °F

δ = Seal clearance, ft

W_s = Seal annulus width, ft

μ = Viscosity of steam, lb_m/ft sec

$\frac{\dot{M}}{A}$ = Mass flow per unit area, lb_m/ft^2 sec

h = Heat transfer coefficient, btu/ft^2 sec °F

In this calculation, the steam properties are contained within the program.

In addition to this coefficient describing the seal behavior, the General Electric rotors require a coefficient describing the heat transfer characteristics of the sides of the diaphragm groove above the labyrinth seals. The expression used to compute this coefficient is (5).

$$h = \left(\frac{\dot{M} c_p}{2\pi r_o W}\right) \left(\frac{\mu W}{\dot{M}}\right)^{0.65} \left[66 + 30 \left[\frac{r_o^2 \omega \rho_1/\mu}{(\dot{M}/\mu W)}\right]\right] \qquad (2\text{-}3)$$

where

h = Heat transfer coefficient, btu/ft^2 sec °F

ρ_1 = Density of steam, lb_m/ft^3

μ = Viscosity, lb_m/ft sec

c_p = Specific heat of steam, btu/lb_m

$\dot{M}$ = Mass flow rate, lb_m/sec

r_o = Rotor radius, ft

W = Gap width between blade and rotor cutout, ft

ω = Rotor speed, radians/sec

The other sections of the rotor, except for the blade attachments, are modelled as either a disk or a shaft rotating in a fluid. For a disk rotating near a wall, the heat transfer coefficient was derived from empirical data given by Metzger (6):

1. For small wall clearance and flow Reynolds number less than 2×10^5.

$$h = \left(\frac{K}{r_o}\right)\left[0.336\left(\frac{\rho_1 \omega r_o^2}{\mu}\right)^{0.505}\right]\left[0.6 + 2.4\left(\frac{Z_o}{r_o}\right)\right] \qquad (2\text{-}4)$$

2. For small wall clearance and flow Reynolds number greater than 2×10^5.

$$h = \left(\frac{K}{r_o}\right)\left[160.0 + 3511 \tanh\left[\frac{\frac{\rho_1 \omega r_o^2}{\mu} - 2 \times 10^5}{4 \times 10^6}\right]\right]\left[0.6 + 2.4\left(\frac{Z_o}{r_o}\right)\right] \qquad (2\text{-}5)$$

When the disk can be treated as moving in an infinite fluid (7),

$$h = 0.0267\left(\frac{K}{r}\right)\left(\frac{r}{r_o}\right)^{1.6}\left(\frac{\mu c_p}{K}\right)^{0.6}\left(\frac{\rho_1 \omega r_o^2}{\mu}\right)^{0.8} \qquad (2\text{-}6)$$

where

h = Heat transfer coefficient, btu/ft^2 sec °F

K = Steam conductivity, btu/sec ft °F

ρ_1 = Density of steam, lb_m/ft^3

ω = Rotor speed, radians/sec

r_o = Radius of rotating disk, ft

μ = Viscosity of steam, lb_m/ft sec

Z_o = Wall clearance, ft

r = An average disk radius, ft

c_p = Specific heat of steam, btu/lb_m

For a shaft in an infinite fluid, the coefficient is (8)

$$h = 0.1139\left(\frac{K}{r_o}\right)\left(\frac{\omega \pi r_o^2}{\nu}\right)^{0.70}\left(\frac{\mu c_p}{K}\right)^{0.35} \qquad (2\text{-}7)$$

where

h = Heat transfer coefficient, btu/ft^2 sec °F

K = Steam conductivity, btu/sec ft °F

r_o = Radius of the rotating shaft, ft

ω = Rotor speed, radians/sec

ν = Kinematic viscosity of steam, ft^2/sec

μ = Dynamic viscosity of steam lb$_m$/ft sec

c_p = Specific heat of steam, btu/lb$_m$

The remaining coefficient is applied at the point of attachment between the rotor and the blades. The metal-to-metal contact over the attachment region is assumed to be perfect, with no mismatch. Hence, the coefficient is a conductive one, given by

$$h = \frac{2k}{9\pi r_o} \tag{2-8}$$

where

h = Heat transfer coefficient, btu/ft^2 sec °F

k = Blade metal thermal conductivity, btu/sec ft °F

r_o = Rotor radius, ft

This expression was derived using the potential field plotting technique; this method is discussed in (9), but will be outlined here. The blade is assumed to be at a constant but nonuniform temperature, with the heat transfer rate from the steam to the blade equal to the rate from the blade to the rotor element. An approximate solution of the steady, two dimensional heat conduction equation for the blade was obtained graphically by potential field plotting. This solution allowed a heat balance expression to be written for the blade. Assuming that the convective heat transfer coefficient between the steam and the blade was large compared to the coefficient across the metal-to-metal contact surface since this contact is not perfect, expression (2-8) resulted from solving the blade heat balance equation.

Examples of Rotor Models

The general features of a model generated by PPMESH are shown in Figures 2-3 and 2-4 for a Westinghouse and a General Electric rotor, respectively. These two figures show the finite element mesh and give some indication of the geometry data required to produce the mesh. This aspect of the modelling is fairly straightforward and hence has not been discussed here; References(1) and (2) give a full description of the details of the geometric modelling.

The two figures do give the surfaces over which the heat transfer coefficients described in the preceding section are applied. These coefficients are shown as:

HC1 - Flow through a labyrinth seal, (2-2)

HC2 - Disk rotating in a fluid, (2-4) - (2-6)

HC3 - Sides of diaphragm grooves, (2-3)

HC4 - Rotor-blade attachment area, (2-8)

HC5 - Shaft rotating in a fluid, (2-7)

A comparison of the two figures shows that there are significant differences between the rotors of the two companies, e.g. the blade attachment area. As more experience with other rotors is gained, it is expected that rotors produced by other companies will be included in the code.

UY(Axial Displacement) = Fixed for Nodes 1 thru 8
UX(Radial Displacement)= Fixed for Nodes 8 and 451
RC = Distance from X = 0 to Node 443
R(1) = Distance from X = 0 to Node 57
RS(1) = Distance from X = 0 to Node 55
R(NSTAGE) = Distance from X = 0 to Node 386
RS(NSTAGE) = Distance from X = 0 to Node 383
RF = Distance from X = 0 to Node 439
RSH = Distance from X = 0 to Node 448
DB = Bore Diameter
HC = Heat Transfer Coefficients

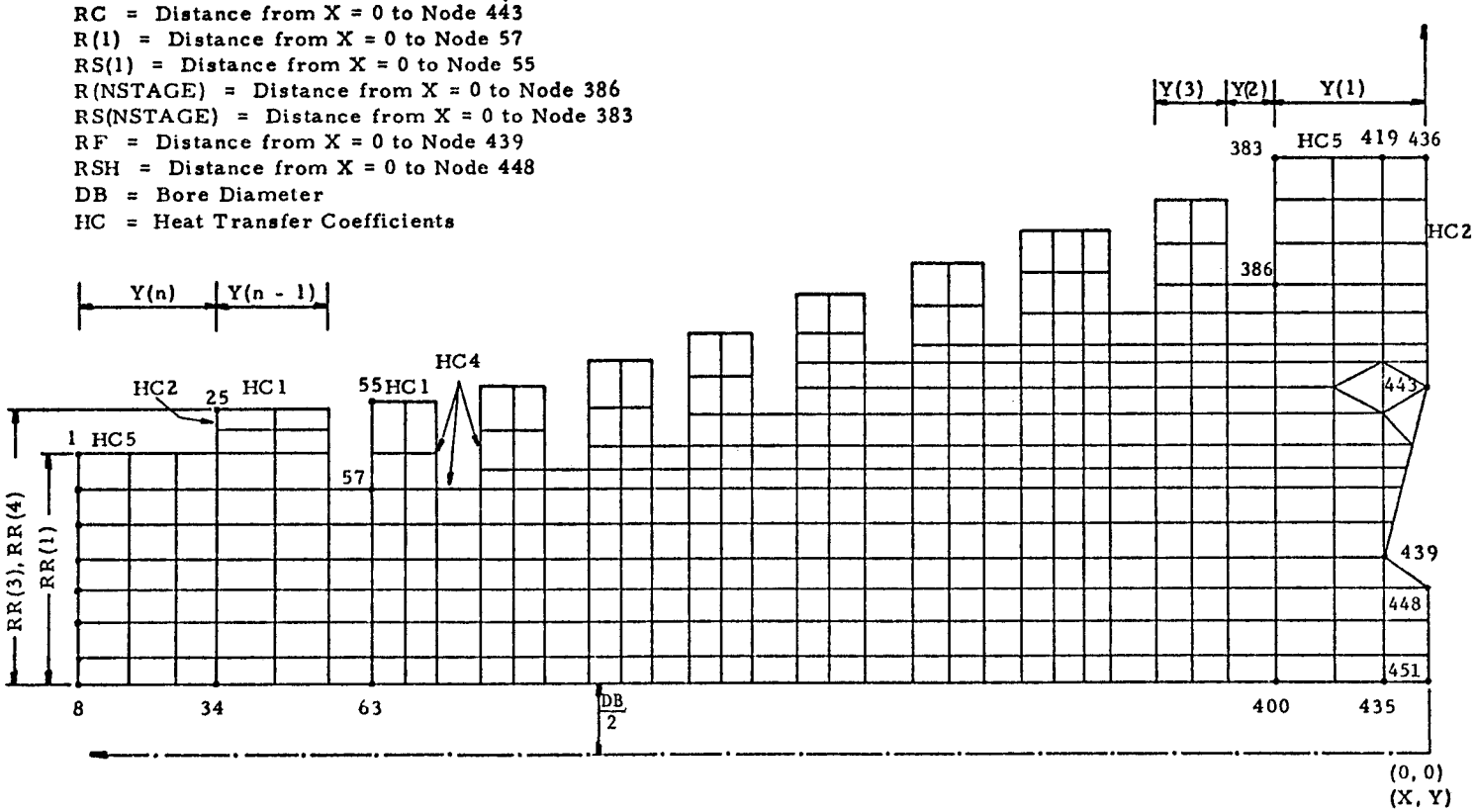

FIGURE 2-3. SCHEMATIC OF CRITICAL WESTINGHOUSE ROTOR INPUT AND ROTOR MESH

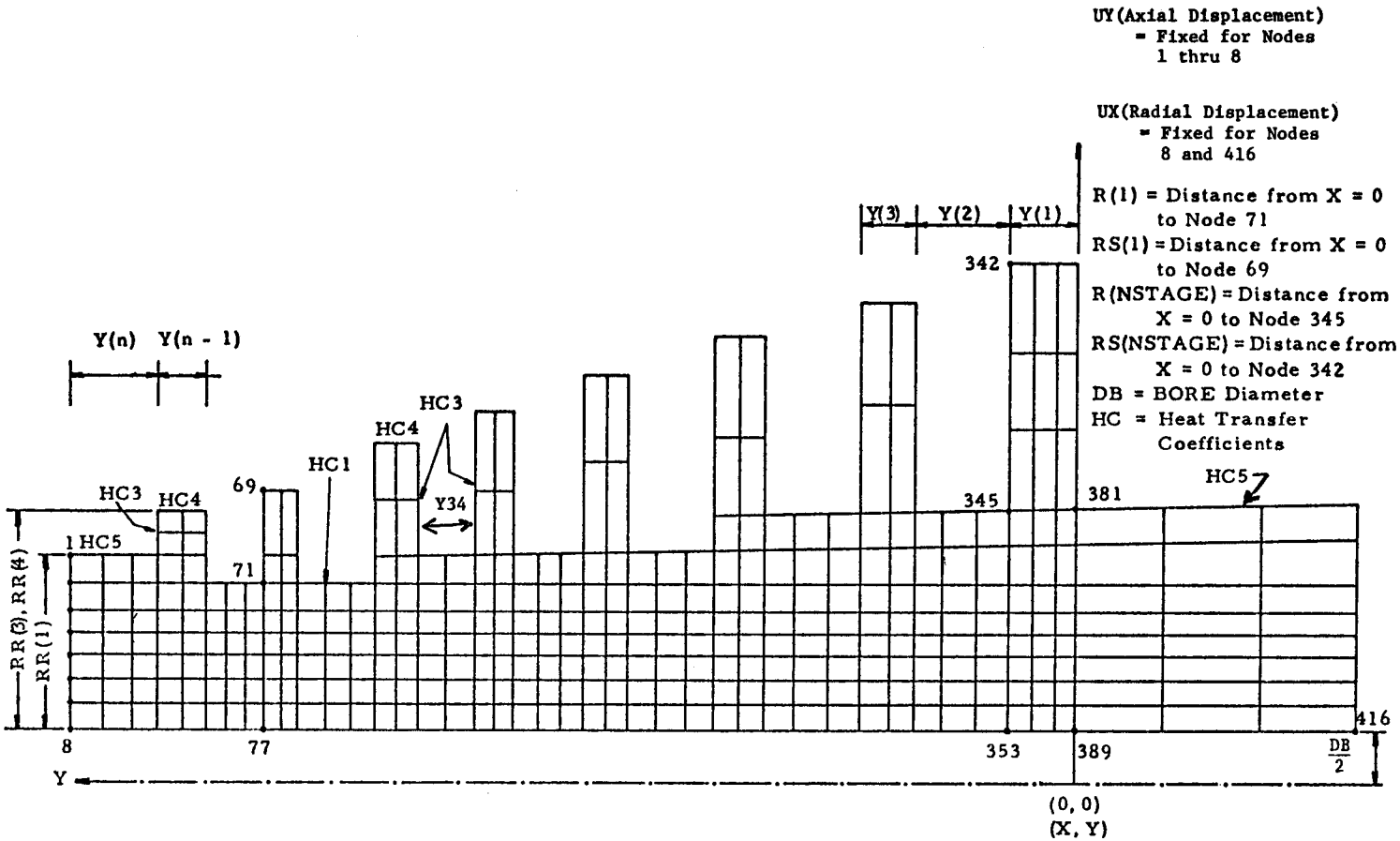

FIGURE 2-4. SCHEMATIC OF CRITICAL GENERAL ELECTRIC ROTOR INPUT AND ROTOR MESH

Section 3

STRESS ANALYSIS CODE

As discussed in the preceding section, specification of the duty cycle establishes the boundary conditions for the heat transfer analysis. Once this analysis has been completed, then the program is ready to determine the stresses in the rotor as a function of time. Since the specification of the duty cycle includes rotor speed as a function of time, the only additional information required to perform the stress analysis is the total blade mass and centroid radius at each blade row. The blade loading is the only mechanical load considered in the analysis.

Five rotors were examined in the course of this program. These rotors were:

1. Gallatin No. 2 IP (Tennessee Valley Authority)
2. Joppa No. 3 IP-LP (Electric Energy, Inc.)
3. Seward No. 5 LP (Pennsylvania Electric Co.)
4. Buck No. 6 IP-LP (Duke Power Co.)
5. Sporn Series IP-LP (American Electric Power Service Co.)

In this section, the duty cycle and resulting stresses and temperature will be discussed for each rotor.

Gallatin No. 2 IP

The duty cycle used to develop the thermal stress analysis is given in Table 3-1. This rotor was initially at 75°F at the beginning of the warmup; the warmup consisted of 190° and 364°F inlet and cooling steam, respectively, with an outlet steam temperature of 180°F. The warmup period lasted for 1.375 hours, after which roll-off commenced. During roll-off the inlet steam temperature was increased slightly and the rotor brought to 3600 rpm over a period of 1.625 hours. The speed vs time history was input as a parabolic function, i.e., the increase in rotational speed was initially rapid but decreased as the speed approached 3600 rpm. Once synchronous speed was reached, loading began immediately. The recorded load-time history was approximated by a linear function so that 80 percent of maximum load was achieved after two hours of loading. The computation

TABLE 3-1. TRANSIENT INPUT GALLATIN #2 IP

% MW Load	(FAHR.) Inlet Steam Temperature	(FAHR.) Cooling Steam Temperature	(FAHR.) Outlet Temperature	(PSIA) Inlet Pressure	(PSIA) Outlet Pressure	(HRS) Time Duration
80.0	820	420	470	324	48.8	
65.0	775	470	380	263.25	39.65	
40.0	700	540	330	162.0	24.4	
25.0	650	581	395	101.25	15.25	2
10.0	490	428	240	40.50	6.1	
0.0	480	422	235	12.297	10.297	Synchronous No-Load
Roll-Off	200	364	185	12.297	10.297	1.625
Warmup	190	364	180	12.297	10.297	1.375

Total Simulated Run Time 5 Hours

Steady State Input Gallatin #2 IP

Inlet Steam Temperature, °F	1050
Outlet Steam Temperature, °F	620
Cooling Steam Temperature, °F	573
Inlet Pressure, PSIA	405
Outlet Pressure, PSIA	61

was terminated at this point as the stresses had reached maximum values, after 4.25 hours had elapsed, and were declining.

Figure 3-1 compares the time dependent temperature of the metal surface with the steam temperature at corresponding locations. The figure shows that while the Rateau stage rapidly reaches the reheat steam temperature, the temperature differential at Stage 7 remains significant, even after five hours of operation. The difference between steam and metal temperature points up the necessity of heat transfer boundary conditions. Figure 3-2 gives an example of the transient temperature distribution for the entire rotor; the isotherms are shown after 0.85 hours of loading.

A steady state analysis of the Gallatin rotor was also performed to evaluate the conditions in the rotor during a long period under load. The steady state operating conditions are given in Table 3-1; these were applied under the same assumptions as were the transient conditions. Steady state isotherms are given in Figure 3-3.

Applying the temperatures generated by the heat transfer analysis and the blade masses listed in Table 3-2 as boundary conditions, the stresses in the Gallatin rotor were determined. Contours of the tangential stresses at the time of their maximum value are shown in Figure 3-4. (These contours are superimposed on the finite element mesh used for the rotor analysis; the details and rationale of the element scheme are given in References (1) and (2). The maximum stress occurred 4.25 hours after the warmup began, or 1.25 hours after attaining synchronous speed. The isostress lines show a strong stress gradient in the region of the sixth and seventh stages. The maximum stress shown on the figures is 60 ksi, but this is at the centroid of an element, 0.67 in. from the bore. Figure 3-5 gives the distribution of tangential stress in the radial direction for the center column of elements between blade stages 7 and 8 in Figure 3-4. Figure 3-5 shows the rapid rise in stress near the bore to a maximum value of 74 ksi at the bore surface. Examination of the stress field for the other two columns of elements that comprise the region between the blade rows shows that there is negligible variation in the axial distribution of tangential stress at this location. This means that there is a considerable volume of material subjected to the high stress field near the bore. The temperature distribution ranged from 272°F at the bore to 425°F at the periphery.

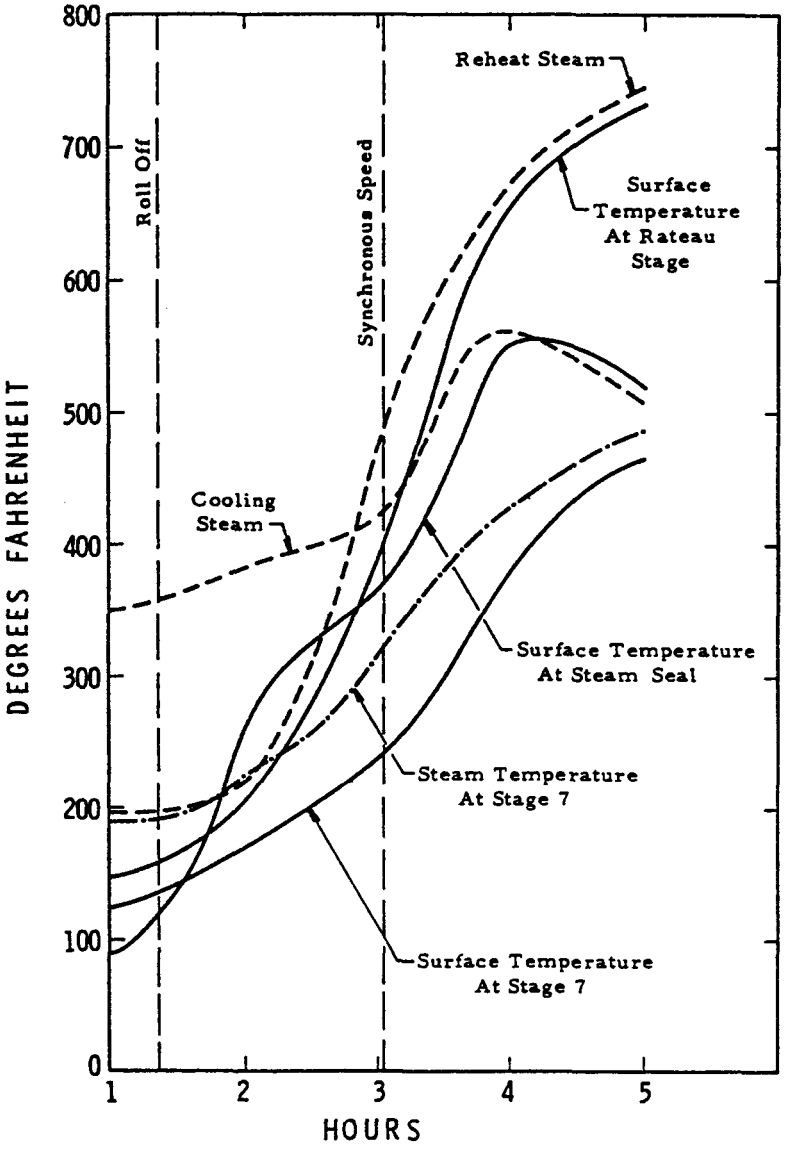

FIGURE 3-1. GALLATIN NO. 2 TRANSIENT STEAM AND SURFACE TEMPERATURE

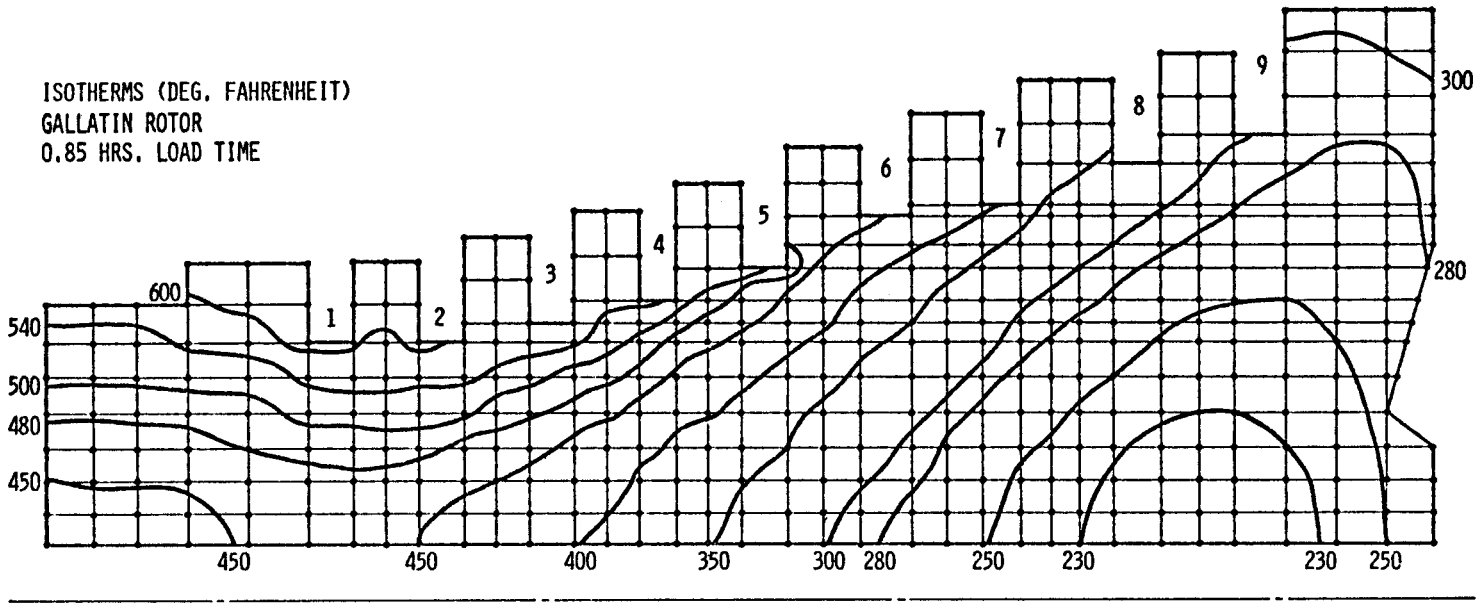

FIGURE 3-2. ISOTHERMS FOR GALLATIN ROTOR
AFTER 0.85 HOURS OF LOADING

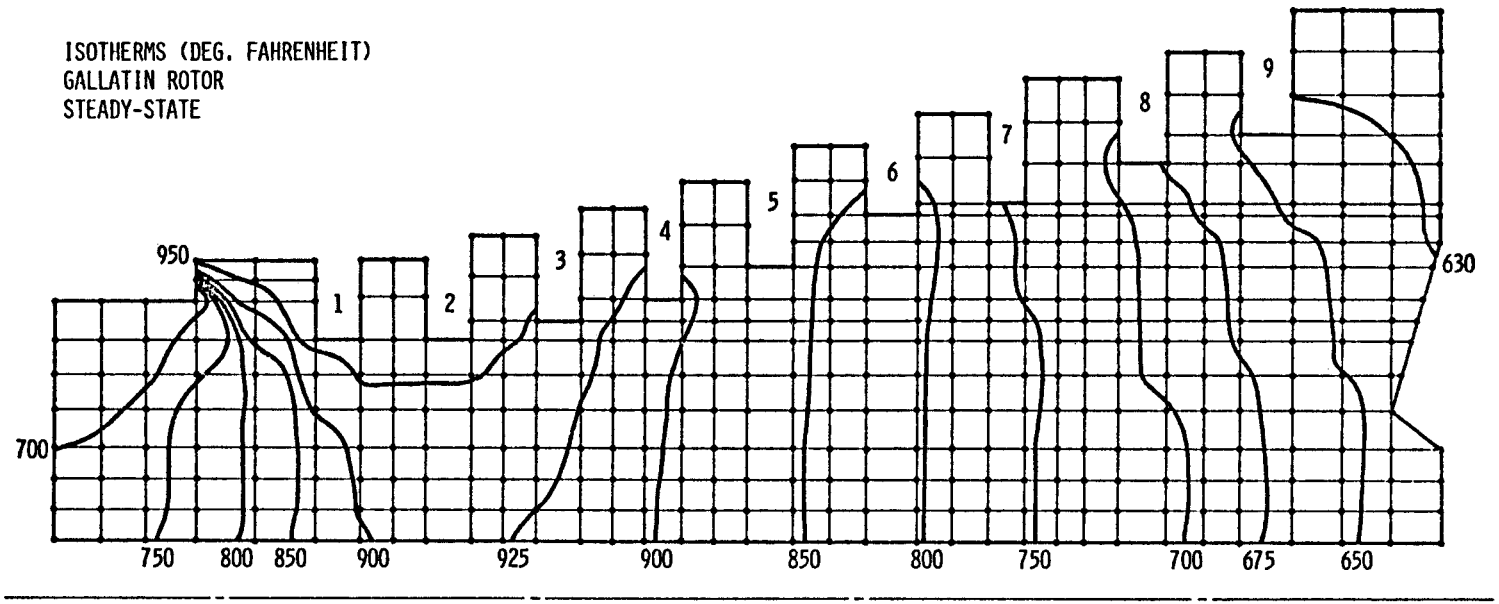

FIGURE 3-3. STEADY STATE ISOTHERMS
FOR GALLATIN ROTOR

TABLE 3-2. BLADE DATA

Blade Row	Gallatin #2 No. Blades	Gallatin #2 (Slugs)+ Blade Mass	Joppa #3 No. Blades	Joppa #3 (Slugs)+ Blade Mass	Seward #5 No. Blades	Seward #5 (Slugs)+ Blade Masses	Buck #6 No. Blades	Buck #6 (Slugs)+ Blade Mass
1	53	10.7243	161	6.1012	180	2.07	143	5.5341
2	57	12.0920	154	6.5324	130	4.33	148	5.5648
3	61	13.0246	164	6.9566	116	7.03	152	6.0952
4	65	14.6410	138	8.4357	98	14.68	155	6.479
5	66	15.4492	144	8.8025	126	31.26	160	7.472
6	98	24.0557	130	12.4100			169	7.8923
7	74	19.008	135	14.1920			149	9.8936
8	84	22.5365	137	14.4304			120	13.14
9	84	24.6814					130	14.209
10							186	5.5056
11							126	5.3172
12							111	12.3765
13							126	19.6686
14							119	18.5759

+Mass of all blades in row.

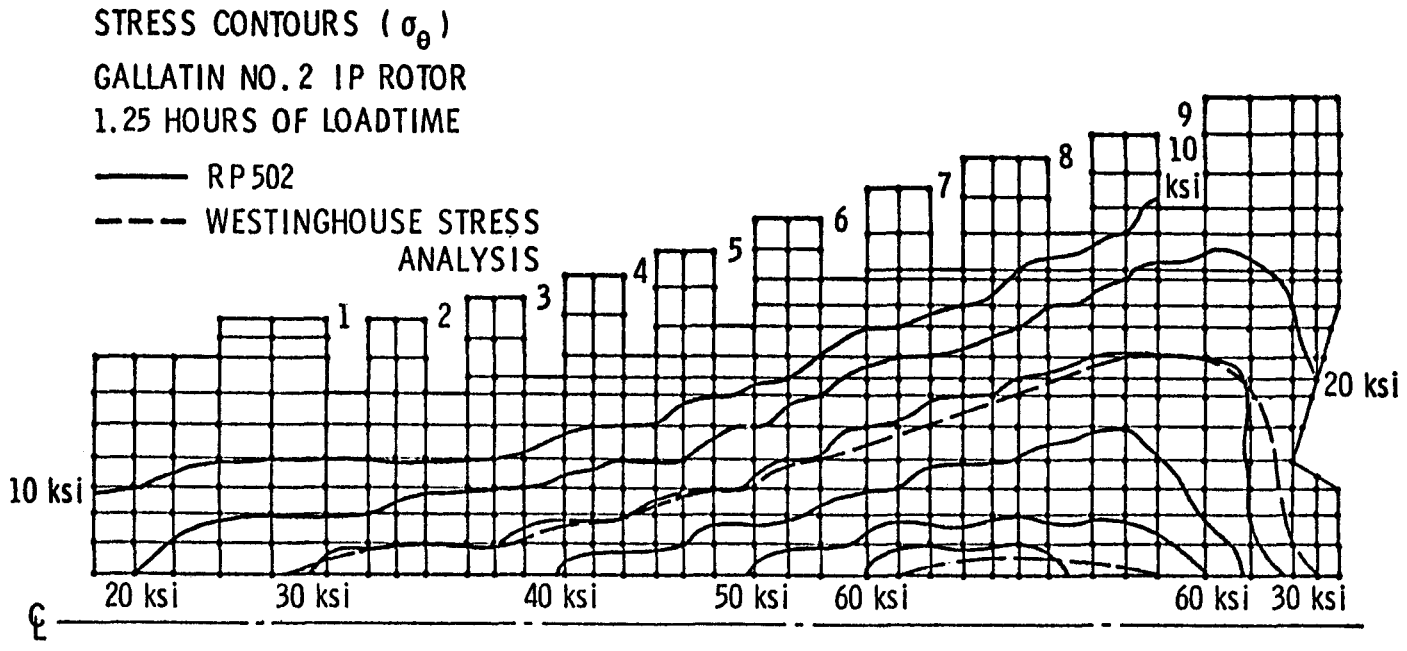

FIGURE 3-4. TANGENTIAL STRESS CONTOURS AT TIME OF MAXIMUM STRESS

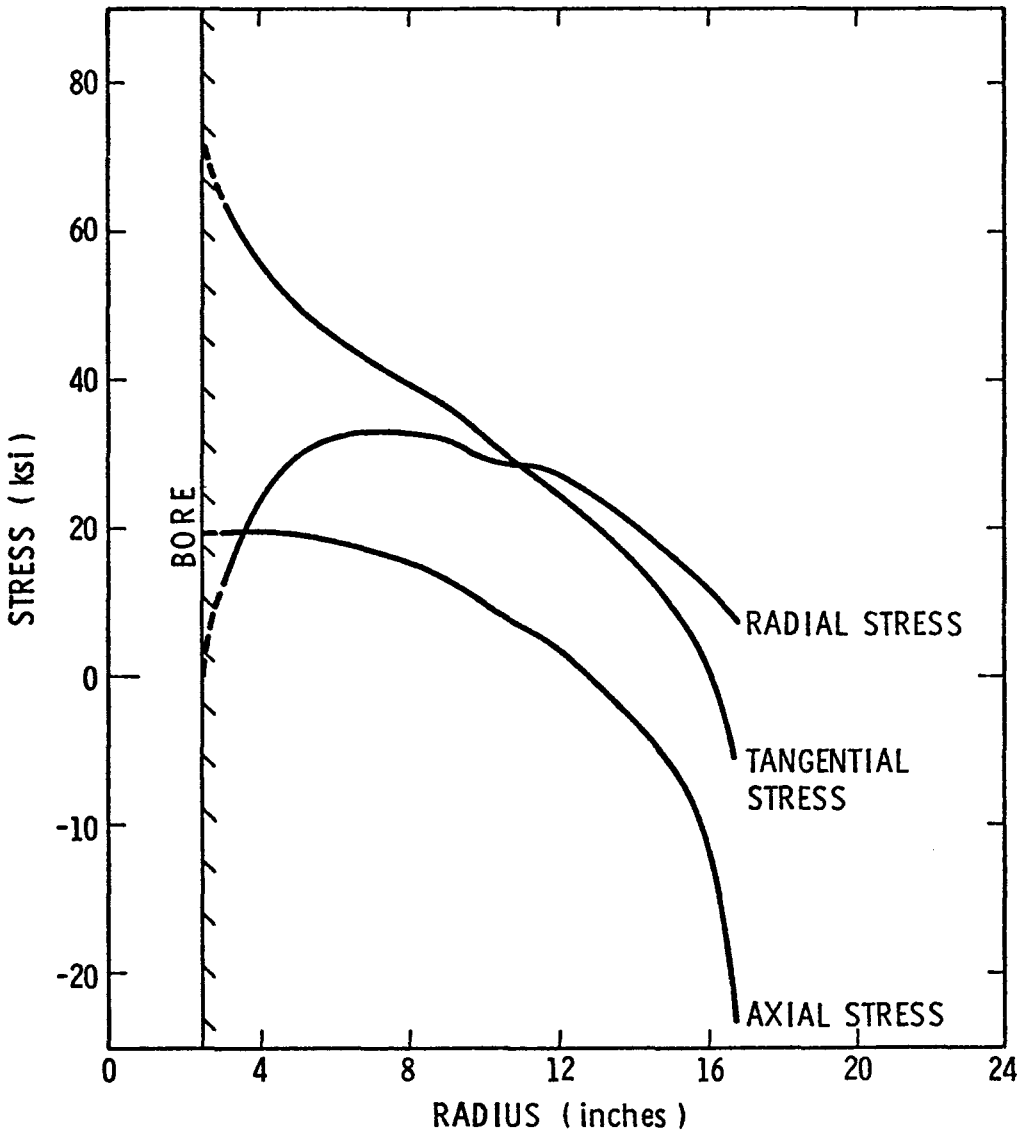

FIGURE 3-5. RADIAL VARIATION OF STRESS AT STAGE 7
OF GALLATIN IP ROTOR; TIME OF MAXIMUM STRESS

Comparing the results of the thermoelastic stress analysis of the Gallatin rotor performed using PPMESH and the published results of the same analysis performed by Westinghouse (10) shown in Figure 3-4, it is evident that the two independent analyses give very close results. The 30 ksi contours follow one another almost exactly except that as the contours pass beneath blade row nine, the PPMESH contour tends to decrease slightly more rapidly. For the 60 ksi stress, the PPMESH tends to encompass a shorter axial dimension than the Westinghouse result. The contour determined by PPMESH starts at the end of blade row six and terminates about the middle of blade row eight, while the Westinghouse computed stress contour initiated midway between blade rows six and seven and ended at the beginning of blade row nine. The difference in height between these two 60 ksi contours leads one to believe that the PPMESH maximum bore stress may be one or two ksi higher than the maximum found in the Westinghouse analysis.

Separate calculation of the steady state stress resulted in a maximum value of 47 ksi at the bore surface, Figure 3-6. Thus, the transient thermal stress is about 27 ksi at the location of maximum stress.

As part of the analysis of the Gallatin rotor, a check was made on the adequacy of the mesh used. Because of the steep stress gradient near the bore, linear strain elements were chosen over constant strain elements, as the former require far fewer elements to describe a rapidly varying stress field. Too coarse a mesh will yield inaccurate results, while a needlessly refined mesh will result in high computation costs. In order to check the mesh shown in Figure 3-4, the simple test case of an externally pressurized cylinder was selected, as shown in Figure 3-7. The mesh size for this test problem was chosen as approximately the same size as the last five elements near the bore below stage 7, as shown in Figure 3-4.

The results of the finite element check analysis are compared in Table 3-3 to the solution given in Wang (11) for a thick cylinder under uniform load. These tabulated results show good agreement between the finite element analysis and the exact solution, with the largest σ_θ disagreement being about 7.4%. As can be seen from Figure 3-8, this difference occurs about 1.18 in. radially out from the bore surface. This may be viewed as an inaccuracy in the element, or, in fact, as an indication

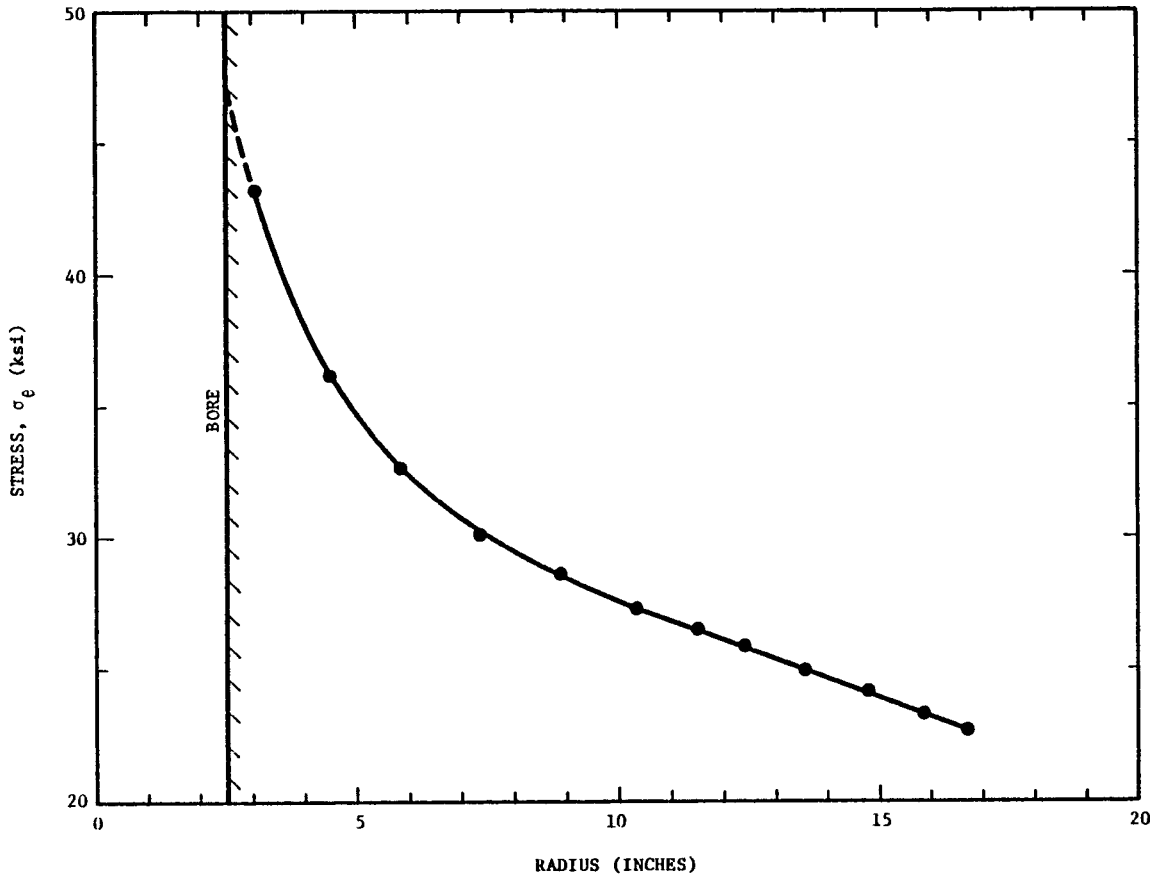

FIGURE 3-6. STEADY STATE STRESS AT STAGE 7 OF GALLATIN IP ROTOR

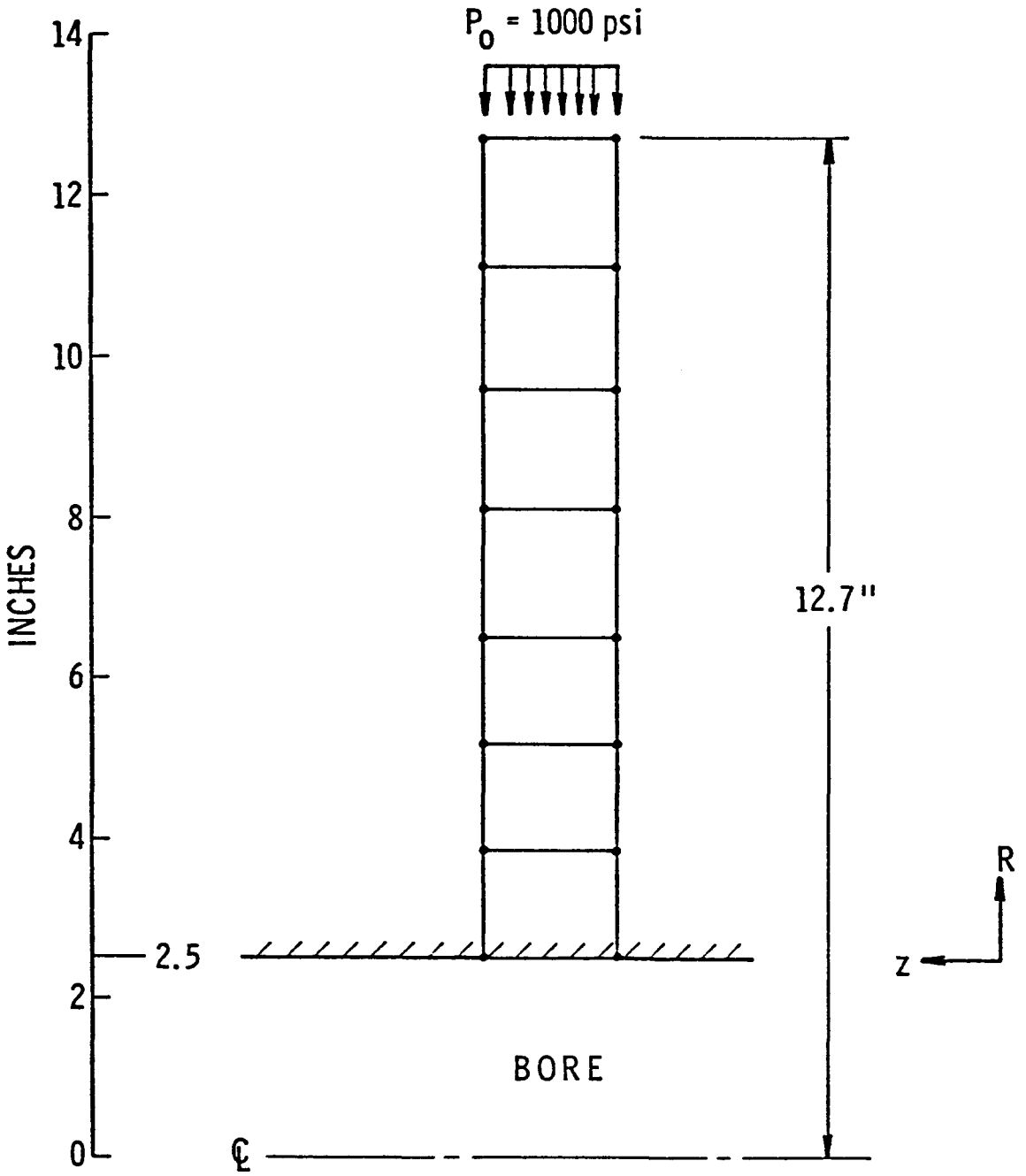

FIGURE 3-7. FINITE ELEMENT IDEALIZATION OF TEST MESH

TABLE 3-3. TABLE COMPARING EXACT STRESS VALUES TO THOSE GENERATED BY F.E.M.

	Finite Element Model (ksi)		Exact Solution* (ksi).		% Dif	
R	σ_θ	σ_r	σ_θ	σ_r	σ_θ	σ_r
2.65	-1.926	-0.133	-1.944	-0.136	-0.9	-2.0
3.17	-1.562	-0.306	-1.672	-0.408	-6.6	-25.0
3.68	-1.397	-0.564	-1.509	-0.571	-7.4	-1.2
3.98	-1.408	-0.621	-1.441	-0.639	-2.3	-2.8
4.50	-1.324	-0.688	-1.353	-0.726	-2.1	-5.2
5.02	-1.283	-0.772	-1.292	-0.788	-0.7	-2.0
5.32	-1.267	-0.800	-1.264	-0.816	0.2	-2.0
5.83	-1.221	-0.832	-1.227	-0.853	-0.5	-2.5
6.35	-1.193	-0.871	-1.197	-0.882	-0.3	-1.2
7.30	-1.160	-0.908	-1.159	-0.921	-0.09	-1.4
8.85	-1.124	-0.952	-1.121	-0.959	0.3	-0.7
11.90	-1.085	-0.993	-1.085	-0.995	0	-0.2

$$\sigma_\theta = -6348.400\ (1/R^2) - 1040.312$$

$$\sigma_r = 6348.400\ (1/R^2) - 1040.312$$

* Reference (11)

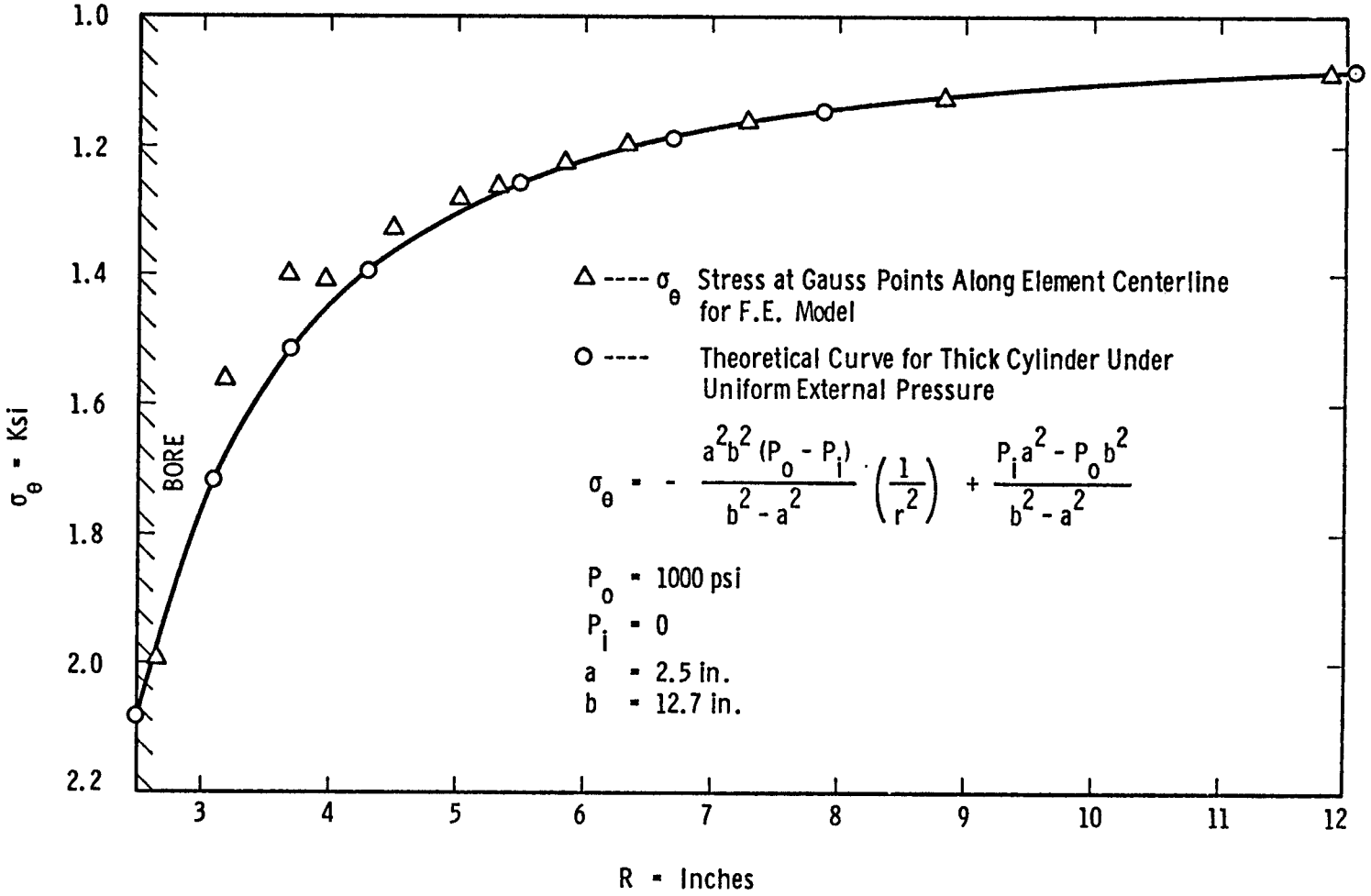

FIGURE 3-8. TANGENTIAL STRESS DISTRIBUTION IN PRESSURIZED RING

that the element is trying to represent the gradient in a refined way (12). This point may be better understood by noting that the points at R = 2.65, 3.17, and 3.68 are all Gauss points contained within the same element. The accuracy of the element along the linear portions of the curve away from the bore may be explained by the linear nature of the element. This same reasoning will serve to explain the inaccuracy near the bore. In order to better define the stress gradient, a more refined mesh would be required.

Although σ_r is not the stress of interest, a comparison between σ_r and the exact solution is shown in Table 3-3 and in Figure 3-9.

Overall, as can be seen in Figure 3-8 and 3-9, this mesh does a good job of predicting the stresses near the bore of this thick cylinder loaded by 1000 psi of external pressure.

In conclusion, the mesh used in the Gallatin analysis can be considered to produce accurate stress results. A more refined mesh will give greater accuracy, but that refinement would lead to a drastic increase in computer cost.

Joppa No. 3 IP-LP

The transient duty cycle for the Joppa No. 3 IP-LP is given in Table 3-4. During this cycle the Joppa rotor was warmed from 75°F for a period of 1.58 hours with an inlet steam temperature of 520°F and a cooling steam temperature of 590°F. The rotor was then brought up to speed in an additional 1.67 hours, again in a parabolic manner as for the Gallatin rotor. Once synchronous speed had been reached, the load was applied as a linear function of time. After 1.5 hours of load, the stresses peaked and then began to decline. The run was halted after 2.25 hours of load and a total elapsed time of 5 hours. The rate of loading of the Joppa rotor was much slower than for the Gallatin rotor; after 2.25 hours, the load had only reached 55 percent of the maximum load.

Figure 3-10 gives the transient temperature distribution for several locations. Again, these are compared to the steam temperature at the same location. At three of the four locations the rotor surface approaches the steam temperature quite rapidly. However, Stage 9 is much slower in reaching the steam temperature.

Table 3-4 also gives the conditions of the steady state analysis.

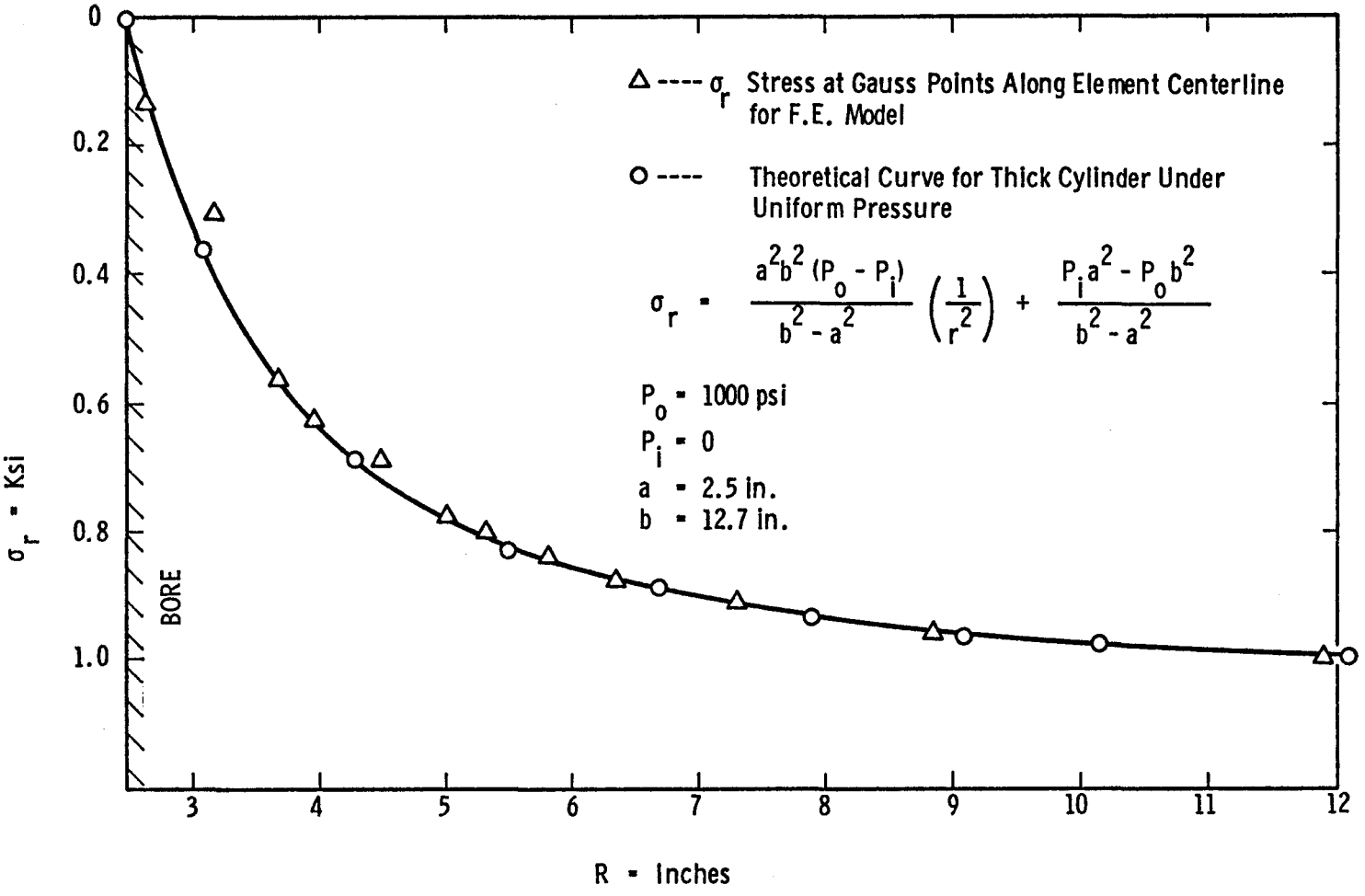

FIGURE 3-9. RADIAL STRESS DISTRIBUTION IN PRESSURIZED RING

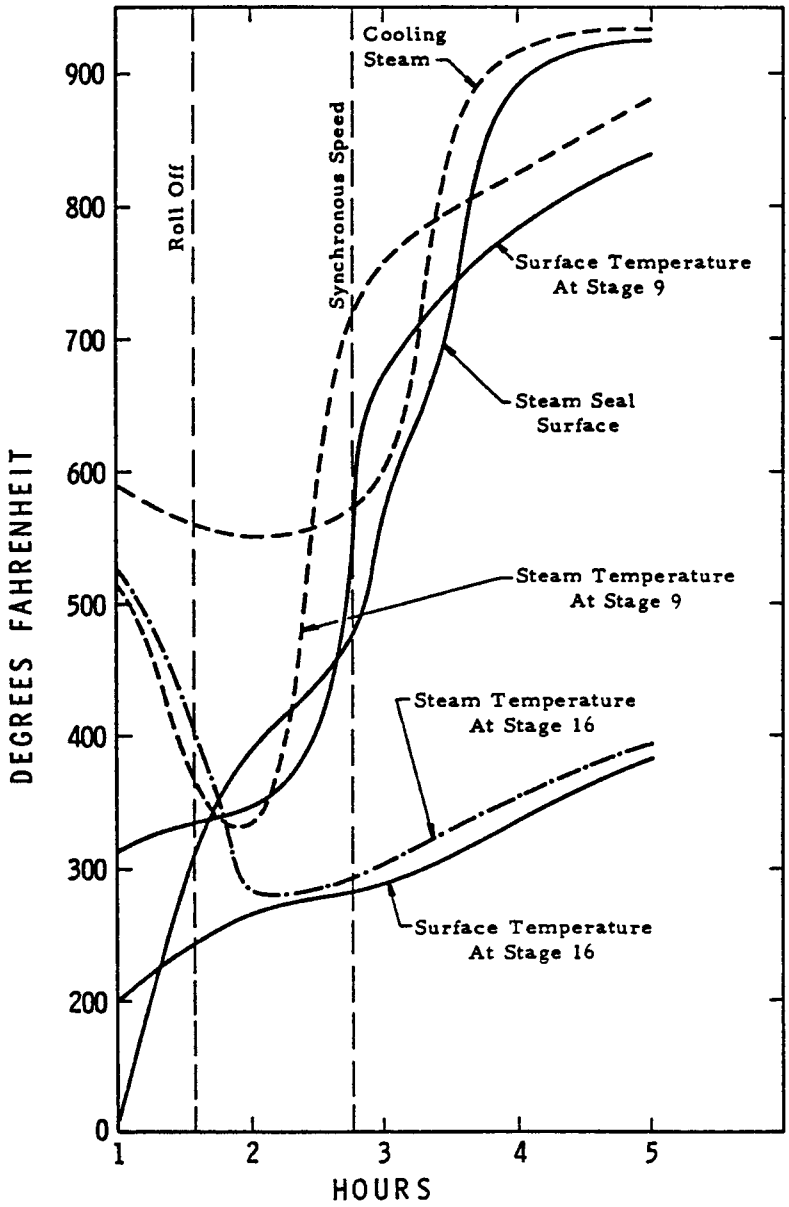

FIGURE 3-10. JOPPA NO. 3 TRANSIENT STEAM AND SURFACE TEMPERATURE

TABLE 3-4. TRANSIENT INPUT JOPPA #3 IP-LP

% MW Load	(FAHR.) Inlet Steam Temperature	(FAHR.) Cooling Steam Temperature	(FAHR.) Outlet Temperature	(PSIA) Inlet Pressure	(PSIA) Outlet Pressure	(HRS) Time Duration
55.2	930.0	930.0	390.0	270.5	22.0	
33.0	870.0	870.0	350.0	161.7	13.3	
11.0	805.0	805.0	300.0	53.9	4.4	2.25
3.0	505.0	505.0	100.0	14.7	1.2	
0	485.0	505.0	485.0	1.0	0.75	Synchronous No-Load
Roll-Off	520.0	550.0	520.0	7.0	6.75	1.1667
Warm-Up	520.0	590.0	520.0	7.0	6.75	1.583

Total Simulated Run Time 5 Hours

Steady State Input Joppa #3 IP-LP

Inlet Steam Temperature, °F	890
Outlet Steam Temperature, °F	425
Cooling Steam Temperature, °F	930
Inlet Pressure, PSIA	500
Outlet Pressure, PSIA	40

Based on this duty cycle and the blade masses given in Table 3-2, the transient thermoelastic stress analysis was performed. The maximum transient stress was reached 1.5 hours after loading commenced. The tangential stress contours at this time are given in Figure 3-11, again superimposed on the finite element model of the rotor. The stresses in this rotor are much smaller than those in the Gallatin rotor.

The maximum transient stress occurs at the bore at the sixteenth stage, which is connected to an extension which simulates the remainder of the rotor. The maximum tangential stress is 31.2 ksi at the centroid of the near bore element; the element temperature is 308°F. Figure 3-12 shows the stress distribution as a function of radius at the sixteenth stage and indicates the steep stress gradient near the rotor bore. When extrapolated to the bore, the maximum tangential stress in the rotor is 37 ksi.

Figure 3-13 shows the steady state tangential stress distribution at the location of maximum transient stress. Comparing the two tangential stress curves, it is clear that the difference between the steady state and transient stress is only 4-6 ksi. This is unlike the Gallatin rotor where the stresses were of comparable magnitude. Extrapolated to the bore, the steady state stress is 31 ksi.

Seward No. 5 LP

The cold start duty cycle assumed in analyzing the Seward LP rotor did not include a separate prewarming, although the initial rotor metal temperature was assumed to be 100°F rather than 75°F used in the first two rotors. The duty cycle is given in Table 3-5 and shows that the steam temperature was maintained at 100°F during the roll-off to 3600 rpm. Once loading commenced, the inlet and cooling steam temperatures were assumed to increase instantaneously to 425°F. Maximum load was reached in an hour.

Figure 3-14 shows the finite element mesh used to model the Seward LP rotor.

The maximum transient stress was reached at the time of maximum load, i.e., after one hour of loading. The isotherms and isostress lines at this time are shown in Figures 3-15 and 3-16 and are examples of the computer graphics output. The maximum stress occurred at the bore near

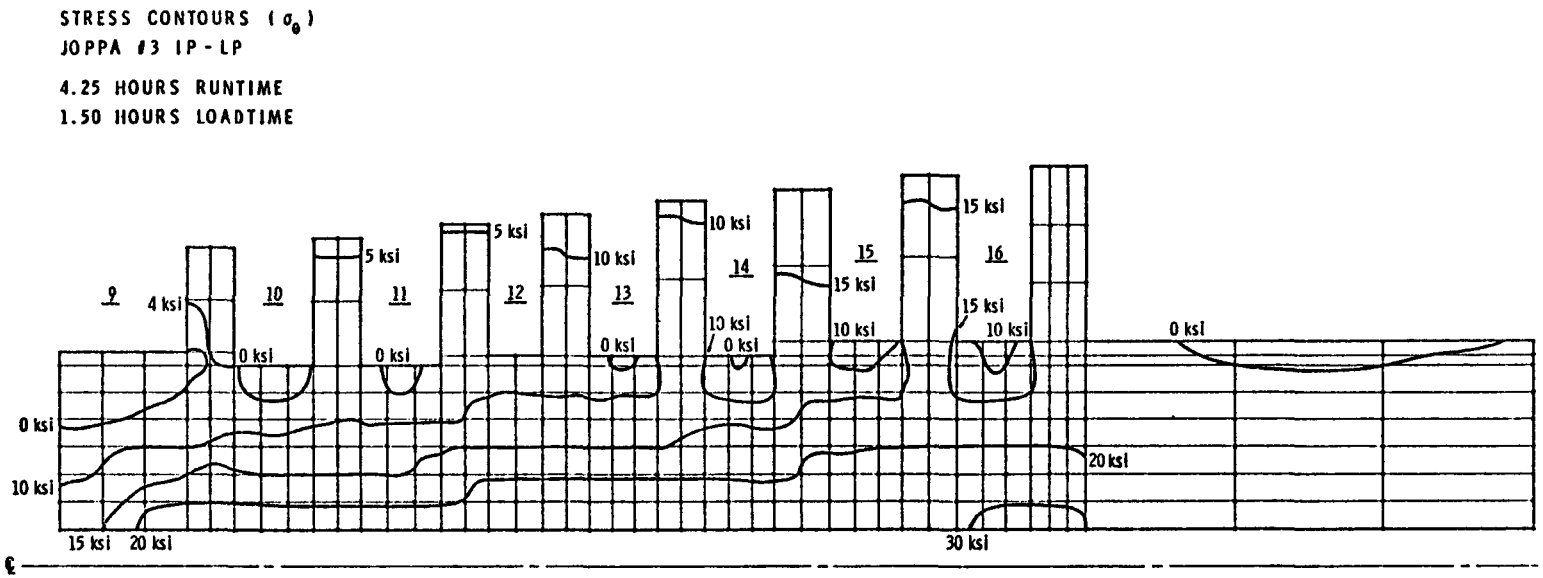

FIGURE 3-11. DISTRIBUTION OF STRESS AT TIME OF MAXIMUM TRANSIENT STRESS

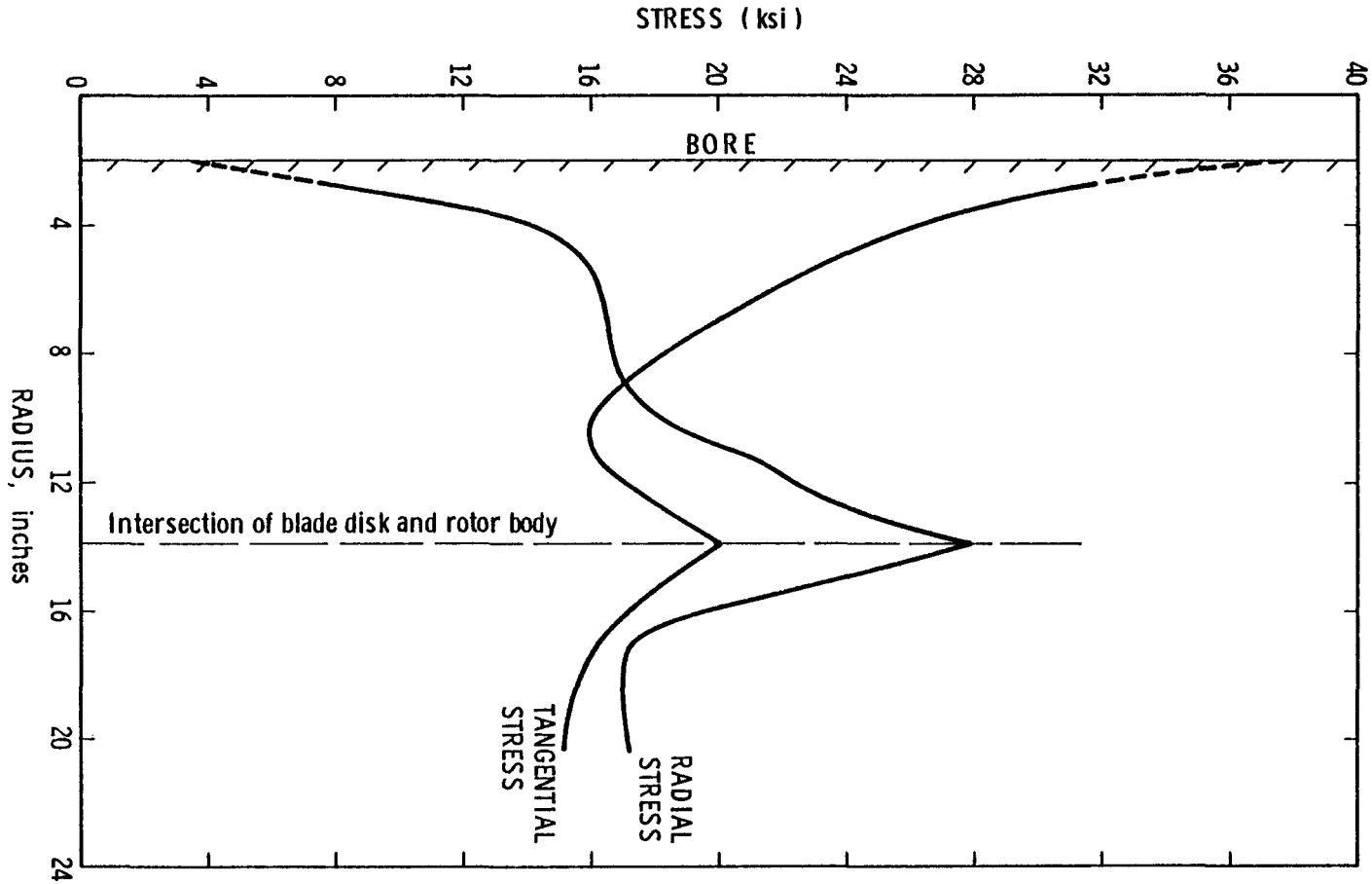

FIGURE 3-12. STRESS DISTRIBUTION AT THE TIME OF MAXIMUM TRANSIENT STRESS, JOPPA IP

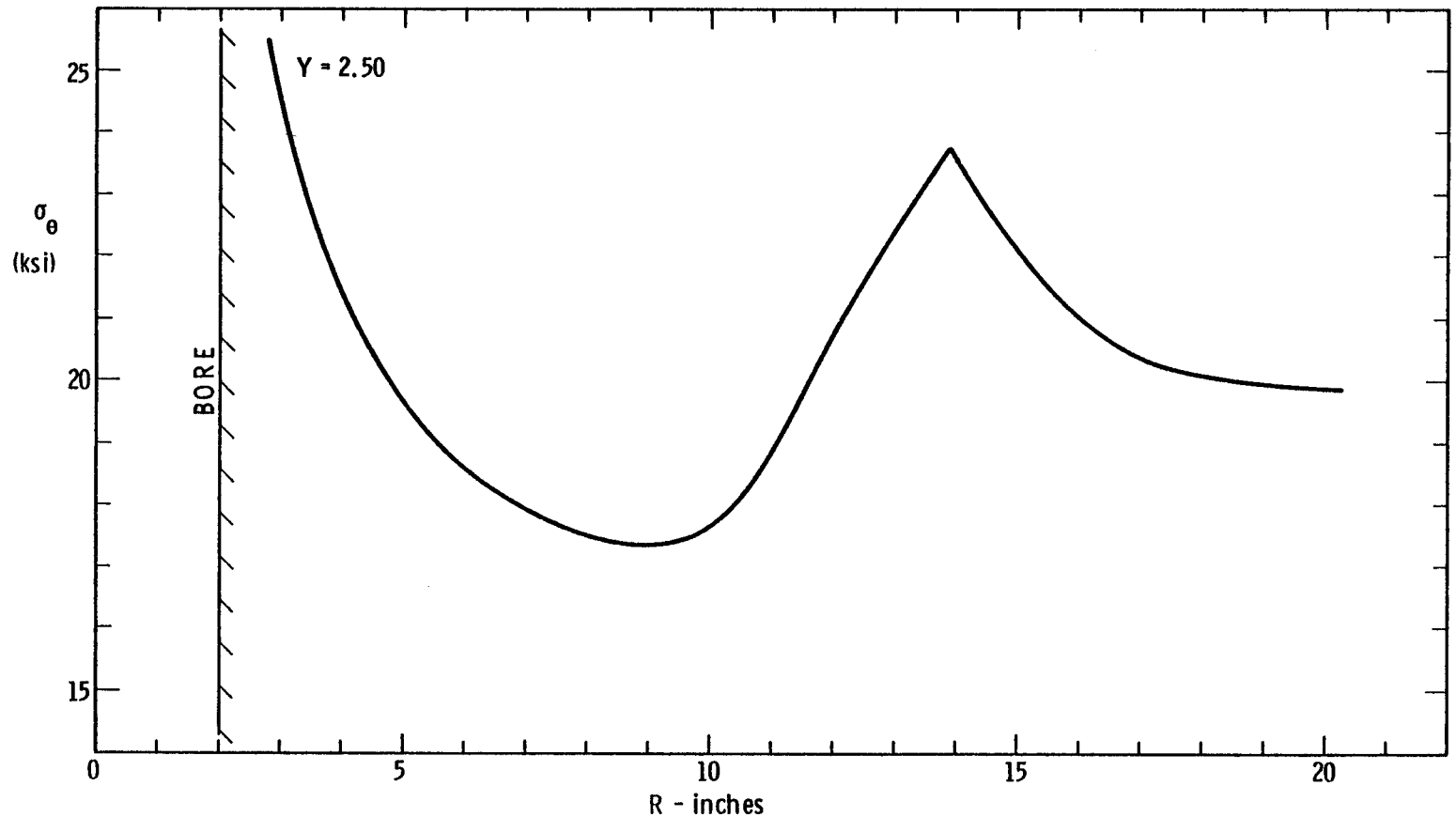

FIGURE 3-13. STEADY STATE TANGENTIAL STRESS AT LOCATION OF MAXIMUM TRANSIENT STRESS, JOPPA IP

TABLE 3-5. TRANSIENT INPUT SEWARD #5 LP

% MW Load	(FAHR.) Inlet Steam Temperature	(FAHR.) Cooling Steam Temperature	(FAHR.) Outlet Temperature	(PSIA) Inlet Pressure	(PSIA) Outlet Pressure	(HRS) Time Duration
100.0	425.0	425.0	92.0	21.50	0.74	
61.6	425.0	425.0	92.0	13.24	0.74	
41.1	425.0	425.0	92.0	8.84	0.74	1
13.7	425.0	425.0	92.0	2.95	0.74	
5.0	425.0	425.0	92.0	1.08	0.74	
0.0	100.0	100.0	100.0	5.0	0.74	Synchronous No-Load
Roll-Off	100.0	100.0	100.0	5.0	4.9	1
Warm-Up	None	None	None	None	None	

Total† Simulated Run Time 3 Hours

† The system was run one hour at maximum load to give this total run time.

Steady State Input Seward #5 LP

Inlet Steam Temperature, °F	346
Outlet Steam Temperature, °F	92
Cooling Steam Temperature, °F	425
Inlet Pressure, PSIA	21.5
Outlet Pressure, PSIA	0.74

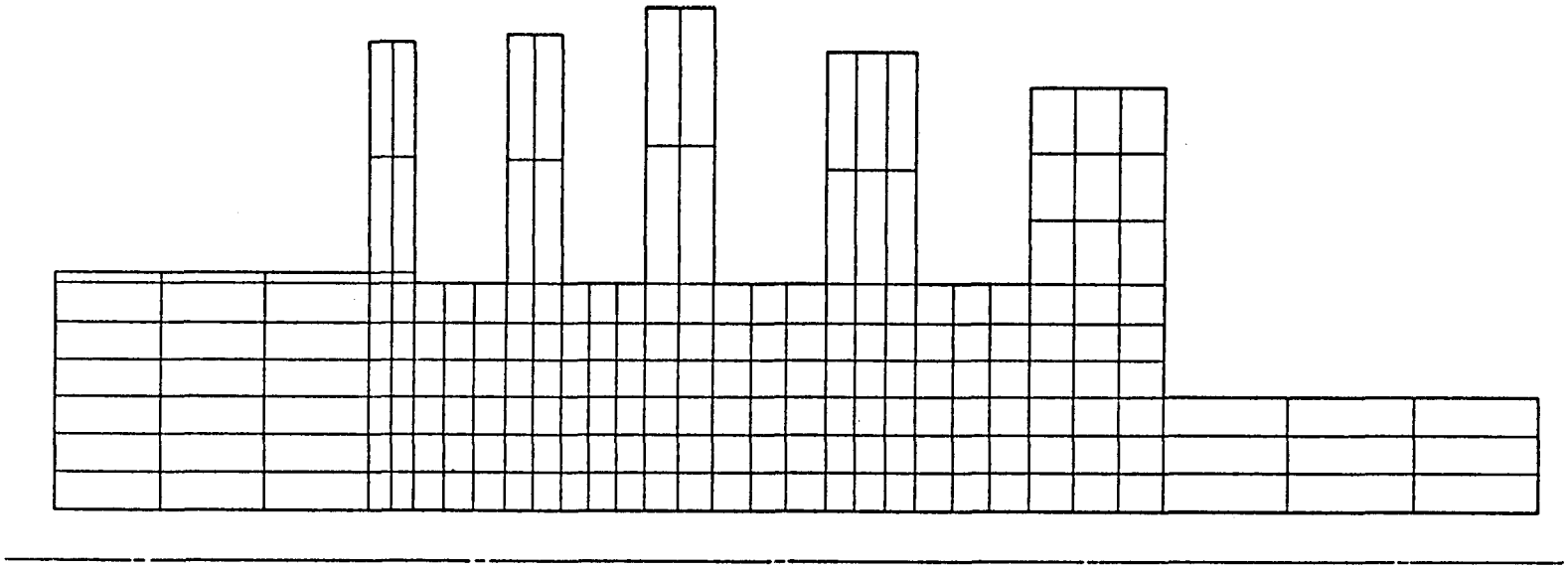

FIGURE 3-14. FINITE ELEMENT MESH OF SEWARD LP

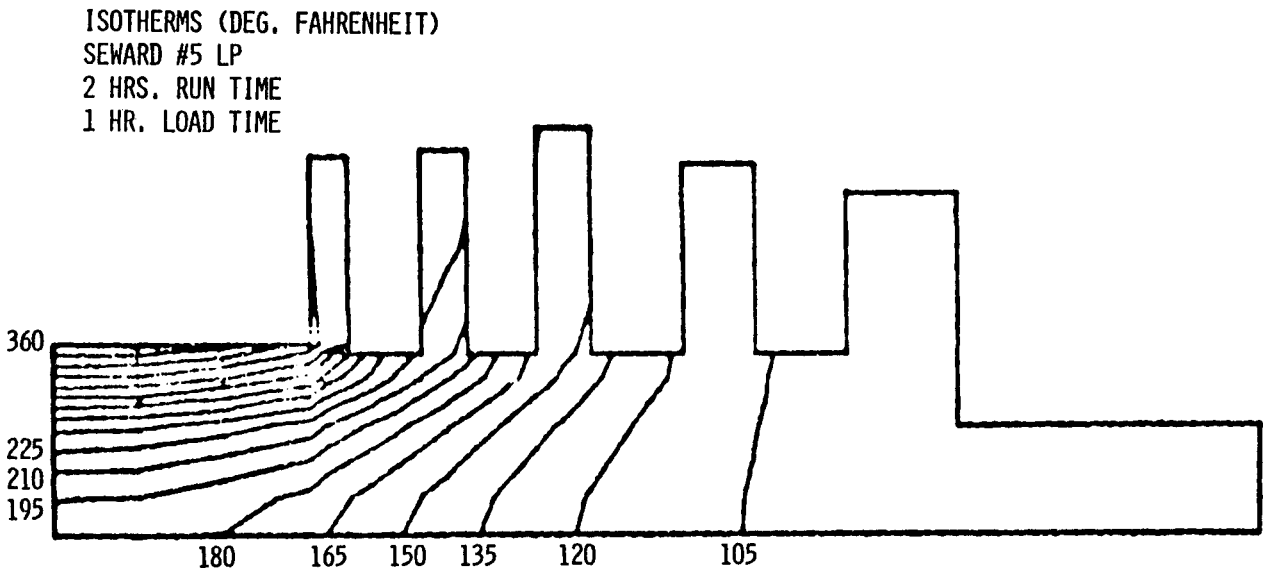

FIGURE 3-15. COMPUTER DRAWN ISOTHERMS FOR SEWARD NO. 5 LP

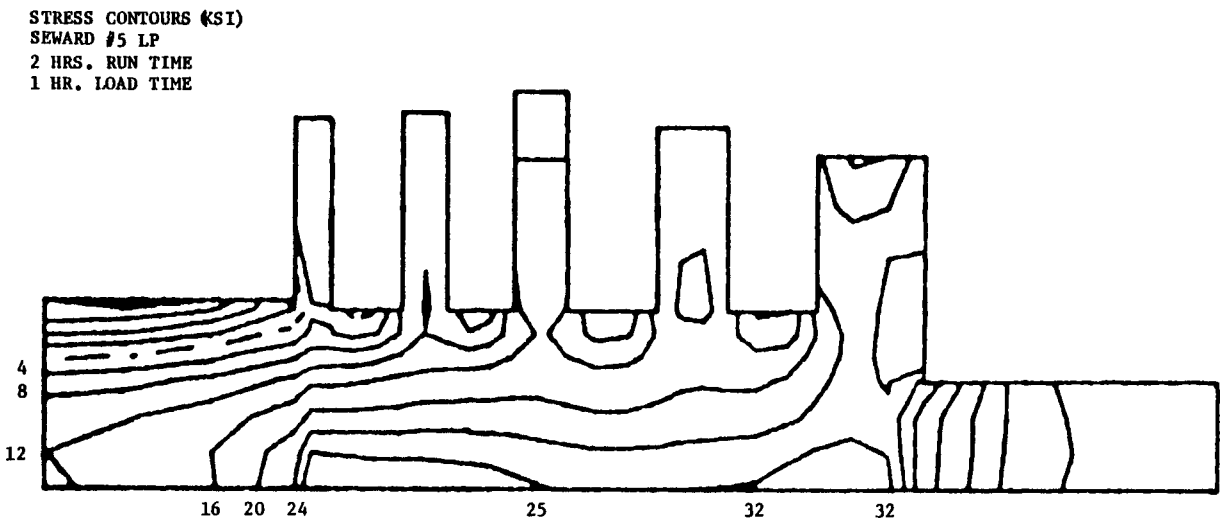

FIGURE 3-16. COMPUTER DRAWN ISOSTRESS LINES FOR SEWARD NO. 5 LP

the twentieth stage when the element temperature was 163°F. The centroidal value of the stress was 34.6 ksi,and when extrapolated to the bore, the value reached 39.4 ksi. The steady state stress at this same centroidal location was 19.4 ksi. It should be noted, however, that the maximum steady state stress did not occur at this location. The maximum steady state stress was found 1 in. upstream from the back face of stage 24 and 8.1 in. radially from the bore centerline. The maximum stress here was 33.0 ksi, and the temperature was 107°F.

Buck No. 6 IP-LP

As given in the duty cycle in Table 3-6, the Buck No. 6 rotor did not receive a separate warmup cycle. The metal temperature was initially assumed to be 100°F. Once synchronous speed was reached, the inlet steam temperature was raised to 485°F and loading begun. Maximum load was reached in an hour, with the maximum transient stress occurring after 0.6 hours of loading. Since the stresses were decreasing as the load increased, the run was terminated. The finite element mesh used to model the Buck rotor is given in Figure 3-17.

The radial distribution of σ_θ at the time and location of its maximum is shown in Figure 3-18. The maximum extrapolated stress is 56 ksi, with an element temperature of 344°F. The steady state stress at this location is 12.7 ksi with a temperature of 884°F. The maximum steady state temperature occurs at the exhaust end of the rotor; a stress of 27.8 ksi and a temperature of 110°F are computed at this location.

Sporn Series IP-LP

The Sporn Series rotor was not part of the RP502 program, but was analyzed using the codes developed during this project as an example of how the codes could be utilized by an operator of a steam turbine. The rotor was evaluated under two duty cycles, one of them a typical cold start, as given in Table 3-7, with the initial metal temperature at 70°F. The second anticipated operating cycle was a hot start with the initial metal temperature at 700°F; details of this cycle are given in Table 3-8. For the hot start, roll-off to synchronous speed was accomplished in 30 minutes, while the time to maximum load was one hour. Once maximum load was achieved, the run was continued for another hour.

TABLE 3-6. TRANSIENT INPUT BUCK #6 IP-LP

% MW Load	(FAHR.) Inlet Steam Temperature	(FAHR.) Cooling Steam Temperature	(FAHR.) Outlet Temperature	(PSIA) Inlet Pressure	(PSIA) Outlet Pressure	(HRS) Time Duration
100.0	1000.0	1000.0	92.0	398.0	0.74	
60.0	747.0	747.0	92.0	237.2	0.74	
40.0	742.0	742.0	92.0	156.0	0.74	1
20.0	702.0	702.0	92.0	79.0	0.74	
4.0	697.0	697.0	92.0	19.0	0.74	
0.0	485.0	485.0	92.0	0.95	0.74	Synchronous No-Load
Roll-Off	100.0	100.0	90.0	0.95	0.70	1
Warm-Up	None	None	None	None	None	None

Total[†] Simulated Run Time 3 Hours

[†] The system was run one hour at maximum load to give this total run time.

Steady State Input Buck #6 IP-LP

Inlet Steam Temperature, °F	1000
Outlet Steam Temperature, °F	92
Cooling Steam Temperature, °F	900
Inlet Pressure, PSIA	398
Outlet Pressure, PSIA	0.74

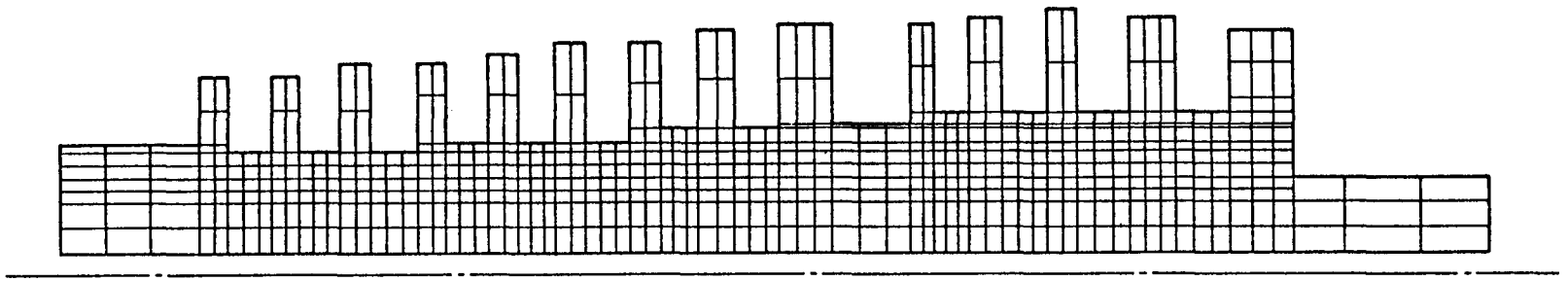

FIGURE 3-17. FINITE ELEMENT MESH FOR BUCK #6 IP-LP

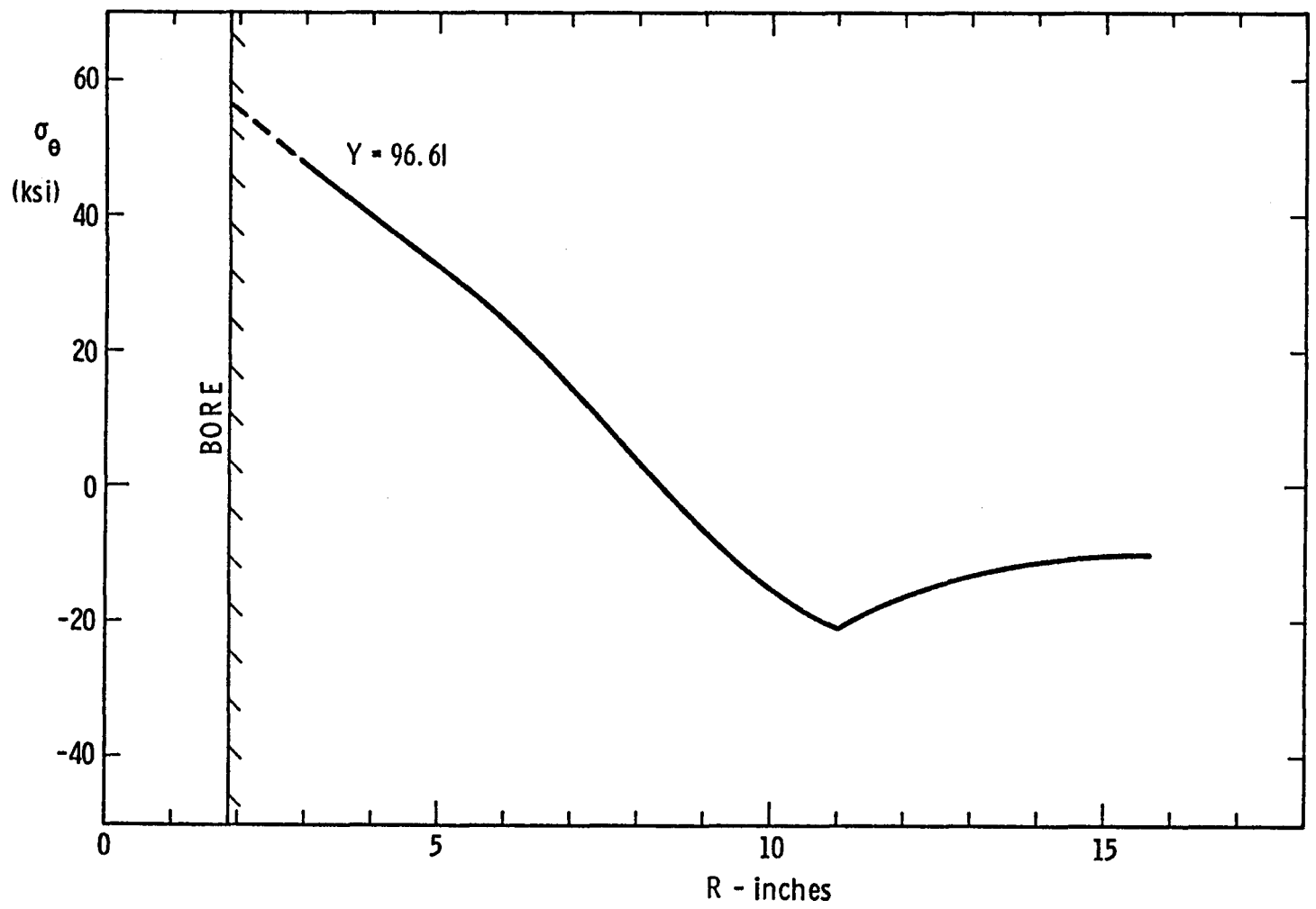

FIGURE 3-18. STRESS DISTRIBUTION AT TIME OF MAXIMUM TRANSIENT STRESS, BUCK #6 IP-LP

TABLE 3-7. TRANSIENT STEAM CONDITIONS FOR COLD START OF SPORN SERIES IP-LP

% MW Load	(FAHR.) Inlet Steam Temperature	(FAHR.) Shaft Sealing Steam Temperature	Stage 13 (FAHR.) Outlet Temperature	(PSIA) Inlet Pressure	Stage 13 (PSIA) Outlet Pressure	(Hrs.) Time	Duration
100.0	1000.0	935.0	468.0	406.0	40.4	7.67	
88.4	1000.0	935.0	474.0	359.0	36.1	7.15	
78.6	1000.0	935.0	462.0	319.0	32.0	6.72	4.42
57.1	912.0	935.0	403.0	232.0	24.0	5.77	
44.3	817.0	875.0	337.0	180.0	18.4	5.21	
0.0	650.0	620.0	260.0	35.0	35.0	3.25	Synchronous
0.0	525.0	620.0	270.0	35.0	35.0	0.8333	3.25
Roll-off	275.0	620.0	275.0	6.0	6.0	0.0	

Metal Temperature at roll-off, 70°F

STEADY STATE STEAM CONDITIONS

Inlet Steam Temperature, °F	1000.0
Stage 13 Outlet Steam Temperature, °F	468.0
Shaft Sealing Steam Temperature, °F	935.0
Inlet Pressure, PSIA	406.0
Stage 13 Outlet Pressure, PSIA	40.4

TABLE 3-8. TRANSIENT STEAM CONDITIONS FOR HOT START OF SPORN SERIES IP-LP

% MW LOAD	(FAHR) INLET STEAM TEMPERATURE	(FAHR.) SHAFT SEALING STEAM TEMPERATURE	STAGE 13 (FAHR) OUTLET TEMPERATURE	(PSIA) INLET PRESSURE	STAGE 13 (PSIA) OUTLET PRESSURE	(HRS) TIME
100.0	1000.0	935.0	468.0	406.0	40.4	1.5
88.4	1000.0	935.0	464.0	359.0	36.1	1.326
78.6	1000.0	935.0	462.0	319.0	32.0	1.179
57.1	912.0	935.0	403.0	232.0	24.0	0.8565
44.3	875.0	875.0	337.0	180.0	18.4	0.6645
0.0	800.0	800.0	260.0	35.0	35.0	0.5
Roll-Off	700.0	800.0	700.0	6.0	6.0	0.0

Metal temperature at roll-off 700°F.

The finite element model of the IP rotor is shown in Figure 3-19. This section of the rotor had been bottle bored, and the rotor was modelled with a constant bore radius equal to that of the bottle bore. A steam seal on the forward section of the rotor was modelled using labyrinth seals.

Figures 3-20 and 3-21 compare the temperature distribution in the rotor at the time of maximum transient stress for the cold and hot start. The maximum cold start temperature at this time is about 890°F and occurs in the region of the steam seals ahead of the reheat stages. As shown in Figure 3-21, the maximum hot start temperature occurs at the same location and is about 40 degrees higher.

Figures 3-22 and 3-23 compare the maximum tangential stress for the two starting conditions. Note that the hot start gives slightly higher stresses; when extrapolated to the bore, the stresses are 27.4 ksi and 23.2 ksi for the hot and cold starts, respectively. The maximum stresses also occur at different locations as the stress contours are shifted forward in the hot start.

The steady state stresses are given in Figure 3-24. The magnitudes of these stresses are low, but they are about 30-40 percent of the peak transient stresses.

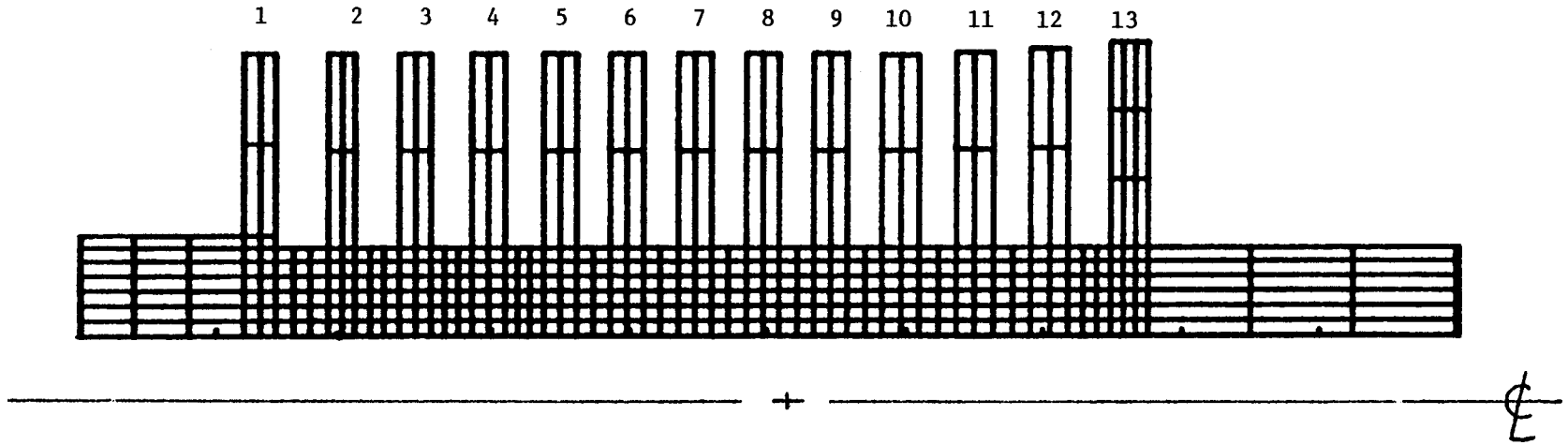

FIGURE 3-19. SPORN SERIES IP ROTOR GEOMETRY

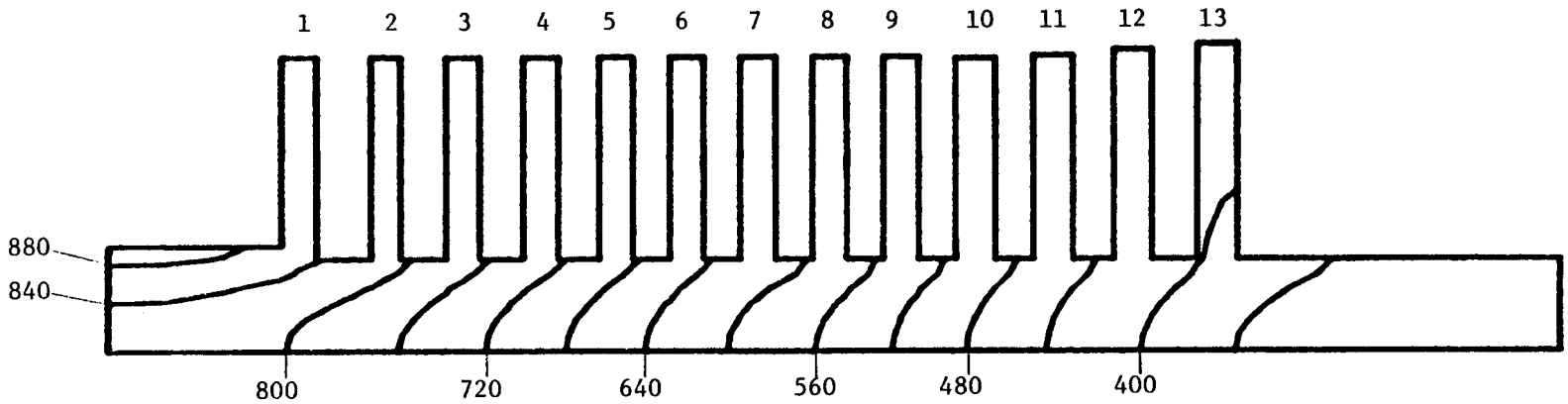

FIGURE 3-20. COLD START: TEMPERATURE AT TIME OF MAXIMUM TRANSIENT STRESS

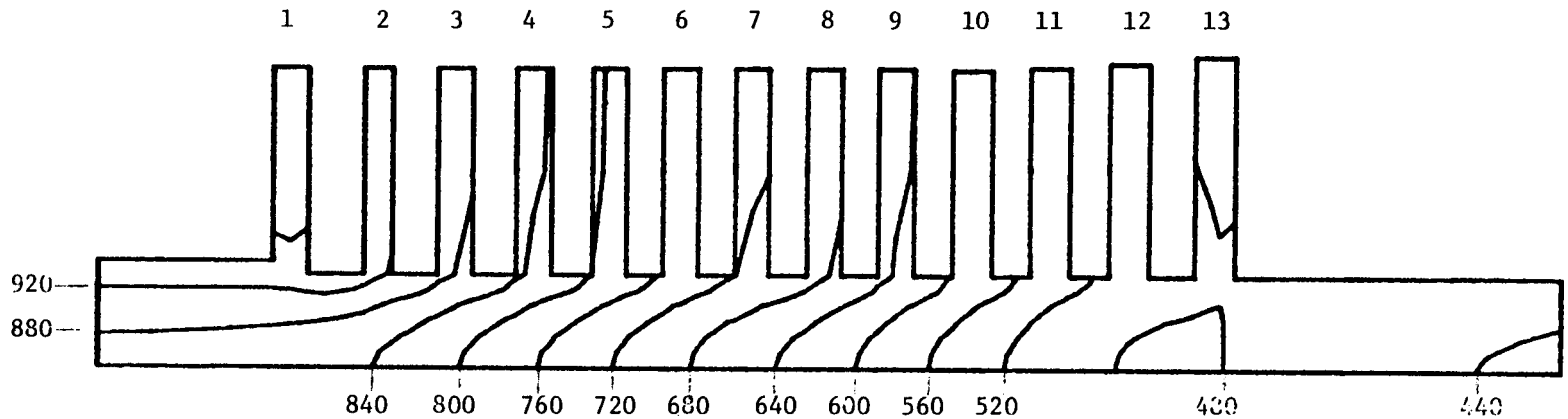

FIGURE 3-21. HOT START: TEMPERATURE AT TIME OF MAXIMUM TRANSIENT STRESS

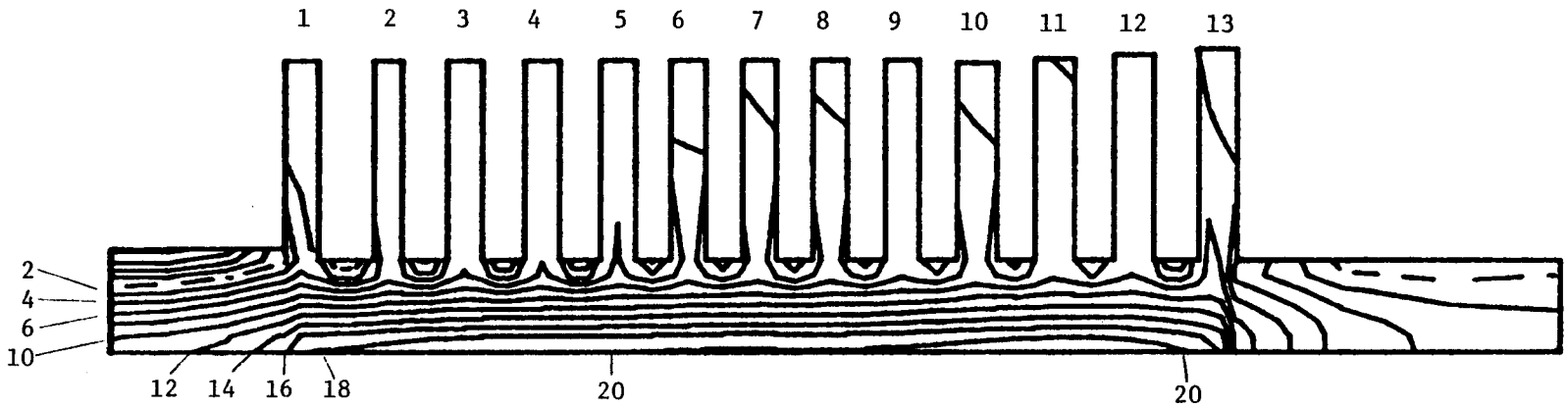

FIGURE 3-22. COLD START: σ_θ AT TIME OF MAXIMUM TRANSIENT STRESS

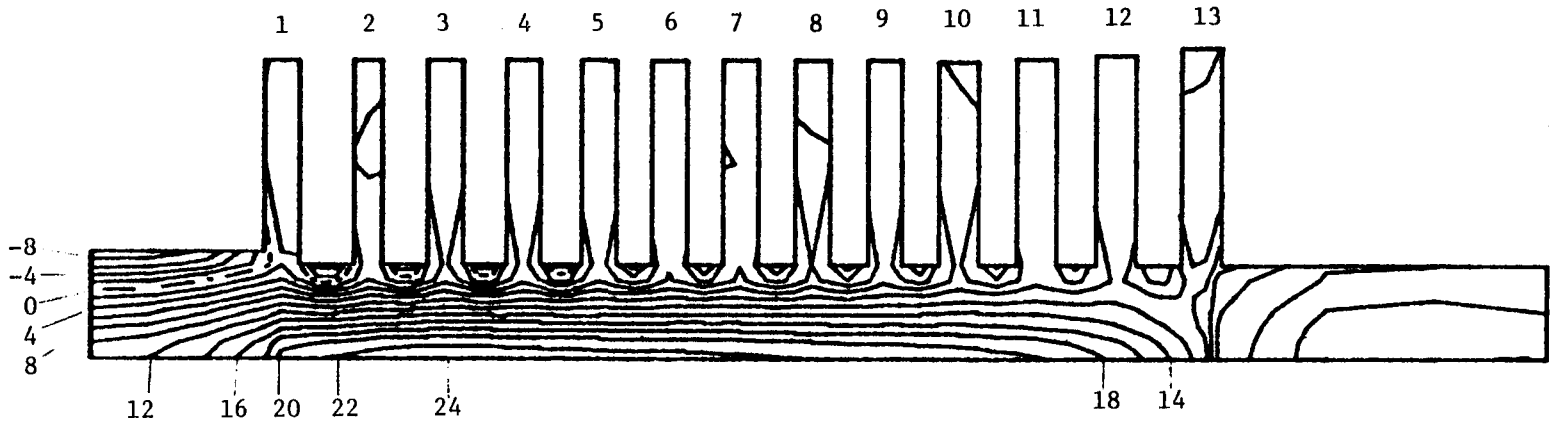

FIGURE 3-23. HOT START: σ_θ AT TIME OF MAXIMUM TRANSIENT STRESS

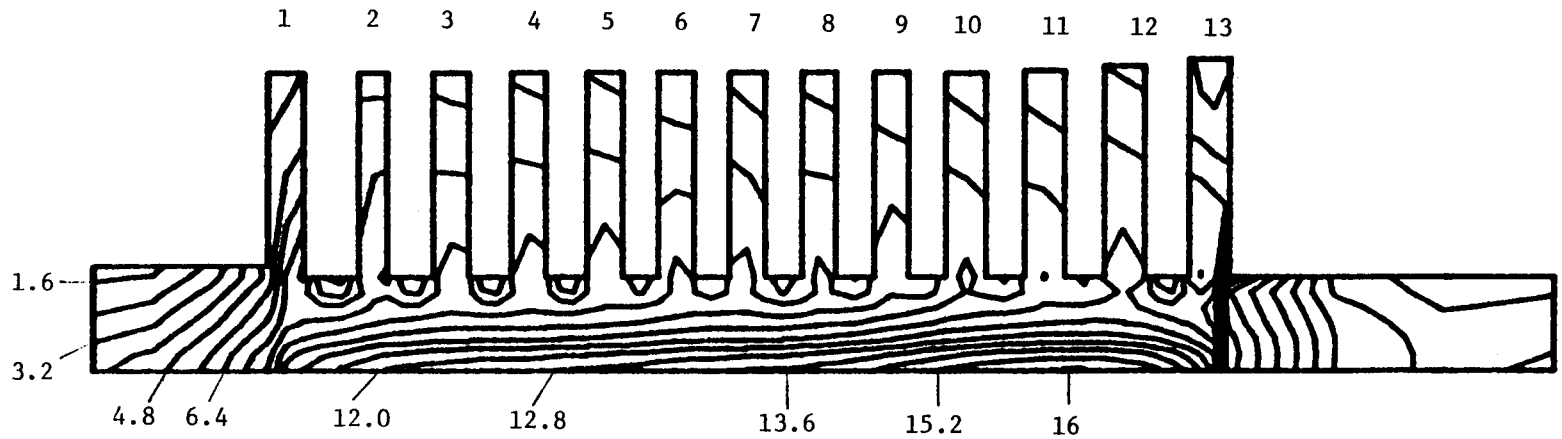

FIGURE 3-24. STEADY STATE HOOP STRESS

Section 4

FRACTURE ANALYSIS

This section presents a discussion of the Fracture Analysis Code postprocessor. While a number of important points of the code will be covered, the discussion will be necessarily limited in scope. For a detailed explanation of the models employed in the code, the programmer's guide, Reference (1), as well as (2), contains all the necessary information.

FRAC - Fracture Analysis Code

The FRAC computer program has been written to provide an assessment of the remaining life of a steam turbine rotor in terms of fracture mechanics concepts. It performs this task by combining the results of the thermoelastic stress analysis of the rotor, typical materials data, and the results of a boresonic nondestructive examination to predict critical rotor locations and to evaluate the threat of designated flaws determined by NDE. The program is generally based on linear elastic fracture mechanics, but it does incorporate other concepts, e.g., the Larson-Miller parameter is used to evaluate the creep-rupture life.

In performing the life assessment of the rotor, the main area of concern is the near-bore region. This is for two reasons. First, the maximum tangential stress occurs at the bore and decreases rapidly away from the bore. Second, the accuracy of current boresonic inspection systems decreases rapidly at distances greater than about four inches from the bore surface. Since the RP502 program code has been designed to work with this type of inspection, the fracture analysis performed by the code is limited to the neighborhood of the bore. This means that the searches of the stress and temperature tables performed by the code are limited to a maximum of five radial elements. Since the near bore region is by far the most highly stressed, this is not a real limitation to the life assessment capabilities of the code. It should be noted, however, that an expanded version of PPMESH and FRAC may eventually be produced that will incorporate greater capabilities for modelling and analyzing the periphery of the rotor. This broader capability would encompass such problems as blade attachment cracking, shrunk on disks, etc.

An overall flow chart for FRAC is given in Figure 4-1. As shown in the figure, the essential steps of the code are as follows:

1. Based on the thermoelastic stress analysis, the smallest crack that can produce unstable fracture during specified startup with overspeed is determined.
2. If specific locations in the rotor are indicated by nondestructive examination to be of concern, the crack size that will cause fast fracture at these locations is computed.
3. The initial crack size that can grow to this critical crack length by low cycle fatigue in a designated number of operating cycles is determined.
4. The potential for creep-rupture and failure resulting from local yielding around inclusions is examined through a simple area fraction model.

Determination of Critical Crack Size

Flaw Geometry

The FRAC computer program has been written to analyze a rotor in terms of one of four different flaw geometries; these geometries are (1) the penny shaped flaw, (2) the elliptical flaw, (3) the stringer flaw, or infinite aspect ratio, and (4) the edge flaw. These four geometries are taken as being representative of flaws encountered in a rotor, as well as containing the most severe flaw geometries. The analysis is limited to these four configurations since the precise flaw geometry will be unknown in many cases; thus, there is little merit in providing a large catalog of possible defect configurations. While we have restricted our attention to four geometries, the code can be expanded in the future to include additional flaw configurations if it is desirable. The program can also handle up to ten different discrete flaw locations in addition to the single critical location. These locations will be determined by the inspection procedure and will be referred to as designated or specific flaws in the following.

In general, the critical crack length is given by

$$a_c = C\left(\frac{K_{IC}}{\sigma}\right)^2 \qquad (4\text{-}1)$$

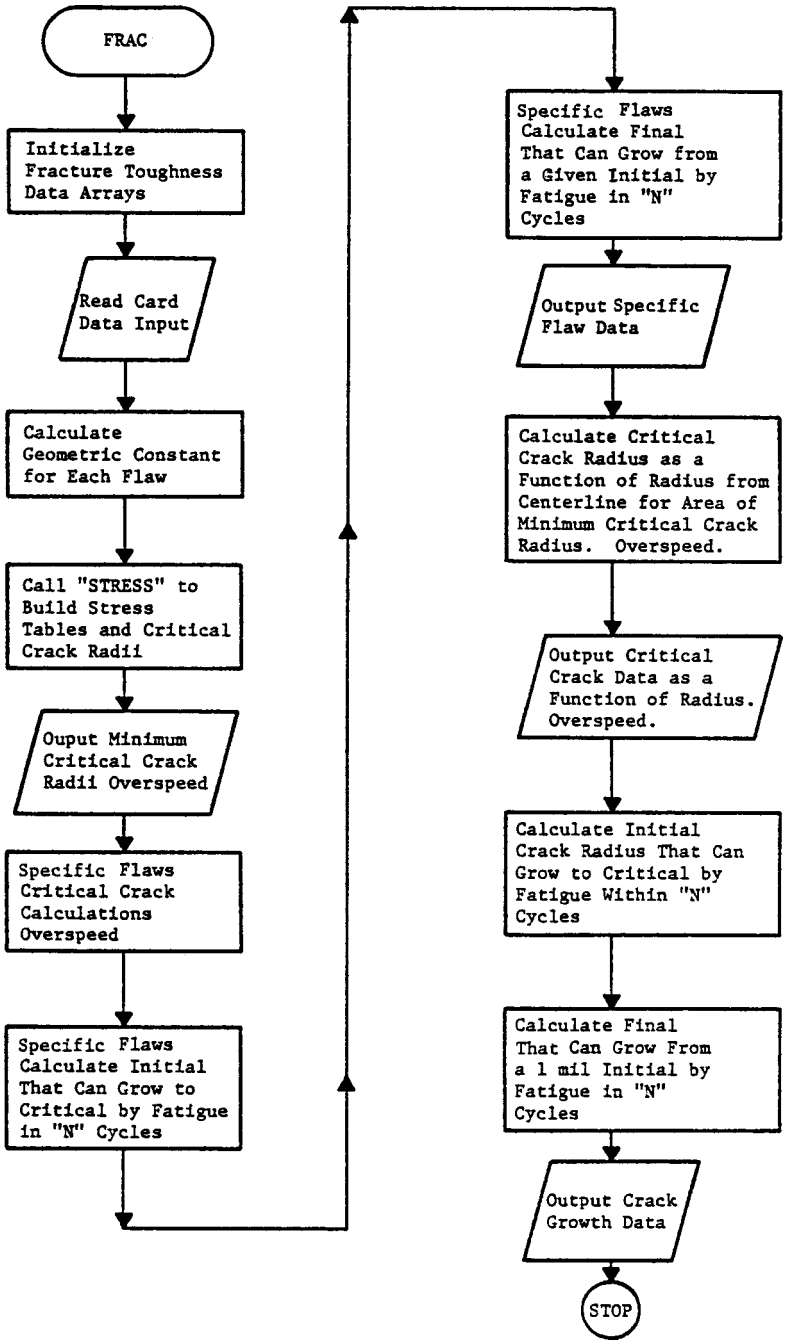

FIGURE 4-1. FLOW CHART FOR FRACTURE ANALYSIS CODE

where

a_c = critical crack half length, inches.

C = a constant determined by the crack geometry,

σ = the tangential stress at the point of interest, ksi

K_{IC} = the material fracture toughness at the temperature of the flaw location, corresponding to the time at which stress σ is developed, ksi$\sqrt{in}$.

Toughness Properties

For a given geometry, the critical flaw size depends on the stress and the fracture toughness, K_{IC}, as expressed in Equation (4-1). The toughness is, in turn, a function of temperature as shown in Figure 4-2. This figure shows toughness data on material obtained from Joppa No. 3 (13) and also the curve used in the FRAC code. It was felt that this curve, while somewhat below the data generated by Westinghouse, should be very conservative since it was feared that the air melt Cr-Mo-V might undergo a service induced loss of toughness. There was, however, no such loss in toughness observed in the initial rotors examined in the RP502 program.

Subsequently, Westinghouse discovered a high fracture appearance transition temperature of 600°F in the reheat stage of the Duke Power Buck No. 6 IP-LP rotor. This increase has been attributed to the high austenitizing temperature of this class of rotors, reported by the manufacturer to be 1850°F. The resulting large austenite grain size, coupled with significant levels of sulfur, phosphorus, tin, and other trace elements, leads to this severe elevated temperature embrittlement during long service exposure in the hot inlet region of the rotor. Neither the TVA Gallatin No. 2 IP nor the Joppa No. 3 IP exhibited this condition. However, another Cr-Mo-V rotor, austenitized at 1850°F, was reported by Argo and Seth (14) to have had an FATT of 575°F.

At the present time, no fracture toughness tests on material from the Buck rotor have been conducted. Only Charpy V-notch tests have been run, which indicate much lower impact energies than Joppa No. 3 over the entire temperature range. Therefore, it appears that a revision to the fracture toughness data used in FRAC will have to be made.

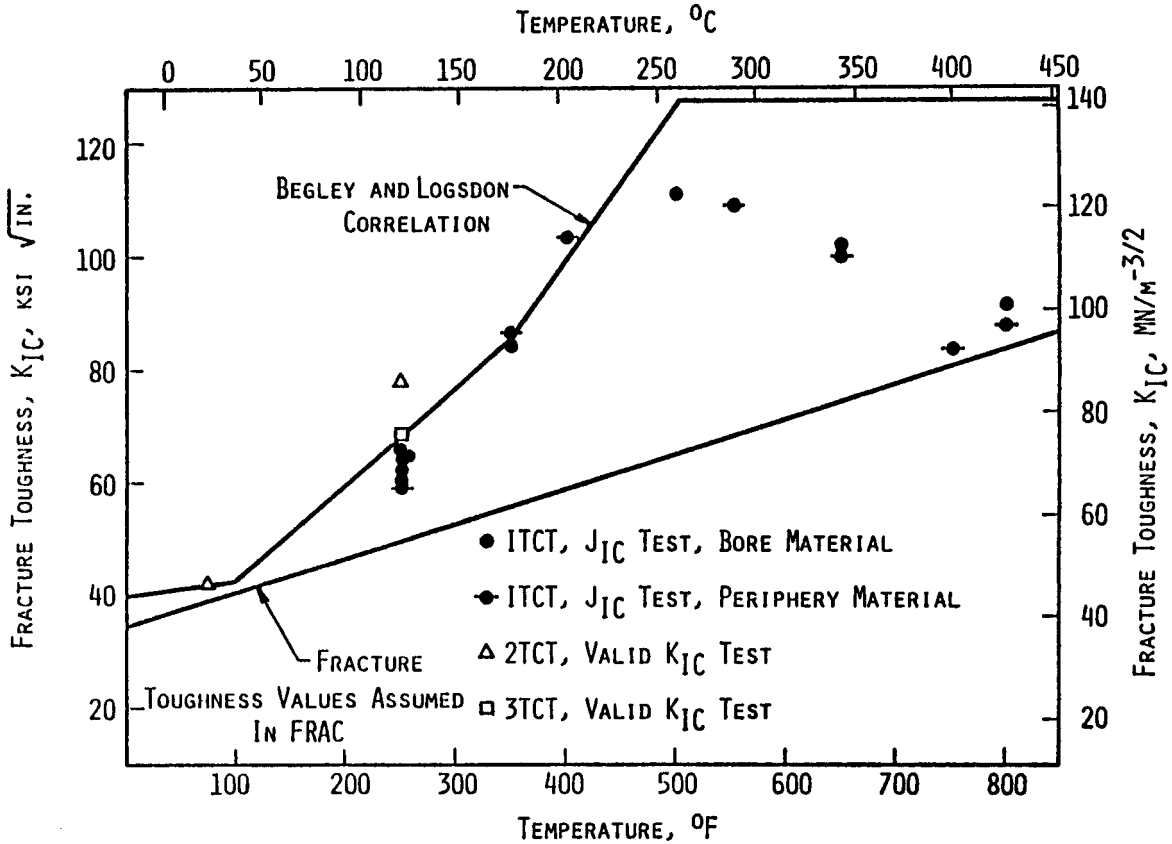

FIGURE 4-2. FRACTURE TOUGHNESS DATA DEVELOPED BY WESTINGHOUSE (13) AND USED IN FRAC

The discovery of the embrittlement poses a severe problem for the life prediction system, at least until the cause of the embrittlement has been completely determined. If the loss in toughness is due to the 1850°F austenitizing and the service temperature, then toughness values corresponding to the steady state temperature of a given rotor location can be determined and the calculation can proceed as presently performed. If, however, the cause of the embrittlement cannot be determined or if it depends on the microstructure, then it may be necessary to obtain and test samples from each rotor under analysis before toughness values can be assigned. Since the embrittlement produces a decrease in critical crack size by at least a factor of three, and it may be as high as an order of magnitude, it will be too conservative to simply take the worst case of toughness. The code has been designed to accept a set of toughness versus temperature values for materials other than Cr-Mo-V. If each rotor has unique toughness values, it may be necessary to supply individual curves for the Cr-Mo-V material also.

Critical Crack Sizes for the Program Rotors

Since the critical flaw size depends on both the temperature and the stress, the initial program operation is to determine the worst combination of these variables. By making an efficient search of the transient stress analysis data files, the location of the maximum rotor stress for each time increment is determined and stored. Once the stress and temperature data has been accumulated for each time step in the transient history, a critical crack size is computed for each time. The smallest of these cracks is the critical crack size at the location of maximum stress.

In an analogous manner, the code stores the temperature and stress at each time step for each designated flaw location. The smallest critical crack size for each designated location is then computed.

While a critical crack size is computed at the location of maximum stress, the variation in fracture toughness with temperature allows the possibility that the minimum critical crack could occur in a lower temperature section of the rotor. Therefore, the cooler end of the rotor, which is considered to be the last ten to twelve inches upstream from the rear face of the last rotor stage, is also searched for its maximum stress. This search results in another stress and temperature table which is used to

compute a critical crack size. This value is compared to the crack size computed from the maximum stress criterion; the comparison yields the minimum critical crack size in the entire rotor.

After the location and value of the minimum critical crack size for the rotor are determined, the stress and temperature distributions as a function of radius from the bore centerline for this location are saved.

Up to this point the computations are based on synchronous speed. Since the operating speed is frequently exceeded during runup, the effect of overspeed on the stress and, therefore, critical crack size must be accounted for. Thus, following the processing of the transient data, the steady state data are read in and stored for all of the locations of interest. With the steady state data and the transient data resident in computer core, the critical crack radius for each of the locations of interest is recalculated based upon a percentage overspeed, which is specified by the operator. The overspeed stress is calculated by the expression

$$S = (OS)^2 \ (SS) + (TS - SS) \qquad (4\text{-}2)$$

where

S = The overspeed stress, ksi

OS = One plus the fraction of overspeed,

SS = The steady state stress, ksi,

TS = The transient thermoelastic stress, ksi.

Then the minimum critical crack size is calculated. The critical crack size at the specific NDE locations is determined in the same way.

Table 4-1 gives the extrapolated bore stresses and temperatures at the time of maximum transient stress for each of the rotors analyzed. The steady state conditions at the same location are also listed. Using this data, Equation (4-2) is used to compute the overspeed stress. Fracture toughness for each location is then obtained from Figure 4-2 using the appropriate temperature from Table 4-1. Once a flaw geometry has been selected, the critical crack size can be computed from (4-1).

If a semicircular bore connected crack is assumed, then the resulting critical crack size for each rotor is given in Table 4-2. The first column lists the sizes based on the data of Figure 4-2 and shows that the radius of the critical crack size covers an order of magnitude. The smallest crack radius occurs in Gallatin, barely a quarter of an inch, while the largest crack radius is predicted for the Sporn Series unit and is over 3 inches.

As has been previously discussed, evidence of embrittlement has been found in the Buck No. 6 rotor. The maximum stress in this unit occurred at the inlet end of rotor, right in the high temperature and, therefore, in the most embrittled region. While no toughness values are yet available on material from this rotor, if we assume a toughness of 30 ksi $\sqrt{in.}$, the critical crack size drops by a factor of 3 from 0.68 to 0.18 inches. This crack size is even smaller than that predicted for the Gallatin unit.

Although there is no evidence that the Sporn Series IP-LP was embrittled, the potential effect of embrittlement on this rotor was investigated. As given in Table 4-2, the effect of service induced embrittlement would be to reduce the critical crack size for the cold start from 3.37 to 0.82 inches. The location of maximum stress in this turbine occurred in the center of the rotor. The steady state temperature at this location was about 525°F, and so the material should not have undergone much embrittlement in the maximum stress region. Hence, the larger value of critical crack size is probably appropriate to this location.

The NDE results of this rotor indicated that there was a flaw near the inlet of this rotor. At the indicated location, the stress is quite low while the temperature at maximum stress is 750°F. The low stress-high toughness combine to yield a critical flaw size of about 24 inches, or larger than the wall thickness. Hence, catastrophic failure from an undetected flaw would be unlikely in this case. This picture changes dramatically when the possibility of service induced embrittlement is introduced. If it is assumed that the service causes a shift in the FATT to about 600°F, then the cold start duty cycle was such that 88% of the peak transient stress is achieved while this location is at or below the FATT. Making the conservative assumption that the toughness is still about 30 ksi $\sqrt{in.}$, the critical crack size is reduced by a factor of eight to 3.4 inches. While it is to be expected that an existing crack of this

TABLE 4-1. MAXIMUM TANGENTIAL ROTOR STRESSES AT SYNCHRONOUS SPEED

Rotor	Transient[1]			Steady State[1]	
	σ_θ, ksi	T, °F	τ, hrs[2]	σ_θ, ksi	T, °F
Gallatin No. 2 IP	74.0	272	1.25	47.2	727
Joppa No. 3 IP	37.0	308	1.50	31.0	450
Seward No. 5 LP	39.4	163	1.00	21.5[3]	302
Buck No. 6 IP-LP	56.0	344	0.60	13.9[3]	884
Sporn Series IP-LP					
(Cold Start)	23.2	421	2.80	17.4	526
(Hot Start)	27.4	615	1.00		

[1]Stresses are computed at element centroids and extrapolated to the bore.

[2]Time after start of loading.

[3]Maximum steady state stress did not occur at location of maximum transient stress.

TABLE 4-2. CRITICAL RADIUS OF SEMICIRCULAR BORE CRACK AT 15 PERCENT OVERSPEED

	a_c, inches	
	Unembrittled	Embrittled*
Gallatin No. 2 IP	0.27	N/A
Joppa No. 3 IP	1.10	N/A
Seward No. 5 LP	0.77	N/A
Buck No. 6 IP-LP	0.68	0.18
Sporn Series IP-LP	3.37	0.82

*300°F increase in FATT

size would be detected by a boresonic inspection, nevertheless the assumption of embrittlement changes the situation from one in which catastrophic fracture is unlikely to one where it may well occur.

The example of these two rotors and the magnitude of the shift in critical crack size illustrates the problem faced in predicting rotor lives. Lower bound toughness values will be too conservative if the rotor is not embrittled, but an embrittled rotor must receive very conservative analysis. Thus, some means of identifying turbines which have undergone service induced loss of toughness must be devised. Alternately, a destructive test specimen may have to be removed from each rotor analyzed.

Fatigue Crack Growth

Fatigue Crack Growth Data Base

Guided in part by the Gallatin No. 2 IP fracture, the initial assumption was made that the subcritical crack growth from multiple defects could be described by linear elastic fracture mechanics using elevated temperature fatigue crack propagation data. This data was generated on the Cr-Mo-V material and is discussed in detail in the Task IV final report (15). These tests were conducted with various hold times and frequencies at several temperatures. It was hoped that the data could be correlated by a single parameter and would represent the significant effects of time and temperature. However, the data failed to conform to parametric generalization.

In tests on the material from the Joppa rotor, it was possible to reduce the data to the form

$$\frac{da}{dN} = C(\nu, T)\Delta K^{2.7} \qquad (4\text{-}3)$$

over the frequency range

$$0.0017 \text{ Hz} \leq \nu \leq 1.0 \text{ Hz}$$

The coefficient $C(\nu, T)$ is plotted in Figure 4-3 as a function of $1/\nu$ using temperature as a parameter.

The data displayed in Figure 4-3 is stored in FRAC in tabular form with C as a function of temperature and period of the duty cycle. This data is stored in a 4 x 4 array and is interpolated, using a cubic spline interpolation function, to generate a table of coefficients as a function of period for a given steady state temperature. The steady

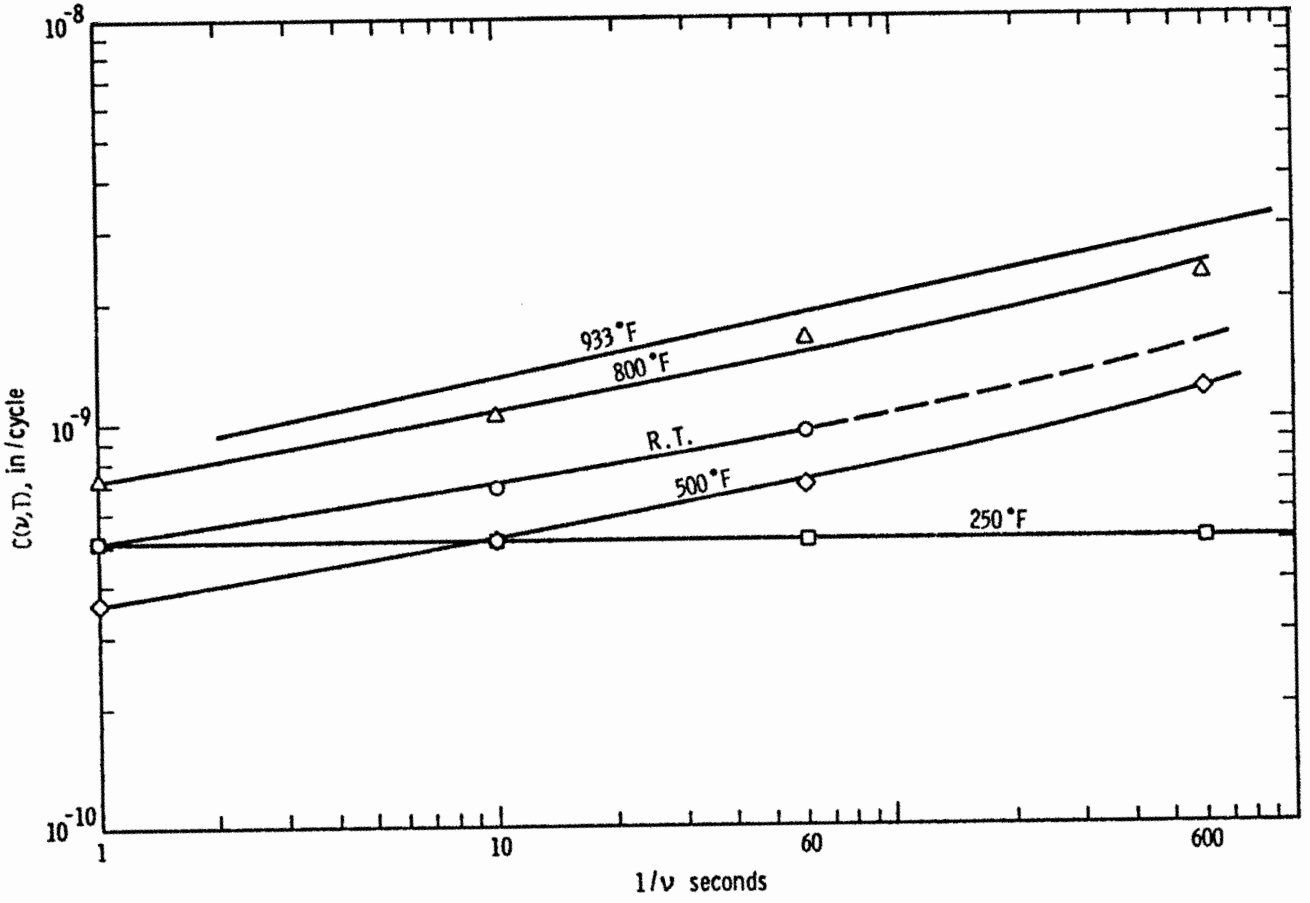

FIGURE 4-3. FATIGUE CRACK GROWTH COEFFICIENT DATA

state temperature is used in order to ensure a conservative coefficient. This final table is interpolated, using a cubic spline interpolation function, to determine the coefficient at the period of the duty cycle being applied to the rotor.

Initial Crack Size Computations

Once the critical crack size has been determined, FRAC next calculates the initial crack size that could grow to the critical size within an operator specified number of duty cycles. Alternately, the operator may specify an initial crack size, based on his boresonic results, and calculate the number of cycles required to reach critical size. These computations use the fatigue growth data base described in the preceding section. Figure 4-4 shows a comparison of the critical crack size and the initial flaw size that will grow to critical size in 1000 cycles for the Gallatin No. 2 rotor; this size is plotted as a function of distance from the bore centerline.

This figure shows that the amount of fatigue crack growth is almost negligible under the selected conditions. Only about 0.01 inch of growth is computed, assuming that the rotor has been subjected to 1000 cold starts. Moreover, this computation is conservative since most rotors have been subjected to 200-300 cold starts in 20 years. On the other hand, the low cycle fatigue crack growth in a peaking cycle turbine may be more significant, since a daily startup will lead to the accumulation of approximately 10,000 cycles in a lifetime of 30 years. In this case, however, the stress range for a hot start is lower, being more nearly equal to the steady state value. In the hypothetical case of a Gallatin IP rotor in a power peaking application, using linear elastic fracture mechanics and assuming the peak stress equals the steady state stress, the crack growth from a 0.19 inch inclusion is only 0.026 inch.

Figures 4-5 and 4-6 show similar plots for the Joppa and Buck rotors, respectively, although these plots are intended more to show the relative effects of several variables than to pinpoint the precise critical crack size. That is, both figures show three curves for the critical crack size. Two of these assume a constant minimum toughness of 40 ksi $\sqrt{in.}$; the lower curve assumes that the rotor experiences a 15 percent overspeed during startup. The plots show that this overspeed

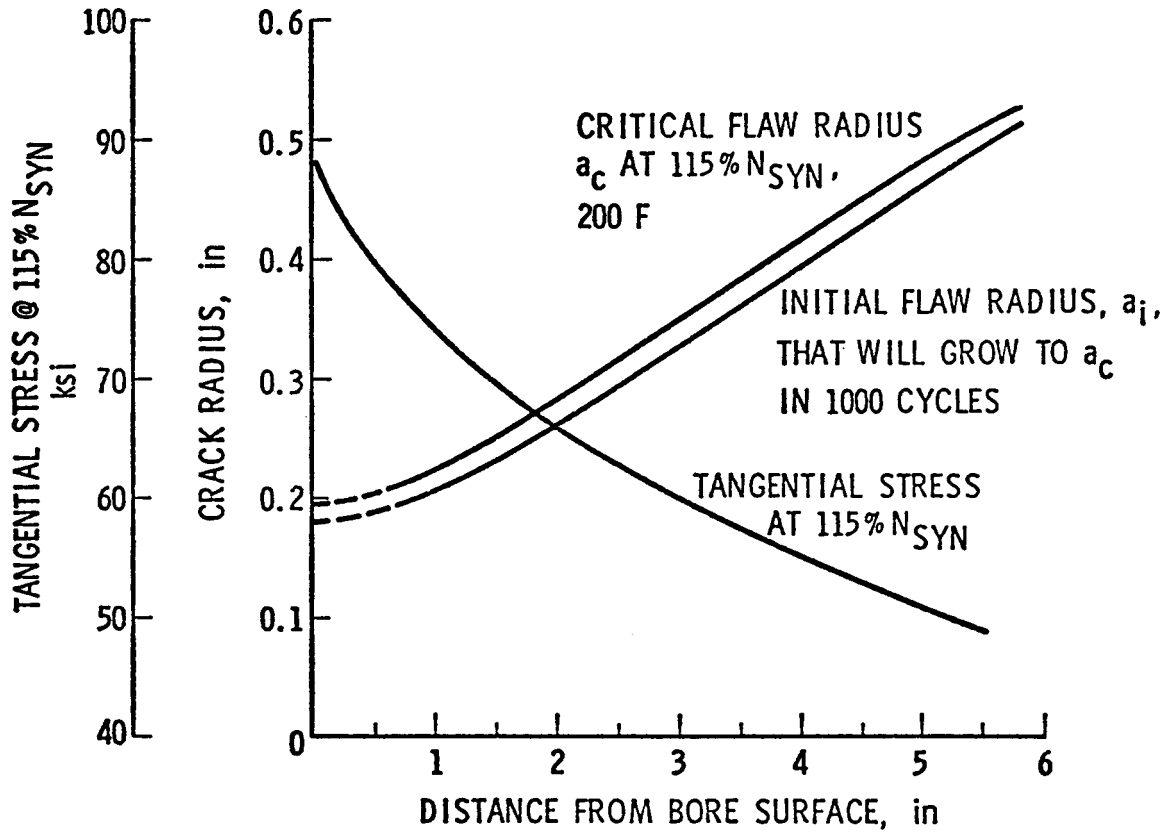

FIGURE 4-4. VARIATION OF INITIAL AND CRITICAL CRACK SIZE WITH RADIUS FOR GALLATIN NO. 2 IP. N_{SYN} IS SYNCHRONOUS SPEED.

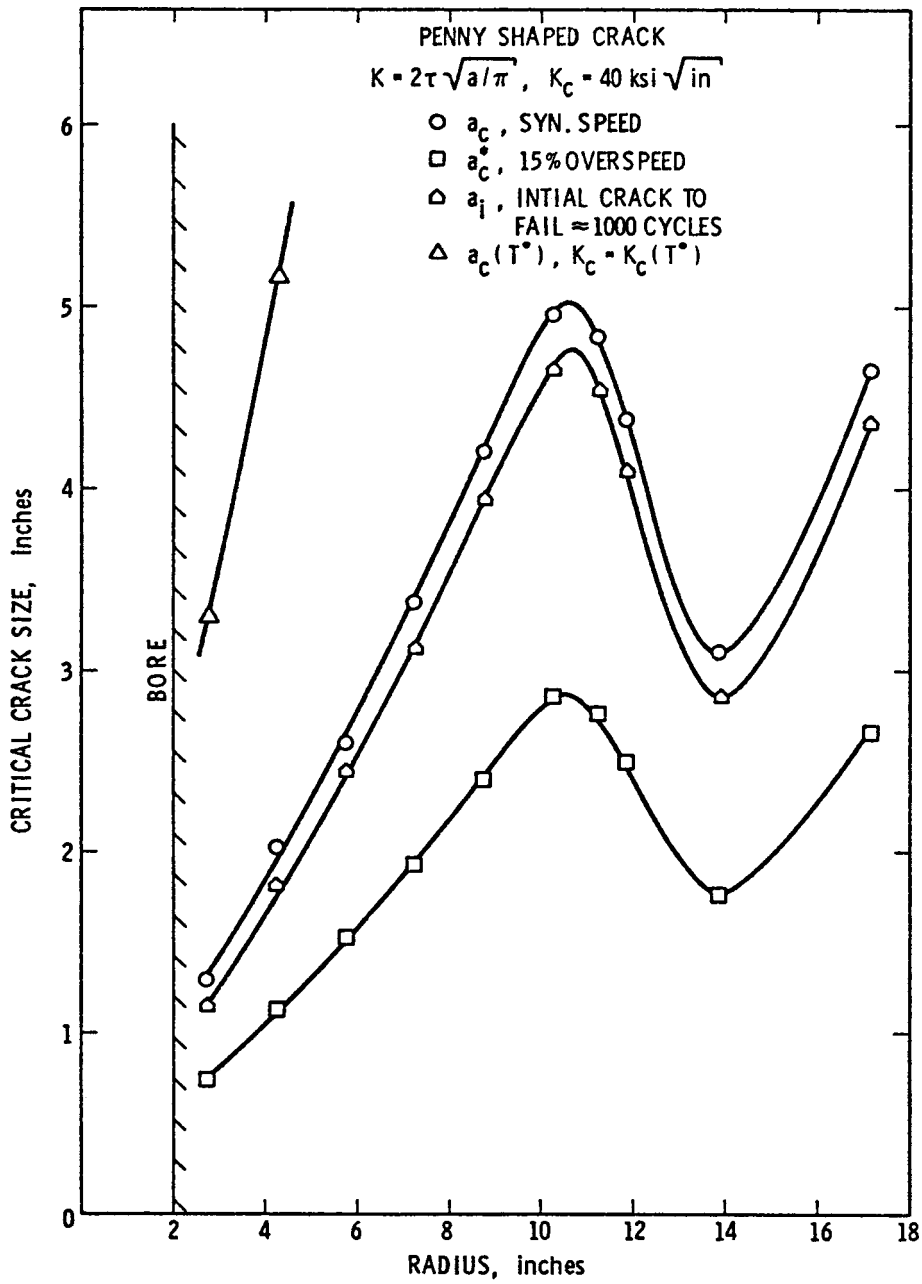

FIGURE 4-5. INITIAL AND CRITICAL CRACK SIZES FOR JOPPA NO. 3 IP

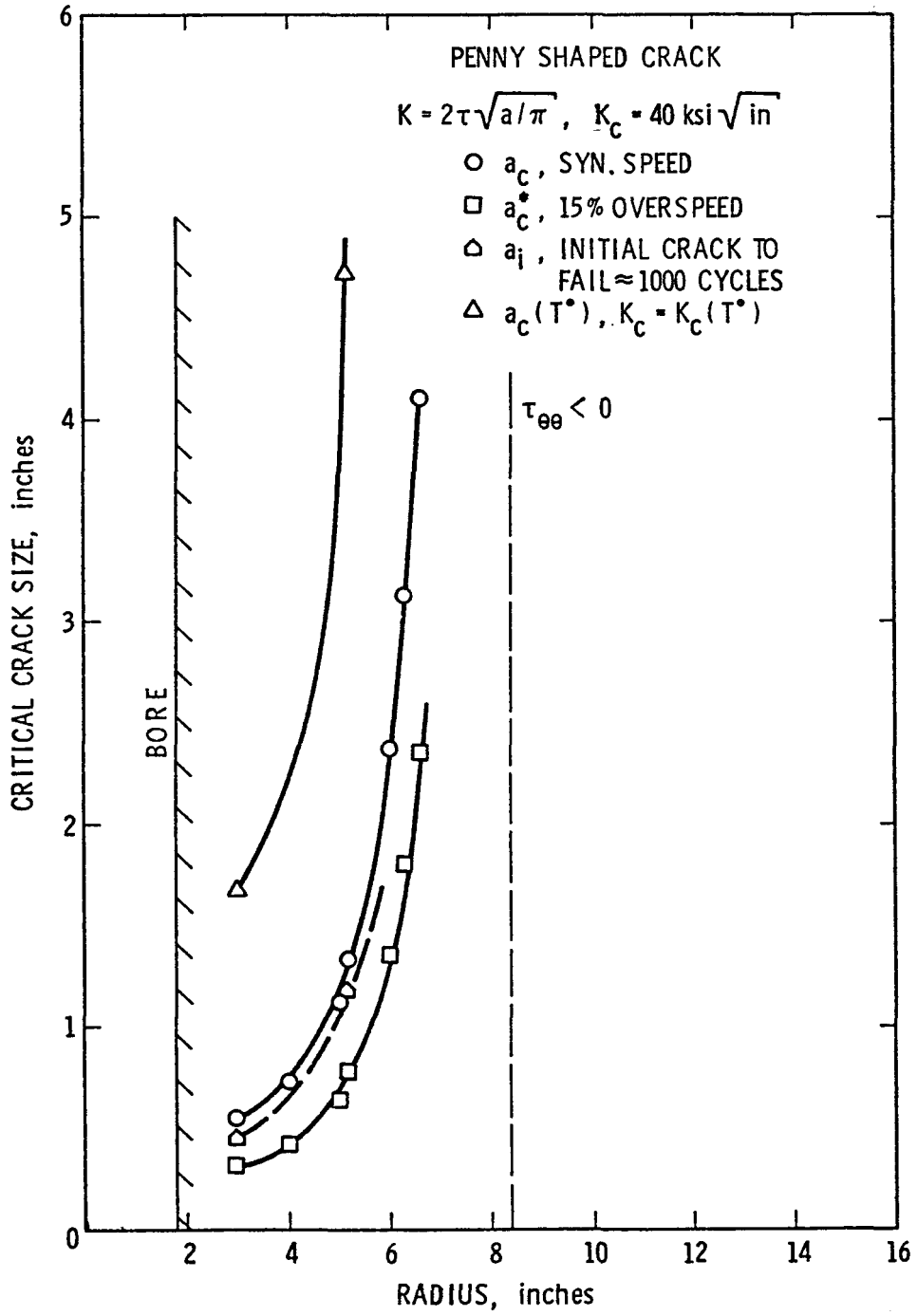

FIGURE 4-6. INITIAL AND CRITICAL CRACK SIZES FOR BUCK NO. 6 IP

produces a large reduction in critical crack size; thus it is necessary to include the effects of an overspeed in any life computations. The figures also compare the effect on critical crack size of using a minimum value of K_{IC}, 40 ksi $\sqrt{in.}$, and a value obtained from Figure 4-2 using the metal temperature at each location. The results show that using minimum properties, in the absence of evidence of service induced embrittling effects, leads to very conservative results.

The fourth curve in Figures 4-5 and 4-6 gives the initial crack size that would grow to critical size in 1000 cycles using a cyclic stress equal to the maximum stress observed in a cold start. As discussed in connection with the Gallatin IP, there is only a small amount of fatigue crack growth in this number of cycles.

Inclusion Clusters and Fracture

In addition to fatigue crack growth of an isolated defect, there are several other possible mechanisms of stable crack growth. The mechanisms are usually associated with a group of defects and are modelled in terms of an inclusion cluster.

The models used to represent such growth are simple, because of the lack of more sophisticated analyses of proven worth. Since the 1950 vintage rotors contain many small pores or inclusions, the analysis attempts to evaluate their potential hazard by three different models. These models assume that, at a given location, a planar cluster of inclusions exists. The ligaments joining the inclusions can fail by yielding, creep rupture or fatigue. Computations are then made to determine the area fraction of inclusions necessary to produce a critical size crack by each of the above mechanisms. In making this analysis, it is recognized that an overspeed will affect a cluster differently than it will an isolated crack. That is, the elevation in stress caused by the overspeed may be sufficient to cause linkup between flaws in the cluster, thereby producing a critical size crack in one cycle. For this reason, the final crack size in the cluster analysis is not taken as a_c but rather as a_i, the size of a single flaw that will grow to a_c in N fatigue cycles. This means that even if an overspeed were to produce linkup within the cluster on the first cycle, the crack would still have to grow from a_i to a_c before causing catastrophic failure.

The ligament yield model assumes that the inclusions are unbonded from the matrix and thereby the load bearing area is reduced. Moreover, once the ligaments yield, they are given no credit for load carrying capability. Hence, it follows that the area of inclusion that will raise the net stress, σ, on the cluster to yield is

$$A_i/A_c = (1 - \sigma/\sigma_y) \tag{4-4}$$

where A_i is the area of the inclusions,

A_c is the area of the cluster,

σ_y is the yield stress.

A second possible cluster failure mode is fatigue crack growth in the ligament joining two inclusions. Since a model of fatigue crack growth in the ligaments would require detailed information on the number and shape of the inclusions, this was not attempted. Moreover, until two circular cracks are within a diameter of each other, there is little interaction between them. Therefore, the amount of fatigue growth within a cluster is estimated by simply computing the crack size, a_i^*, that would grow to a_i in N fatigue cycles. While a cluster geometry could be assumed, there usually will not be any justification for modelling a specific grouping of inclusions. Therefore, the same geometry is used in this computation as in the determination of the critical crack size. The area fraction in this case is

$$A_i/A_c = \left(\frac{a_i^*}{a_i}\right)^2 \tag{4-5}$$

It is anticipated that a more sophisticated elastic-plastic model will be incorporated in the future.

In the event that stress-rupture or an interaction of creep-fatigue takes place, a modification of the Larson-Miller parameter is used to determine a third area fraction. This yields an inclusion area fraction similar to (4-4),

$$A_i/A_c = (1 - \sigma/\sigma_{1m}) \tag{4-6}$$

where σ_{lm} is the Larson-Miller rupture stress given by the data of Figure 4-7.

Figure 4-7 shows a plot of rupture stress versus the Larson-Miller parameter (P) where P is given as follows:

$$P = (T + 460)(20 + LOG_{10}\ t_R)/1000.0$$

and

P = Larson-Miller parameter

T = Local temperature in degrees Fahrenheit

t_R = Time to rupture, hours.

The solid curve is stress rupture data generated by Westinghouse (15), which agrees with (16). The dashed line is also stress-rupture data, but with periodic fatigue cycles (17). The interspersed fatigue cycles caused a reduction in life by a factor of three over the stress-rupture lives. Since we cannot predict the effect on creep life of intermittent fatigue cycles, it is assumed that the factor of three represents a creep-fatigue interaction. The dashed curve is, therefore, used to predict the behavior of material subject to fatigue cycles with long hold times.

The minimum area fraction is then selected. The value of the area fraction determined indicates the likelihood of failure by the particular mechanism. The fraction can be compared to the inclusion content of the rotor as indicated by the NDE data.

It is intended that the fracture analysis code, FRAC, will ultimately contain correlations between true flaw volume fraction and flaw volume fraction as indicated by results of boresonic examination, as well as a computation scheme to determine the maximum effective area fraction for such three-dimensional clusters. These correlations do not now exist, and the evaluation of flaw density on the basis of ultrasonic signal amplitude currently requires substantial conservatism and subjective interpretation. The data analysis currently in use to reduce the volumetric density to an area fraction is external to FRAC and assumes the effective width of the cluster ($r\Delta\theta$) to be twice the diameter of the largest equivalent flat bottom hole reflector indicated in the cluster. Within this width, all flaw areas, expressed as equivalent flat bottom hole diameters, are projected upon a single (r,Z) plane for comparison with FRAC computations.

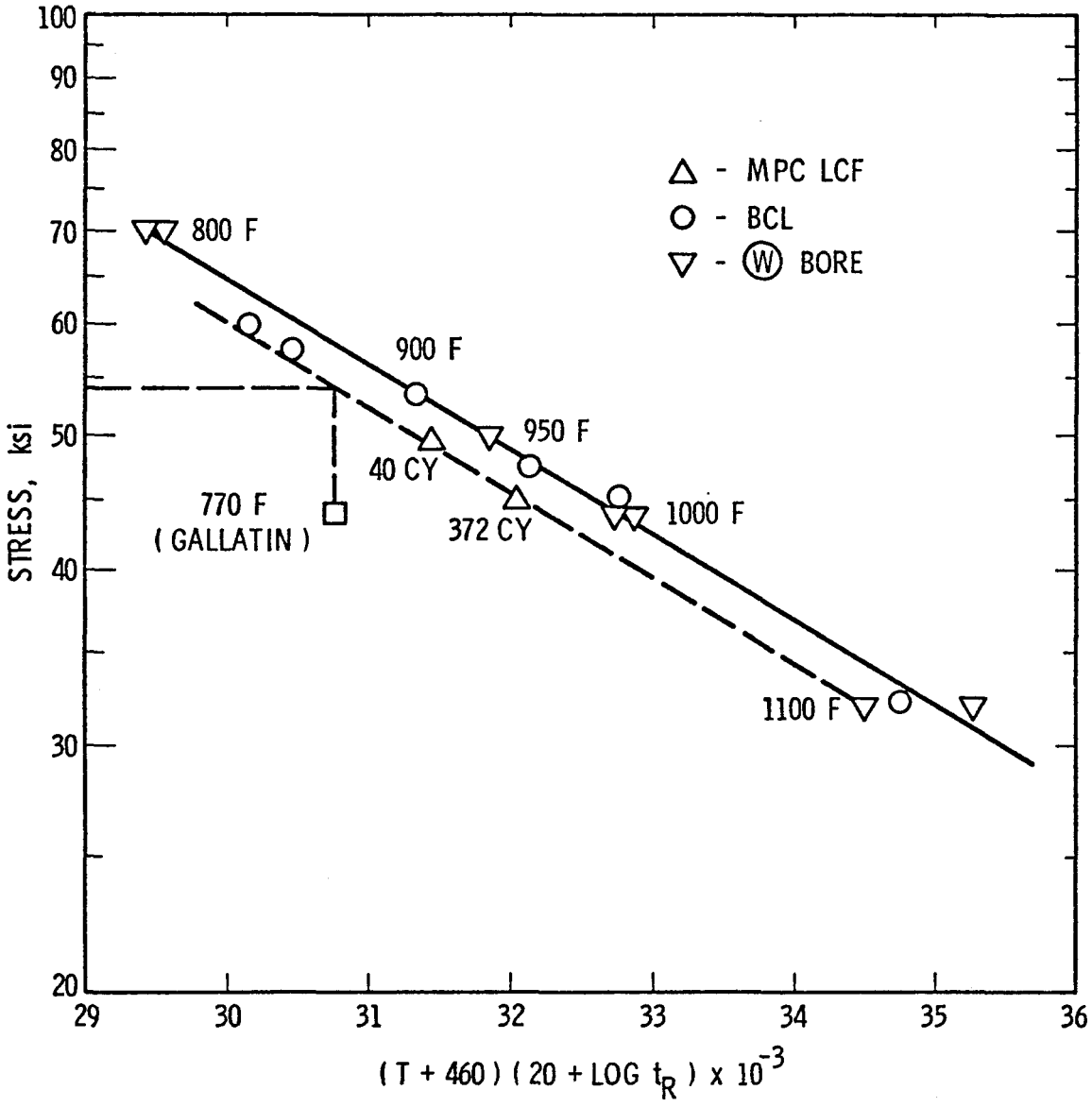

FIGURE 4-7. LARSON-MILLER REPRESENTATION OF MPC, BCL, AND WESTINGHOUSE DATA

Section 5

REFERENCES

1. H. G. Pennick, T. S. Cook, and C. H. Wells, "Programmer's Guide for Fracture Analysis of Steam Turbine Rotors," Report on EPRI Project RP502, May 1978.

2. H. G. Pennick, "Development of a Computerized Rotor Lifetime Analysis System," M. S. Thesis, St. Mary's University, 1978.

3. H. M. Martin, "Steam Leakage in Dummies of the Ljungstrom Type," Engineering, 3 January 1919, p. 1.

4. V. M. Kapinos and L. A. Gura, "Investigation of Heat Transfer in Labyrinth Glands on Static Models," Teploenergetika, 17, 11, 1970, pp. 38-41.

5. D. E. Metzger and J. W. Mitchell, "Heat Transfer from a Shrouded Rotating Disk with Film Cooling," 1965 Transactions of the ASME, Journal of Heat Transfer, Paper No. 65-WA/HT-20.

6. D. E. Metzger, "Heat Transfer and Pumping on a Rotating Disk with Freely Induced and Forced Cooling," Transactions of the ASME, Journal of Engineering for Power, 1970, Volume 92, No. 3, pp 342-348.

7. J. M. Owen, "The Effect of Forced Flow on Heat Transfer from a Disc Rotating Near a Stator," Int. J. Heat Mass Transfer, 1971, Volume 14, pp 1135-1147.

8. F. Krieth, Principles of Heat Transfer, International Textbook Company, 1958, p. 324.

9. W. H. McAdams, Heat Transmission, McGraw Hill, New York, 1954, p. 7.

10. D. A. Weisz, "Analysis of TVA Gallatin No. 2 Rotor Burst. Part II - Mechanical Analysis," 1976 ASME-MPC Symposium on Creep-Fatigue Interaction, R. M. Curran, Ed., American Society of Mechanical Engineers, G00112, 1976, New York, p. 25.

11. C. Wang, Applied Elasticity, McGraw-Hill, New York, 1953, p. 54.

12. O. C. Zienkiewicz, The Finite Element Method in Engineering Science, McGraw-Hill, New York, 1971, p. 168.

13. T. T. Shih and G. A. Clarke, "The Effect of Temperature and Frequency on the Fatigue Crack Growth Rate Properties of a 1950 Vintage Cr-Mo-V Rotor Material," Westinghouse Scientific Paper 77-507-Rotor-P1, September 1977.

14. H. C. Argo and B. B. Seth, "Fracture Mechanics Analysis of Ultrasonic Indications in Cr-Mo-V Alloy Steel Turbine Rotors," Case Studies in Fracture Mechanics, T. P. Rich and D. J. Cartwright, Eds., Army Materials and Mechanics Research Center, AMMRC MS 77-5, 1977, p 3.2.1.

15. G. A. Clarke, T. T. Shih, and L. D. Kramer, "Evaluation of the Fracture Properties of Two 1950 Vintage Cr-Mo-V Steam Turbine Rotors," Final Report, Research Project EPRI RP502, Task IV, March 1978.

16. C. E. Jaske and H. Mindlin, "Elevated Temperature Low-Cycle Fatigue Behavior of 2-1/4 Cr-1 Mo-1/4 V Steels," Symposium on 2-1/4 Chrome 1 Molybdenum Steel in Pressure Vessels and Piping, Metal Properties Council, Second Annual Pressure Vessels and Piping Conference, Denver, September 1970, ASME Publication G11, 1971, pp 137-210.

17. R. M. Curran and B. M. Wundt, "Continuation of a Study of Low-Cycle Fatigue and Creep Interaction in Steels at Elevated Temperatures," 1976 ASME-MPC Symposium on Creep-Fatigue Interaction, ASME Publication G113, 1976, pp 203-282.

Steam Turbine Rotor Reliability - Task Details

Task 2. Nondestructive Evaluation

Prepared by

BATTELLE, COLUMBUS LABORATORIES
505 King Avenue
Columbus, Ohio 43201

Principal Investigators

M. J. Golis
J. R. Fox
S. D. Brown
R. J. Warren

Blank Page

CONTENTS

ILLUSTRATIONS

TABLES

SUMMARY

This is the final report on the first phase of a research program directed at determining the effectiveness of nondestructive means for assessing the presence of objectionable discontinuities within the volume of steam turbine rotors. It discusses the results of both field and laboratory studies conducted primarily during 1977 that resulted in a state-of-the-art report on boresonic examination as well as the technical findings discussed in this report. The general results suggest that significant improvements can be made in the technologies associated with rotor examination, particularly when the NDE results are to be used as the data base for making failure predictions founded on fracture mechanics concepts. Numerous areas of concern are identified, particularly those associated with data gathering (transducers and mechanical positioners) and informational displays (test data formats and completeness). This first phase is to be followed by a comprehensive comparison of the current NDE capabilities with advanced inspection schemes which are designed to optimize the correlation of NDE findings with the data input needed for life-time predictions.

Section 1

INTRODUCTION

This is the Final Technical Report on the Task II-Nondestructive Evaluation activities associated with the EPRI Research Project (RP-502) to improve the reliability of steam turbine rotors. This task addressed the current state of rotor NDE, the performance characteristics of two commercial systems, the multiple inspection of two retired rotors, and identification of those research areas and standardization procedures which should be addressed to improve inspection reliability. Of particular interest are the basics of inspection technique, calibration and data analysis.

The study was a two-phase effort in which Phase A addressed the determination of current bore inspection methodology, while Phase B addressed the effectiveness of the methodology in the inspection of two retired rotors. Included in the effectiveness evaluation was how accurately inspection systems could (1) define flaw location within each rotor and (2) what system elements were in need of further development. This report discusses the findings of these phases through the first two years of the program.

The major accomplishments achieved by Task II include the following:

- Establishment and publication of a state-of-the-art report on steam turbine rotor inspection (EPRI Interim Report NP-744, April 1978)
- Identification of areas in need of technical development for improved inspection
- Selection and coordination of the inspection of two retired rotors
- The findings to date have graphically shown that there are critical areas in need of improvement if the sensitivities and resolutions implied by the requirements of fracture mechanics are to be met in the near future.

As discussed below, new techniques are needed in the areas of data acquisition, display, and interpretation in order to make future inspections faster, more accurate, and in general, more reliable. This report addresses the areas which were explored during the course of the program. A major contribution was a study of the state-of-the-art of turbine inspection and this is summarized in

the following section. A large contributor to measurement of system and particularly transducer performance was the laboratory performance studies conducted at the Battelle-Columbus Laboratories. The major results of these studies are summarized in the subsequent section. The segment of the program that had the largest impact on the state-of-the-art work was the field evaluation studies conducted whenever the rotors were being inspected. All of these topics as well as our conclusions and recommendations are described in the following sections of this report.

Section 2

GENERAL STATE OF TURBINE ROTOR INSPECTION

INDICATIONS OF SIGNIFICANCE

The NDE signals of most interest are those which indicate the presence of discontinuities most likely to initiate catastrophic failures in the near future. Fissures having major dimensions on the order of 0.25 inch and in highly stressed regions of a large rotor are a size and location combination which are considered critical under cold start-up conditions. Such discontinuities should be detectable with a better than 95 percent probability.

Generally speaking, available NDE techniques are only effective in giving location data, and are rather vague regarding size and orientation. Clusters of indications and their volumetric extent are being noted, but area or volume fractions are not being calculated routinely nor can the source of an indication be accurately identified, e.g., an inclusion versus a fissure. This failure is largely due to the relatively large elemental volume which the boresonic beam is using to interrogate the rotor (1/2" x 1/2" x 1/10" nominal). Note that higher performance boresonic systems can improve considerably on this but a corresponding increase in inspection time is the penalty paid for the improved resolution capabilities.

The Nature of the NDE Process

The NDE examination normally falls into two categories: (1) detecting and locating imperfections, and (2) characterizing the imperfections in detail. Historically, the same equipment is used for both tasks to expedite inspections. Thus, inspection systems are designed to have a reasonable probability for detecting imperfections while at the same time, being sufficiently discriminatory to do a satisfactory job of characterizing the detected imperfections. Unfortunately, this dual approach appears to be incapable of generating the degree of detail needed to make an accurate fracture-mechanics prediction because the input information is inadequate. On the other hand, optimally designed systems are showing great promise for producing the information required to give

real credibility to the fracture-analysis predictions. Thus, the most informative procedure is to search the rotor (in a detection mode) to locate all of the questionable regions, then to reinspect (using a highly selective characterization mode) to map out the orientations, sizes, volume fractions, and similar data needed as input to the analytical solutions of failure prediction.

The NDE systems used for rotor inspection represent a compromise between an optimum detection and an optimum characterization capability. It follows that the effectiveness of these systems relies heavily on the data-interpretation capability of their operators. It also relies on each operator's thoroughness. Thus, operator performance is a critical element in current inspections.

Some reduction in operator dependence (or in a sense, some measure of standardization of rotor inspections) is being achieved through the use of calibration schemes, but even these are not universal. Calibration schemes and operating thresholds set the general level of system sensitivity for each inspection. Two types of test targets are used. They are side-drilled holes (SDH) and flat-bottomed holes (FBH). The FBHs range in size from 3/64 to 1/16 inch in diameter. The SDHs are usually 1/8 inch in diameter with one exception at 3/8 inch. These holes are placed in test blocks at different depths so the depth-dependent response of each ultrasonic system can be estimated. Figure 2-1 shows a block developed on this program which is a composite of these types of calibration reflectors. The response of signal amplitude with increasing depth can often be accounted for through compensating electronic circuitry.

The ultimate sensitivity of a boresonic system is often measured by its ability to detect a given size FBH at a specified distance. A typical example would be a 3/64-inch FBH, 1/8 inch from the bore surface. This could represent the minimal detectable flaw for a given system; however, it does not state the probability of detecting such a flaw under normal dynamic inspection conditions. For in-service inspection purposes, a high probability of detecting imperfections of interest is necessary. However, the detection probability should not be accompanied by an excessive number of reported false indications (e.g., those due to nonuniform beam profiles which can lead to duplicate indications, spurious indications caused by variations in coupling media, or similar causes of examination uncertainty).

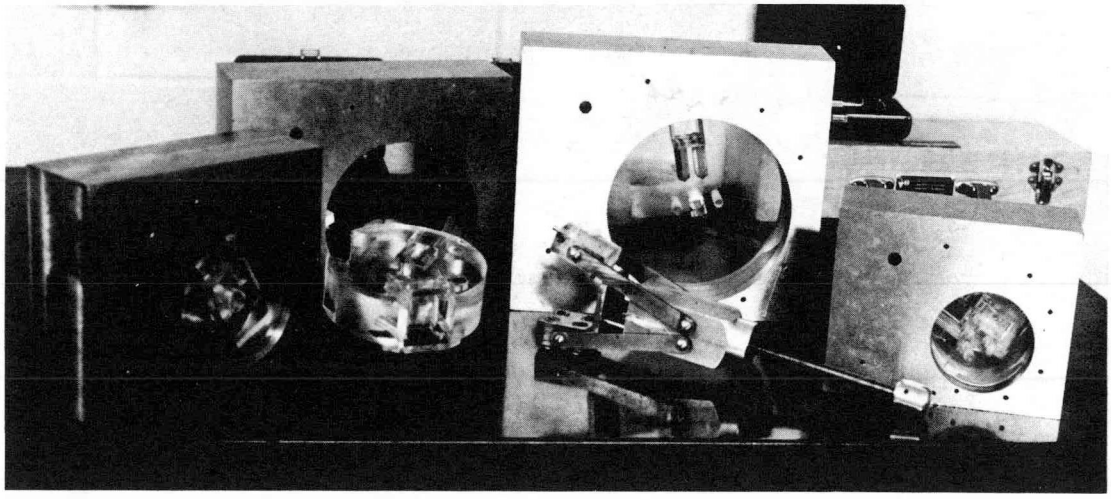

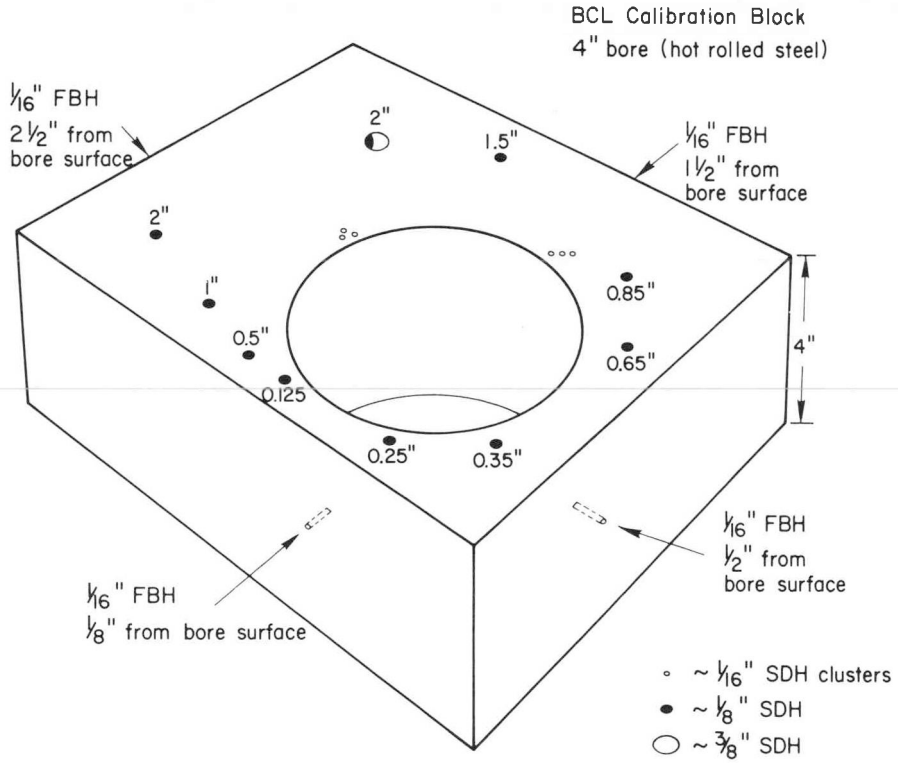

Figure 2-1. Composite Block Showing Types of Calibration Reflectors

A DESCRIPTION OF CURRENT INSPECTION PRACTICES (1-6)

Routine inspections are a loosely coordinated series of surface, near surface, and volumetric examinations of the rotor material. The methods used from the bore include visual, wet-magnetic particle, and pulse-echo ultrasonic examination (boresonic). Occasionally, ultrasonic confirmations are made from the periphery. Table 2-1 lists the types of examinations being performed and their general regions of coverage.

Visual Examination

The visual examination is via borescope and is done before and after bore preparation. Visual examination before bore preparation allows assessment of general conditions regarding the extent of corrosion and oxide formations since the last inspection. Specific items of interest to visual examination include: locations and depths of bottle bores, dimples (local ground-out areas), presence of large cracks, excessive pitting, and any sign of inclusion concentrations or other imperfections which might be exposed by the boring process. The presence of such areas is usually recorded on sketches made by the examiners. These sketches sometimes have supporting photographs where these are useful.

The limitations and uncertainties associated with visual examinations are closely associated with the thoroughness and experience of the operator conducting the examination. There is little assurance that the entire surface of the bore is examined with equal care and attentiveness. The completeness of the reported data, which may have an impact in later examinations (ultrasonics for example), is entirely up to the thoroughness of the examiner.

Magnetic-Particle Examination

The magnetic-particle examination (MT) is by the wet method. In this method, the magnetic particles are suspended in a fluid vehicle to enhance the flow, mobility, and sensitivity of the examination. A current-carrying rod (or a supported cable) is inserted into the bore and made to contact the rotor at the far end of the bore (for blind bores). Another contactor is attached to the outside of the rotor and close to the blind end of the bore. The current passed through the conductor is set at values between 200 and 500 amps/inch of bore diameter.

Table 2-1

EXAMINATION METHODS USED DURING ROTOR INSPECTION

EXAMINATION METHOD	GENERAL REGION OF INTEREST	GENERAL FINDINGS	COMMENTS
Visual (done before and after bore prep to assess general bore conditions)	Bore surface	Surface conditions (cracking, grinding marks, oxide coatings, and general corrosion -- usually pitting)	Bottle bores and grinding marks are indications of previous work done on the bore and suggest potential problem areas. Ground areas adversely affect coupling during boresonic examinations.
Magnetic Particle	Surface and near surface of the bore (effective radial depth, surface to 0.125 inch)	Cracking, segregation, inclusion, pits	Presence of some oxides tend to yield false indications. Incomplete removal may also mask valid indications.
Boresonic	Near surface to OD	Subsurface reflectors such as nonmetallic inclusions, hydrogen flakes, cracks, porosity, and regions of localized alloy segregation	Interpretation of cause for indications very difficult. Location of reflector most accurate information available. Echo amplitude alone is not a reliable indicator of actual size, shape, or type of internal discontinuity.
Pitch/catch	0.125-3.0 inches		
Radial L wave*	0.50 to OD		
Radial S wave**	0.25 to OD		
Axial S wave	0.25 to OD		

*L wave is the longitudinal wave directed outward toward the OD.

**S wave is the shear or transverse wave usually directed at angles of 45 (axial) and 60 (rotational) degrees.

While the current is still being applied, the liquid containing the black suspended particles is sprayed over the upper half of the rotor bore. (Note that the lower half of the bore is flooded with liquid and thus no indications can be found there.) The current is discontinued, the conductors are removed, and the borescope is inserted to view the indications. Relevant indications are reported by hand and photographed if of particular interest. The rotor is then rotated 180 degrees and the procedure is repeated.

The MT data are collected in a manner similar to that of visual inspection with the same inherent limitations. With magnetic particles, however, the probability of detecting fine surface cracks and near-surface large discontinuities is enhanced due to (1) the inherent contrast associated with dull black magnetic particles viewed against a shiny metallic background, and (2) the magnetification qualities associated with the accumulation of particles near a region exhibiting a strong leakage magnetic field. The MT indications are normally slightly more extensive than those found by visual examination since they represent both surface and near-surface discontinuities. Very small cracks that can be missed easily during visual inspection are discovered by MT because small cracks can yield relatively strong leakage fields.

The sensitivity of magnetic-particle examination was generally evaluated on rotor grade materials and summarized in Figure 2-2. It is evident that when an entire magnetic half-space exists (as in the case of a rotor bore), the sensitivity to subsurface discontinuities drops dramatically. We suspect there exists an uninspected annulus around the bore since the depth of magnetic-particle detection does not meet or overlap, the minimum depth at which boresonic examinations become effective, in some cases. The size of this annulus varies as the near bore surface resolution of the boresonic systems.

BORESONIC EXAMINATION

The boresonic apparatus constitutes the major capital investment in equipment associated with rotor inspection. Mechanical devices position ultrasonic search units (transducers) precisely and electronic detection and signal processing devices display the search unit findings. The electronic packages for ultrasonic pulse generation and detection are usually commercially available configurations. The automatic gating systems are also commercially available but the specific selection of components and their assembly into a single

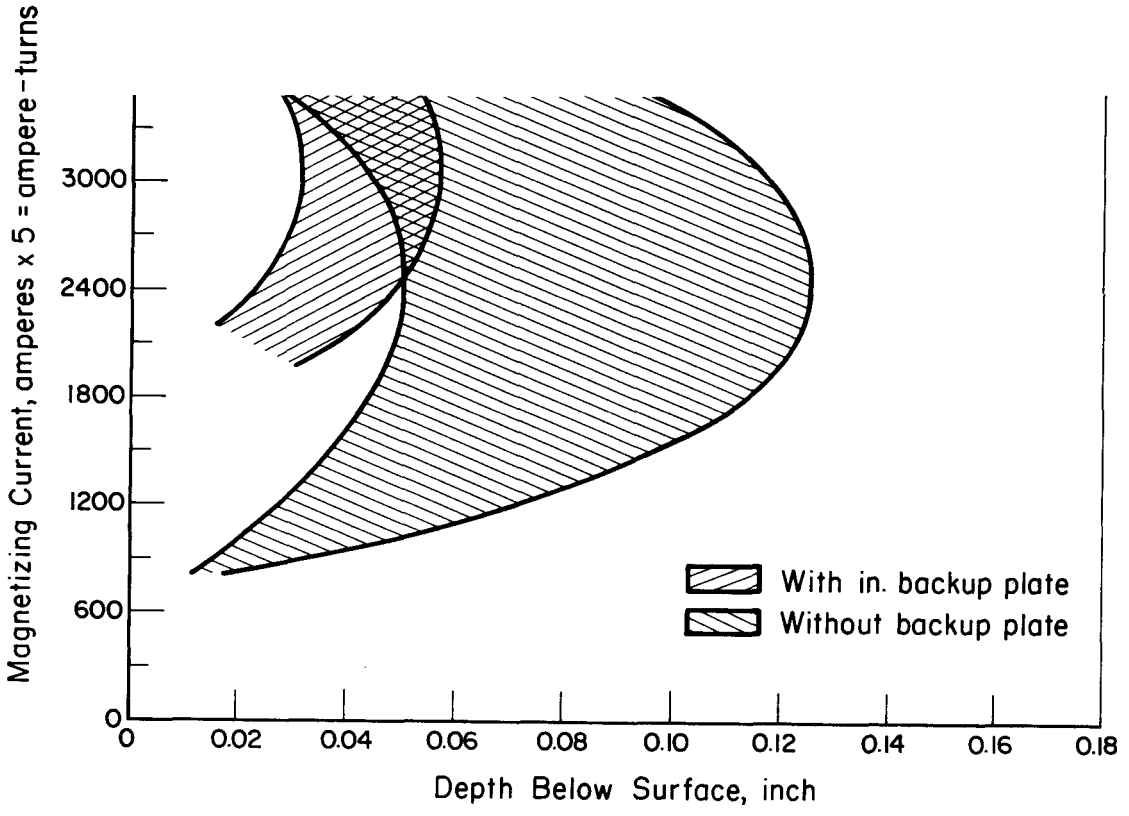

Figure 2-2. Sensitivity of Magnetic-Particle Examination to Subsurface Discontinuities as Measured on Flay Bottom Holes in 1/4 Inch Plate of Retired Rotor Material. The Lower Sensitivity is Found when the 1/4 Inch Plate is Backed by an Additional 1 Inch of Rotor Steel.

package is normally directed by each inspection group. Figure 2-3 shows schematically the major elements of a typical boresonic system.

Details of the Operational Boresonic Examination

The extent of boresonic coverage varies depending on equipment adjustment. Most positioning equipment is automatic with a manual override. The time/amplitude gates used when automatic recording usually do not follow the contour of the rotor outside diameter (OD). The gates are usually set according to the minimum distance from the transducer (within the bore) to the geometrically varying OD reflecting surface.

Scanning patterns usually call for 0.25-inch axial increments when continuous rotational scans are being made while 5-degree circumferential increments are used when continuous axial scans are being made. These choices of axial and circumferential increments represent engineering judgements based on a compromise between the ultimate resolution of the inspection apparatus and the necessity for gathering a large amount of data in a very short time period. The boresonic data must be accumulated and assimilated in a reasonable time (usually a few days) to keep the cost of inspections to a minimum. Our studies have shown, however, that these increments are too wide for effective correlation of NDE results based on fracture-mechanics requirements.

The bore of each rotor to be inspected must be prepared by honing to remove the accumulated oxide layers and general corrosion products which form during service. This removal is less critical for boresonic examination than it is for effective visual and magnetic-particle examination based on comments by several inspection personnal. However, the extent of the honing has been of some concern to several inspection groups since visual and magnetic-particle (MT) indications may be masked and artifacts induced if all of the oxide film is not removed. Some inspection groups require the bore to show bare metal throughout. In the field, 0.01 to 0.02 inches of material are typically removed from the bore surface. This amount does not always assure complete removal of oxide layers, particularly in areas which have been ground out previously.

The "shoes" which carry the search units into the bore may be designed to give as many as four modes of examination. These modes and their areas of application are listed in Table 2-2. Schematic representations of each of them are shown in

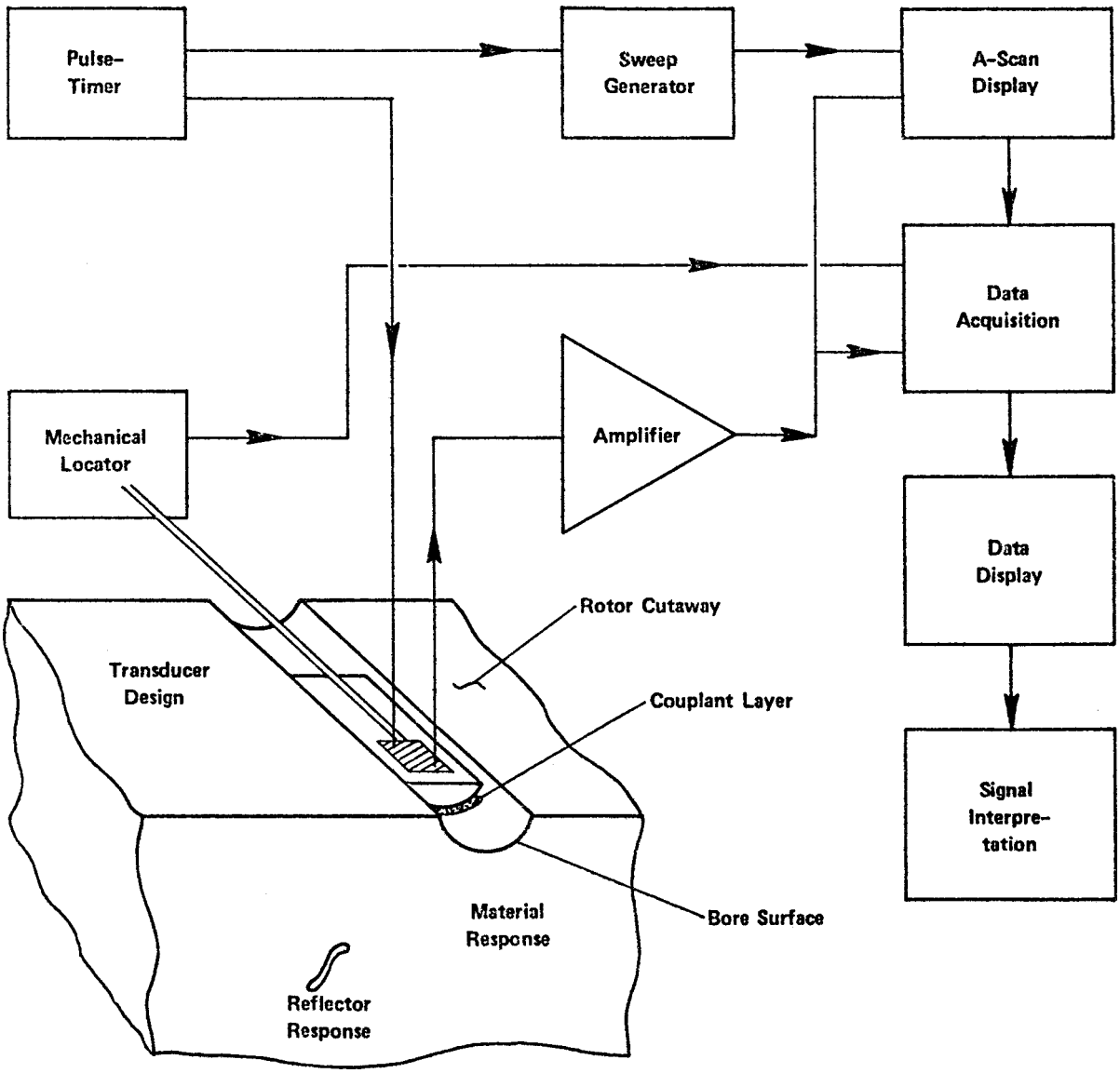

Figure 2-3. Schematic representation of a typical boresonic system indicating the major electrical, mechanical, and electroacoustical elements.

Figure 2-4. The radial-longitudinal mode is used for overall volumetric scanning and is effective from near the bore to the OD of the rotor. It is also used to locate the shoe precisely within the bore since this mode generates an outline of the OD contour as the shoe progresses along the bore. The radial-(longitudinal wave) pitch/catch mode concentrates on the region directly adjacent to the bore. This mode is considered by some to be the most useful mode of boresonic examination since it is carefully examining the most highly stressed region of the rotor. The lateral (or spatial) resolution is good since reflectors are close to the search unit. However, this resolution is still limited by the size of the transducer; larger transducers yield poorer resolutions.

Table 2-2

BORESONIC EXAMINATION MODES

MODE	APPLICATION AREA
Radial - (Longitudinal Wave)	General volumetric discontinuity throughout the body of the rotor. Most sensitive to reflective surfaces concentric with the bore surface.
Radial - Pitch/Catch (Longitudinal Wave)	Discontinuities within 1/8 inch to a few inches of the bore. Most sensitive to reflective surfaces concentric with the bore surface.
Radial - Shear Wave	General volumetric discontinuity throughout the body of the rotor. Most sensitive to reflectors perpendicular to the direction of wave propagation (60 degrees CW and CCW).
Axial - Shear Wave	General volumetric discontinuity throughout the body of the rotor. Most sensitive to reflectors oriented transversely to the axis of the rotor and inclined at an angle of 45 degrees with respect to the rotor axial center line.

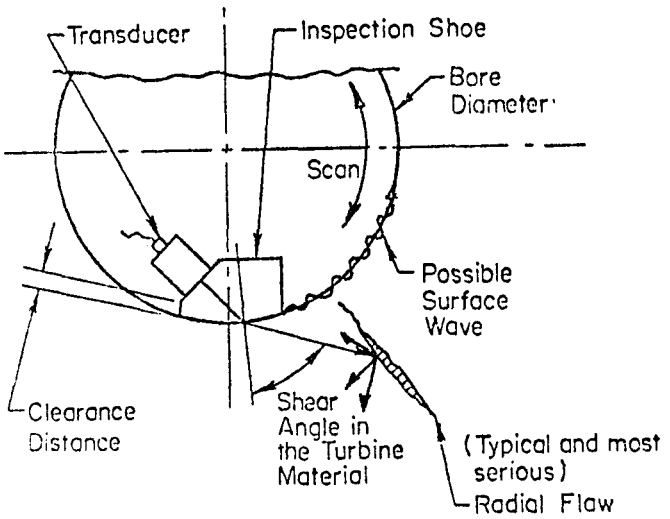

(a) RADIAL SHEAR

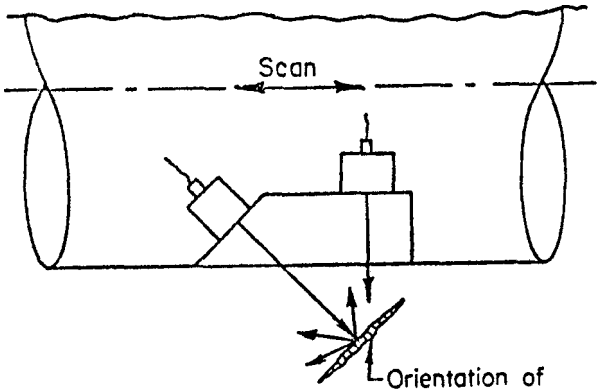

(b) AXIAL SHEAR AND RADIAL LONGITUDINAL

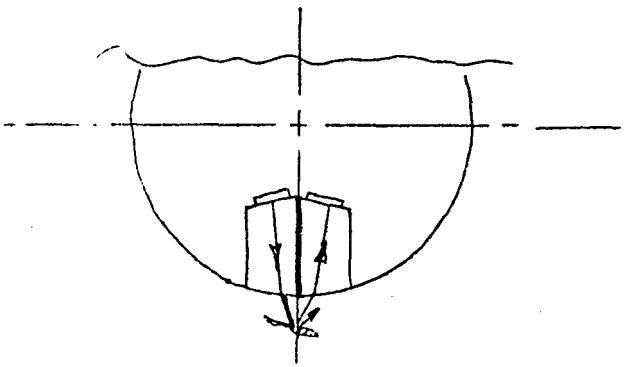

(c) Radial Pitch/Catch in "Line Focus" Orientation

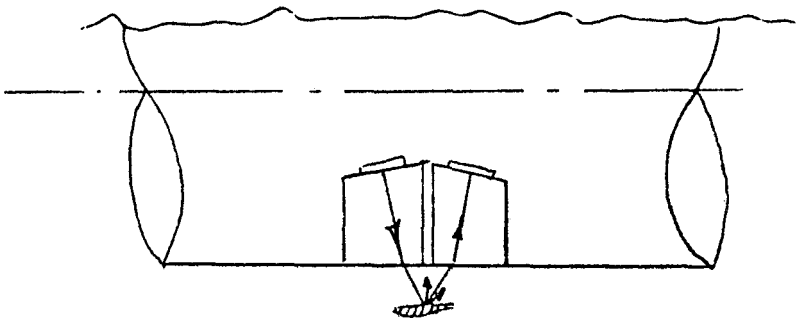

(d) Radial Pitch/Catch in "Point Focus" Orientation

Figure 2-4. Boresonic Modes of Examination

It should be recalled that catastrophic rotor failures are often initiated at the near-bore region. The radial shear and axial shear modes are considered by some to be the best attempts to date to be sensitive to radially oriented discontinuities. But even these modes, which introduce the ultrasonic waves at relatively steep angles, must still have the reflector send some component of the wave back to the sending transducer. (Note that in Figure 2-4a that most of the sound reflected from the flaw would not return to the sending transducer.)

The boresonic equipment being used both in shops and in the field represents a rapidly changing technology. The special gating and distance amplitude correction (DAC) accessories are often custom designed for the boresonic application. Interestingly enough, the piezoelectric transducers being used by two out of three of the best known inspection groups are supplied by a single manufacturer.* Today's field inspection equipment incorporates recent changes in available hardware and still more improved units are on order. The system improvements on order lie mostly in the accessories and only a little in the fundamental ultrasonic signal gathering units, i.e., the transducers. We feel that some fundamental improvements are needed in transducer design.

Also needed are modifications to the bookkeeping of gathered data. The analysis, display, and interpretation of ultrasonic indication data may be expedited with the projected use of computer analysis schemes but these are still in the planning or early prototype stages.

Mechanical positioning and scanning equipment is of generally sound design with a fair degree of repeatability. Finer resolution is available from the systems in use today, but it usually is not used since finer scan increments extend the overall inspection time. When a specific indication is considered of interest, the resolution of these systems can be made finer so that slow, detailed scans of particular regions of interest can be made with the intent of improving interpretation possibilities; however, spatial resolution is not improved since the same transducers are being used for detection and characterization. The mechanical designs have also been upgraded within the past two years and are believed to be sufficiently accurate for general surveillance of rotor forgings but their use for detailed, in-service inspection (ISI) characterization is questionable.

---

*Harisonic Laboratories, Inc., 215 Stillwater Avenue, Stamford, CT 06902

Numerous parameters influence boresonic examination. Some typical examples include the system's electronic component settings, methods of data recording, coupling techniques, transducer designs, and mechanical positioning configurations. These all have an effect on the system's capability to detect natural flaws, gage their depth and lateral resolution, and discriminate against unwanted background noise and false indications. Impressions obtained from technology reviews and observations of inspection teams and their respective systems are shown in Table 2-3. The parameters in Table 2-3 are listed from the most to the least significant.

The curves in Figure 2-5 have been generated from experimental data gathered using commercial transducers constructed to the designs of pitch/catch units currently in field use. A 3/8-inch SDH was used to normalize all signal levels whether they be from SDH or FBH. Thus, these curves are a composite estimation of the performance of two calibration standards (1/8-inch SDH and 1/16-inch FBH), three examination transducers (all pitch/catch), and three thresholds commonly used to establish recordable indications.

In practice, the precise level of these thresholds is somewhat arbitrary in that some operators may elect to record signals below the thresholds. For example, a given indication may appear to be part of a cluster. Some of the cluster may have been above the threshold and in the immediate vicinity of the given indication. Thus, the indication can help to define the extent of the cluster.

It is significant that the effective maximum sensitivity exhibited by boresonic systems can range anywhere from less than 1/32-inch effective flat bottom hole (EFBH) diameter to greater than 1/8-inch EFBH diameter within the nearest half inch from the bore. The system showing the greatest control within the dynamic range of its performance as well as the highest sensitivity in the first 1/4 inch from the bore is System B in Figure 2-5. The region between the bore surface and the first 1/10 inch from the bore is examined, largely, through the use of magnetic-particle methods.

Some General Comments on Rotor Inspection

The most quantitative data available from rotor inspection are associated with the location of (1) bore surface imperfections and (2) subsurface reflectors

Table 2-3

PARAMETRIC INFLUENCES IN BORESONIC EXAMINATION

PARAMETER	GENERAL EFFECTS	SPECIFIC EFFECTS
Bore Condition	Ground out areas and/or bottle bores can make boresonic examination impossible (oxide residues have little effect).	Loss of couplant and irregular coupling of transducers make it impossible to have ultrasound enter rotor volume uniformly.
Coupling Techniques	The flowing system is subject to shoe noise and numerous mechanical difficulties.	Interferes with interpretation of indications and slows progress of the tests.
	The presoak method when coupled with high-pressure shoes reduces noise and mechanical uncertainty.	More uniform mechanical system behavior.
Mechanical Positioning Equipment	Quite effective for general scanning. Questionable for use in detailed comparisons of test results from one ISI to the next.	Mechanical design (which indirectly affects coupling uniformity) is considered one of the weakest system elements in today's inspections with much room for improvement.
Recording Threshold	Establishes the severity of a reflector needed before the boresonic system will consider it as an indication at all.	This major inspection procedure parameter has been shown to disallow consideration of potentially critical reflectors.
Operating Frequency	High frequencies show better depth and cluster resolution.	Shorter wavelengths offer higher reflectivity to internal discontinuities.
Calibration Methods	Can subject sensitivity of boresonic inspection to moderate variations based on areas of interest. No adequate calibrations exist for the MT inspection.	Sets the thresholds of gates and alarms which control those indications which are considered critical to service.

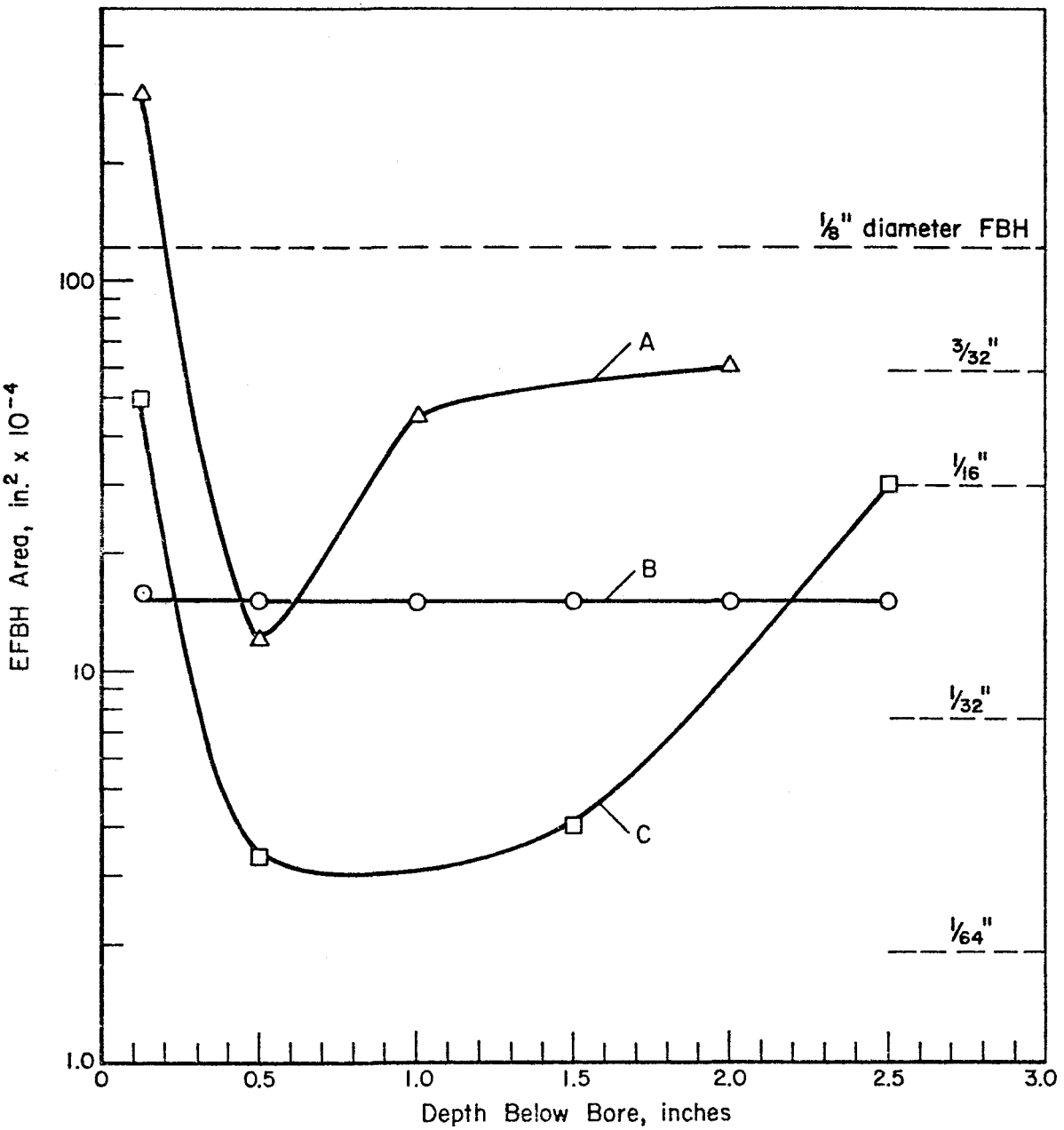

Figure 2-5. Comparative system sensitivities expressed in typical engineering units (pitch/catch). The B system is depth independent and most sensitive in the near bore region.

(through ultrasonic means.) This locational information may be supplemented with severity and/or complexity data when seen by the operator on the ultrasonic instrument's oscilloscope. Supplemental information could include (1) the amplitude of the pulse received from a sound wave reflector, (2) the area over which a single indication persists, (3) the variation in range between the transducer and the reflector as the transducer is translated (either axially or rotated around the bore) for "traveling indications", (4) the presence of other nearby reflectors suggesting a cluster of reflectors, (5) the shape or spectral content of the reflected pulse, and (6) a detailed correlation of reflectors detected from different aspect angles and modes of examination. Although all of this information is available, the most commonly recorded parameters are only (1) the amplitude of the received pulse, (2) whether the pulse is part of a cluster of indications, and (3) whether it "travels" with movement of the transducer. Only for large indications and clusters of indications, is the area over which reflections persist recorded.

It is readily recognized by personnel performing rotor inspections that these measured parameters are but generalizations of the actual conditions within the rotor and are rather questionable with regard to predicting, with a high degree of accuracy, the magnitude, orientation, and acuity of an internal fissure. Thus, the interpretation of the boresonic examination results (size, shape, orientation and location) is largely up to the operator. Ultrasonic data cross correlations can be run between what is "seen" within the rotor from several different directions and under several different examination conditions with a corresponding improvement in the reliability of any given inspection. This is in fact done in special cases where it is suspected that a large fissure is in the rotor, but it is rarely done during routine inspections.

Problems arise most often when identifying finely dispersed collections of reflectors because of the limited resolution (both depth and laterally) of the ultrasonic systems. This limitation makes it difficult to separate echos from other nearby fissures (within 1-2 diameters when the fissures are about 1/16-inch FBH). Thus, it is usually impossible to differentiate between a singular indication and a closely packed collection of several small reflectors. Preliminary laboratory results show that reflectors about 1/16-inch diameter (or less) are not resolvable using typical commercial transducers and when found as clusters separated by 1-2 diameters of each other.

THE MOST PROBABLE CAUSES OF INSPECTION UNCERTAINTIES

Rotor inspection uncertainty can arise in three fundamental areas. These are (1) the random physical nature of the discontinuities found within the rotor (shape, size, surface roughness, and acoustic impedance), coupled with the inability of ultrasonic methods to uniquely characterize their shapes and sizes, (2) the inaccuracies and physical limitations associated with the inspection equipment, and (3) the human factors associated with the gathering and translation of large volumes of detailed information into a readily interpretable format. These uncertainties are discussed, as appropriate, according to each of the examination methods now used in rotor ISI.

Visual and Magnetic-Particle Examination Uncertainties

The major problems in these two surface techniques are (1) the human factors activity of translating the visual observations into a reliable report and (2) the absence of a quantitative estimation of crack depth. Bore access being only through a borescope makes data interpretation from either source entirely up to the operator. Although the jobs being done are considered generally acceptable, uniformity of coverage and interpretation level is a potential source of inspection uncertainty.

The magnetic fields being established in the bores for magnetic-particle examination are of such a strength that some background noise (spurious indications) are being formed on the rotor material surface. Thus, the examination sensitivity is estimated to be near an optimum. The uniformity of examination, on the other hand, relies largely on operator diligence in applying the magnetic-particle fluids uniformly. The depth of penetration and ability to detect subsurface discontinuities of magnetic-particle examination, however, is limited to approximately 1/8, at most, as shown in Figure 2-2. Thus, it is critical that a good, near-surface boresonic system be used to complement the magnetic-particle examinations being performed if uniform coverage with depth below the bore surface is to be achieved.

Boresonic Examination Uncertainties

Boresonic examination can be influenced by all three causes for rotor inspection uncertainty. Since several types of discontinuities are of interest (cracks, inclusions, segregation, distributed fissures, etc.), their random presence makes it impossible to set the performance characteristics of the boresonic

system in such a manner as to assure identifying any one type of discontinuity. Based on studies to date, if an internal fissure is about 1/8 inch or larger, volumetric in nature, and within a few inches of the bore, its presence can probably be uniquely determined. When the fissures are less than 1/16 inch, there is little chance that the current ISI systems are capable of returning to the same location and identifying the same reflector with a high degree of reliability under normal inspection circumstances. If the reflectors are generally planar, radially oriented and possibly skewed with respect to the rotor axis, these sizes can increase substantially. To what extent they increase is not known based on current experience.

Much of the difficulty in lack of repeatability comes from the inability of the mechanical systems to precisely repeat their travel paths from one scan to the next. This is particularly true when the positioning equipment is totally disassembled and then repositioned on the rotor. There also appears to be a mismatch between ultrasonic beam characteristics and scan increments as dictated by the boresonic written procedures. Figure 2-6 shows a typical transducer characterization as measured on a pitch-catch transducer. The width of the beam near the peak detection region is less than $\pm$0.100 inch. Yet the normal scan pattern in the axial (Z direction) is 0.25 inch. This indicates that at least 0.05 inch of material is not being inspected every 0.25 inch of axial translation. The situation is somewhat compounded when side lobes are present in the beam profiles leading to redundant recordings of the same geometrical reflector.

Generally speaking, inspection groups feel that the overall condition of a rotor can be reasonably assessed from the statistical number of small indications and their general distribution throughout the rotor. This information would be augmented with the location of larger indications when they are present. However, the characterization potential of boresonic examination is not being exploited to the extent that it could or should be.

Translating precise position data to a generalized format suffers from the human factor effects common to visual data interpretation as well as the limitations inherent in automatic systems. Some data are gathered by operators viewing position indicators with inherent parallax problems and if care is not taken to account for this condition, random variations can be expected in the positional data. Slight errors can be expected in duplication of data recording

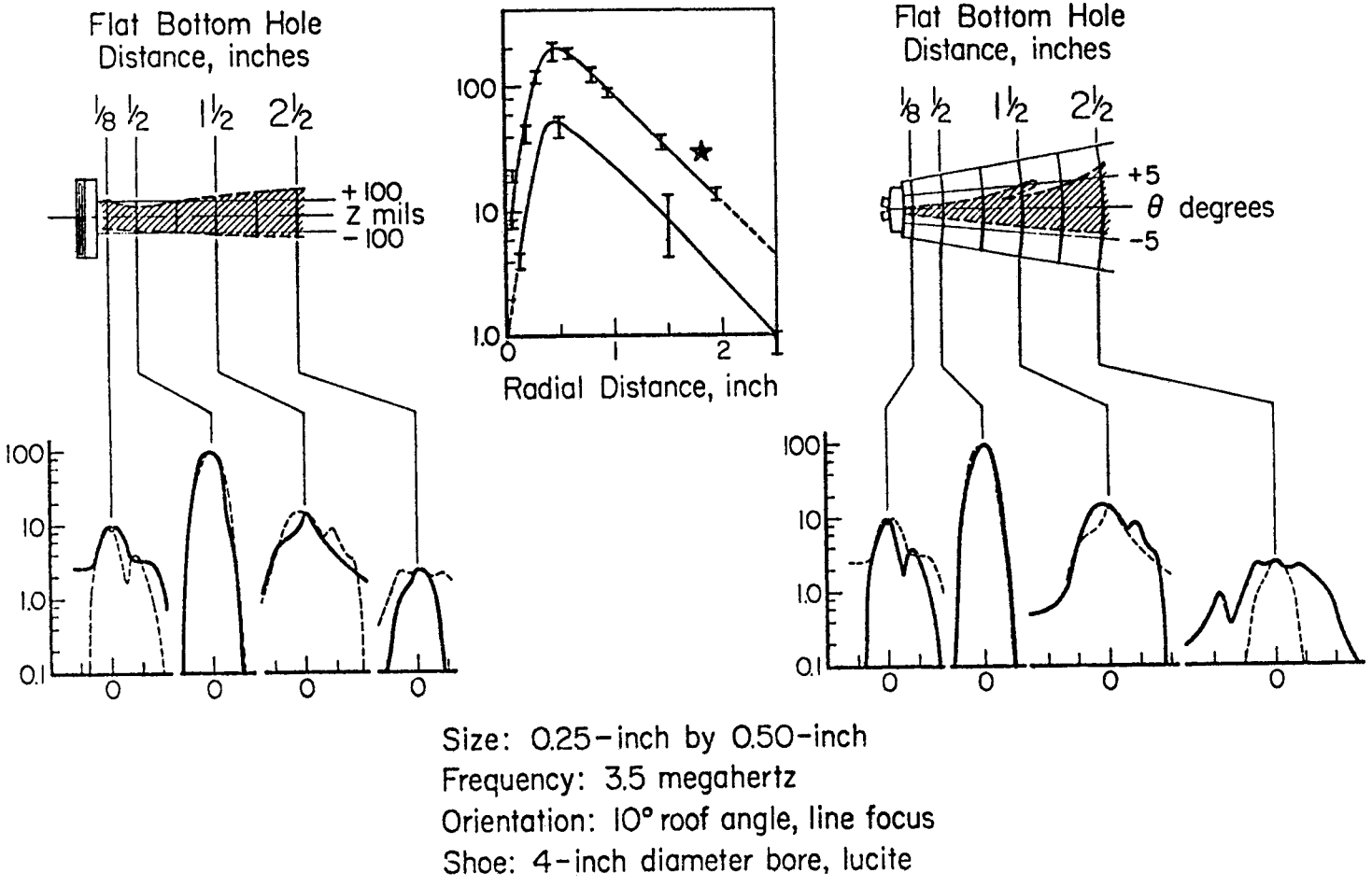

Figure 2-6. Summary sheet showing the overall propagation characteristics of a typical boresonic transducer including beam spread and decay of signal amplitude with distance from the bore surface.

since some indications are recorded by hand. Even different machine-based problems arise with automatically recorded signals since some ambiguities have been found regarding the exact correlation of a detected flaw's location and its recorded ultrasonic signal amplitude. There may even be variations in the precise threshold levels at which signals are recorded. Lastly, the response with depth of some systems is not uniform and thus automatic recording schemes can lead to signal level errors on the order of $\pm$ 30 percent, depending on the indication depth below the bore surface.

All systems are not equally sensitive to rotor internal discontinuities because of differences in calibration standards and preference for one type of transducer or another. These differences and preferences may have been partially identified through the detailed sectioning of the inspected rotor. Some groups rely on shear wave data (these data appear to be more reliable in the opinion of the operators of one system.) On the other hand, another group relies heavily on data gathered via the pitch/catch mode of examination. Note that when discontinuities are essentially isotropic, this differentiation probably makes no particular difference. However, when discontinuities are preferentially oriented and highly anisotropic (e.g., radially propagating cracks), this difference would surely yield different inspection results. Plots of the volume fractions of different types of flaws using these two systems have shown marked differences as shown later in this report.

The general conclusion is that the uncertainties associated with rotor inspection are not unlike those found in other applications of nondestructive examination when the work must be done to a high precision and in a remote, difficult environmental situation. We feel, however, that significant improvements can be made and would result in much more reliable inspections.

Section 3

LABORATORY PERFORMANCE STUDIES

Although the major thrust of this program has been the field evaluation of operational inspection systems, numerous specific areas had to be addressed in a laboratory setting by virtue of their long-term data gathering characteristics as well as the need for interactions with large computer systems which were helpful in data reduction. This section discusses a few of these selected studies which have made a significant impact on our overall assessment of the state-of-the-art of turbine inspection.

TRANSDUCER PERFORMANCE STUDIES

The effectiveness of ultrasonic transducers was evaluated through the detailed plotting of their respective beam profile characteristics using typical calibration holes as test reflectors. Thus pitch-catch transducers of the same designs as those used in the field were carefully scanned past the side drilled holes and flat bottomed holes of the special calibration block shown in Figure 2-1 of this report. A typical example was shown in Figure 2-6. The net result has been an estimation of the beamwidths available for guidelines to the setting of increment lengths when rotor scanning procedures are being established. As noted earlier, the $\pm$ 0.10 inch beamwidths found in some of the more selective P/C units are too narrow to be used for a totally assured scan of the rotor when increments of 0.25 inch are the scanning increment.

The widths of the beams varied from a minimum of approximately $\pm$ 0.10 inch to a maximum of $\pm$ 0.75 inch. Since this broad a range can be encountered in practice, it is necessary that the displacement increment for scanning be selected on the basis of each transducer's beamwidth. For typical pitch-catch units, the increments should be on the order of 0.2 inches. For the larger shear wave transducers, the minimum increments can be increased to 0.4 inches due to the larger size of the transducers. Appendix C shows several of the typical scans developed during the laboratory studies of transducer performance.

PROBABILITY OF FLAW DETECTION CALCULATIONS

The transducer-response curves of Appendix C can be used to determine the probability of flaw detection and its variation as a function of the axial incremental distance Δz between successive scans. Our objective is to use the "width" of the transducer-response curve to specify the Δz required to achieve a given level of inspection performance in terms of probability of detection. This concept provides the field operator with a practical procedure for setting the axial scanning inspection increment based on field-generated transducer beamwidth data.

Figure 3-1a is an axial response curve for a hypothetical transducer. For scanning in the θ direction, this response curve represents the behavior of the transducer transverse to its direction of scan. The effective width of the response curve is determined by the threshold alarm level. In Figure 3-1a the alarm level sets the effective width to 400 mils based on a half peak value threshold. Any incoming signal exceeding the alarm level is recorded as an indication. Signals below this value level are ignored. Thus the alarm level criterion changes the initial transducer response curve to that shown in Figure 3-1b.

The probability of flaw detection can now be calculated on the basis of geometrical considerations. Figure 3-1c shows the alarm-adjusted response curve superimposed on the probability density curve for any given size calibration standard being located anywhere within a given Δz. The probability of detection is the ratio L/L'. Probability of flaw detection curves based on the laboratory data were collected and are plotted in Figure 3-2 and Appendix D. In each of these figures, the further to the left the curves are located, the higher is the probability of flaw detection for any given transducer. In Figure 3-2, an axial scanning increment of 0.100 would result in about a 100% probability of detection for reflectors above the alarm threshold level. The probability drops to 0.8 in the near bore area (1/8" below bore surface) for this particular case. If the scan increment is increased to 0.250 inches (the common increment found in inspection at the start of this program), reflectors 1/8" from the bore would be missed about 2/3 of the time while those reflectors 1/2 inch from the bore would be missed about 1/3 of the time. All reflectors below about 1 inch would be detected all of the time.

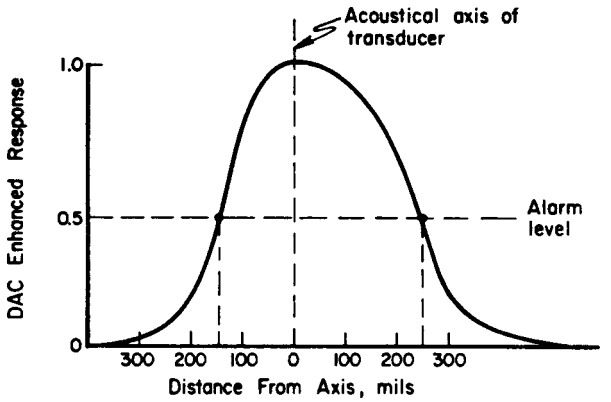

Figure 3-1a.

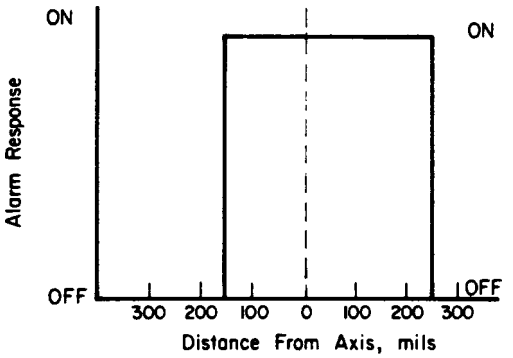

Figure 3-1b.

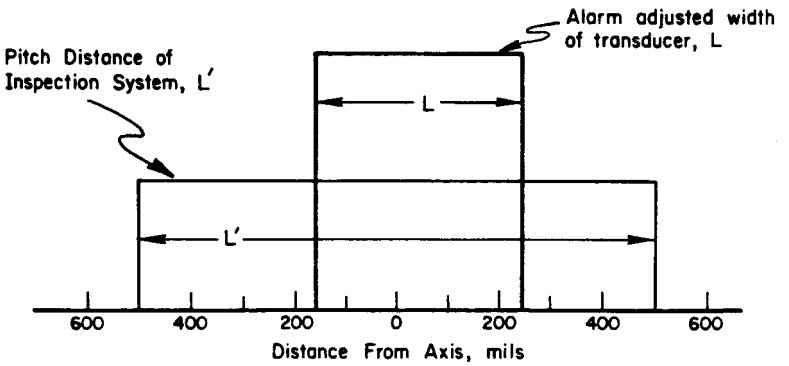

Figure 3-1c.

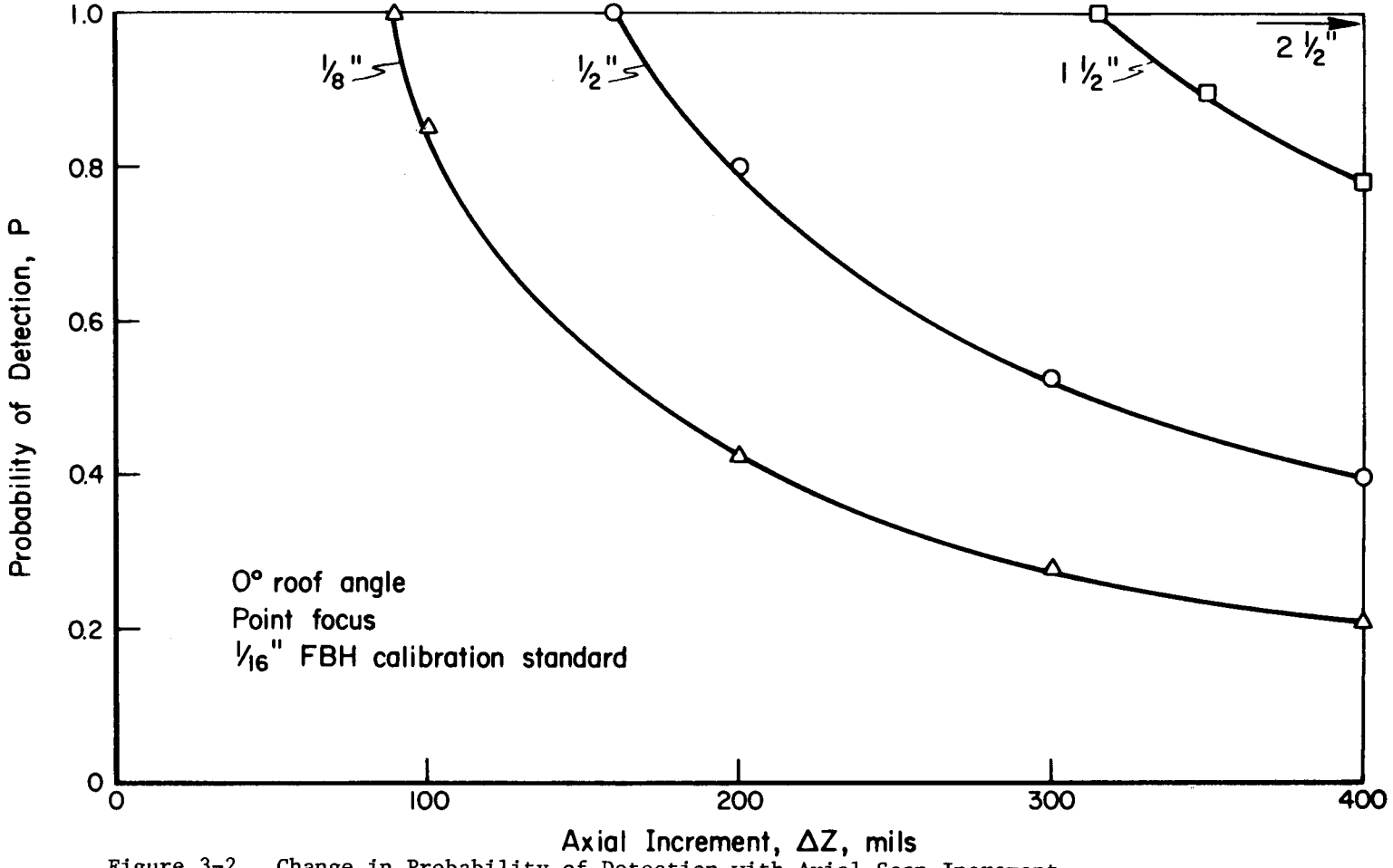

Figure 3-2. Change in Probability of Detection with Axial Scan Increment

Section 4

FIELD EVALUATION STUDIES

MECHANICS OF ROTOR STUDIES

Rotor Selection

The selection of rotors was a process of requesting candidate rotors from utilities by EPRI, tabulating the information available on each rotor, gathering additional information where necessary, and final selection of the rotors based on the needs of the RP 502 program.

Based on the initial list provided by EPRI, various utilities were contacted as to the availability of rotors for use on the RP 502 program. Mechanical property data and inspection data were requested and received on eight rotors. This information was summarized and tabulated for use in selecting the rotors to be used for nondestructive inspection and dissection. The tables of the Joppa #3 and Buck #6 mechanical property and inspection data are shown as examples in Tables 4-1 and 4-2.

Selection of rotors was based on the following criteria:

- Size-preferably greater than 100 M watt
- LP-IP emphasis
- Near-bore nondestructive indications
- Prior to 1954 vintage rotor subjected to $\sim$ 1850^{o}F second cycle austenitizing temperature heat treatment (Grade C)
- Clean bore condition - without grindouts and bottle bore regions.

To aid in the assessment of rotors prior to actual selection, BCL constructed a scanner for use in field rotor ultrasonic evaluation. The scanner was a hand-operated device capable of manipulating typical boresonic transducers for general assessment of rotor conditions. The unit was used later in the program for spot checking regions of the rotors prior to rough cutting and for a recheck on the general location of reflectors prior to final rough cutting. The Joppa #3 turbine rotor was selected as the initial Task II inspection candidate. Its

Table 4-1

JOPPA #3 MECHANICAL AND INITIAL NDT DATA

MANUFACTURING NDT

Peripheral sonic test revealed few scattered indications, A=5-10% at midbody, 0<r<2"

MECHANICAL

	r_1	r_2
σT (kpsi)	123.8	123.3
σY (kpsi)	96.9	92.3
% Elong.	14.0	15.0
% R/A	39.5	44.0

IN-SERVICE NDT

VISUAL (Bore)

Ind. from bore end to 9th stage, L-1/8"

MAGNETIC (Bore)

Same as visual, grind-caused ind. to appear & disappear

BORESONIC

- Specific Ind. - 86

  A = 5-25%
  Position
  7/8"<r<3"
  Location (Stage)
  20th-5 Ind.
  14th-19th-71
  9th & 10th-10

- Area Ind. - 6

  A = 3-15%
  Position
  0<r<3.5"
  Location(Stage)
  Gen. end coup. to 18th stage.
  13th-16th.
  9th & 10th.
  1st rotor packing

PERIPHERAL SONIC

- Specific Ind. - 28

  A = 10-30%
  Position
  1/4"<r<3 3/4"
  Location (Stage)
  10th-19th

- Area Ind. - 12

  A = 5-40%
  Position
  0<r<4 3/4"
  6"<r<8" (9th stage)

- Area & Level Ind. - 8

  A = 5-60%
  Position
  r_{max} = 9"
  Location
  In unbored sect. from turbine end jnl. to 1st rotor pack

Table 4-2

BUCK #6 MECHANICAL AND INITIAL NDT DATA

MANUFACTURING NDT

Peripheral UT. Several ind. ~5-10% A, r=3" in the IP end

MECHANICAL

	R_1	R_2
σ_T (kpsi)	130.0	128.0
σ_Y (kpsi)	100.0	100.0
% Elong.	15.0	13.5
% Red. Area	34.1	31.5

IN-SERVICE NDT

VISUAL (Bore)

Five areas which had been ground. Z = 5'4", 6'-4", 7'-3-1/2", 8'-8-1/2", & 11'-4" from turbine end had been ground to depths of 1/2", 3/8" & 3 at 1/8", respectively. (Done during manufacturing.)

MAGNETIC (Bore)

Numerous ind. Most were 1/16"<ℓ<1/8". In the region of the 21st to 22nd stage, semicontinuous ind. with ℓ-6-3/8". This reflects a change from the '67 report.

BORESONIC

- Discrete Ind. - 149

  A = 3-25%

- Cluster Ind. - 16

  A - 3-10%

- Cloud Ind. - 11

  A - 3-10%

  Position (All Ind.)
  1/8"<r<5"

  Location
  7-1/2" to 160" from turbine end

PERIPHERAL SONIC

- Discrete Ind. - 71

  A = 5-110%

- Cloud Ind. - 110

  A = 5-40%

  Position (All Ind.)
  1"<r<8"
  most within 4"
  Location
  Full length of bore

selection was governed primarily by two factors: (1) The Joppa 3 is an (IP/LP) rotor which is of interest to the other program participants, and (2) the bore was extremely clean throughout its length.

Prior to the selection of the second Task II inspection candidate, Task I and Task III participants were polled as to their recommendations. Several candidates were recommended. The Buck #6 was chosen since it was in line with input recommendations from the polled individuals. It is of interest because again it is an (IP/LP) and, in addition, appeared to contain relatively large cloud-type indications based on the initial inspection data.

Glenwood #4 was also chosen for the program for use as material for manufacturing calibration standards. The HP stage was rough cut into discs 1-foot-thick and transported with the IP stage to BCL. Most of this rotor is still intact and is planned to be used for equipment capability demonstrations.

Rotor Inspection

Buck #6 and Joppa #3 were transported to the facilities of the two teams used to prepare and inspect the rotors. Both teams were directed to treat the rotors as typical in-service candidates and to use their normal bore preparation and inspection procedure. The results of the inspections were evaluated and compared. Team A was asked to perform an ultrasonic reinspection of Joppa #3 and Team B was likewise asked to reinspect Buck #6, to determine the reproducibility of the boresonic inspection for each team.

The results of each inspection performed by both teams are presented in detail in the following sections.

Joppa #3. The Joppa #3 was shipped to the facilities of Inspection Team A. BCL directed the team to treat the rotor as a typical in-service candidate and to use their normal bore preparation and inspection procedures. The bore was visually inspected, the results of which are shown in Figure 4-1. Subsequent to the visual inspection operations, bore preparation operations were initiated. Both "Floppy-Wheel" and automated power honing techniques were utilized. An estimated 20-30 mils were removed from the bore surface. After completion of the bore preparation, boresonic inspection of the Joppa #3 was accomplished followed by the magnetic-particle testing. The bore was then cleaned, lightly coated with oil, and plugged for shipment to Inspection Team B.

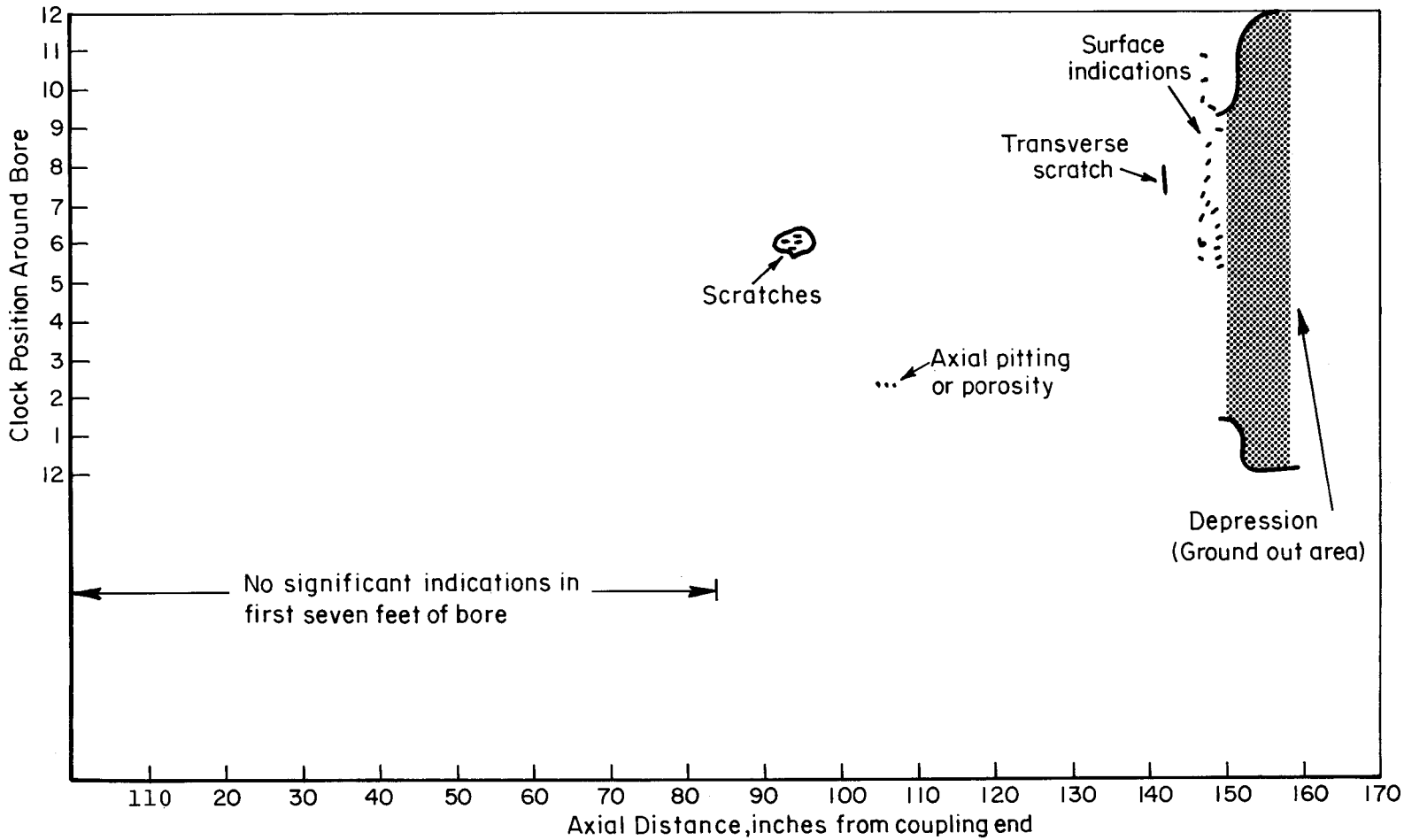

Figure 4-1. Team A Visual Inspection Results

Upon arriving at Team B facilities, the bore was re-examined and judged unacceptable for magnetic-particle inspection due to corrosion during shipping. After consultation with BCL, Team B was authorized to perform additional bore preparation. Bore preparation work was initiated using a "Floppy-Wheel" technique where an estimated additional 2-5 mils was removed from the bore surface. The bore preparation was followed by a magnetic-particle inspection and finally the boresonic inspection. Team B was then requested to perform an ultrasonic reinspection. Team B's visual and magnetic-particle results are summarized in Tables 4-3 and 4-4, and Figures 4-2, and 4-3, respectively. A summary of the boresonic inspection results for both Teams is given in Figure 4-4.

Buck #6. The Buck #6 rotor was shipped to Team A facilities where it was visually inspected and then prepared in the same honing and grinding process as was Joppa #3. The rotor was then magnetic-particle and boresonically inspected. The rotor was then shipped to the Team B facilities where it was magnetic-particle, visual, and boresonically inspected. Team A then traveled to a remote site, performed a honing-floppy-wheel polish bore preparation, subsequent visual magnetic-particle and boresonic reinspection of the rotor.

The results of the initial visual and magnetic-particle inspection for Team A are shown in Figure 4-5 and 4-6, for Team B in Table 4-5 and Figures 4-7 and 4-8. The initial and repeat boresonic inspection results are shown in Figure 4-9.

Rotor Dissection

Regions of Buck #6 and Joppa #3 were removed from the rotors and progressively sectioned to determine the actual flaw characteristics of each region. The actual rough cutting and progressive sectioning was performed by Task III. Additional regions were removed from each rotor and mechanically tested to determine mechanical properties in flawed and unflawed regions of the rotor. The boresonic inspections of Team A and B were used as input to determine the regions for sectioning and mechanical testing.

The areas to be sectioned were chosen for two principal reasons: (1) to provide input to the failure prediction model in Task 1 and (2) to provide the basis for evaluating the performance of the boresonic inspections. In order to

Table 4-3

SUMMARY OF TEAM B VISUAL INSPECTION RESULTS

Indication	Distance (Axial)	Clock Position	Length of Indication	Comments
1	80"	2:00	.03x.06"	Porosity
2	102"	4:00	1-.06"dia. 1-.03"dia. 2-.02"dia	Porosity & Non-metallic
3	102.5"	7:00	4 ind's each .06"	Cluster in approx. .38" dia. area. Porosity.
4	114"	8:00	3 ind's., .03 to .06"	Cluster in .12" dia. area.
5	113"	4:00	.03"	Porosity
6	142.5"	10:00	2 ind's. .06	Appears to be ruptures propagating from non-metallics.
7	141.7"	12:00	Ditto	Ditto
8	130.5"	1:00	5 ind's .03-.06"	Cluster in area .38" dia.
9	140.5"	3:00	Ditto	Ditto
10	154	5:00	4 ind's .03-.06"	Cluster of non-metallics
11	152"	5:00	5 ind's .03-.06"	Cluster in area .5" dia.
12	152.2"	6:00	Ditto	Cluster of Porosity and non-metallics in .75" dia. area.
13	146.5"	1:50	.03-.09	Cluster approx. 30 ind's in a 1.5" dia. field.

Table 4-4

TEAM B MAGNETIC PARTICLE INSPECTION RESULTS

Indication	Distance (Axial	Clock Position	Length of Indication	Comments
1	26.7"	6:30	.09"	Tight Split type
2	79.5"	2:30	.03"	Cluster of 3-inds.
3	85.7 to 88.7"	8:00 to 10:00	.02 to .09	Approx. 50 inds. Axial and angular orienated
4	80"	12:00	.03 to .12	5 ind.
5	92"	4:00	.03 to .12	8 ind.
6	98"	2:00	.03 to .12	20 ind.
7	100 to 101.7"	2:30	.03 to .25"	Approx. 50 ind. Axial and angular
8	106.2	2:00	.03 to.09"	Cluster of 8
9	106.5 to 118.2"	2:00 to 4:00	.03 to .12	Approx. 50 inds. continuous stringers
10	113.5"	9:00	.03 to .12	Same area as #4 on visual exam-approx. 8 inds.
11	118"	3:00	.03 to .09	Cluster of 4 ind. axial orientated
12	118" to 146.2	12:00 to 3:00	.03 to .25"	Numberous indications continuous stringers. Axial and angular orientated
13	152" to 156	All Clocks	.03" to .12"	Ditto
14	100"	4:00	.03" to .12"	Same area as #2 area on visual exam
15	101.2"	5:00	.03" to .25"	Cluster of Inds. Axial and Angular orientated

Table 4-4. (Continued)

Indication	Distance (Axial)	Clock Position	Length of Indication	Comments
16	100"	7:00	.03" to .12"	Similar to #15
17	132"	9:15	.25"	
18	138" to 156	3:00, 6:00 9:00	.03" to .25"	Numerous clusters - similar to #12

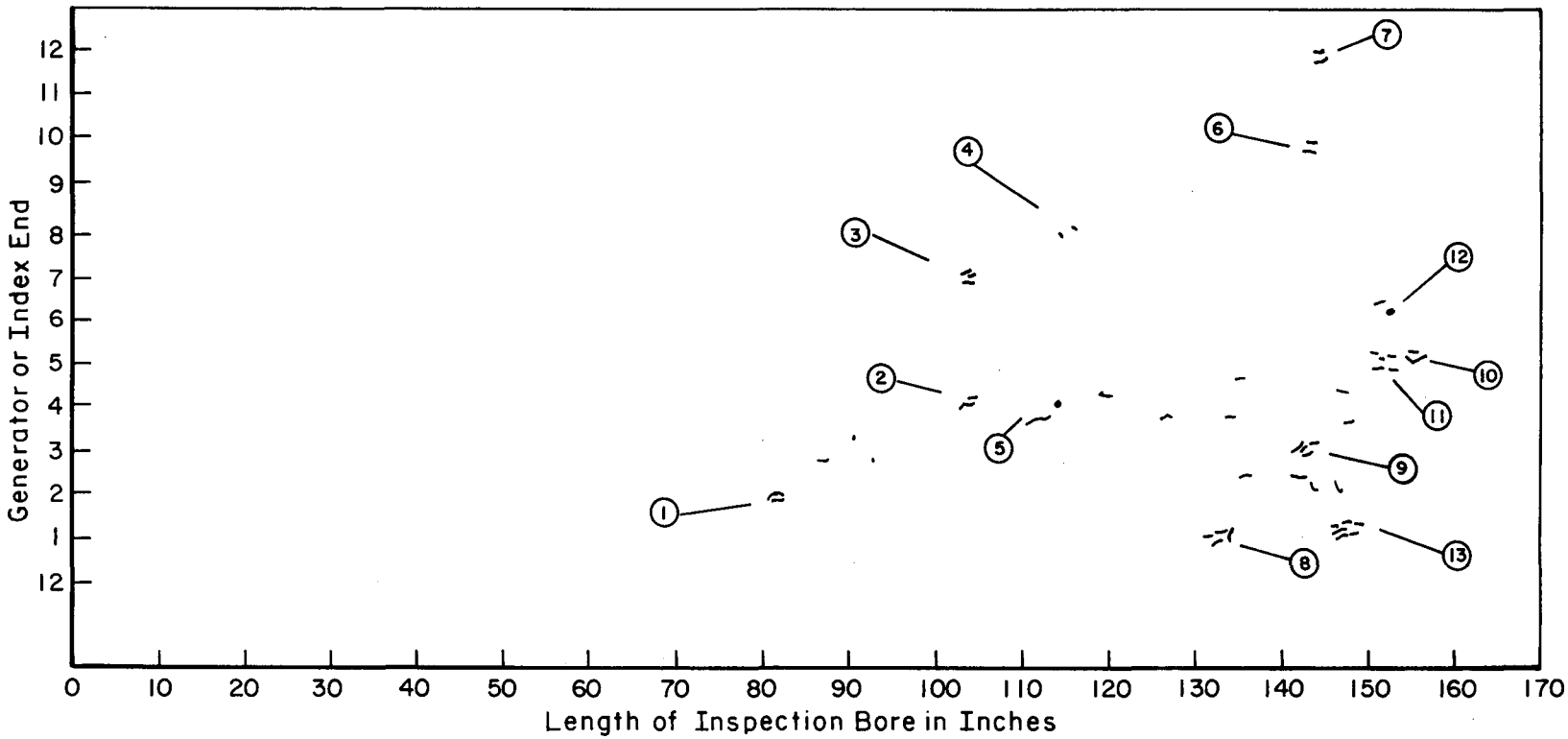

Figure 4-2. Plot of Team B's Visual Indications

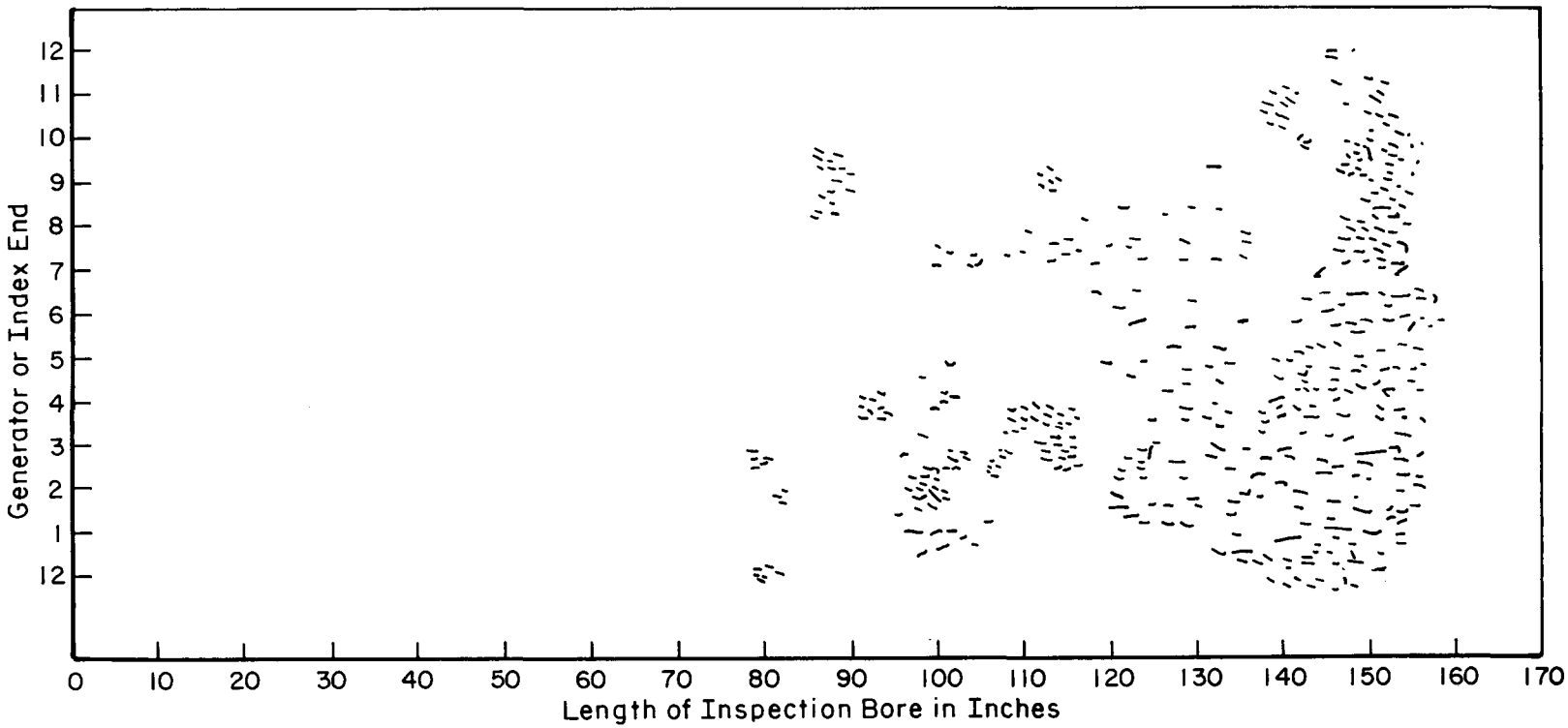

Figure 4-3. Plot of Team B's Magnetic-Particle Indications

INDICATIONS DETECTED

TEAM	INDICATIONS P/C	S	R	SIZE RANGES 0-1/16	1/16-1/8	1/8>
(A)	191	126	12	246	82	1
(B)	4182	0	0	2987	1193	4

LARGEST INDICATION

TEAM	SIZE (inch)	POSITION Z	θ	R
(A)	~1/8	101.8	320°	0.35
(B)	~5/32	100.8	131°	0.5
(B)	~1/8	57.0	84°	0.44

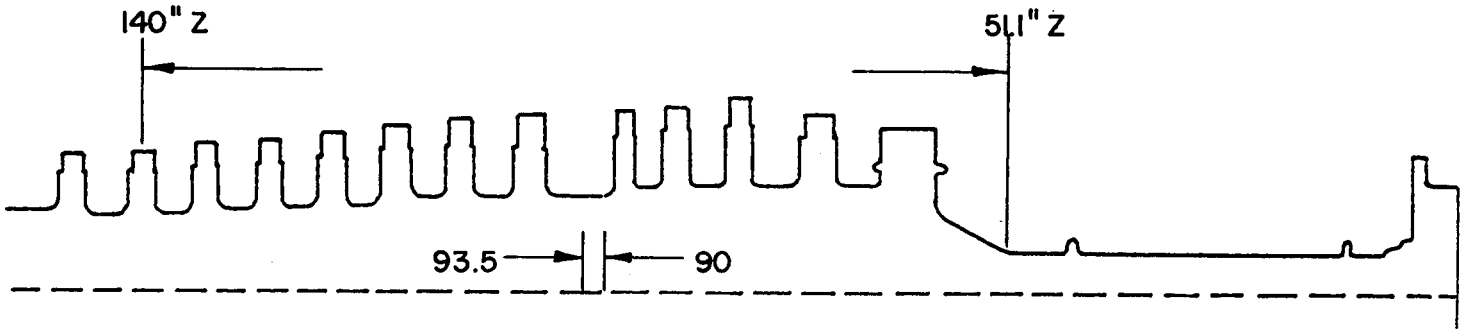

TEAM	Indications Initial Scan P/C	S	R	Indications Repeat Scan P/C	S	R	SIZE RANGES 0-1/16	1/16-1/8	1/8>
(A)	14	12	0	Did Not Repeat				Did Not Repeat	
(B)	226	0	0	277	0	0	207	69	1

Figure 4-4. Ultrasonic Indications Found in Joppa #3

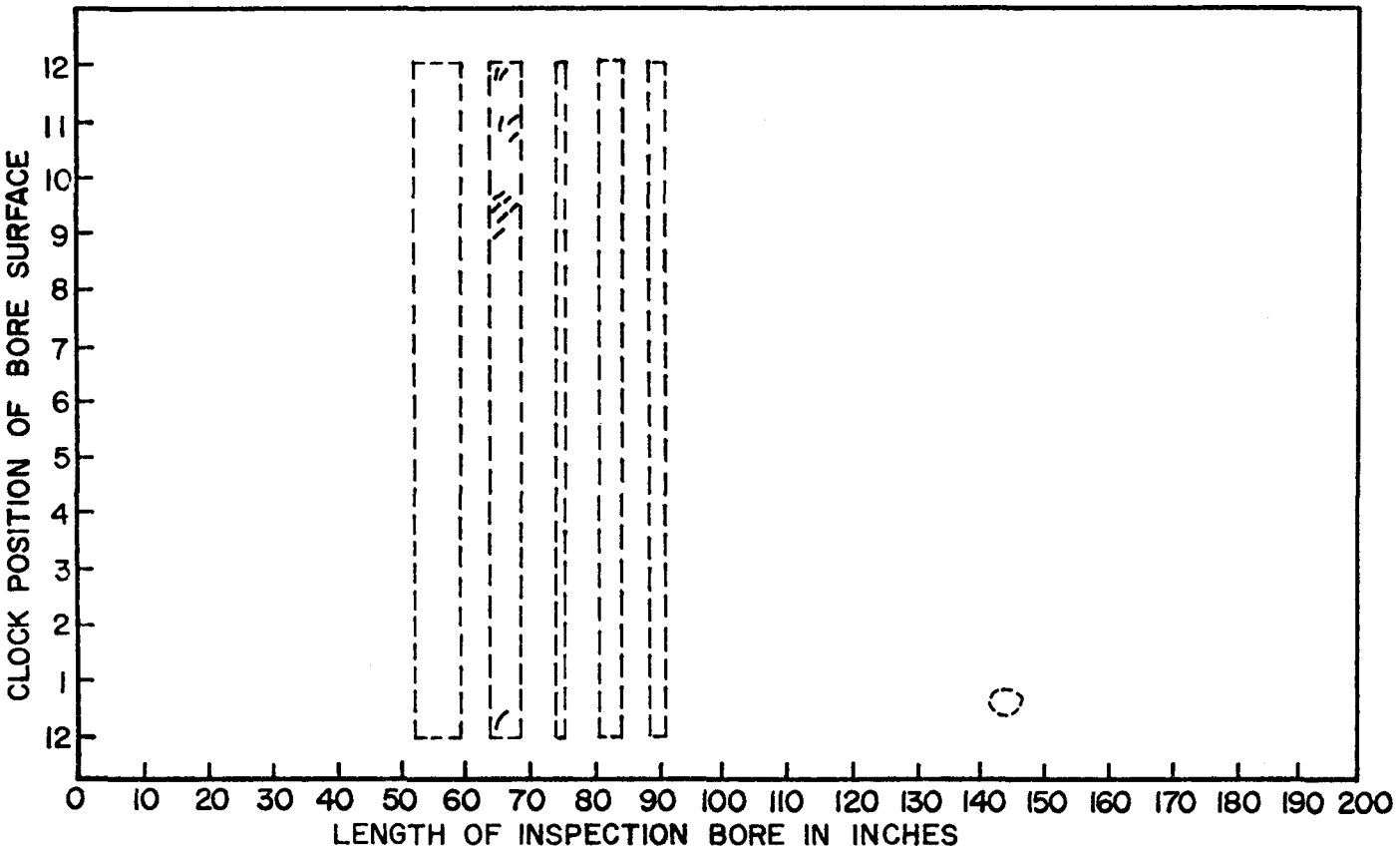

Figure 4-5. Plot of Team A's Visual Examination of Buck #6

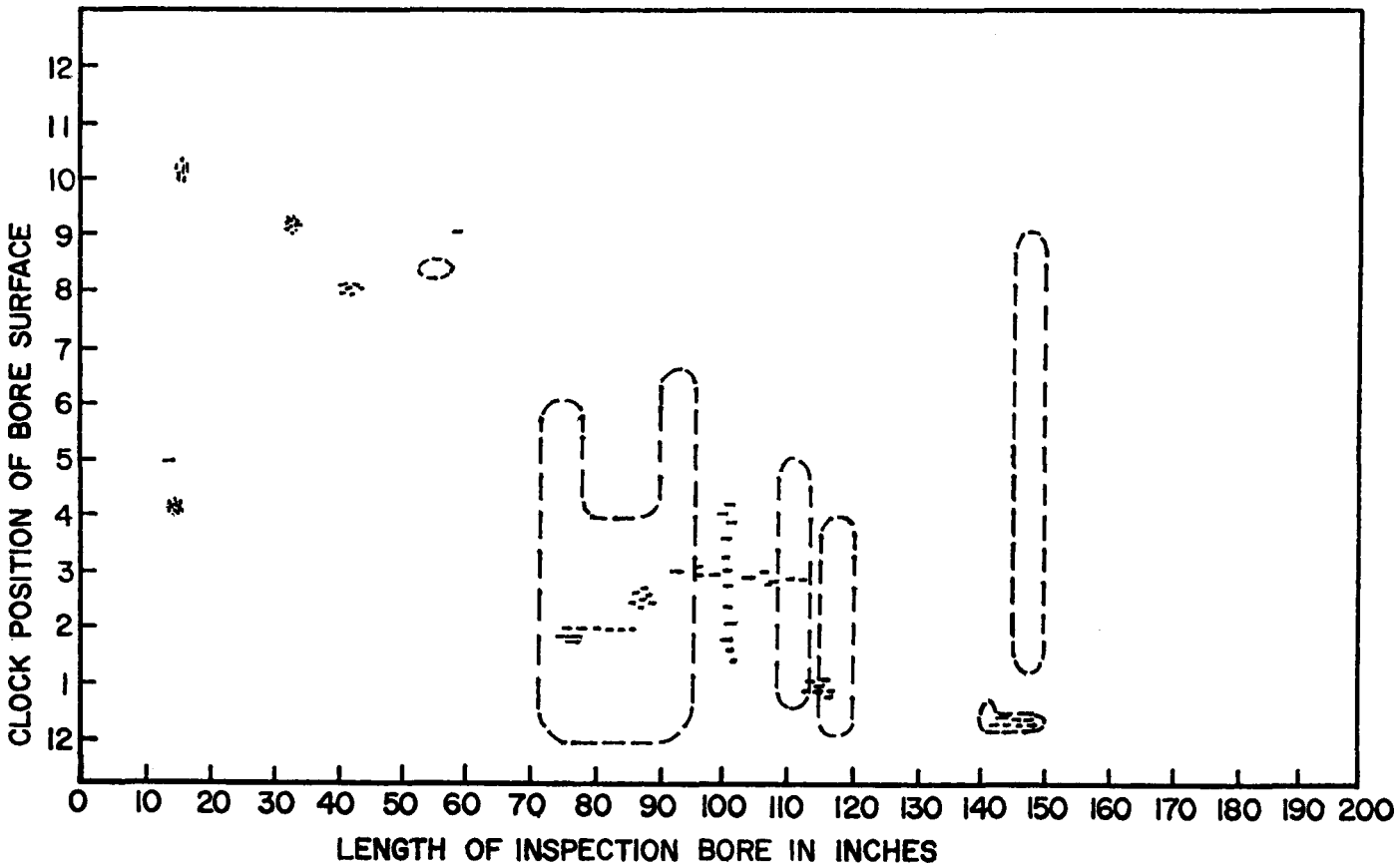

Figure 4-6. Plot of Team A's Magnetic-Particle Indications for Buck #6

Table 4-5

VISUAL DEFECTS NOTED IN BUCK #6 BY TEAM B

Indication No.	Distance from Gov. End	Length of Indication	Clock Position	Remarks
1	45"	1/32-1/16	2:30	Scattered Porosity
2	45"	"	8:30	" "
3	66.7"	"	6:00	" "
4	106.0"	"	5:00	" "
5	112-115"	"	2:00-5:00	Chain of Scattered Porosity
6	123"	"	4:30	Cluster of Porosity
7	126"	"	6:00	" " "
8	135"	"	3:00	" " "
9	132"	"	5:00	" " "
10	136"	"	5:00	" " "

NOTE - Visual defects noted do not include those in dimpled areas.

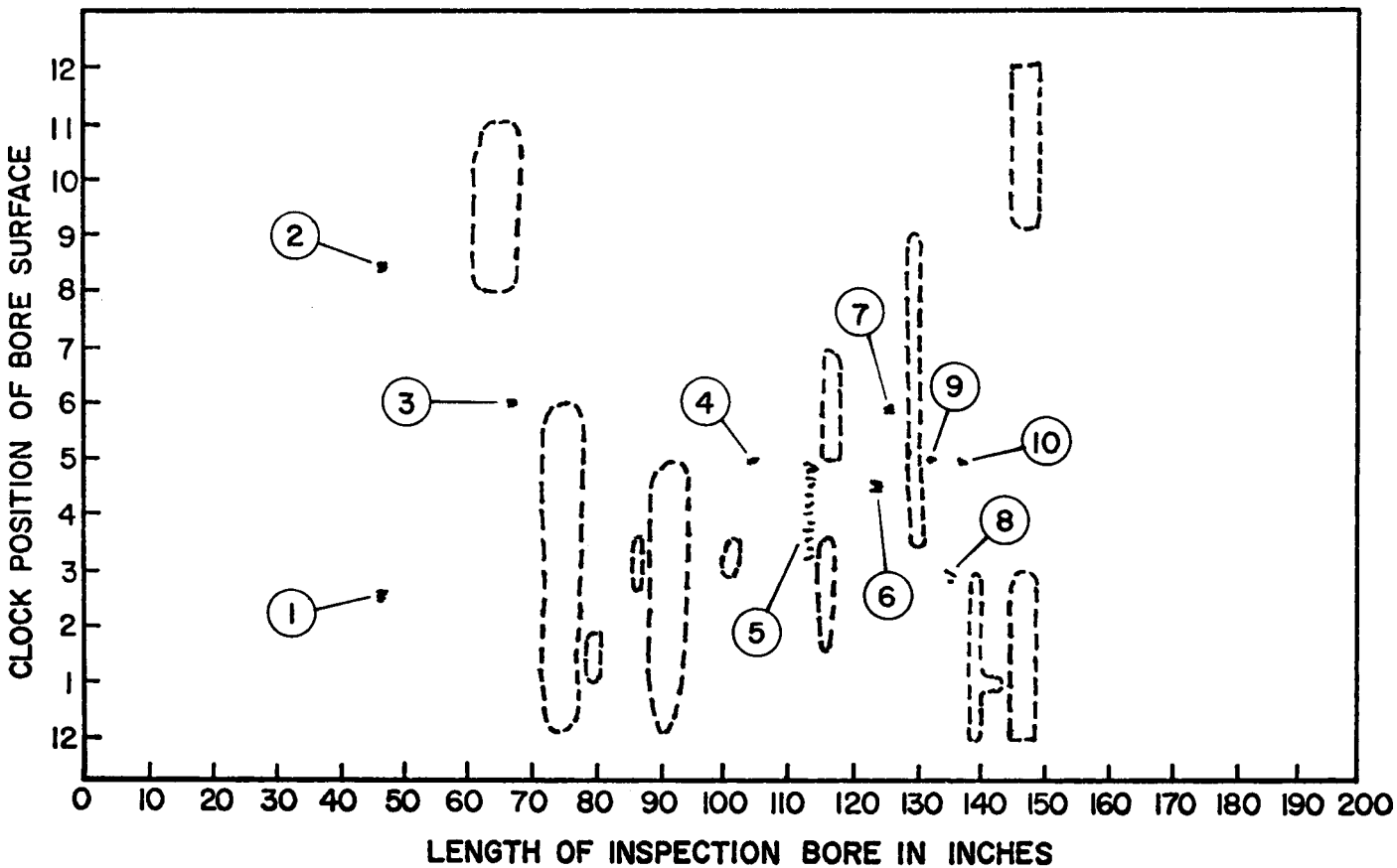

Figure 4-7. Plot of Team B's Visual Examination of Buck #6

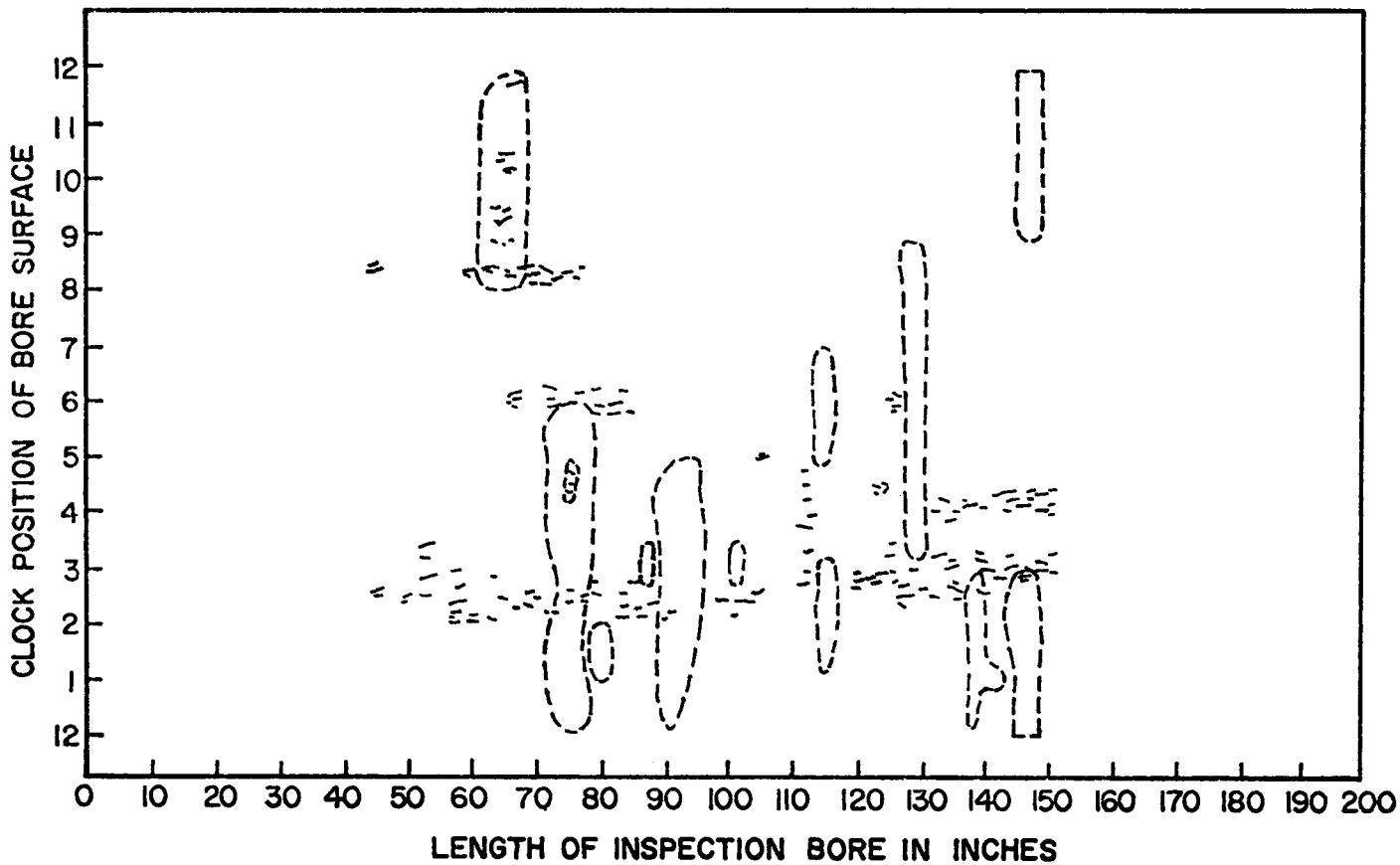

Figure 4-8. Plot of Team B's Magnetic-Particle Indications for Buck #6

	INITIAL SCAN						REPEAT SCAN					
	INDICATIONS			SIZE RANGES			INDICATIONS			SIZE RANGES		
TEAM	P/C	S	R	0-1/16	1/16-1/8	1/8	P/C	S	R	0-1/16	1/16-1/8	1/8
(A)	(-)	307	(-)	266	40	1	0	28	(-)	0	27	1
(B)	2496	26	0	1918	603	1	Did Not Repeat					

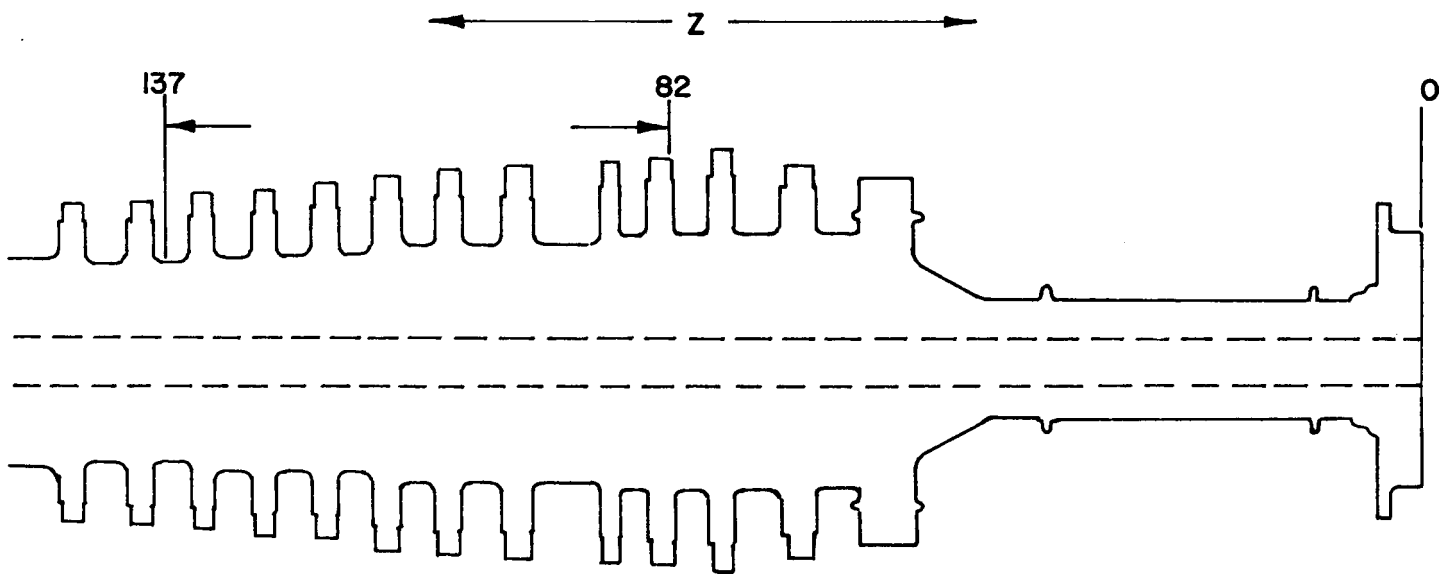

LARGEST INDICATION

TEAM	SIZE (inch)	POSITION Z		R
(A)	1/8 in.	89	94°	0.14
(B)	1/8	105.3	150°	1.25

Figure 4-9. Ultrasonic Indications Found in Buck #6

provide input to the failure prediction model it is necessary to determine the regions of highest flaw density or flaw volume fraction (V_f). To evaluate the performance of the boresonic inspections it is necessary to examine regions of disagreement between the two teams evaluated. Moreover, it is also necessary to evaluate regions of agreement to determine the relative difference between boresonics and actual flaws. This should be done for all types of flaws distinguished in the rotors, i.e., clouds, clusters, and singular indications. This detailed study should tell the ultimate resolution, detection, sensitivity, and characterization capabilities of state of the boresonic inspection process.

Eight regions from each rotor were selected for progressive sectioning as shown in Table 4-6. They essentially met the requirements described above for both of the needs of the program. A large singular indication in Joppa #3 at 58-1/2 was sectioned in addition to the eight regions which contained cluster type of indications. Prior to rough cutting and sectioning this indication was characterized under a BCL directed study using a typical boresonic scanner and various boresonic transducers. This area was then sectioned to provide one-to-one correlation between ultrasonics and actual flaw geometry.

Table 4-6

FLAW DENSITY LEVELS IN SELECTED SPECIMENS FROM BUCK AND JOPPA ROTORS AS DETECTED BY BORESONICS

Joppa 3			Buck 6			
	Flaw Density		Specimen ID		Flaw Density	
Specimen ID	Team A	Team B	Task II	Task III	Team A	Team B
J 7A1-6	Low Large Indications	High	A	112	High Large Cluster	*
J 7A-31	High	High	B	114	High Large Cluster	*
J 7A-81	Low	High	C	114	High Large Cluster	*
J 7AS-14	Low	High				
J 7AS-15	Low	Low	U	212	Medium	None Detected
J 7AS-12	Low	Low	I	312	Medium	*
J 6A-2	Low	Low	P	313	Medium	*
J 7-1	Medium	High	Y	372	Low Large Cluster	*
J F-3	Large Singular Indication	Large Singular Indication	W	372	Low Large Cluster	*

DESCRIPTION OF NONDESTRUCTIVE EVALUATION RESULTS

Data Formats

Results from the boresonic inspections conducted in the Joppa and Buck rotors were reported to BCL in a tabular format. The indications were identified in numerical order in the sequence in which they were detected. Each indication was identified as to location (R, Z, θ) in the bore, some sort of designation as to size - either flat bottom hole or amplitude, a designation of the transducer which detected the indication, and a comment concerning the type of indication; the designated flaw size was based on the method of calibration used. Since one inspector uses flat bottom holes (FBH) for calibration the amplitude could be directly converted to FBH equivalent size. The other inspection agency calibrates in side drilled holes (SDH) which could not be directly related to equivalent FBH size. BCL conducted a laboratory study with various FBH's and SDH's in the same block; hence variation versus depth curves could be drawn to relate the amplitudes from SDH's to that of FBH's. The comments contained in the data sheet were usually the type of indication (cluster, cloud, or holding indications) and the number of indications when multiple indications were detected simultaneously.

The information on the tabulated data sheets were fed into the computer for ease in analysis. The indications were then represented by polar (R-θ) plots (Figure 4-10) and axial (θ-Z) plots (Figure 4-11) with indication size ranges indicated by various symbols. The plots could be made to represent various size rotor segments by altering the thickness displayed in a plane.

Two data-analysis routines were developed in an attempt to segregate the test rotors into optimum areas for destructive sectioning. These were:

1) A Cluster Routine
2) An Area-Fraction Routine.

The cluster routine analyzed indications according to the distance separating closely-spaced indications (i.e. based on the ligament between defects). The length of the ligament was varied from 0.1 to 0.5 inches. Using this method, the areas which contained the "highest" concentrations of defects per unit area were identified.

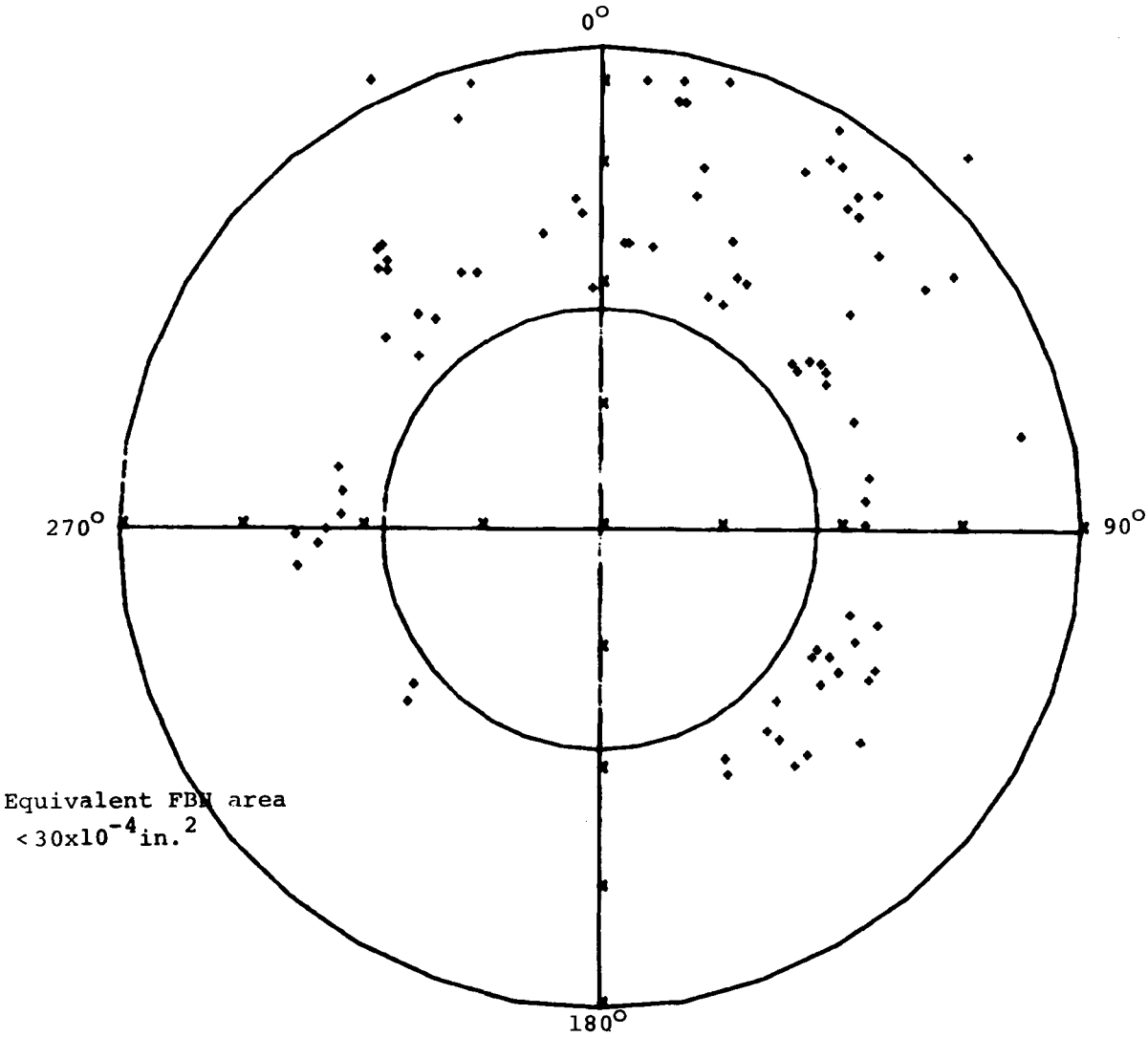

Figure 4-10. Team B Polar Plot of Boresonic Indications, Z=99-100"

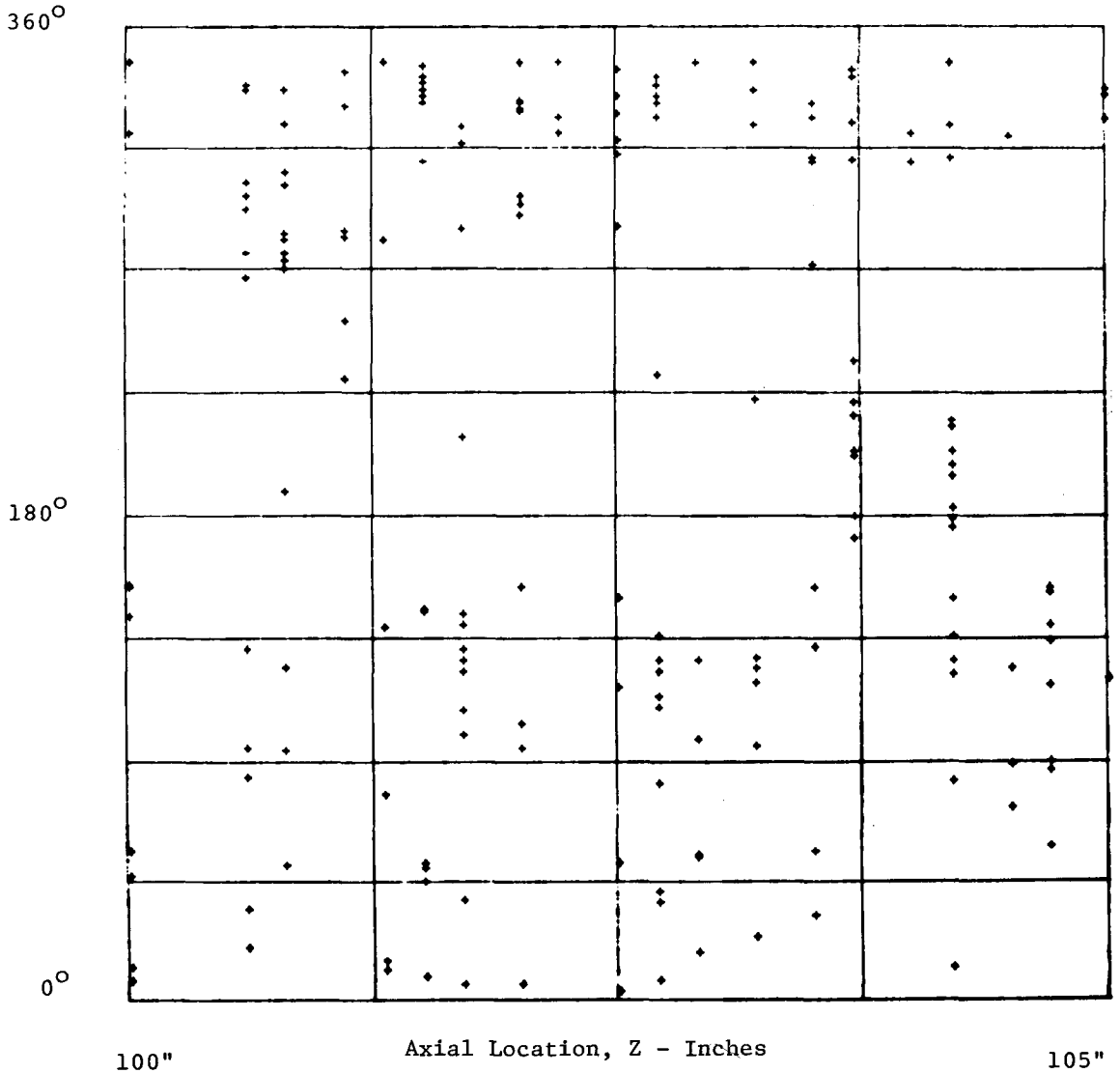

Figure 4-11. Boresonic Indications Projected Onto Bore Surface for Reflectors with EFBH Areas < 30 x 10^{-4} in^2 and Regardless of Radial Depth

The area fraction program examined a specified volume which was then incremented through the volume of the rotor. The volume under analysis would contain an associated number of "defects" with assigned EFBH sizes. In the calculation of the volume fraction, each "defect" was assumed to be spherical. The aggregate "defect" was then collapsed onto a R-Z or θ-Z plane and a representative area fraction calculated. The test volume size could be increased or decreased, as necessary, depending on the test volume size of interest. The two routines were used concurrently to display relative concentration's of inspection results and to statistically characterize regions of the test rotors for later comparison with the destructive sectioning results.

Summary of Boresonic Statistical Results

A cursory review of the test data obtained from the Joppa 3 rotor shows that the number of indications from one inspection group (4,693) was substantially greater than that of the other team (329). This same magnitude of difference was demonstrated in the inspection of Buck 6. The initial scan of Buck revealed 2,522 indications whereas the second inspection team reported 307 indications. This 10:1 difference in total number of reported indications represents an extremely poor correlation based on the total number of indications. When the results are examined in greater detail it is found that the inspection team reporting the larger number of indications detected almost all of them with a pitch catch transducer. Most of the indications reported by the other team were obtained using shear wave transducers. The only general agreement found between inspection teams was the trends of indication concentration as a function of bore position; i.e. they reported the same general regions as being acoustically dirty. This is shown in Figure 4-12 in which the number of reported indications in the Joppa rotor are plotted as a function of position along the Z axis.

The number of indications reported in any given size range also exhibits the same order of magnitude difference between inspection teams, i.e., the number of indications reported for a specific size range were an order of 10:1 between inspection groups. Table 4-7 summarizes the statistical results obtained by the two inspection teams for the two rotors used in this study.

Some Comparative Results

Studies of the relative system performances on specific reflectors were conducted. In addition to examining the total number of indications and comparing the

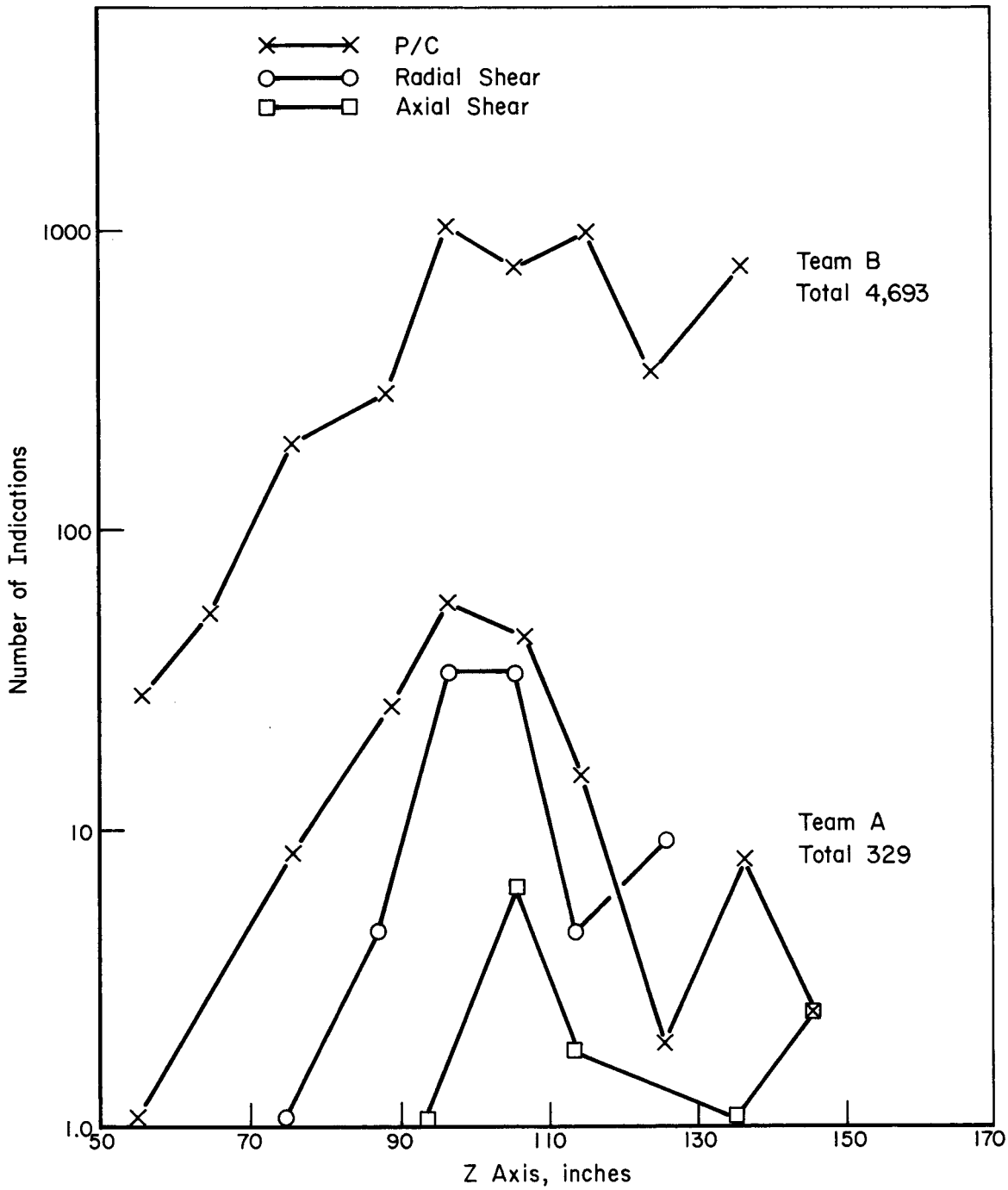

Figure 4-12. Number of Boresonic Indications in Joppa 3 Along Z

Table 4-7

SUMMARY OF STATISTICAL RESULTS

TEAM		JOPPA #3							BUCK #6						
INDICATIONS REPORTED															
		INITIAL			REPEAT			Range	INITIAL			REPEAT			RANGE
		P/C	S	R	P/C	S	R	Z	P/C	S	R	P/C	S	R	Z
	(B)	4184	0	0	--	--	--	(51.1-140.5)	2496	26	0	--	--	--	(82-137)
	(A)	191	126	12	--	--	--		(-)(2)	307	(-)	0	28	(-)	
	(B)	226	0	0	277	0	0(1)	(90-93.5)							
	(A)	14	12	0	--	--	--								
SIZE RANGES															
		INITIAL			REPEAT				INITIAL			REPEAT			
		0-1/16	1/16-1/8	1/8>	0-1/16	1/16-1/8	1/8>		0-1/16	1/16-1/8	1/8>	0-1/16	1/16-1/8	1/8>	
	(B)	2987	1193	4	207	69	1		1918	603	1	--	--	--	
	(A)	246	82	1	--	--	--		266	40	1	0	27	1	
LARGEST SINGLE INDICATIONS															
		SIZE			POSITION				SIZE			POSITION			
		(inch)			Z	θ	R		(inch)			Z	θ	R	
	(B)	∿5/32			100.8	131°	0.5		1/8			105.3	150°	1.25	
	(B)	∿1/8			57.0	84°	0.44								
	(A)	∿1/8			101.8	320°	0.35		1/8in.			89	94°	0.14	

(1) Includes 17 clusters of 2 points and 3 clusters of 3 points initially as opposed to 39 clusters of 2 points and 7 clusters of 3 points when repeated.

(2) Data has not been analized by Team (B).

boresonic size range predictions. Comparative sensitivity, reproducibility, positioning accuracy, flaw sizing and characterization studies were attempted to determine the reliability of relative performance capability of boresonic inspections. Specifically, the following comparative studies were conducted:

1) Joppa and Buck Rescans by at Least One Team Each
2) Multi-Scans of Both BCL and Commercial Calibration Block
3) Detailed Correlations on Single Indications
4) Correlation of Nondestructive and Destructive Sectioning.

The details and results of these comparative studies are described below.

Rescans of Joppa and Buck. In order to determine the reproducibility of boresonic inspection, each team was asked to reinspect specific areas of the Joppa or Buck rotors. Joppa was rescanned by our team between Z = 90 inches to 93 inches. The results of that rescan are represented in polar form in Figures 4-13 through 4-18. These show the initial scan (Figures 4-13, 14, and 15) and the rescan (Figures 4-16, 17, and 18) with the Z increments set at one-inch for each figure. Comparing the scans inch by inch we see little evidence of detailed correlation, particularly in the region between 91 and 92 inches. If we use a relatively wide spatial tolerance of ΔZ = 1 inch, $\Delta\theta$ = 5 degrees, and ΔR = 1/4 inch, and if we do not attempt to correlate according to amplitudes, but only 3-dimensional locations, the following numerical correlation is found through this same region:

Axial Position	Percent Correlation
90 - 91 inches	24.6
90 - 92 inches	26.6
92 - 93 inches	19.5

Thus the same team could only duplicate the geometrical location of about 25% of the indication found on the first scan where they rescanned this section using the same procedures and equipment. If we consider boresonic examinations as only a general assessment of rotor integrity, e.g. based on the dirtiness of the rotor, then the relative number of indications might be a valid consideration. In this case, the initial scan averaged over 3 inches, yield 226 indications, while the rescan revealed 277 indications. These are within an order of magnitude and thus are encouraging. Note that when we examine this same region at 1 inch intervals the numbers do not show the same degree of correlation. The magnitudes are reasonable, the trend is inconsistent from Scan 1 to Scan 2.

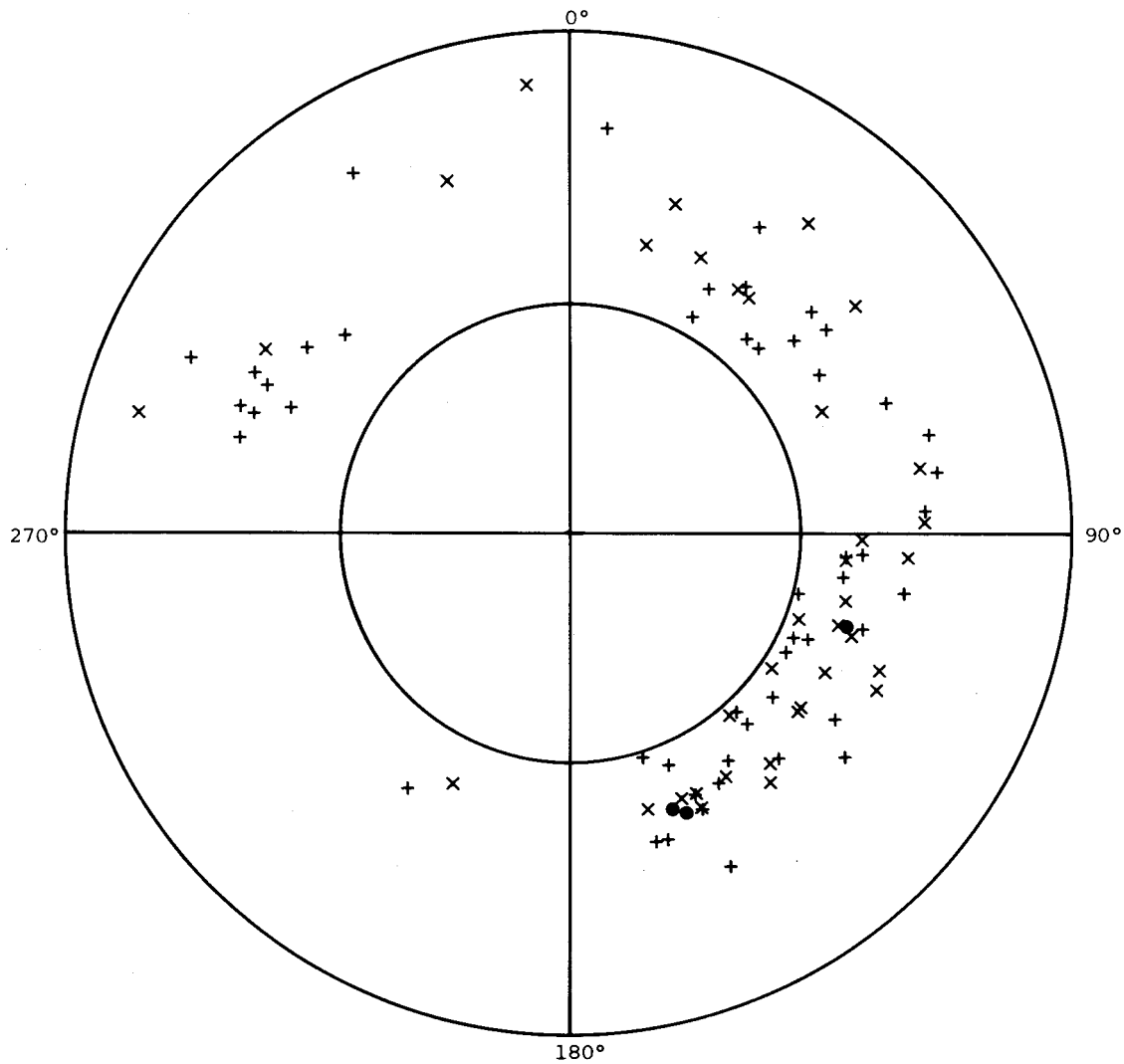

Figure 4-13. SCAN 1 ULTRASONIC INDICATIONS
90" ≤ z ≤ 91" JOPPA

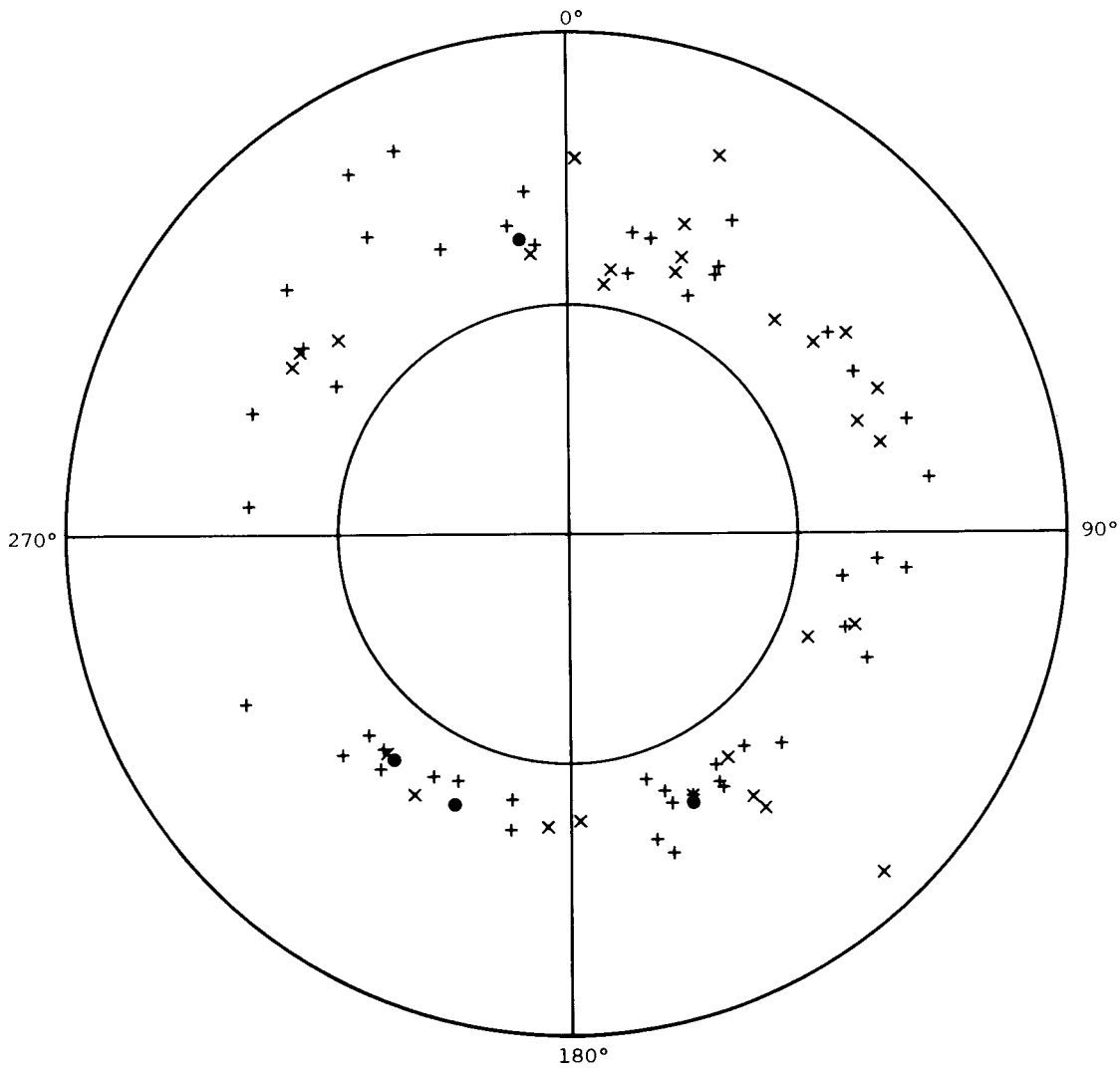

Figure 4-14. SCAN 1 ULTRASONIC INDICATIONS
91" ≤ z ≤ 92" JOPPA

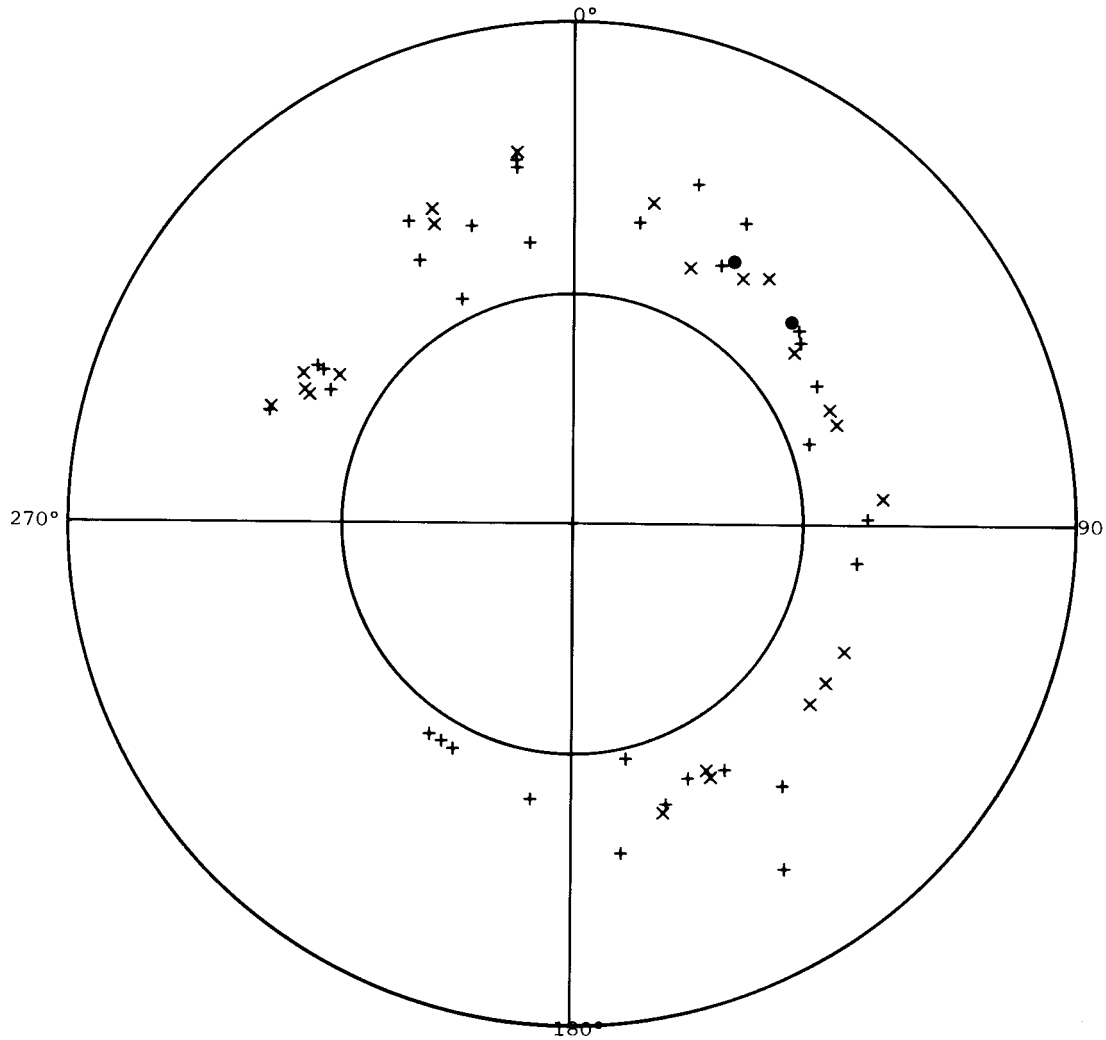

Figure 4-15. SCAN 1 ULTRASONIC INDICATIONS
92" $\leq$ z $\leq$ 93" JOPPA

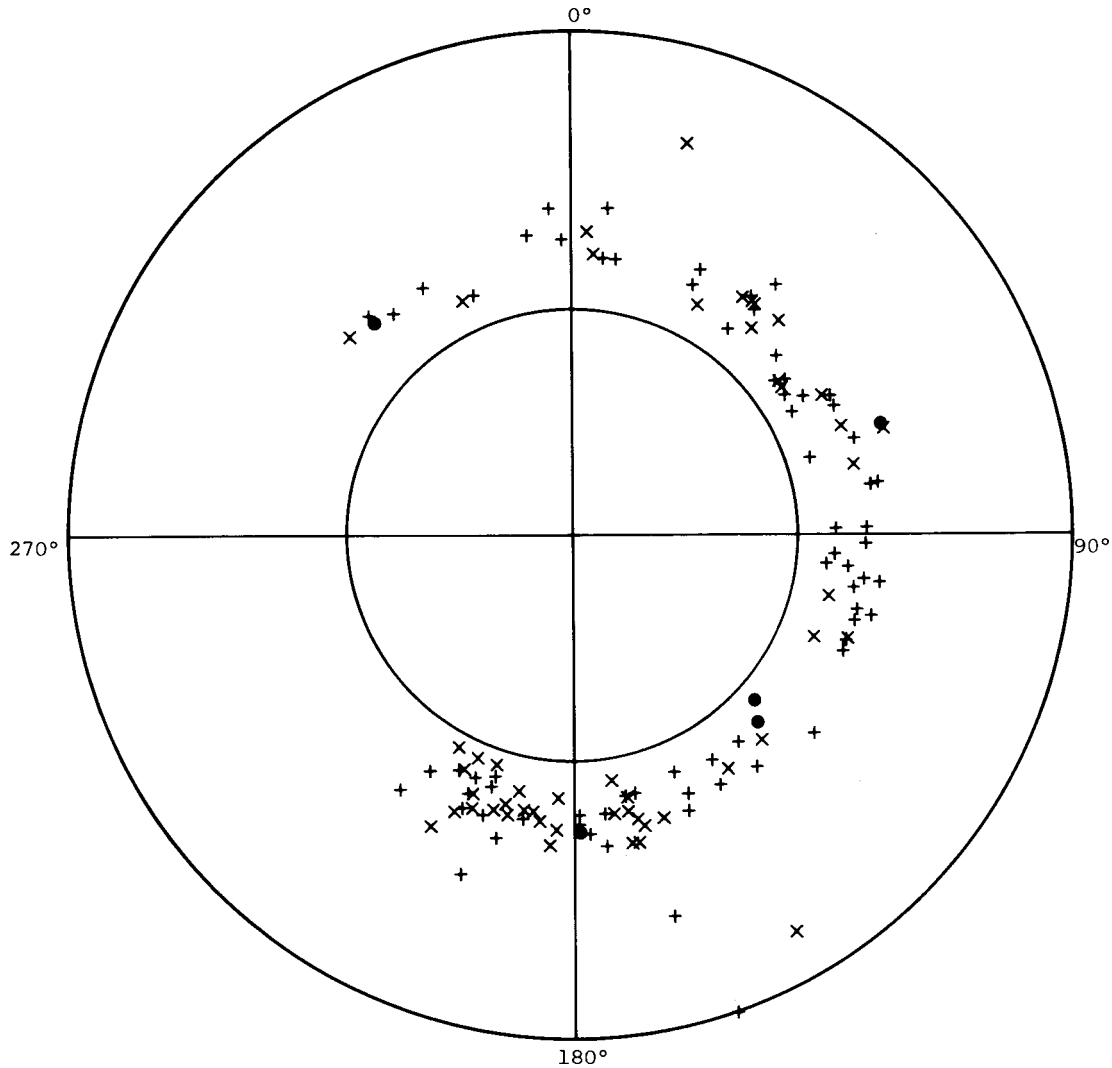

Figure 4-16. SCAN 2 ULTRASONIC INDICATIONS
90" ≤ z ≤ 91" JOPPA

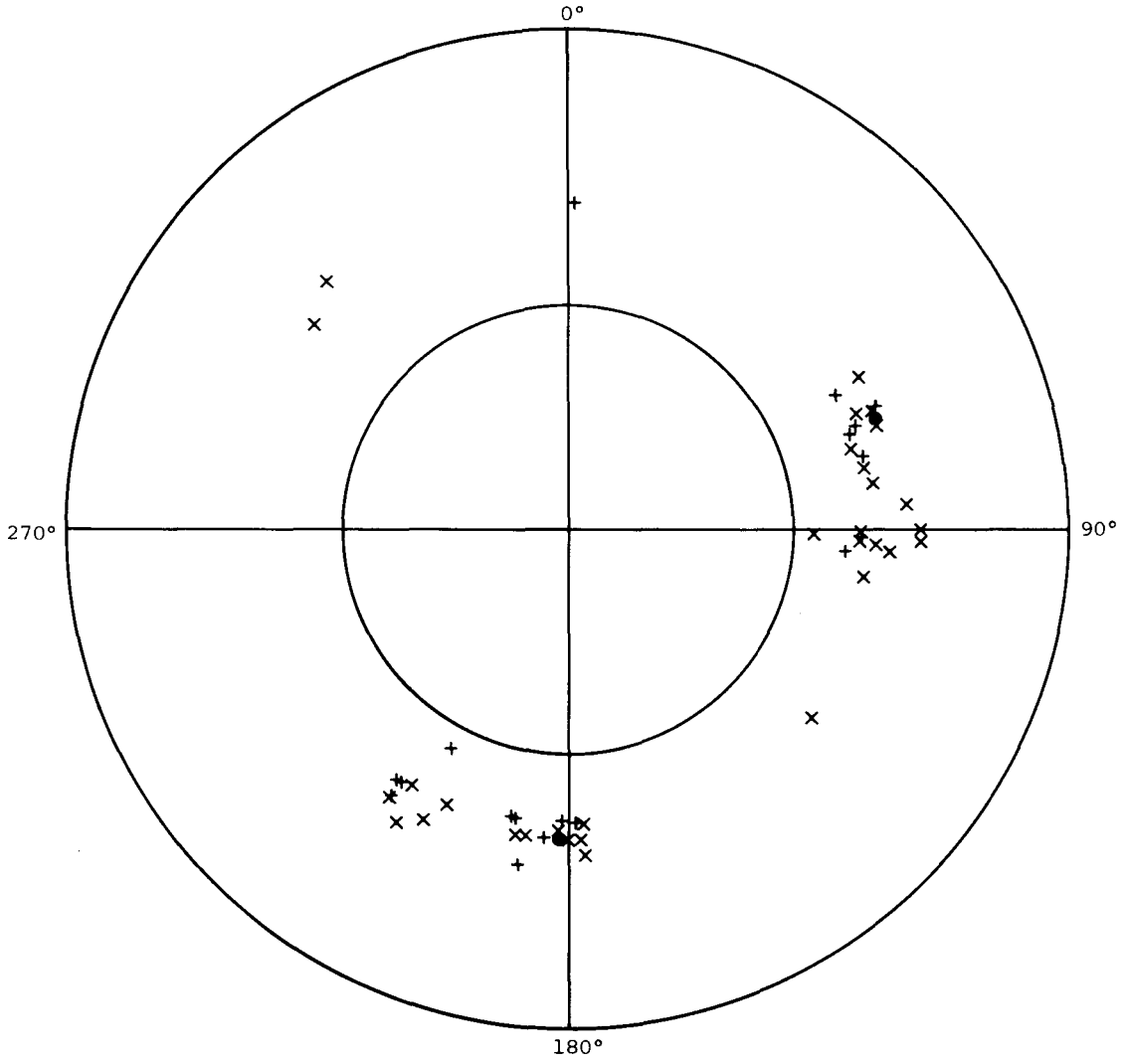

Figure 4-17. SCAN 2 ULTRASONIC INDICATIONS
91" ≤ z ≤ 92" JOPPA

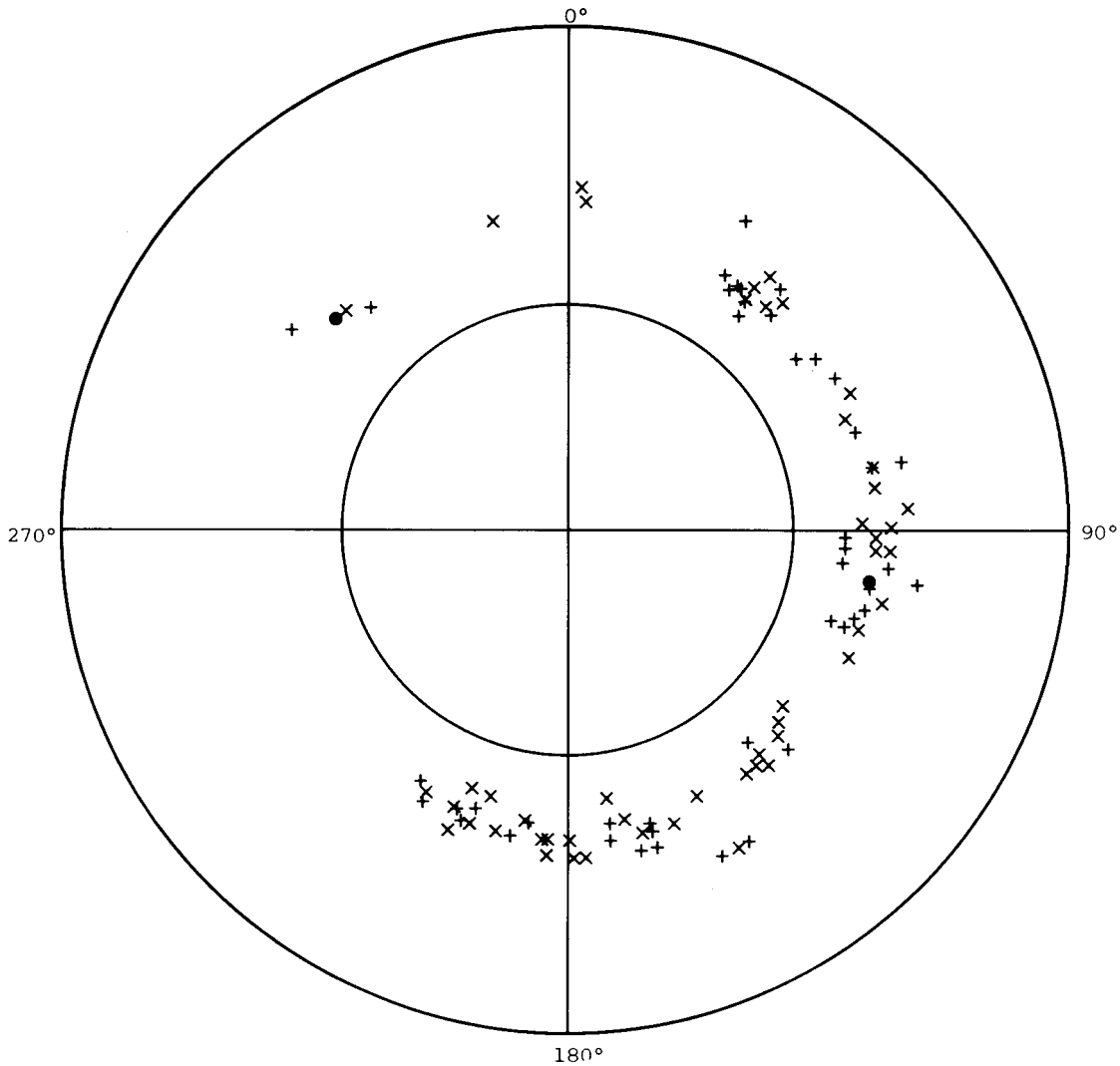

Figure 4-18. SCAN 2 ULTRASONIC INDICATIONS
92" ≤ z ≤ 93" JOPPA

Axial Position	Number of Indications	
	Scan 1	Scan 2
90 - 91	89	131
91 - 92	80	51
92 - 93	57	95

Thus the correlation apparently degrades, the finer we reduce the area examined.

Buck 6 was reinspected in a similar manner, however, due to the relatively small number of indications reported, a much larger region of the rotor was re-examined (Z = 32 inches to 137 inches). The initial examination revealed 307 indications while the rescan only detected 28 indications. None of the 28 indications correlated point by point with the indications in the initial scan with a tolerance of $\pm$ 30° in θ, and $\pm$ 0.5 inches in both Z and R. Furthermore, none of the indications correlated with indications reported by the other inspection team in their initial inspection of the Buck rotor. These results are extremely unsatisfactory but are considered valid for the equipment used and the size reflectors being reported (less than 1/8 inch EFBH).

Calibration Block Studies. In order to explain the deviation between the statistical number of indications found by the two inspections on Joppa and Buck it is necessary to first analyze the variations in sensitivities between inspection systems. To conduct such an analysis it is essential that known reflectors are used and that these reflectors are simulated in a bore condition. It is also necessary to have this test conducted with the boresonic system so that all sensitivity deviations which usually occur in a normal inspection are incorporated. To this end the inspection team was asked to scan the BCL calibration block which was mounted directly onto the rotor during the reinspection of Buck 6. The BCL block contained an array of 1/8 inch diameter SDH's and 1/16 inch diameter FBH's. In addition, BCL personnel conducted an independent calibration block field study using this typical field boresonic system. Most of the transducers analyzed in the RP 502 program (Appendix C) were included in this field study.

The results of the calibration studies are shown in Figures 4-19 through 4-26. Figures 4-19 through 4-22 are examples of pitch-catch transducer deviations between static and dynamic scanning of calibration blocks. Figure 4-19 is essentially a field comparison between sensitivities of the FBH's and SDH's used as calibration standards for boresonic inspection. Figures 4-20 and 4-21

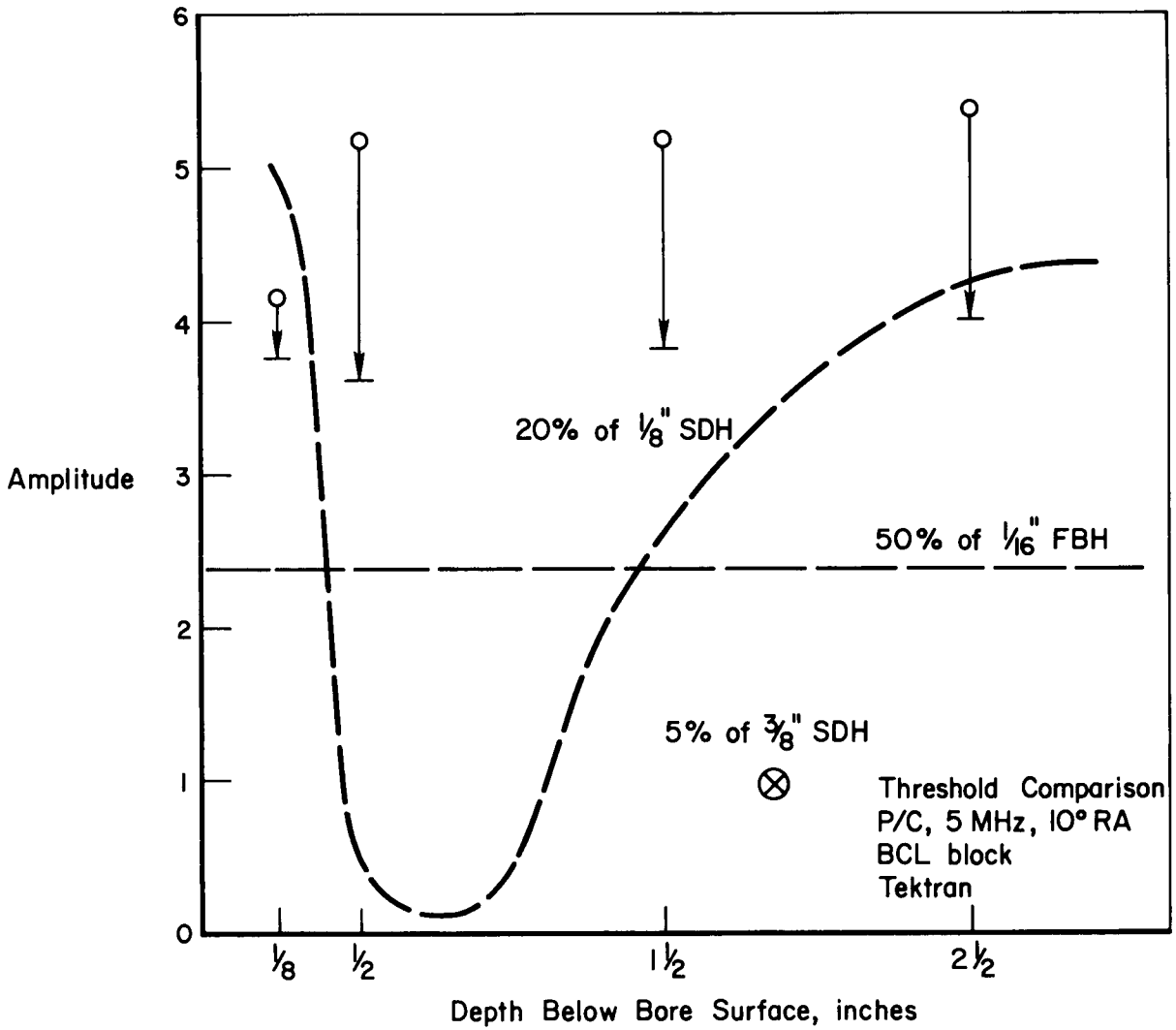

Figure 4-19. Threshold comparison between 20% of the response to 1/8" SDH and 50% of the response to 1/16" FBH using a 5 MHz P/C transducer. Included are the error bands associated with multiscans of the 1/16" FBH response as seen on a Tektran Ultrasonic Instrument.

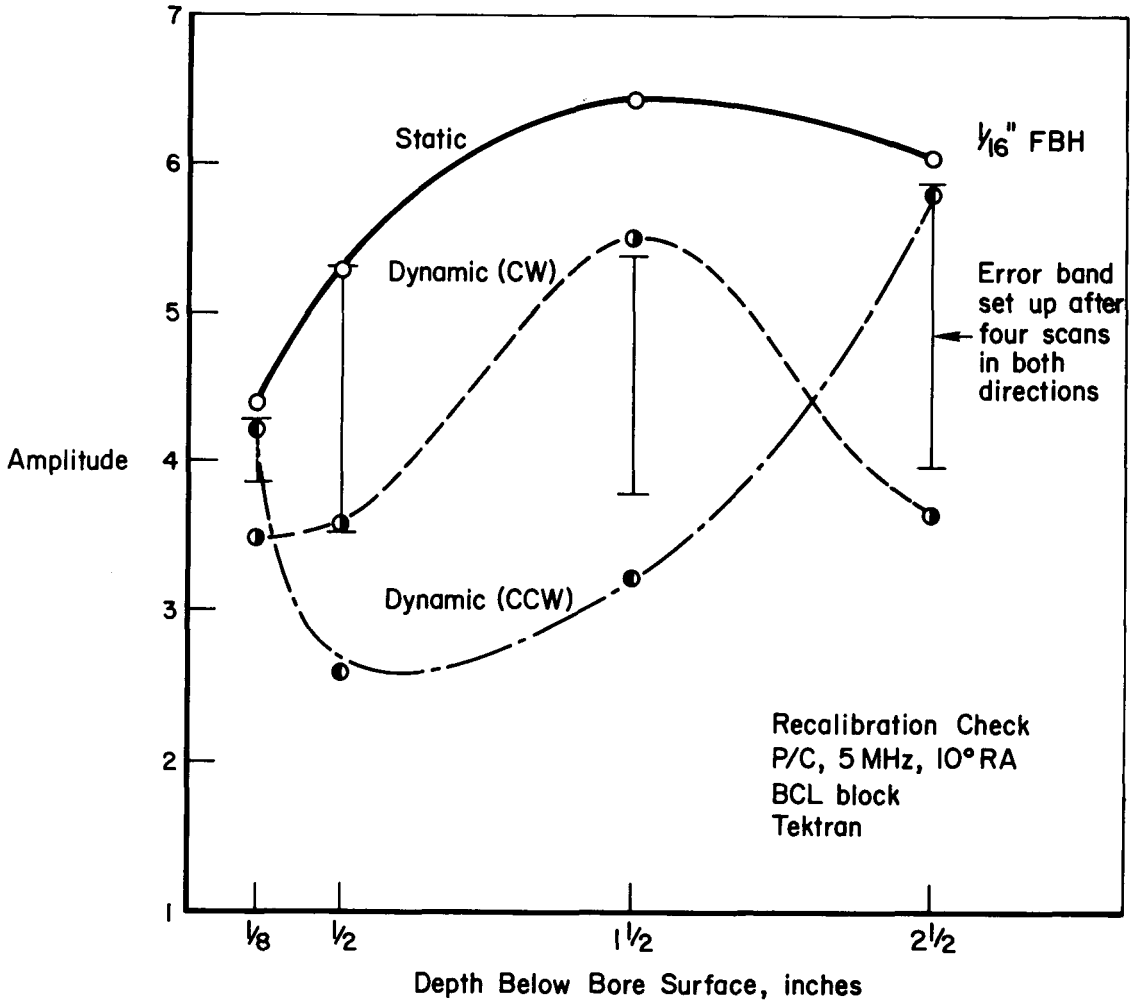

Figure 4-20. The dynamic scanning response to 1/16" FBHs and their associated error bands as opposed to the static response to 1/16" FBHs using a 5 MHz P/C transducer and a Tektran Ultrasonic Instrument.

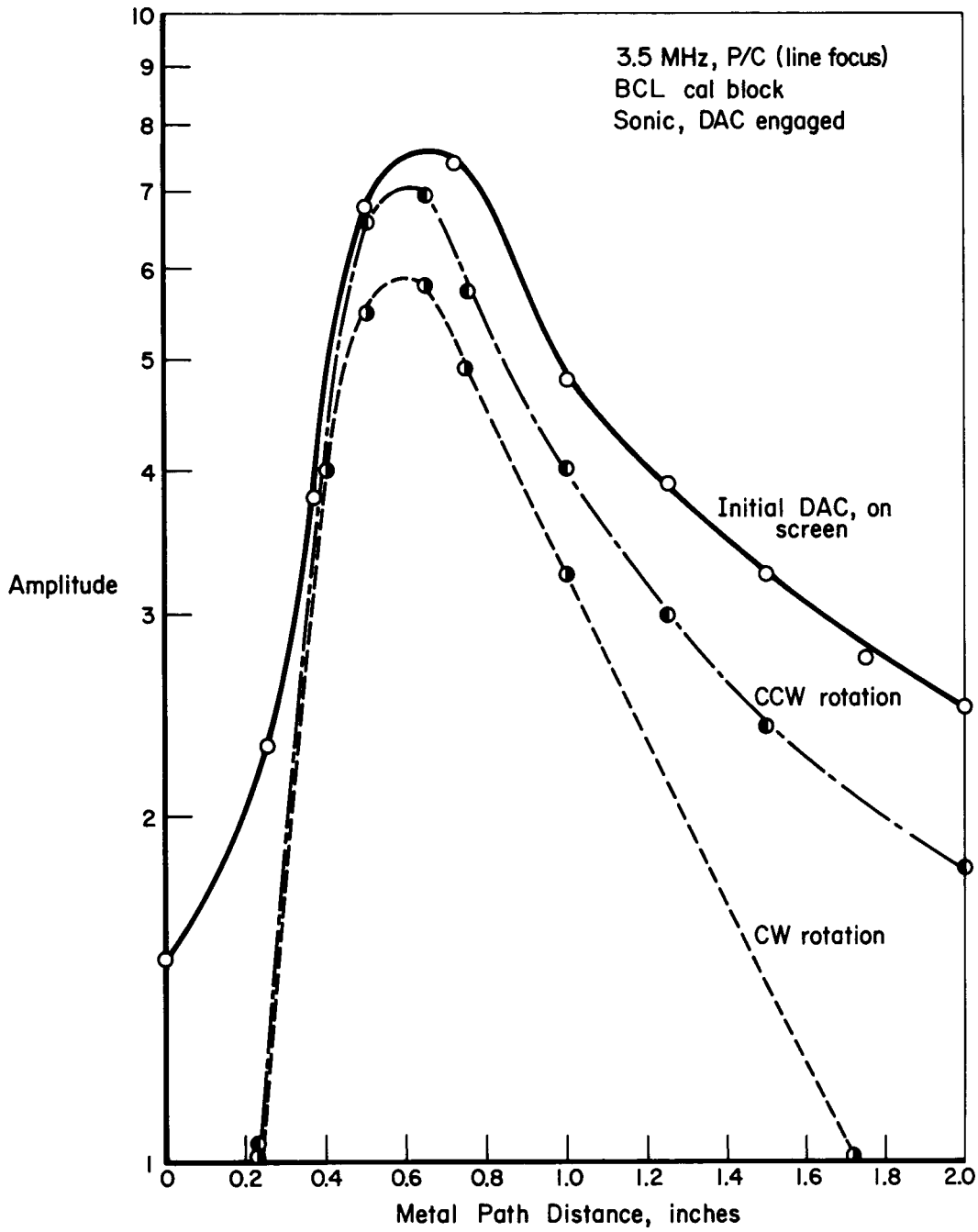

Figure 4-21. Dynamic and static comparisons of responses to 1/8" diameter SDH using a 3.5 MHz P/C transducer with a Ultrasonic Instrument.

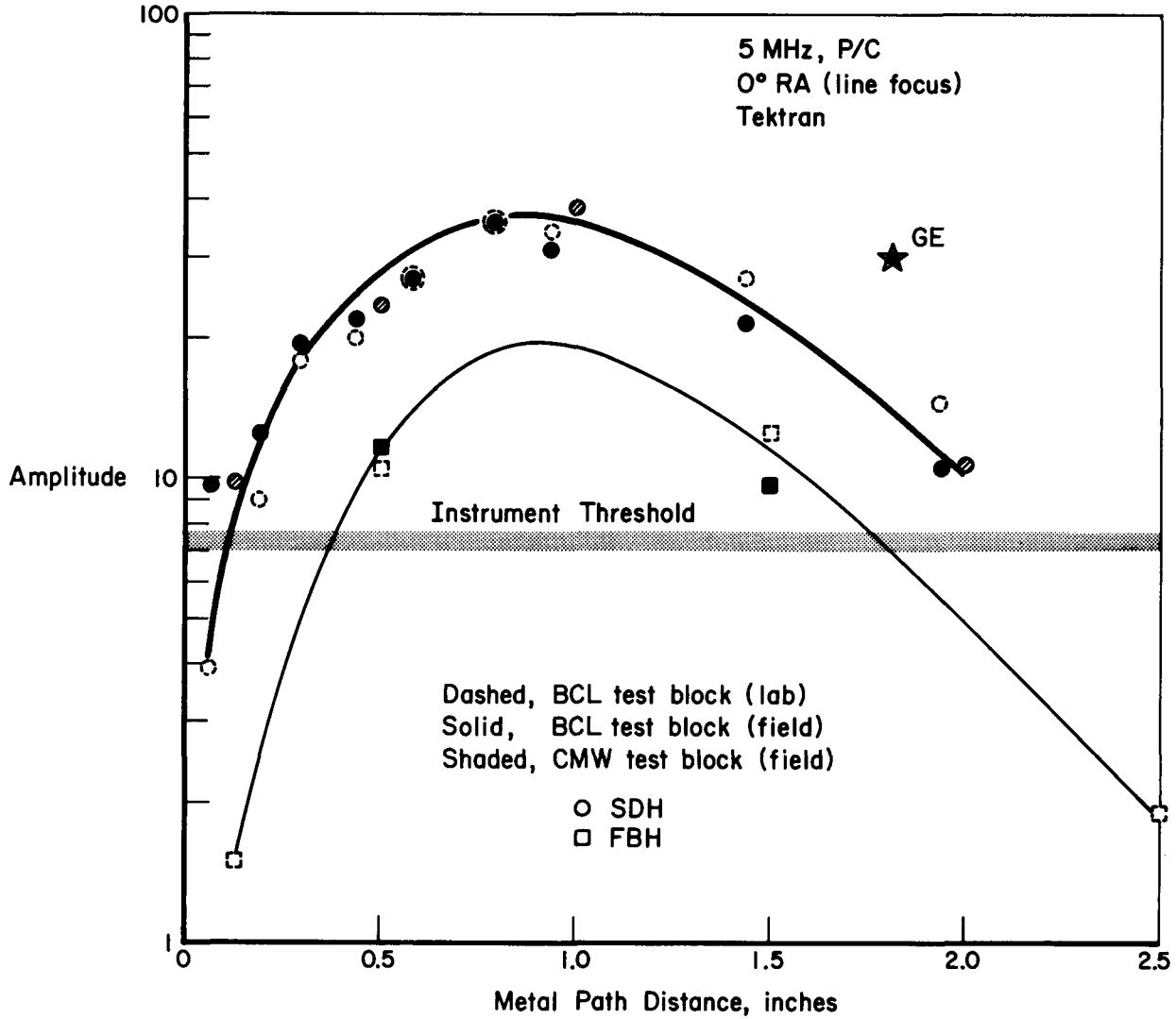

Figure 4-22. Comparative responses to various test blocks between field studies and Laboratory studies using a 5 MHz P/C transducer.

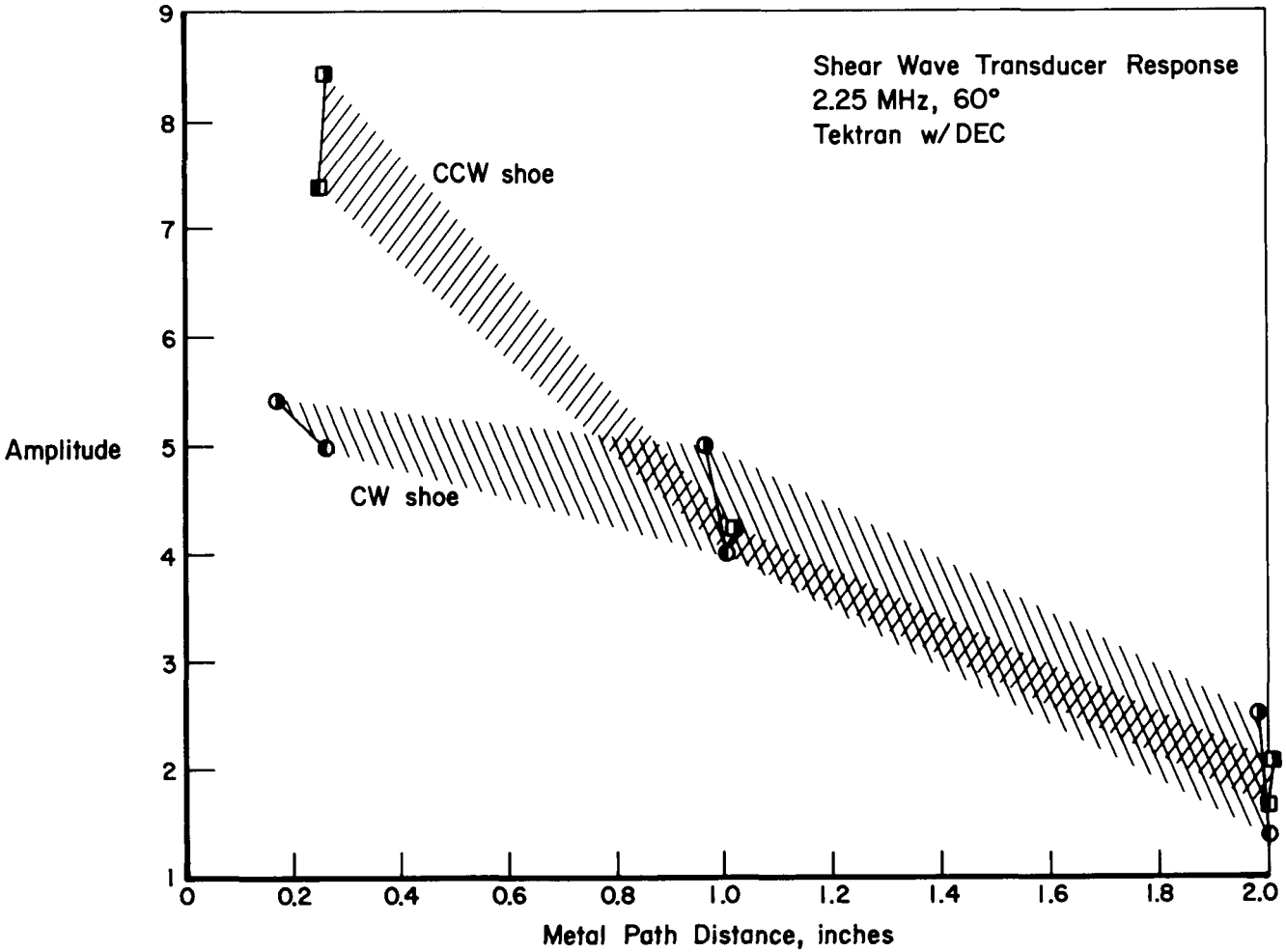

Figure 4-23. Comparisons between clockwise and counterclockwise scan response to 1/8" SDH using 2.25 MHz shear transducer and a Tektran Ultrasonic Instrument.

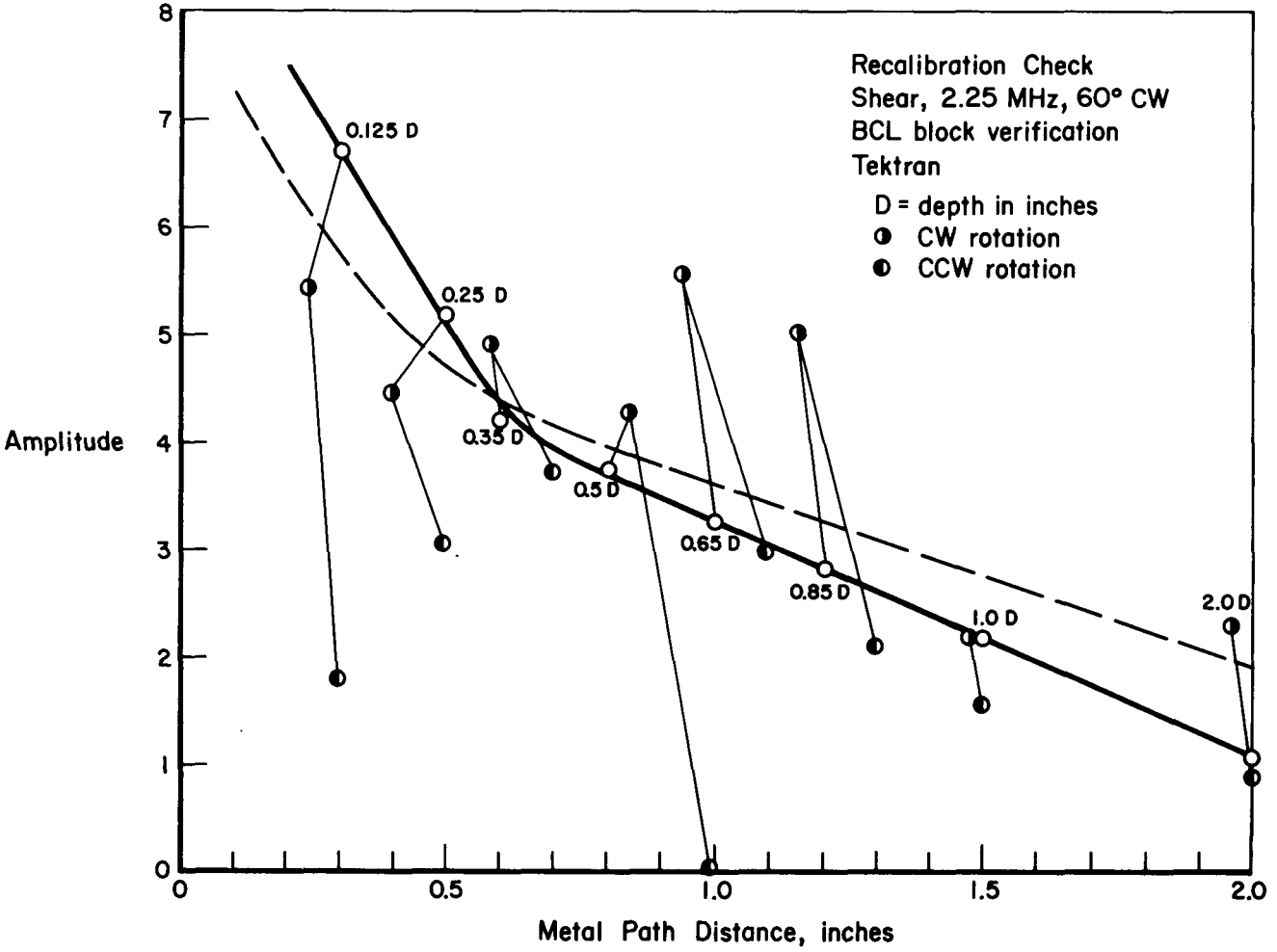

Figure 4-24. Static versus dynamic response to 1/8" SDHs using 2.25 MHz 60° shear transducer and a Tektran ultrasonic instrument.

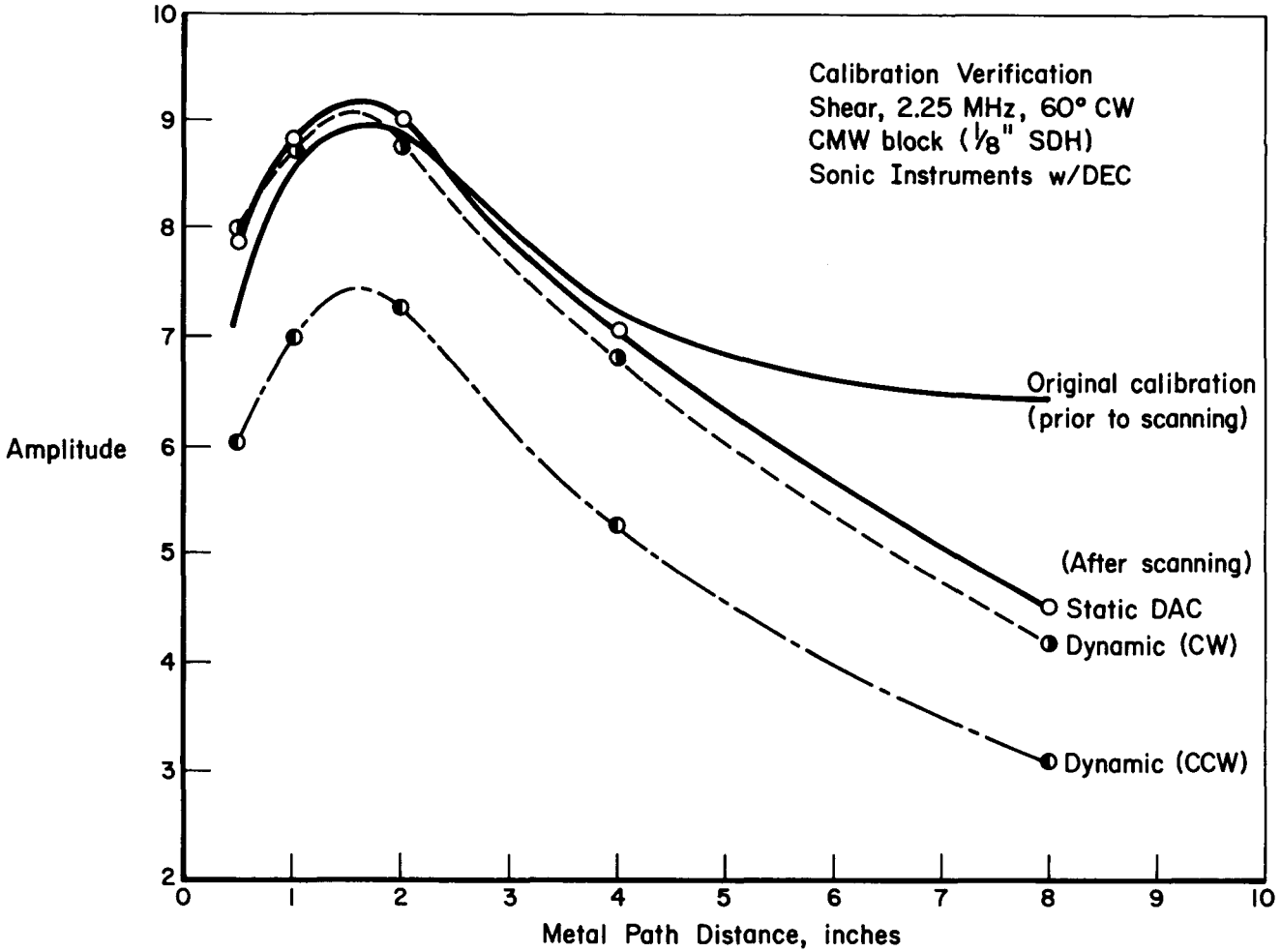

Figure 4-25. Static versus dynamic response to 1/8" SDHs as compared to the original calibration prior to scanning a 30" rotor segment using a 2.25 MHz 60° clockwise shear transducer.

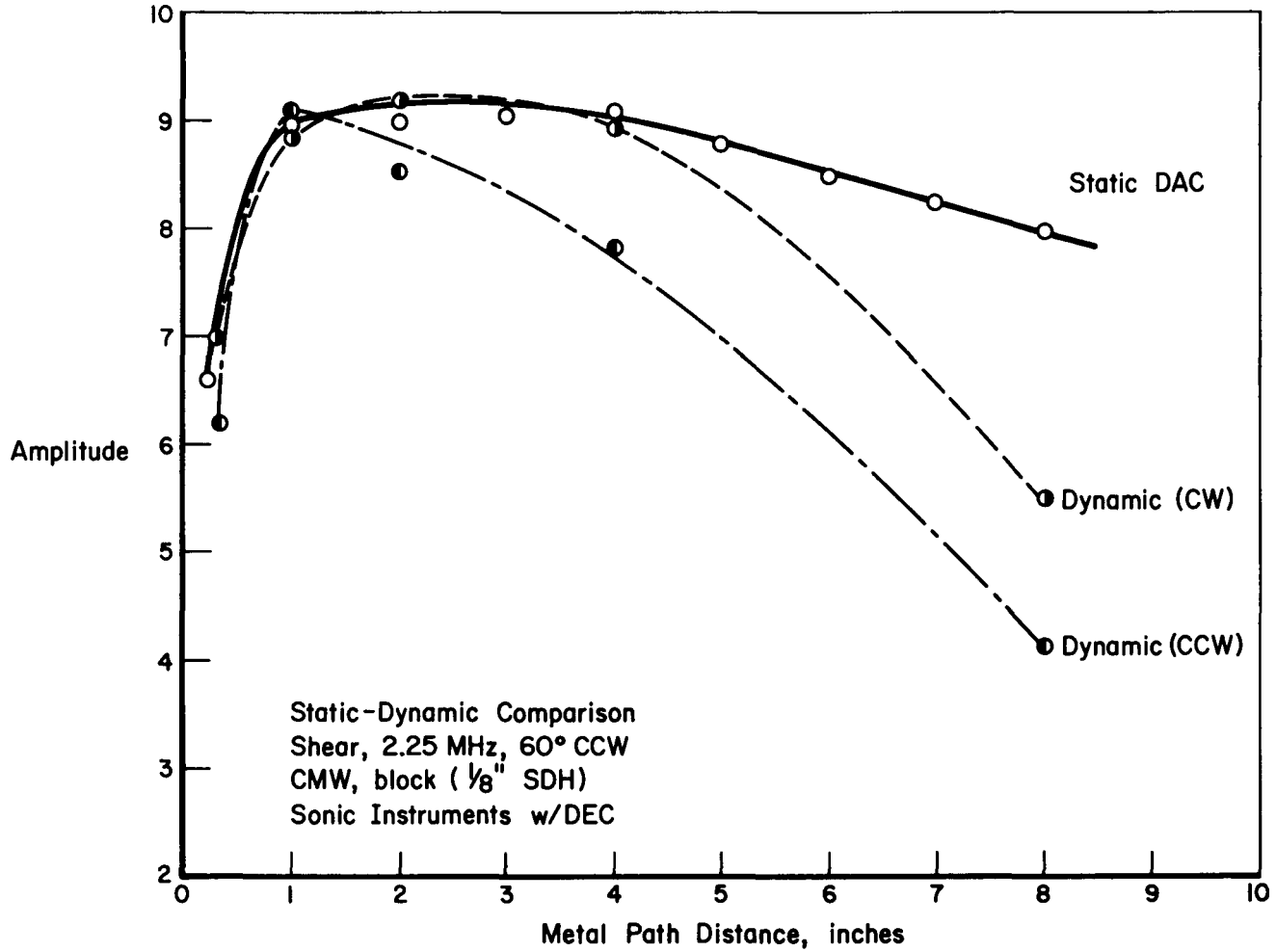

Figure 4-26. Static versus dynamic response to 1/8" SDHs using a 2.25 MHz 60° counterclockwise shear transducer.

demonstrate how deviation in sensitivity levels can occur depending on the direction of scan as well as static as compared to dynamic response to the same reflector. The same correlation is demonstrated for Shear transducers in Figures 4-23 through 4-26. Figure 4-22 relates the calibration levels seen in the field to that previously experienced in laboratory studies held at BCL.

Several observations can be made from these studies on calibration blocks. First, scanning sensitivity can deviate by as much as 80% of the sensitivity established by calibration. This sensitivity demonstrates a greater fluctuation than seen by multiple static calibrations. Second, scanning sensitivity deviations are on the average approximately 50% greater in one direction than in another explaining why more indications are reported by one shear transducer than another in the previous rotor inspections by one team. Third, calibration sensitivities can become altered as much as 45% during an inspection of a rotor. Fourth, 25-50% greater fluctuations are demonstrated by FBH calibration reflectors than SDH calibration reflectors.

Correlation on an Isolated Reflector

Relatively large, isolated indications are ideal to unequivocally establish a one-to-one correspondence between two independent rotor inspection data sets. Unfortunately, the Joppa 3 and Buck 6 rotors had very few of these types of indications. There is, however, one area at about Z = 57 inches in Joppa (axial position) where a relatively large indication was reported. Table 4-8 shows the reported results of both teams. Additional Team B indications in this area can be correlated with the single large indication suggesting that we have a "holding" type indication or one which exhibits some axial extent to it. Both Team A and Team B portrayals of this area are shown in Figure 4-27. There are drastic variations in amplitude (or EFBH) for the Team B indications. Also the EFBH area as measured by each of the two inspection teams is significantly different. At this axial position, however, the two teams are aligned in angle but appear to be offset in axial location by approximately 0.6 inch.

The "actual" location of the reflector within the rotor can only be confirmed destructively. Since both inspection teams sample the rotor volume at 0.25 inch increments and each have their own unique mechanical drive systems and associated errors, there exists the possibility that alignment for maximum signal reflection was not achieved. Note: Laboratory experiments with the Joppa 3 rotor have

TABLE 4-8. COMPARATIVE INDICATIONS FROM A SINGLE LARGE REFLECTOR

Team	R	θ	Z	Amplitude (EFBH)
B	0.44"	90°*	57.0"	154 x 10^{-4} in^2
A	0.6"	88°	57.62"	27 percent DAC (30 x 10^{-4} in^2)

* In reviewing the video tapes of the inspection it was discovered that the angle was reported incorrectly at 84 degrees.

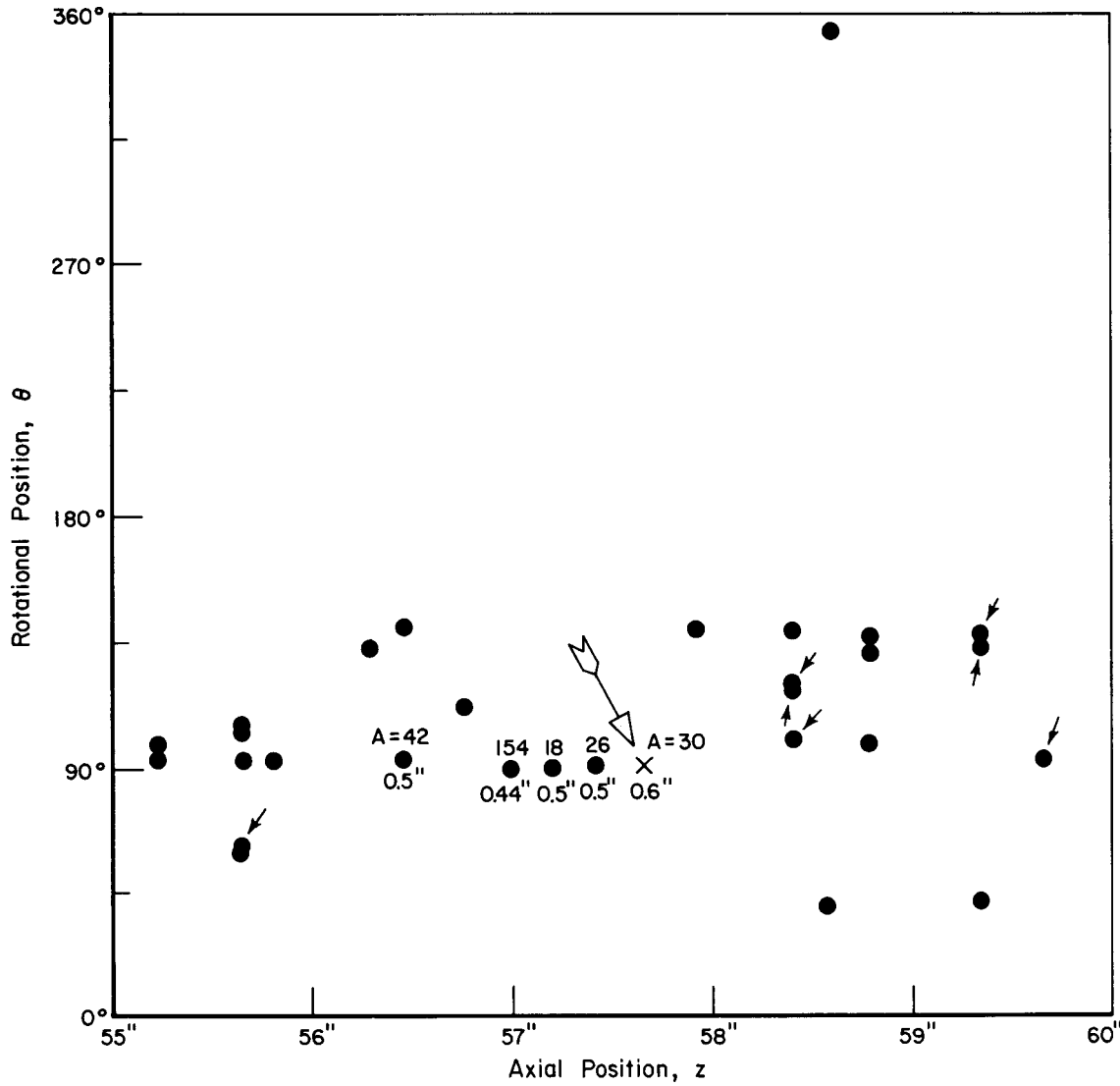

Figure 4-27. Graphical representation of reported ultrasonic indications for a relatively large, singular indication in Joppa. The arrow shows the only reported indication for our team while the solid dots show the many indications of the other team, including a possible "holding" indication at a depth of about 0.5 inches and an amplitude representation of 154 $(10)^{-4}$ inches ^{2} in area.

shown that a 0.050-inch axial change in the boresonic head can result in an amplitude decrease of 6 db, i.e., 50 percent reduction. Thus, we can only state that each of the teams has reported a relatively large indication, at approximately the same location in Joppa 3.

Further evaluation of the indication at Z between 57 and 58 inches in Joppa was conducted by BCL personnel in a special study. A field scanning system consisting of components from each of the inspection teams was used for this exercise. Various transducers at different sensitivities were used to record the variations in the indications (shape and amplitude) from this larger, singular reflection and examine them as a function of transducer beam geometry and frequency. Figure 4-28 shows three ultrasonic characterizations of the flaw indication. The indication was recorded from the time a signal was detected until it disappeared again into the baseline when scanned in both Z and θ directions. The sensitivity levels recorded in Figure 4-28 were the response to a 1/8" SDH established DAC. When the indication is compared to the beam profiles of the transducer associated with each plot, it is found that the recorded flaw size is approximately the same size as the beam at the depth of the flaw. This leads to the probable conclusion that the flaw is smaller than the beam diameter of the transducers used and all that is being "plotted" in the flaws "characterization" is the beam geometry at the depth of the reflector.

The region from 57 - 58 inches in Z was removed from the rotor, radiographed and destructively sectioned. This piece is referred to as JF 3 in the Task III report. The dissection revealed a series of Type II flaws (small porosity type indications 0.005 x .030 inch aligned along the Z axis). The flaws were centered at approximately 57.8 inches Z, $94^{o}\theta$, and 0.5 inches R. The flaws revealed by destructive sectioning are shown in Figure 4-29. Care was taken during JF 3's rough cut removal from the rotor to assure that the indication was indeed in the specimen by continuously monitoring the indication using a hand held transducer. Note: Variations from the "true" location of an internal reflector can be as great as 0.25 inch due to saw run-out as well as inaccuracies in measurement.

The results of the initial boresonic inspections, the BCL studies, and destructive sectioning of the area from Z = 56-58 inches in Joppa suggest the following. First, the dissection at 58 inches showed that the EFBH detected by a shear wave transducer was a more accurate predictor of flaw size than that of the P/C transducer. Second, the discrepancy between the reported location and

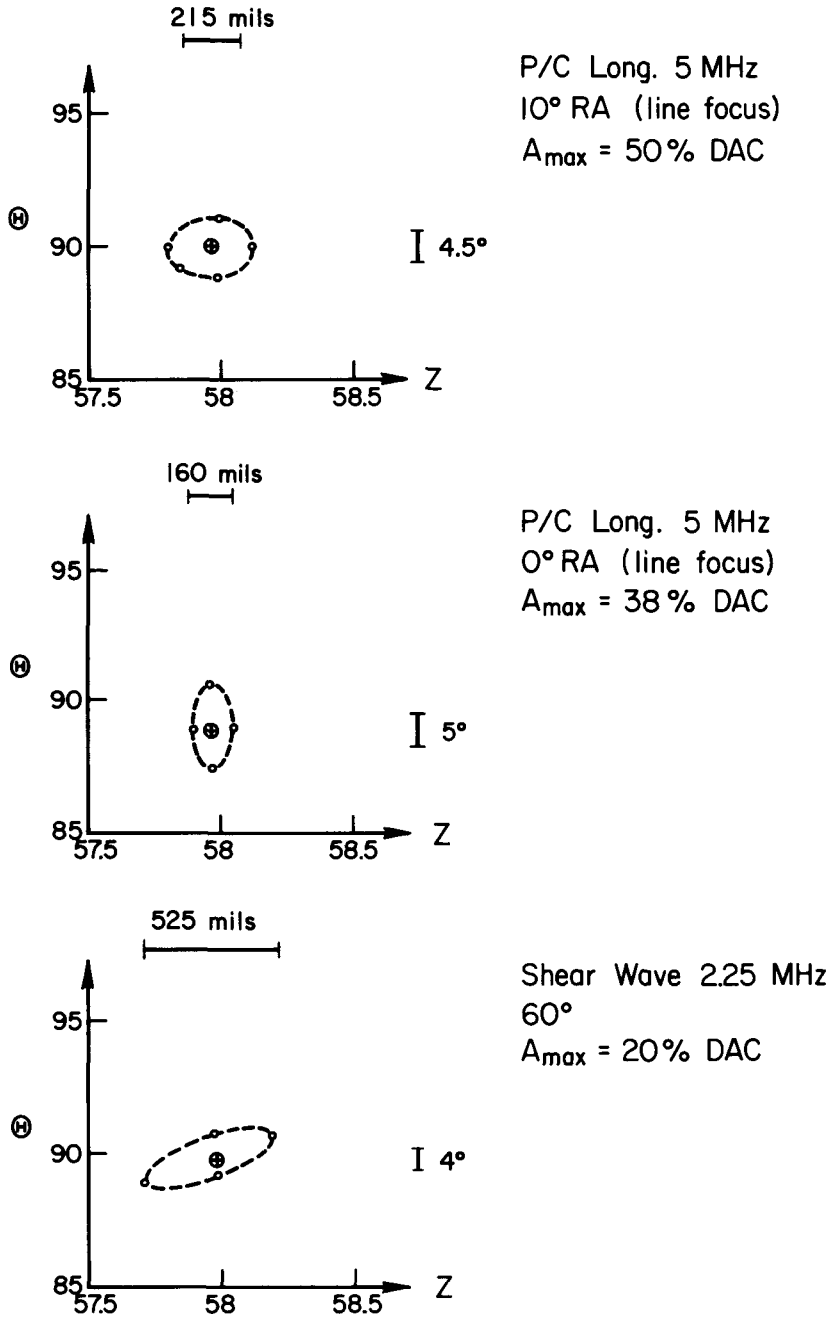

Figure 4-28. Flaw geometry observed by various transducers on the area at 58" Joppa.

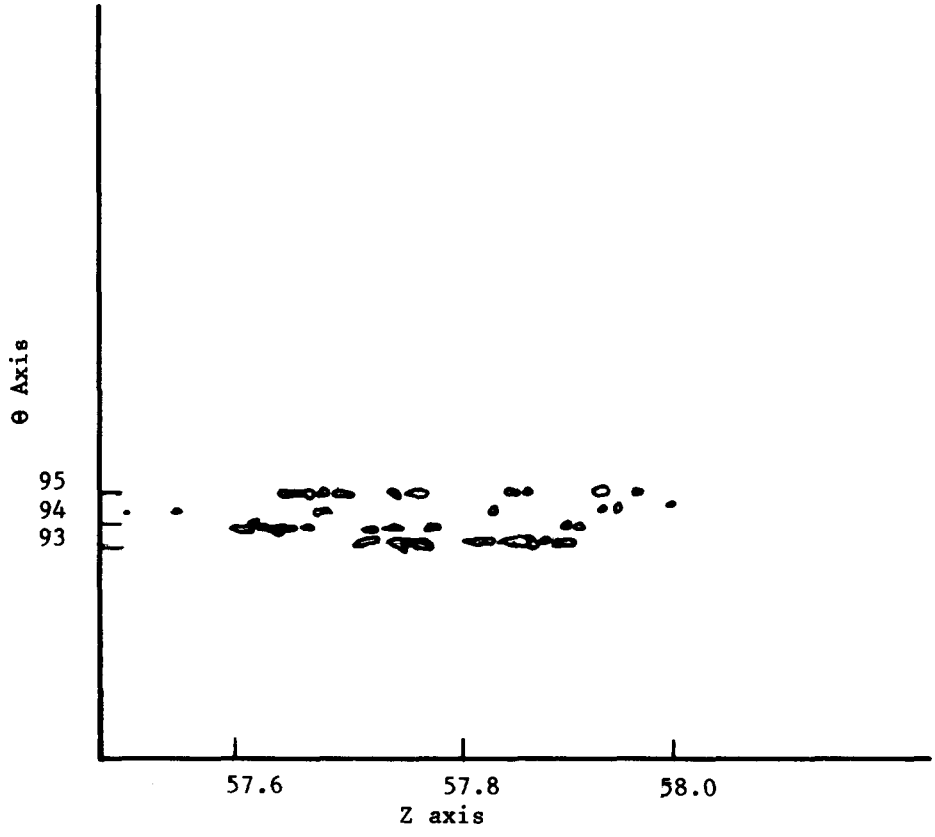

Figure 4-29. Plot of Type II flaws destructively sectioned in the area of Zc 57 - 58" Joppa.

the destructive results was approximately 0.6 inches.

Comparisons between NDE and Progressive Dissection of Other Segments of Joppa 3 and Buck 6. Nine specimens were removed from Joppa 3 and eight from Buck 6 as discussed in Table 4-6. The progressive dissection of 6 of the Joppa segments and 4 of the Buck segments resulted in a metallographic volume fraction for each of these areas of interest. The NDE boresonic data were corresponding reduced into a volume fraction for each segment. This was done by establishing an equivalent flat bottom hole area from the amplitude of each indication in the region of the specimen. This EFBH size was rotated to become a spherical volume which was in turn added to all other flaw volumes projected for the specimen and divided by the total volume of the specimen. The results of the analysis of the 10 specimens are shown in Figure 4-30.

It can be seen by analyzing the Vf plot in Figure 4-30 that most of the volume fractions reported by one group are above the 45 degree line and the other teams results fall below the 45^{o} line. The 45^{o} line would be a perfect correlation between destructive and nondestructive results. It should also be noted that the results from only one inspection are shown for Buck 6. The other inspection team was unable to scan these regions due to the bore condition caused by poor multiple grindout.

Relatively good correlation between destructive and nondestructive Vfs are demonstrated on specimens J7a1-8, J 7-1, B 312, J 7A5-15 and B 112 by one team as well as J 6A-2 and J 7A1-3 by both teams. Excessive over-estimation of specimens J 7A-1 and J 7A1-81 is hypothesized to be caused by the large signal amplitude reflected by a Type II flaw to a pitch/catch transducer. The cause of the underestimation of flaws in the other areas (by both teams) cannot be explained with a single reason. These tend to reflect the general uncertainty of boresonic inspections due to deviations in sensitivity levels, position inaccuracies, and general mechanical properties associated with each system. It should be noted, however, that the sectioned regions of the rotors revealed gross quantities (as many as 100 on a 1" x 1" plane of polish) of relatively small (30×10^{-4} square inches) flaws. No major flaw was found during sectioning.

It can also be hypothesized that the plot reflects a preference of the shear wave transducer of one team over the P/C transducer of the other team. That is, the pitch/catch transducer would be most sensitive to the Z-θ oriented reflectors

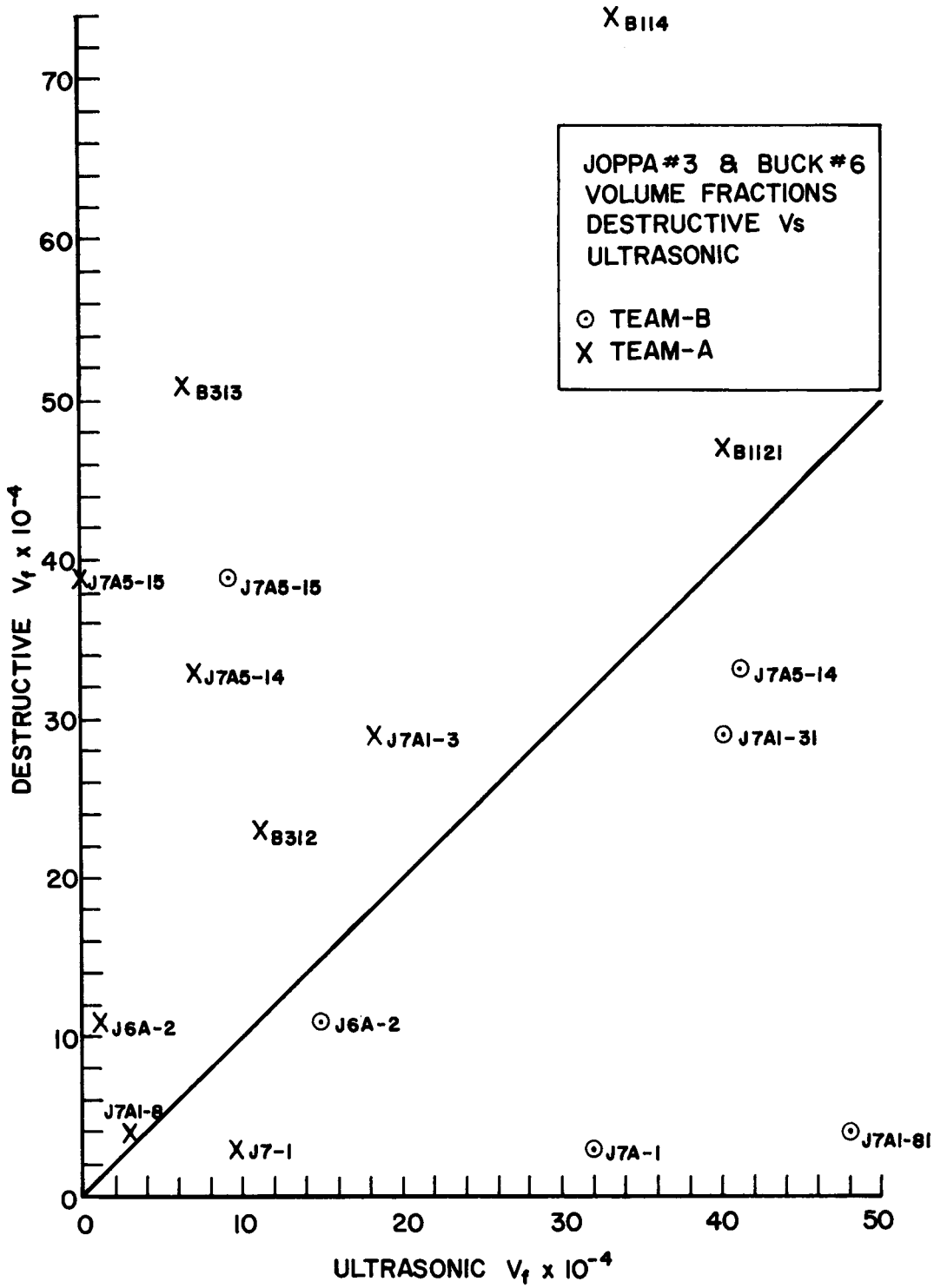

Figure 4-30. Comparison between destructive Vf and ultrasonic Vf.

within the specimens whereas the shear wave units would tend to yield lower amplitude responses to these same reflectors.

Section 5

CONCLUSIONS

There have been several sets of results developed on this program which have led us to the following general conclusions:

(1) The NDE practices used in the field at the start of this program were generally acceptable for giving a survey of the presence of discontinuities distributed throughout the rotor. They were not sufficient to characterize the details of reflectors found on a scale required by fracture mechanics considerations (resolution on the order of 1/16 inch).

(2) The ability for current ultrasonic techniques to detect and characterize subsurface, radially oriented cracks has not been proven conclusively since no such cracks were present in any of the rotor material scanned during the program. Shear wave transducers were found to be able to detect radially oriented EDM notches when their side walls were slightly roughened, but no proof of detectability has been obtained on natural cracks.

(3) A relatively low degree of repeatability was found during reinspection of the same rotor areas when the reflectors were on the order of 1/16 to 1/8 inch in diameter. This lack of detailed repeatability could be caused by several factors, including mechanical scanner systematic errors, inspection head coupling uncertainties, data transferral from instruments to data sheets as well as operator variations in calibration settings.

(4) The limited ability of current systems to characterize in detail the nature of natural reflectors lies in the system design philosophy of using transducer configurations which serve as both detection and characterization units, simultaneously.

(5) On a volume fraction basis, the radial shear wave transducers tend to predict undersized while the P/C units tend to over estimate the size of the flaws observed non-destructively.

Section 6

REFERENCES

1. Timo, D. P., and Placek, R. J., "Inspection and Evaluation of In-Service Turbine Rotor Forgings", presented at the 39th Annual Meeting of the American Power Conference, April 18-29, 1977.

2. Gottelt, H. R., "On-Site Ultrasonic Inspection of Turbine Rotors", Power Engineering, September, 1974, pp. 56-57

3. Renner, R. W., Greenberg, H. A., and Clark, W. G., "Ultrasonic and Metallurgical Evaluation of Flaws in Large Rotor Forgings", Proceedings, 5th International Conference on Nondestructive Testing, 1967, pp. 37-42.

4. Liversidge, D. B., Fearn, G. A., and Dodgson, M. W., "Ultrasonic Assessment of Unbored Rotor Forgings", Nondestructive Testing, November, 1968, pp. 385-400.

5. Sauer, D. L., and Matters, R. G., "Nondestructive Inspection of Turbine Generator Parts During Manufacture and Service", Nondestructive Testing, November, 1968, pp. 385-400.

6. Golis, M. J., and Reinhart, E. R., "Improved Reliability of Steam Turbine Rotors Through Effective NDE", Eighth World Conference on Nondestructive Testing, Cannes, France, September, 1976.

APPENDIX A - GLOSSARY OF TERMS AND SYMBOLS

Amplitude Gate - An electronic circuit designed to supply an analog signal proportional to the amplitude of any ultrasonic pulse which occurs within a selected time period.

Area Fraction - The ratio of the defect area observed on a plane within a specified region to the total area of the region, expressed as a percentage. The defective area can be a single site, but it is usually the summation of numerous small sites. Note that an area fraction measured ultrasonically can be different numerically than that measured using destructive sectioning. See: Volume Fraction.

"Area" Indications - The term one inspection group uses synonymously with a cluster. See: Cluster.

Beam Profile - The curve produced when the radiated peak amplitude signal (detected at a point location of the sound field of an ultrasonic transducer) is plotted as a function of distance from the central axis of the radiation field (the detector displacement being parallel to the face of the transducer).

Blind Bore - A hole drilled coincident with the axis of a rotor but not entirely through it. Thus, it can be entered from only one end.

Bore Preparation - The removal of end plugs, substances (such as oxide layers) adhering to the bore surface, and surface roughness due to pitting corrosion. The surface is usually smoothed using flapper wheels and/or power honing devices.

Borescope - A tubular device equipped with internal illumination and viewing lenses used for visual observation of interior surfaces which are not readily accessible.

Boresonic - A term coined for the pulse-echo ultrasonic examination of rotor shafts when the transducers are located within a central hole and radiating outward into the volume of the rotor. It can take on numerous forms depending on the design and mode of the transducers used.

Bottle Bore - A region along the bore of a rotor which has been enlarged for the purpose of removing defective material. The enlargement is equally distributed around the circumference of the bore. Local areas may be ground out for the same reason, and these are referred to as dimples. The transition from original bore size to the new bottle bore size may be tapered by machine or ground for a reasonably smooth contour.

Cloud - Designation given to the boresonic indication when several closely spaced pulses appear as a group but are not clearly resolved with respect to one another. See: "Level" Indications.

Cluster - Designation given to the boresonic screen indication when several closely spaced but clearly distinguishable pulses appear as a group. These can be due to numerous discrete reflectors within the rotor as well as multiple reverberations between sizeable reflectors. See: "Area" Indications.

DAC - Distance Amplitude Curve - The curve showing signal amplitude received as a function of depth below the bore surface and established through the use of calibration holes placed at varying distances from the bore surface. Also used for Distance Amplitude Correction which in this report is designated DEC (see below).

DEC - Distance Electronic Correction - The compensation circuitry used to normalize the observed decay of signal strength to a uniform height, usually to allow gating devices to serve as accept/reject alarms. Also referred to as Time Corrected Gain (TCG).

Depth Resolution - An ultrasonic system's capacity to differentiate reflectors which lie at closely spaced but different distances from the transducer. It is expressed as the minimum distance at which the system can still identify the presence of two discrete reflectors. See: Spatial/Lateral Resolution.

EFBH - Effective Flat Bottom Hole - A measure of severity used to describe a natural discontinuity; the FBH size needed at the specific location of the natural discontinuity to give the same pulse echo amplitude as detected from the natural discontinuity.

Elapsed-Time Gate - An electronic circuit which monitors the time interval from a reference pulse (usually the main bang or inspection initiating pulse) and the first received pulse which exceeds a predetermined pulse amplitude threshold. It is used as an estimate of the distance from the ultrasonic transducer to the reflecting surface.

Examination vs Inspection - These terms are often used interchangeably in the general literature but in this report, inspection refers to the overall quality-control activity of assuring the condition of the rotor while specific examinations such as visual, boresonic, and magnetic particle refer to conducting tests to gain technical information.

FBH - Flat Bottom Hole - A reflective target used as a calibration reflector for boresonic examination. The target consists of the flat bottom of a drilled hole and its size is expressed in terms of its diameter. See: SDH.

Holding Indication - A boresonic echo pulse which continues to show a sizeable amount of reflected ultrasonic energy beyond what would be expected of a point source, as the ultrasonic search assembly is moved either axially or circumferentially along the surface.

Inspection Head - The mechanical device used to hold boresonic transducers in their proper orientation, at a prescribed pressure, and with a suitable flow of acoustic couplant.

ISI - In-Service Inspection - The quality assurance steps taken to verify that a system or component has not degraded due to operational causes since the previous inspection (either preservice or an earlier in-service inspection).

"Level" Indications - Synonymous with cloud indications. See: Cloud.

Longitudinal Wave Transducer - A boresonic examination element which radiates a sound beam normal to the bore surface (slightly inclined in the case of a pitch/catch unit).

Magnetic-Particle Examination - A scheme whereby a circumferential magnetic field is established within the near bore region of a rotor and leakage magnetic flux lines within the bore are used to attract powders exhibiting high magnetic permeabilities and whose clumping into localized regions indicate the presence of a flux-inhibiting surface (or near-surface) discontinuity.

Pitch/Catch - An ultrasonic transducer having a pair of piezo-electric elements housed in the same structure. One element is used to transmit the ultrasonic pulses and the second is used for echo reception. This design maximizes sensitivity to near-surface reflectors.

Rotor Cylindrical Coordinates -

R - Radial distance, usually measured from the bore surface.

θ - Rotational position often measured with respect to the No. 1 balance hole of a rotor and expressed in degrees or clock position as viewed from the generator flange.

z - Axial location, measured from the generator flange end of a rotor.

SDH - Side Drilled Hole - A reflective target used as a calibration reflector and found most useful when angular independence is critical, as in the use of shear wave transducers. The side of the hole is used as the target surface and the size is expressed in terms of hole diameter.

Shear Wave Transducer (Radial vs Axial) - A boresonic examination element which radiates a sound beam inclined at an angle with respect to the bore entry surface. The beam may be axial (inward or outward in a plane containing the bore axis) or radial (clockwise or counterclockwise in a plane transverse to the bore axis).

Spatial/Lateral Resolution - An ultrasonic system's capacity to differentiate closely spaced reflectors which lie equidistant from the transducer. It is expressed as the minimum distance at which the system can still distinguish the presence of two discrete reflectors. See: Depth Resolution.

Tangential Bore Stress - The tensile stresses found near the bore, in a plane transverse to the bore axis and tangent to the bore surface.

Transducer - The piezoelectric element used to convert electrical impulses into ultrasonic stress waves as well as the converse effect (convert stress waves into electrical pulses).

Traveling Indication - A boresonic echo pulse which changes range as the ultrasonic search assembly is moved either axially or circumferentially along the surface; e.g., this range change is expected from a point reflector as a shear wave transducer is rotated around a bore. It is also expected of an extended reflector which is included at an acute angle with respect to the bore axis.

Volume Fraction - The ratio of defective volume located within a specified region to the total volume of the region, expressed as a percentage. See: Area Fraction.

APPENDIX B - SUPPLEMENTAL MAGNETIC PARTICLE SENSITIVITIES FOR BOTH NOTCHES AND DRILLED HOLES WITH AND WITHOUT A 1-INCH-THICK BACKING PLATE TO SIMULATE CONDITIONS IN THICK FORGINGS

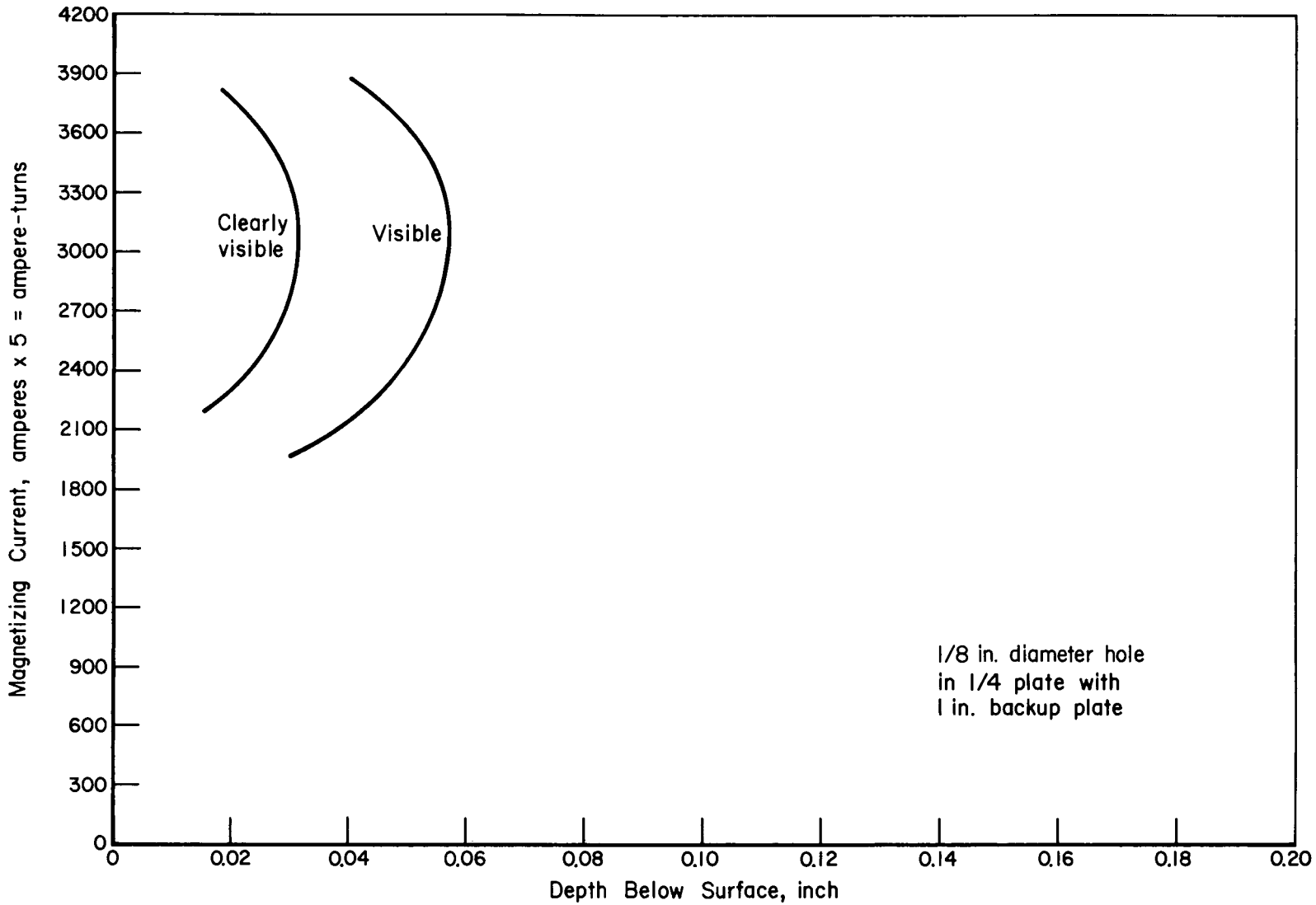
Magnetizing Current, amperes x 5 = ampere-turns
4200
3900
3600
3300
3000
2700
2400
2100
1800
1500
1200
900
600
300
0
Clearly visible
Visible
1/8 in. diameter hole
in 1/4 plate with
1 in. backup plate
0
0.02
0.04
0.06
0.08
0.10
0.12
0.14
0.16
0.18
0.20
Depth Below Surface, inch

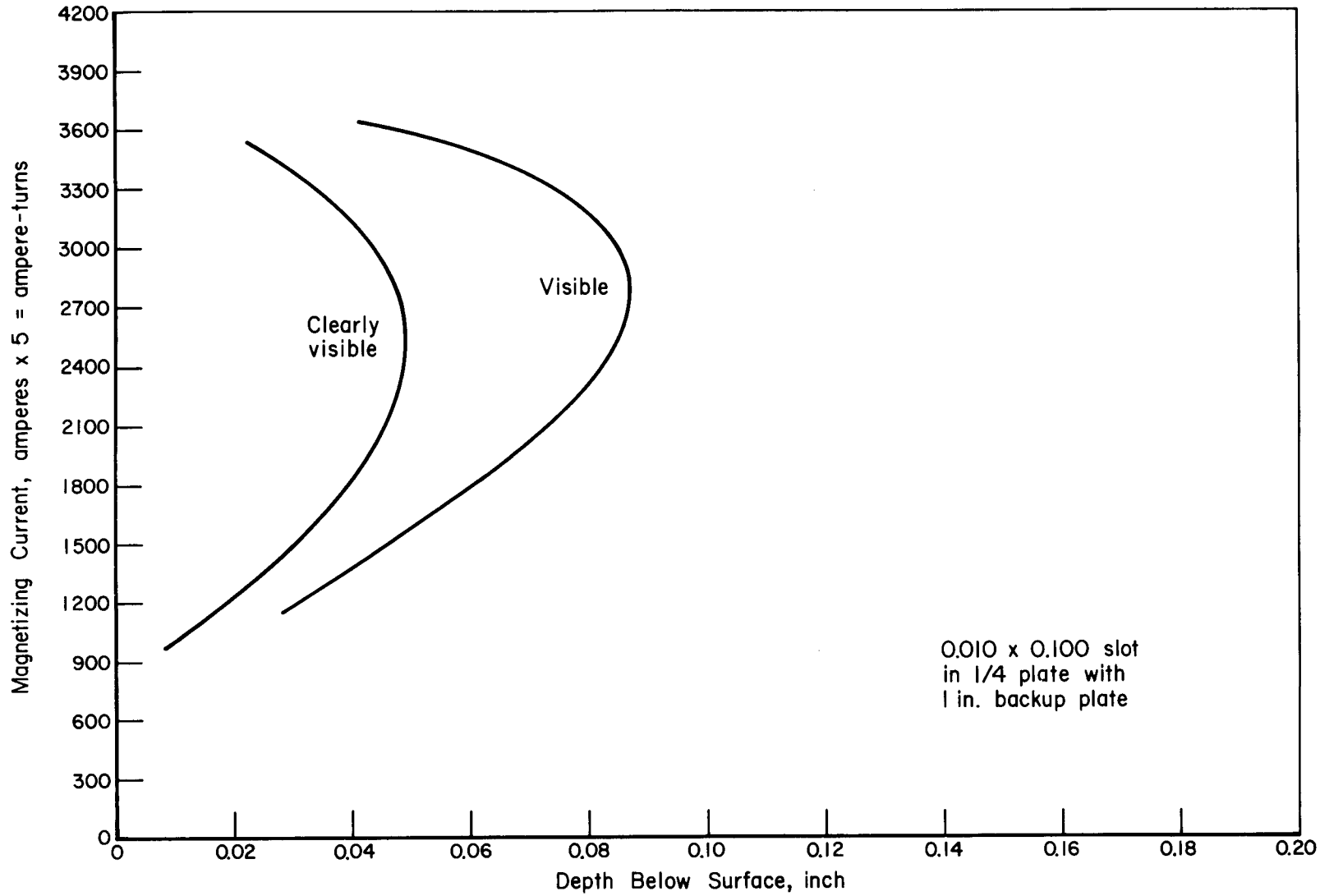
4200
3900
3600
3300
3000
2700
2400
2100
1800
1500
1200
900
600
300
0
Magnetizing Current, amperes x 5 = ampere-turns
Clearly visible
Visible
0.010 x 0.100 slot in 1/4 plate with 1 in. backup plate
0
0.02
0.04
0.06
0.08
0.10
0.12
0.14
0.16
0.18
0.20
Depth Below Surface, inch

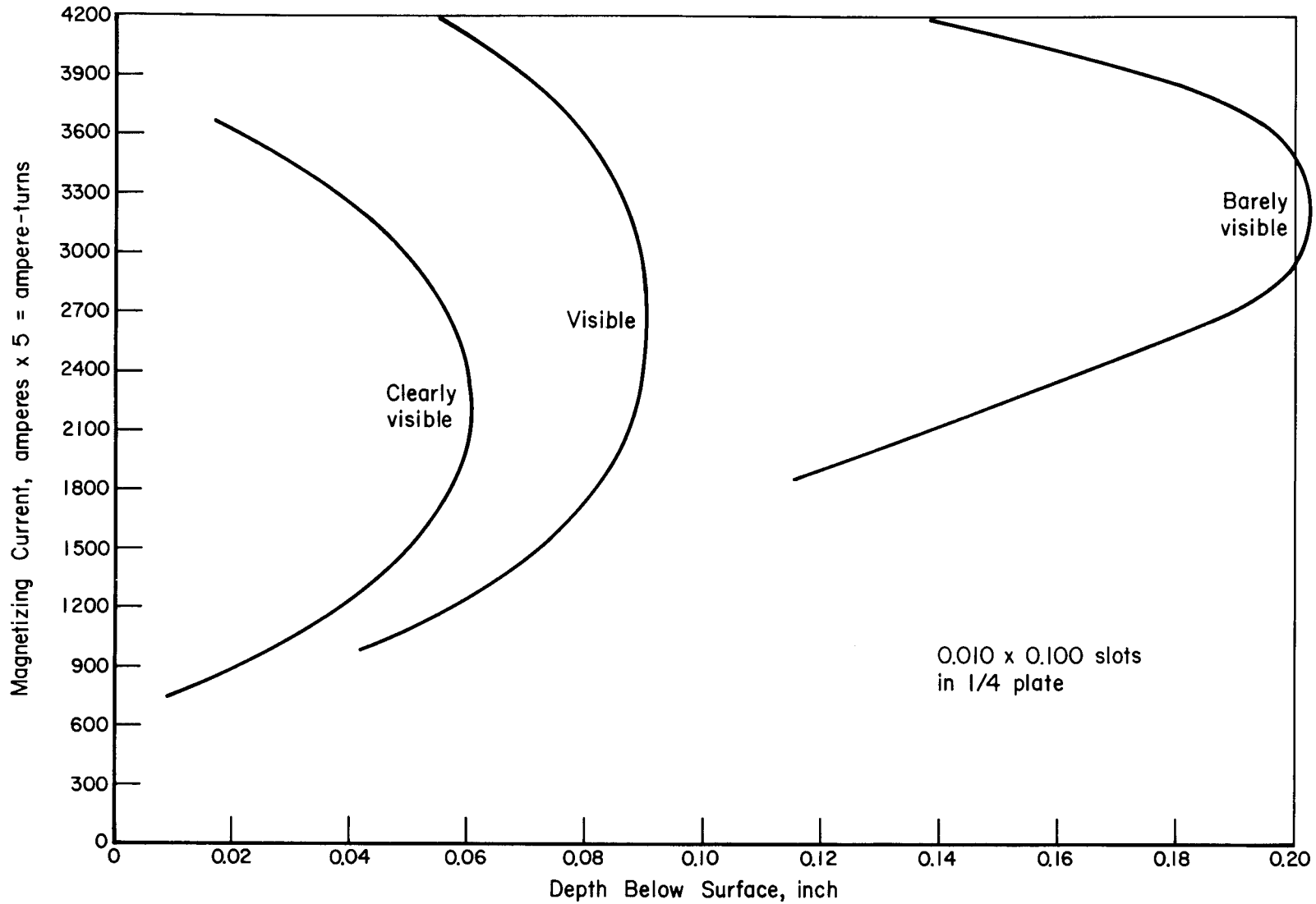
Magnetizing Current, amperes x 5 = ampere-turns
4200
3900
3600
3300
3000
2700
2400
2100
1800
1500
1200
900
600
300
0
0
0.02
0.04
0.06
0.08
0.10
0.12
0.14
0.16
0.18
0.20
Depth Below Surface, inch
Clearly visible
Visible
Barely visible
0.010 x 0.100 slots in 1/4 plate

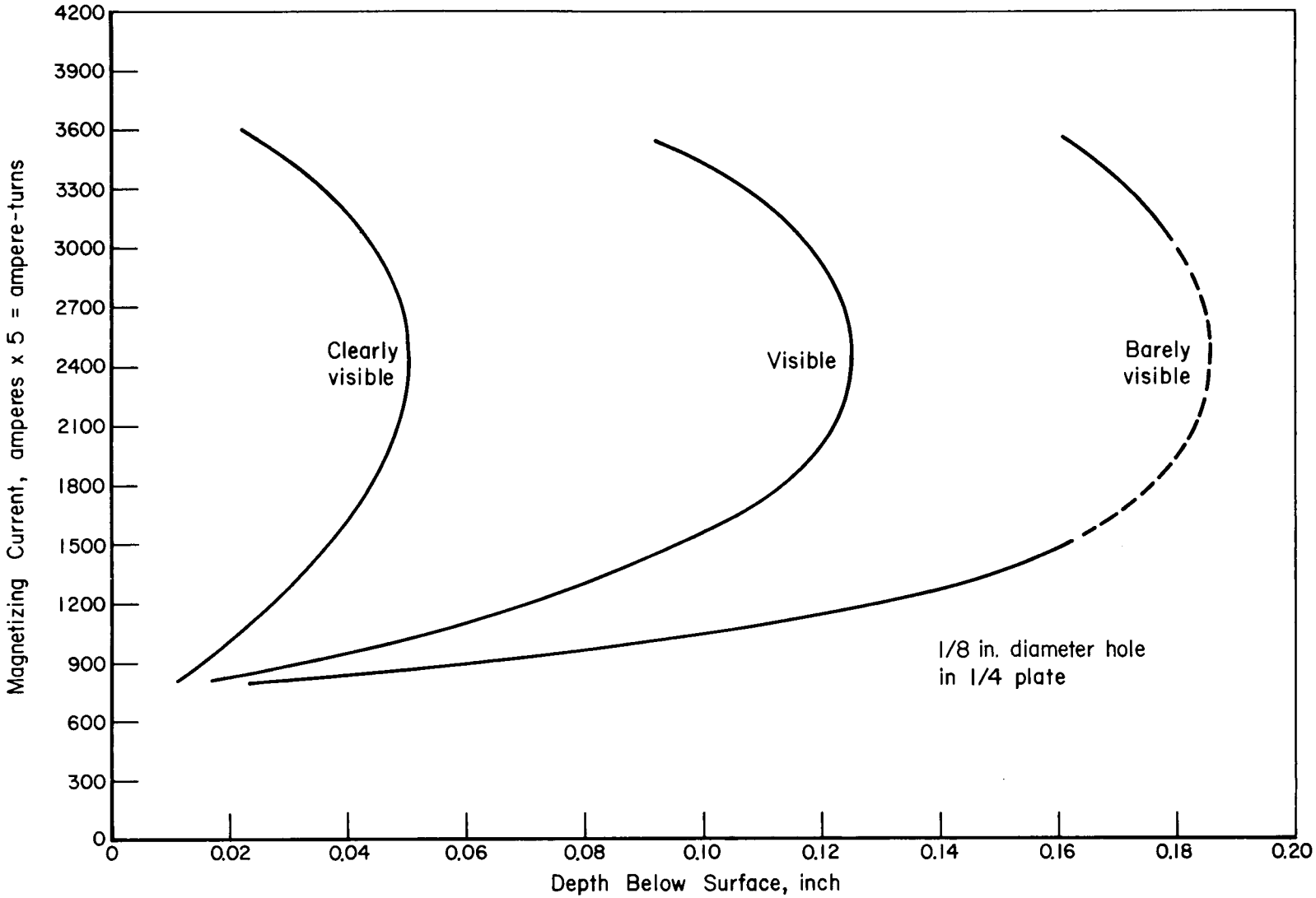
Magnetizing Current, amperes x 5 = ampere-turns
4200
3900
3600
3300
3000
2700
2400
2100
1800
1500
1200
900
600
300
0
0
0.02
0.04
0.06
0.08
0.10
0.12
0.14
0.16
0.18
0.20
Depth Below Surface, inch
Clearly visible
Visible
Barely visible
1/8 in. diameter hole in 1/4 plate

APPENDIX C - TRANSDUCER BEAM PROFILE SCANS

This appendix is a compendium of summary scan data developed through a comprehensive laboratory evaluation of ten pitch/catch transducers and two shear wave transducers. These units comprise both typical field evaluation units, as well as a few experimental configurations which have shown promise to various groups involved in boresonic inspection.

In each case, the upper center curves represent the uncorrected distance amplitude correction curves for each transducer. The upper curve represents the response from a 1/8-inch SDH. The lower curves are the response from a 1/16-inch FBH. The shear wave FBH's were inclined at a suitable angle so that the normal to the FBH was approximately parallel to the beam centerline. Where a collection of indications are shown on these sets of curves, they represent multiple occasions when the data were taken; thus they represent the deviation in the measured response from the transducer under repeated exercises and thus are an indication of the reliability of the particular type of reflector as the basis for a standardization or calibration block.

The series of curves to the lower left represent the beam profiles measured transverse to the beam's axis and at these distances indicated in the figure. The scans were made by traversing each transducer in the Z direction (bore axis) using a 1/16-inch FBH as a reflector target. The series to the lower right were made in the same manner with the scan being taken in the θ direction. Smooth, bell-shaped, curves are in general in agreement with theoretical predictions associated with such transducers. The highly irregular responses of some transducers suggest nonideal behavior and in extreme cases could lead to the recording of ambiguous data due to the presence of multiple indications caused not by more than one reflector, but rather the presence of more than one lobe in the interrogating beam.

The pictographic renditions of the beam cross-sections in the upper left and upper right corners are made from the half amplitude points as observed and

recorded in the scans of the beam profiles. These last two descriptions of the beam profiles are most important in that they should be used for the determination of the overall inspection scan increments in both the Z and the θ directions.

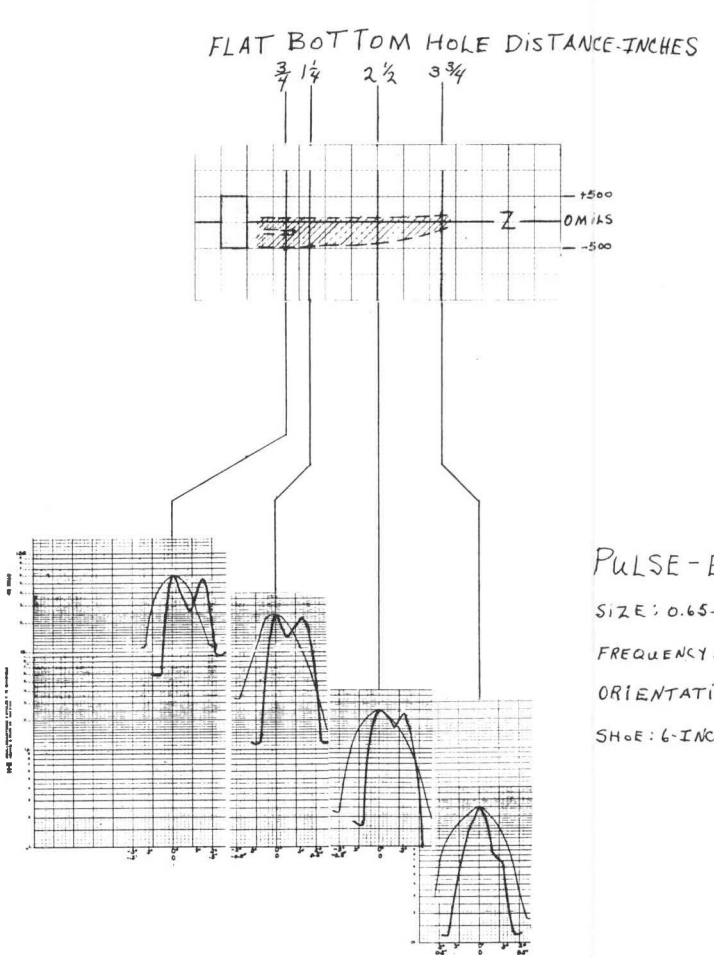

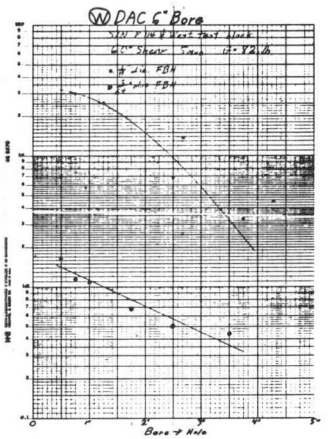

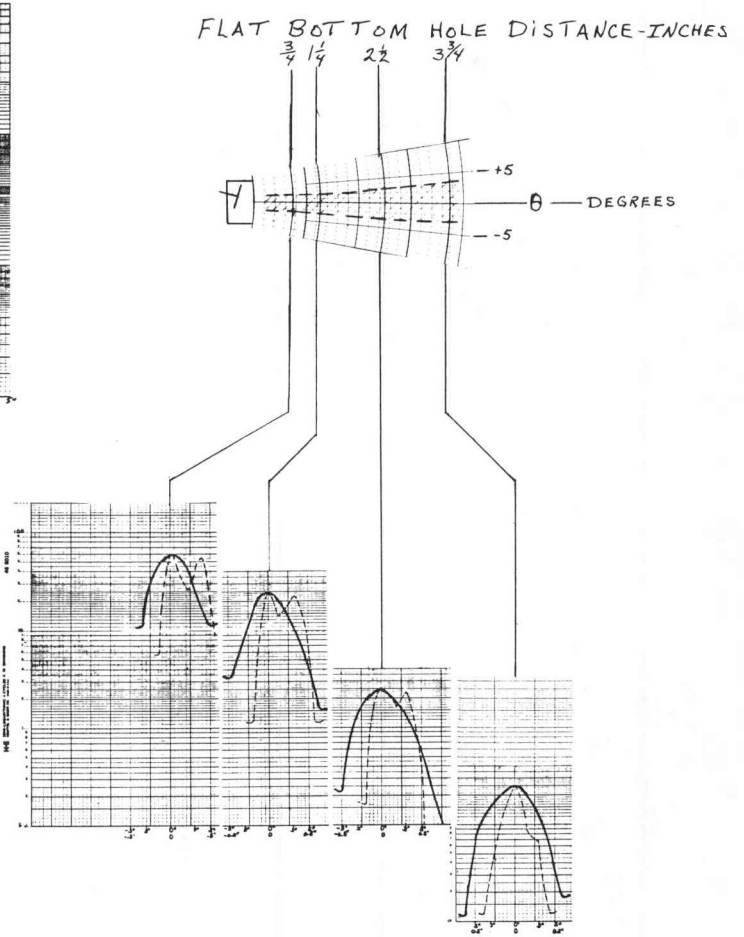

PULSE-ECHO TRANSDUCER

SIZE: 0.65-INCH by 0.20-INCH

FREQUENCY: 5 MEGAHERTZ

ORIENTATION: 60 DEGREES SHEAR WAVE

SHOE: 6-INCH DIAMETER BORE, LUCITE

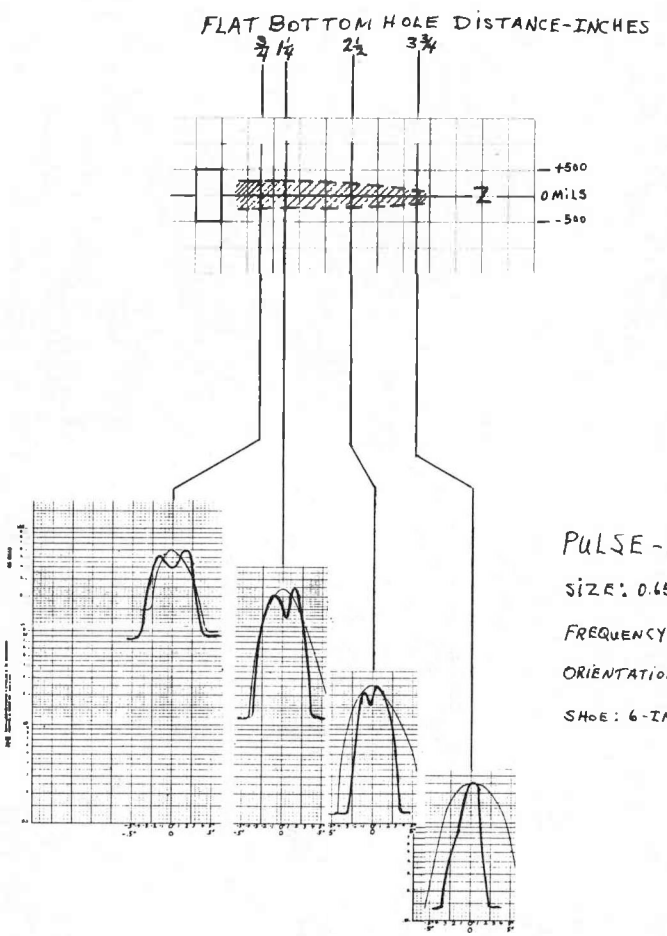

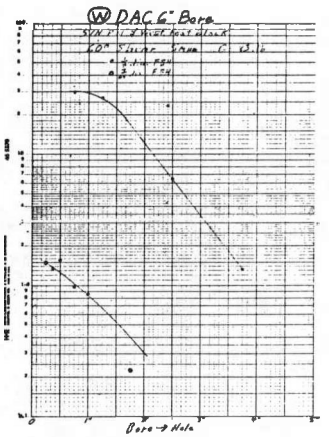

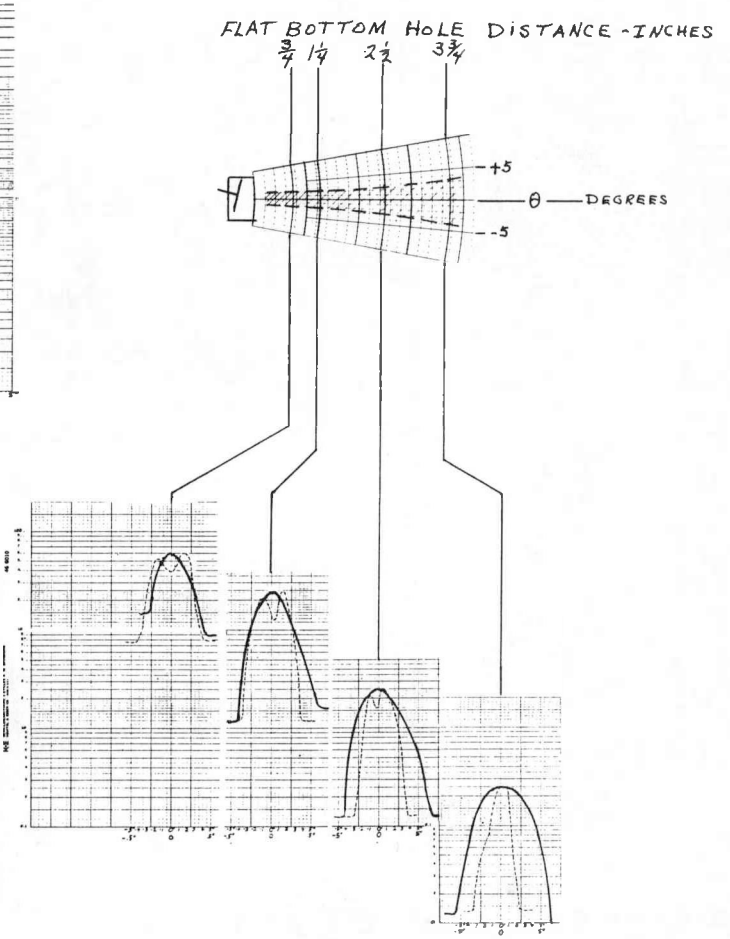

PULSE-ECHO TRANSDUCER

SIZE: 0.65-INCH BY 0.20-INCH

FREQUENCY: 5 MEGAHERTZ

ORIENTATION: 60 DEGREES SHEAR WAVE

SHOE: 6-INCH DIAMETER BORE, LUCITE

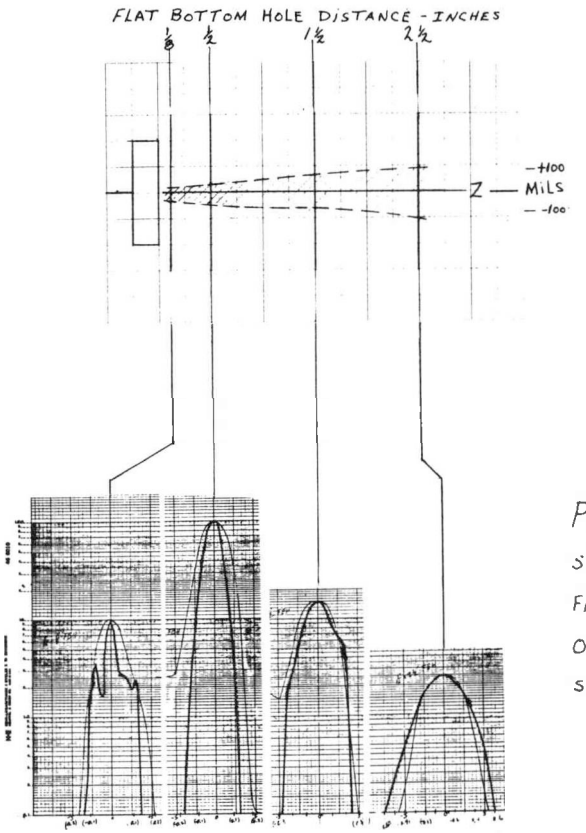

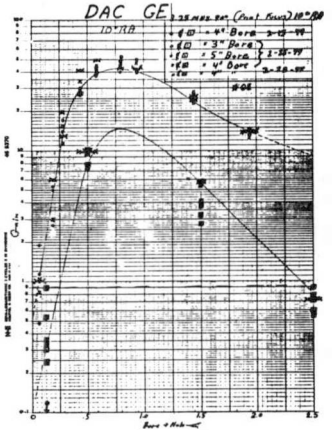

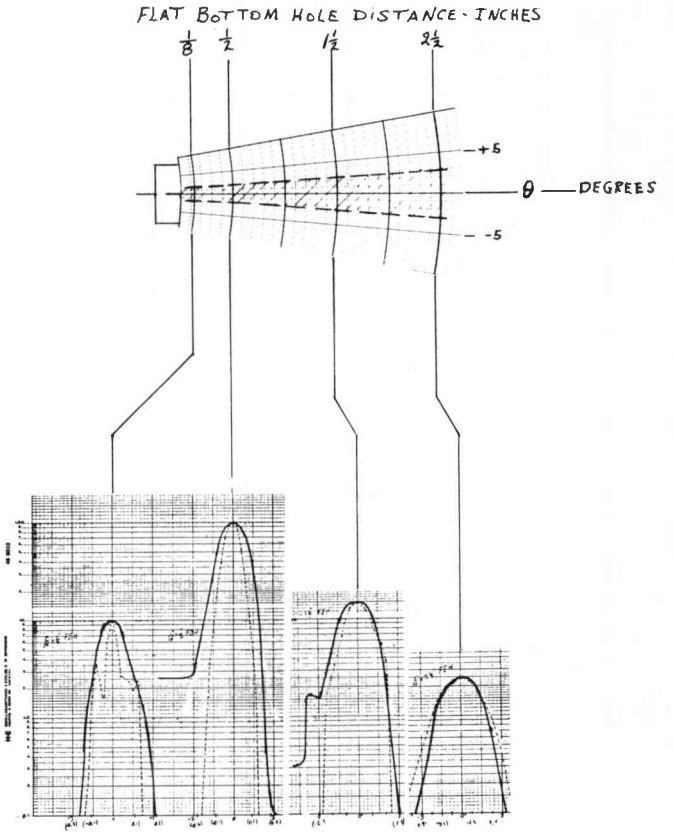

PITCH-CATCH TRANSDUCER

SIZE: 0.25-INCH by 0.50-INCH

FREQUENCY: 2.25 MEGAHERTZ

ORIENTATION: 10 DEGREES ROOF ANGLE, POINT FOCUS

SHOE: 4-INCH DIAMETER BORE, LUCITE

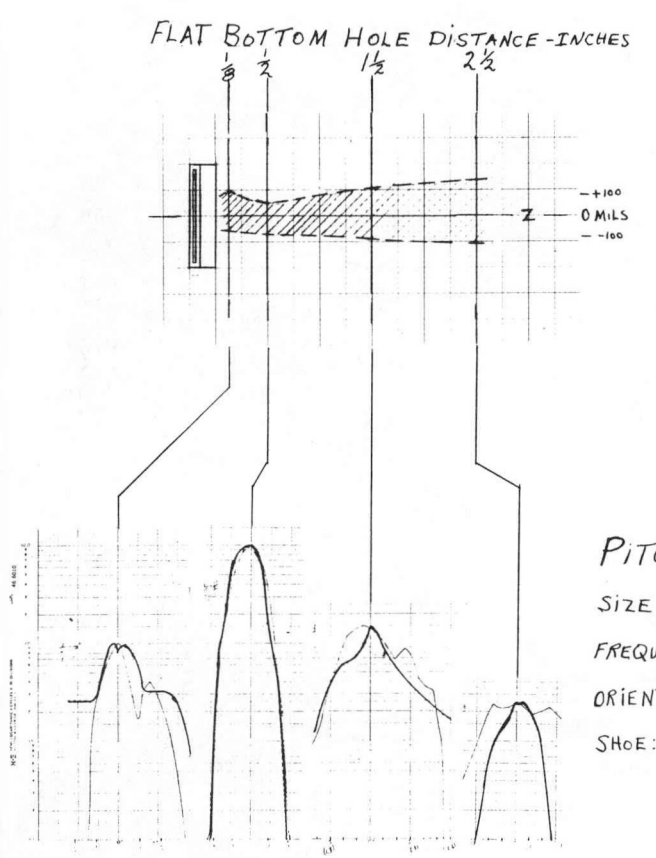

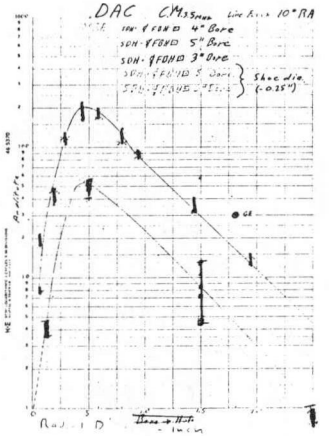

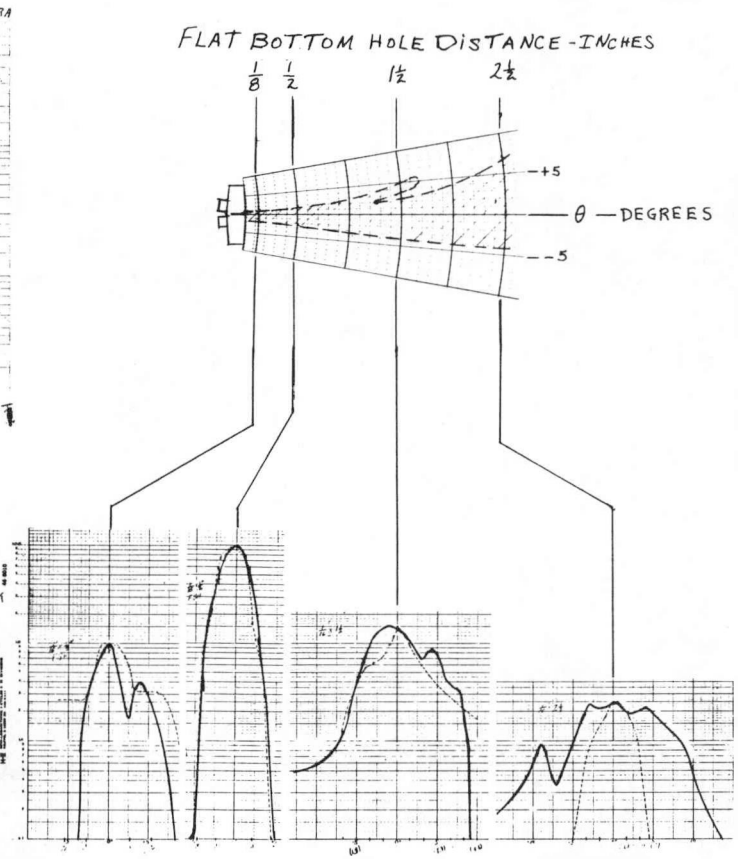

PITCH-CATCH TRANSDUCER

SIZE: 0.25-INCH by 0.50-INCH

FREQUENCY: 3.5 MEGAHERTZ

ORIENTATION: 10 DEGREES ROOF ANGLE, LINE FOCUS

SHOE: 4-INCH DIAMETER BORE, LUCITE

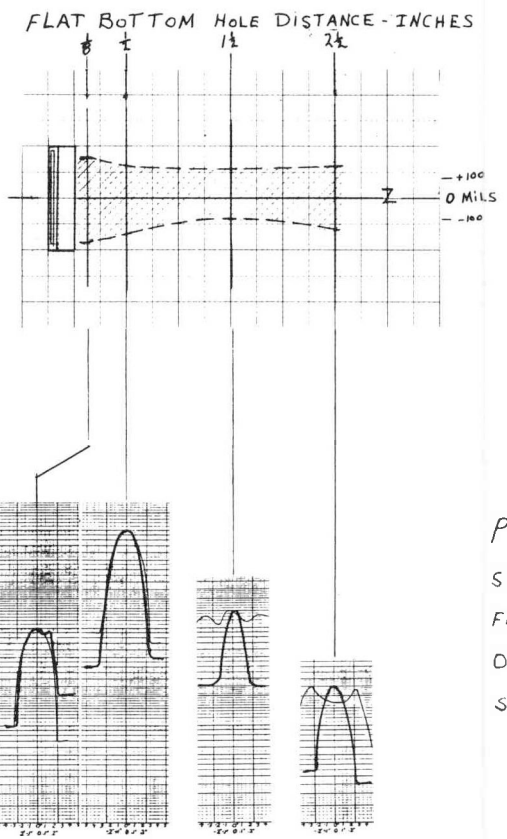

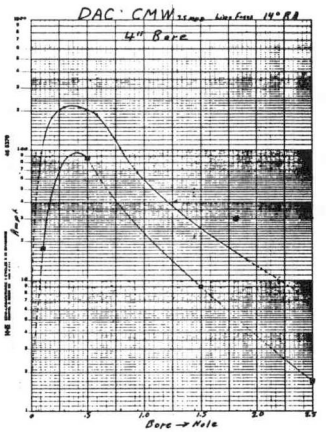

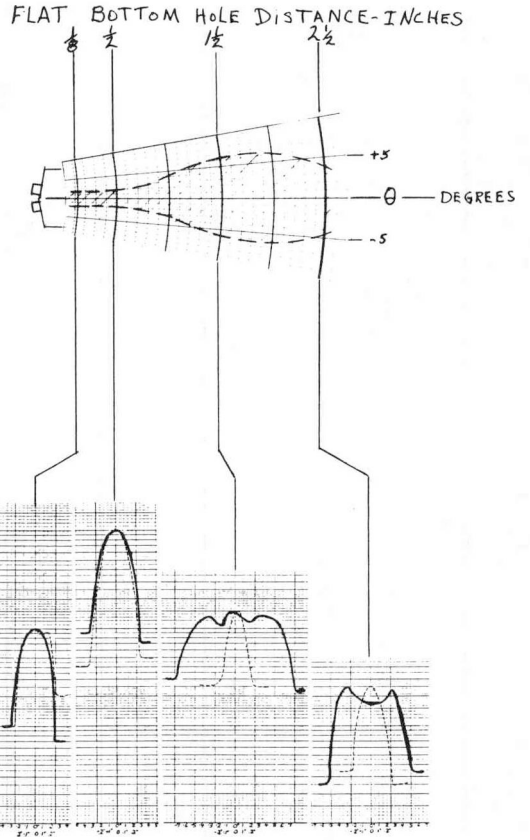

PITCH-CATCH TRANSDUCER

SIZE: 0.25-INCH by 0.50-INCH

FREQUENCY: 3.5 MEGAHERTZ

ORIENTATION: 14 DEGREES ROOF ANGLE, LINE FOCUS

SHOE: 4-INCH DIAMETER BORE, LUCITE

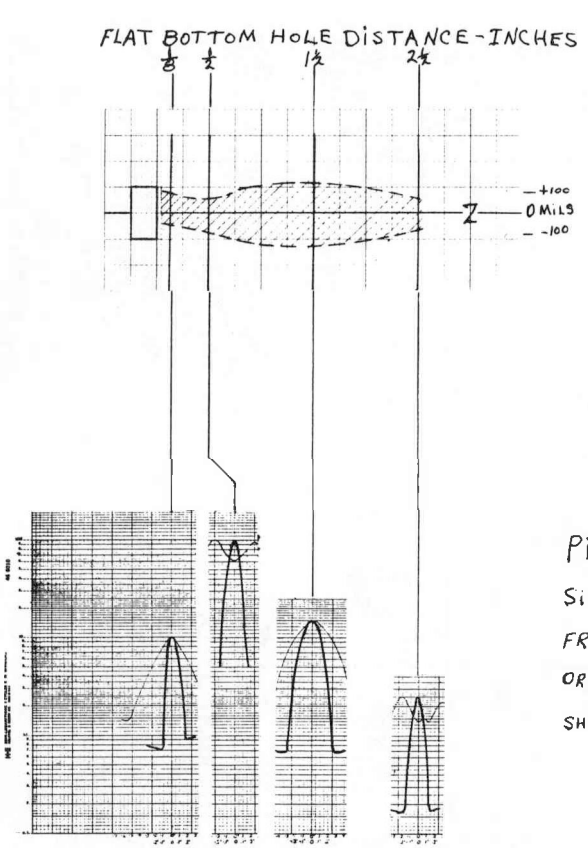

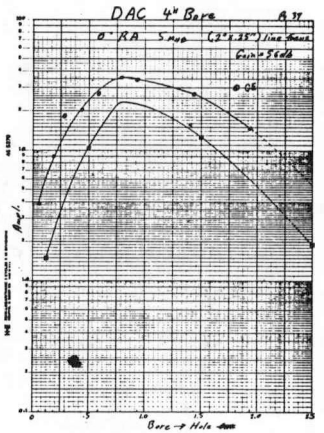

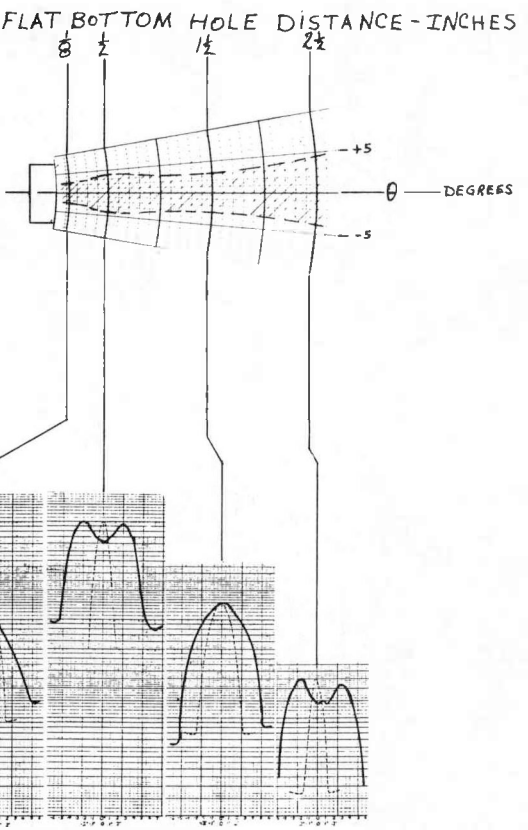

PITCH-CATCH TRANSDUCER

SIZE: 0.20-INCH BY 0.25-INCH

FREQUENCY: 5 MEGAHERTZ

ORIENTATION: 0 DEGREE ROOF ANGLE, LINE FOCUS

SHOE: 4-INCH DIAMETER BORE, LUCITE

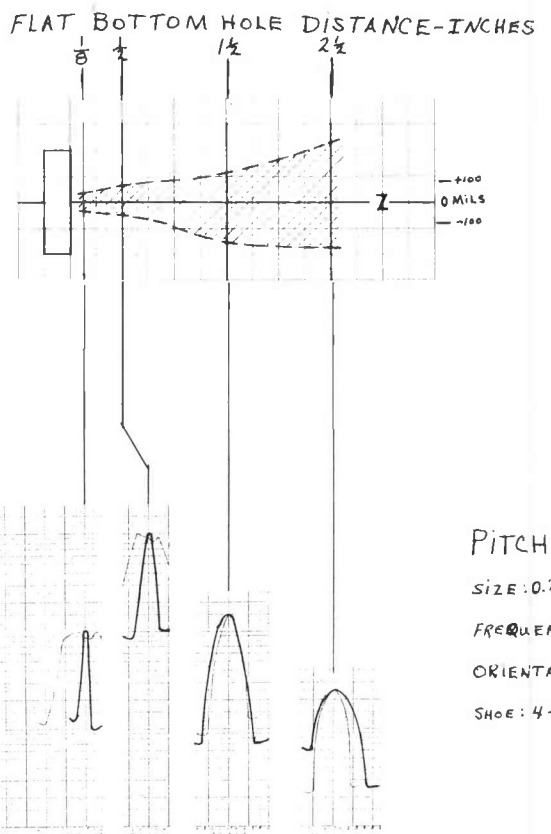

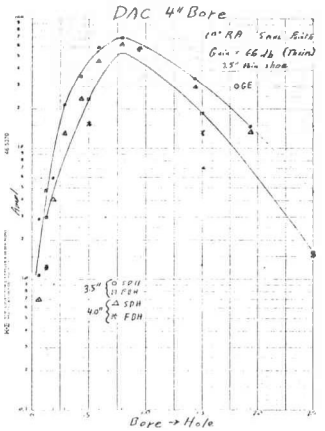

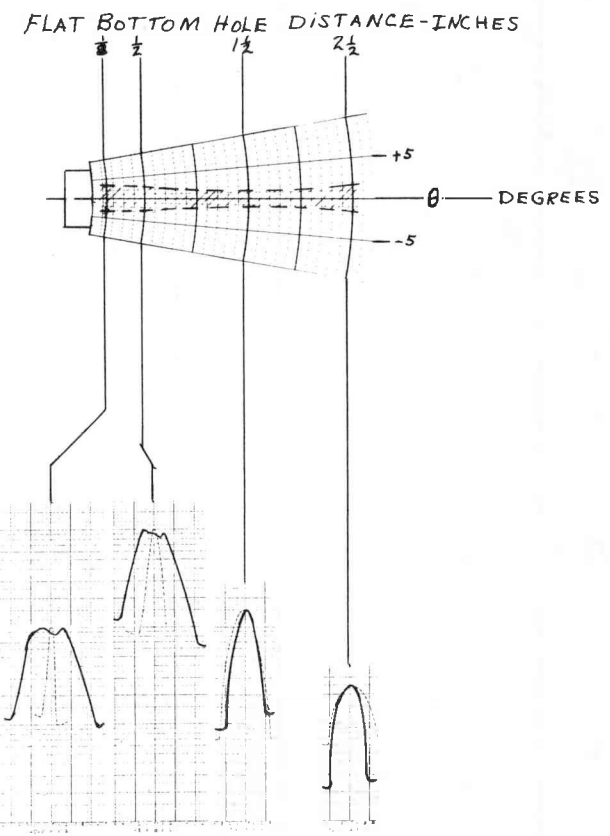

PITCH-CATCH TRANSDUCER

SIZE: 0.25-INCH BY 0.50-INCH

FREQUENCY: 5 MEGAHERTZ

ORIENTATION: 10 DEGREES ROOF ANGLE, POINT FOCUS

SHOE: 4-INCH DIAMETER BORE., LUCITE

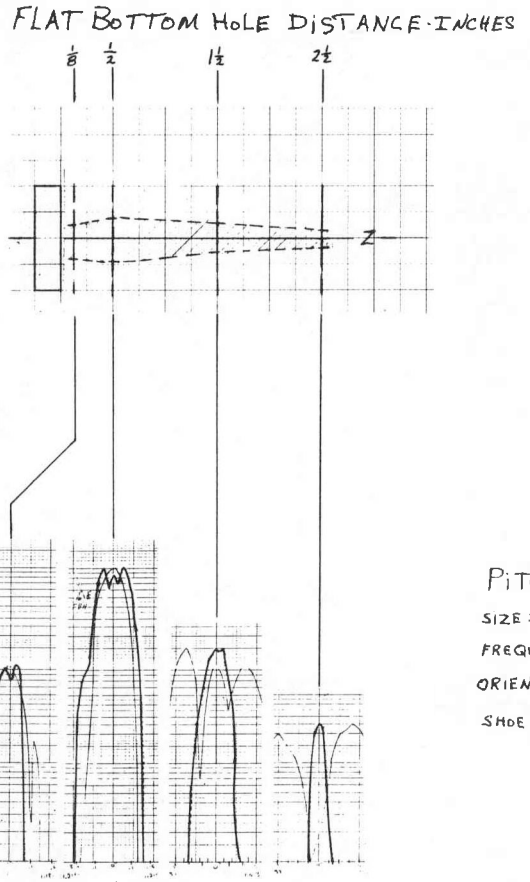

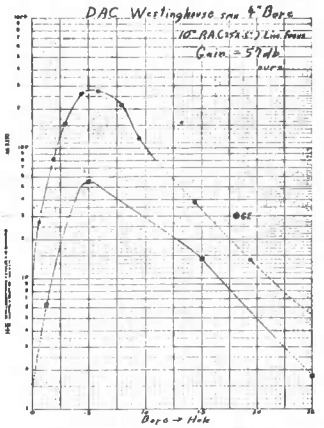

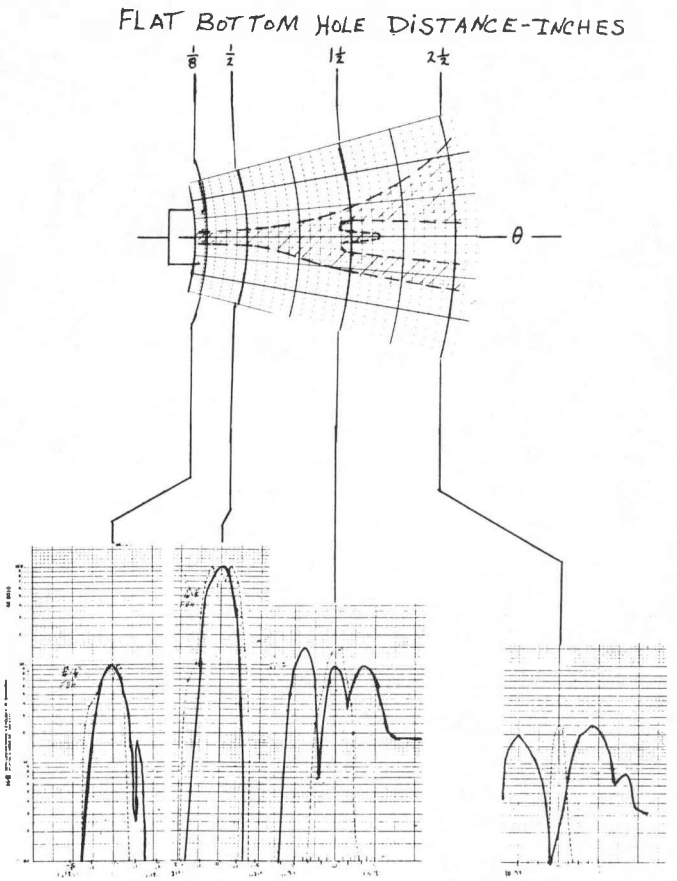

PITCH-CATCH TRANSDUCER

SIZE: 0.25-INCH by 0.50-INCH

FREQUENCY: 5 MEGAHERTZ

ORIENTATION: 10 DEGREES ROOF ANGLE, LINE FOCUS

SHOE: 4-INCH DIAMETER BORE, LUCITE

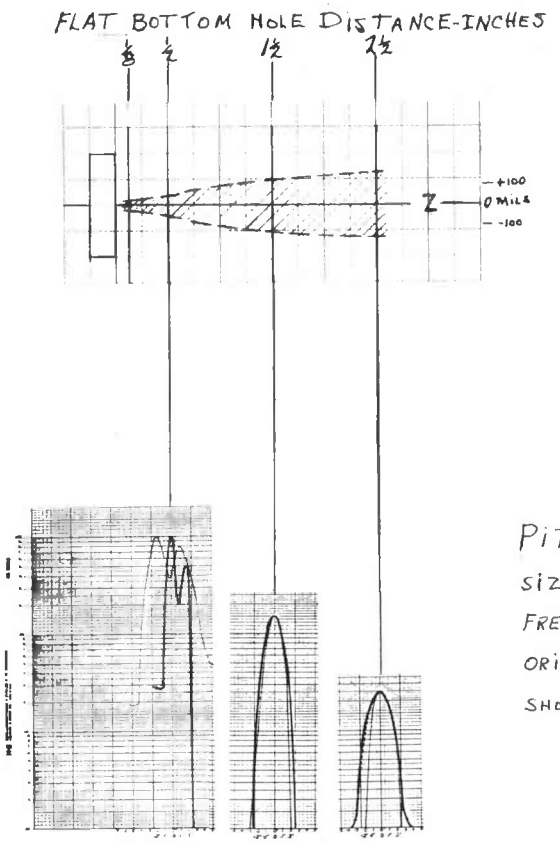

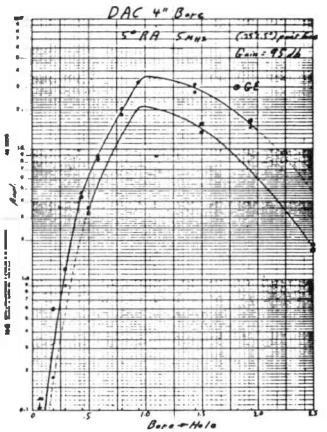

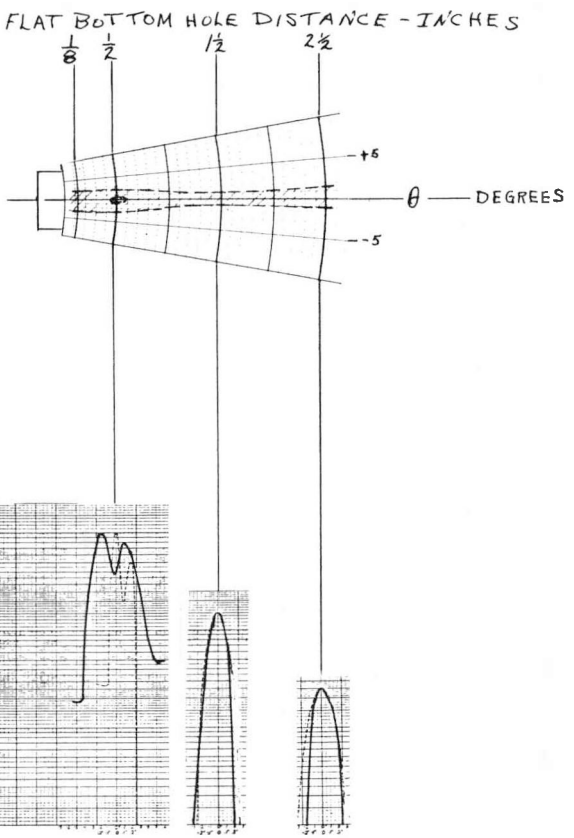

PITCH-CATCH TRANSDUCER

SIZE: 0.25-INCH BY 0.50-INCH

FREQUENCY: 5 MEGAHERTZ

ORIENTATION: 5 DEGREES ROOF ANGLE, POINT FOCUS

SHOE: 4-INCH DIAMETER BORE, LUCITE

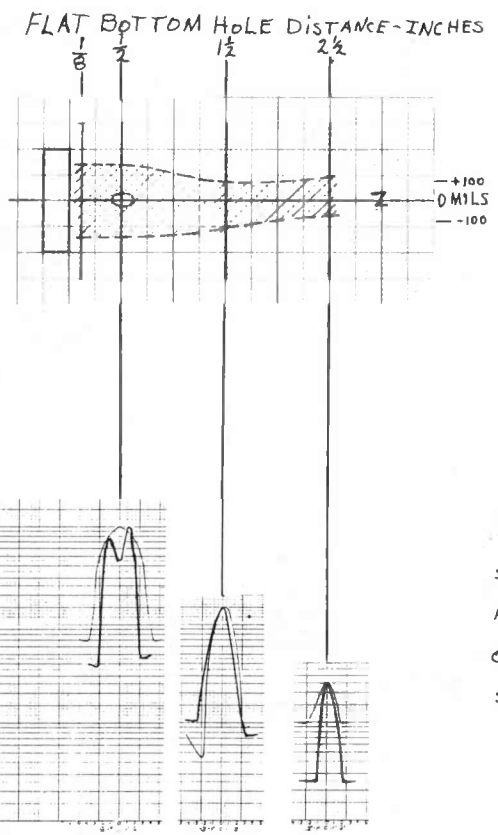

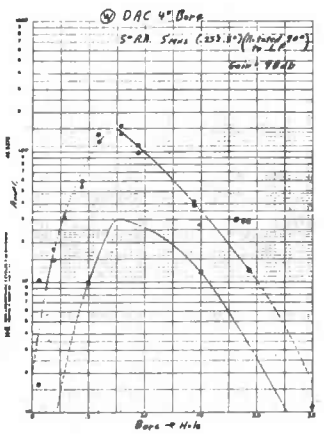

PITCH-CATCH TRANSDUCER

SIZE: 0.25-INCH BY 0.5-INCH

FREQUENCY: 5 MEGAHERTZ

ORIENTATION: 5 DEGREES ROOF ANGLE, LINE FOCUS

SHOE: 4-INCH DIAMETER BORE, LUCITE

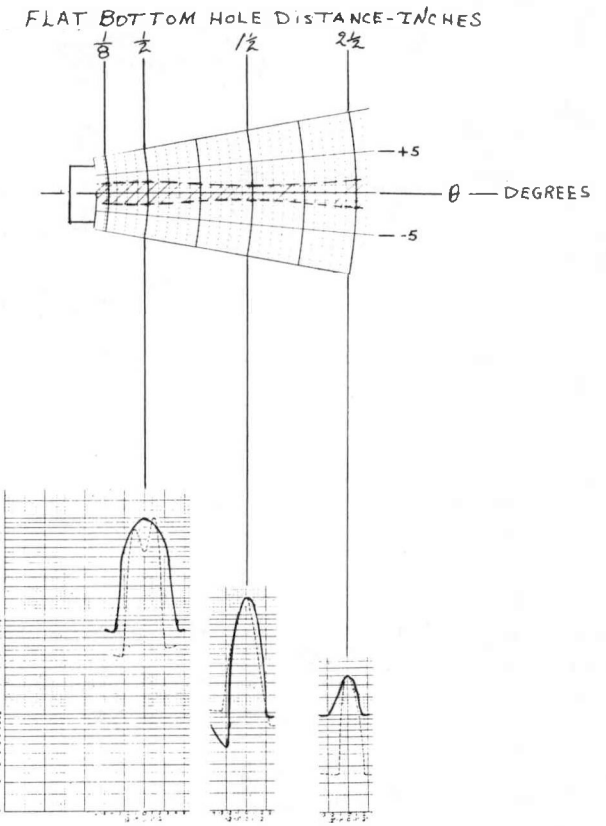

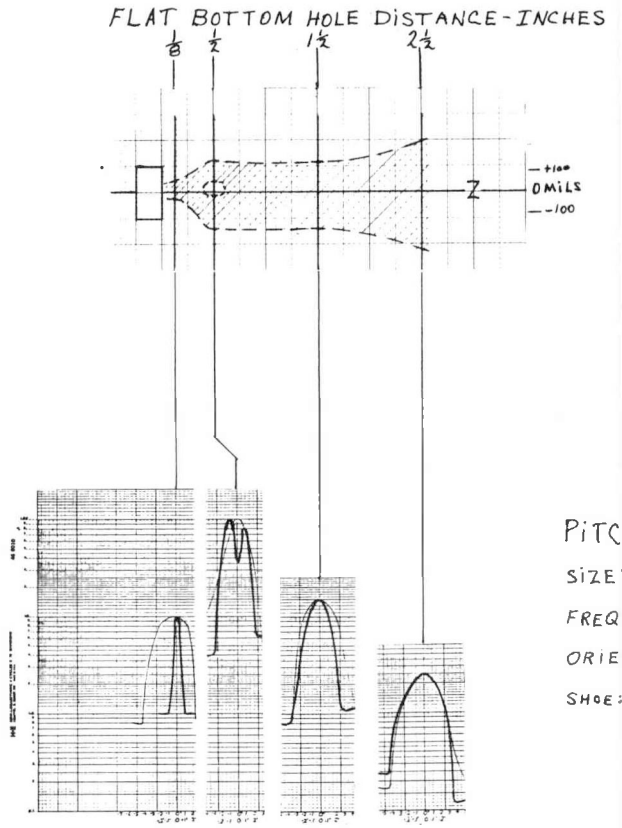

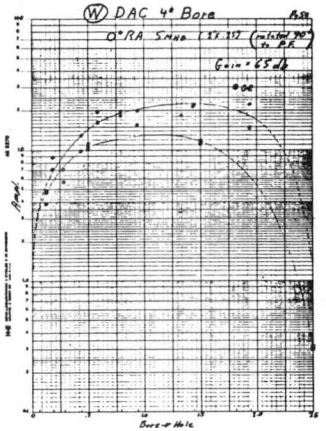

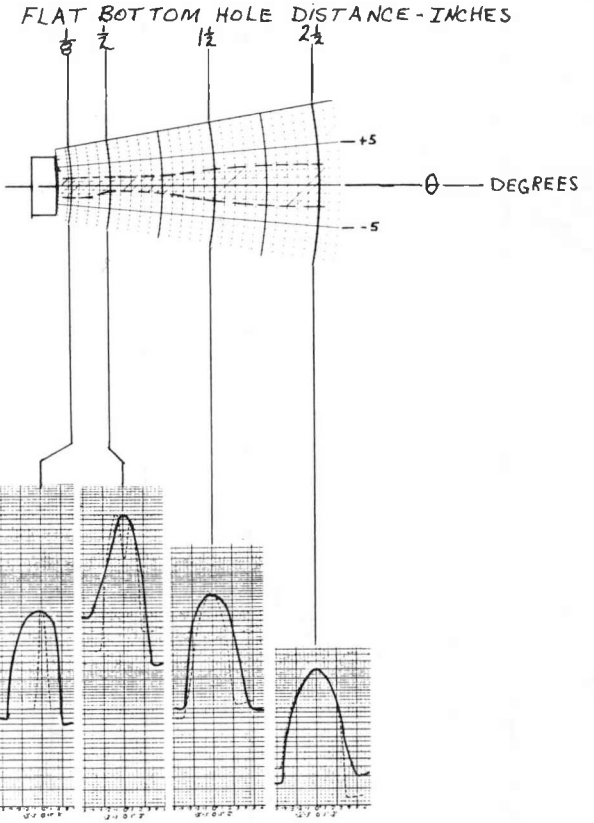

PITCH-CATCH TRANSDUCER

SIZE: 0.20-INCH BY 0.25-INCH

FREQUENCY: 5 MEGAHERTZ

ORIENTATION: 0 DEGREE ROOF ANGLE
POINT FOCUS

SHOE: 4-INCH DIAMETER BORE, LUCITE

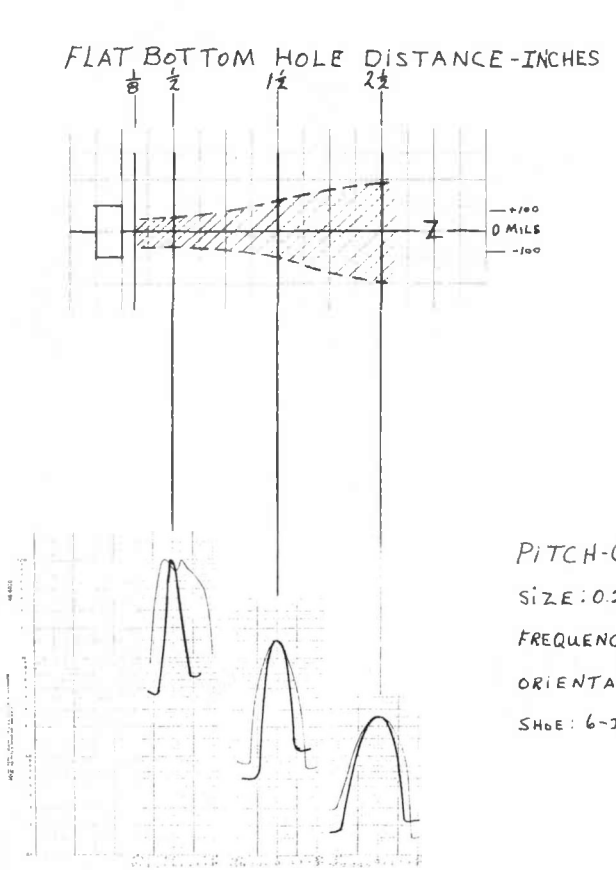

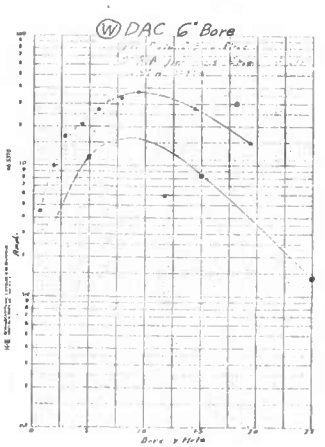

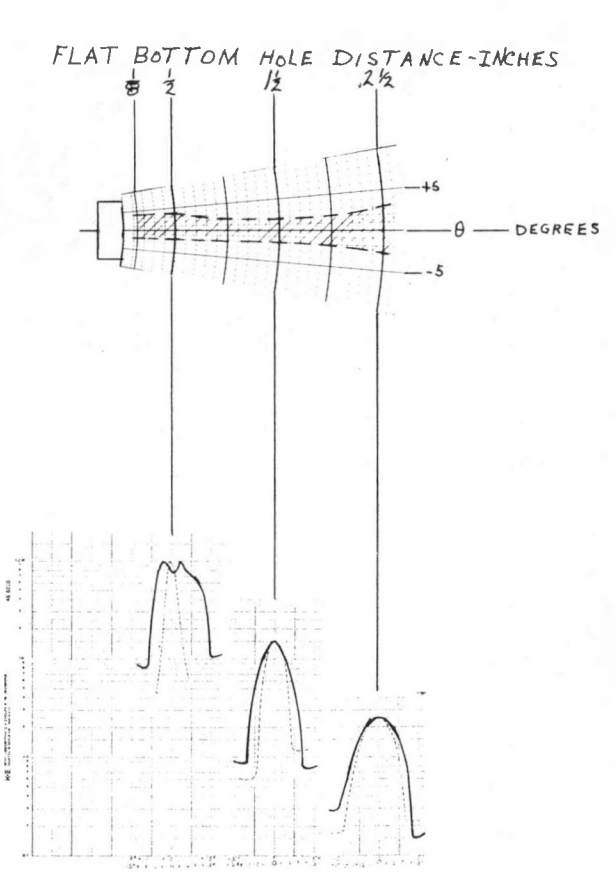

PITCH-CATCH TRANSDUCER

SIZE: 0.20-INCH by 0.25-INCH

FREQUENCY: 5 MEGAHERTZ

ORIENTATION: 0 DEGREE ROOF ANGLE, LINE FOCUS

SHOE: 6-INCH DIAMETER BORE, LUCITE

APPENDIX D - SUPPLEMENTAL PROBABILITY OF FLAW DETECTION CURVES

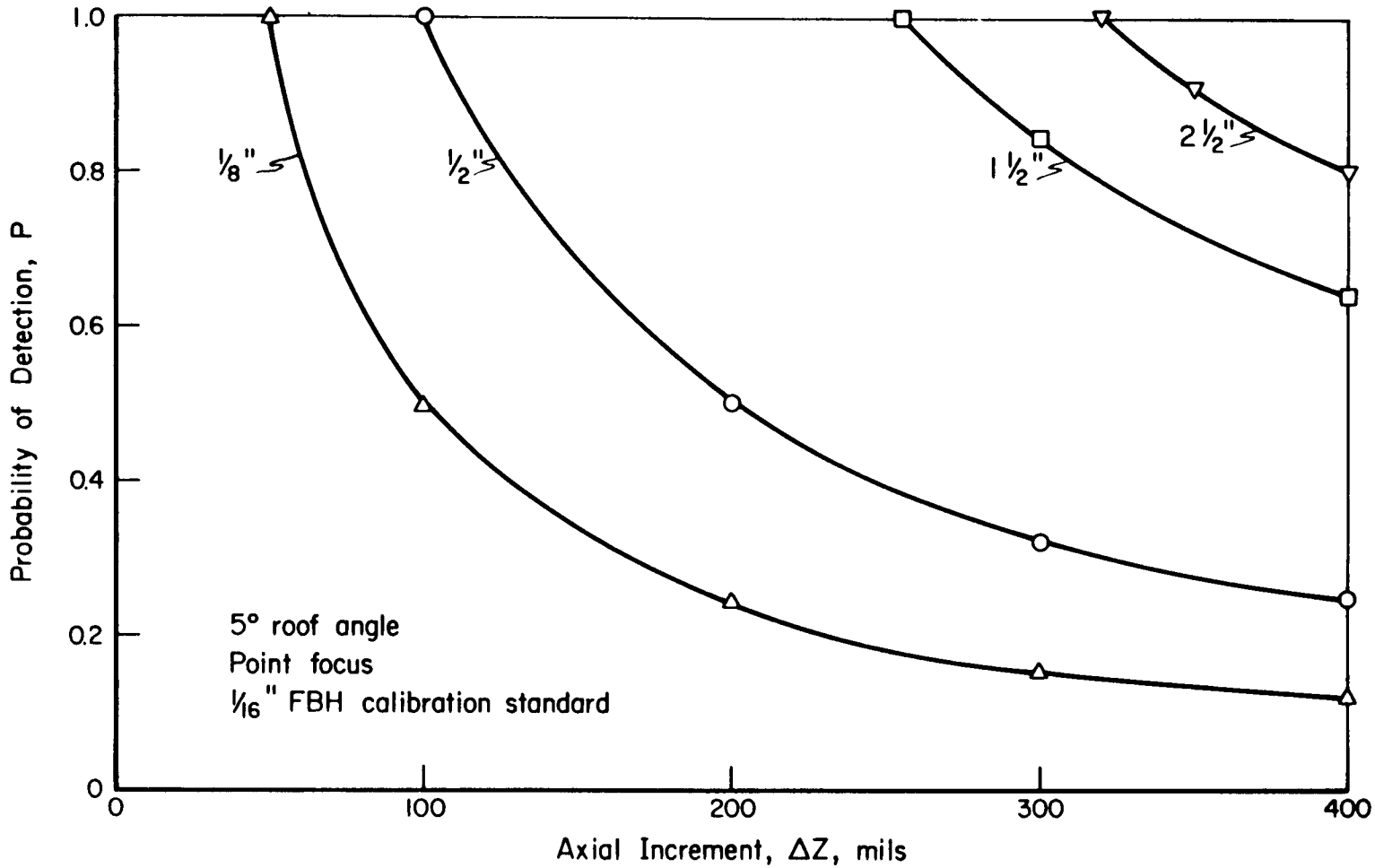

Figure D-1. Change in Probability of Detection With Axial Scan Increment

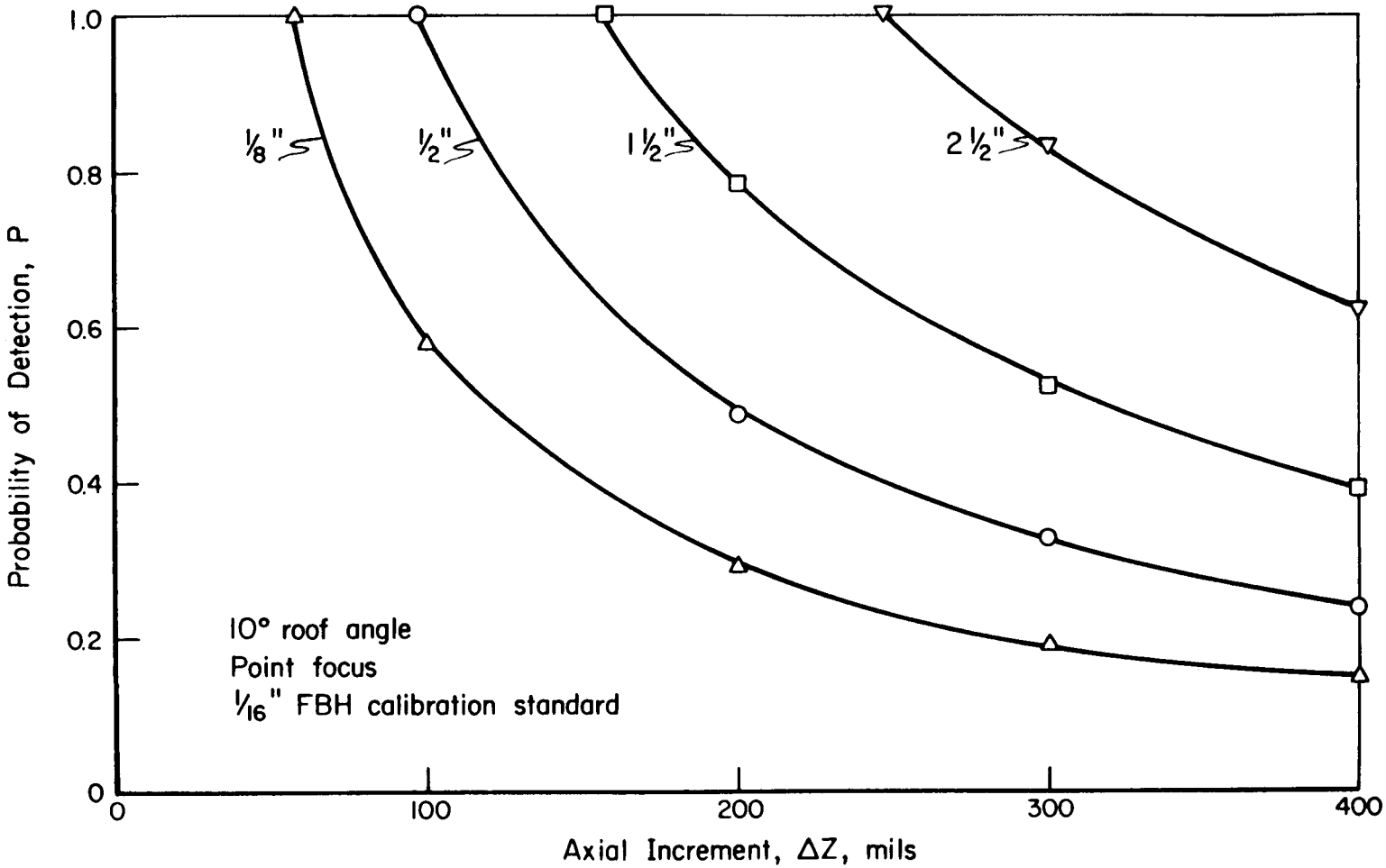

Figure D-2. Change in Probability of Detection With Axial Scan Increment

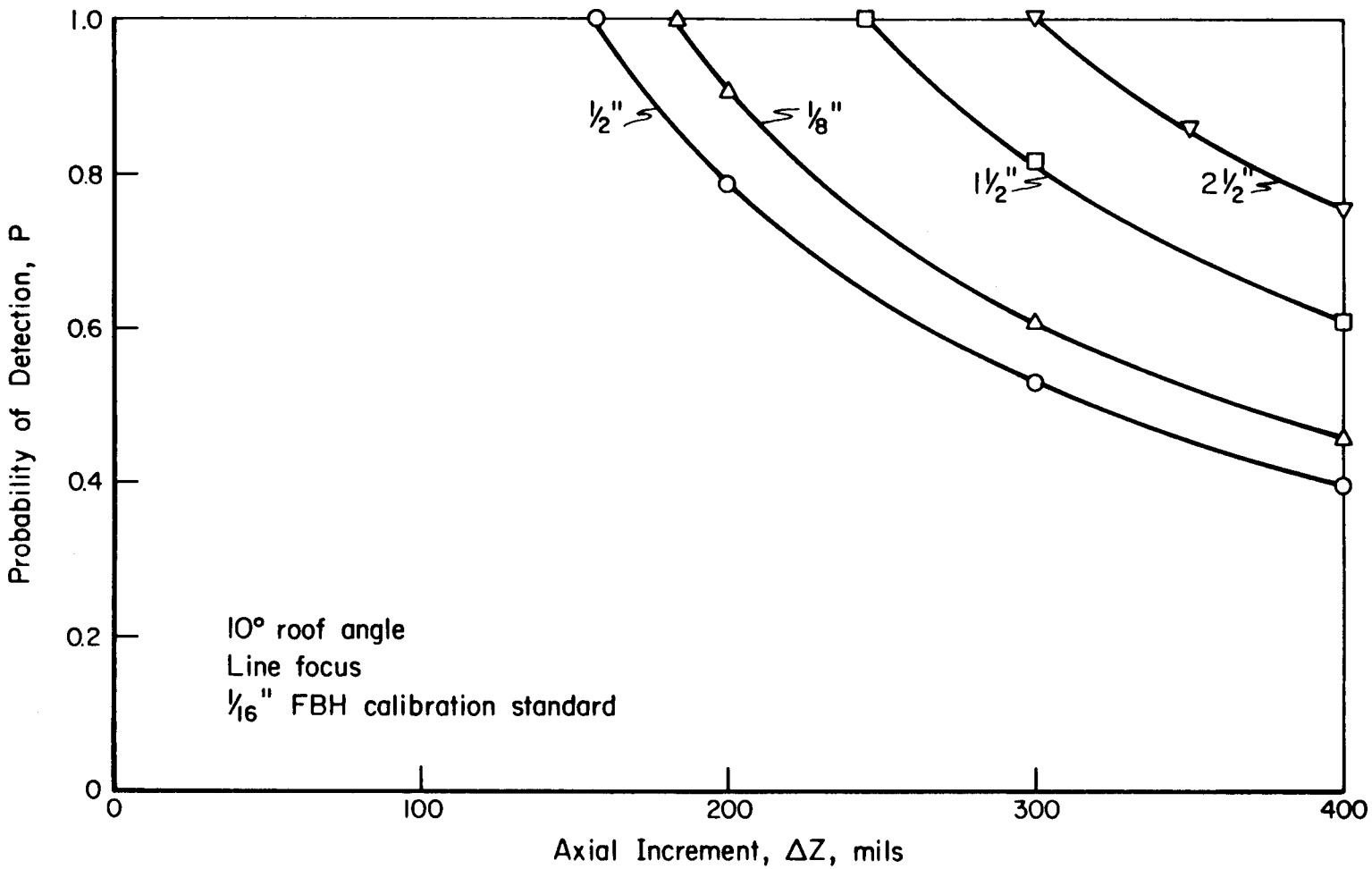

Figure D-3. Change in Probability of Detection With Axial Scan Increment

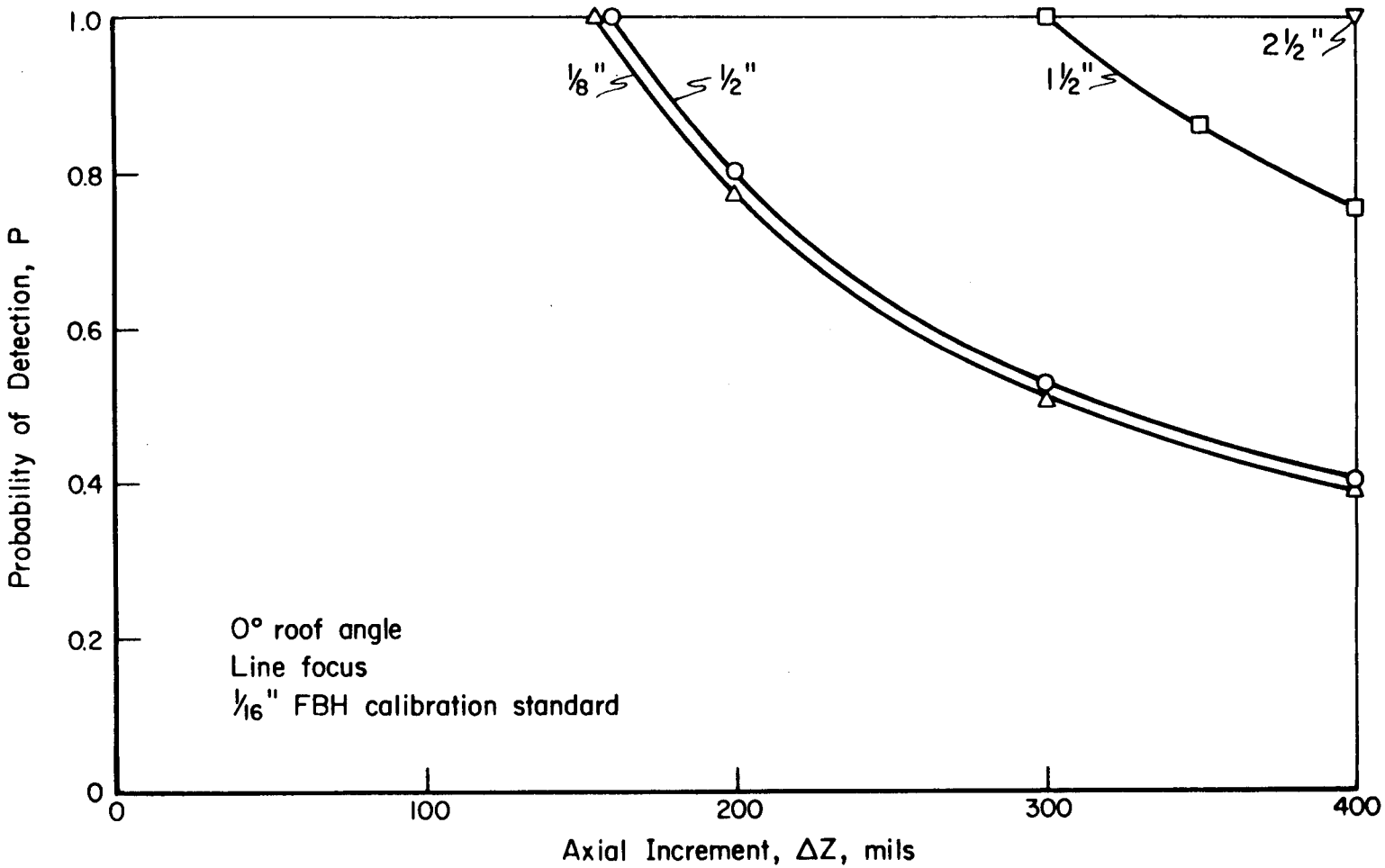

Figure D-4. Change in Probability of Detection With Axial Scan Increment

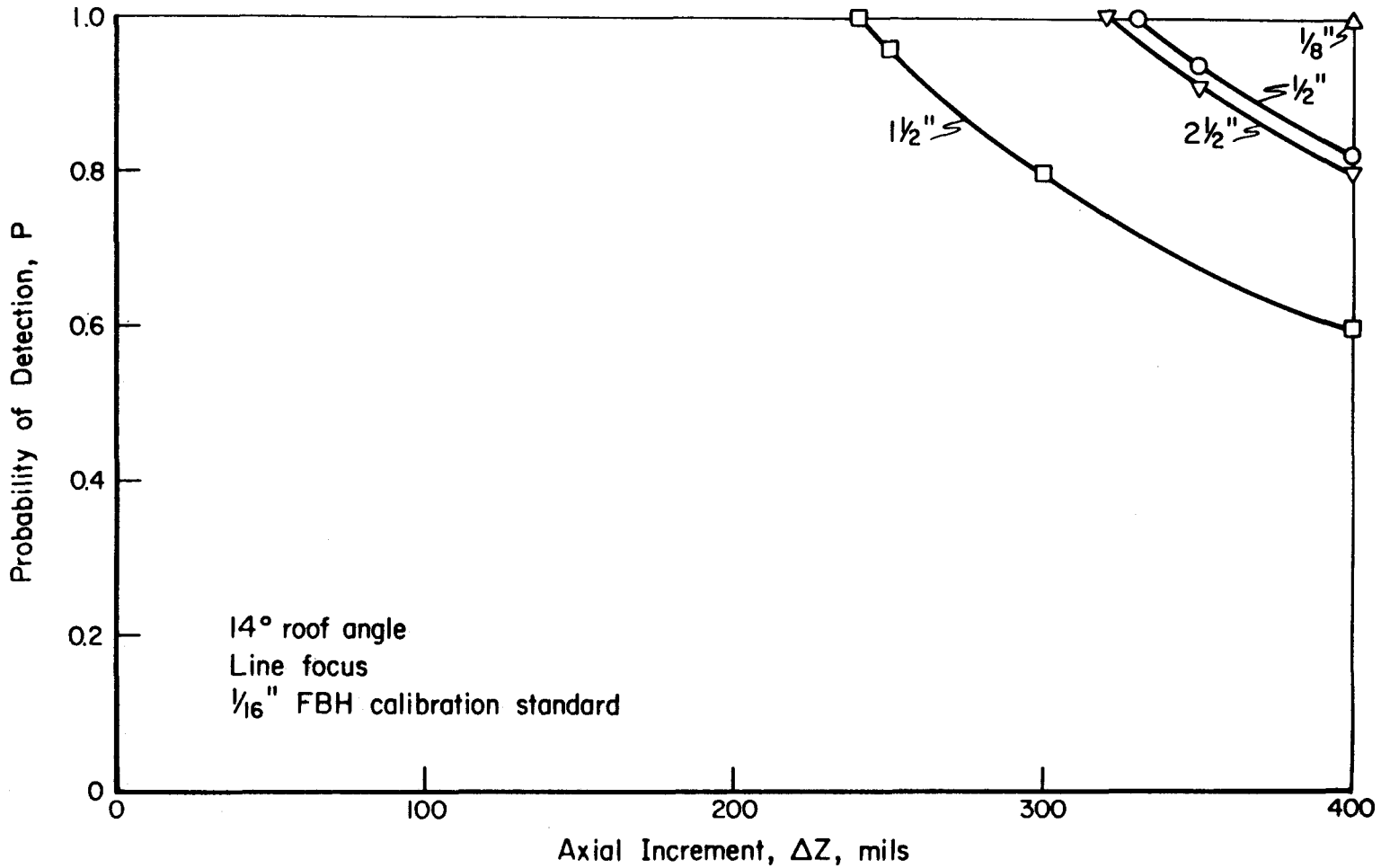

Figure D-5. Change in Probability of Detection With Axial Scan Increment

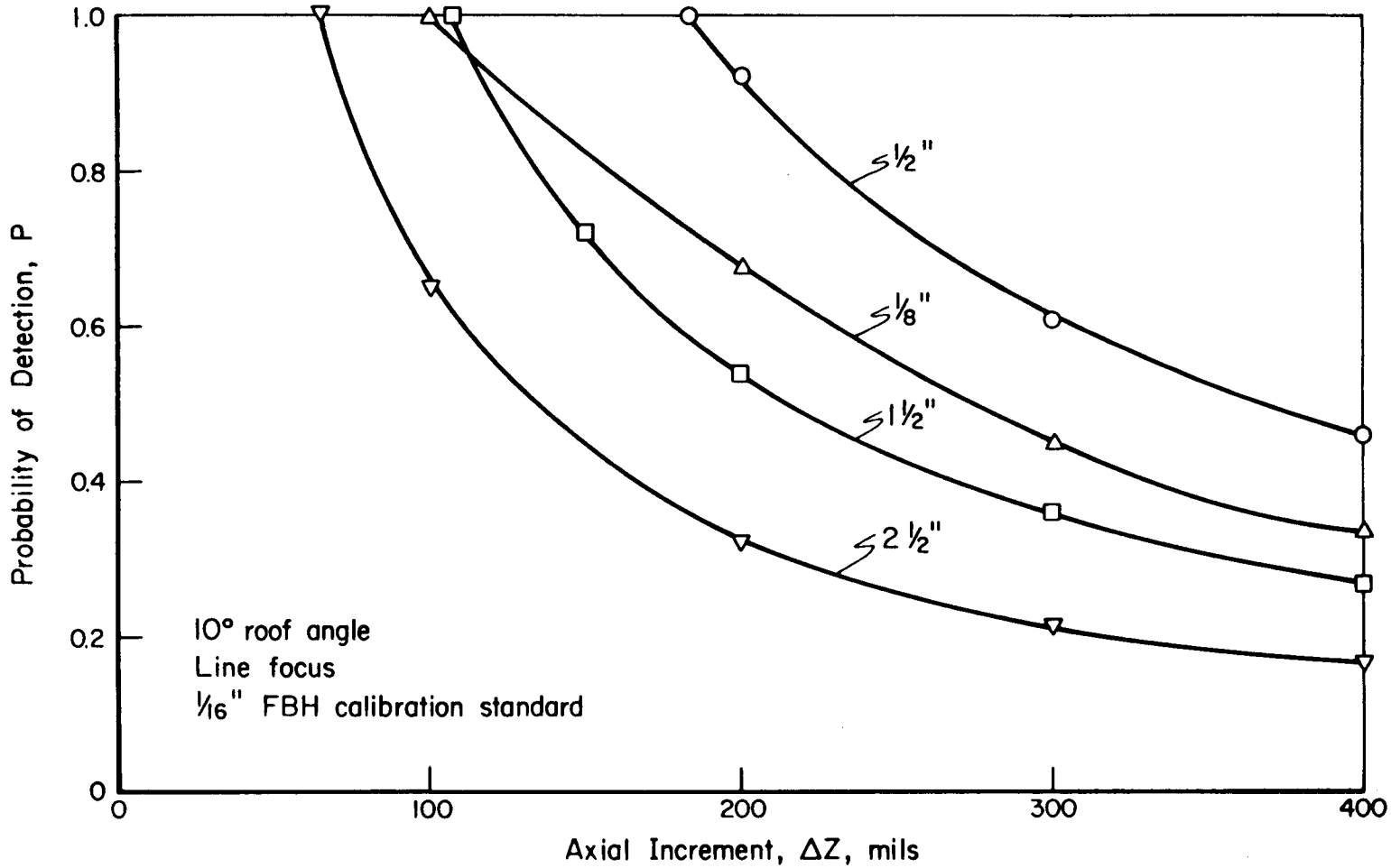

Figure D-6. Change in Probability of Detection With Axial Scan Increment

Steam Turbine Rotor Reliability - Task Details

Task 3. Destructive Testing

Prepared by

WESTINGHOUSE ELECTRIC CORPORATION
Lester Center
P. O. Box 9175
Philadelphia, Pennsylvania 19113

Principal Investigator

J. W. Cunningham

Blank Page

CONTENTS

SUMMARY

This document describes the techniques and results of Task III of a four task EPRI program investigating the "Reliability of Steam Turbine Rotors". The aim of the overall program was to develop a life prediction model which uses nondestructive (NDE) test data generated mainly by in-service boresonic inspection as input. The Task III object was to destructively section retired turbine rotors which had been boresonically inspected in order to determine the metallurgical and flaw structure which existed at the time of retirement, and to determine the degree of correspondence between the actual flaws and what was reported by NDE.

Two retired IP/LP rotors, Joppa 3 and Buck 6, manufactured in the early 1950's were cut up in performing this task. Small pieces cut from selected near-bore regions of the rotors were subjected to C-scan, radiography, and progressively polished at small intervals through flawed areas. The flaws revealed were quantified with respect to location, area and volume fraction, size, and nearest neighbor distance. Location and size were compared to boresonic results.

Although no metallurgical anomalies were found, both rotors contained a large number of small flaws, generally confirming the results of the commercial boresonic inspections. However, due to the small size and close spacing of flaws relative to uncertainties in position arising from boresonic techniques and cutting, a one-to-one correlation between a specific boresonic indication location and size, and a specific dissected flaw was rarely possible.

In spite of the large number of flaws, the area fraction and the volume fraction of flaws in both rotors, averaged over dimensions considered critical by Task I modeling, was less than 0.01. Inspection of

low cycle fatigue specimen fractures from the Joppa 3 rotor disclosed that subcritical cracks generated under high cyclic stresses in laboratory tests made large deviations from the expected fracture plane in order to follow the path of least resistance established by the flaws in spite of their low volume fraction.

The general conclusion reached is that existing NDE boresonic techniques, while probably adequate for large flaws, do not provide a good representation of detailed flaw structure in rotors such as Joppa 3 and Buck 6 where a small size and spacing of flaws exists.

I. Introduction

In early 1976, the Electric Power Research Institute funded a two-year program, RP 502, on the "Reliability of Steam Turbine Rotors". The overall program objective was "to establish and test the viability of a component lifetime predictive system which is rooted in finite element stress analysis and fracture mechanics, and utilizes field spindle-bore nondestructive examination (NDE) results as input". The program was split into four Tasks with four separate contracts to three different companies as follows:

Task I - Lifetime Prediction Analysis System. Contractor: Southwest Research Institute.

Task II - Nondestructive Evaluation. Contractor: Battelle Columbus Laboratories.

Task III - Destructive Tests. Contractor: Westinghouse R&D Center, Materials Evaluation and Application Research Department.

Task IV - Material Mechanical Properties Measurements. Contractor: Westinghouse R&D Center, Structural Behavior of Materials Department.

This report details the results of the Task III, Destructive Sectioning, efforts. The prime objective of Task III was to determine the actual flaw size, shape, nature and location associated with selected NDE indications found in the retired turbine rotors inspected as part of Task II of RP-502 (Nondestructive Evaluation).

At the time the program objectives were established, it was expected that the rotors of concern would contain a few (less than one hundred) relatively large flaws (say greater than 1/4 in. dia in projection) consisting of porosity, inclusions and/or cracks as either single defects or tight clusters or clouds. Consequently Task III was to destructively examine 8 to 12 flaws of this nature per rotor in some detail. However, when the first retired rotor, Joppa 3, was inspected from the bore, many more indications than expected were found and, apparently, none were of the anticipated size. However, Southwest Research Institute, who are developing the Lifetime Prediction model and thus determine the

nature of the NDE data needed, is concerned with crack growth and link-up in areas containing many close small flaws. This concern makes it important to know the amount of flaw discrimination and resolution attainable between profuse discrete small flaws by NDE examination in the near bore areas. Accordingly, Task III conducted the destructive examination of the rotors with the goal of determining not only the true nature of the rotor structure but also how well the two commercial boresonic inspections permitted locating and distinguishing between relatively small individual flaws.

The original program called for five turbine rotors to be nondestructively tested, sectioned, fracture toughness determined, and the data incorporated into a lifetime prediction model. Complications resulting largely from the small size and distribution of the rotor defects in both the first and second rotors inspected as part of the program caused a re-orientation of the program with more emphasis on improved ultrasonic inspection techniques. As a consequence only two rotors were treated, Joppa 3 and Buck 6.

II. Experimental Procedures

IIA. Sectioning Procedures

This section describes the procedures used in cutting the rotor into the carefully located small cubes necessary for microscopic examination.

Two methods of sectioning the rotors, each weighing approximately 15 tons with maximum diameters of about 45 in. and 17 foot long, were considered. Sectioning into discs on a lathe was most desirable due to the dimensional precision which would result, but cost was high and time delays prohibitive. Cutting by band saw was the technique chosen since it was about half as expensive and rapid service was available.

IIA.1. Deblading

As received, the rotors were still bladed. Thus, sections cut from them would have been cumbersome to handle. Originally the sawyer had planned to cut the martensitic stainless blades off at the platform by plasma wand but he experienced some difficulty in doing this, and changed

to cutting the shrouds with a torch and driving the blades off with an air hammer (gaps were oxyacetylene cut into the rotor rims every 90° to facilitate removal). This technique has the advantage of giving a cleaner, safer to handle piece and also permitted us to determine dimensions and weight on blades from each row in order to provide information for Southwest Research Institute's stress calculations.

IIA.2. Choice of Cutting Areas

Areas chosen for sectioning were determined by concensus of all contractors and EPRI. The basis of selection was principally the results of commercial boresonic inspections in the case of the Joppa 3 rotor and, for Buck 6, the results of improved boresonic techniques developed by Battelle on Task II of the program. In the case of Joppa, areas containing high densities of relatively large flaws in dense clusters were usually chosen, particularly where these occurred in the most highly stressed region of the rotor. One clean area containing an isolated large ultrasonic test indications (JF3) was chosen in an attempt to avoid the complications introduced by neighboring flaws. Areas in Buck were picked to reveal the nature of specific UT indications of relatively large size, as determined by BCL in their non-standard reinspection.

IIA.3. Cutting Sequence

The rotors were stamped with coordinate identifying numbers at frequent intervals before deblading. A cylindrical coordinate system was chosen as most suitable to the rotor geometry. The origin of the Z dimension, the longitudinal axis, is at the open end of the blind bores, the angular dimension, θ, is zero degrees at an arbitrary point chosen by Battelle and increases in the clockwise direction looking from the $Z = 0$ end of rotor. The radius dimension, R, is reported as distance into the rotor along a radial line measured from the bore surface. To get the true cylindrical coordinate, R', the bore radius must be added.

The first saw cuts were made transverse to the rotor axis, removing discs four to ten inches thick containing the flawed areas of interest. The discs were then cut into pie shaped segments by radial cuts and chordal cuts made to discard material beyond a radius of 5 to 6 inches (boresonic UT indications were only reported to about 4 in. from the rotor center line). Further cuts were then made perpendicular to the Z axis in order to achieve relatively thin pieces for radiography or UT inspection in the Z direction. Figure 1 shows a typical disc cross section with the cuts discussed above. In this case the pieces marked J7A1 and J7A3 are the pieces of interest for further sectioning. Similar sketches were made of most cuts in order to secure a permanent record of piece location. Typical flaws sometimes revealed on saw cut surfaces at this stage are shown in Fig. 2.

In order to expose the flawed areas of interest for comparison to the boresonic UT data and to develop quantitative data for use by the Task I portion of the program on the Lifetime Prediction Analysis, it was decided that the RZ plane across which maximum stresses would exist should be the plane of polish. Figure 3 shows a schematic of the manner in which the approximately 1 inch x 1 inch x 1 inch cubes chosen for detailed examination were situated in the rotor body. Figures 4, 5 and 6 show an actual cutting sequence as it continues from Fig. 2. The specimens were polished and microscopically examined at 0.03 inch to 0.06 in. intervals along the direction tangent to the bore (the θ direction). In Fig. 3 it should be noted that as each successive plane is removed in the θ direction (going from the right hand face toward the left hand face), the plane deviates more and more from a true RZ orientation. This occurs in all specimens examined, and it is felt by all concerned that the deviation is not great enough in the total of 0.5 in. to 0.7 in. removed to be of concern to the interpretation of results.

Each sequence of progressive planes of polish was photographed at a magnification of 6X to secure a record of the flawed areas. The photographs were used to locate the larger flaws in the rotor coordinate system and to measure the percent area of flaws in each plane as described

later. Occasional planes were etched and metallographically examined to determine if anomalies in metallurgical structure could be detected.

IIA.4. Other Methods of Flaw Location

In the course of sectioning several other techniques were occasionally utilized to examine the specimens for flaws. After the truncated pie shaped segments shown in Fig. 2 were cut out, attempts were made to locate Joppa 3 flaws from the bore with hand held transducers of both 2.25 and 5 MHz fitted with a shoe which duplicated the curvature of the bore. Correlation with boresonic results was not good. For instance, the single largest flaw reported by the Westinghouse boresonic inspection of Joppa 3 had an Equivalent Flat Bottom Hole (EFBH) diameter of 0.16 in. but could not be located by a hand held transducer. It was located only with great difficulty with an EFBH diameter of 0.09 in. by a small mechanical positioning device made by Battelle. Evidently the contact pressure which is high and closely controlled by hydraulics in the commercial boresonic inspection apparatus is necessary for good results with small flaws; the Battelle tool permits some pressure but hand pressure is not at all adequate for the sensitivity needed.

In addition to the use of hand held transducers, some of the specimens were inspected by the ultrasonic C-scan technique. In C-scan, the piece to be examined is immersed in water and the ultrasonic transducer traversed across the specimen in the water about 2 in. above the specimen surface. The water acts as the couplant. By moving the transducer systematically over the entire surface and automatically recording the presence of reflections above a set amplitude, a drawing of the specimen with projected flaw locations is attained. The recording device gives no idea of flaw amplitude, although these can be obtained by stopping the traversing mechanism and reading the CRT in the conventional manner. It is possible to set the depth gate so that the recorder ignores indications which are not within a desired small interval of depth. Figure 7 shows the effect of flat bottomed hole size and depth below the metal surface for the 10 MHz C-scan used in this program. This figure may be

used as a calibration chart to attain an estimate of the flaw sizes shown in C-scans of various specimens later in the report.

Radiography was found to be the most useful technique for revealing the location and extent of larger flaws and flawed areas before progressive grinding and polishing commenced. Some positive prints of radiographs are included in the detailed descriptions of the various flawed specimens later in this report.

III. Treatment of Results

The primary objective of destructive rotor sectioning was to determine the actual flaw structure of the rotors in order to permit interpretation of the commercial boresonic UT results in a manner useful to the Lifetime Prediction Model being developed by the Task I contractor. An additional objective of the sectioning was to reveal areas where improvements in boresonic test techniques would be necessary if the Task I requirements were to be met.

Since both the Joppa 3 and Buck 6 rotors contained a large number of small flaws widely distributed throughout the near-bore area, input to the Lifetime prediction model was in terms of volume fraction of flaw averaged over a volume with dimensions approximately equivalent to the critical crack size calculated for the specific rotor alloy and stress. This was on the order of a 1 in. x 1 in. x 1 in. cube for both rotors. To get volume fraction it was necessary to experimentally determine area fraction of flaw on the planes of polish. This was determined as an average over the entire RZ plane of each polished section; i.e., at intervals of 0.03 in. to 0.06 in. through the θ direction of each approximately 1 in. x 1 in. x 1 in. specimen which was progressively sectioned.

Area fraction was measured by placing an arbitrary array of points over the polished surface, and counting the number of these points which lie in flaws (either holes or inclusions). This number divided by the total number of points in the array is the area fraction. It is a statistical method, becoming more and more accurate as the number of points in the array increases. It may also be shown (Metals Handbook, Vol. 8, American Society for Metals, p. 38) that, under the assumption of

a fairly uniform distribution of flaws in the volume of the rotor being considered, the area fraction determined in the above manner is equivalent to volume fraction; volume fraction is calculated for each of the specimens progressively polished by averaging the area fractions of each plane polished throughout the approximately 0.7 in. of metal removed.

Two methods of forming the array and counting the points in flaws were used. The usual method was to place a transparent grid containing 100 points per cm^2 over a 6X photograph of the plane of polish and visually count the points laying on flaws. The montages shown in following sections were used for this purpose. Use of this technique placed 28,000 points on each square inch of specimen. In making the visual count it was found that flaws below about 0.005 in. in maximum extent could be ignored without significantly affecting the resultant area fraction.

The second counting method used was an automatic image analyzer. This instrument, the Leitz Classimat, imaged a fraction of the polished specimen surface onto a special video screen at about 350X, electronically sampled about 13,000 points on each image to determine which were in the flaws (the holes and inclusions of the as-polished specimen surfaces produced very adequate contrast for this determination), stored this count in a microcomputer, automatically traversed the specimen to a new field, repeated the process, and, after the entire surface of the specimen had been scanned, the computer calculated the area fraction. The Classimat is also capable of classifying the flaw sizes at the same time area fraction is determined. The maximum diameter of each flaw is measured, and the number within each 25 micrometer diameter range calculated. This measurement was performed on several planes of polish and the results summarized in a later section of this report.

The Classimat technique probably yielded more accurate area fraction data than the manual overlay technique due to the large number of points sampled (about 2,000,000/$in.^2$ compared to 23,000/$in.^2$) and also the fact that it counted flaws as small as 0.0005 in. However, both techniques yielded area fractions of about the same size. Since time delays were encountered in gaining access to the Classimat, most of the area fraction data was generated by manual counting.

In order to form a quantitative correlation between actual flaws found by dissection and the indications reported by the various boresonic inspections, the position of selected flaws revealed in the planes of polish were converted by graphical or mathematical methods to the cylindrical coordinates of the rotor from the Cartesian coordinates of the dissected specimens. This technique was satisfactory to establish the position of relatively large single flaws which are then compared directly to individual boresonic results.

However, there were so many small flaws which were frequently densely clustered that the tremendous amount of individual flaw position data could not be assimilated to form a useful understanding of the structure. In several of the dissected specimens densely flawed areas of this nature were treated by calculating the volume fraction in 0.06 in. x 0.06 in. x 0.03 in. cells in the plane of polish and treating cells with greater than 0.1 volume fraction as a single flaw. All such "flaws" were then plotted onto RZ or θR projections through the various dissected specimens. The boresonic data from the same area was plotted onto the same figures to determine correlation (e.g., Figs. 63 and 64).

IV. Results

IVA. Joppa 3 Rotor

The 175MW, IP/LP Joppa 3 rotor was placed in service in 1954. It is an integral forging about 17 ft long, has a maximum diameter of 46-1/4 in. and contains a 3.625 in. diameter blind bore approximately 157 in. deep. No manufacturing information is available on melting, ingot or forging practice.

IVA.1. Chemical Composition

The chemical composition taken at the bore near 100 in. Z is as follows:

Cr	0.99	Ni	0.10
Mo	1.10	Si	0.30
V	0.25	P	0.017
C	0.26	S	0.0046
		Mn	0.74

IVA.2. Metallography

Microstructure

Figure 8 shows a low magnification view of a polished and etched RZ face of the Joppa 3 rotor near Z = 100 in. The intermixed light and dark etching areas are remnants of the cored ingot structure. Coring results from localized minor segregation of nominal alloying elements during ingot solidification; this segregation is always present, particularly in large ingots, and while it does not usually have a serious effect on mechanical properties, it is frequently of sufficient magnitude to effect the attack rate of chemical etchants.

Figure 9 shows the microstructure (Picral etch) of the Joppa 3 rotor in the near bore area near Z = 100 in. The photomicrographs reveal the expected bainitic structure with a very faint trace of proeutectoid ferrite at the prior austenite grain boundaries. Figure 10 shows the microstructure in the same area as etched in STBS (Sodium Tridecyl Benzene Sulfonate). The lower photo of Fig. 10 contains microhardness indentations used to determine if there was a difference in hardness between the light and dark etching areas of Joppa; no difference was found.

IVA.3. Typical Flaws

Three specific types of flaws were found in Joppa 3. Figures 11, 12 and 13 are typical examples. For purposes of this program the three types have been labeled as follows:

Type I. Relatively large holes and associated laps that are probably the result of gas and shrinkage porosity which has been only partially closed by forging.

Type II. Small elongated (in the Z direction) holes, with sharp angular edges which contain angular translucent inclusions. These holes are hypothesized to be the result of small scale interdendritic shrinkage that has not been affected by forging.

Type III. Manganese sulfide inclusions. These are generally of two forms; the first relatively large and slightly elongated, frequently lying in the laps associated with Type I defects (Fig. 14); the others are small spherical manganese sulfide inclusions, Figs 15 and 16, distributed rather densely on some planes of polish. These small manganese sulfides are occasionally densely clustered around Type I holes as seen in Fig. 17.

Two more examples of laps associated with holes are shown in Fig. 18. Some question arose as to whether these features might not be cracks instead of laps, particularly when they occurred in the region of Joppa 3 which was calculated to see the highest service stress (i.e., the bore near Z = 100 in.). High magnification light photomicrographs of several laps are shown in Fig. 19. Further investigation to answer this question was carried out on the Scanning Electron Microscope (SEM). High magnification SEM photomicrographs of several laps are shown in Figs. 20 and 21. These features have fairly smooth edges, with no abrupt steps which would characterize a cleavage fracture. They also frequently show signs that the forces exerted during polishing have collapsed metal along the crack, indicating the presence of a hole in the vicinity. When an isolated lap was found on a polished surface (i.e., no associated visible hole), it was usually possible to collapse the metal around the lap into a subsurface hole with a pointed tool. Thus, the evidence points to laps formed by the partial closing of holes during forging rather than cracks formed during service.

An idea of the extensive distribution of the manganese sulfide inclusions is given by the sulfur print of Fig. 22. In this print the plane is tangent to the bore and the vertical axis is parallel to Z.

IVA.4. Fractography

Some fractographic investigations were conducted for the Task IV contract on Material Properties. A detailed report of this fractography is included in the Task IV report, but for the sake of completeness some photos of the fracture surface showing flaw involvement are included here.

The fracture surface of interest is from a Low Cycle Fatigue (LCF) specimen which contained an actual bore surface. Figure 23 is a low magnification view of the RZ plane of fracture. The dull gray semi-circular portion of the fracture toward the top of the photo is the fatigue portion of the crack, while the shiny faceted remainder of the surface is the overload portion which failed by cleavage. Several smaller fatigue portions also appeared on the fracture. The fatigue portion was extremely rough, contrary to the usually flat smooth nature of fatigue cracks. Peak to base depths in this crack are on the order of 1/4 in. It is believed that this extensive departure of the crack from the RZ plane of maximum stress is due to the cracks attempt to follow flaws in the structure. Figure 24 is a Scanning Electron Microscope (SEM) photo-micrograph of a flaw detected on the fatigue fracture. Figure 25 is a higher magnification shot in the same area as Fig. 24 and shows that many of the inclusions laying in the fracture surface are angular in nature. This corresponds to the shape of the inclusions in Fig. 12, and leads to the belief that this is a Type II flaw. An EDAX analysis (an X-ray analysis performed on the small inclusions in the SEM which identifies chemical elements but not the quantity present) on several of the particles identified the presence of aluminum and silicon as primary constituents with some calcium also present. These inclusions were probably washed into the ingot from refractories.

Figure 26 shows a flawed area in the cleavage (overload) portion of the fracture. The cleavage fracture was fairly flat and closely followed the RZ plane. Flawed areas were easy to see by light microscopy in the cleavage area and the area fraction appeared somewhat larger than the amount of area

fraction expected from the typical number of flaws seen on various polished sections of Joppa 3. The extremely rough nature of the fatigue portion of the fracture made determination of flawed area very difficult there; it appears as if 500X or higher magnification on the SEM would be necessary to do this and to cover the large fatigue fracture surface seen in Fig. 23 would be very time consuming and expensive. In the short time available to us, heat tinting the fracture surface was tried. On the cleavage portion of the fracture, this produced a drastic difference in color between the already evident pre-existing flawed areas and the newly formed fracture. Similar color differences appeared on the fatigue portion of fracture. If the assumption is made that pre-existing flaws and fresh fracture surfaces in the fatigue area tint in the same way as in the overload area, it may be estimated that roughly 20% of the RZ projected area of this very rough fracture is due to pre-existing flaws. Data of this nature should be useful to the Lifetime Prediction work of Task 1, but should be confirmed by additional fractography.

IVA.5. Progressive Dissection

The following section describes the flaws found in the individual specimens of the Joppa 3 rotor which were progressively sectioned and polished. In many cases correlation with the findings of the two commercial boresonic inspections are attempted.

Specimen J7A1-6

This specimen is centered about Z = 100.6 in., θ = 328° and R = 0.1 in. to R = 1.3 in. in the most highly stressed region of the Joppa 3 rotor. It was progressively sectioned on approximate RZ planes parallel to 332° for a distance of 0.9 inches. See Figs. 4, 5 and 6.

Figure 27 shows results of an ultrasonic C-scan at 10 MHz through the RZ plane of the specimen before progressive sectioning was begun. Figure 28 shows a calibration chart for the 10 MHz C-scan which permits a comparison between the size of reflectors in the specimen and flat-bottomed round holes of various diameters drilled into a steel test block. Note that the

indicated C-scan flaw size varies with depth. The C-scan confirms in general the commercial Westinghouse boresonic inspection results of large numbers of small indications.

Radiography of the same specimen is shown in Fig. 29. The large flaw corresponds to the large UT indication in the lower right corner of the Fig. 27 C-scan.

Dissection revealed that this indication was indeed a large hole with many lobes and side arms, extending about 0.25 in. in the Z direction, 0.15 in. in the R direction and more than 0.4 in. in the θ direction as shown in Fig. 30. The following table compares the center position of this hole in rotor (cylindrical) coordinates, as found during dissection, to the results of the commercial boresonic inspections of Westinghouse (Ⓦ) and Commercial Machine Works (CMW).

Largest Flaw Exposed by Dissection of J7A1-6

$\Delta Z \approx .25"$ $\Delta R \approx .15"$ $\Delta\theta \approx .4"$

(Δ indicates maximum extent of flaw in coordinate direction)

	Z"	θ°	R"	Amplitude	
Dissection	101.2	325	7/8	$\sim 600 \times 10^{-4}$ in.^{2}	
Radiography	101.3	325	0.9	$\sim 234 \times 10^{-4}$ in.^{2}	
C-scan	101.2	322	0.9	---	
Hand held	101.3	323	0.7	Large	
Ⓦ boresonic	101.1	324	3/4	77×10^{-4} in.^{2}	P/C
Ⓦ boresonic	101.1	325	3/4	85×10^{-4} in.^{2}	P/C
Ⓦ boresonic	101.1	326	3/4	55×10^{-4} in.^{2}	P/C
Ⓦ boresonic	101.3	323	3/4	97×10^{-4} in.^{2}	P/C
Ⓦ boresonic	101.5	322	1-1/16	115×10^{-4} in.^{2}	P/C
CMW boresonic	101.6	321	.65	17% S/P	P/C
CMW boresonic	101.8	320	.35	129% S/P	Shear

Westinghouse used 5 MHz transducers in the pitch-catch (P/C) mode while CMW used 3.5 MHz transducers in P/C and two shear modes. (Details of the boresonic inspections may be found in the Task II report of the Battelle Columbus Laboratories).

It is interesting that the Westinghouse boresonic inspection reported a series of indications for this flaw. This probably results from the highly irregular nature of the hole coupled with the increased resolution available from the 5 MHz frequency used. Also the fact that the boresonic tool was moved in approximately 1/4 in. increments along the rotor axis may have contributed several indications from this relatively large flaw. Figure 31 shows the approximate shape of this large flaw on the θZ projection through specimen J7A1-6 along with the location of the reported boresonic indications. Figure 32 shows the θR projection. In these figures the size of the circles or triangles representing the boresonic indications are roughly proportional to the amplitude reported. The small holes in the lower left of these figures are shown in the polished sections of Figs. 33 and 34. Table 1 compares these to the results of the boresonic inspection results in this area of Joppa 3.

The correlation between the above flaws revealed by sectioning and the boresonic inspections was very good considering that most of the flaws were rather small. However, it should be noted that in general it was not possible to establish a one-to-one correspondence between actual flaws and boresonic indications. As Fig. 35 typically shows there are many flaws on any given plane of polish in this specimen. Table 2 lists all flaws greater than about 1/32-in. in largest extent found on just one plane of polish and Table 3 lists all boresonic indications recorded in the rotor volume near this plane. By comparing the two tables the difficulty in forming a one-to-one match can be appreciated. Probable reasons for this lack of correlation on small flaws are covered in the Discussion Section of this report.

Specimen J7A1-31

This specimen is centered at Z = 98.85 in., θ = 347°, R = 0.1 in. to 1.3 in. It is a neighbor of J7A1-6 in the most highly stressed region of Joppa 3 (Fig. 5).

Specimens J7A5-14 and J7A5-15

These Joppa 3 specimens are located as shown in the radiograph of Fig. 61. They were chosen for progressive dissection because of the flaws revealed by radiography. Both specimens were polished back 0.75 in. in 0.03 in. steps and 6X photographs taken of each plane of polish. Specimen J7A5-14 contained 0.0033 volume fraction of flaws and J7A5-15 contained 0.0039.

J7A5-14 contained only one notably flawed area, the balance having a sparse fairly uniform distribution of small Type II and III defects. The densely flawed area was a cluster of holes, and the following table compares this location to commercial boresonic indications reported in its neighborhood.

Location Method	Z, Inches	θ°	R, Inches	Amplitude
Dissection	98.3	28	0.875	--
CMW Boresonic	98.6	36	0.50	15% P/C
CMW Boresonic	98.6	33	0.45	13% P/C
CMW Boresonic	98.6	20	0.55	13% P/C
CMW Boresonic	98.2	30	0.14	35% Shear
CMW Boresonic	99.7	25	0.84	27% Shear
CMW Boresonic	98.9	35	0.56	32% Shear
Ⓦ Boresonic	98.0	22	0.75	42×10^{-4} in.^{2}
Ⓦ Boresonic	98.0	20	0.75	77×10^{-4} in.^{2}
Ⓦ Boresonic	98.2	22	0.875	44×10^{-4} in.^{2}
Ⓦ Boresonic	98.2	26	0.875	34×10^{-4} in.^{2}
Ⓦ Boresonic	98.2	33	0.875	24×10^{-4} in.^{2}
Ⓦ Boresonic	98.2	33	0.875	58×10^{-4} in.^{2}
Ⓦ Boresonic	98.4	31	1.5	31×10^{-4} in.^{2}
Ⓦ Boresonic	98.4	28	0.625	21×10^{-4} in.^{2}
Ⓦ Boresonic	98.4	24	0.875	21×10^{-4} in.^{2}
Ⓦ Boresonic	98.8	29	0.44	92×10^{-4} in.^{2}

Sectioning revealed that J7A5-15 contained what is an almost continuous flaw through all 0.75 in. removed during polishing; the radiograph shows this as the large flaw near the center of the plane of polish indicated by the arrow and as a relatively linear stringer running in the direction of the arrow slightly to the left of the large flaw. The large flaw is of Type I as shown in the progressive sections of Fig. 62.

The following table lists the location of this flaw and shows the location of commercial boresonic indications in the general area.

Location Method	Z, Inches	θ°	R, Inches	Amplitude
Dissection	98.5	41	1.2	--
CMW Boresonic	98.3	40	0.42	28% Shear
CMW Boresonic	98.6	36	0.5	15% P/C
CMW Boresonic	98.6	33	0.45	13% P/C
CMW Boresonic	98.9	35	0.56	32% Shear
CMW Boresonic	99.1	45	0.56	41% Shear
Ⓦ Boresonic	98.2	39	1.5	31×10^{-4} in.^{2}
Ⓦ Boresonic	98.4	35	0.875	21×10^{-4} in.^{2}
Ⓦ Boresonic	98.4	31	1.5	31×10^{-4} in.^{2}
Ⓦ Boresonic	98.6	45	1.5	26×10^{-4} in.^{2}
Ⓦ Boresonic	99.0	50	1.5	47×10^{-4} in.^{2}
Ⓦ Boresonic	99.0	55	1.5	37×10^{-4} in.^{2}

The boresonic inspections do not reveal anything very large in the vicinity of the flaw although the many Ⓦ indications at 1.5 in. depth do fairly well correspond to the flaw and its long linear extension in the θ direction.

J7A5-15 was also treated for the first 0.5 in. of polishing by the cell technique described for Specimen J7A1-31. The results are shown in Figs. 63 and 64. The oddly shaped area outlined by a heavy black line in Fig. 63 and cross-hatched in Fig. 64 contains the flaw discussed above.

Specimens J7A5-12 and J7A5-22

These specimens were chosen for dissection to generate more volume fraction data and because radiography from the bore showed what appeared to be a lengthy linear flaw extending from J7A5-1 into J7A5-2 which might have been a crack in the RZ plane. Figure 65 shows this flaw (arrows). Figure 66 and Fig. 61 show orthogonal radiographs to Fig. 65.

Dissection revealed nothing unusual in either specimen; i.e., no cracks were found. The radiographic indication near the center left edge of J7A5-12 was a single large flaw, extending about 1/4 in. into θ, 1/8 in. into Z, and 3/8 in. in the radial direction. The location of this flaw and some neighboring boresonic data is shown below:

Location Method	Z, Inches	θ	R, Inches	Amplitude
Dissection	98.65	82°	0.7	--
CMW Boresonic	98.88	81°	0.45	15% P/C
CMW Boresonic	99.12	81°	0.40	19% P/C
CMW Boresonic	99.88	84°	0.7	16% P/C
CMW Boresonic	98.75	80°	0.17	?
Ⓦ Boresonic	98.4	80°	0.625	20×10^{-4} in.^{2}
Ⓦ Boresonic	98.6	91°	0.44	59×10^{-4} in.^{2}
Ⓦ Boresonic	98.8	92°	0.625	41×10^{-4} in.^{2}

The only flawed area of any significance in J7A5-22 is shown in Fig. 67. This area has a θ extent of about 0.06 in. to 0.09 in. since it only appears in three planes of polish and is about 3/8 in. wide in the Z direction and about 1 in. along a near radius direction. (Note that this figure is at 8.5X not 6X). The linear flaw of Fig. 65 was not evident during dissection and was probably due to a coincidental projection of overlaying flaws in the radiograph.

Volume fraction in J7A5-12 was determined to be 0.0046, and in J7A5-22 it was 0.0050. These were the dirtiest specimens examined in Joppa 3.

Specimen J6A-2

This is a specimen containing the bore as part of the plane of polish. It is centered at Z = 91.5 in., θ = 120°, and R = 0.45 in. with the plane of polish parallel to 130°. Some of the mechanical property data of Task 4 came from this area. Figure 68 is a radiograph looking along the bore from Z = 90.6 in. to Z = 92.4 in. The piece is not heavily flawed and the radiograph had to be heavily exposed to show what little was there. Figure 69 reveals that relatively large flaws can exist at the bore. This flaw appears in only one plane of polish and so has less than 0.06 in. extent in the θ direction.

Volume percent flaw in the approximately 0.9 in. (R) x 1.5 in. (Z) x 0.7 in. (θ) removed from this specimen was 0.0011.

Specimen J7-1

This specimen also contained the actual bore surface and was centered at Z = 97.6 in., θ = 65°, R = 0.5 in. and polished parallel to 74°. Some mechanical property specimens also came from this area. The specimen was very clean as the radiograph of Fig. 70 shows. BCL analysis of the boresonic data indicated that this specimen came from a fairly dirty area contrary to what sectioning disclosed. However, polished cross sections as shown typically in Fig. 71 reveal a heavy concentration of Type II flaws and, as discussed previously for Specimen J7A1-81 and later for JF-3, this type of flaw appears to give a disportionately large UT signal.

Flaw volume fraction was not measured in this specimen since only a few planes were polished.

Specimen JF-3

This specimen was centered at Z = 59.8 in., θ = 90°, R = 0.5 in. It was chosen because it contained one isolated large boresonic flaw in an otherwise very clean area of Joppa 3, and it was felt that it would offer an excellent opportunity to check the location accuracy of the boresonic inspection techniques in the absence of possible interference

from neighboring flaws. Both boresonic inspection teams had located this flaw using routine techniques applied during commercial inspections; it was further confirmed by a manual tool built by BCL which permitted positioning a UT transducer several feet into the rotor bore, and was again found by a hand held transducer after the rotor was partially cut into a pie shaped segment. The following table lists the flaw positions found by the above techniques along with the dissection location:

Location Method	Z, Inches	θ°	R, Inches	Amplitude
CMW Boresonic	57.62	88	0.6	27% P/C
Ⓦ Boresonic	57.70	84	0.44	154×10^{-4} in.^{2}
BCL Tool	57.37	90	0.5	92×10^{-4} in.^{2}
Hand Held	57.8	93	0.5	No DAC
Dissection	57.8	94	0.5	--

The correlation is very good except for the angle. Some problem with saw run-out during the radial cuts on this piece may have introduced several degrees of this error.

The radiograph of Fig. 72 attempts to show the flaw structure of the specimen. Only one small needle shaped flaw could be seen on the actual radiograph, about 1/32 in. long in the Z direction and about 0.005 in. or less wide in the R direction. This can be seen on the print of the radiograph only with great difficulty just slightly to the right and down from the center of the Fig. 72 print. A radiograph orthogonal to this view showed nothing. This area of Joppa 3 was much cleaner than any of the other Joppa specimens examined.

Figures 73 and 74 show sections polished at 0.03 in. intervals through the area of this flaw. This view is the same direction as the radiograph but the specimen is rotated 90° and the metallograph used to photograph the specimen has inverted the picture. The Type II flaws seen in these photographs appear to be densely grouped through 0.09 in. to 0.12 in. in θ and might present an apparent solid disc-shaped area to

the ultrasonic beam coming from the bore (as radiography also indicates). However, even then the density could not be nearly as bad as some of the groupings of Type I and III defects shown in many of previous figures of this report. Although it could occur, it is not likely that Type II defects are thin discs laying in the θZ plane (i.e., discs perpendicular to the radius). θR planes have been examined and the Type II defects are found in approximately circular clusters of small diameter as one would expect from the transverse cross section of a needle-like defect. Figure 75 shows an example of this for a Type II defect with about as much spreading (0.005 in.) in the θ direction as could be found.

The Ⓦ boresonic inspection reported an indication at this location with an equivalent flat bottomed hole (EFBH) diameter of 0.14 in., a very large indication relative to most of the 4300 indications reported. CMW boresonic also reported a large flaw relative to the other P/C indications they found and the BCL tool found an EFBH diameter of about 0.11 in. It must be concluded that there is some accentuation of the ultrasonic reflection by either the geometry and orientation of Type II defects and/or the nature of the aluminum-silicate inclusions associated with this flaw type.

IVB. Buck 6

The 125 MW, IP/LP rotor was placed in service in 1953. It is an integral forging very similar in all dimensions to Joppa 3. Once again, no manufacturing data is available.

IVB.1. Chemical Composition

The chemical analysis of a specimen from the bore near Z = 155 in. is as follows:

Cr	0.99	Ni	0.10
Mo	1.10	Si	0.28
V	0.25	P	0.019
C	0.26	S	0.0102, 0.0097
		Mn	0.75

IVB.2 Metallography

Figure 76 presents a low magnification view of a polished and etched RZ plane of Buck 6. This figure is badly pitted due to a poor etch but it does show the same coring due to chemical segregation during ingot solidification as was found in Joppa 3.

Figure 77 shows the general bainitic microstructure of Buck 6, and Fig. 78 gives a higher magnification showing some small amount of proeutectoid ferrite at the grain boundaries. There appears to be less ferrite in Buck than in Joppa. Figure 79 shows a still higher magnification view of some grain boundaries containing what are probably carbides. All microstructures are from near-bore specimens from under the major diameter of the rotor.

IVB.3. Typical Flaws

The flaws found in Buck 6 were similar to those found in Joppa 3 with only minor variations. Type I was present in both and was not significantly different. Type II was identical to Joppa but less numerous, at least in the areas examined. The Type III manganese sulfides were noticeably different from Joppa 3. They were often present in branching alignments as shown in Fig. 80 whereas this was an infrequent arrangement in Joppa 3. This figure also shows that individual inclusions contained a second phase and were of odd shapes. Figure 81 is a view of this at higher magnifications. This variation in Type III inclusion form probably does not affect UT results. The presence of a different phase in the inclusion does indicate a chemical change, possibly an addition such as a rare earth element.

IVB.4. Bore Condition

The Buck rotor differed from Joppa in that some work had been done on the bore after manufacturing, undoubtedly to remove flawed areas that showed up during magnetic particle or visual borescopic examination of the bore ID. At frequent locations along the bore, a grinding tool had been used. This process is called "dimpling" and leaves very shallow indentations smoothly blended into the bore wall. Figure 82 shows a low

magnification view of a dimpled area. In the areas of the Buck 6 bore exposed during sectioning, these were extremely shallow (estimated as about 0.010 in.) and were apparent visually more because of a difference in the coarseness of the grinding marks than because of a physical dimension change.

IVB.5. Progressive Dissection

The areas chosen for progressive dissection in Buck 6 were based upon the results of a reinspection of the rotor (both CMW and Ⓦ had run commercial boresonic inspections identical to what was done on Joppa) by Battelle Columbus Laboratories (BCL). This reinspection used techniques which are described in Battelle's Task II report on the program.

The reinspection identified 15 major indications over the fraction of the bore which was boresonically tested, and the contractors agreed upon 8 of these for at least partial dissection. The reinspection results for the 8 indications are:

Ⓦ Specimen No.	BCL Designation	Location			Extent	
		Z	θ°	R"	ΔZ"	Δθ°
B112	A	67.2	36	1.27	0.46	8
B114	B	69.8	49	2.03	0.47	14
B114	C	70.3	40	2.12	0.52	13
B212	U	98.9	101	1.36	0.31	9
B312	I	117.2	133	0.25	0.40	13
B313	P	118.3	140	0.74	0.92	13
B372	Y	118.2	223	0.6	0.23	10
B372	W	118.3	212	0.66	0.32	15

Wedge shaped segments containing the indicated flaws were cut as thin as possible in the Z thickness and radiographed as shown in Figs. 83 and 84. The arrow and crosses on these figures show the center of the location where the BCL boresonic results indicated a significant

flawed area (see above table). At this point Specimen B372 (Indications X and Y) were not pursued further due to the clean radiograph. Specimen B212 was also abandoned due to the unpromising results of radiography.

The remaining four specimens containing five BCL indication locations were further cut to small pieces containing the indications, re-radiographed and progressively polished. These specimens were polished at 0.06 in. intervals.

Montages of B114 (BCL Flaws B&C) are presented in Figs. 85 through 99, B1121 (BCL Flaw A) is shown in Figs. 100 through 112, and B313 (BCL Flaw P) in Figs. 113 through 116. The only flawed area in B312 (BCL Flaw I) may be seen in Fig. 117.

The locations of largest flaws or very densely flawed areas in the Buck specimens are compared to the boresonic results in the table on the next page.

No commercial boresonic inspection results were available for comparison since they did not inspect these areas because of dimpling.

The correlation between dissection and the BCL boresonic re-inspection was excellent for Flaws P, I and A, whereas Flaws B and C did not correlate well, although the general area was confirmed. Flaws B and C were more than 2 in. from the bore and in a generally very dirty area. This may account for poor correlation because of beam spread and interference from neighboring flaws.

Volume fraction flaw was calculated for the Buck specimens with the following results:

Specimen No.	Volume Fraction Flaw
B1121	0.0047
B114	0.0074
B312	0.0023
B313	0.0051

Specimen or Flaw	Location Method	Coordinates of Flaw Center Z"	θ°	R"	Extent ΔZ	Δθ°	ΔR°	Comment
B114	Dissection	69.1	39	2.22	.12	8	.17	Long, continuous
B114	Dissection	69.0	34	2.85	.16	2	.20	Badly broken
B114	Dissection	69.6	34	2.15	.30	3	.30	Broken
B	BCL boresonic	69.8	49	2.03	.47	14	--	--
C	BCL boresonic	70.3	40	2.12	.52	13	--	--
B313	Dissection	118.0	145	0.6	.17	4	.10	Single
P	BCL boresonic	118.3	140	0.74	.92	13	--	--
B312	Dissection	116.7	132	0.0	Contacts bore			Band narrow in θ
B312	Dissection	117.6	133	0.35				and R, 0.9" long in Z.
I		117.2	133	0.25	.4	13		
B1121	Dissection	66.9	41	1.15	.16	4	.14	Single Flaw
A		67.2	35	1.27	.46	8	--	

Excepting B312, the volume fractions of flaws in dissected specimens are higher in Buck than in Joppa. This may have been due to the more careful selection of Buck specimens at specific areas in which BCL boresonic inspection indicated large flaws, rather than a specially increased flaw content in Buck.

V. Discussion

VA. Metallurgy

The chemical analysis of both Joppa 3 and Buck 6 corresponded to Cr-Mo-V steels, although manufacturers specifications were not available for comparison. The two rotors were almost identical in composition except that the sulfur content of Buck was about 2 times higher than Joppa. It is very possible that much of the sulfur difference can be attributed to sample location; i.e., the Buck sample may have come from a segregated area with high sulfur and the Joppa sample from an area of low sulfur. There was a definite difference in the sulfide inclusion morphology in the two materials which may be partially due to the chemical difference.

The bainitic microstructures of the two alloys were similar, with none of the unusual ferrite structure seen in the failure origin of the Gallatin rotor. There was some pro-eutectoid ferrite in both Joppa and Buck, slightly more in Joppa than Buck, but nothing unusual in view of the slow cooling rates during heat treating that are expected in heavy sections.

VB. Flaw Structure

Both rotors displayed a large amount of unconsolidated shrinkage and/or gas porosity in the near bore. This indicates that there was insufficient forging reduction to heal ingot defects. This is further confirmed by the sulfide inclusions which are not distributed in linear arrays as would occur if heavy reductions in ingot cross sections had occurred. However, the Type II defects were much longer in the direction of the rotor axis than in the other directions, even though they showed little forging distortion.

The flaws revealed on the Joppa 3 LCF specimen fracture surfaces did show much elongation along the rotor axis. These specimens came from near the extreme end of the rotor (Z = 140 in. to 150 in.) and Fig. 118 confirms that flaws in this area were largely elongated Type II defects.

The volume fraction of flaws found by progressive dissection of the two rotors is somewhat higher in Buck 6 than in Joppa 3; however, the Research Institute (SWRI) analysis indicates that even the worst case found is insignificant and given the rotor stresses they calculate and the material properties determined by Task 4.

Dissection disclosed no defects such as cracks that could be attributed to cyclic start-up stresses or creep during the many years of operation of the rotors. Even the unhealed folds frequently found in association with relatively large voids in the near bore regions showed no signs of opening due to service stresses.

Fractography conducted on low cycle fatigue specimens of Joppa 3 did indicate that flawed areas can play a role in subcritical crack growth as shown by large departures from the maximum RZ plane of stress. However, these specimens were failed at much higher (approximately 2X) cyclic stresses than SWRI calculations indicated had been seen by the rotor.

If the number of objects laying in a plane is known, and if the assumptions made that the objects are randomly and homogeneously distributed over a volume of concern, the average distance between the center of one object and the center of its nearest neighbor can be calculated by the statistical techniques of stereology (see Quantitative Microscopy, p. 283, Dehoff and Rhines, McGraw-Hill, 1968). The average nearest neighbor center to center distance on a plane of polish is $\bar{\lambda}_A = 1/2\ (N_A)^{-1/2}$ where N_A is the number of flaws per unit area. The average nearest neighbor center to center spacing in the volume of alloy is given by $\bar{\lambda}_V = 0.554\ N_V^{-1/3}$ where N_V is the number of objects per unit volume. The data collected by microscopy gives only N_A since only a planar section can be polished and

inspected. N_V can be calculated from N_A if simplifying assumptions are made as described below.

As an example, the above calculations may be made for a very dirty Joppa plane of polish which is shown in Fig. 46. The number of flaws (holes and inclusions) per square inch (N_A) in this plane was established to be 3734 by the Classimat. The average nearest neighbor approach (center to center) in the plane is then calculated to be 0.008 in. The Classimat also gives the average flaw dimension in this plane as 0.00086 in. This figure can be used to calculate an average surface to surface approach of nearest neighbors (which would be a measure of the average distance a crack would have to grow in the RZ plane through sound metal to link the flaws) by assuming the flaws have circular cross sections in the plane. This approach distance is equal to ($\lambda_A - D_{ave}$) where D is flaw diameter. The result is 0.0073 in., which gives a ratio of linkage path to flaw diameter of 9; the hypothesis for flaw linkage used by Task 1 indicates that this ratio must be less than one before the cloud of flaws is of concern in Joppa 3.

Since fractography showed that the sub-critical LFC fatigue cracks in the Joppa 3 specimen deviated drastically from a plane apparently in an effect to follow flaws, the closeness of approach ratio in the volume would probably be more indicative of the path that the cracks really follow than the ratio in an RZ plane.

This calculation is made using the technique described in DeHoff and Rhines, pp. 133-134. The assumption used in addition to those described above is that all flaws are spheres of identical diameter; while the results are coarse approximations, they do give an idea of the average nearest neighbor approach in the volume calculated from data collected by averaging over many planes of polish. By this technique the number of flaws per cubic inch, N_V, is calculated as 2,578,510, the diameter of the spheres is 0.0014 in. (this is greater than in the plane of polish since the plane would rarely intercept the maximum diameter of the flaws), and the center to center average distance to a nearest neighbor is 0.004 in. This yields a linkage path to average flaw diameter ratio of about 2. This is a much shorter linkage path through the volume than on a plane, although the crack would

have to deviate from the plane of maximum stress to follow it. This is just what has happened in the sub-critical fractures of the LCF specimens. This is almost a worst case calculation for Joppa 3, but it does indicate that clouds of flaws found in Joppa can be quite closely packed. Also the above calculations are averages over fairly large areas and volumes, and where flaws are grouped or occur in bands the approach ratios within these features can be less than the averages indicate.

The majority of small flaws counted by the Classimat and used in the above calculations are well below the size detected by boresonic examination. The 5 MHz frequency used by the commercial Ⓦ boresonic inspection reported the largest number of indications, 4300 in the approximately 2800 $in.^3$ of the Joppa 3 bore examined versus about 150 by the 3.5 MHz CMW inspection, while calculations based on the Classimat data gave on the order of 20,000 flaws in 1 $in.^3$ even in some of the less dirty specimens examined. The smallest flaw reported by Ⓦ was about 0.03 in. Equivalent Flat Bottomed Hole (EFBM) diameter or about 20 times the average size counted by the Classimat. Since the rotor life prediction model being developed by Task 1 has to operate on input from in-service boresonic inspections, the fine detail used in the above calculations is beyond the capability of boresonics and thus has no utility to Task 1. It was mainly for this reason that the Classimat work was abandoned.

VC. Correlation Between Flaws and Boresonic Inspection

Attempts to obtain an exact correspondence between indications reported by the boresonic inspection and individual flaws found by dissection were generally unsuccessful, as shown by the various correlations discussed for individual specimens in foregoing sections of this report. This is not surprising in view of the very many small flaws that occur. The major reason is that the dimensions of individual flaws are smaller than the dimensional uncertainties resulting from both the boresonic inspection and the cutting of the rotor. It is estimated that these various dimensional uncertainties are on the order of 1/4 in.

Both commercial boresonic inspections on both rotors reported an average indication size on the order of 0.05 in. to 0.06 in. EFBH diameter, while dissection revealed at least an equivalent number of flaws in this size range plus many much smaller. Thus, the boresonic indications and actual flaws were on the average 4 times smaller than the region within which their location could be specified, and in most cases several flaws were located within the uncertainty volume.

The uncertainties in boresonic location arise from minor positioning errors in the boresonic transducers, backlash in the tooling, and ultrasonic beam spread, etc. Perhaps the largest single source of uncertainty results from the fact that the transducers interrogated the rotor only in steps on one of the dimensions. The Ⓦ inspection used a stepwise jump of 1/4 in. in moving the transducer along the rotor axis (the Z dimension) while the CMW inspection used a stepwise jump in the θ dimension. Both techniques not only frequently cause mislocation of indications but may even miss detecting some flaws altogether. Also the amplitude of the signal returned from a flaw will frequently be misstated since the transducer is not being maneuvered to maximize the signal. Figure 31 gives a graphic illustration of this, showing a missing gap in Z at the large flaw that is probably due to not interrogating continuously in Z, and also showing an underestimation of flaw size (amplitude). This figure also points out another problem that arises from the many lobes or side branches of the large hole (see Fig. 30); i.e., multiple reflections from a single flaw. It also indicates the magnitude of combined boresonic and cutting mislocation errors. The large CMW indication, which was the largest they reported in Joppa, is almost certainly the large flaw shown, but the flaw and the indication fail to correspond by about 0.5 in. in Z and by 0.5 in. in R (Fig. 32).

Perhaps the best illustration of the commercial boresonic limitations when dealing with these profuse small flaws is given by the attempts of both inspection teams to repeat an inspection over a short section of a rotor. Westinghouse had removed their boresonic setup from the rotor bore but replaced it and reinspected a one foot length with the

same operators and instrumentation. They found approximately the same number and sizes of indications but not with the same positions, nor could plots of the two sets of inspection data be translated and/or rotated to correspond. Commercial Machine Works reinspected several months after the first inspection with different operators and found much fewer flaws than the first inspection. A one-to-one correlation of actual small flaws found by dissection with the commercial boresonic results cannot be expected in view of these results. If the rotors had contained isolated large flaws (1/2 in. diameter or so), in all probability both teams would have located the individual flaws with sufficient precision for adequate analysis.

One anomaly did arise in the examination of Joppa 3. The isolated flaw, JF3, found by boresonic inspection near 57.7 in. was reported as being relatively large (see page 21) by all inspections. However, dissection showed it to be a very small group of Type II flaws which nominally would not have had enough area to return the signal amplitude reported by either Ⓦ, CMW or the Battelle tool. The same type of phenomena occurred in specimens J7A1-81 and 7A1 both of which contained many Type II flaws. The reason for this is not known; we can only speculate that the geometry of these holes and associated inclusions enhance the reflected UT signal.

The re-inspection of Buck 6 by the modified techniques of Battelle did appear to offer better correlation between dissection and the boresonic results. How much of this was due to improved boresonic techniques and how much was due to improvements in dissection techniques and more painstaking boresonic inspection is problematical. Where relatively isolated large flaws or clusters of flaws are close to the bore (R = 1 in. or less), good mating between the flaw and the boresonic signal is found. When the flaw is 2 in. or more from the bore, resolution is lost.

VI. Conclusions

1. Dissection revealed that both the Joppa 3 and Buck 6 rotors contained very many small flaws. The flaws were of three types: large relatively unoriented holes which frequently were partially collapsed and folded together to form unhealed seams; small rod shaped holes with saw tooth edges oriented along the rotor axis, which frequently contained angular alumino-silicate inclusions; manganese sulfide inclusions only occasionally aligned with each other and the rotor axis.

2. Flaw density was always less than 0.01 volume fraction when averaged over volumes of 0.5 to 1.0 $in.^3$. The maximum area fraction flaw on an RZ plane (maximum stress plane) was 0.02.

3. The ratio of the average nearest neighbor distance to the average flaw diameter can be as low as 2 in dirtier volumes of the rotor.

4. Flaw linkage is involved in areas of subcritical cracks in low cycle fatigue specimens ran at relatively high stresses, as evidenced by high area fraction of flaws on the fracture surfaces and drastic deviations from the plane of maximum stress.

5. In general, the results of commercial boresonic inspection, which indicated many small flaws in the near-bore regions of both rotors, were confirmed by dissection. However, a one-to-one correlation of the actual position of single flaws or flaw clusters to specific boresonic indications was not possible. A major reason was that the size and spacing of the flaws was smaller than the uncertainties in location introduced by both boresonics and cutting. The correlation improved as flaws became larger and/or more isolated and their distance from the bore decreased (ignoring the dead zone immediately adjacent to the bore).

6. Anomalously large reflection amplitudes came from the elongated rod shaped Type II flaws. In some instances, this caused volume fraction of flaw as determined from the boresonic data to be much larger than revealed by dissection.

7. Existing boresonic inspection techniques do not provide a good representation of the detailed flaw structure in rotors when a profuse number of small flaws are present as in Joppa 3 and Buck 6.

VII. Recommendations

In any future work, specimens chosen for dissection should first be precracked in fatigue on an RZ plane and then examined by progressively polishing an Rθ plane perpendicular to the crack. This approach would still permit determination of flaw size, distribution, and calculation of volume fraction flaw, plus additionally revealing the degree of flaw involvement in the path chosen by the crack.

TABLE 1

Densely Flawed Volume in Piece J7A1-6 From Joppa 3 in RZ Planes. Letters Refer to Figure 34

Revealed by Dissection

Flaw	Mils Removed Below 332° Plane	Z, in.	R, in.	θ°	Size in RZ Plane, in.
A	875	100.98	0.50	309	0.035 in. x 0.035 in.
C	850	100.97	0.46	310	0.050 in. x 0.020 in.
D	850	100.98	0.52	311	0.045 in. x 0.020 in.
E	825	100.90	0.43	310	0.070 in. x 0.030 in.
F	825	100.90	0.48	311	0.070 in. x 0.020 in.
G	800	100.95	0.41	311	0.060 in. x 0.010 in.
H	800	100.96	0.53	312	0.050 in. x 0.030 in.
Fig. 33	750	100.84	0.34	312	0.045 in. x 0.015 in.

Boresonic Results in Same General Volume

Flaw Identity	Z, in.	R, in.	θ°	Amplitude
Westinghouse 1405	100.6	3/8	310	49×10^{-4} in.^{2}
Westinghouse 1407	100.8	3/8	307	45×10^{-4} in.^{2}
Westinghouse 1468	100.8	3/8	308	31×10^{-4} in.^{2}
Westinghouse 1469	100.8	7/16	310	46×10^{-4} in.^{2}
Westinghouse 1470	100.8	1/4	315	63×10^{-4} in.^{2}
Westinghouse 1477	100.8	3/8	312	174×10^{-4} in.^{2}
Westinghouse 1479	100.8	3/8	316	69×10^{-4} in.^{2}
Westinghouse 1531	101.3	1/2	305	49×10^{-4} in.^{2}
CMW	101.6	0.68	313	19% S/P (pitch-catch)
CMW	102.2	0.42	310	17% S/P (axial shear)

TABLE 2

Sizable Flaws Exposed by Cutting and Progression Grinding on ∿RZ Plane of Piece J7A1-6 from Joppa 3

Z (inches)	R (inches)	Θ (degrees)	Approx. Largest Extent. (inches)
98.6	1/2	360	0.03
98.7	1-1/8	352	0.03
98.8	1-1/8	356	0.03
98.8	3/8	354	0.08
98.9	1/2	354	0.05
98.9	1/2	360	0.06
99.0	7/16	360	0.03
98.9	1-1/4	360	0.03
99.5	1.4	356	0.03
99.5	1.35	352	0.03
99.7	0.5	332	<0.03
100.4	0.5	360	0.03
100.4	0.8	360	0.03
100.4	1.1	360	<0.03
100.7	0.5	332	0.03
100.8	0.6	332	0.03
100.9	0.8	332	0.03
101.0	1.2	331	0.03
101.2	1.8	336	<0.03
101.15	7/8	325	Very large
101.4	0.8	360	<0.03
101.4	1.0	360	<0.03
101.4	1.5	360	<0.03

TABLE 3

All Boresonic Results Near Flaws Listed in Table 2

CMW

Z	R	Θ	Amplitude (%)	Type of Transducer
98.87	.35	340	17	45° shear
98.88	.78	359	19	P/C
98.88	.60	356	16	P/C
99.01	.21	355	23	45° shear
99.09	.28	345	22	45° shear
99.12	.65	355	16	P/C
99.12	.78	1	16	P/C
99.14	.28	340	29	45° shear
99.27	.35	350	24	45° shear
99.38	.63	344	33	P/C
99.39	.53	335	42	45° shear
99.77	.35	355	19	45° shear
99.88	.72	336	15	P/C
99.88	.55	330	13	P/C
100.20	.35	0	34	45° shear
100.20	.42	345	46	45° shear
100.30	.42	350	17	45° shear
101.52	.35	355	19	45° shear
101.81	1.06	335	36	45° shear

Westinghouse

Z	R	Θ	Amplitude (EFBH x 10^{-4} in.^{2})	Type of transducer
98.6	1/2	334	34	P/C
98.6	7/16	345	77	P/C
98.6	5/8	350	91	P/C
98.6	1-1/4	355	34	P/C
98.6	7/16	0	49	P/C
98.8	7/8	340	65	P/C
98.8	1/2	350	34	P/C
98.8	5/8	354	23	P/C
98.8	1/2	358	18	P/C
98.8	7/8	0	24	P/C
99.0	1/2	339	52	P/C
99.0	1-5/8	340	46	P/C
99.0	9/16	351	52	P/C
99.0	3/4	351	58	P/C
99.0	7/8	0	54	P/C

TABLE 3 (Cont'd) - 2

Westinghouse

Z	R	Θ	Amplitude (EFBH x 10^{-4} in.^{2})	Type of transducer
99.0	7/8	6	48	P/C
99.0	3/4	6	58	P/C
99.2	2-1/2	335	31	P/C
99.4	5/8	334	49	P/C
99.4	3/4	335	34	P/C
99.4	9/16	339	31	P/C
99.4	1-3/4	340	29	P/C
99.4	3/4	350	34	P/C
99.4	7/8	355	20	P/C
99.4	1/8	357	20	P/C
99.4	1/8	358	31	P/C
99.4	7/16	0	69	P/C
99.4	9/16	5	34	P/C
99.6	3/4	332	43	P/C
99.6	2-1/2	333	18	P/C
99.6	1/2	333	12	P/C
99.8	3/4	336	48	P/C
99.8	2	343	31	P/C
99.8	5/8	348	34	P/C
99.8	1/2	0	34	P/C
99.8	1/2	4	27	P/C
100.0	3/4	333	34	P/C
100.0	1/2	339	130	P/C
100.0	1/2	345	92	P/C
100.0	3/4	350	31	P/C
100.0	3/4	356	29	P/C
100.0	7/8	356	50	P/C
100.0	9/16	4	31	P/C
100.0	2-1/4	5	18	P/C
100.2	1	336	34	P/C
	Head pulled. Skipped to 100.6 Z When Re-started.			
100.6	5/8	335	24	P/C
100.6	1	337	18	P/C
100.6	9/16	339	46	P/C
100.6	9/16	340	31	P/C
100.6	1/2	343	61	P/C
100.6	7/16	347	48	P/C
100.6	1/2	344	34	P/C
100.6	7/8	354	34	P/C

TABLE 3 (Cont'd) - 3

Z	R	Θ	Amplitude(EFBH x 10^{-4} in.^{2})	Type of transducer
100.8	9/16	334	95	P/C
100.8	1-1/2	335	73	P/C
100.8	1/4	335	21	P/C
100.8	5/8	337	91	P/C
100.8	1/2	340	39	P/C
100.8	3/4	353	35	P/C
100.8	3/4	359	70	P/C
100.8	7/8	3	58	P/C
101.1	1	336	31	P/C
101.1	3/4	342	29	P/C
101.1	1/2	342	26	P/C
101.1	3/4	345	46	P/C
101.1	3/4	348	34	P/C
101.3	7/8	337	61	P/C
101.3	3/4	341	39	P/C
101.3	3/4	346	48	P/C
101.3	3/4	353	97	P/C
101.3	3/4	359	27	P/C
101.3	1/2	4	39	P/C
101.5	1-1/2	336	34	P/C
101.5	1/2	336	61	P/C
101.5	3/4	335	41	P/C

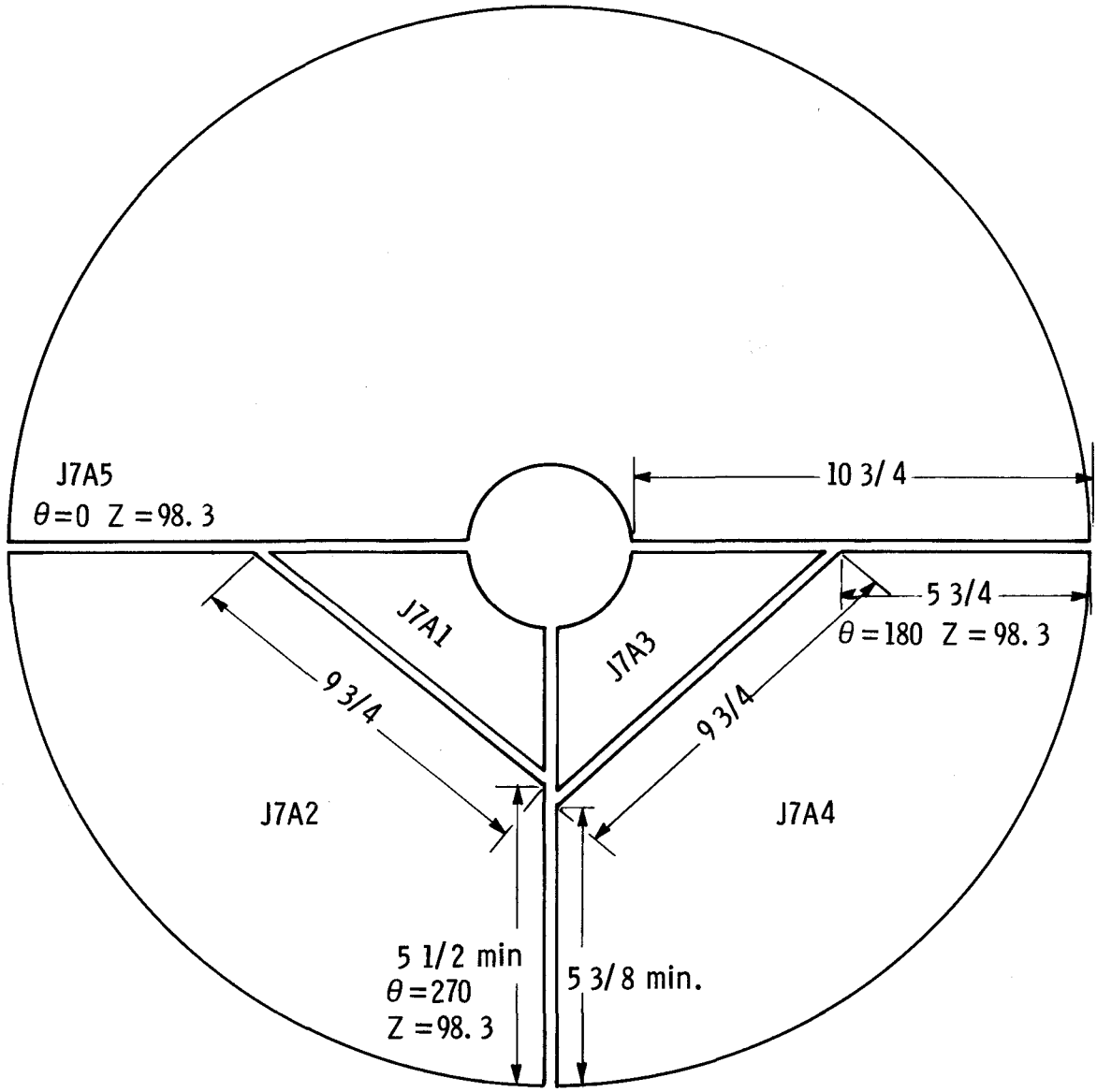

Fig. 1 —Cutting schematic for disc J7A of Joppa 3

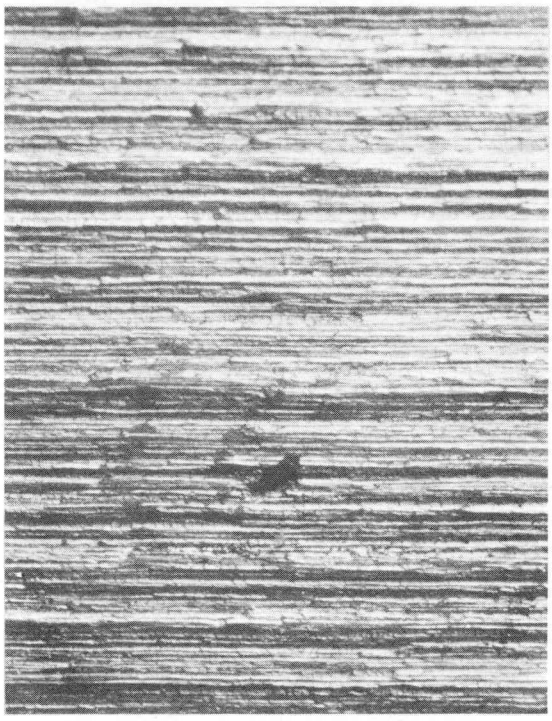

Z = 100.4", R = 0.81", θ = 360°

Z = 98.7, R = 0.81", θ = 360°

Z = 102.3", R = 2.31", θ = 3.57°

Z = 102.3", R = 2.06", θ = 357°

FIG. 2 - Holes in Joppa 3 Revealed by Saw Cuts.
Mag. 10X

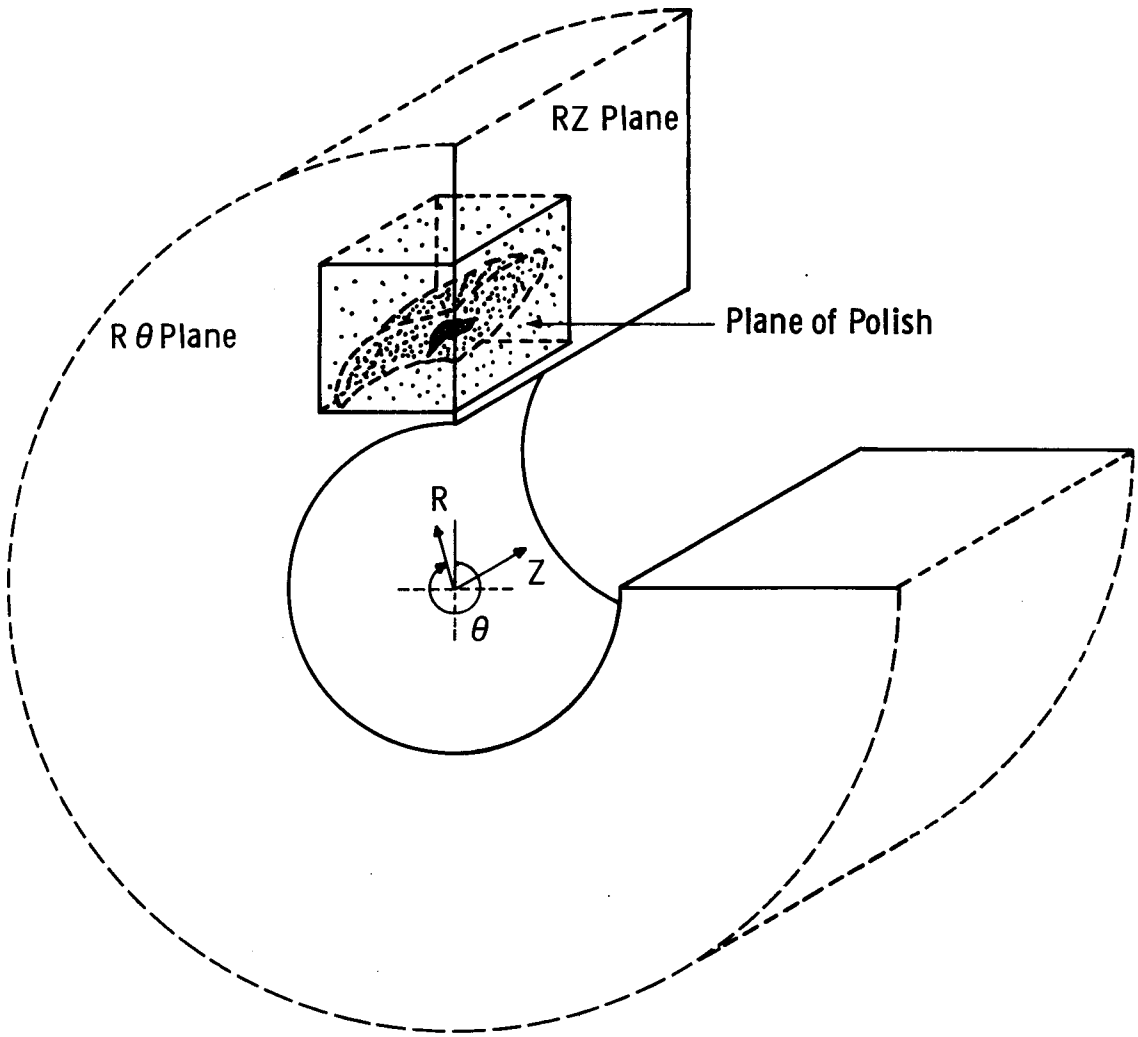

Fig. 3 – Schematic of specimen position in Rotor

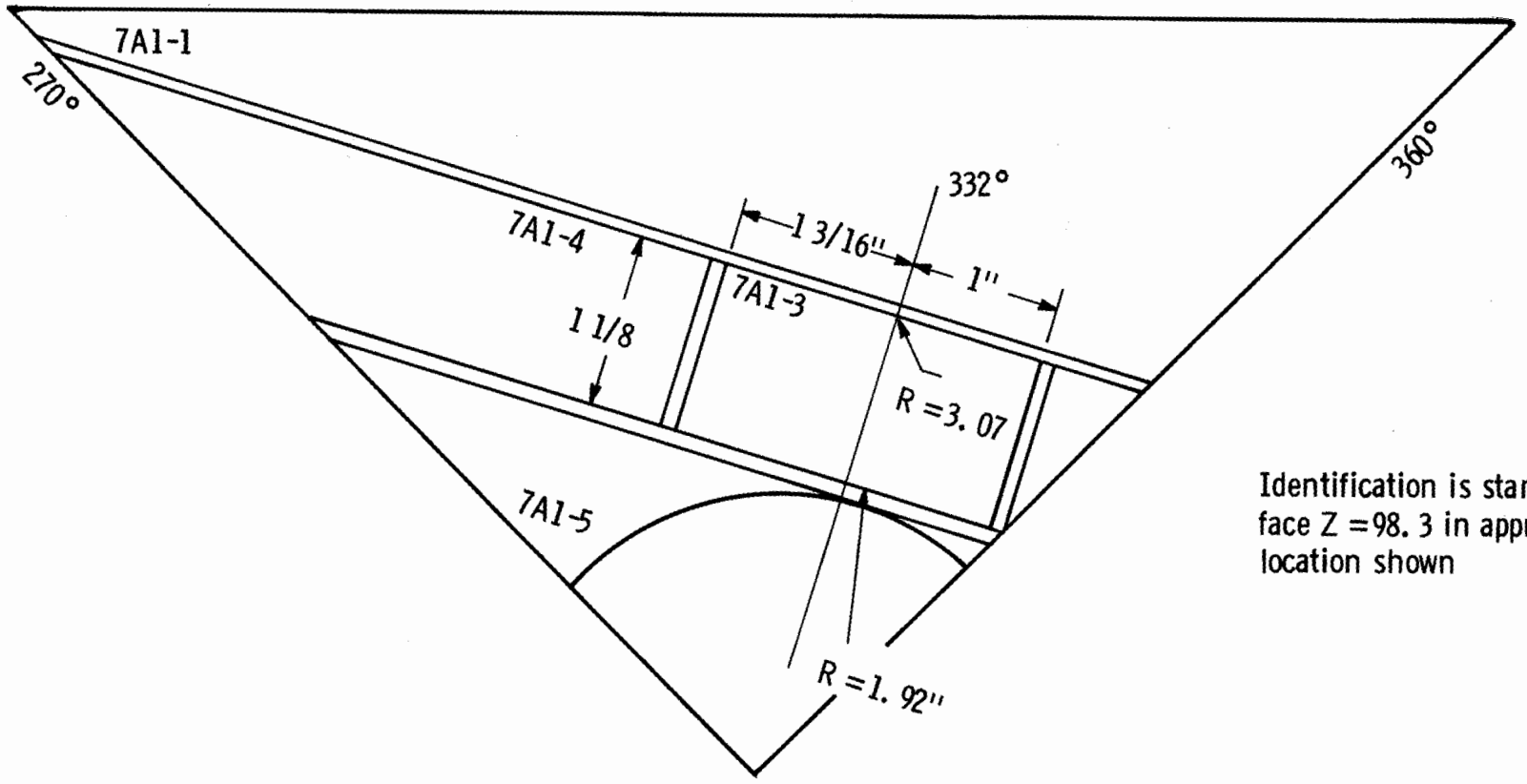

Identification is stamped on face Z =98. 3 in approximate location shown

Fig. 4 — R - θ view of cutting layout for pc. J7A1

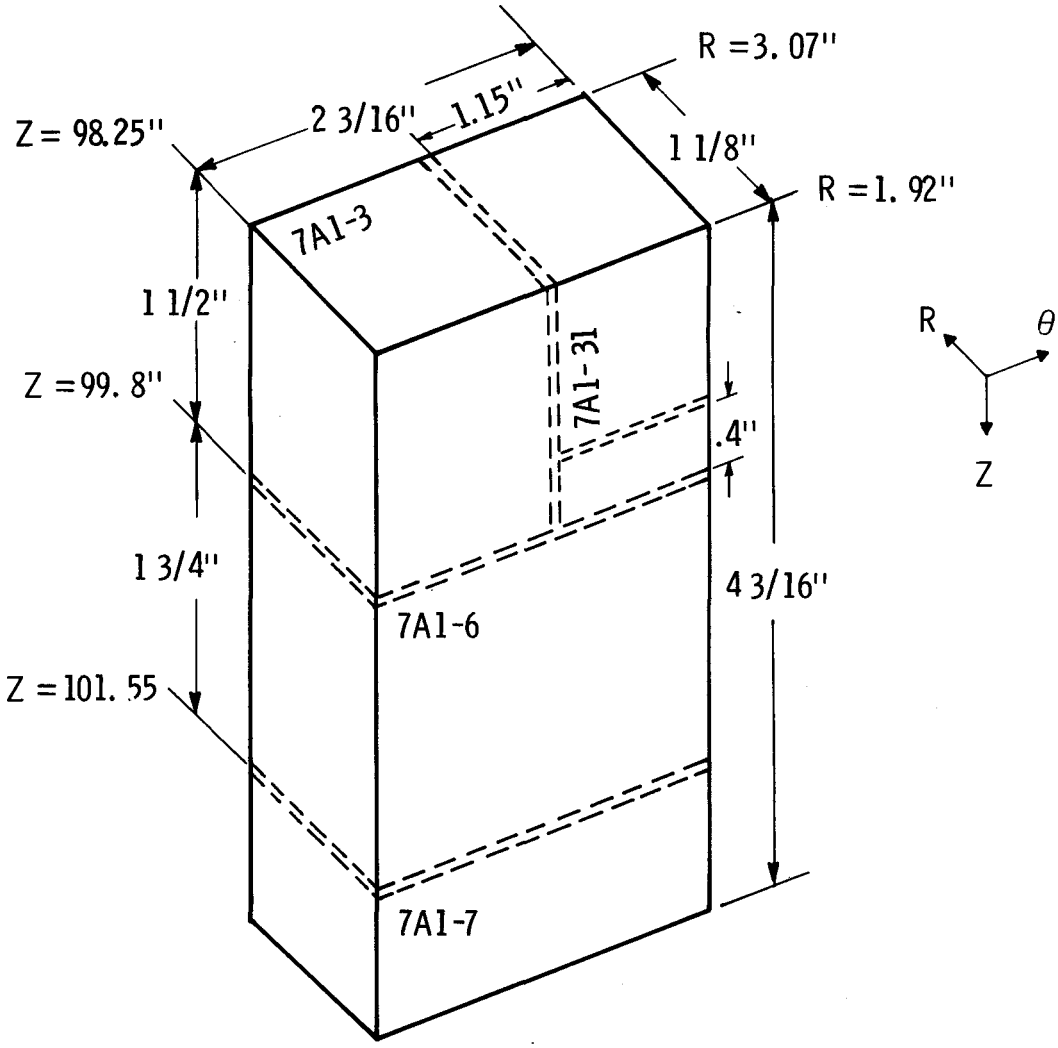

Fig. 5 — Further cutting of J7A1-3 of Fig. 4

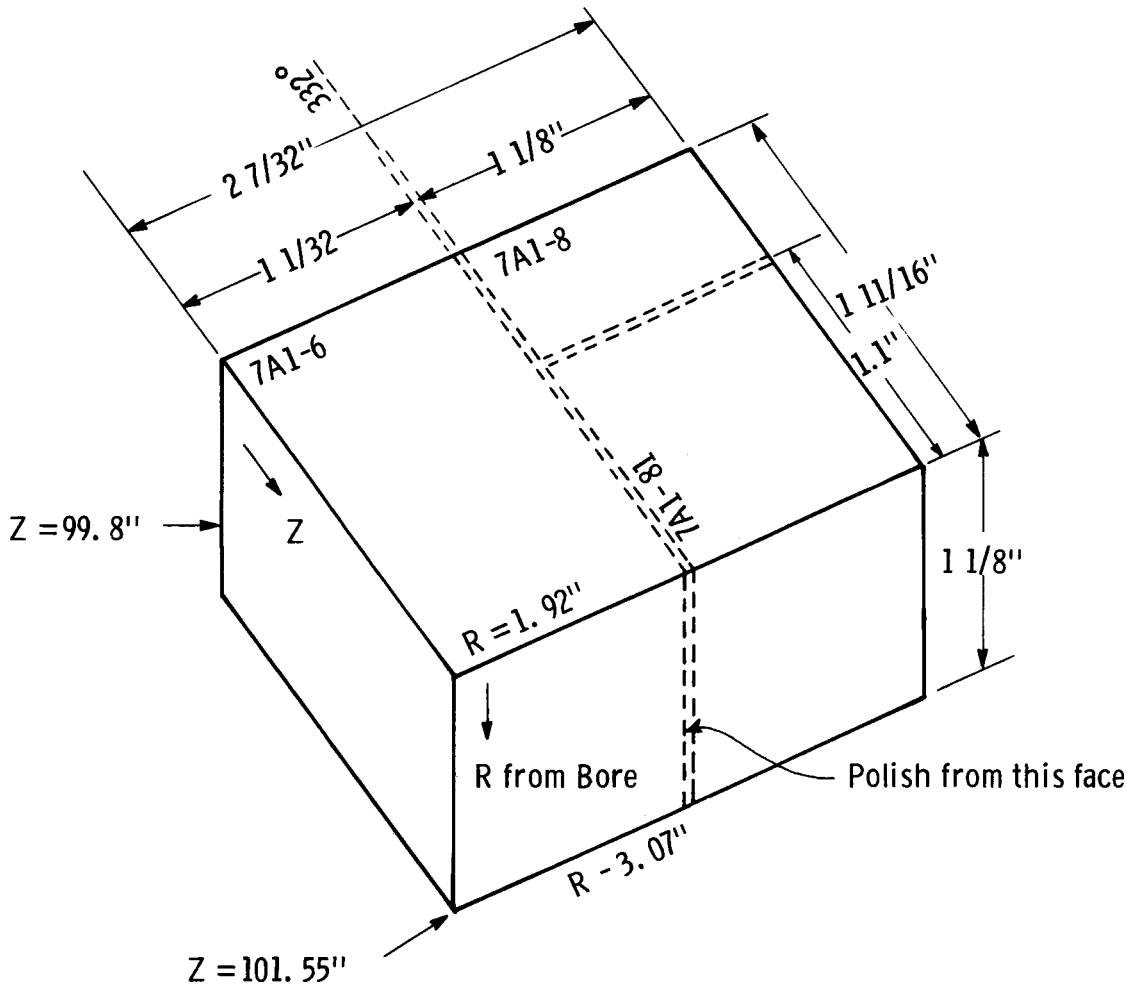

Fig. 6 – Further cutting of pc. J7A1-6 of Fig. 5

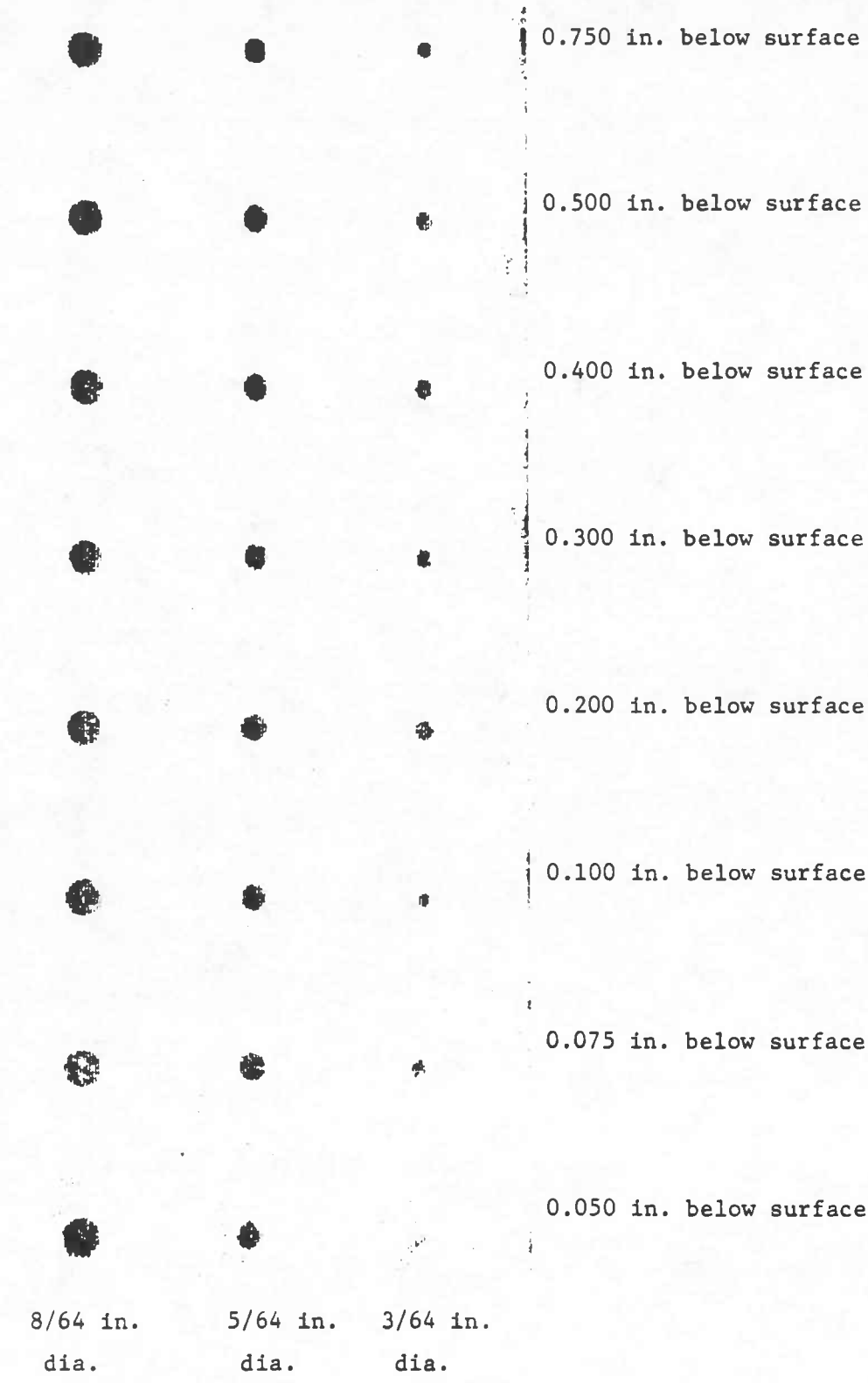

FIG. 7 - Calibration C-Scan of Flat-Bottomed Holes at Various Depths. Freq. 10 MHz

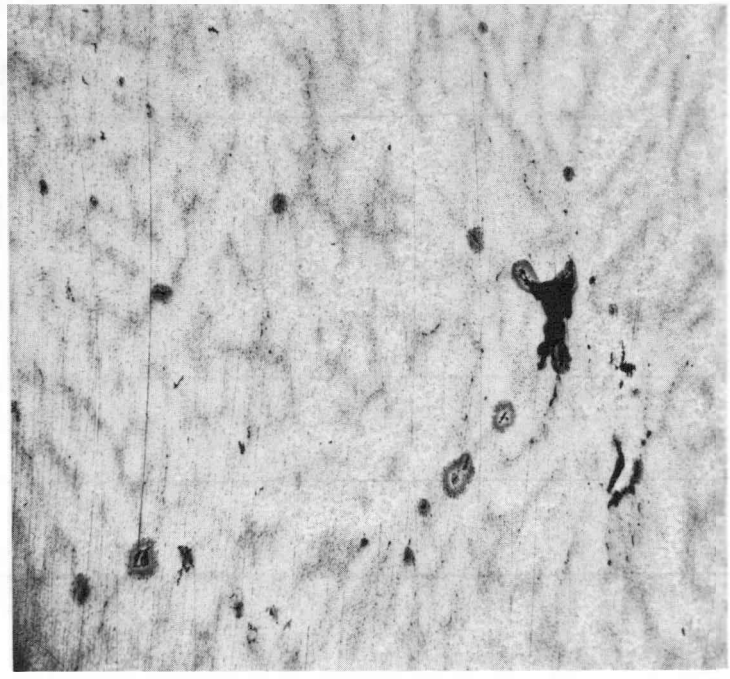

Mag. 6X

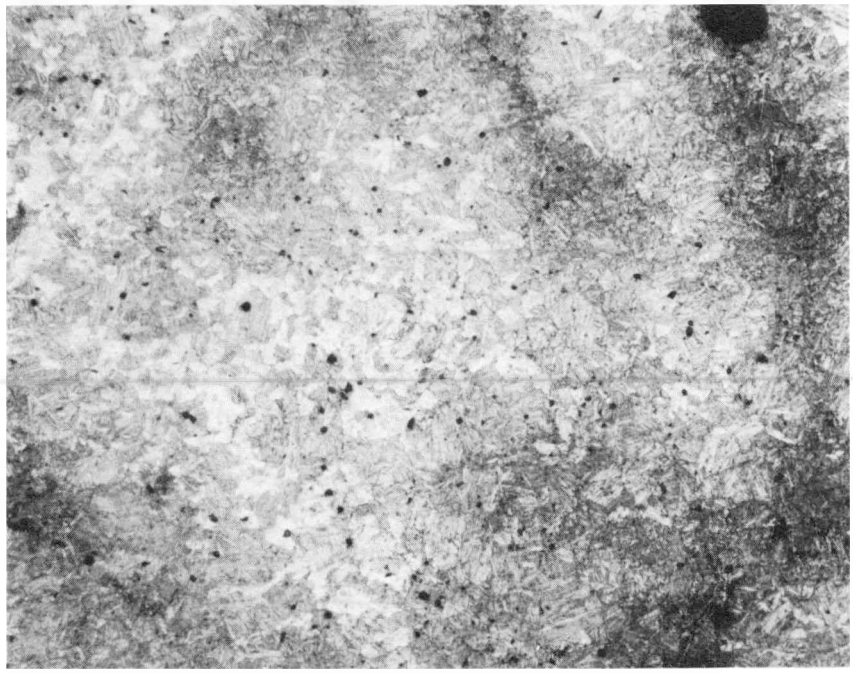

Mag. 30X

FIG. 8 - Polished and Etched RZ Plane of Joppa 3 (Piece J7A1-6). STBS Etchant.

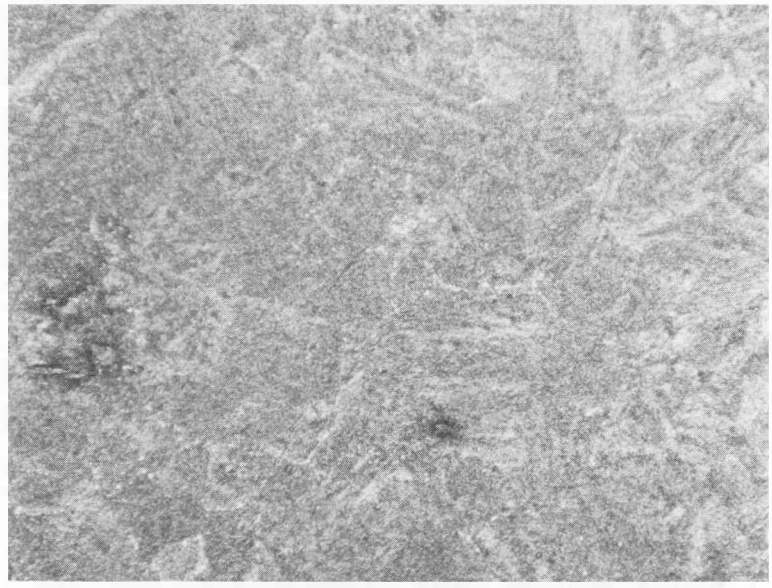

Mag. 300X

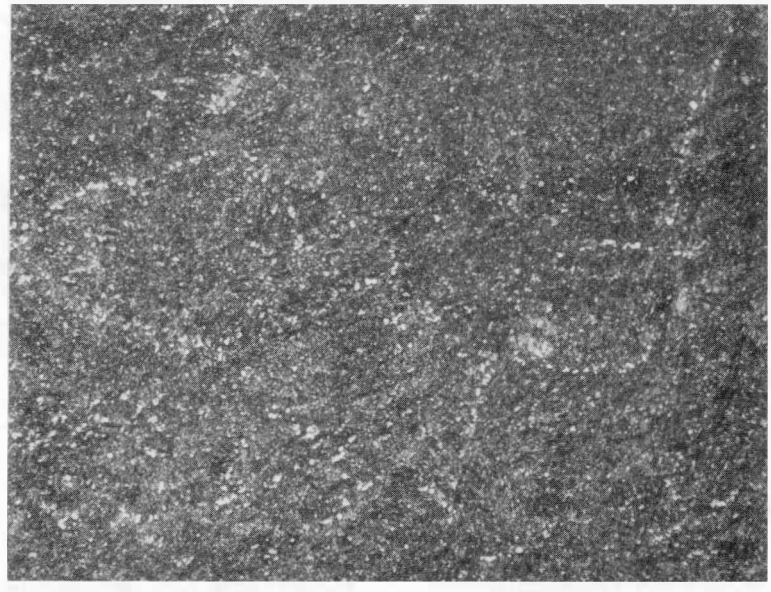

Mag. 500X

FIG. 9 - Microstructure of Joppa 3.
Picral Etch.

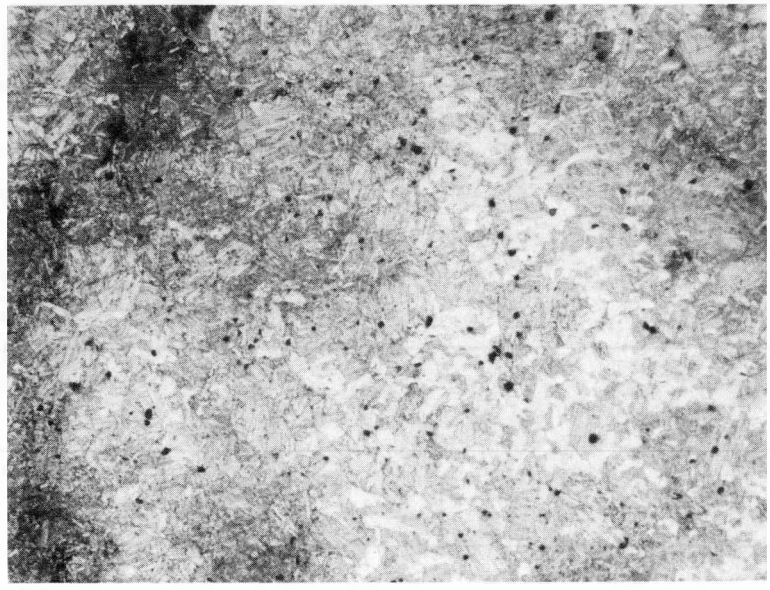

Mag. 30X

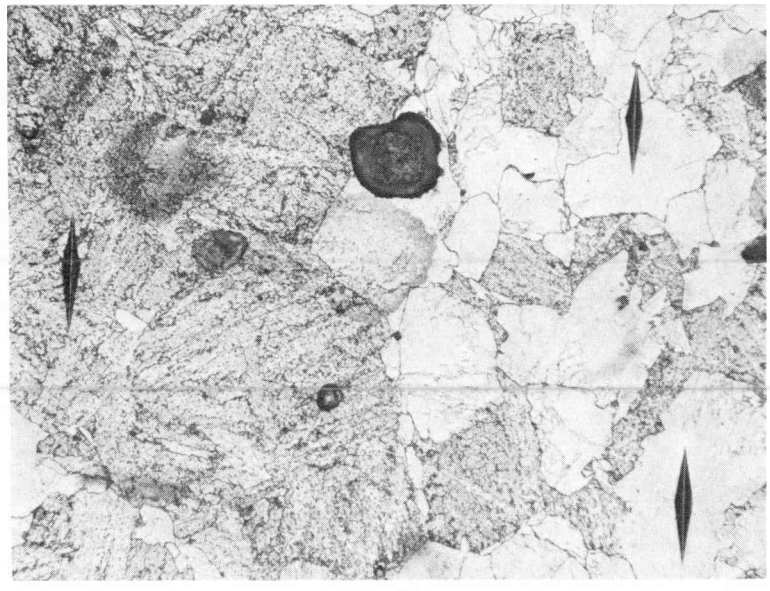

Mag. 200X

FIG. 10 - Microstructure of Joppa 3.
STBS Etch.

Mag. 50X

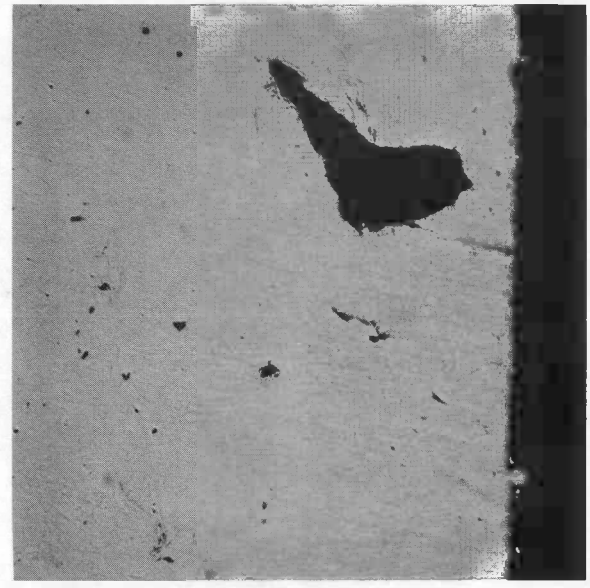

Mag. 50X

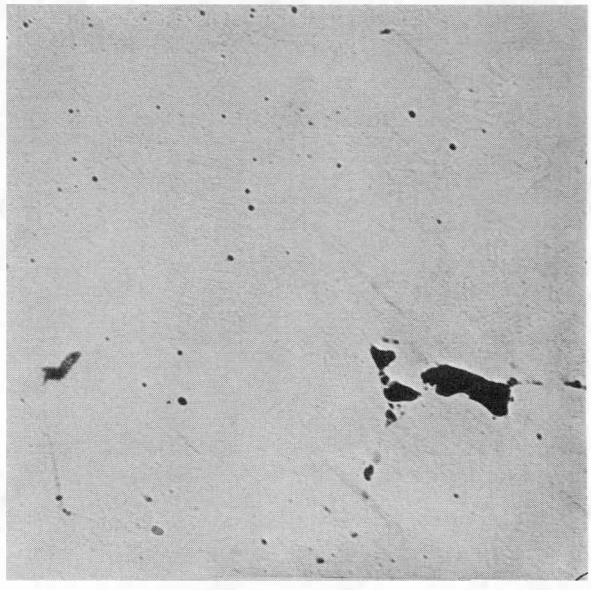

Mag. 50X

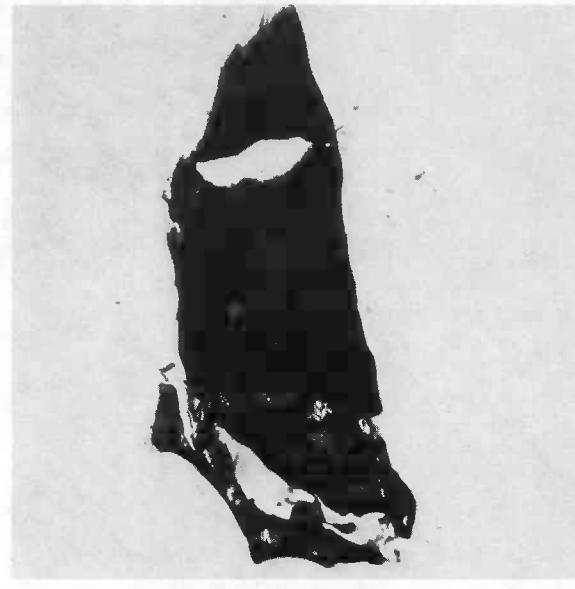

Mag. 100X

FIG. 11 - Examples of Type I Flaws in Joppa 3.

Mag. 50X

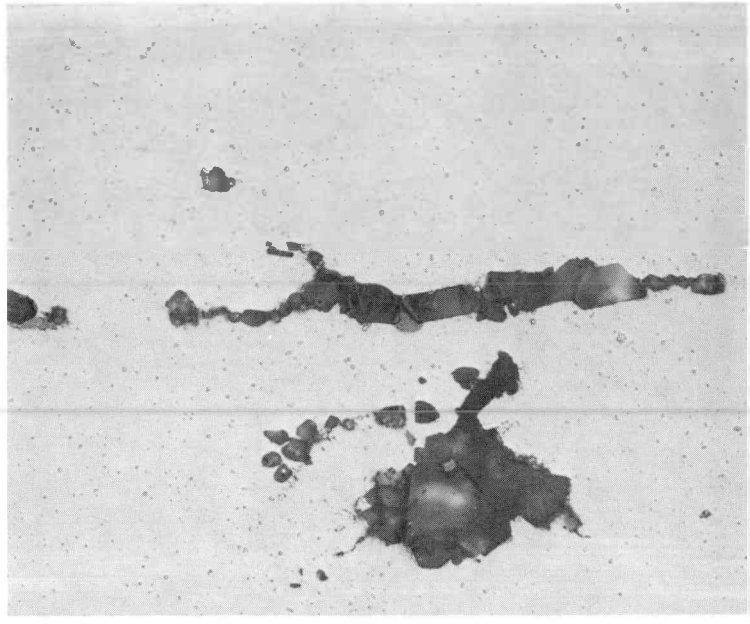

Mag. 500X

FIG. 12 - Examples of Type II Flaws in Joppa 3.

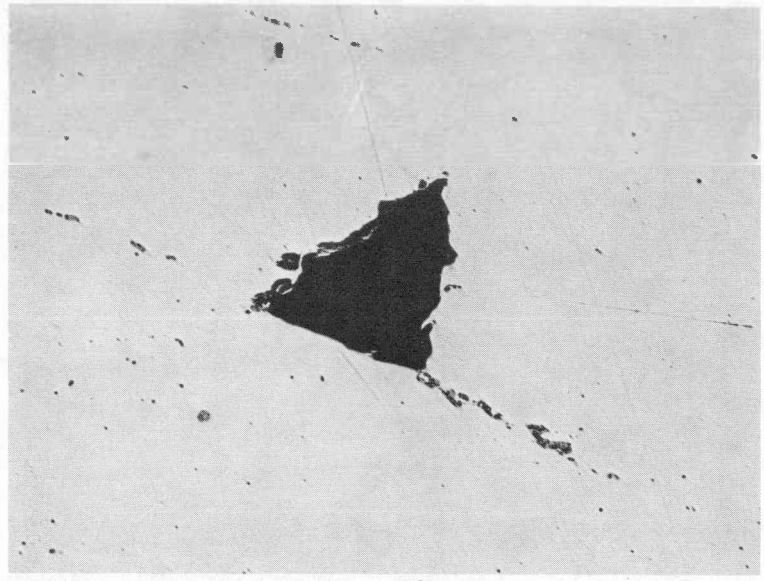

a. Mag. 50X

b. Mag. 50X

FIG. 13 - Examples of Type III Flaws in Joppa 3. In 'a' the Sulfides are Associated With a Type I Void.

Mag. 500X

FIG. 14 - Magnified View of Inclusion Stringer Coming from Lower Right Corner of Fig. 13a. Note Forging Laps.

FIG. 15 - Typical Small Spherical Manganese Sulfide Inclusions in Joppa 3. RZ Plane of Polish. Mag. 100X

Unetched Mag. 500X

FIG. 16 - High Magnification View of Small Sulfides Found in Joppa 3.

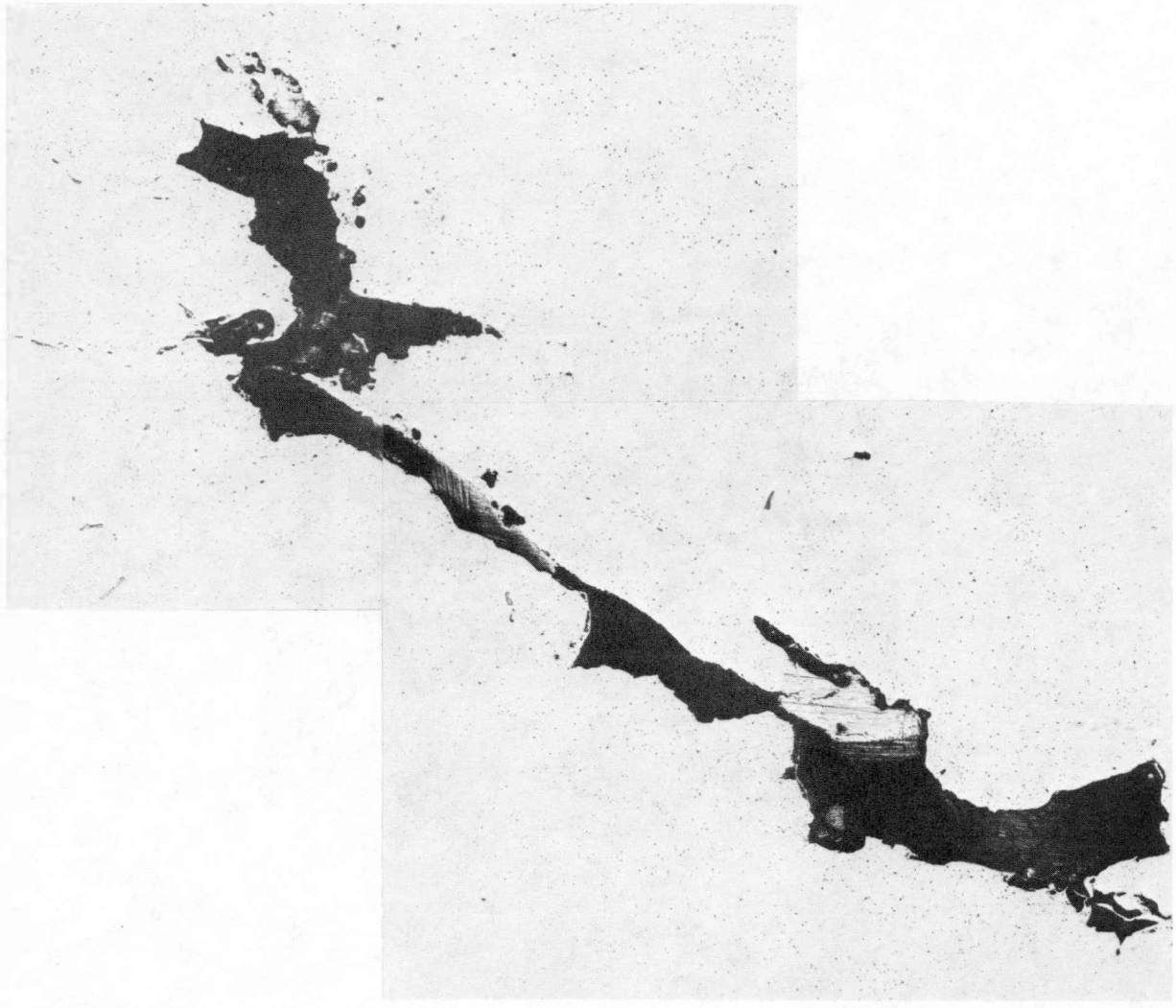

FIG. 17 - Examples of Small MnS Inclusions Densely Grouped Near Type I Holes in Joppa 3. Mag. 100X

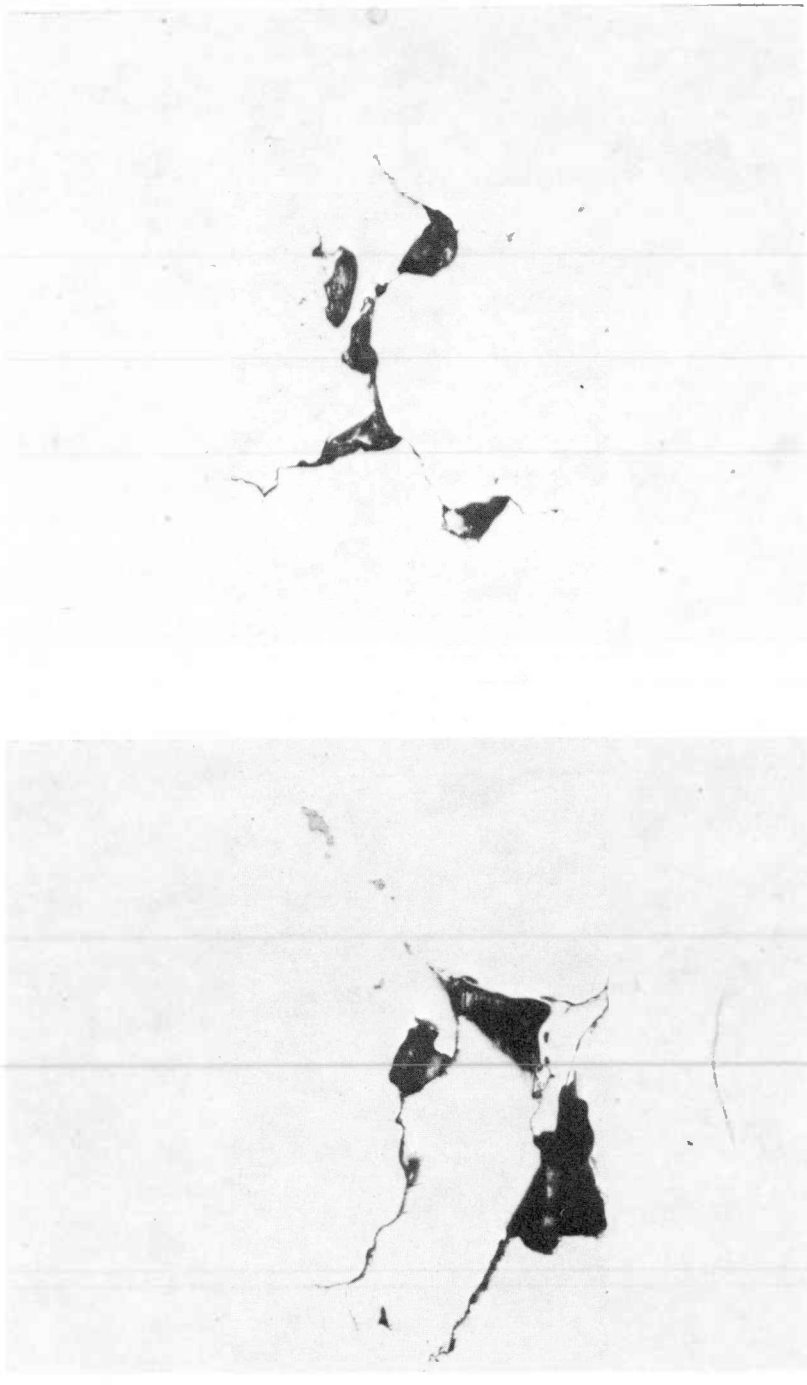

FIG. 18 - Lapped Areas Near Type I Holes in Joppa 3. RZ Plane of Polish. Mag. 100X

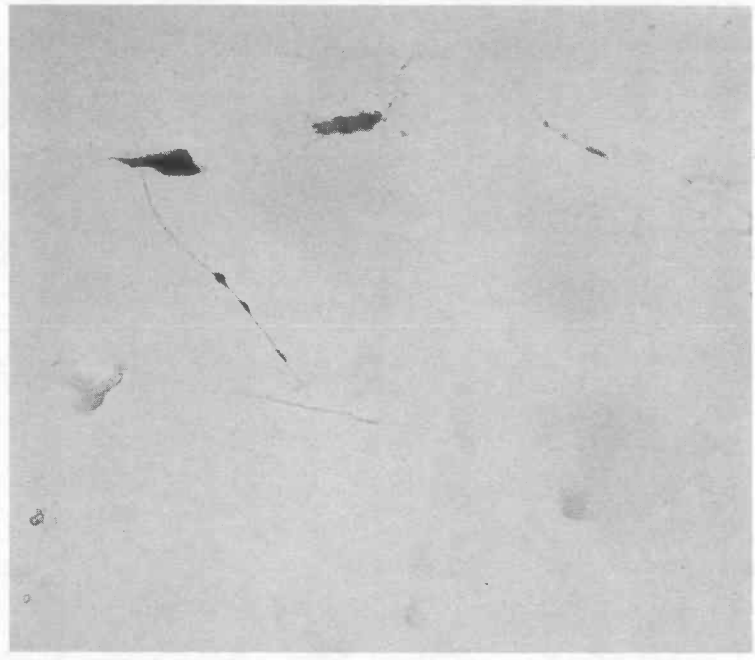

Mag. 500X

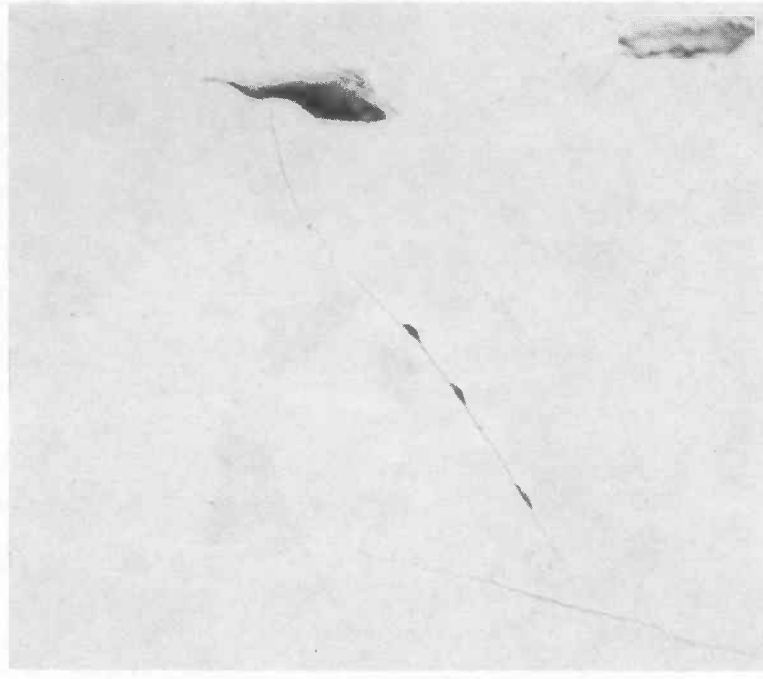

Mag. 1000X

FIG. 19 - Light Photomicrographs of Typical Laps in Joppa 3.

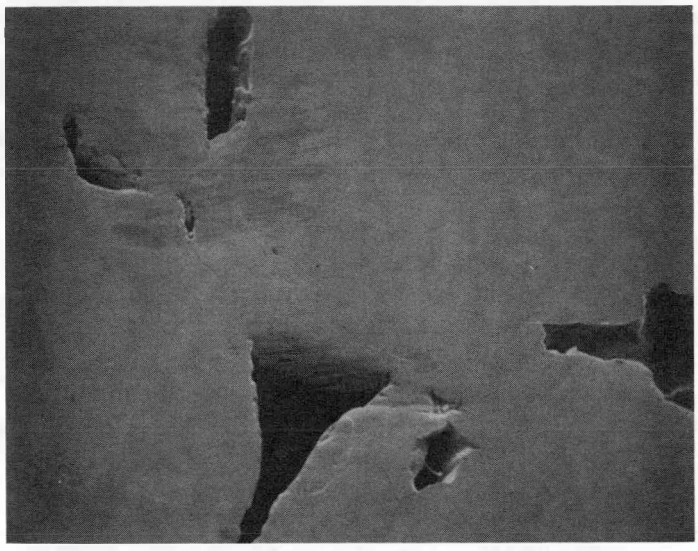

Mag. 240X

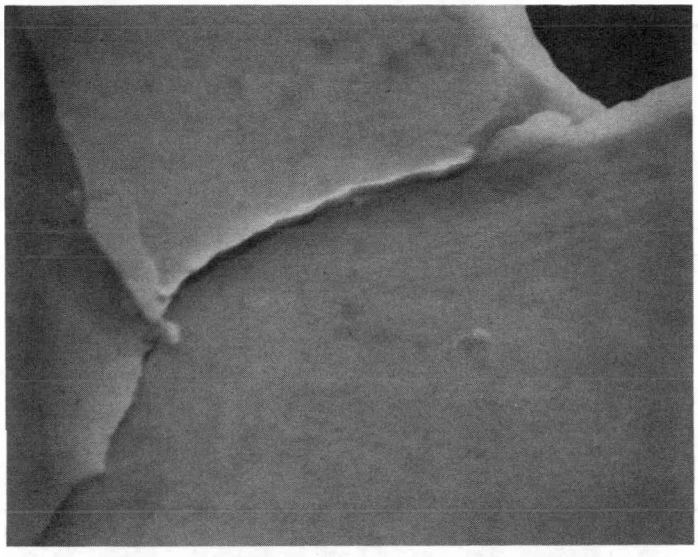

Mag. 2400X

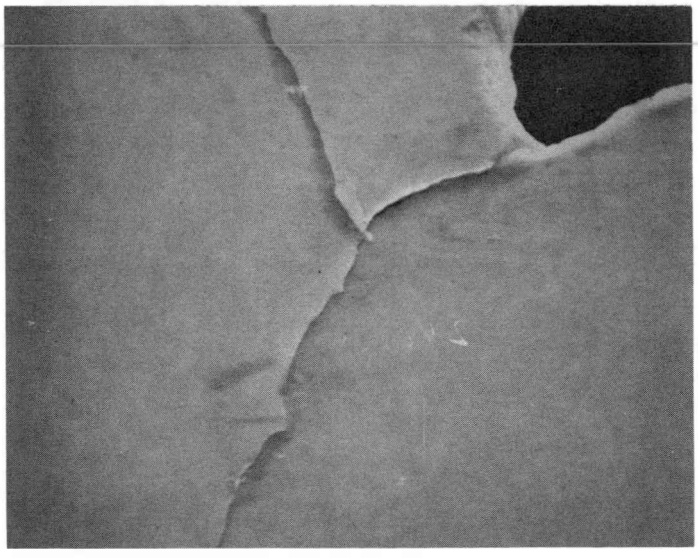

Mag. 5900X

FIG. 20 - Scanning Electron Photomicrographs of Laps and Holes in Joppa 3.

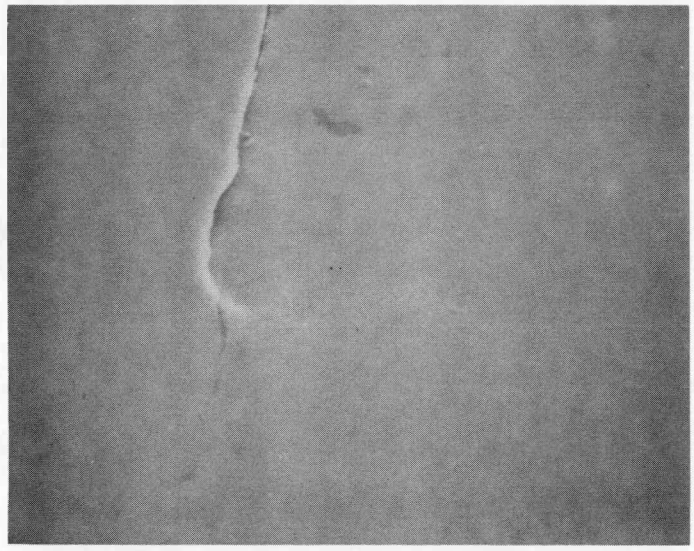

Mag. 2400X

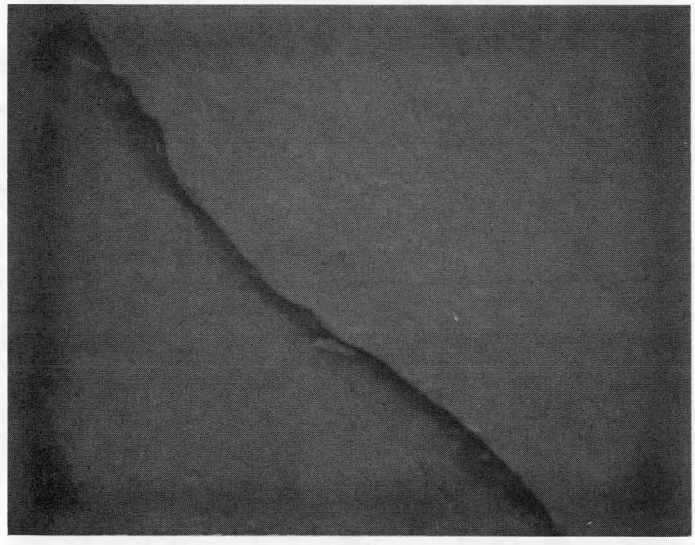

Mag. 2400X

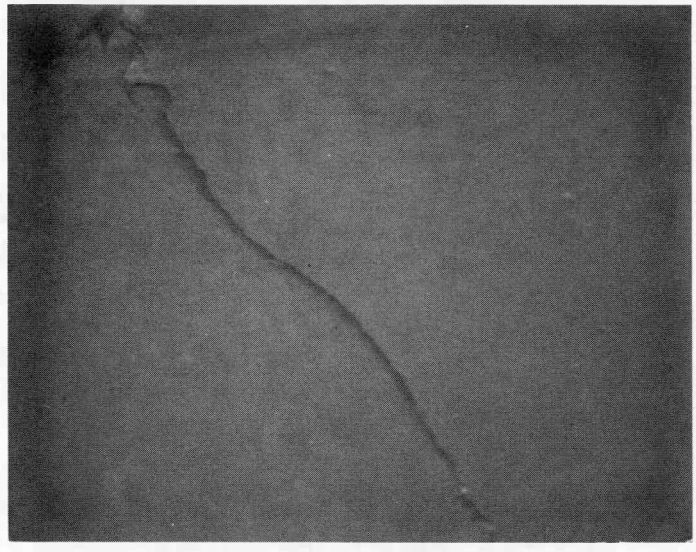

Mag. 5900X

FIG. 21 - Scanning Electron Photomicrographs of Laps in Joppa 3.

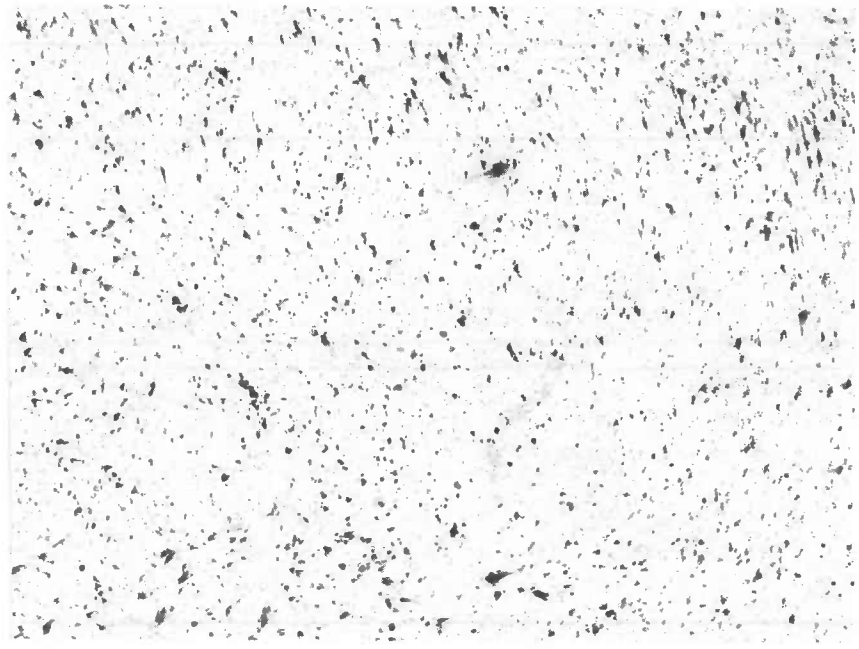

Mag. 1X

FIG. 22 - Sulfur Print of Zθ Plane of Joppa 3 About 2 in. From the Bore.

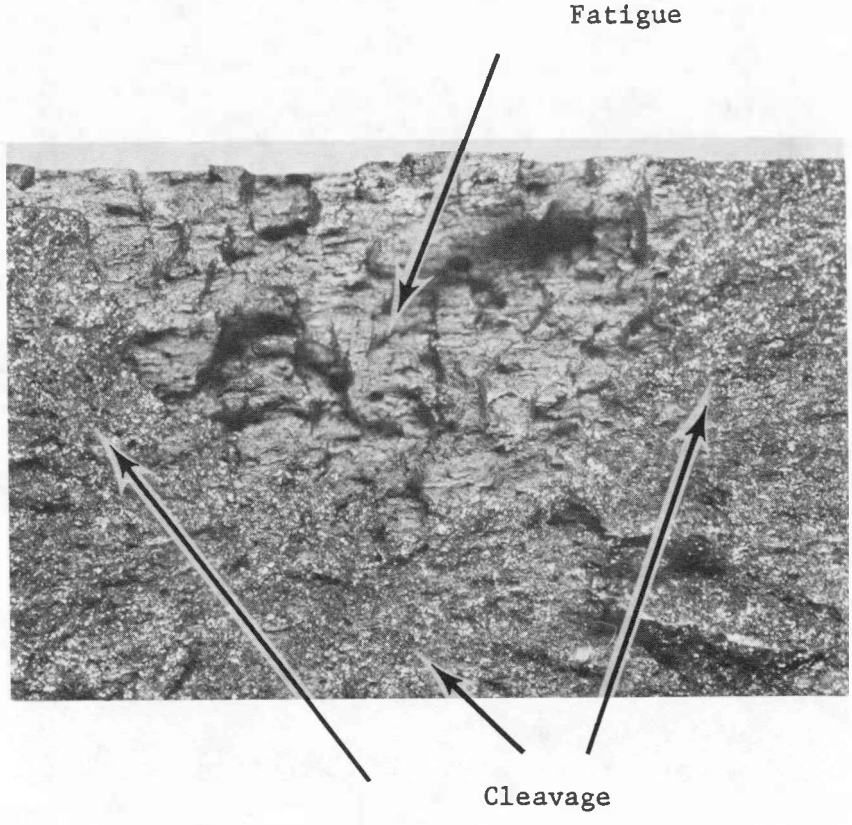

FIG. 23 - Light Photomicrograph of Low Cycle Fatigue Specimen Fracture on RZ Plane of Joppa 3. Mag. 3.5X

FIG. 24 - Scanning Electron Photomicrograph of Flaw Area in Fatigue Portion of Failed Low Cycle Fatigue Specimen from Joppa 3. Mag. 200X

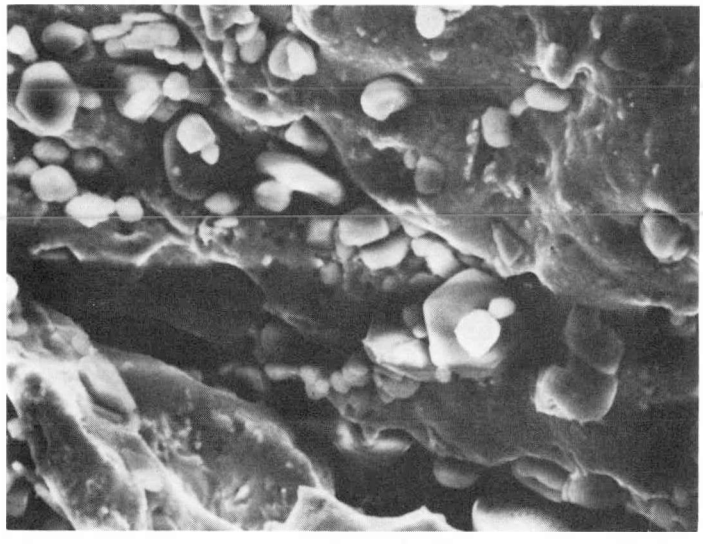

FIG. 25 - Same as Fig. 24 but Mag. 1000X.

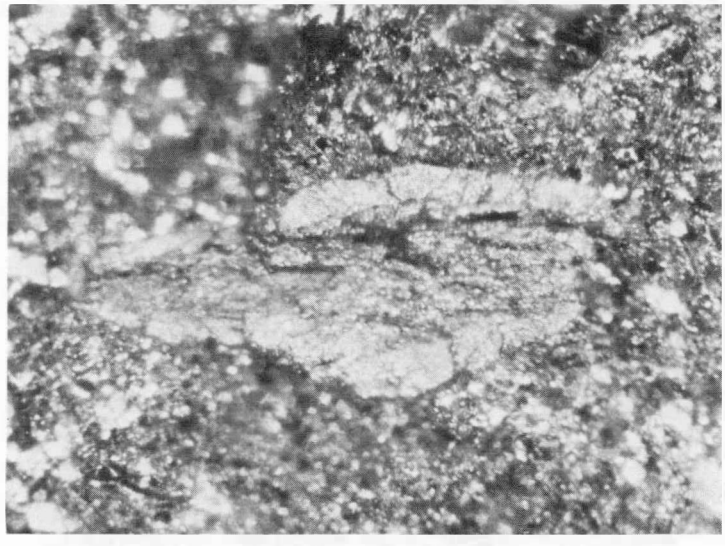

FIG. 26 - Light Photomicrograph of Flaw in Cleavage Portion of Low Cycle Fatigue Specimen Fracture. RZ Plane of Joppa 3. Mag. 40X

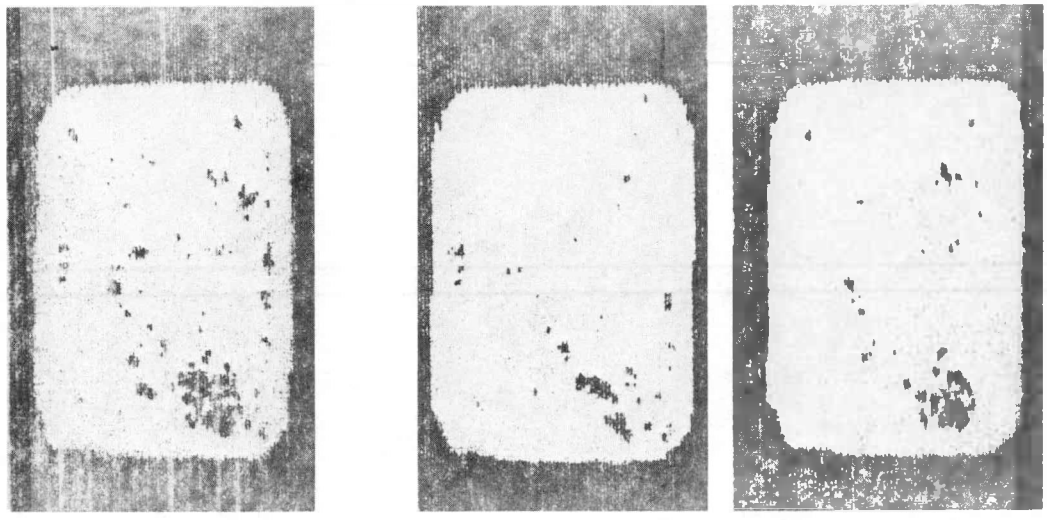

a)	b)	c)
Full Thickness	0.13" to 0.25"	0.25" to 0.375"

FIG. 27 - 10 MHz C-Scan from θ = 332° Face of Piece J7A1-6. Gated at Depths Indicated. Top Edge at Z = 99.8 in., bottom at Z = 101.5 in., Front Left Edge at R = 0.11 in. and Front Right Edge at R = 1.3 in.

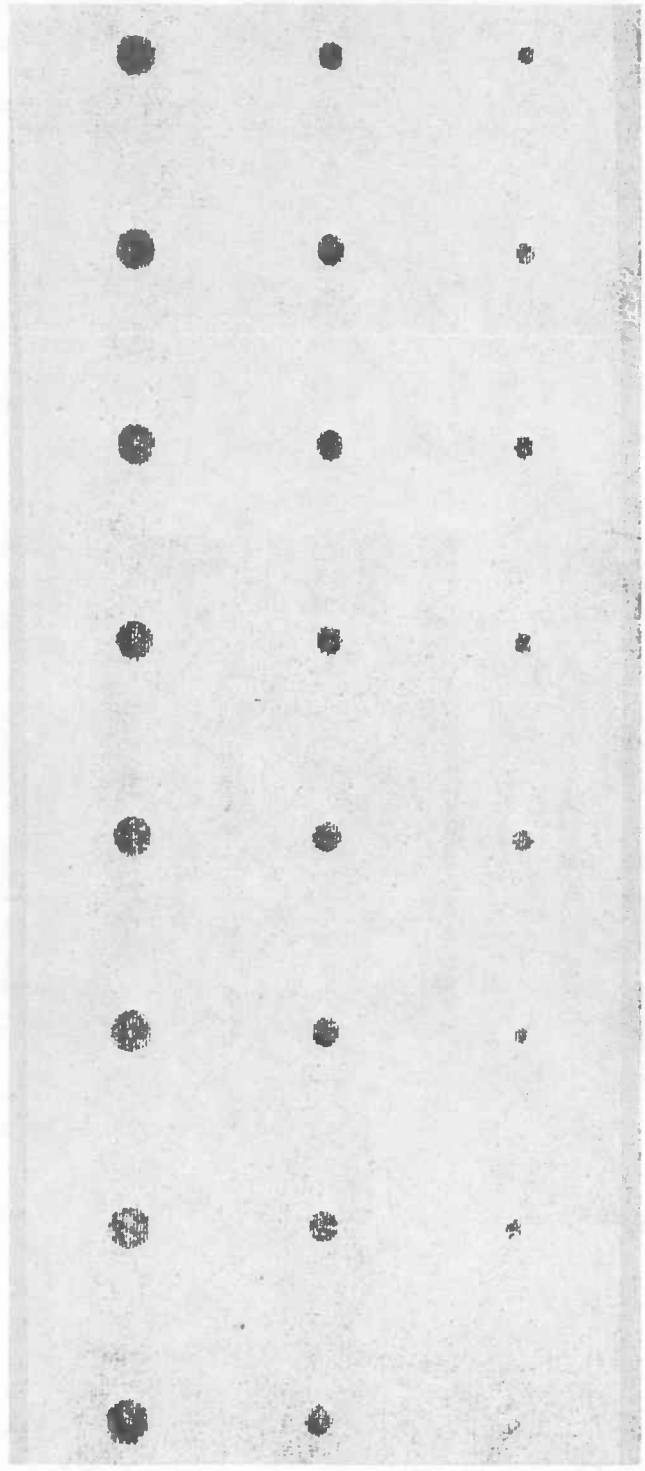

FIG. 28 - Calibration C-Scan of Flat-Bottomed Holes at Various Depths. Freq. 10 MHz

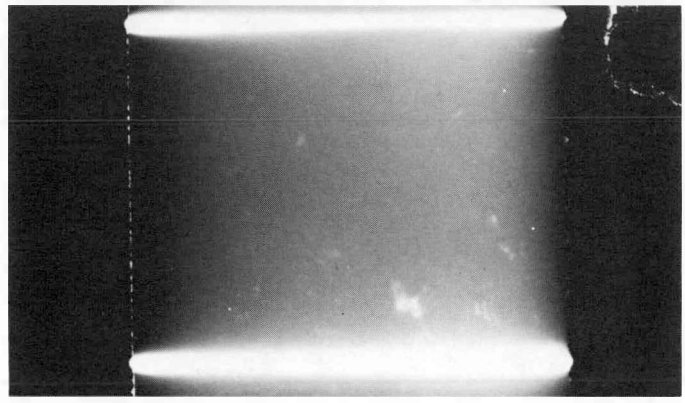

J7A1-6 before separation into -6 and -8 portions of Fig. 21. Top edge at Z = 99.8 in., bottom at 101.5 in., left and right edges are reversed from Fig. 19; i.e., view is toward bore.

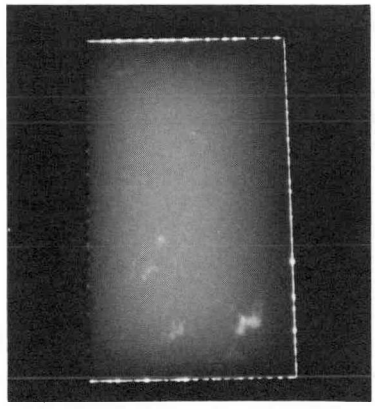

J7A1-6 after final cut. Top at Z = 99.8, bottom at Z = 100.5 in., right edge is 332°.

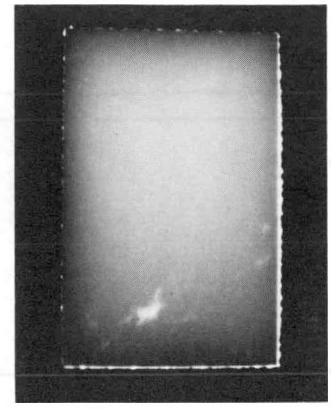

J7A1-6 after final cut. Top and bottom as before, view is approximately in the θ direction.

FIG. 29 - Radiographs of Piece J7A1-6 from Joppa 3. Calculation of flaw position in cylindrical coordinates must either be done graphically in conjunction with Fig. 4 or mathematically.

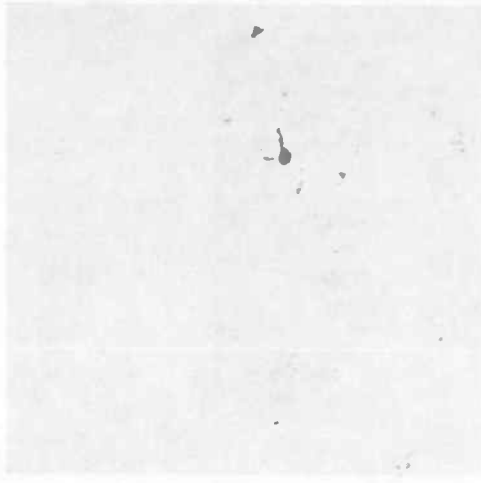

0.035 in.

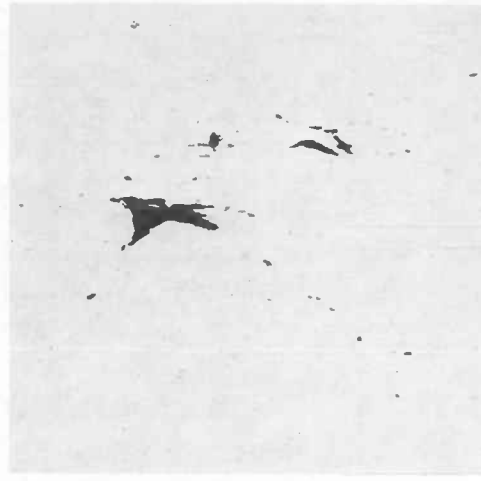

0.100 in.

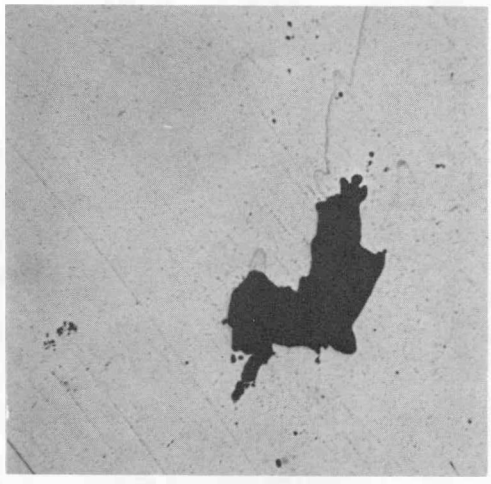

0.300 in.

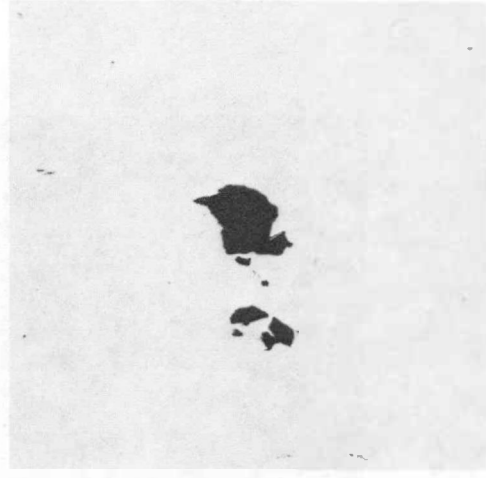

0.350 in.

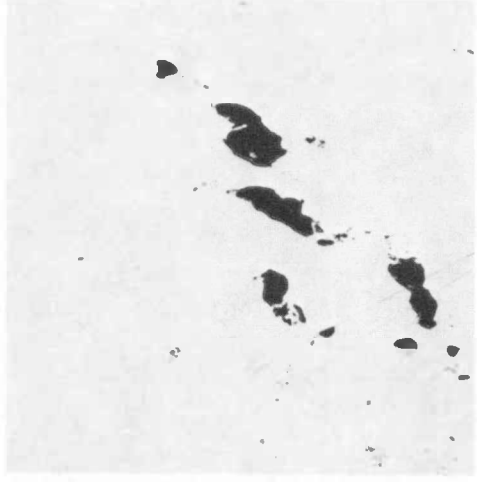

0.400 in.

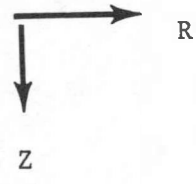

FIG. 30 - Large Flaw from Joppa 3 Piece J7A1-6. Material Removed from 332° Plane of Polish is Indicated. Mag. 6X

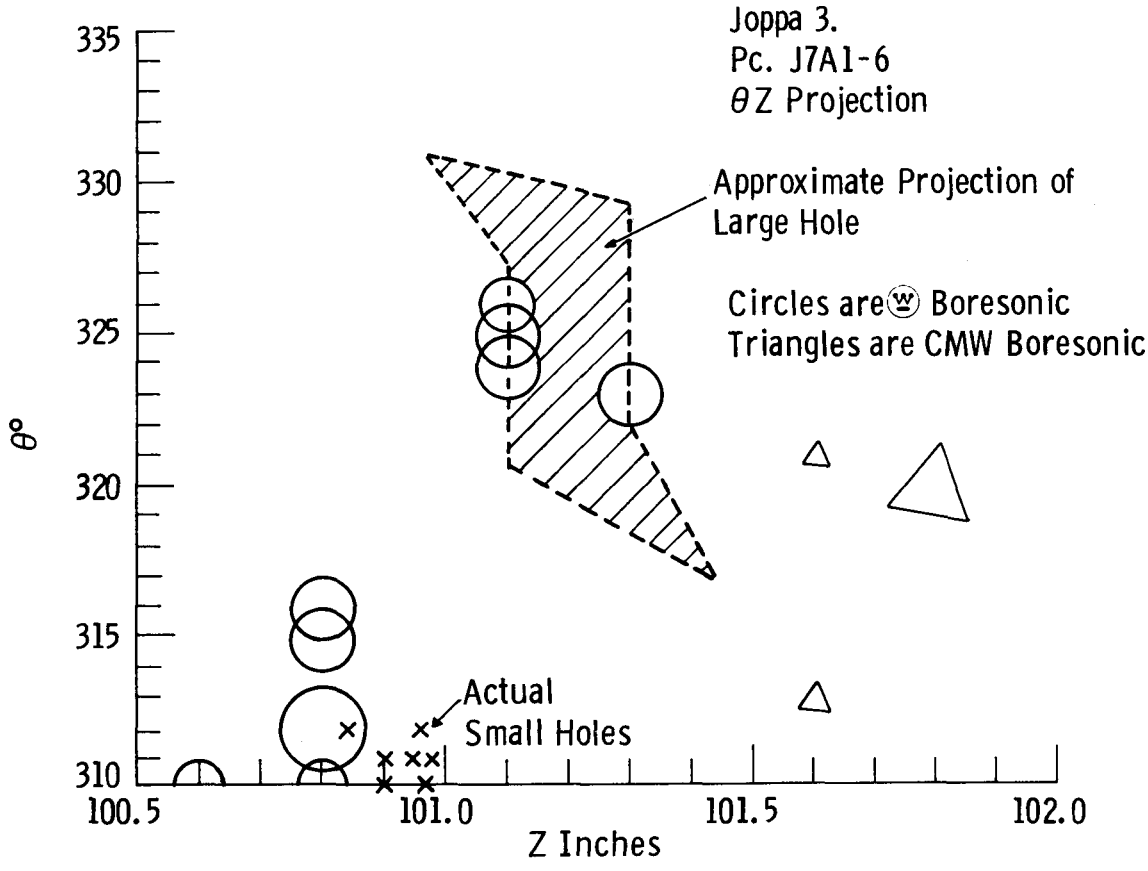

Fig. 31 – Boresonic indications versus actual flaw position in J7A1-6

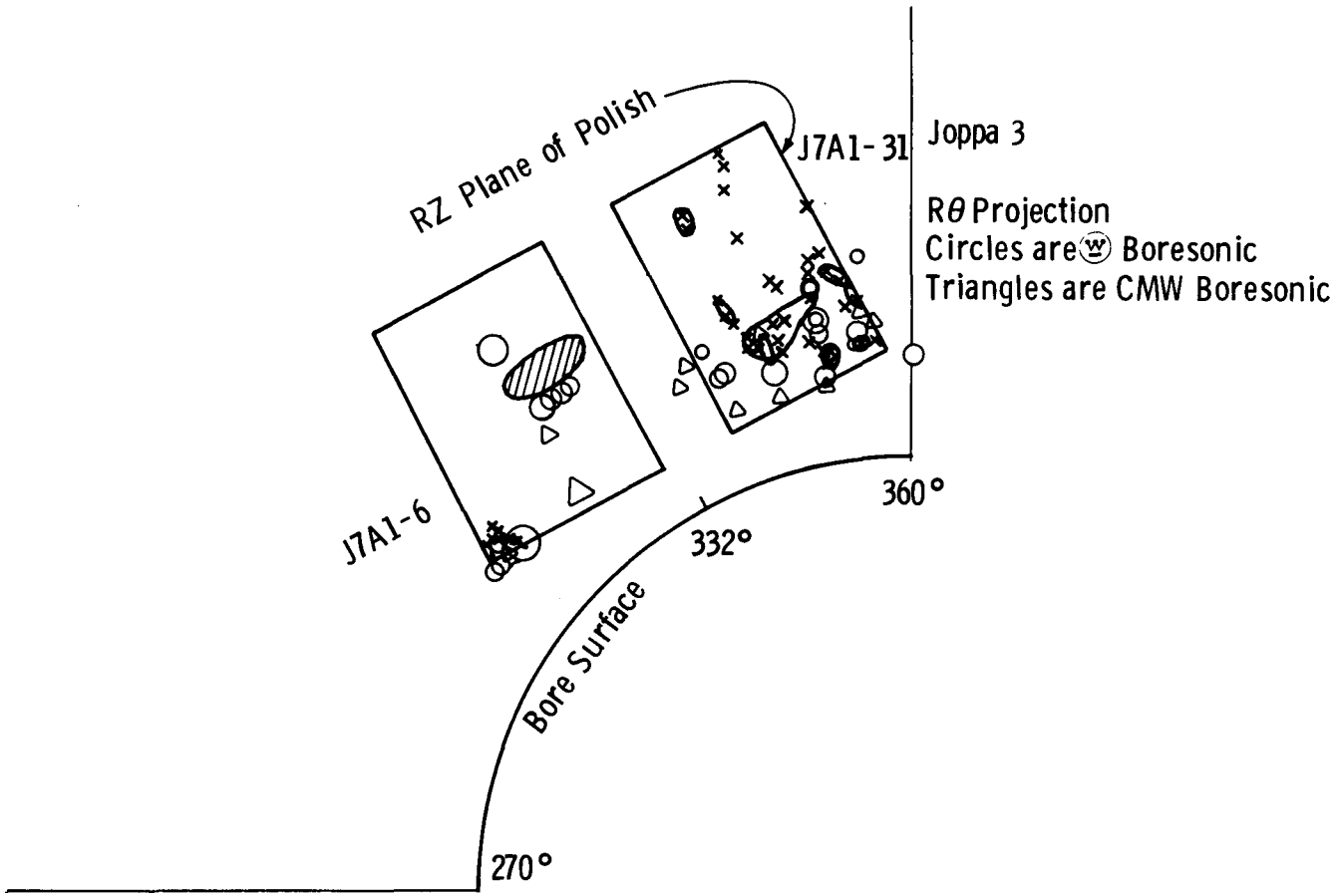

Fig. 32 — R θ projections of actual flawed areas and boresonic results

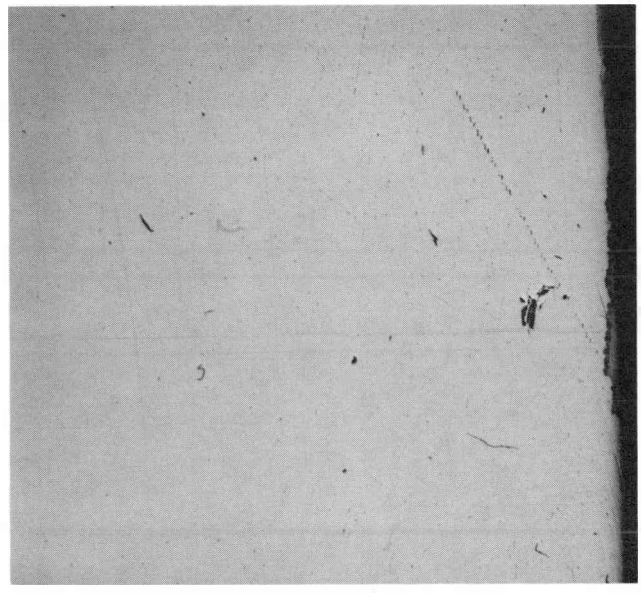

750 mils removed

FIG. 33 - Flaw in Piece J7A6-1 from Joppa 3 Located at 100.8 in. Z, 0.34 in. R and 312° θ. (Approximate RZ Plane of Polish). Mag. 6X

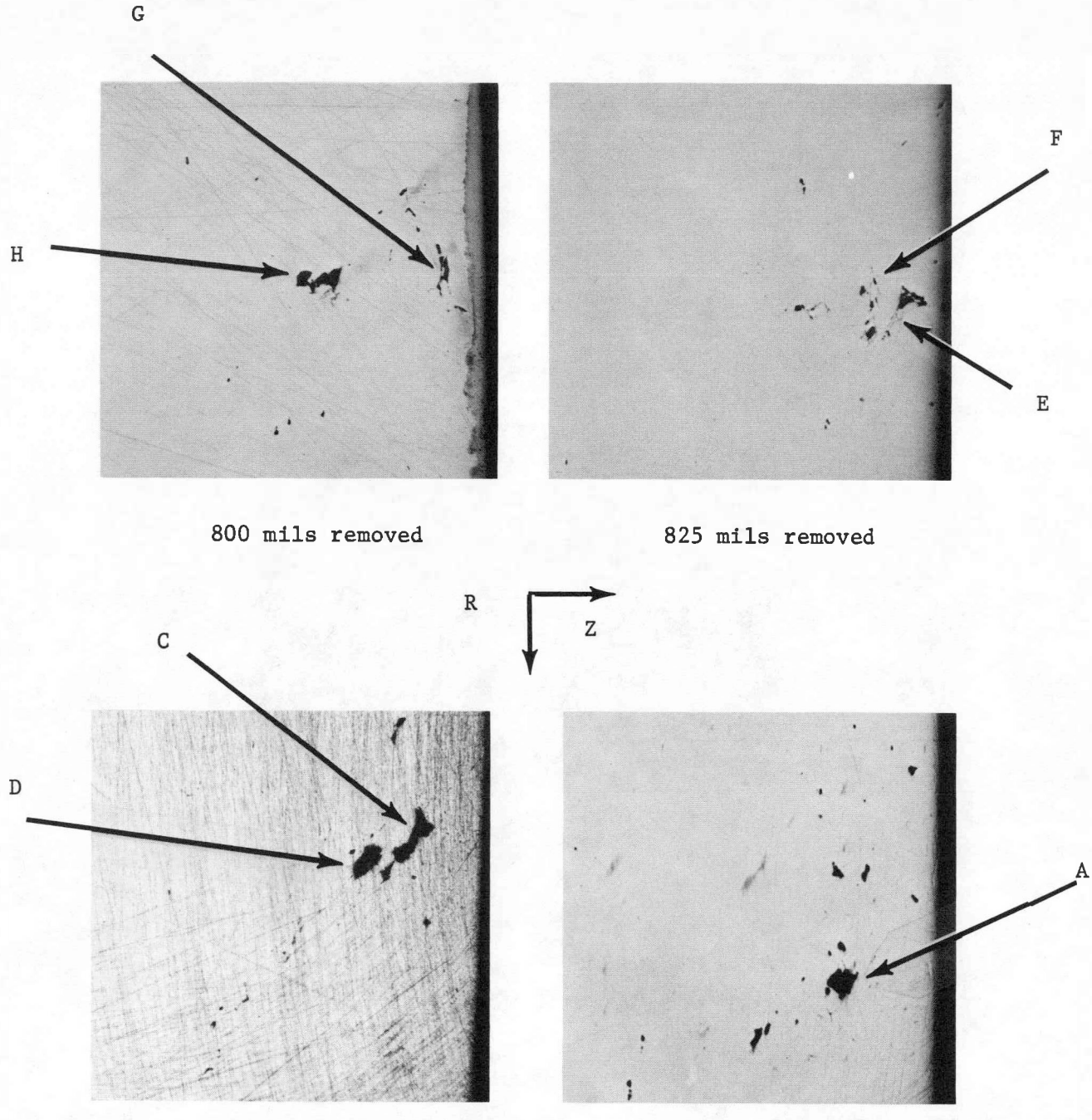

FIG. 34 - Planes of Polish in 0.025 in. Increments.
Letters Refer to Flaws in Table I.

FIG. 35 - Montage of Polished RZ Plane of Piece J7A1-6 from Joppa 3.
Mag. 6X

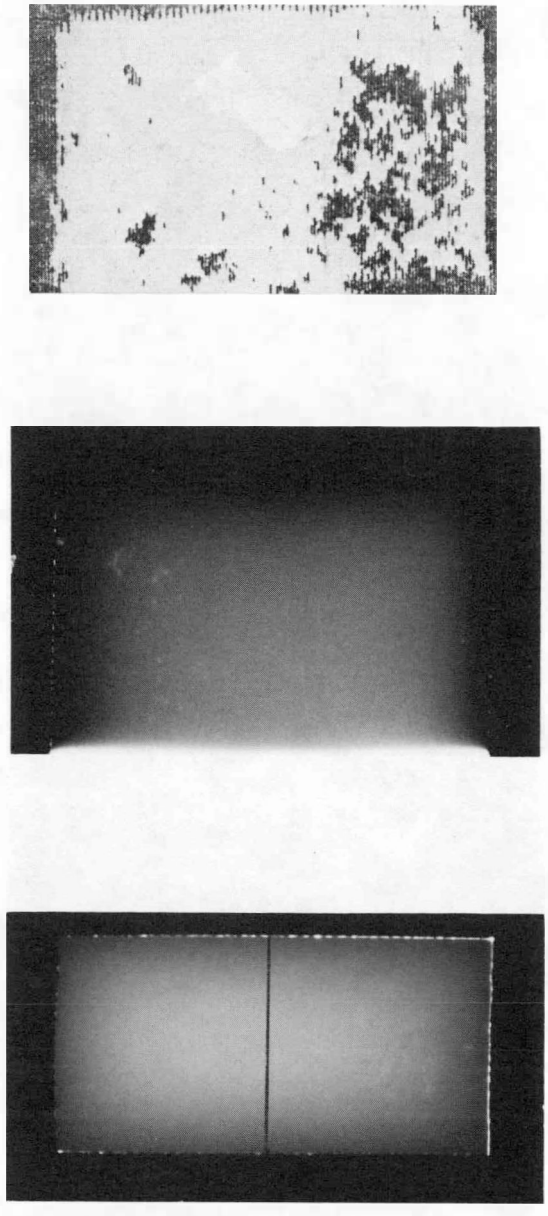

FIG. 36 - C-scan and Radiography of Piece J7A1-31 from Joppa 3.

The C-scan and top radiograph are identical views looking out from the bore along the 332° radius. The bottom edge is 0.1 in. from the bore at a point midway between the left and right edges. The bottom radiograph looks along the Z axis in the direction of increasing Z and is perpendicular to the other radiograph. The plane of polish of the following figures is the right edge of the bottom radiograph and the metal is removed progressively toward the left.

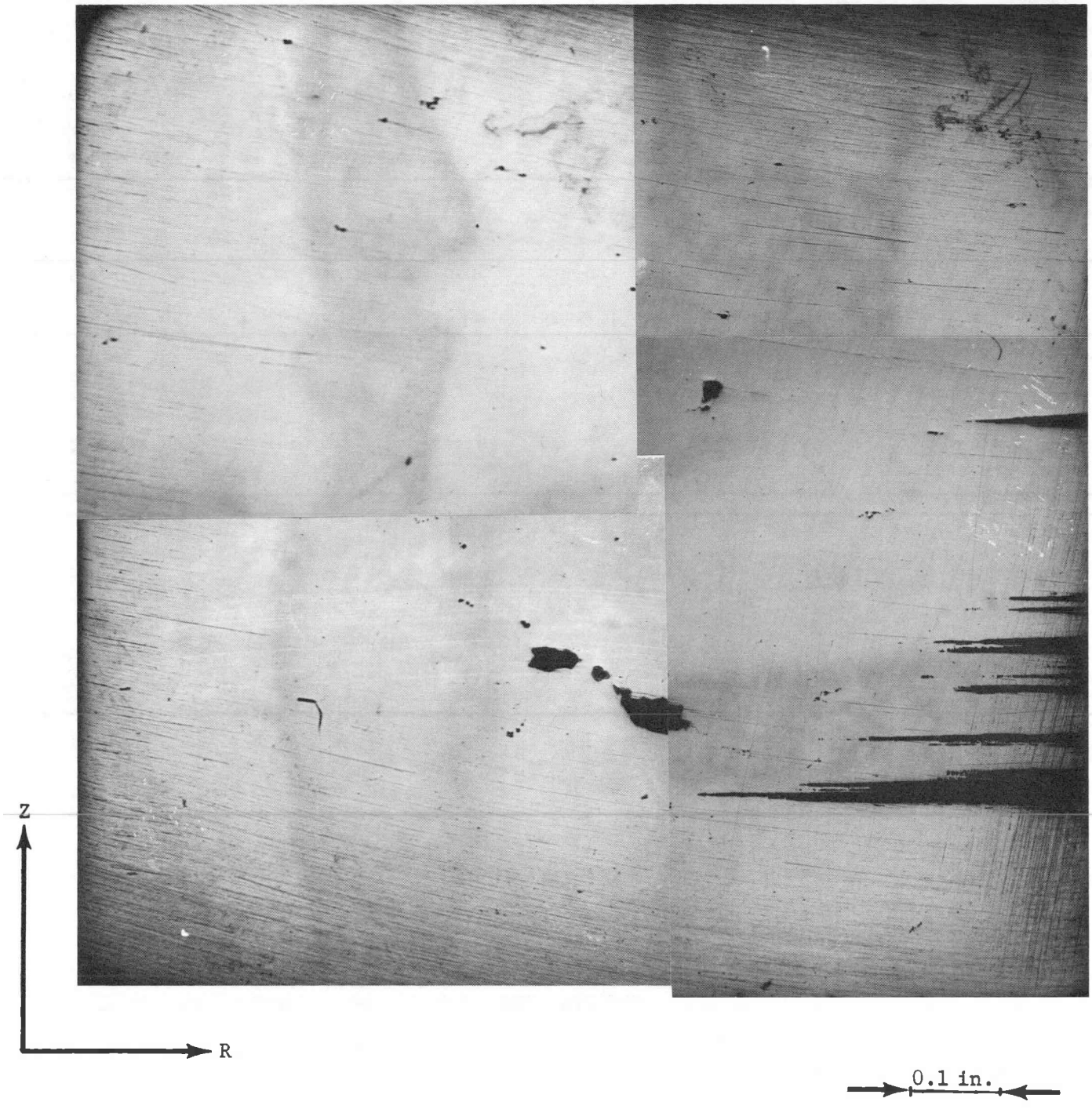

FIG. 37

Piece J7A131 from Joppa 3 - 0.009 in. removed.
Area Fraction of Flaws is 0.0048.

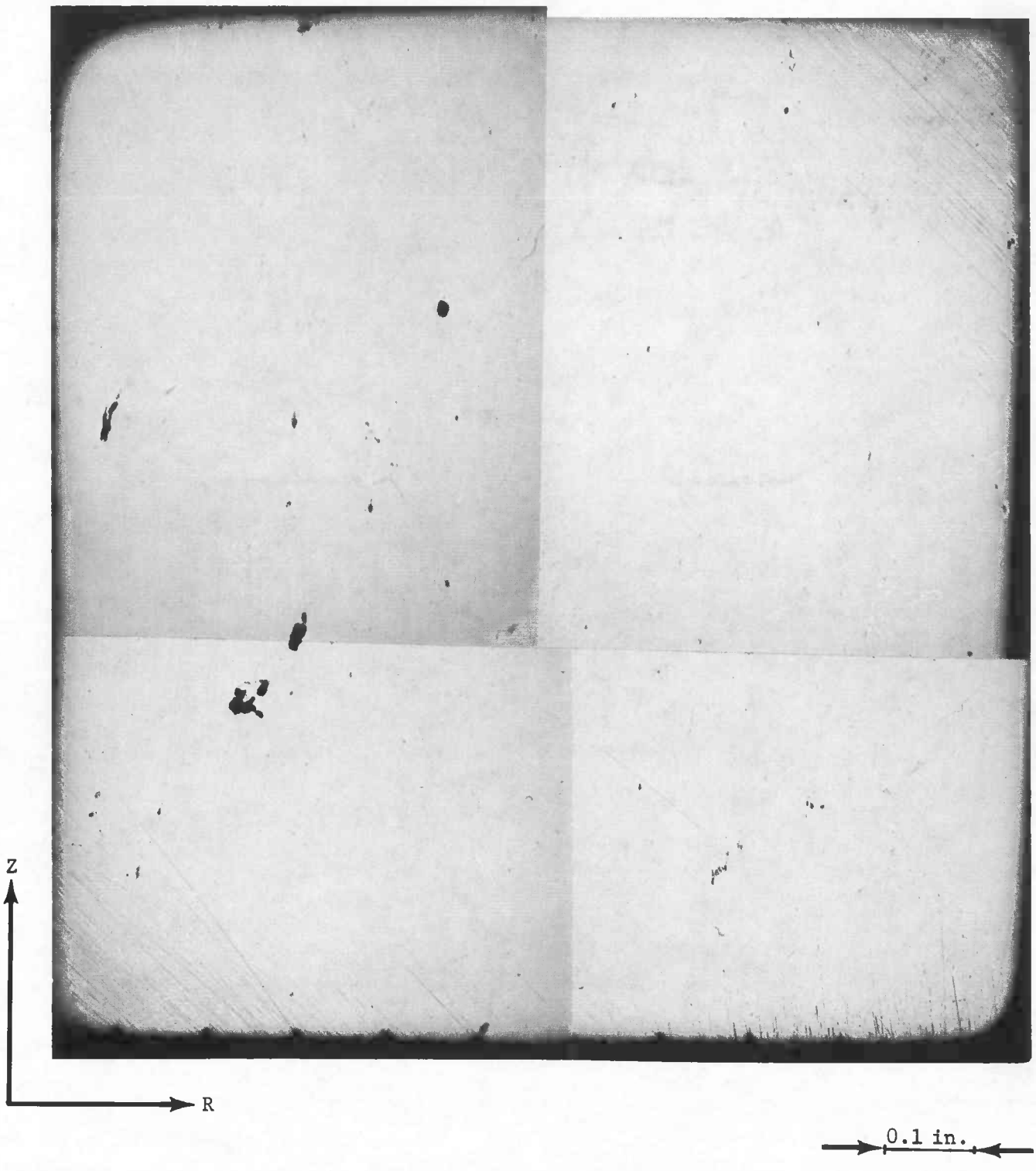

FIG. 38

J7A131 - 0.036 in. removed.
Area Fraction of Flaws is 0.0026.

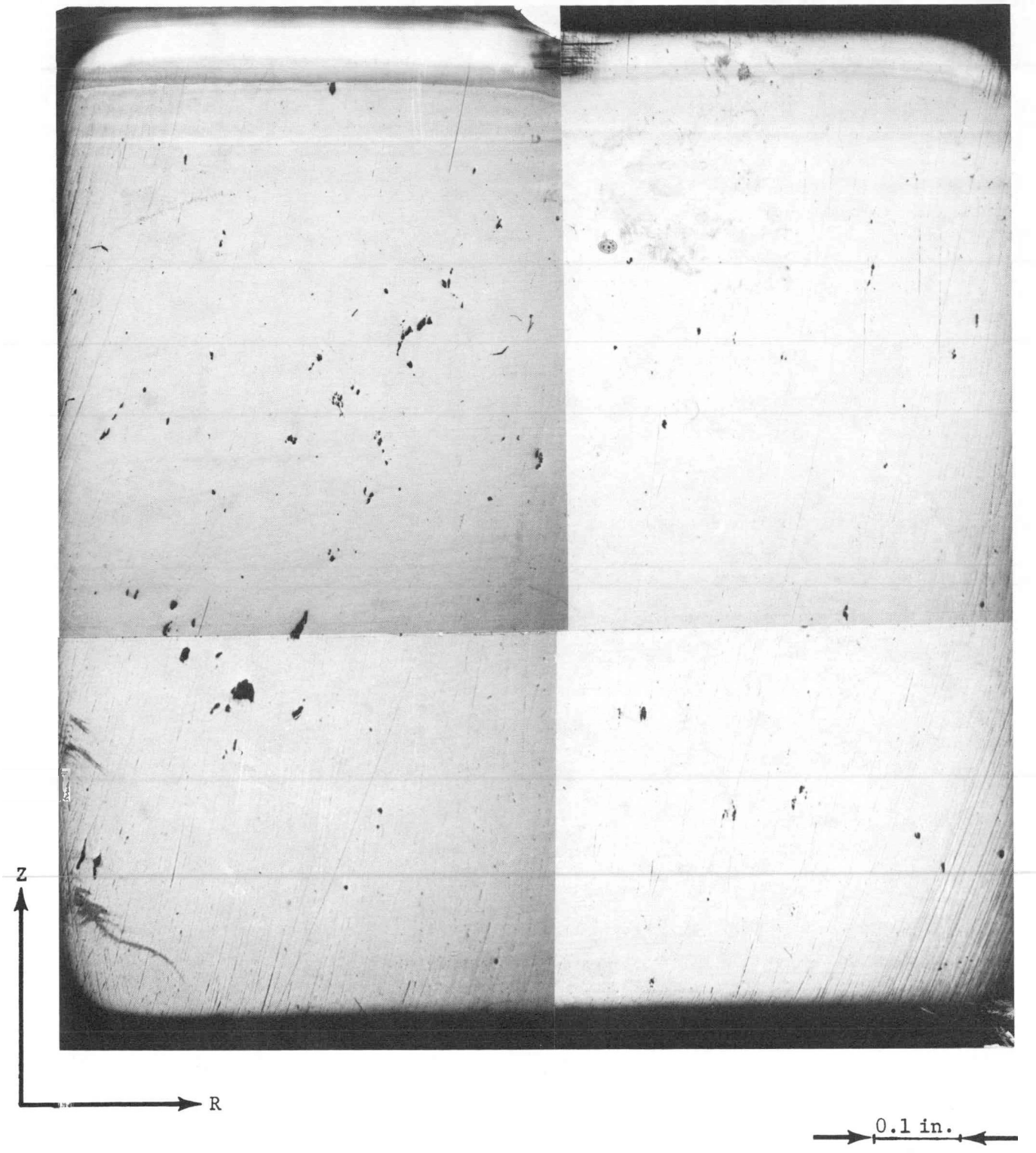

FIG. 39

J7A131 - 0.056 in. removed.
Area Fraction of Flaws is 0.0045.

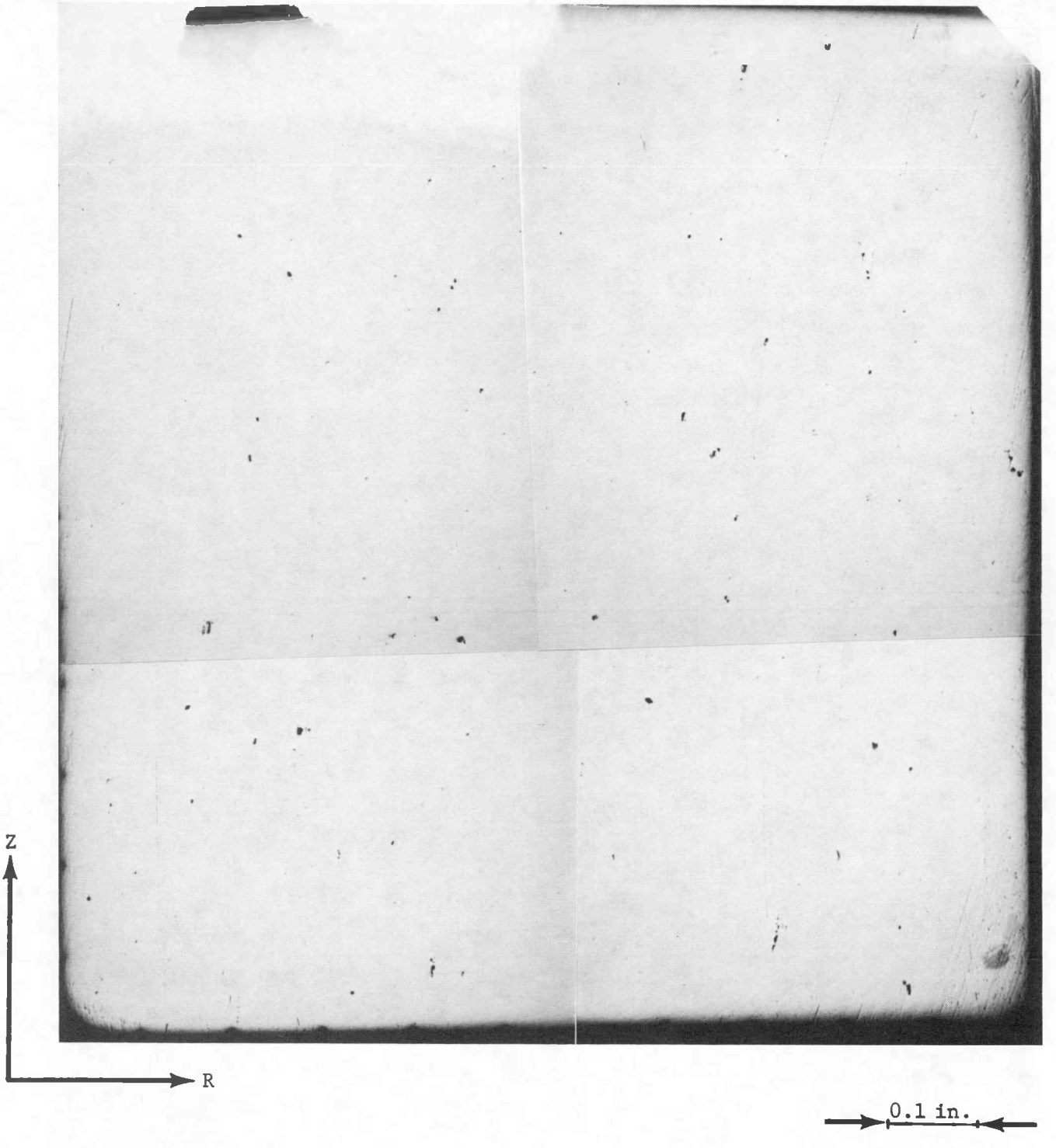

FIG. 40

J7A131 - 0.085 in. removed.
Area Fraction of Flaw is 0.0016.

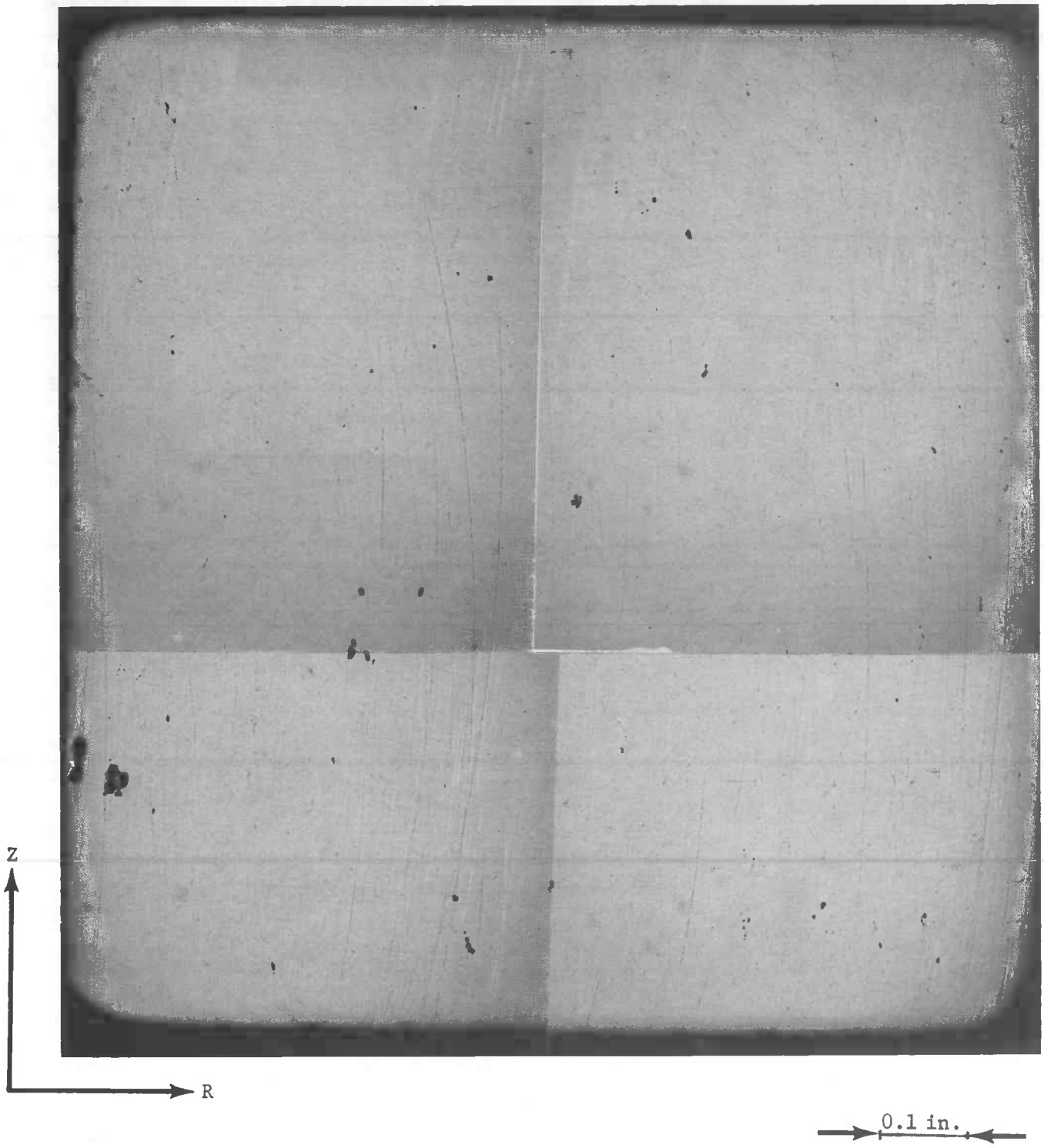

FIG. 41

J7A131 - 0.114 in. removed.
Area Fraction of Flaw is 0.0026.

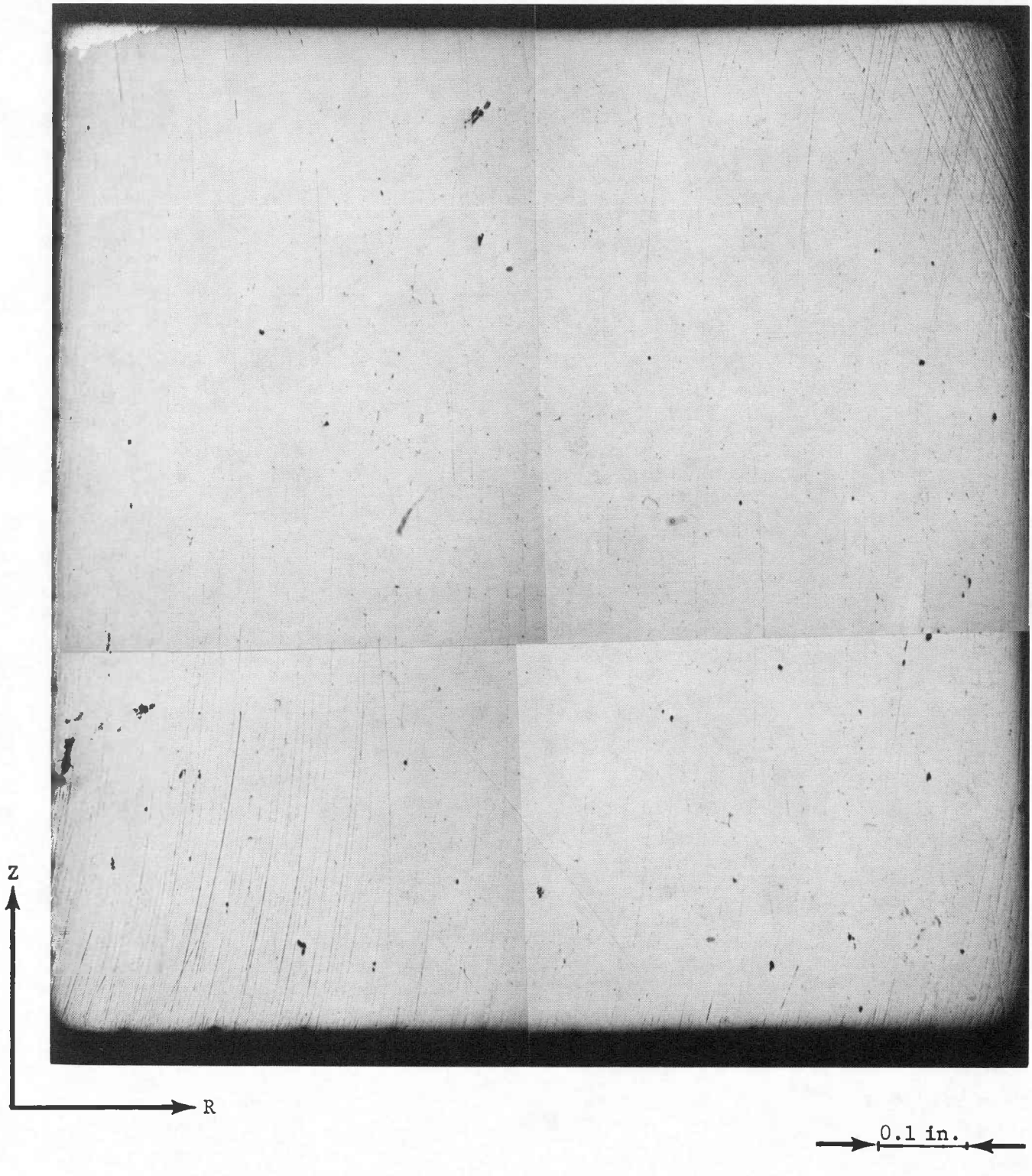

FIG. 42

J7A131 - 0.144 in. removed.
Area Fraction of Flaw is 0.0024.

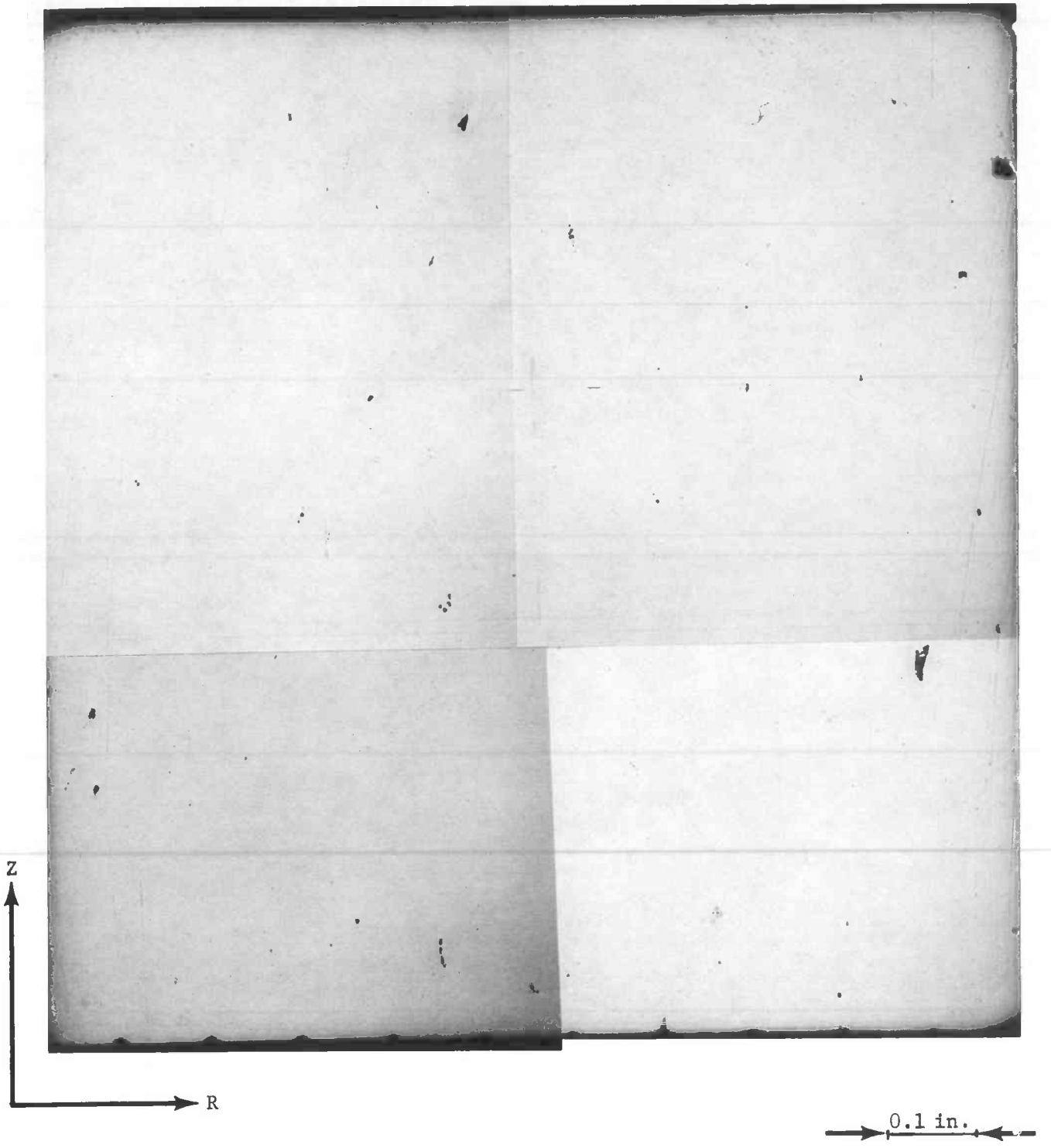

FIG. 43

J7A131 - 0.174 in. removed.
Area Fraction of Flaw is 0.0016.

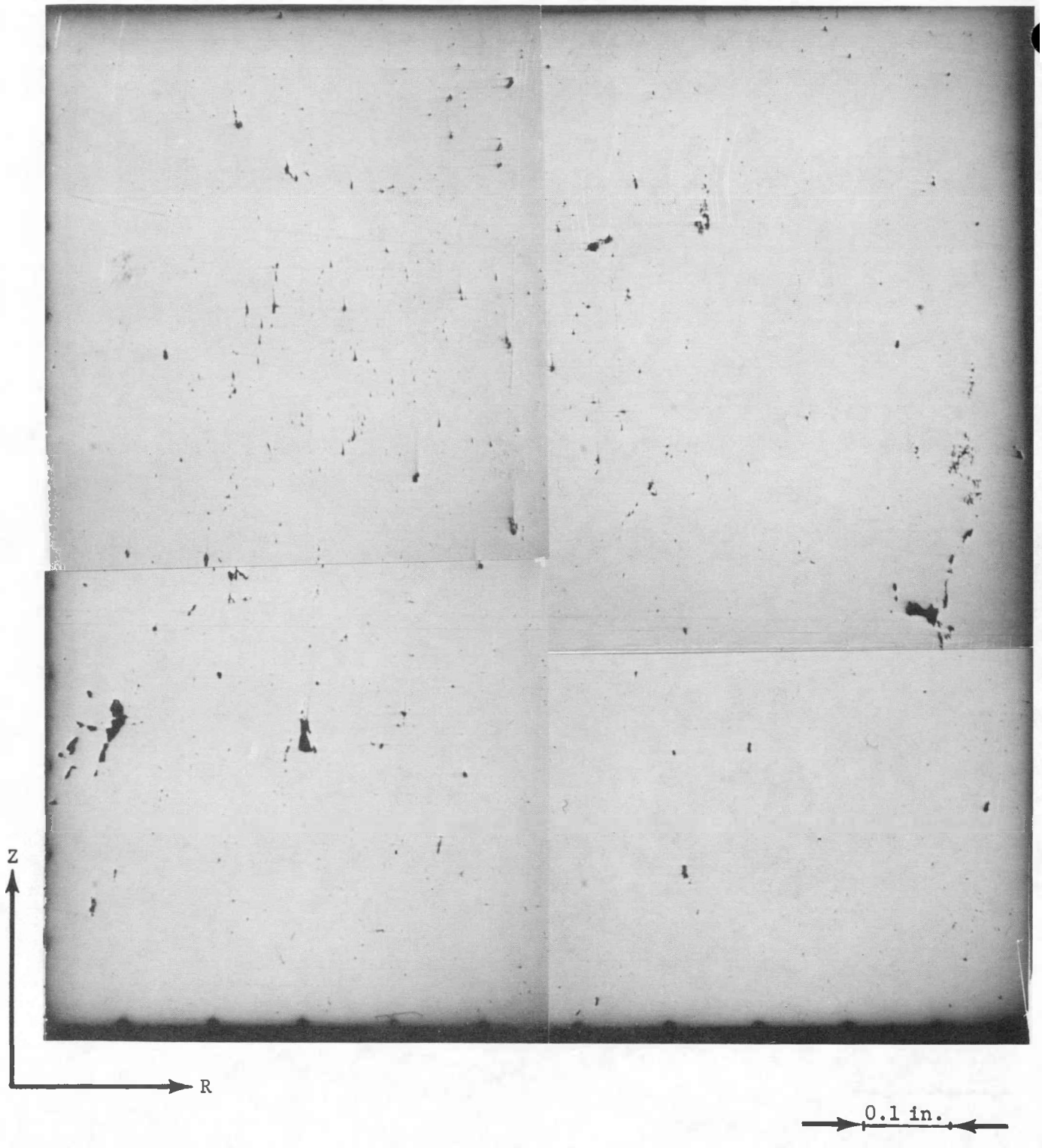

FIG. 44

J7A131 - 0.234 in. removed.
Area Fraction of Flaw is 0.0049.

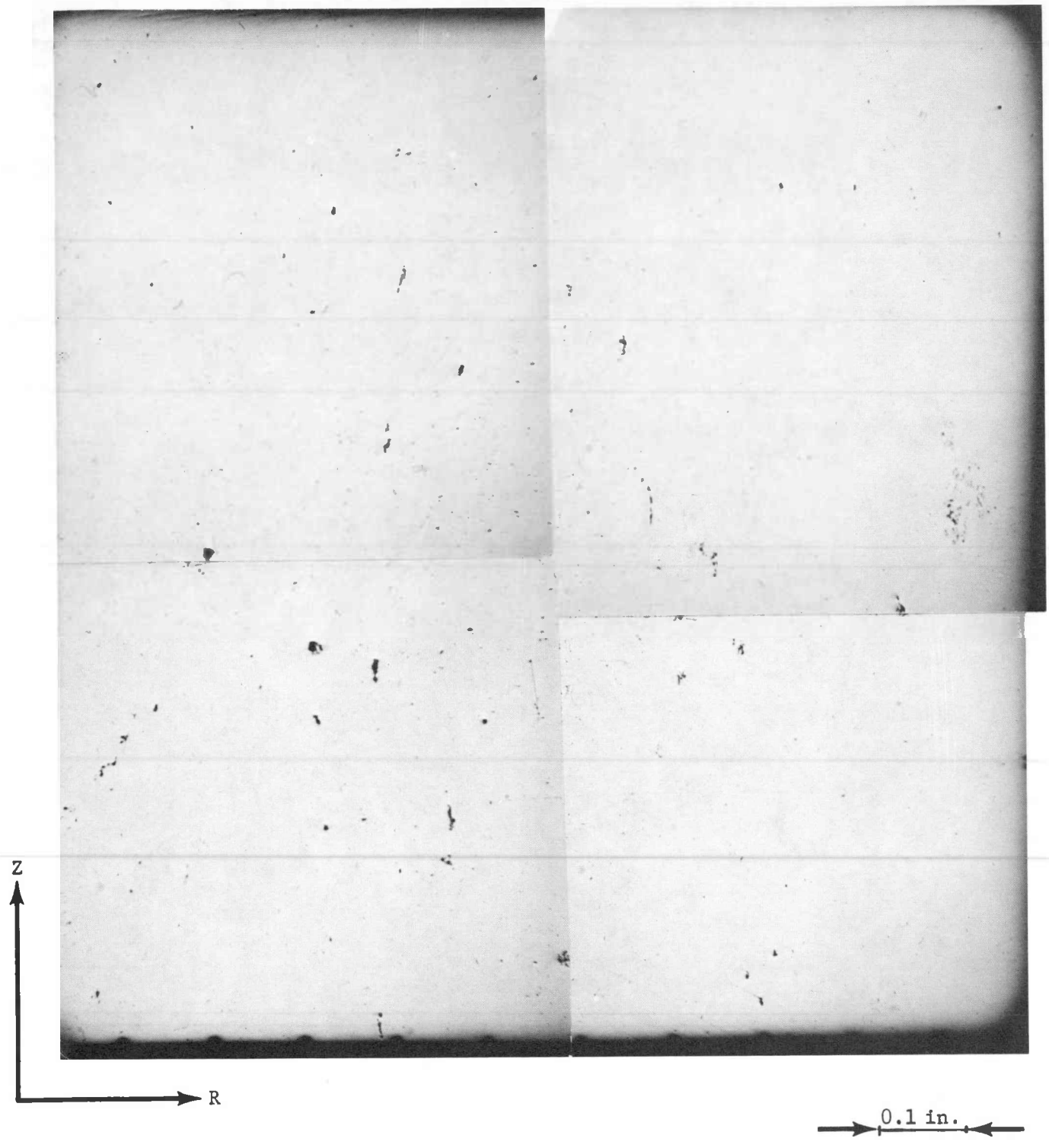

FIG. 45

J7A131 - 0.264 in. removed.
Area Fraction of Flaw is 0.0031.

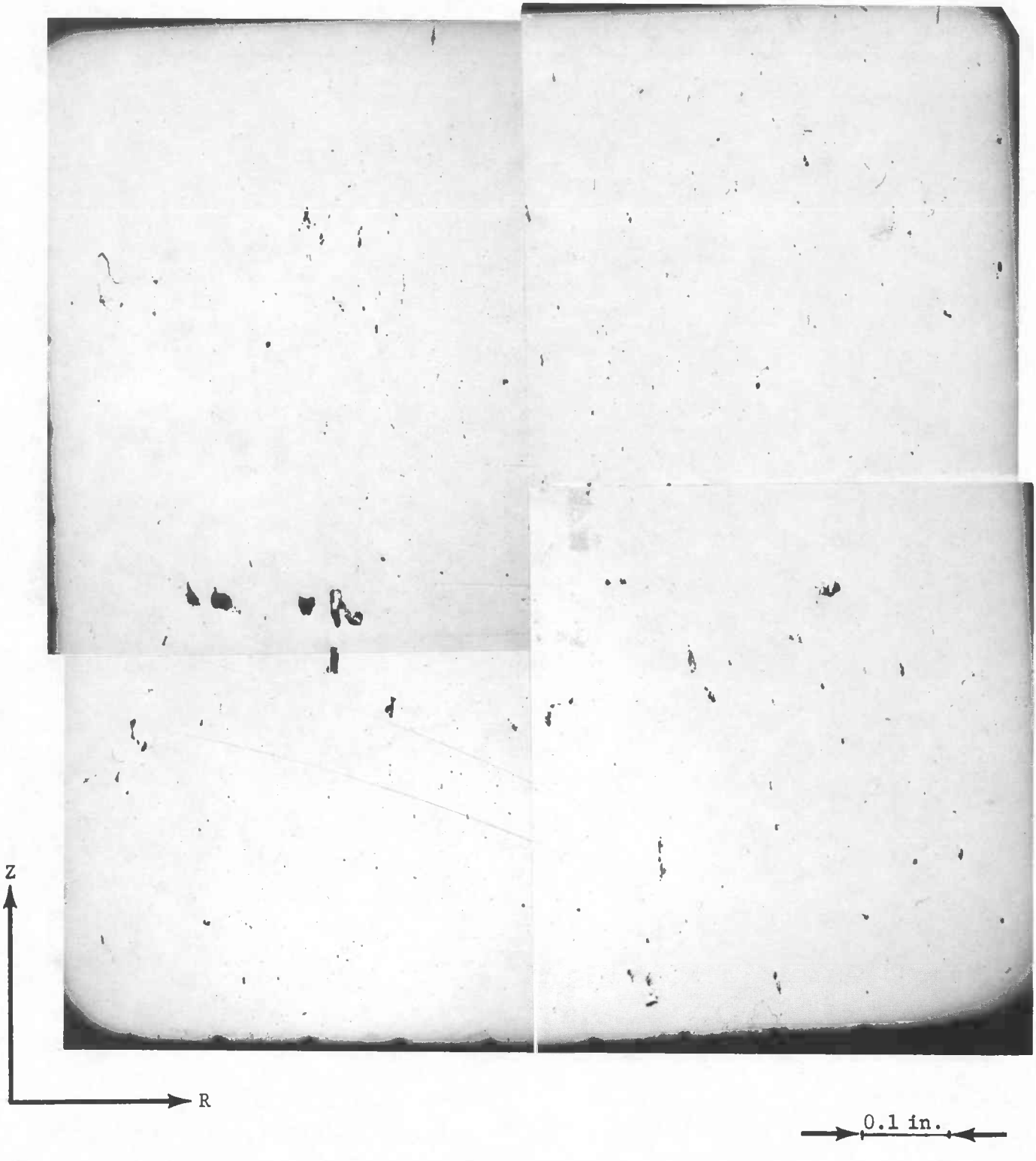

FIG. 46

J7A131 - 0.205 in. removed.
Area Fraction of Flaw is 0.0041.

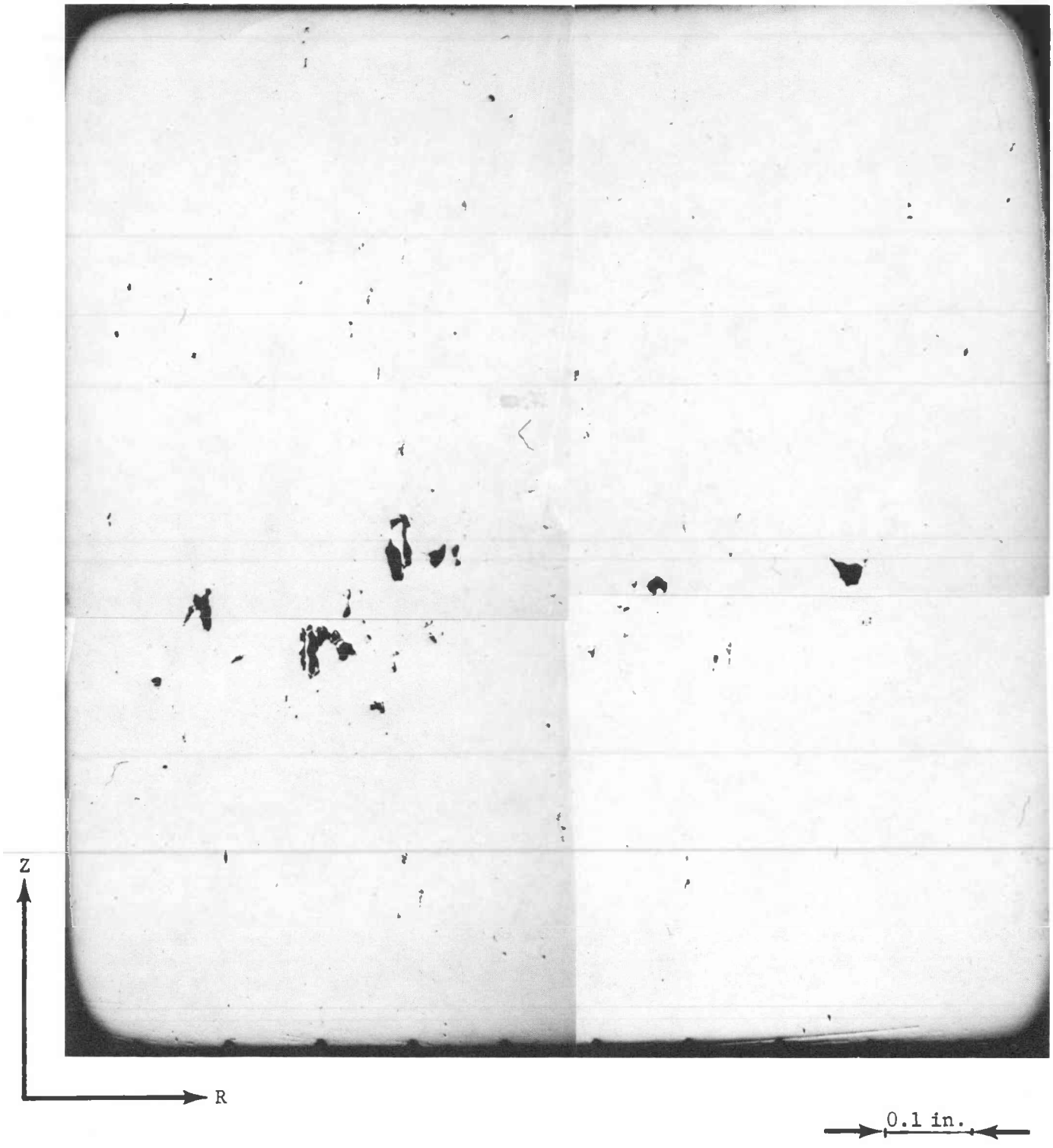

FIG. 47

J7A131 - 0.325 in. removed.
Area Fraction of Flaw is 0.0051.

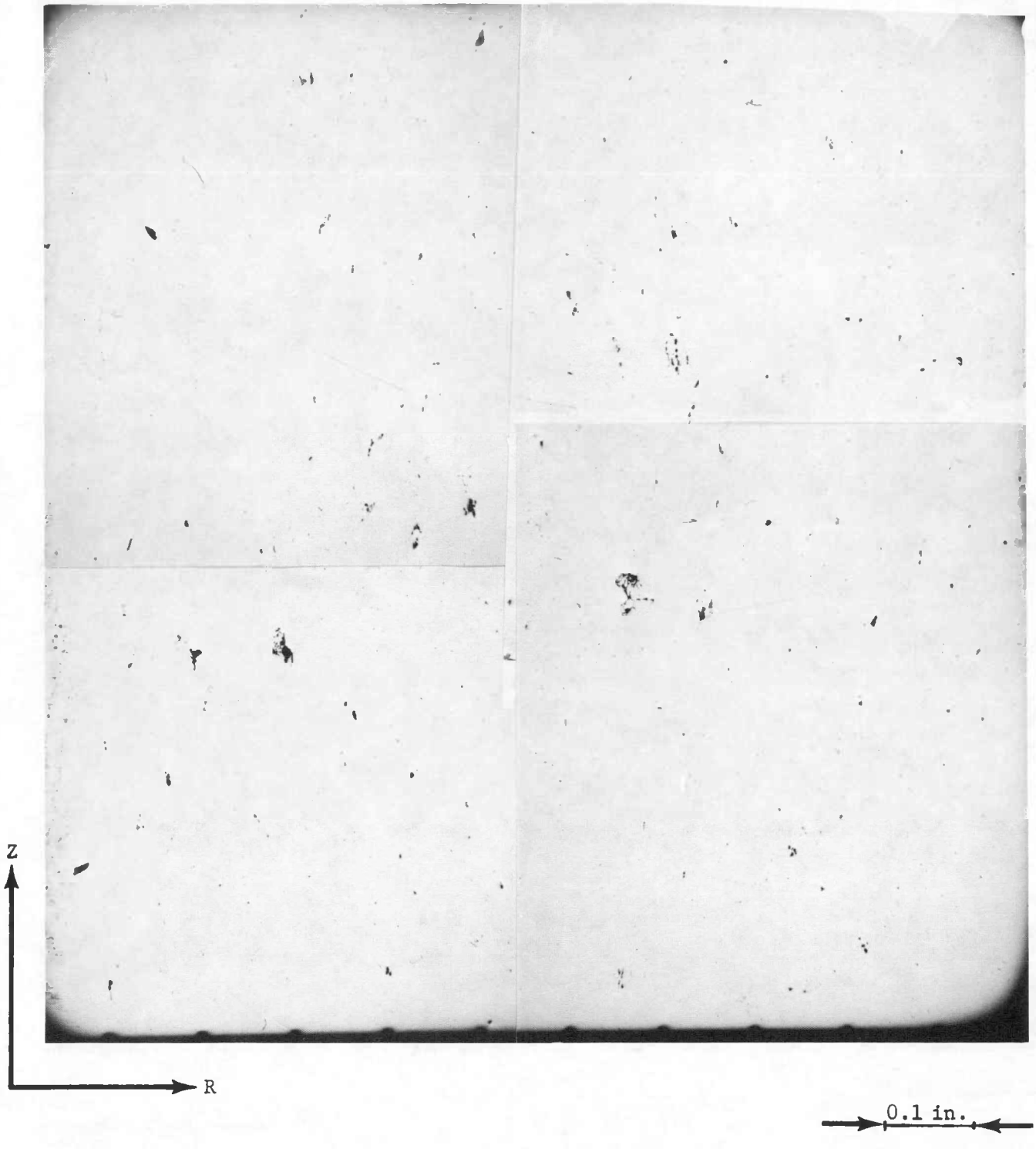

FIG. 48

J7A131 - 0.354 in. removed.
Area Fraction of Flaw is 0.0022.

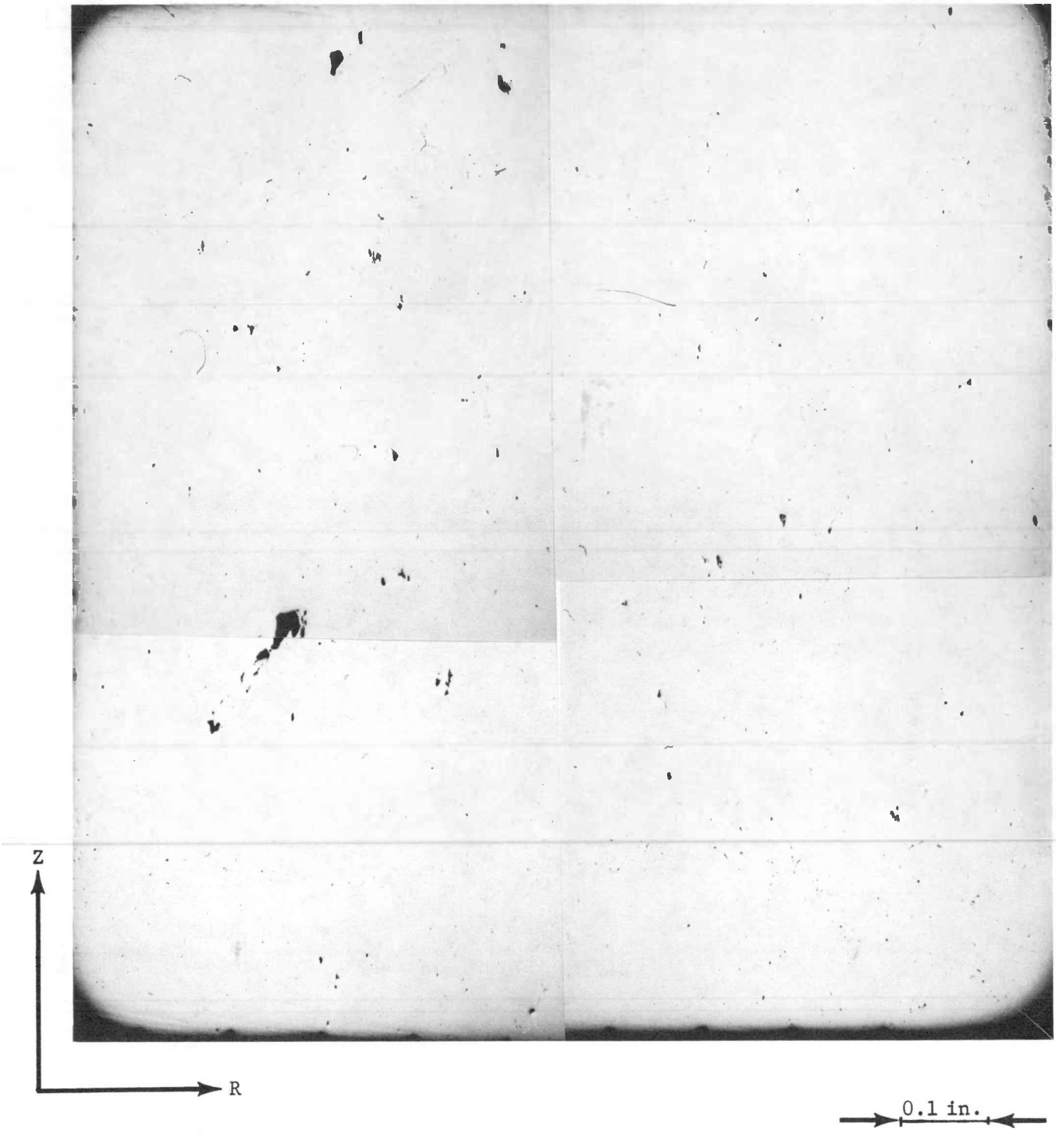

FIG. 49

J7A131 - 0.387 in. removed.
Area Fraction of Flaw is 0.0021.

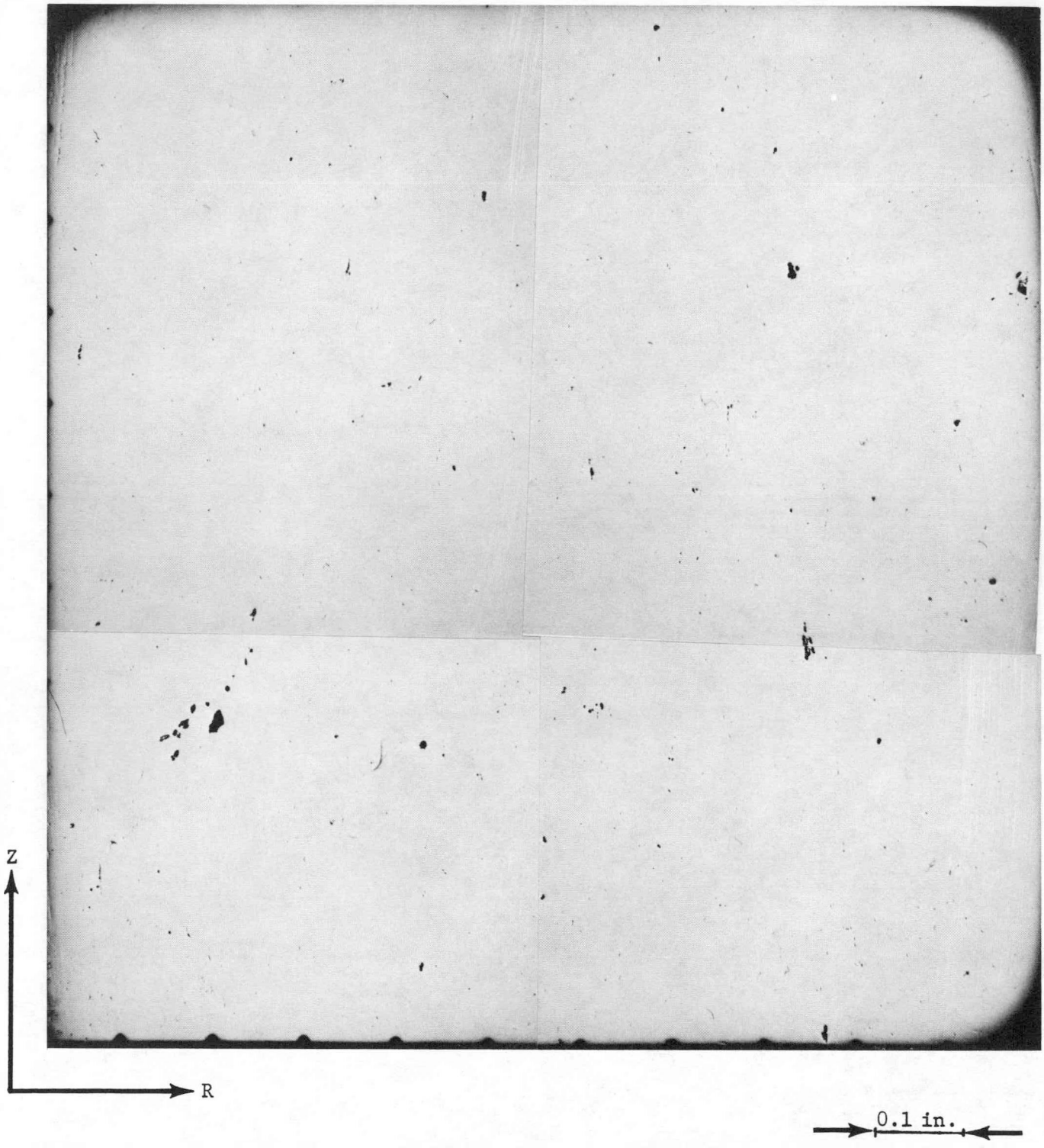

FIG. 50

J7A131 - 0.417 in. removed.
Area Fraction of Flaw is 0.0010.

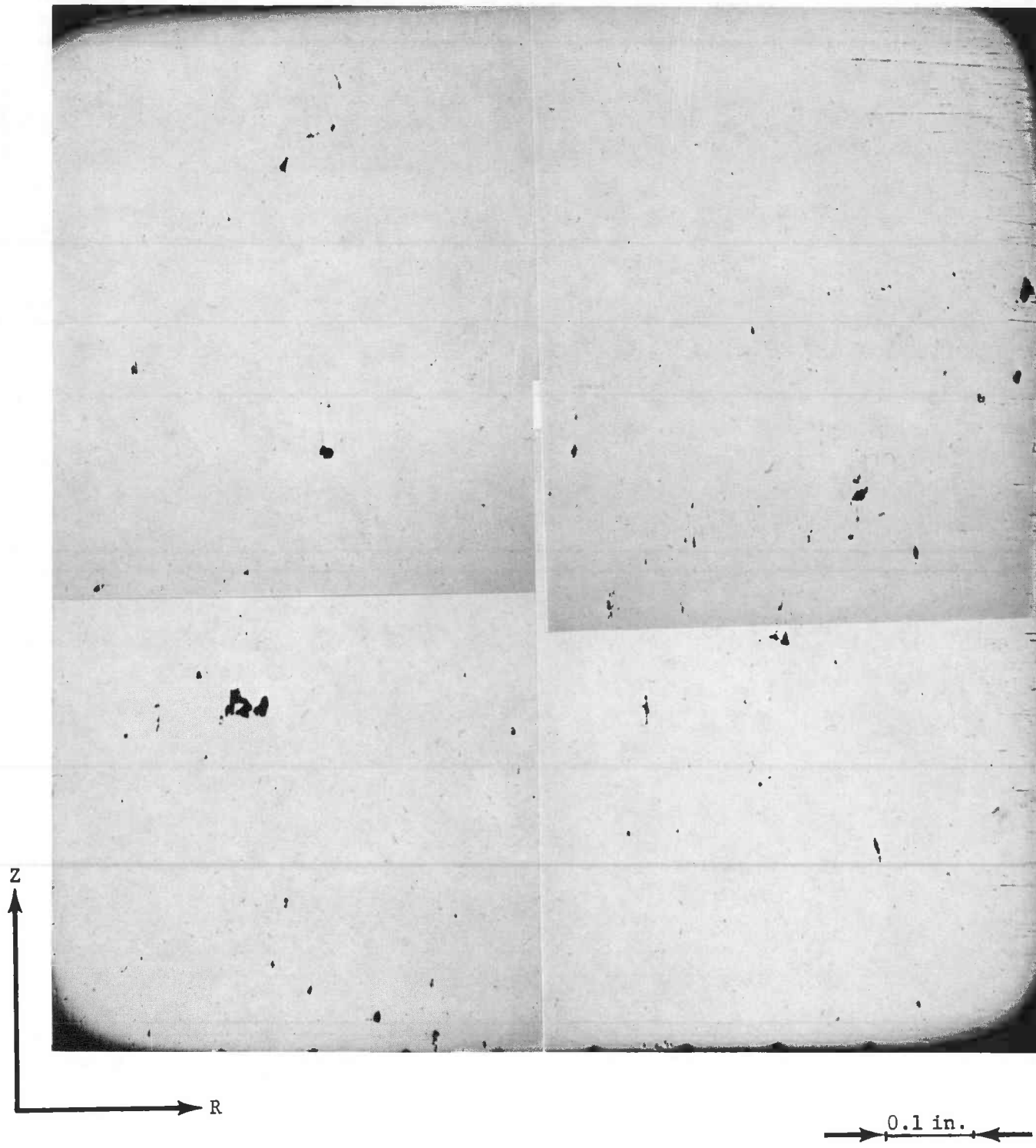

FIG. 51

J7A131 - 0.448 in. removed.
Area Fraction of Flaw is 0.0018.

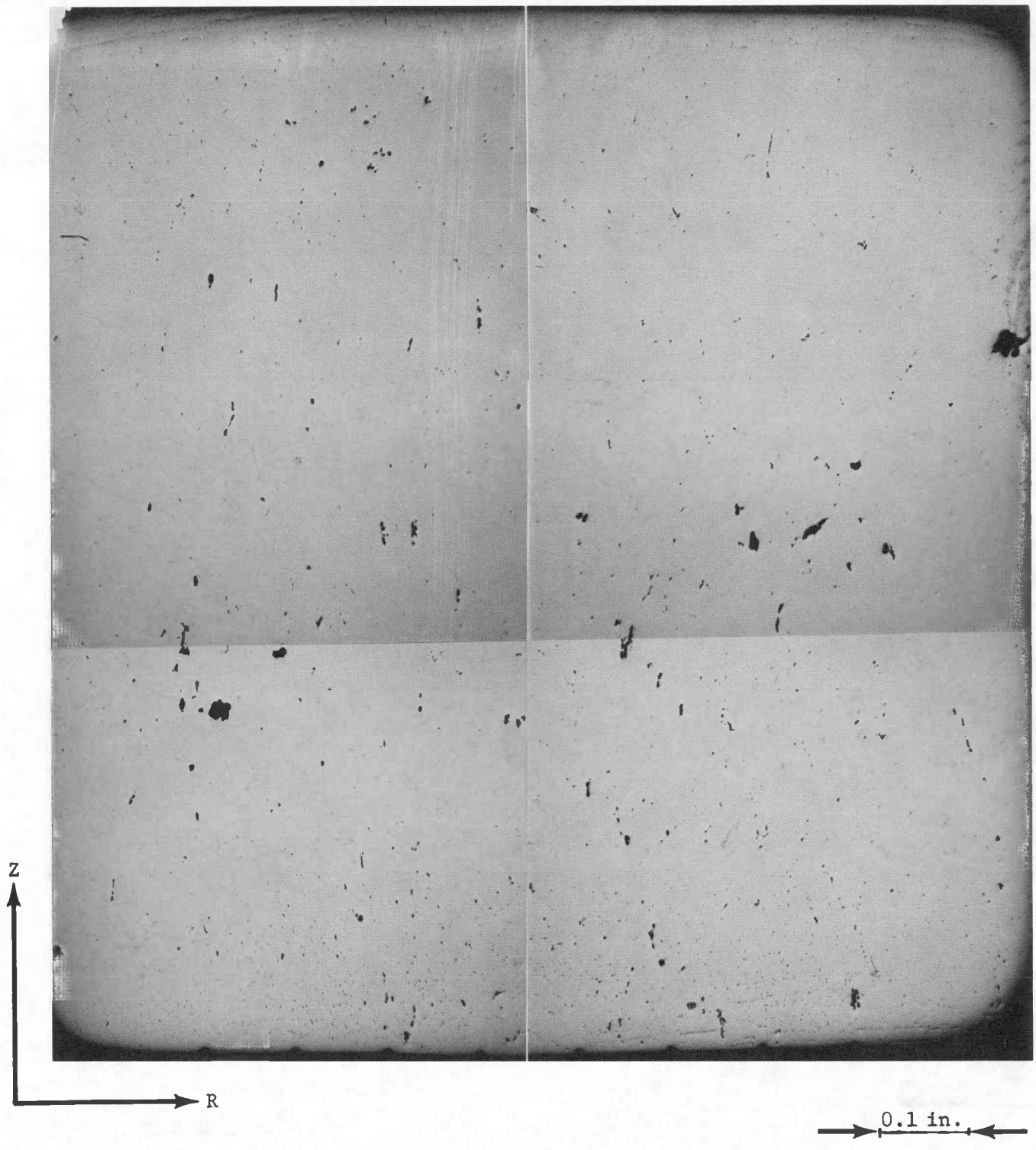

FIG. 52

J7A131 - 0.478 in. removed.
Area Fraction of Flaw is 0.0045.

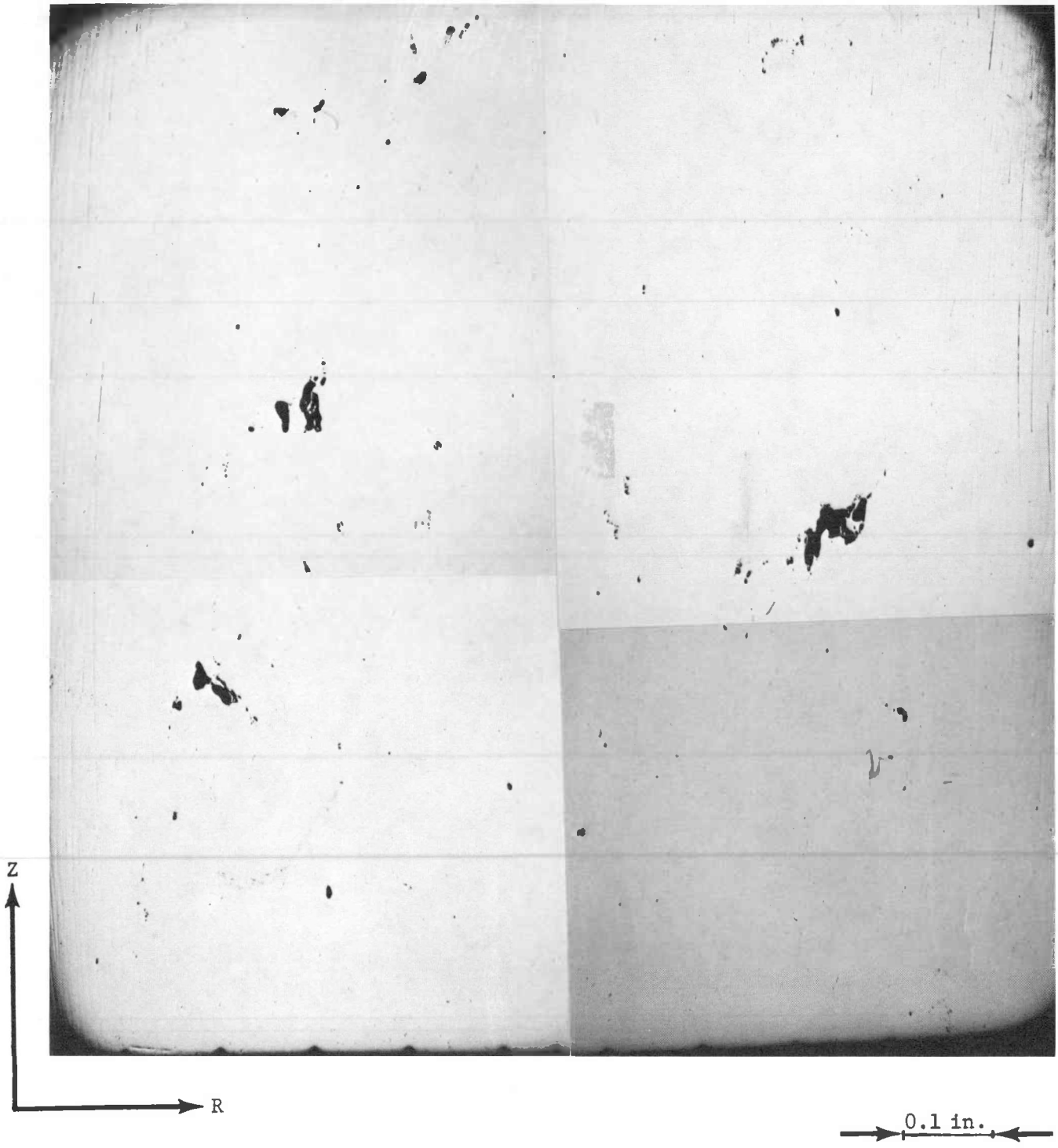

FIG. 53

J7A131 - 0.509 in. removed.
Area Fraction of Flaw is 0.0045.

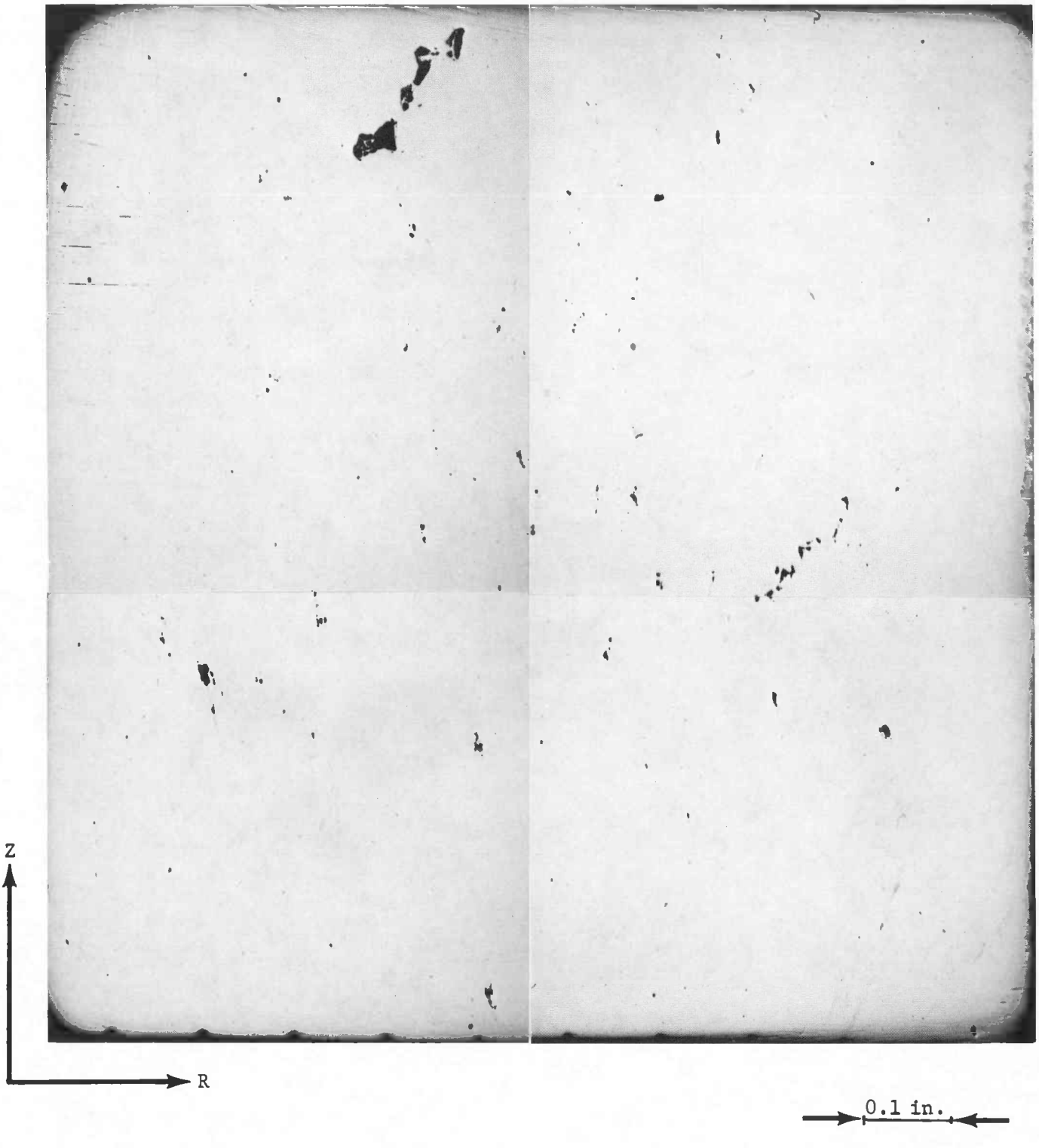

FIG. 54

J7A131 - 0.540 in. removed.
Area Fraction of Flaw is 0.0029.

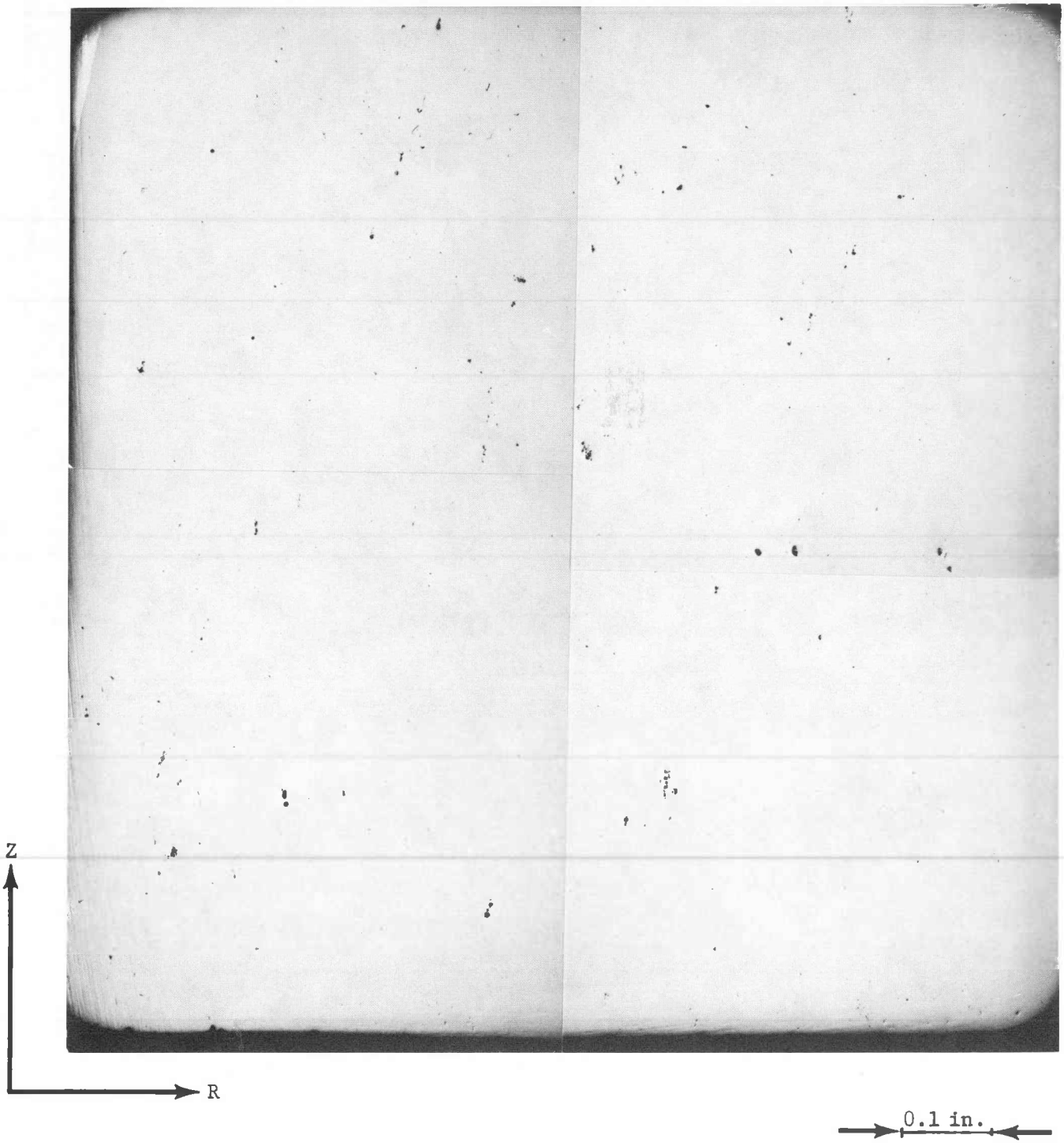

FIG. 55

J7A131 - 0.570 in. removed.
Area Fraction of Flaw is 0.0009.

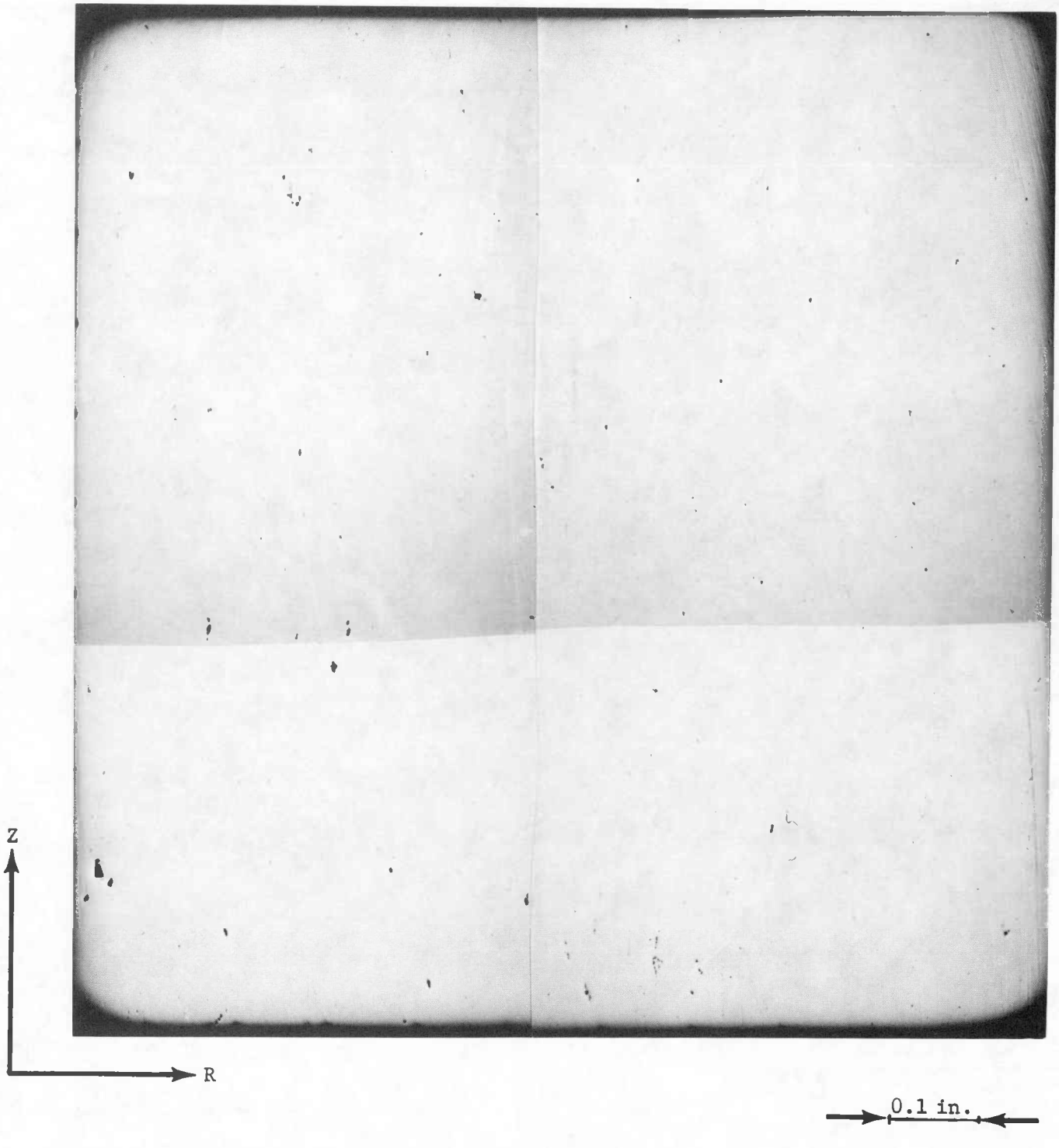

FIG. 56

J7A131 - 0.601 in. Removed.
Area Fractions of Flaws is 0.0006.

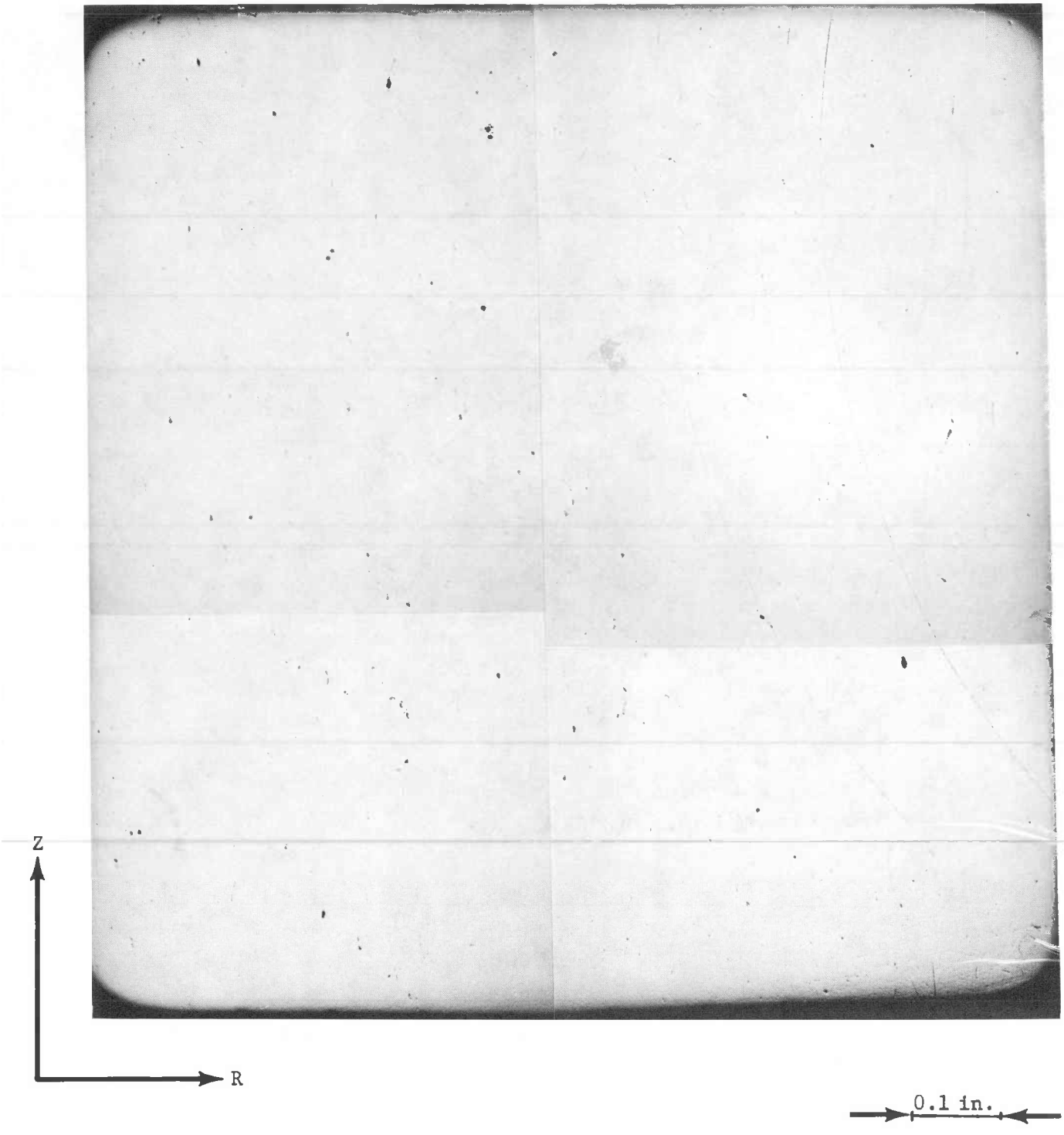

FIG. 57

J7A131 - 0.632 in. Removed.
Area Fraction of Flaws is 0.0004.

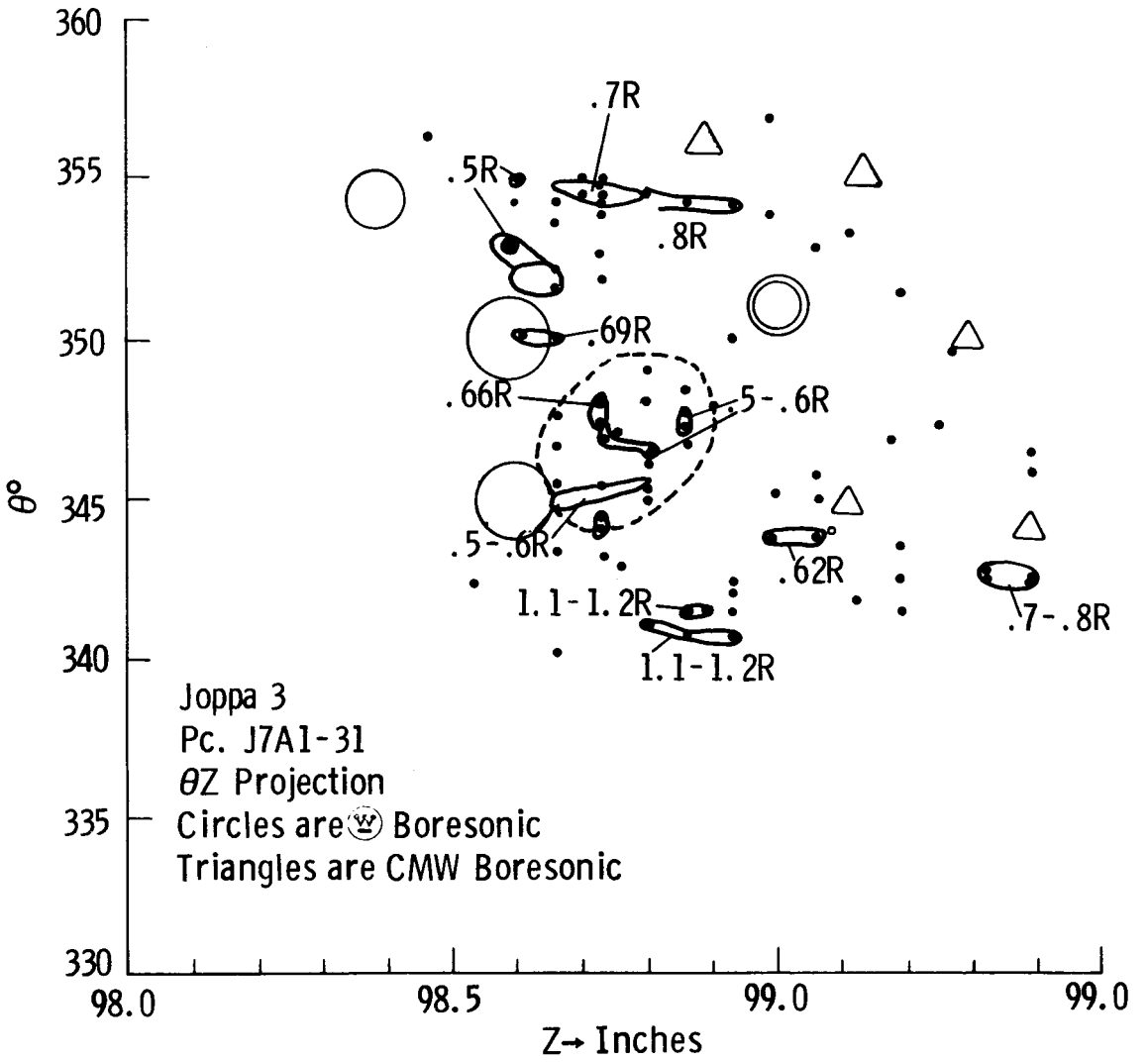

Fig. 58 – θZ projection of flawed cells and neighboring boresonic indications for J7A1-31 from Joppa 3.

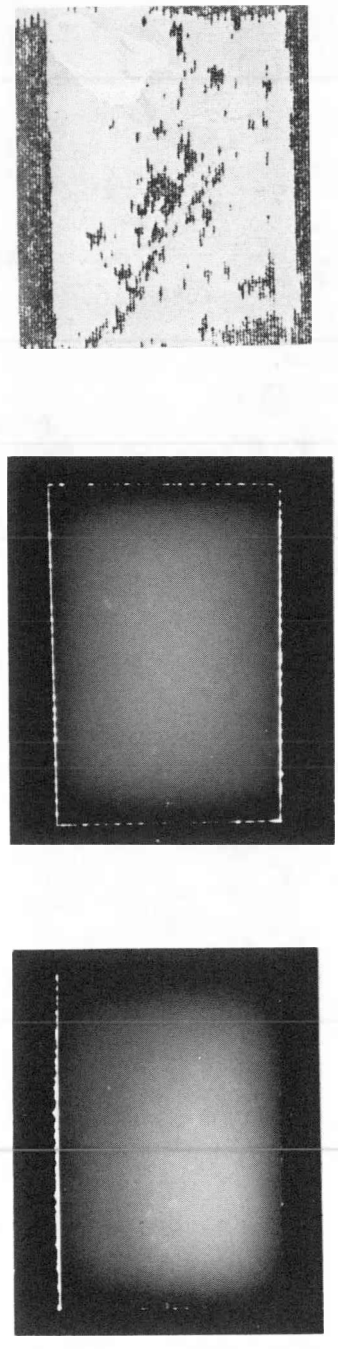

FIG. 59

C-Scan and Radiographs of Piece J7A1-81 from Joppa 3.

C-scan and top radiograph looking from bore toward periphery, right edge is plane of polish. Bottom radiograph orthogonal to other and is the RZ plane of polish.

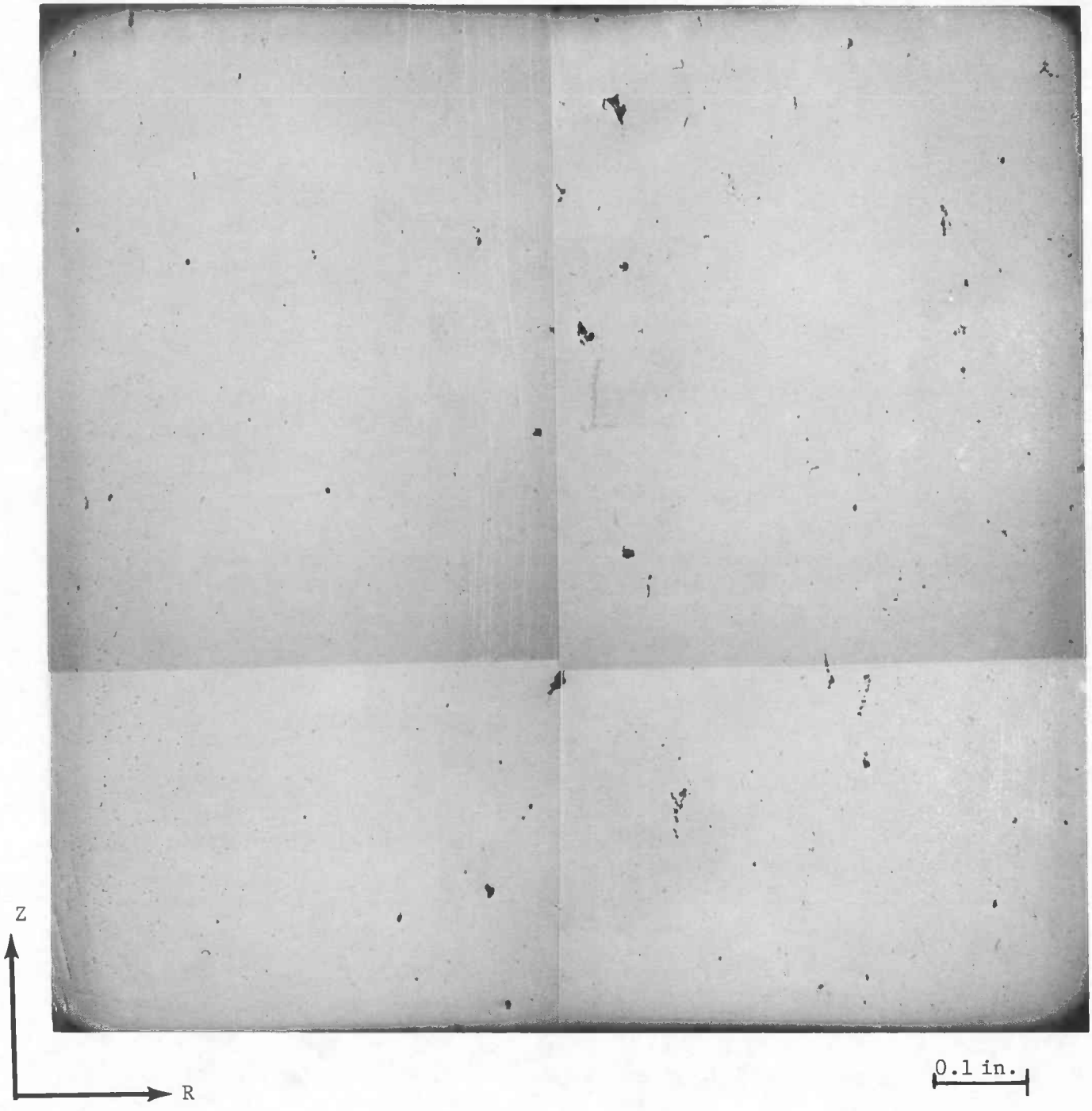

FIG. 60

Specimen J7A1-81 from Joppa 3. Plane of Polish Showing Profuse Type II Defects at the Right Side.

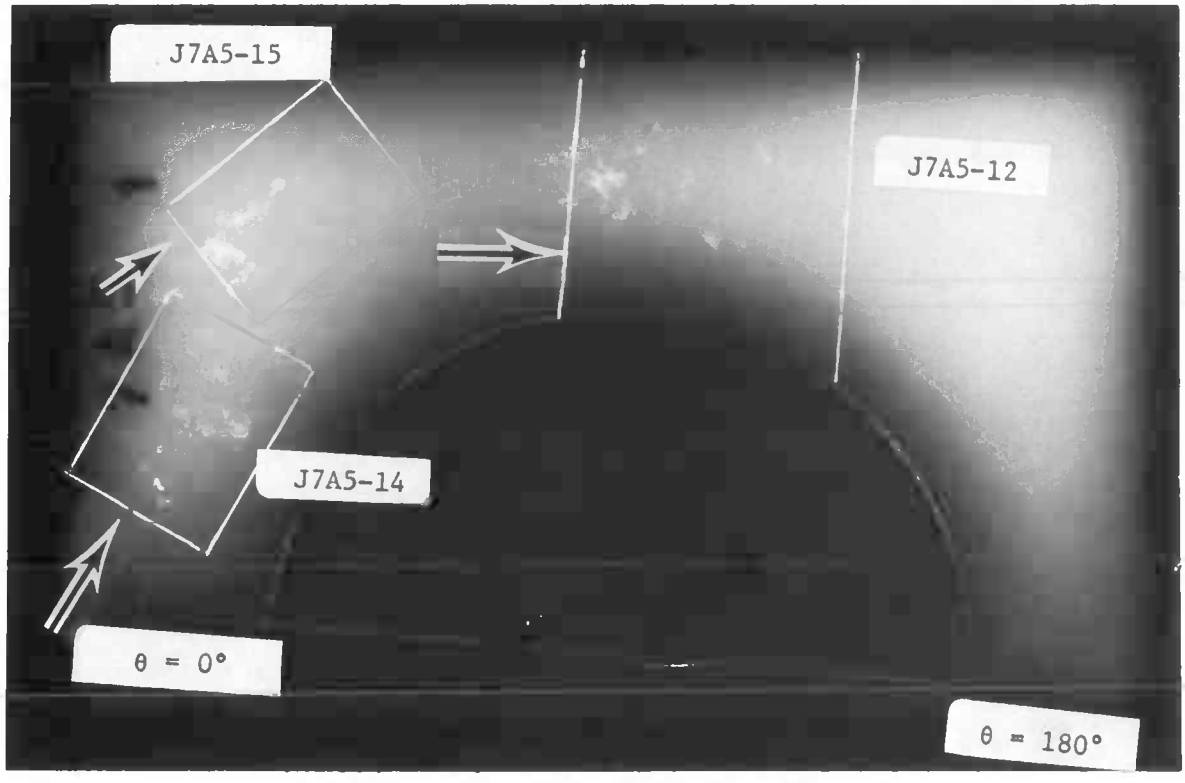

FIG. 61

Radiograph of Piece J7A5 from Joppa 3 Showing the Locations of J7A5-14, J7A5-15 and J7A5-12. Arrows Show Plane and Direction of Polish. Radiograph Looking Along Z Axis from Z 98.3 in. to 99.6 in.

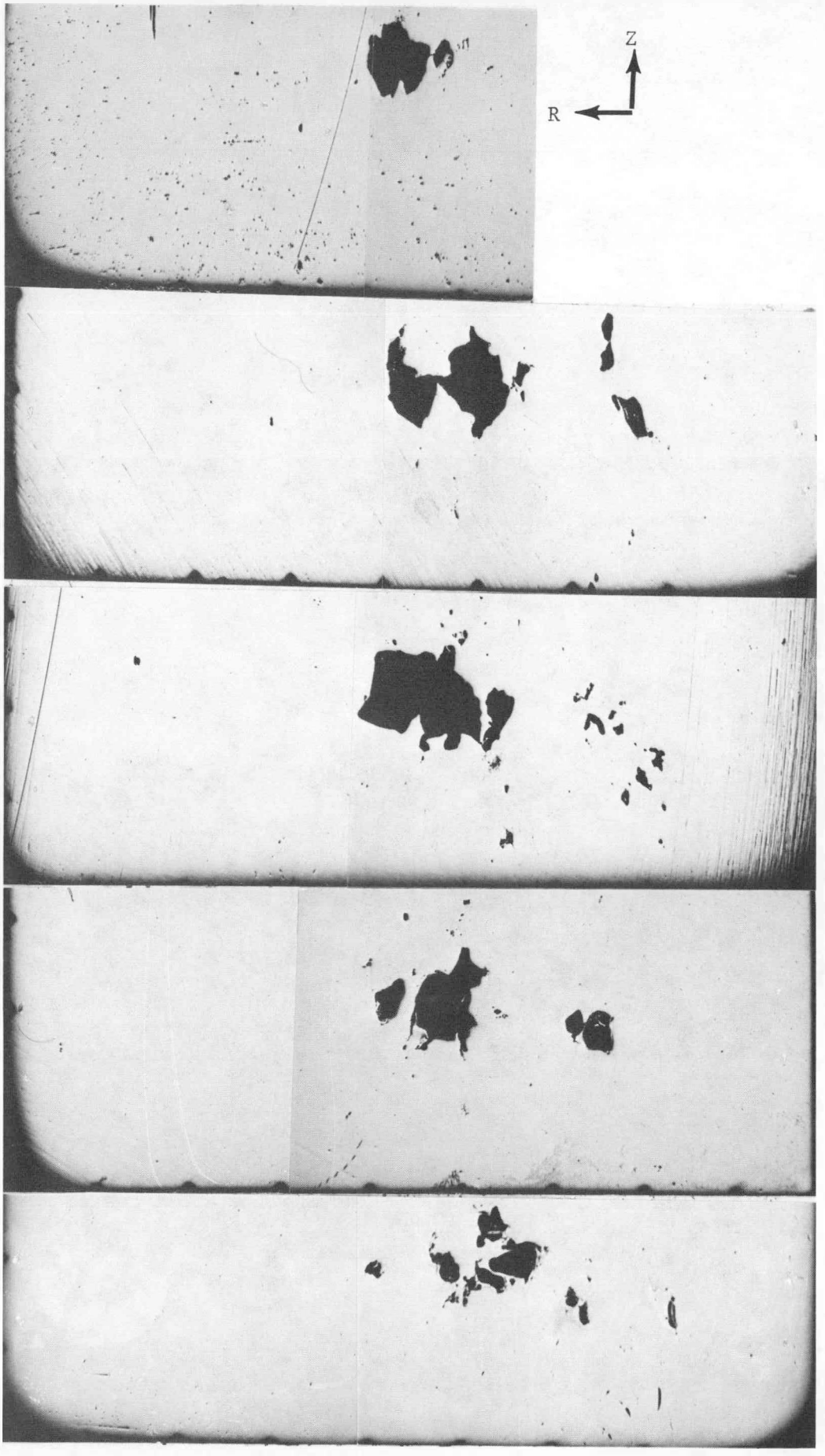

FIG. 62

Large Flaw in Piece J7A5-15 from Joppa 3 Shown at 0.03 in. Intervals into θ. Mag. 6X.

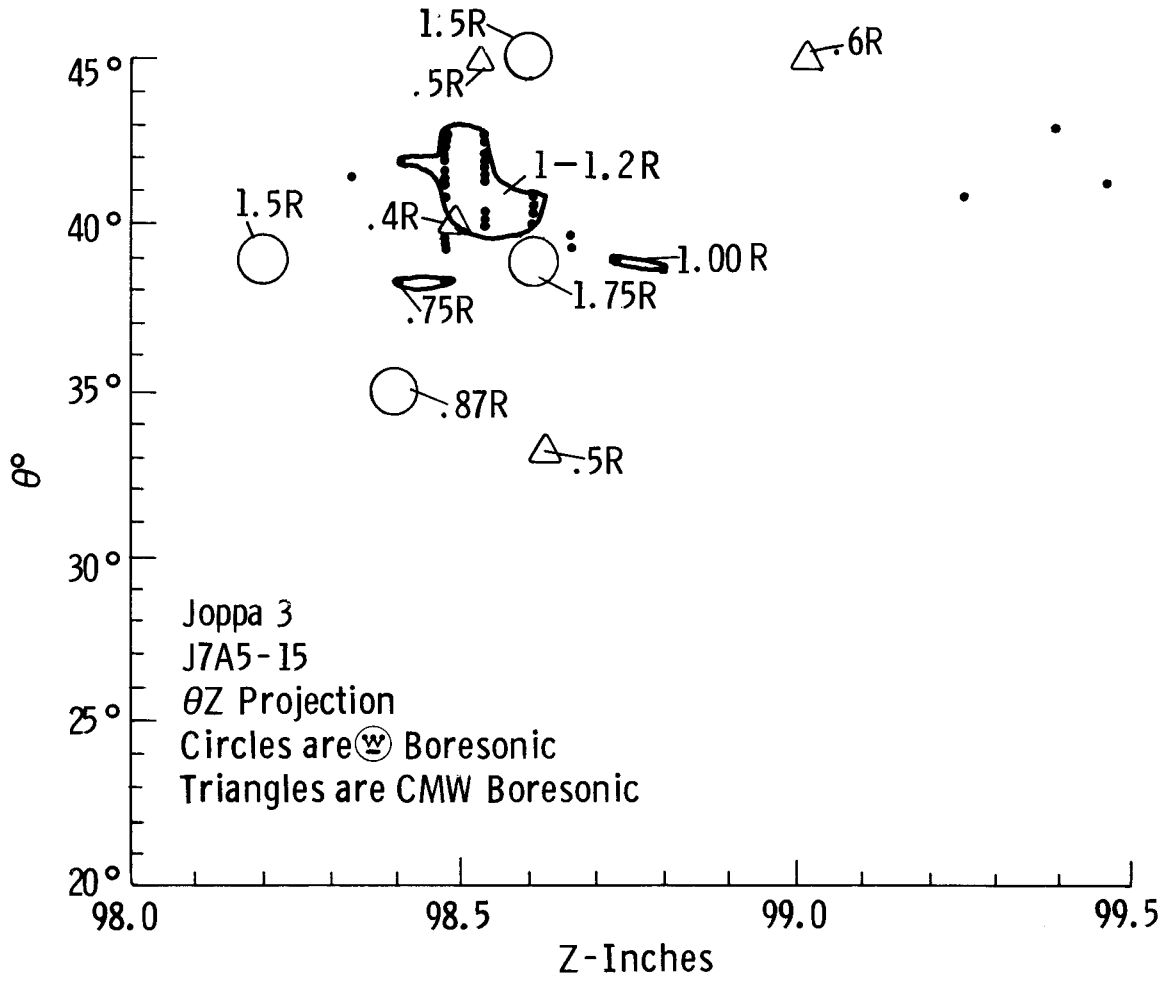

Fig. 63 — Location of densely flawed areas of J7A5-15 versus boresonic indications. Dots indicate local areas with volume fraction of flaws > 0.1

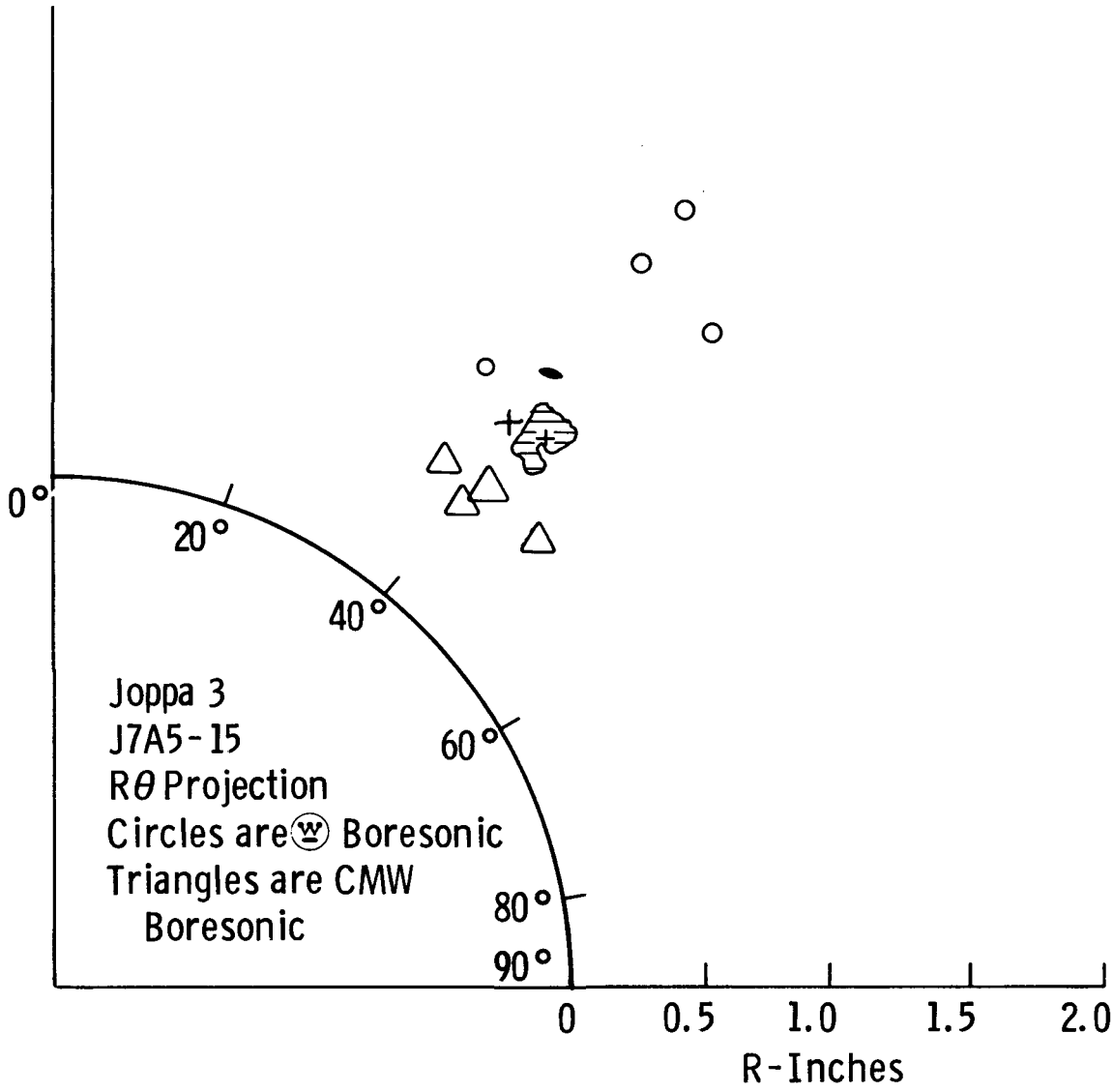

Fig. 64 — Location of densely flawed areas of J7A5-15 versus boresonic indications

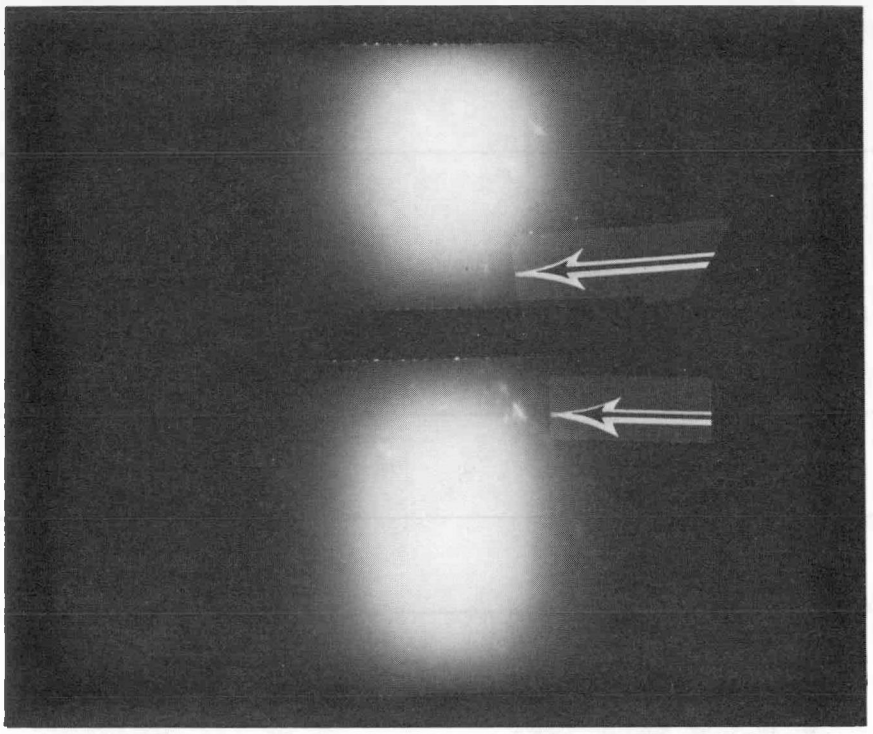

FIG. 65

Pieces J7A5-12 (top) and J7A5-22 from Joppa 3. Arrows Indicate Linear Defect. Looking from Bore.

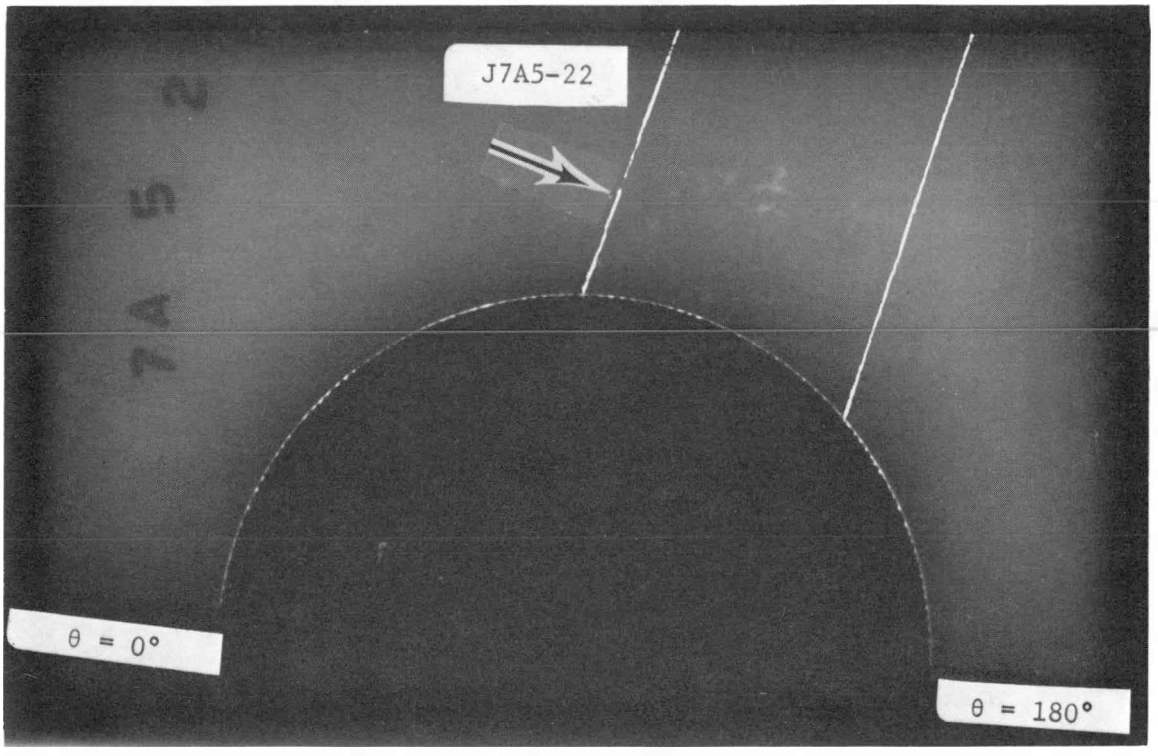

FIG. 66

Z-Axis Radiograph of Piece J7A5-22 from Joppa 3. Looking from Z = 100.4 in. to Z = 102.1 in.

FIG. 67

Radially Oriented Flaw in Piece J7A5-22 from Joppa 3. Bottom is Actual Bore Surface, Z Increasing Right to Left. Mag. 8.5X.

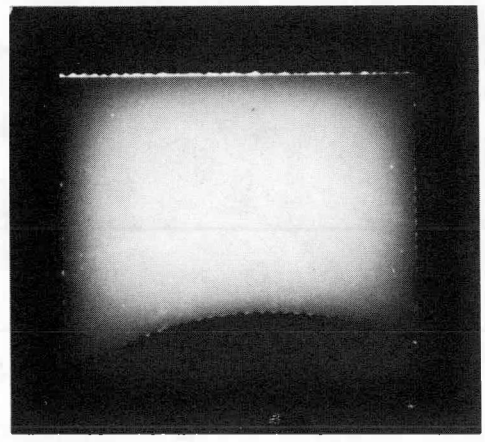

FIG. 68

Radiograph of Piece J6A-2 from Joppa 3.

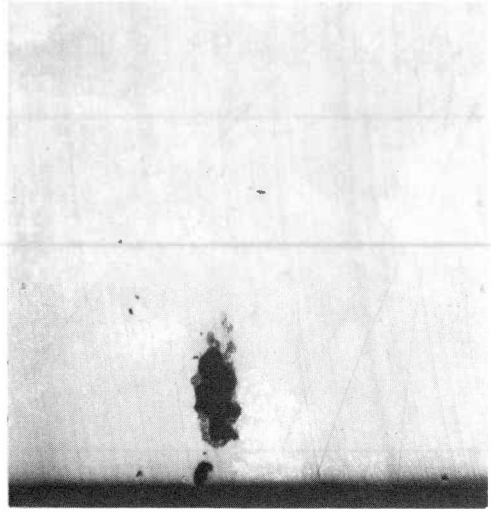

FIG. 69

Flaw at Bore (Bottom Edge) of Piece J6A-2 from Joppa 3. Mag. 6X.

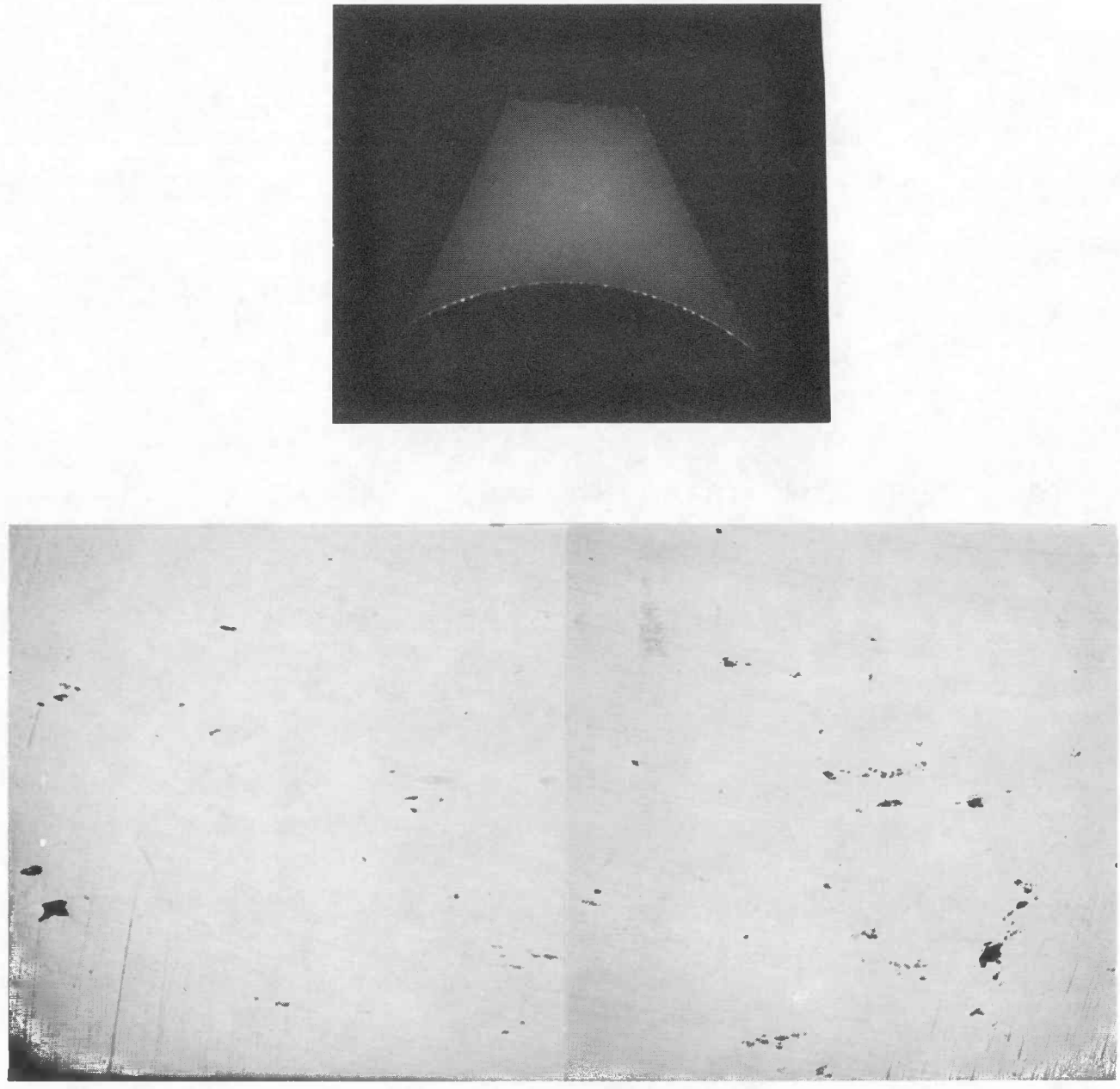

FIG. 71

Type II Flaws in Piece J7-1 from Joppa 3.
Bore Surface at Bottom. Mag. 6X.

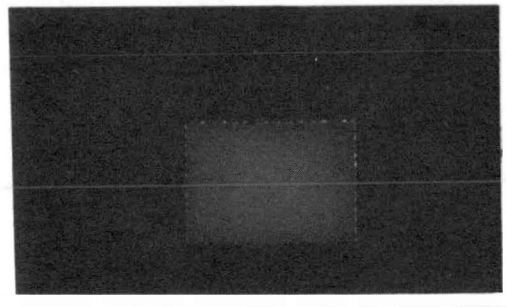

FIG. 72

Radiograph of Piece JF3 from Joppa 3.
Z Direction Right to Left, Radial
Direction Bottom to Top.

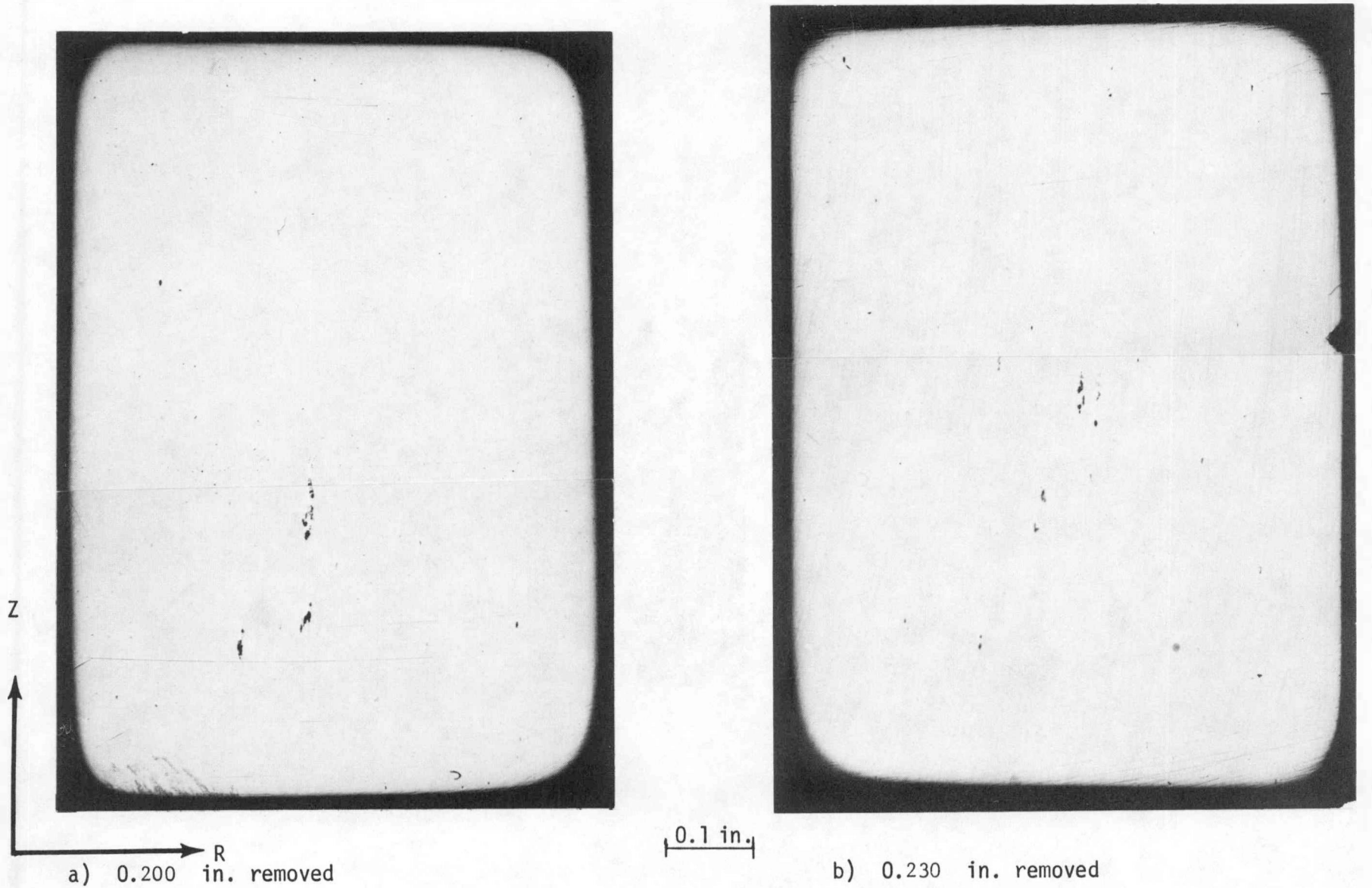

a) 0.200 in. removed

b) 0.230 in. removed

FIG. 73

Specimen JF3 from Joppa 3.

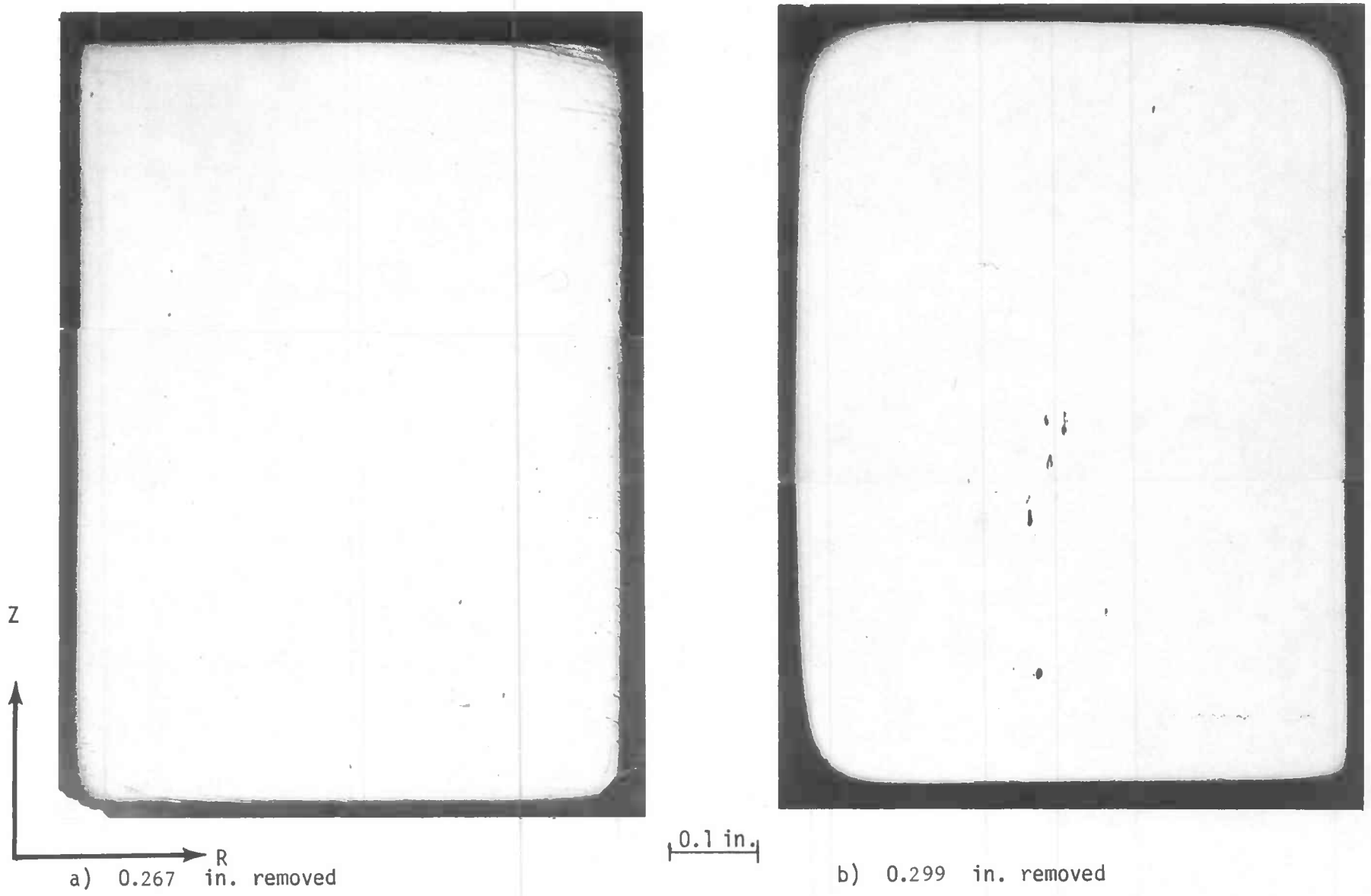

a) 0.267 in. removed

b) 0.299 in. removed

FIG. 74

Specimen JF3 from Joppa 3.

FIG. 75

Typical Type II Flaw Viewed in θR Plane of Polish. Mag. 200X.

FIG. 76 - Cored Structure in Buck 6.
STBS Etch. Mag. 6X

FIG. 77 - General Microstructure of Buck 6.
2% Picral Etch. Mag. 100X

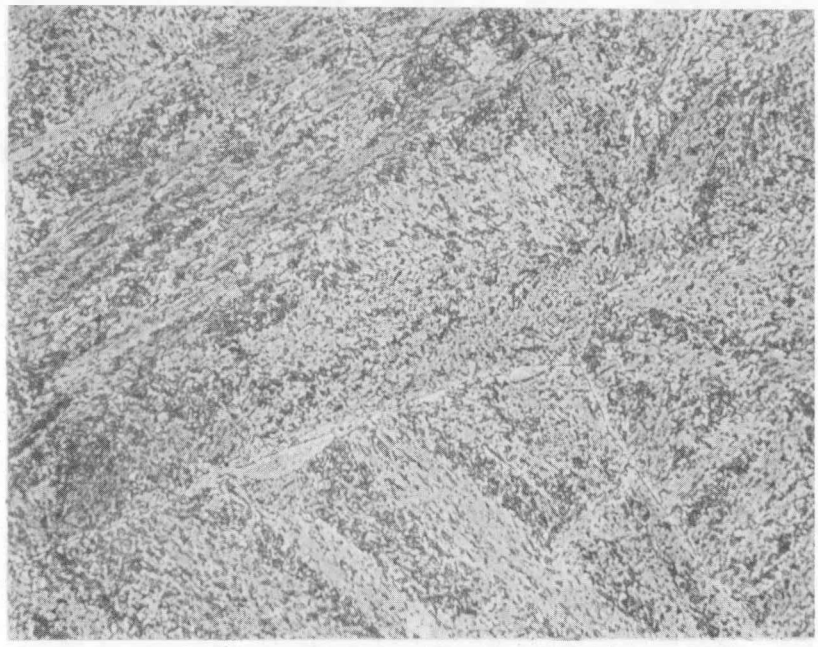

FIG. 78 - Microstructure of Buck 6.
2% Picral Etch. Mag. 500X

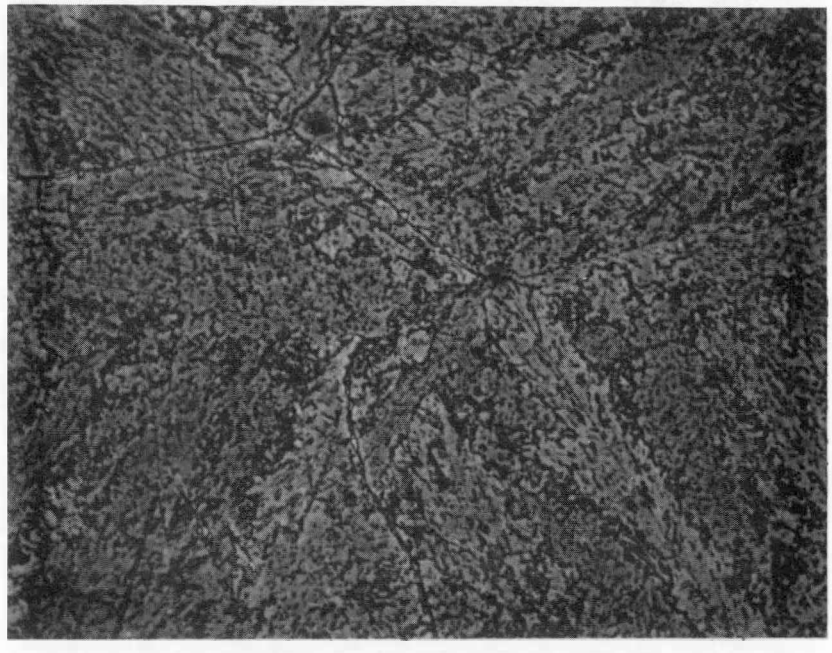

FIG. 79 - Buck 6 Grain Boundaries.
2% Picral Etch. Mag. 1000X

FIG. 80 - Type III Inclusions in Buck 6.
Unetched. Mag. 100X

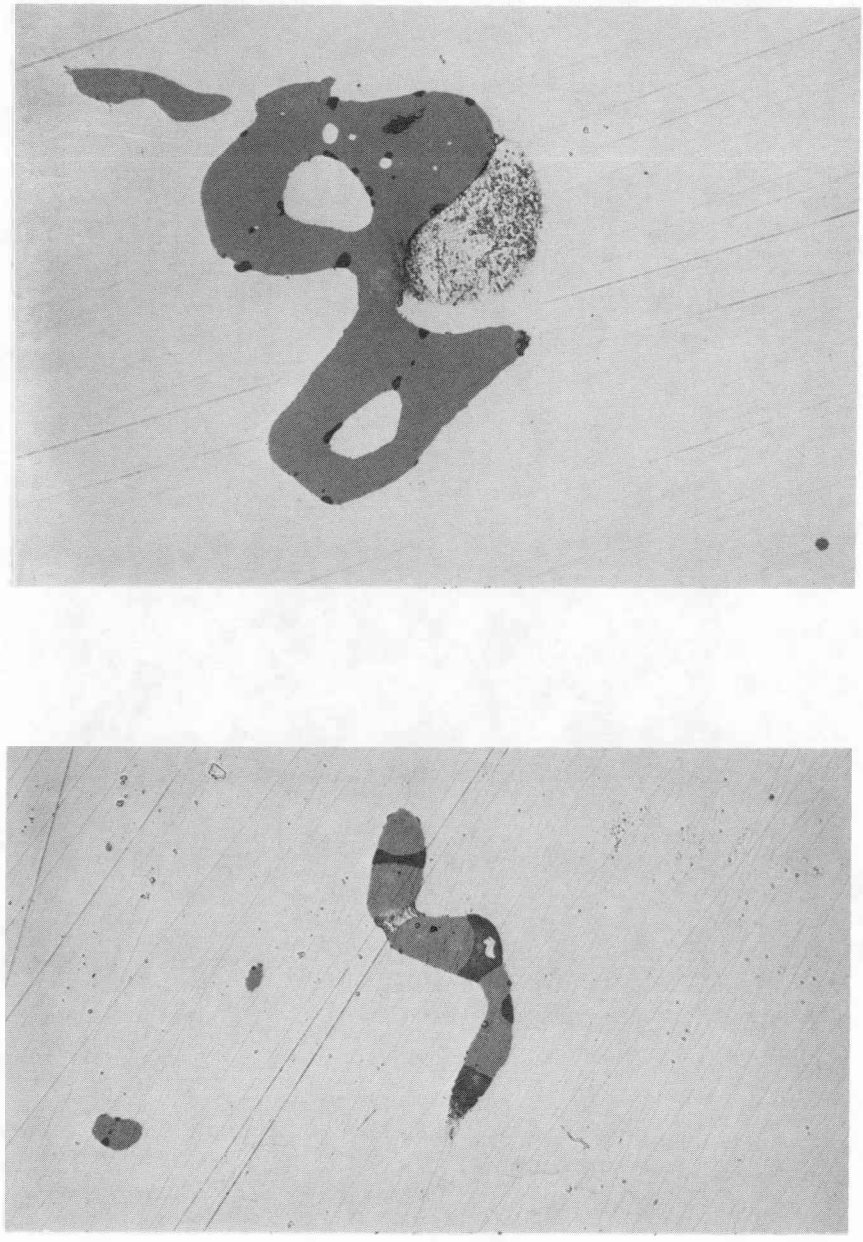

FIG. 81 - Type III Inclusions in Buck 6. Unetched. Mag. 500X

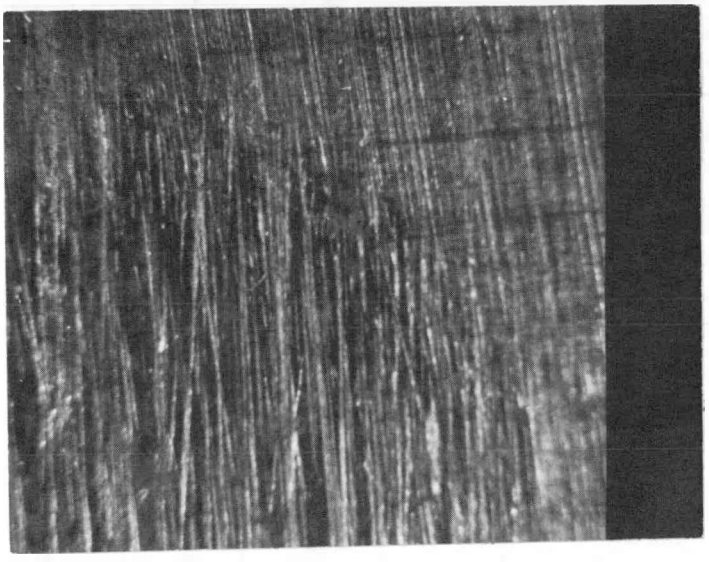

FIG. 82 - Dimpling on the Buck 6 Bore. The upper right hand corner is dimpled, and the dimple boundary curves from the upper left corner to the lower right corner. Mag. 7.7X

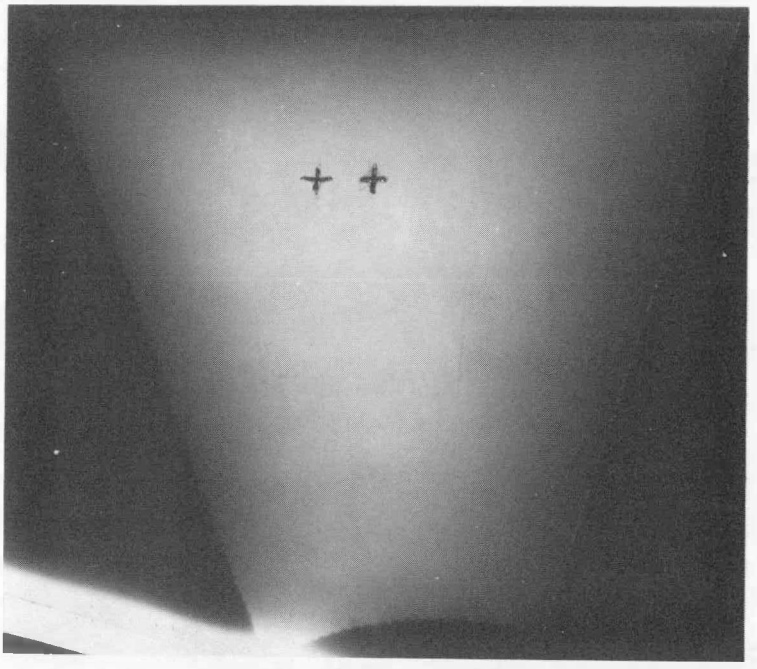

B114

Z = 69.0" to 71.0"
Right hand θ = 63°
Left hand θ = 25°
Left cross flaw C
Right cross flaw B

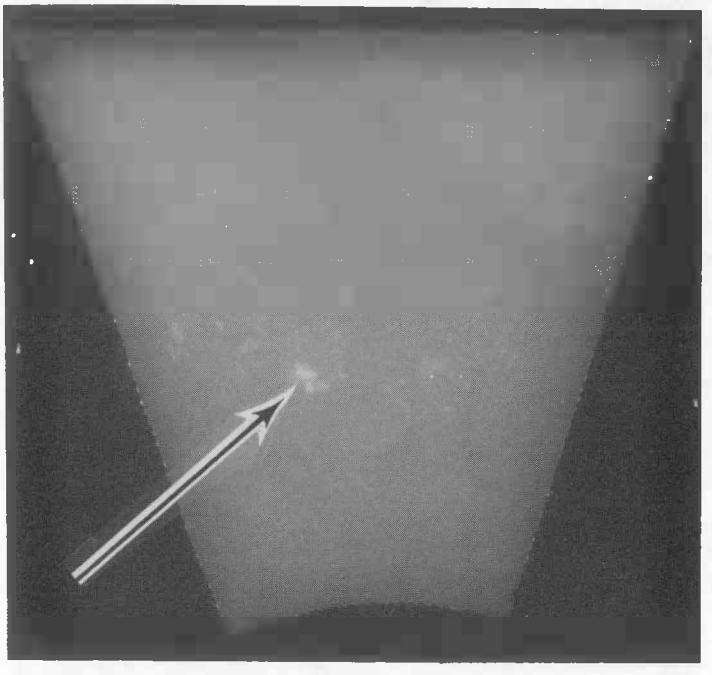

B112

Z = 66.75" to 67.75"
Right hand θ = 63°
Left hand θ = 25°

Arrow shows boresonic flaw A location

FIG. 83 - Radiographs of Buck 6 Sections.

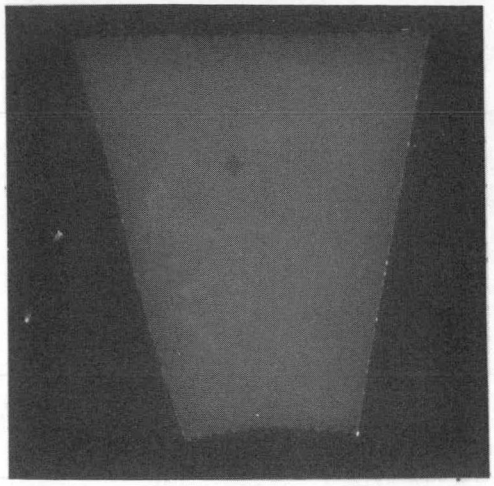

B212

Z = 98.3" to 99.2"
Right hand θ = 115°
Left hand θ = 90°

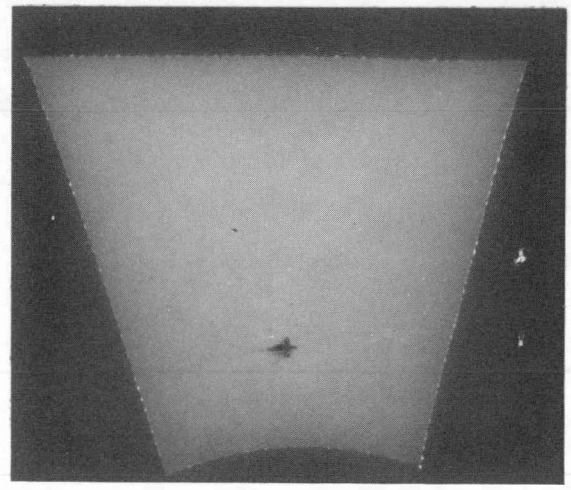

B3723

Z = 117.6" to 118.9"
Right hand θ = 235°
Left hand θ = 195°

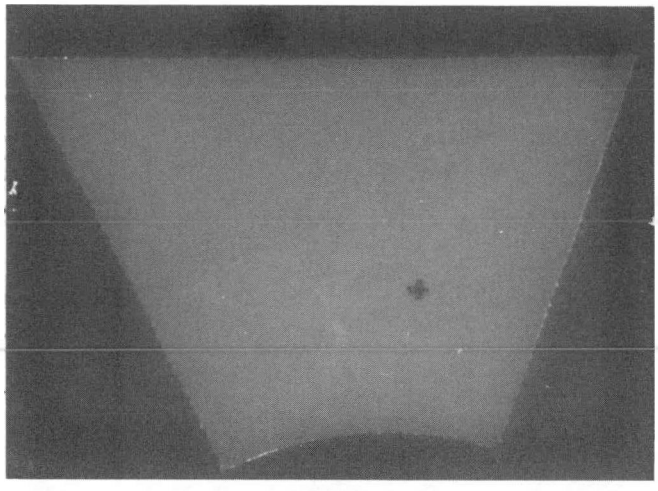

B313

Z = 117.6" to 118.9"
Right hand θ = 115°
Left hand θ 110°

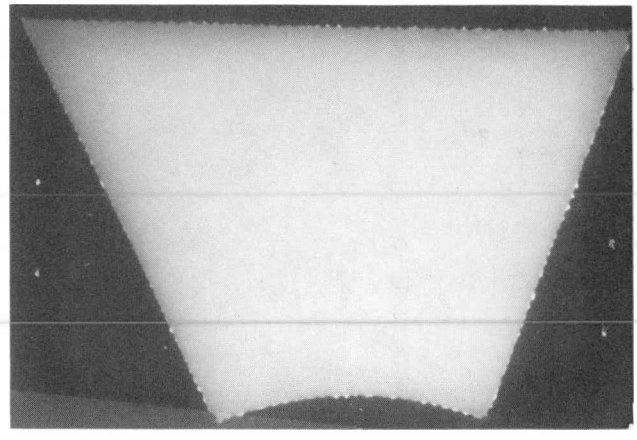

B312

Z = 116.7" to 117.5"
Right hand θ = 155°
Left hand θ = 110"

FIG. 84 - Radiographs of Buck 6 Sections.

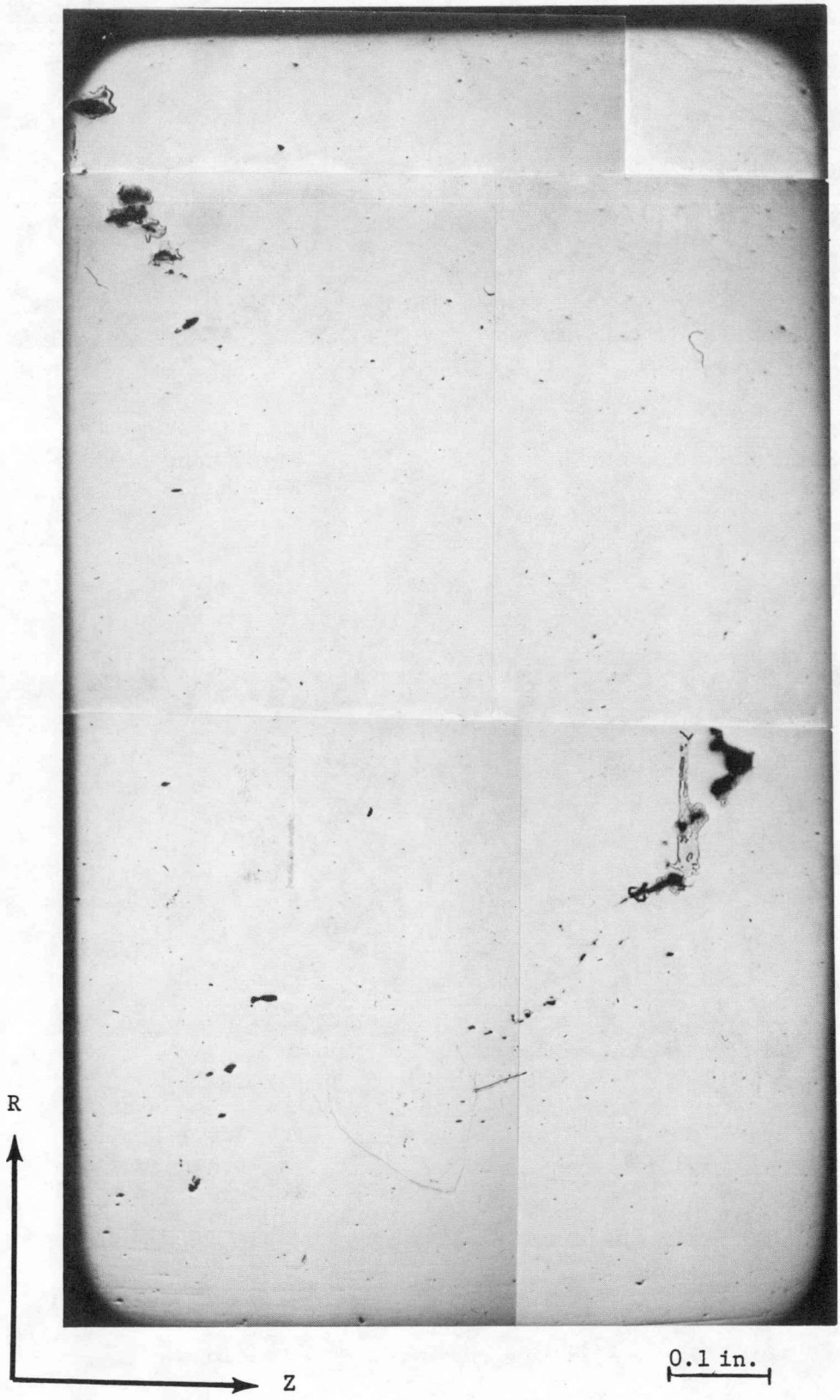

FIG. 85

Piece B114 from Buck 6 - 0.002 in. Removed.
0.0117 Area Fraction Flaw.

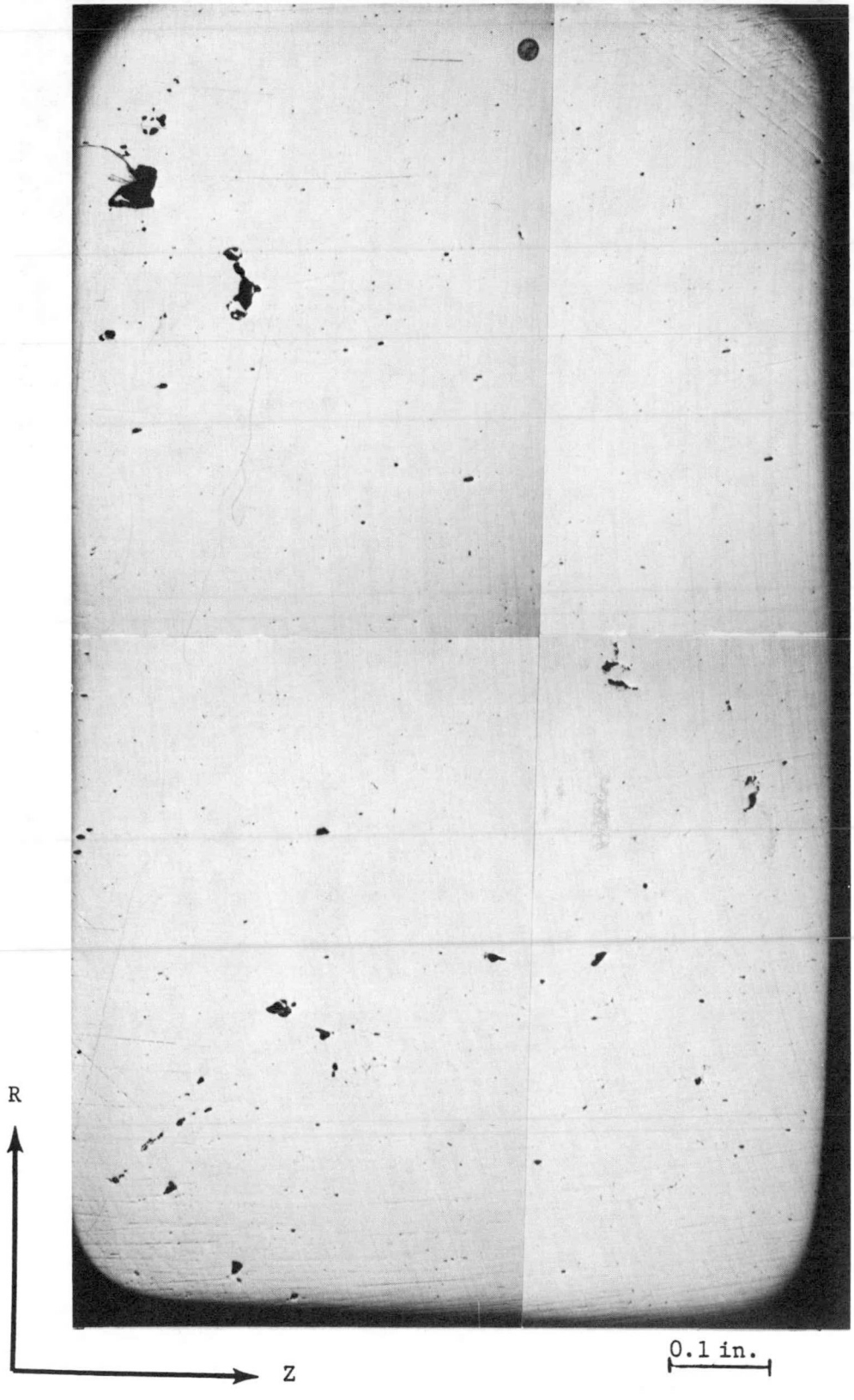

FIG. 86

Piece B114 from Buck 6 - 0.066 in Removed.
0.0092 Area Fraction Flaw.

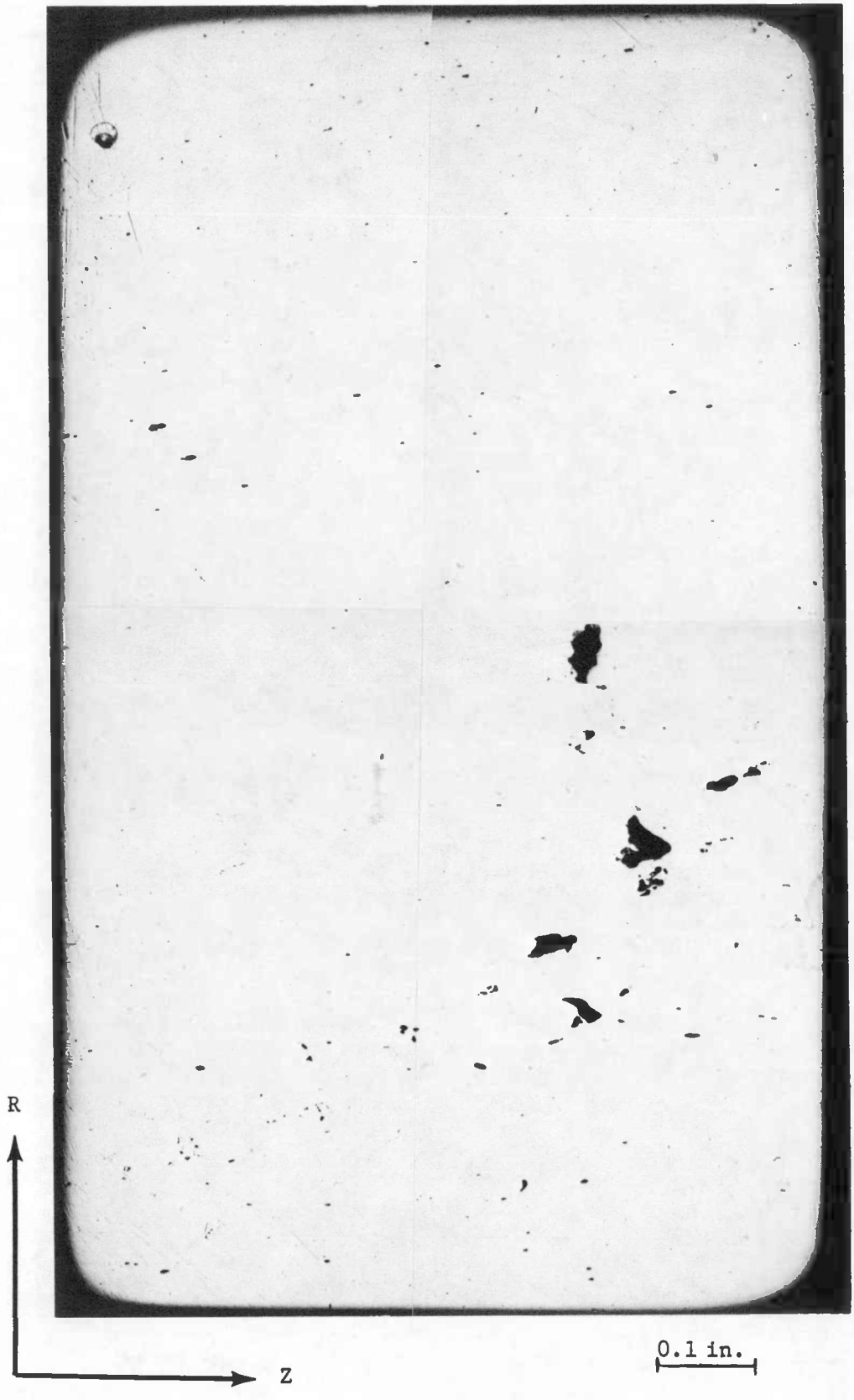

FIG. 87

Piece B114 from Buck 6 - 0.128 in Removed.
0.0079 Area Fraction Flaw.

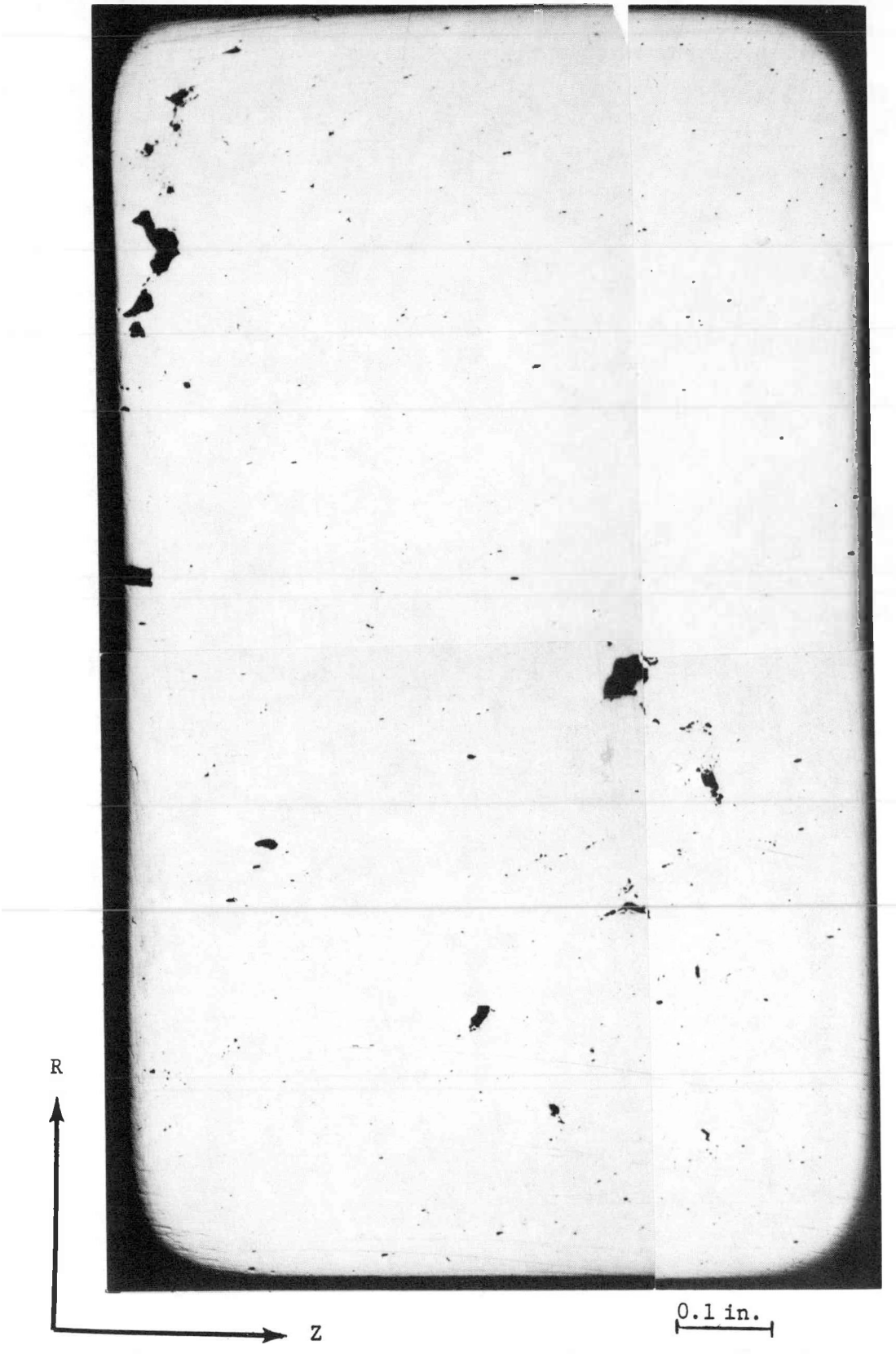

FIG. 88

Piece B114 from Buck 6 - 0.189 in. Removed.
0.0082 Area Fraction Flaw.

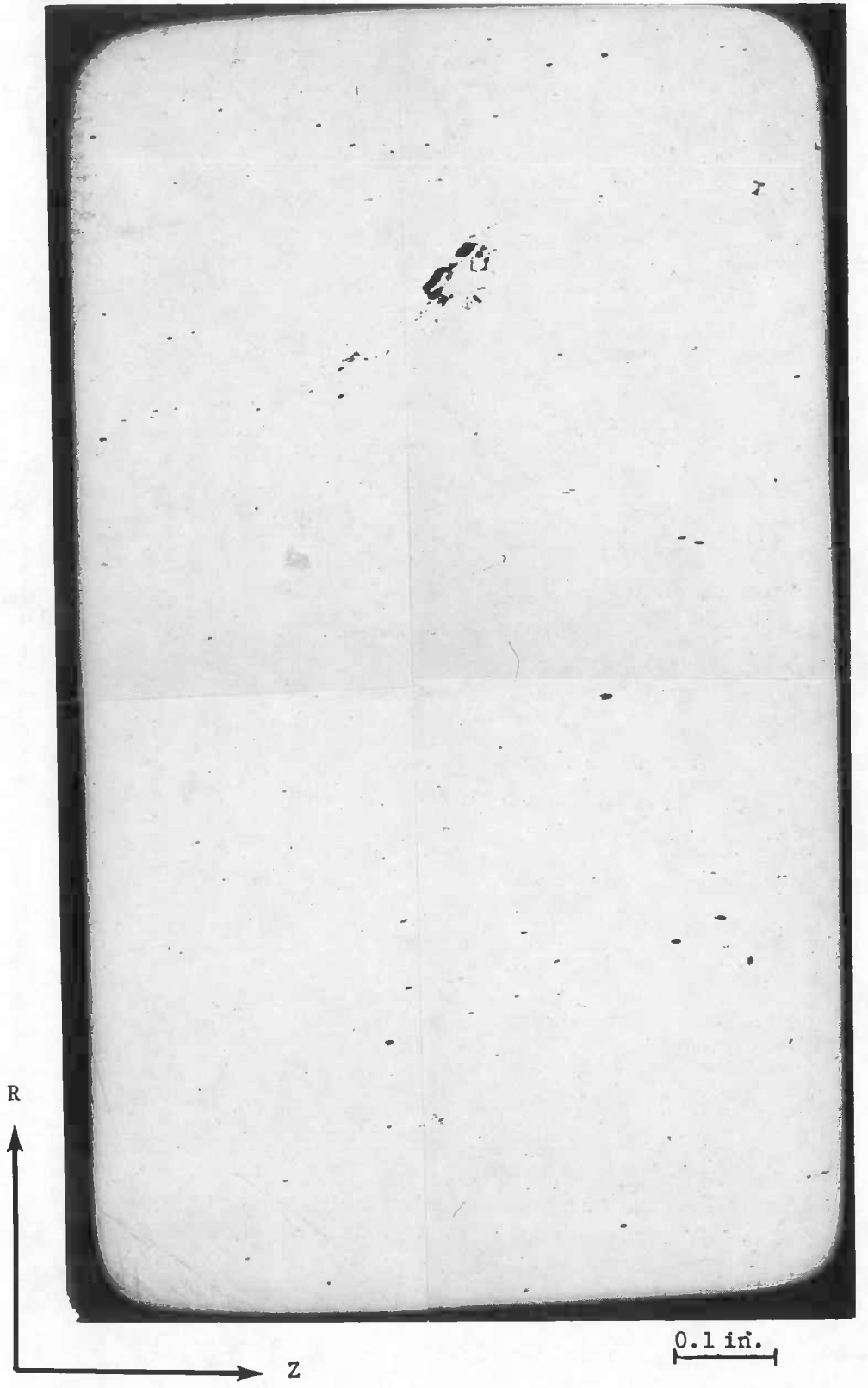

FIG. 89

Piece B114 from Buck 6 - 0.253 in. Removed.
0.0031 Area Fraction Flaw.

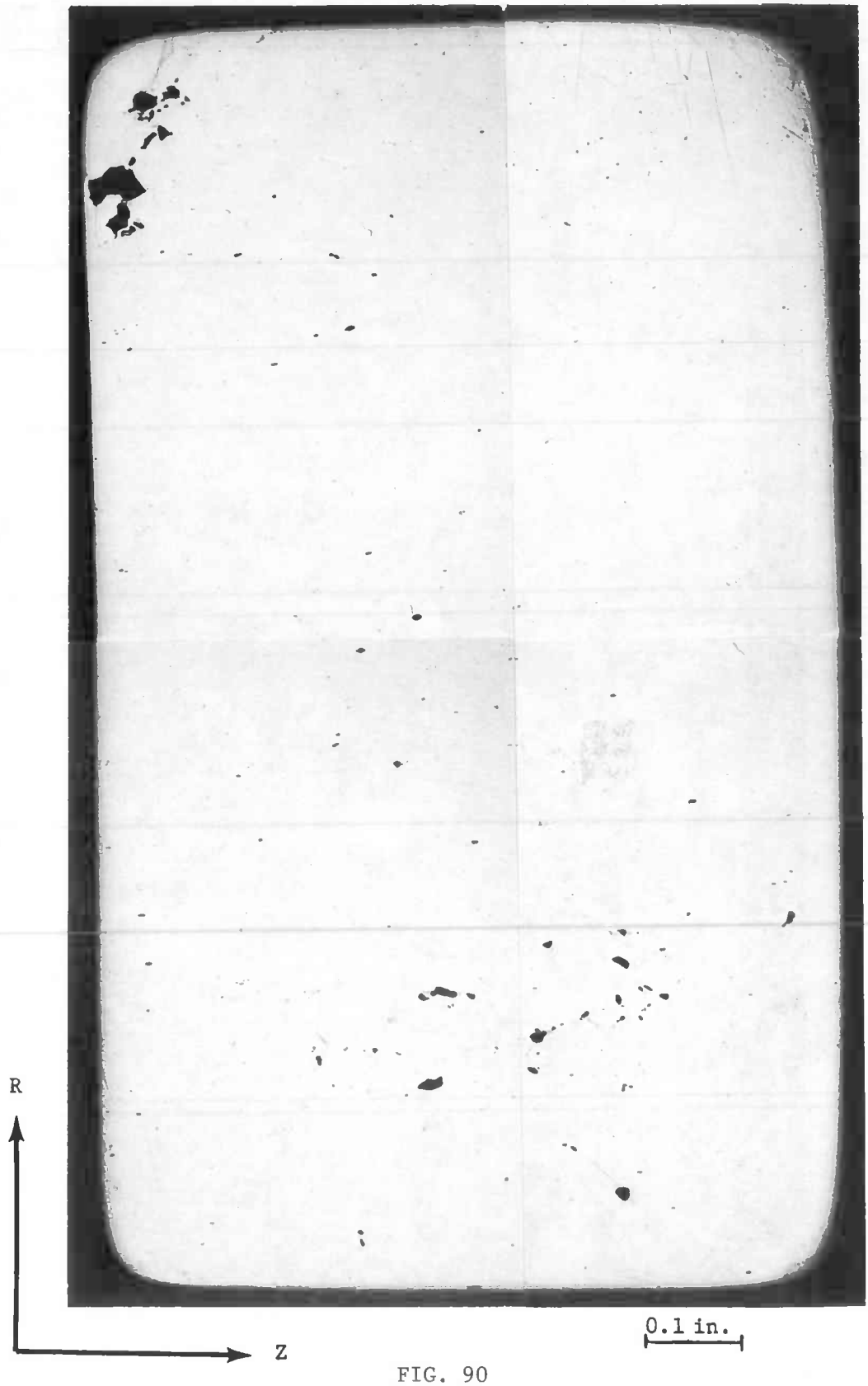

FIG. 90

Piece B114 from Buck 6 - 0.317 in. Removed.
0.0070 Area Fraction Flaw.

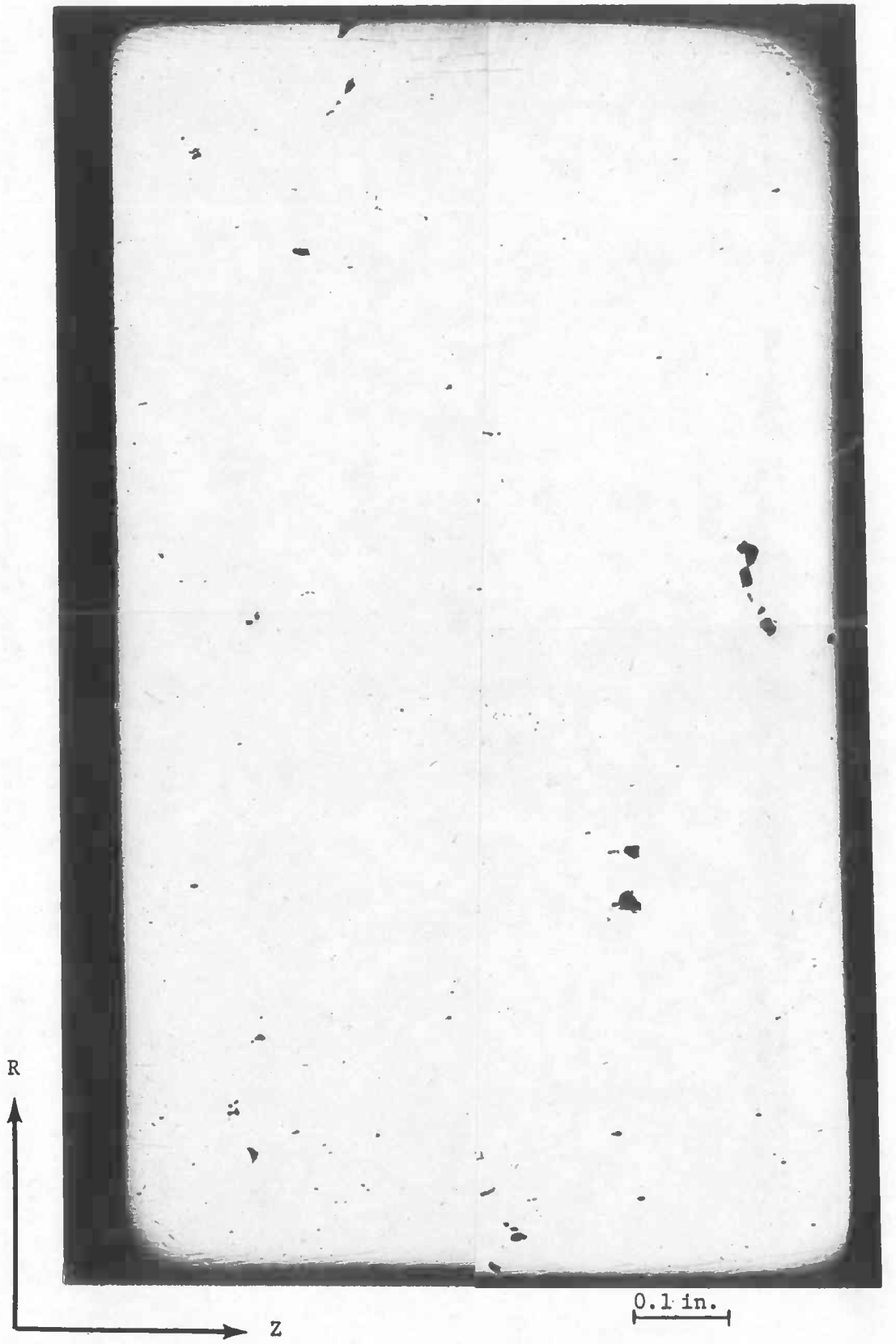

FIG. 91

Piece B114 from Buck 6 - 0.381 in. Removed,
0.0048 Area Fraction Flaw.

FIG. 92

Piece B114 from Buck 6 - 0.443 in. Removed.
0.0110 Area Fraction Flaw.

FIG. 93

Piece B114 from Buck 6 - 0.505 in. Removed.
0.0114 Area Fraction Flaw.

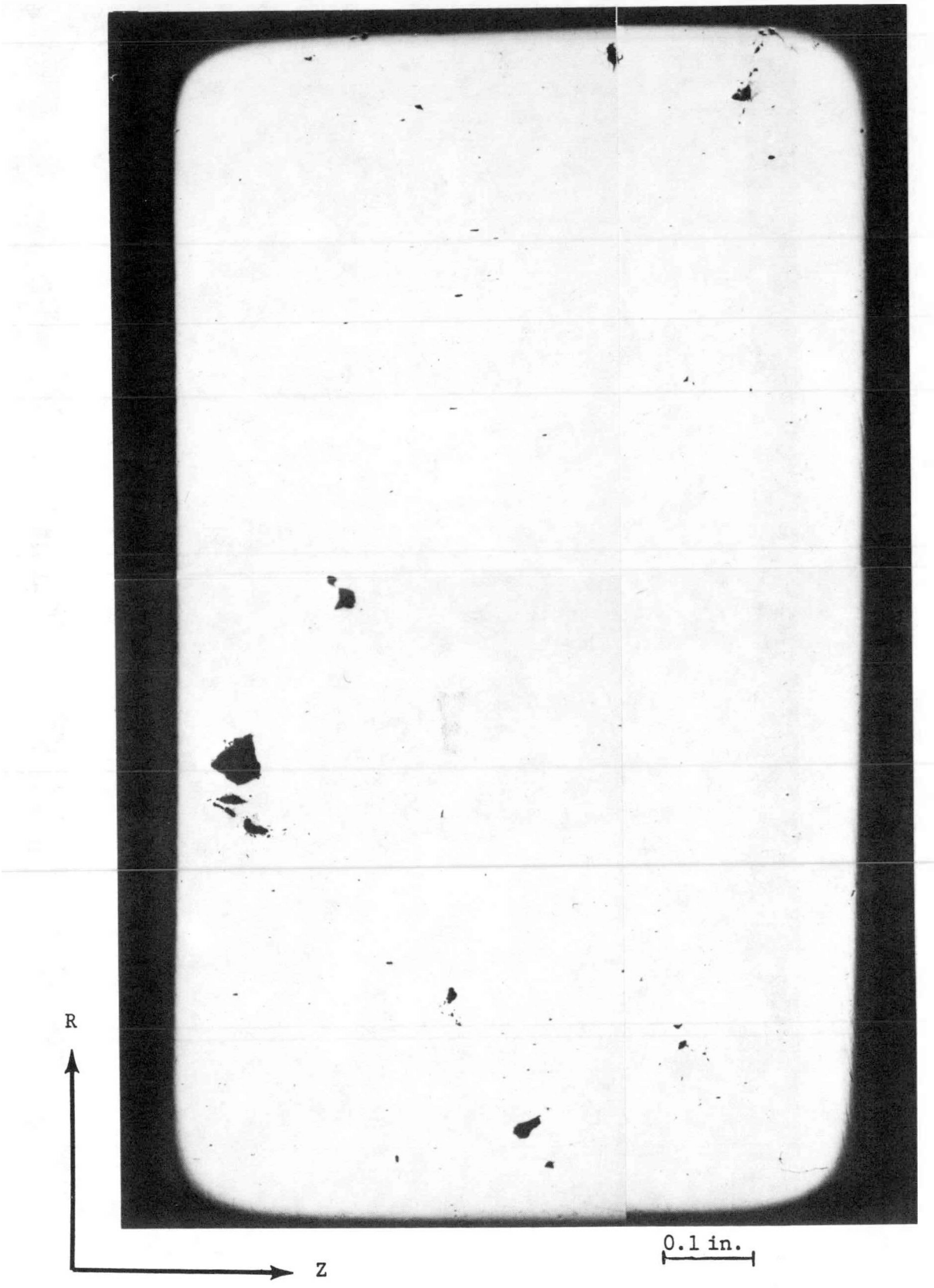

FIG. 94

Piece B114 from Buck 6 - 0.568 in. Removed.
0.0058 Area Fraction Flaw.

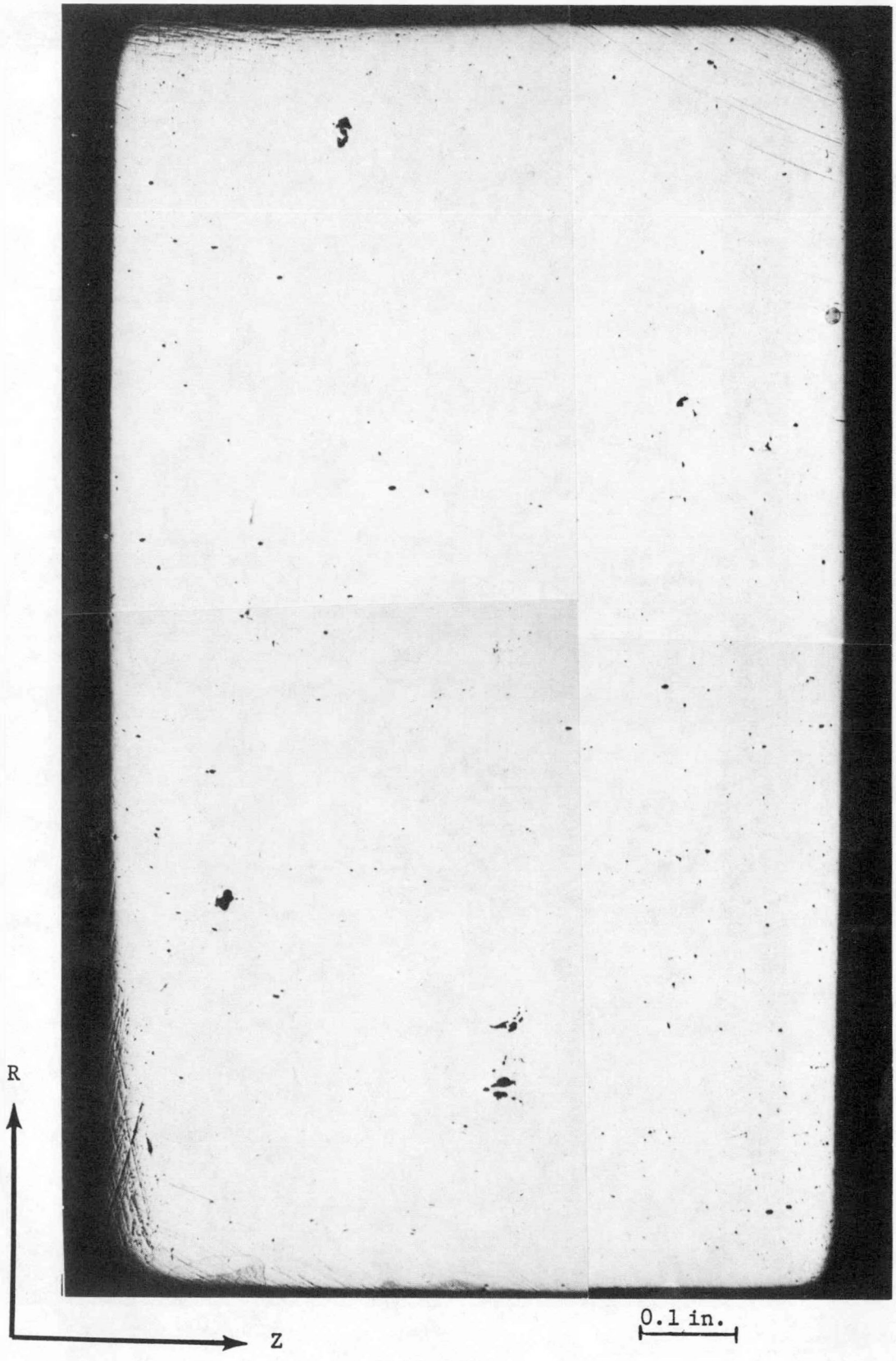

FIG. 95

Piece B114 from Buck 6 - 0.630 in. Removed.
0.0027 Area Fraction Flaw.

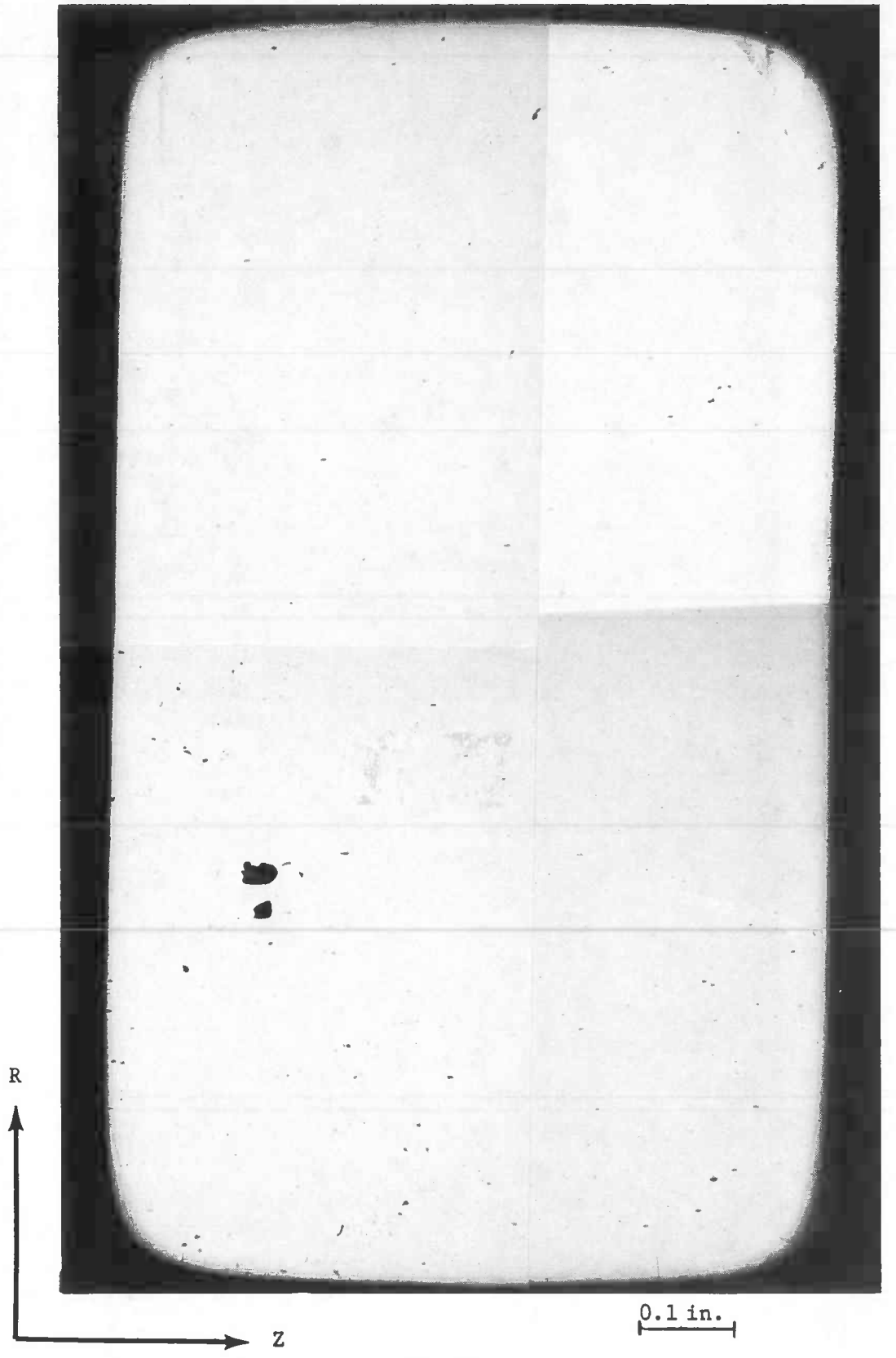

FIG. 96

Piece B114 from Buck 6 - 0.692 in. Removed,
0.0024 Area Fraction Flaw.

FIG. 97

Piece B114 from Buck 6 - 0.755 in. Removed,
0.0045 Area Fraction Flaw.

FIG. 98

Piece B114 from Buck 6 - 0.819 in Removed,
0.0076 Area Fraction Flaw.

FIG. 99

Piece B114 from Buck 6 - 0.886 in. Removed,
0.0138 Area Fraction Flaw.

FIG. 100

Piece B1121 from Buck 6 - 0.002 in. Removed.
0.0027 Area Fraction Flaw.

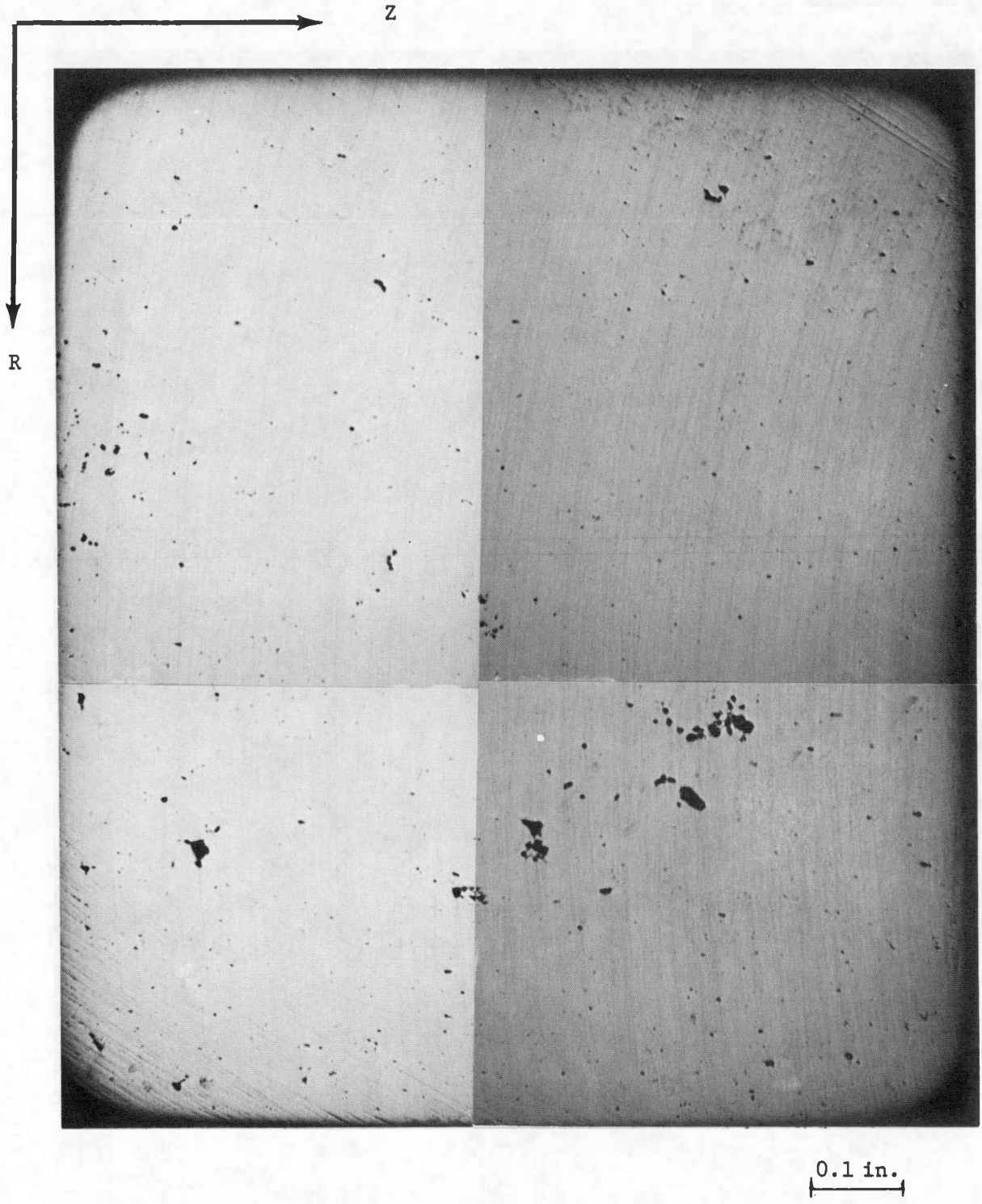

FIG. 101

Piece B1121 from Buck 6 - 0.065 in. Removed.
0.0071 Area Fraction Flaw.

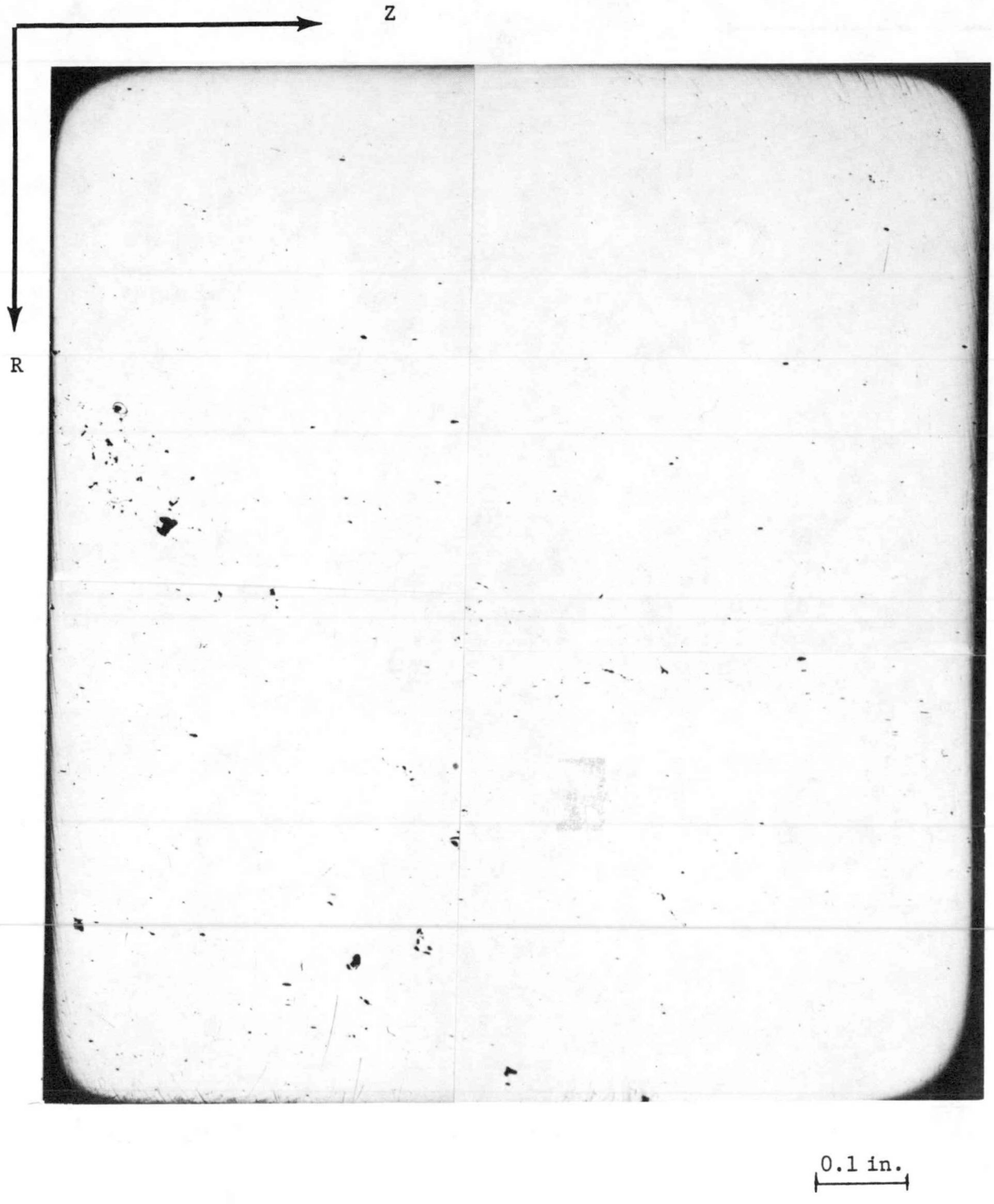

FIG. 102

Piece B1121 from Buck 6 - 0.131 in. Removed.
0.0022 Area Fraction Flaw.

FIG. 103

Piece B1121 from Buck 6 - 0.194 in. Removed,
0.0047 Area Fraction Flaw.

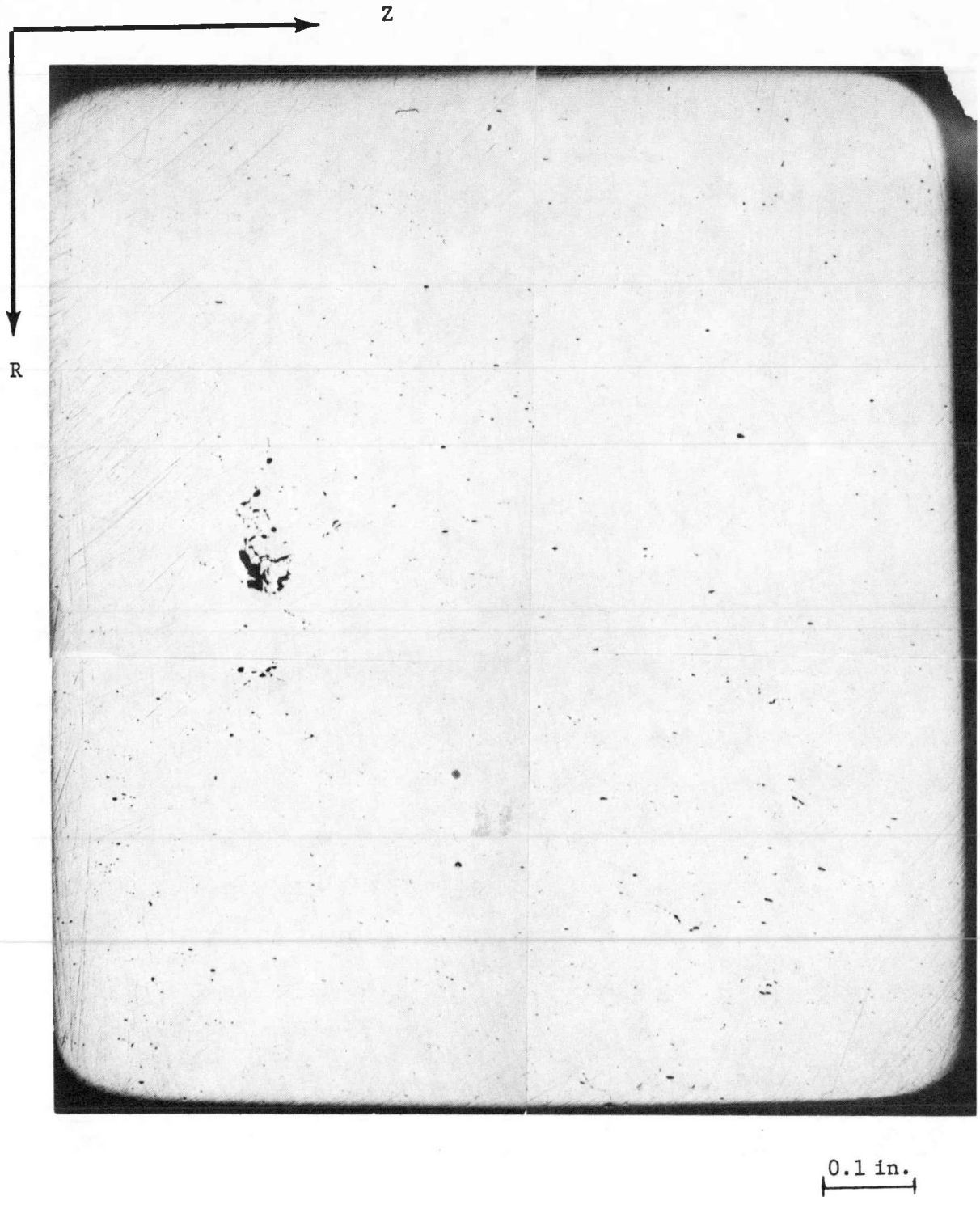

FIG. 104

Piece B1121 from Buck 6 - 0.255 in. Removed.
0.0020 Area Fraction Flaw.

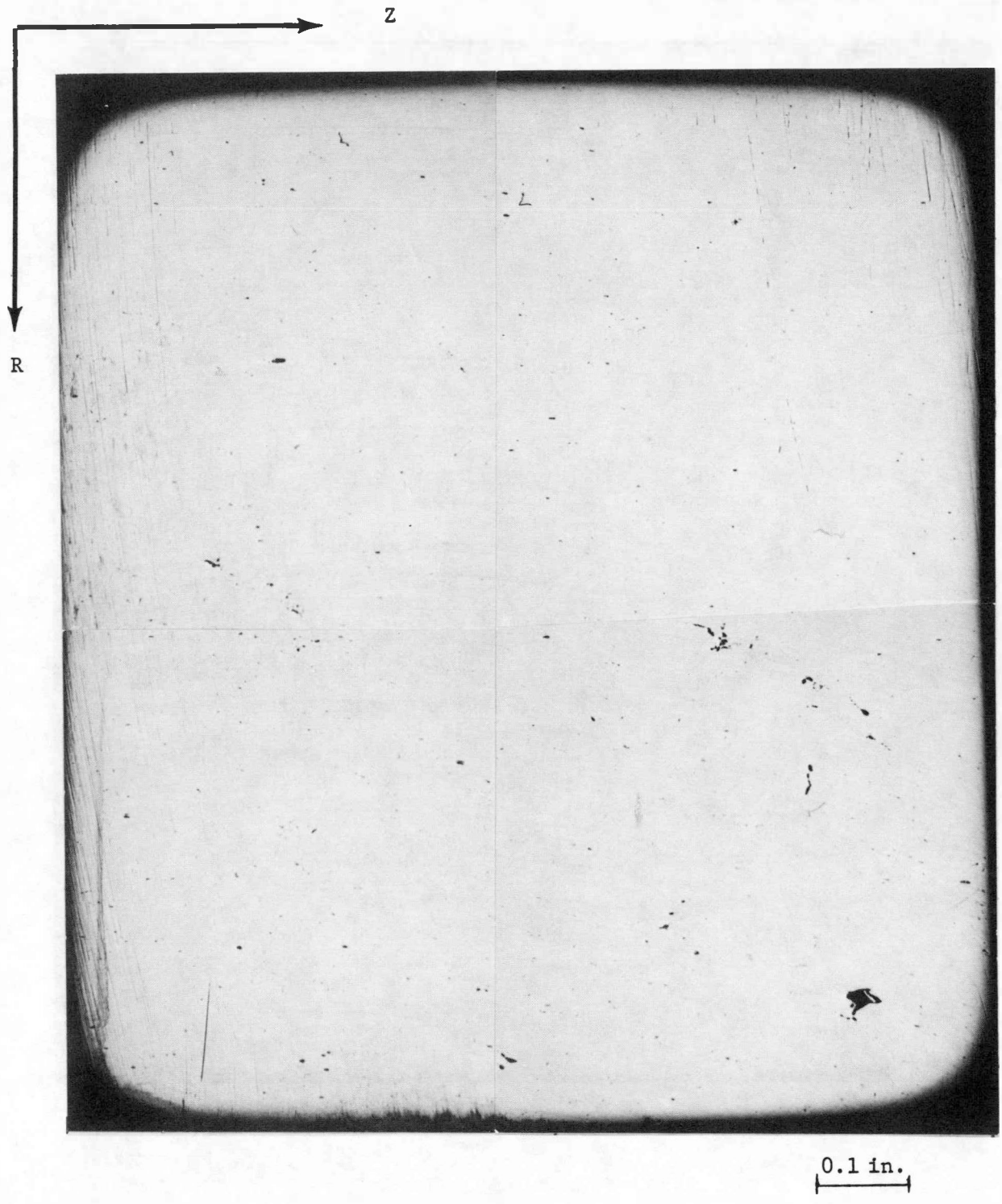

FIG. 105

Piece B1121 from Buck 6 - 0.323 in. Removed.
0.0018 Area Fraction Flaw.

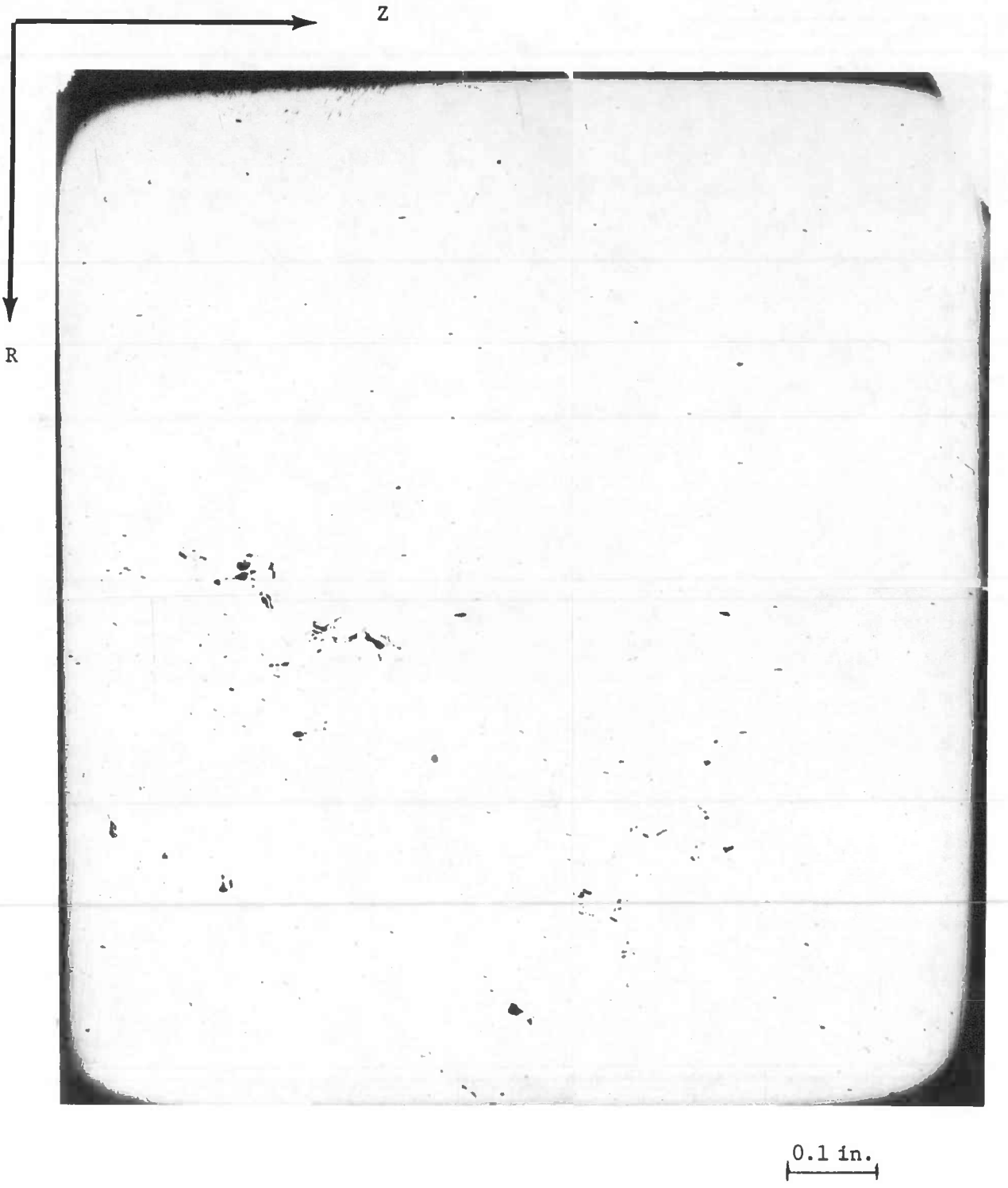

FIG. 106

Piece B1121 from Buck 6 - 0.386 in. Removed.
0.0022 Area Fraction Flaw.

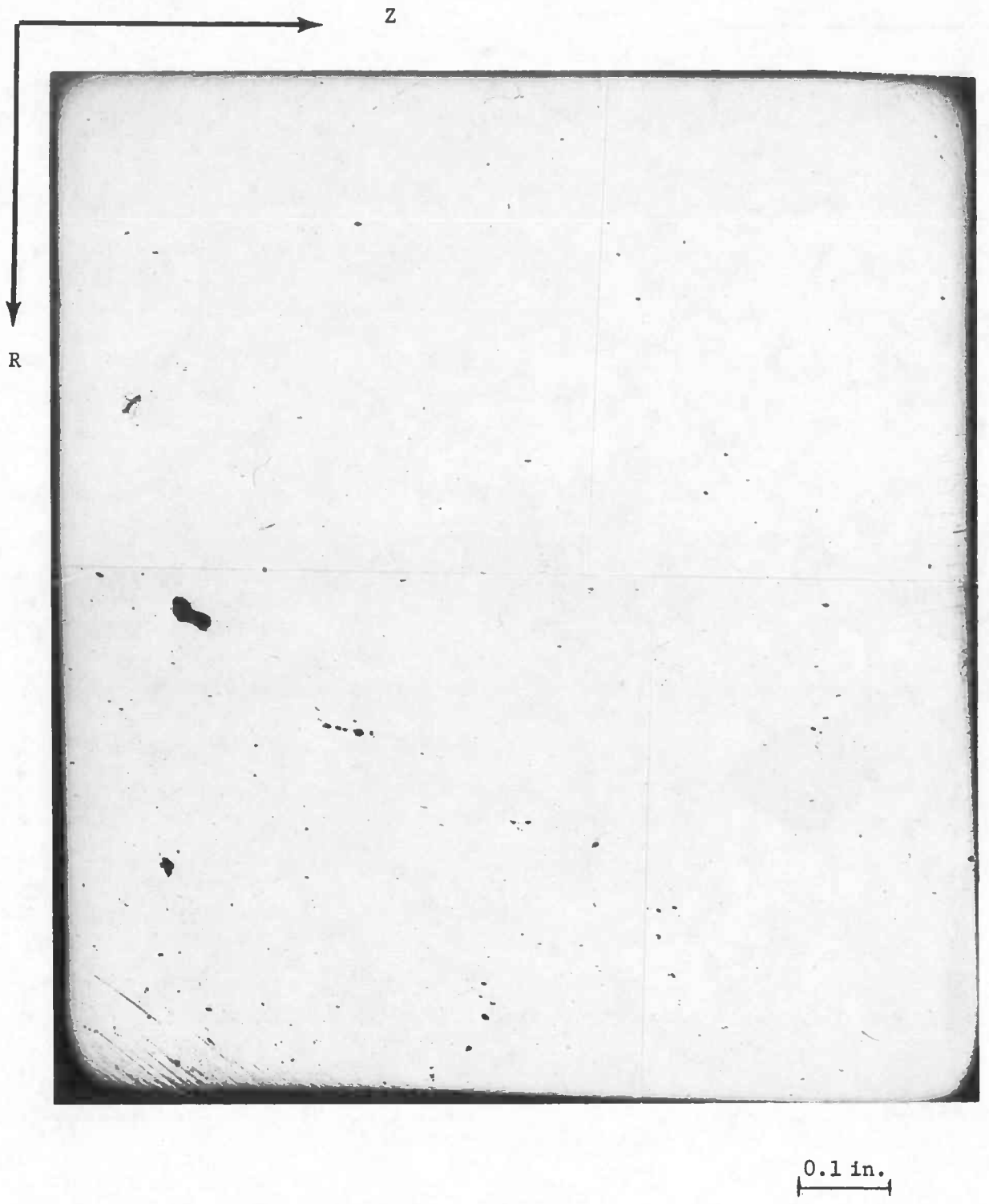

FIG. 107

Piece B1121 from Buck 6 - 0.448 in. Removed.
0.0022 Area Fraction Flaw.

FIG. 108

Piece B1121 from Buck 6 - 0.512 in. Removed,
0.0045 Area Fraction Flaw.

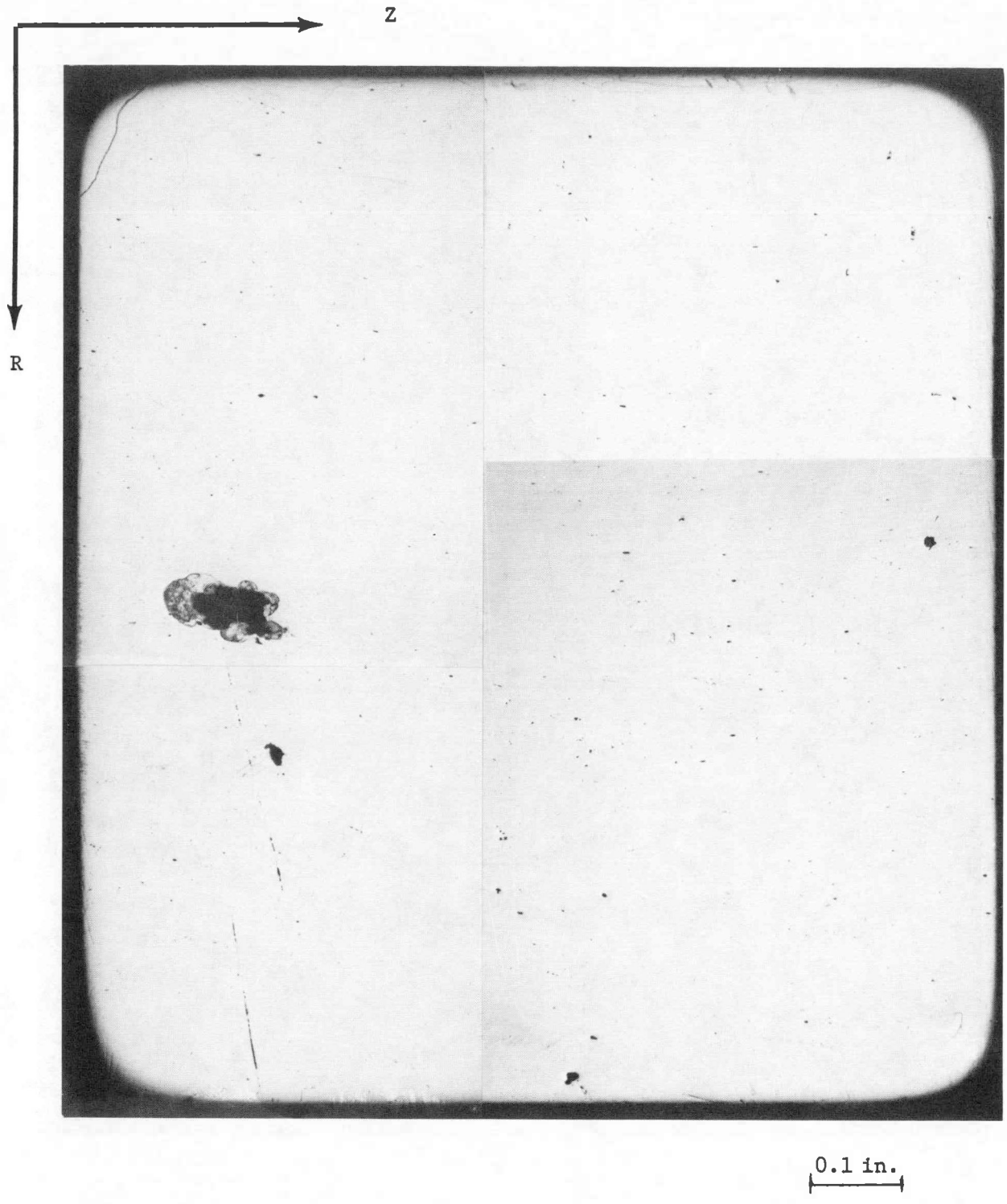

FIG. 109

Piece B1121 from Buck 6 - 0.574 in. Removed,
0.0037 Area Fraction Flaw.

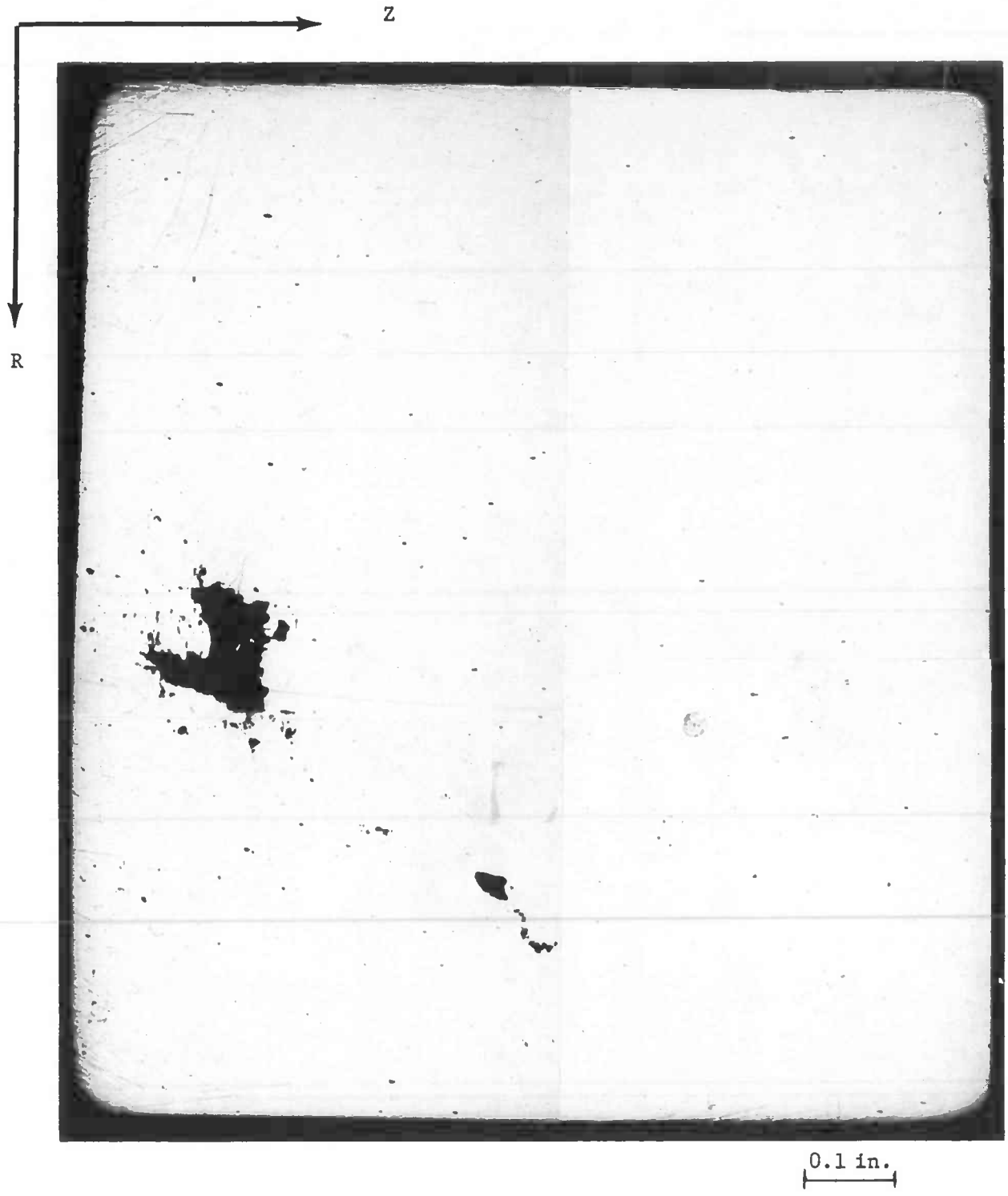

FIG. 110

Piece B1121 from Buck 6 - 0.636 in. Removed,
0.0107 Area Fraction Flaw.

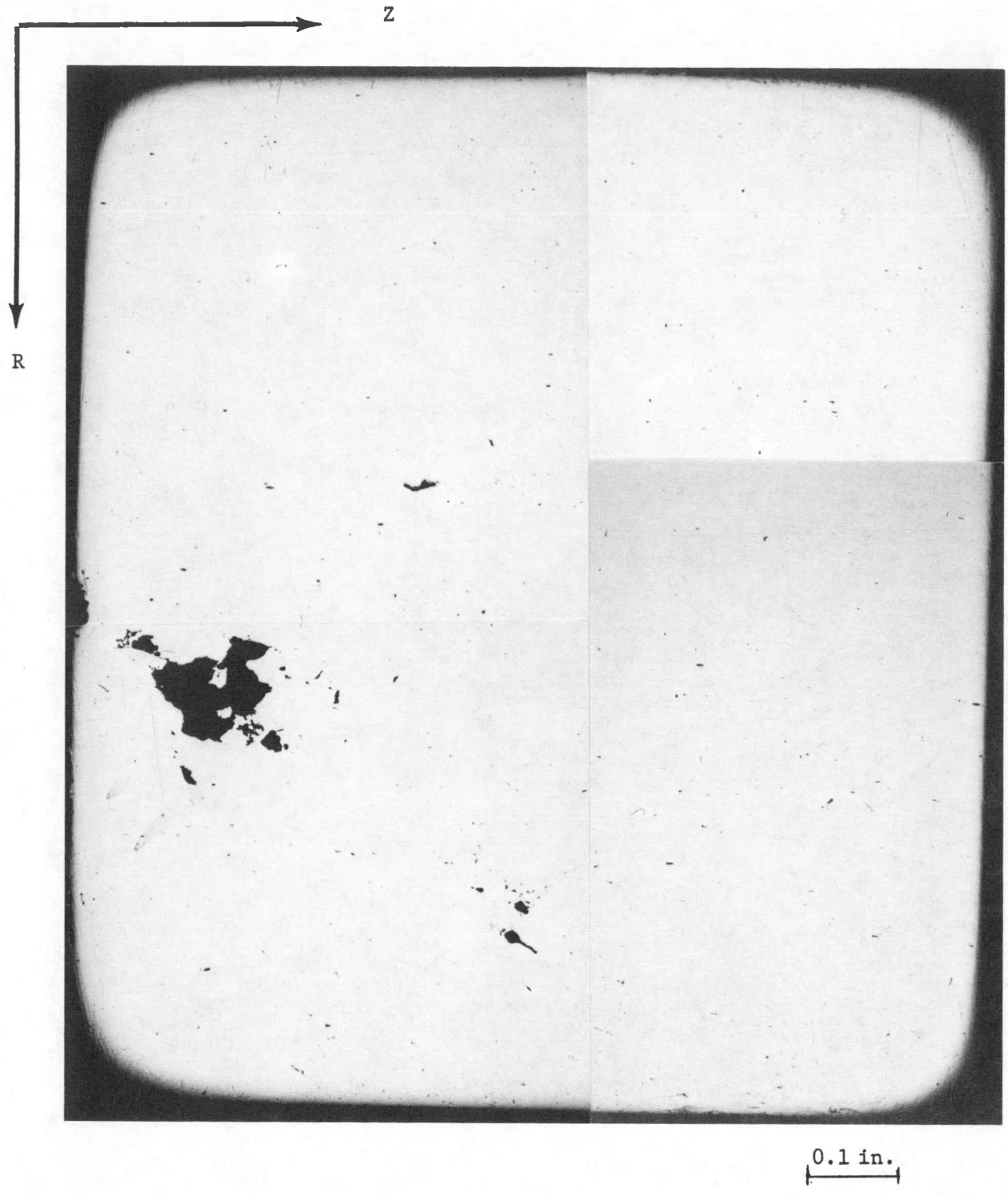

FIG. 111

Piece B1121 from Buck 6 - 0.698 in. Removed.
0.0079 Area Fraction Flaw.

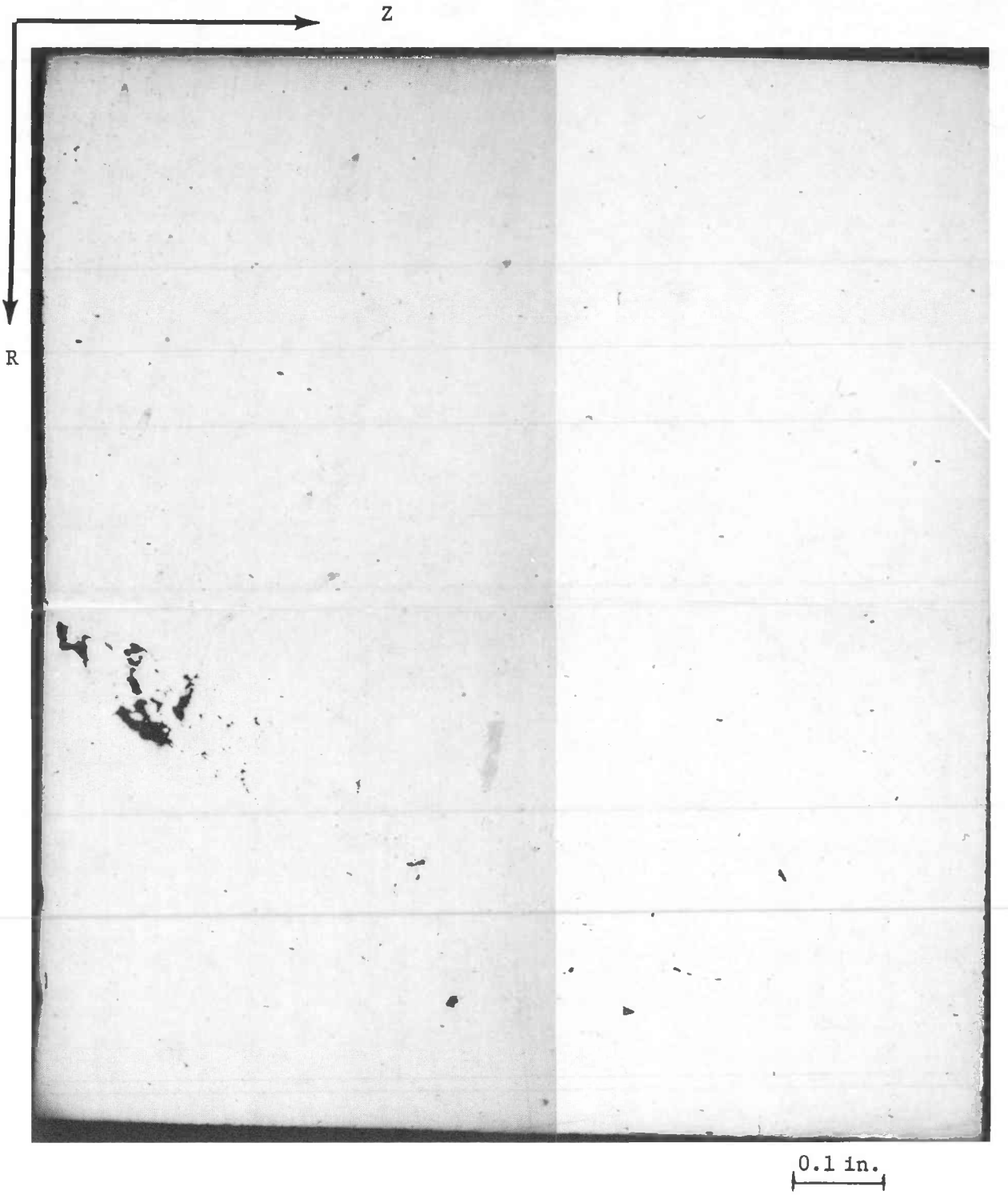

FIG. 112

Piece B1121 from Buck 6 - 0.761 in. Removed,
0.0038 Area Fraction Flaw.

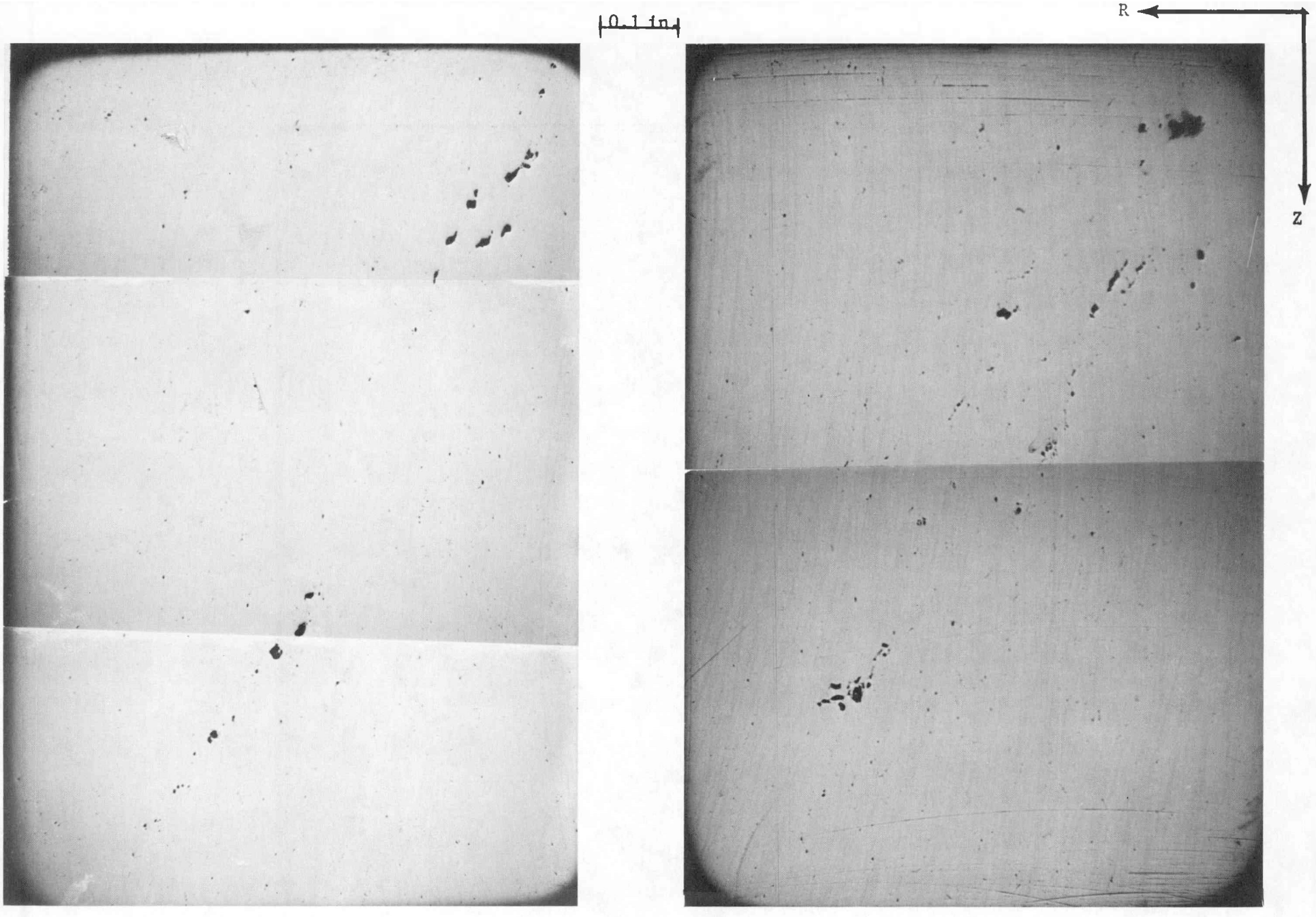

a) 0.002 in. removed.
0.0021 area fraction flaw.

b) 0.063 in. removed.
0.0030 area fraction flaw.

FIG. 113

Specimen B313 from Buck 6.

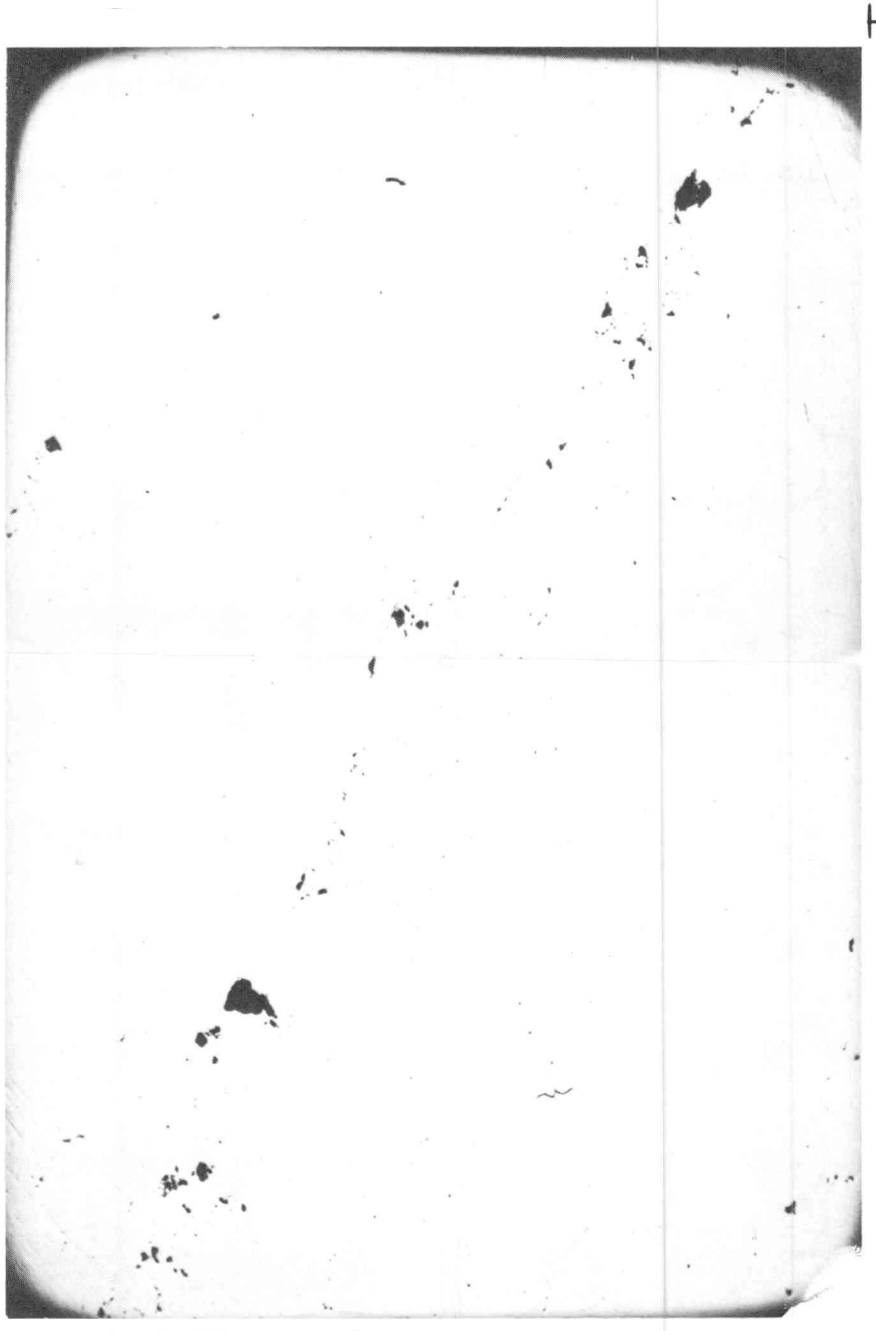

a) 0.101 in. removed.
0.0043 area fraction flaw.

b) 0.187 in. removed.
0.0116 area fraction flaw.

FIG. 114

Specimen B313 from Buck 6.

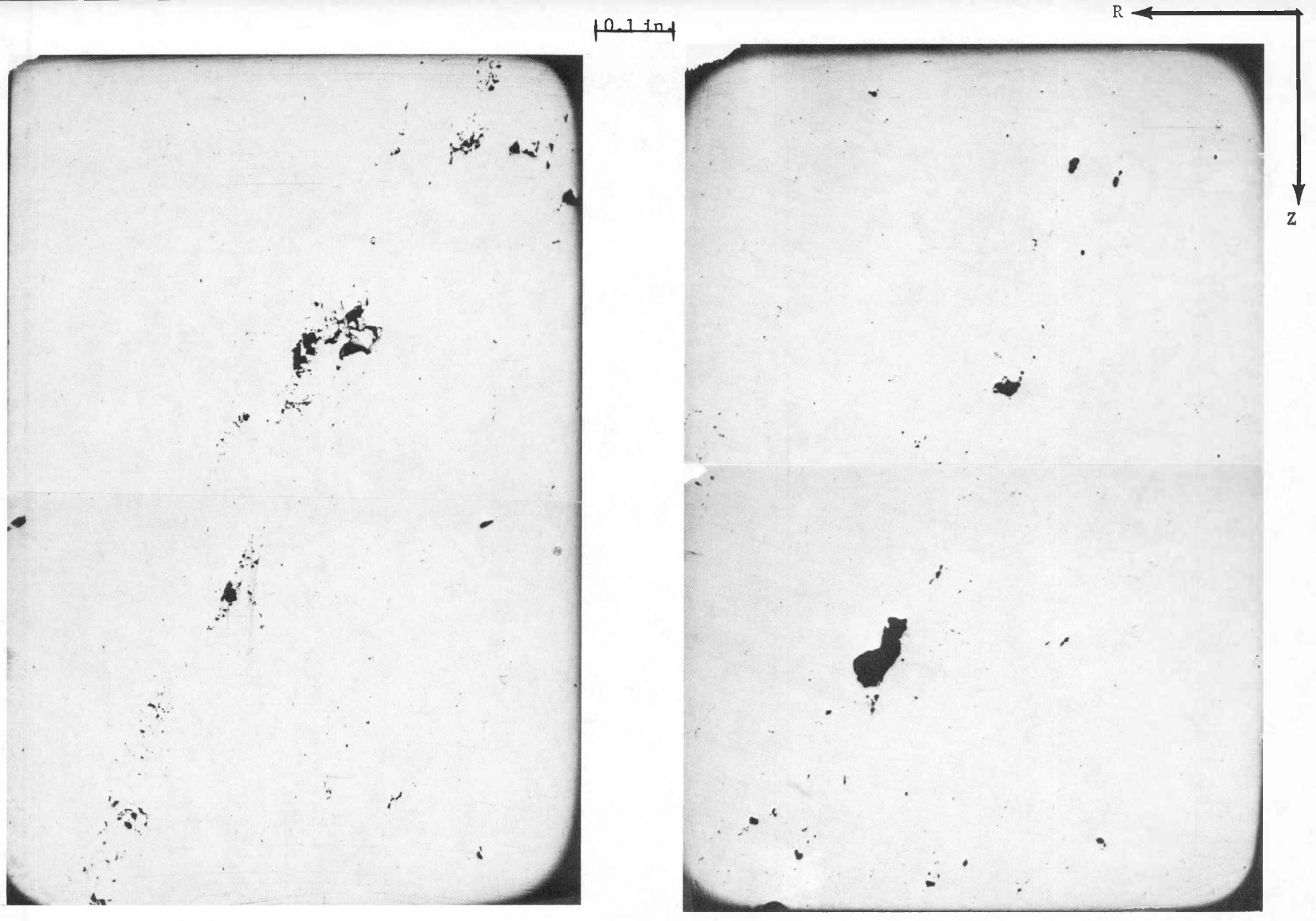

a) 0.252 in. removed.
0.0062 area fraction flaw.

b) 0.311 in. removed.
0.0061 area fraction flaw.

FIG. 115

Specimen B313 from Buck 6.

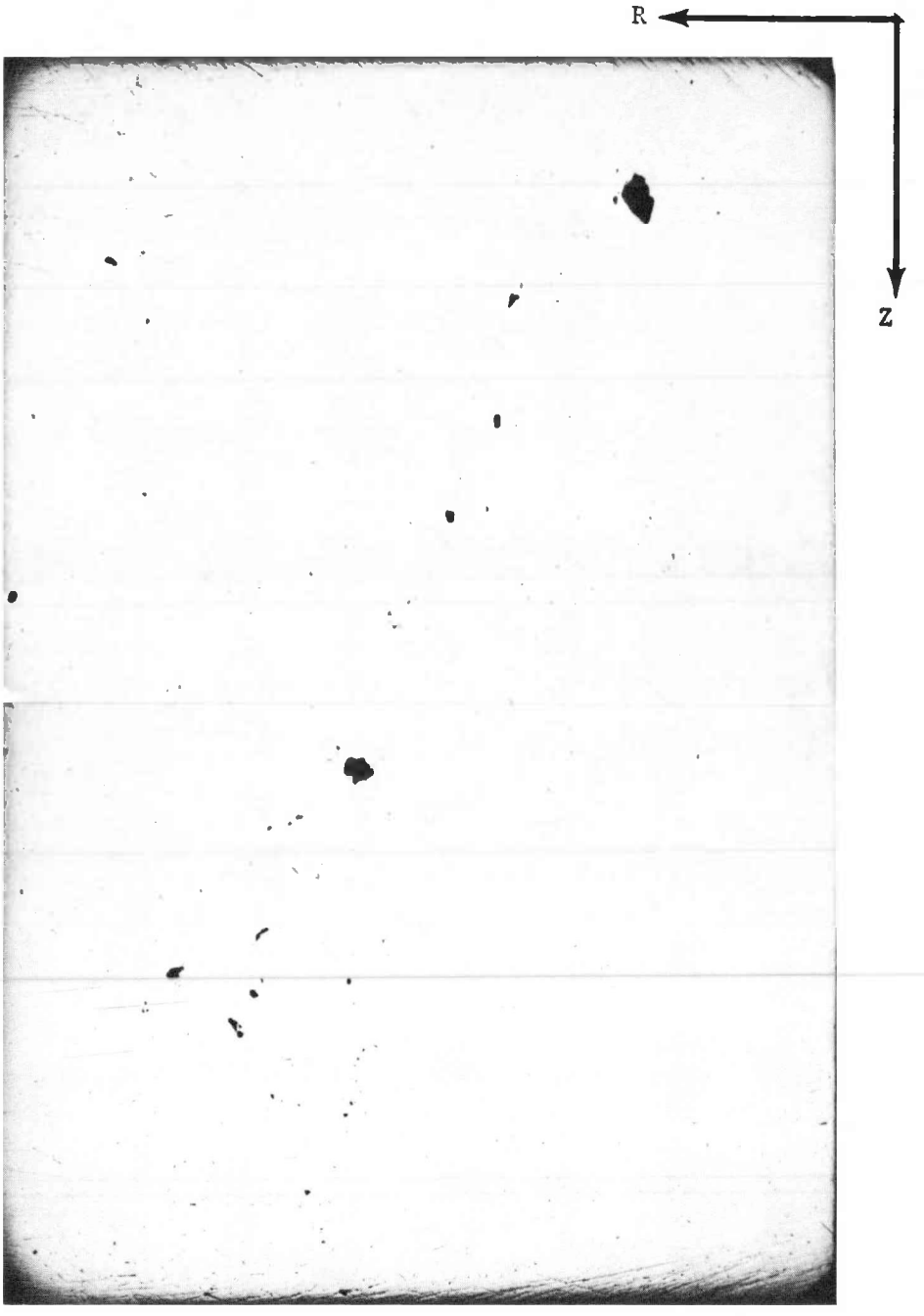

0.372 in. removed.
0.0027 area fraction flaw.

FIG. 116

Specimen B313 from Buck 6.

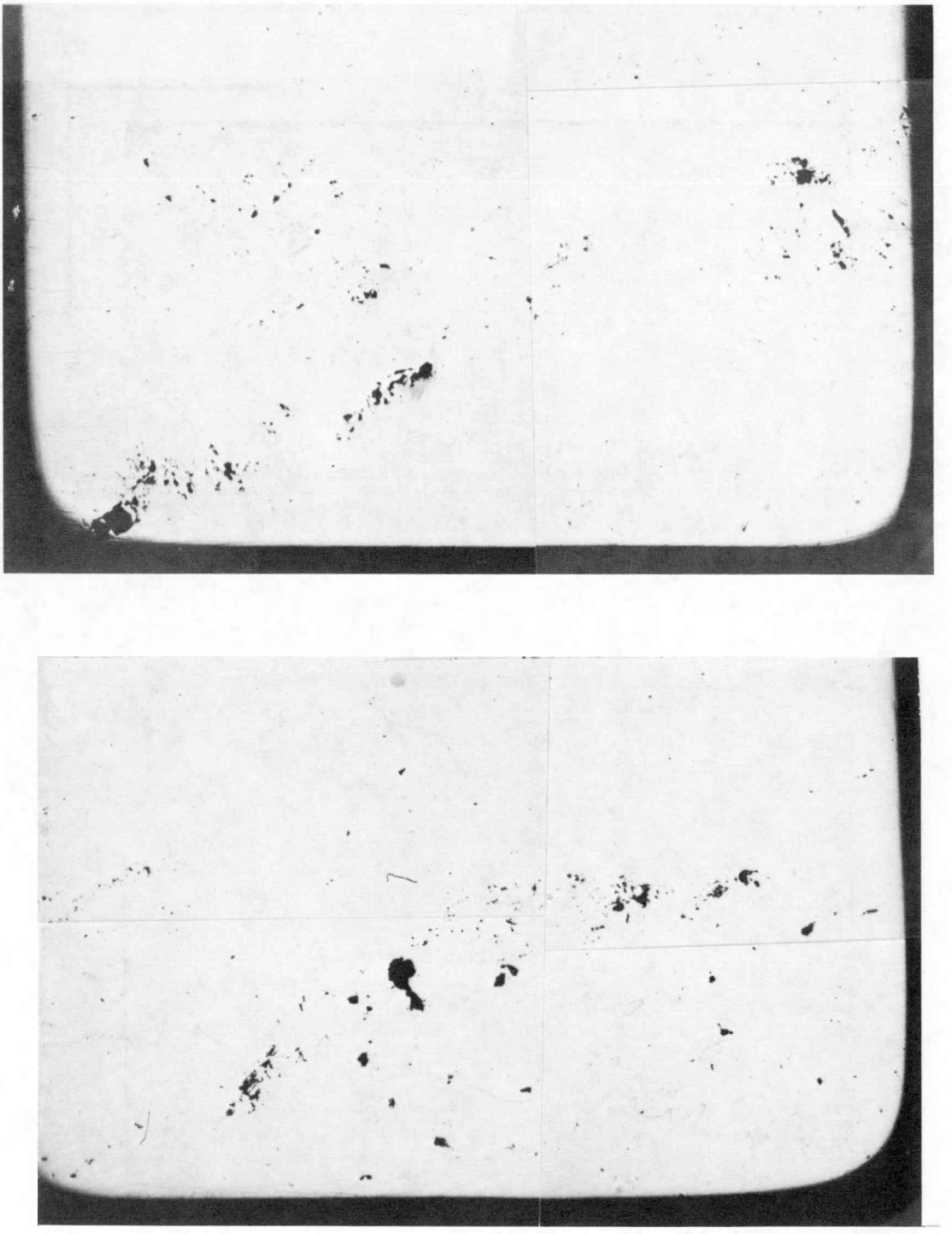

FIG. 117

Flawed Areas of Piece B312 from Buck 6. Bottom Edges are at Bore. Planes 0.06 in. Apart. Mag. 6X.

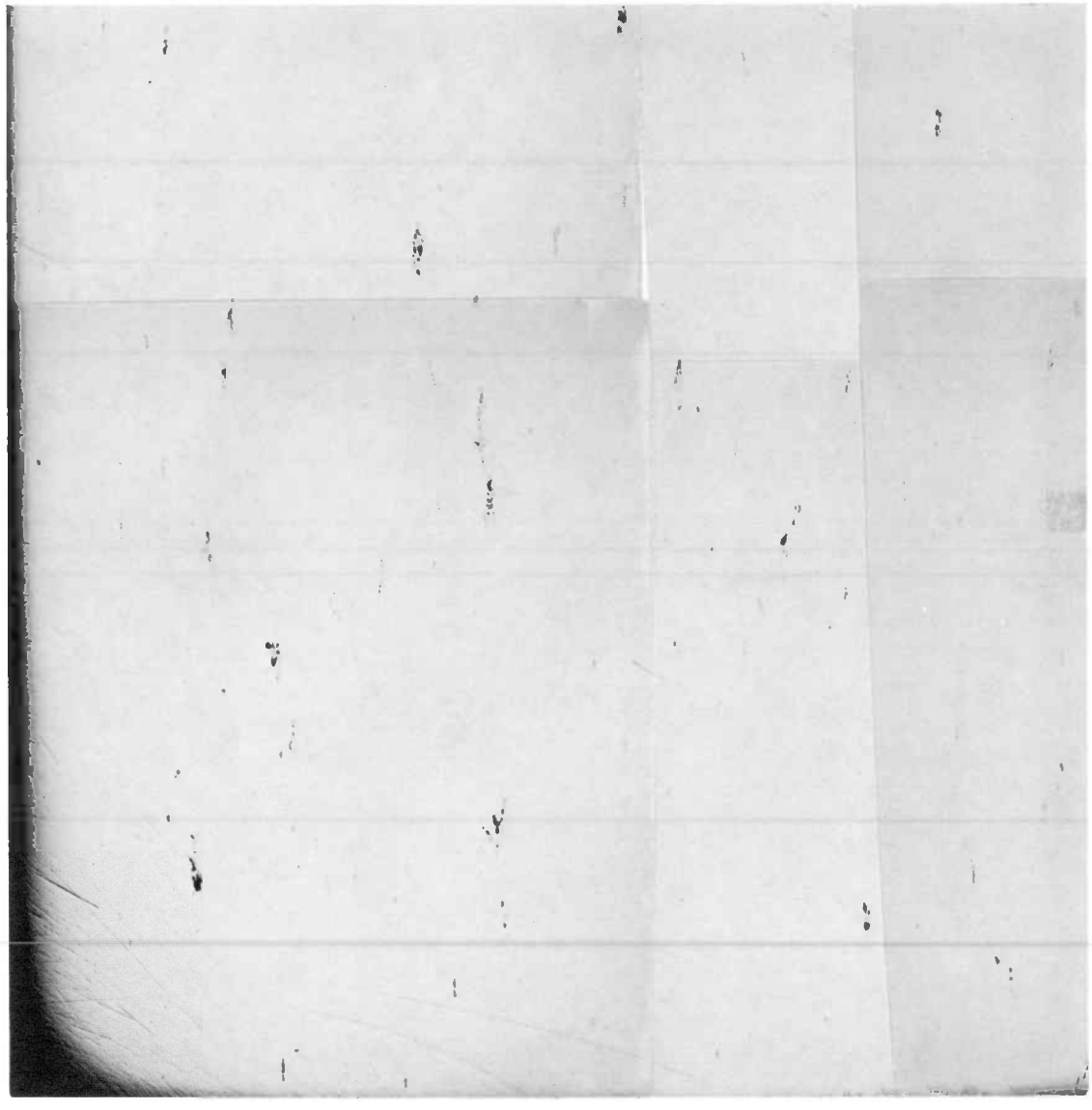

FIG. 118

RZ Plan of Polish 1/4" Below Fracture Surface of Joppa 3 LCF Specimen. Z = 145". Original Bore of Left Side, Z Axis Vertical. Mag. 6X.

Steam Turbine Rotor Reliability - Task Details

Task 4. Material Mechanical Properties Measurements

Prepared by

WESTINGHOUSE ELECTRIC CORPORATION
Research and Development Center
1310 Beulah Road
Pittsburgh, Pennsylvania 15235

Principal Investigators

G. A. Clarke
T. T. Shin
L. D. Kramer

Blank Page

ACKNOWLEDGMENTS

The authors would like to acknowledge the work of members of three separate Westinghouse Laboratories for their part in the completion of this program.

1. The Steam Turbine Divisions Materials Engineering Laboratory.
2. The Materials Testing and Evaluation Laboratory at the Research and Development Center.
3. The Structural Behavior of Materials Laboratory at the Research and Development Center.

In particular, the work of John Olszewski and Ashok Hattangadi of the Steam Turbine Division, along with Dick Hewlett and Pete Barsotti of the Research and Development Center is gratefully acknowledged. A special note of thanks goes to Bill Pryle for managing to keep the many specimens from various locations identified and recorded. The help of Charles Brenneman of the R&D ultrasonic group is also noted. The substantial effort from Andy Madeyski regarding the fractographic examination of the test specimens deserve a special acknowledgment along with the many pages of typing by Donna Gongaware. Final acknowledgment goes to the Project Manager of this task, Ed Wessel for his guidance and technical expertise and to W. G. Clark, Jr. as well as B. B. Seth for their critical review and helpful comments.

Blank Page

CONTENTS

SUMMARY

An extensive evaluation of the mechanical properties of two 1950 vintage air-cast CrMoV steel rotor forgings was conducted to provide data for an Electric Power Research Institute sponsored program (EPRI RP502) to develop an improved reliability prediction methodology for steam turbine rotors. The rotors investigated included the T.V.A. Gallatin Station No. 2 IP-LP rotor which burst in June 1974 and the Electric Energy Inc. Joppa Station No. 3 IP-LP rotor which was retired after 17 years of service. Tensile, Charpy, impact, fracture toughness, fatigue crack growth and low cycle fatigue data were developed for both rotor materials under a wide variety of loading conditions. Creep and blunt notch fatigue crack initiation tests were also conducted with the Gallatin material.

In addition to the mechanical testing, detailed fractographic examination of broken test specimens was undertaken to both characterize and identify the controlling fracture mechanisms. The fractographic features associated with various testing conditions were compared with the fractographic evaluation of the Gallatin rotor burst. A brief summary of the Gallatin rotor failure scenerio is also included. With regard to the mechanical testing of the Gallatin material, it was found that the mechanical properties were similar to other 1950 vintage rotors. The only test performed which showed any evidence of intergranular cracking, similar to that found in the Gallatin rotor, was a 23 hour dwell time low cycle fatigue test conducted at a nominal strain range of 2.98% at 800°F (427°C). A biaxial state of stress had no effect on the initiation of fatigue cracks in blunt notched CT specimens when tested at 800°F (427°C) with a one hour dwell period. This result as well as the absence of any intergranular cracking at the initiation site, suggests that a creep phenomena did not play a dominant role in the initiation of cracks in these specimens.

An evaluation of peak load dwell time effects on cyclic loading revealed a three fold increase in fatigue crack growth rate with an increase in dwell time from 15 minutes to 22-2/3 hours at 800°F (427°C). Again, it was noticed that fatigue cracking was trangranular.

The mechanical properties of the Joppa No. 3 rotor was found to be uniform throughout the axial and radial extent of the rotor. These properties were also found to be similar to the properties of other 1950 vintage CrMoV rotors. The uniformity of the Charpy impact properties would suggest that the Joppa rotor saw little if any in service degradation. The fatigue crack growth rate of the Joppa rotor was found to be similar to the Gallatin rotor as well as two other Westinghouse retired rotors. A three dimensional surface representing log da/dN - log T - log ν was found to describe the interaction of temperature and frequency of the fatigue crack growth rate for this material.

A complete toughness versus temperature curve was developed for the Joppa material using K_{Ic} and J_{Ic} techniques. A good agreement was found between the estimated value of toughness using the Begley-Logsdon correlation method and actual test results.

The large low cycle fatigue specimens showed a classic example of the linkup process between defects. It was observed that in an approximately constant stress field, the linkup process occurred in a three dimensional pattern, with the crack front searching out defects on various nearby planes. Further investigation is needed to understand and characterize the linkup process in order to develop an accurate life prediction model for this behavior.

1. INTRODUCTION

Failures of turbine and generator rotors generally have been due to a combination of factors involving stresses, temperature, material properties and discontinuities, all acting collectively in an unfavorable manner. The catastrophic circumstances associated with such failures have well documented[1.1, 1.2, 1.3]. In order to reduce the possibility of a rotor failure, a comprehensive understanding of the individual events that may lead to the final failure is essential. Further, it is important to determine what interaction these individual events can have on each other.

During the past 20 years, significant improvements in steel making practice, improved inspection capability, and improved material properties have resulted in both larger as well as structurally more sound rotors. This has caused a dichotomy in steam turbine reliability in as much as the larger, more efficient steam turbines are being used for continuous service, while the older, less efficient machines are being used for what may be more severe daily duty cycle. To ensure the continued reliability of these older turbines,it has become necessary to make more frequent in-service inspections of the turbine rotors. To evaluate the integrity of a turbine rotor once an inspection has taken place is at best a complex and often an approximate procedure.

To aid the electrical industry in the understanding of the various mechanisms affecting the reliability of rotors and to make a more educated judgment as to the condition of a specific rotor, EPRI has sponsored a project, RP502, on "The Reliability of Steam Turbine Rotors". This project was divided into four sections with specific tasks being undertaken as follows:

Task I - The Lifetime Prediction Analysis System (Southwest Research Institute)

Task II - Nondestructive Evaluation (Battelle Memorial Institute)

Task III - Destructive Tests (Westinghouse R&D - Materials Evaluation and Applications)

Task IV - Material Mechanical Properties Measurements (Westinghouse R&D - Structural Behavior of Materials)

This report describes the various mechanical testing and fractographic analyses completed under the Task IV portion of this program. A detailed discussion of how the results affect the possible outcome of the lifetime prediction analysis scheme prepared by Southwest Research Institute, is also included.

While this project was not designed to demonstrate that the life prediction analysis would have predicted the Gallatin failure if prefailure ultrasonic test records had existed, it was hoped that a more clear understanding of the failure mechanism attributed to the Gallatin rotor burst[1.4, 1.5] would air in determining any inherent weakness in the predictive system. It is with this goal in mind that the report is essentially made up of three parts: (1) the results of a microstructural analysis of the Gallatin rotor material, (2) the mechanical and fractographic test results on Gallatin rotor material and (3) the mechanical and fractographic test results of the Joppa #3 material.

1.1 REFERENCES

1.1 Emmert, H. D., "Investigation of Large Steam Turbine Spindle Failure," Trans. ASME, 1956, 78, pp. 1547.

1.2 Deforest, D. R., Grobel, L. P., Schabtach, C. and Sequin, B. R., "Investigation of the Generator Rotor Burst at the Pittsburgh Station of the Pacific Gas and Electric Co.," ASME Paper No. 57-PWR-12, 1957.

1.3 Schabtach, C., Fogleman, E. L., Rankin, A. W., and Winne, D. H., "Report of the Investigation of Two Generator Rotor Fractures," Trans. ASME, 1956, 78, pp. 1567.

1.4 Kramer, L. D. and Randolph, D. D., in the 1976 ASME-MPC Symposium on Creep-Fatigue Interaction, R. M. Curran, Ed., ASME, New York, 1976, pp. 1-24.

1.5 Weisz, D. A., in the 1976 ASME-MPC Symposium on Creep Fatigue Interaction, R. M. Curran, Editor, ASME, New York, 1976, pp. 25-40.

2. MICROSTRUCTURAL STUDIES OF THE GALLATIN ROTOR

It would be a fruitless exercise, if the life prediction computer program were developed with total disregard to the failure mechanism attributed to the Gallatin rotor burst. However, a number of questions regarding the microstructure found at the failure origin remained unanswered. Therefore, a detailed evaluation of the microstructure in the Gallatin material was necessary. The tests performed in this evaluation included metallographic, fractographic, Auger and residual gas analysis of the segregated regions in the Gallatin rotor. The results of these tests are presented, following a brief summary of the scenerio of the Gallatin rotor failure.

2.1 The Failure Scenerio of the Gallatin Rotor as Determined by Westinghouse Steam Turbine Division

Prior to the inception of EPRI 502 program, the failure analysis of the Gallatin #2 steam turbine IP-LP rotor from the Tennessee Valley Authority Gallatin Station was analyzed by the Steam Turbine Division of the Westinghouse Electric Corporation. A detailed documentary ranging from the fabrication of the rotor to the actual failure was reported by Kramer, et al.[2.1] The salient high lights of this description are presented below.

The manufacturing records of the Gallatin rotor forging revealed that there was nothing unusual in the process cycle for this 1954 rotor. The rotor was forged from an ingot which was fabricated with state-of-the-art techniques at the time of manufacture. These techniques would not, however, be considered as adequate by present day steel making practices. The ingot from which the Gallatin forging was made was air-cast whereas modern forgings are made from vacuum-degassed ingots. The older air-cast ingots were generally richer in low level chemical elements such as sulfur. The Gallatin rotor was one of

two 55" dia. x 224" long forgings taken from a 108 inch inner diameter mold. Again, this multiple forging practice is not normally used today.

From the fractographic analysis it was observed that the failure origin was located near the bore under the seventh row of blades in the IP end of the rotor. This location nearly corresponds to the ingot center line approximately one third of the axial distance from the stool piece cropping location, as shown in Figure 2.1. During the ingot solidification process, the material surrounding the origin would be expected to have a well developed columnar microstructure. An example of this structure can be seen as dark streaks in Figures 2.2 and 2.3. These streaks represent interdendritic areas containing positive alloy segregation which was developed by the rejection of the solute elements into the liquid phase ahead of the advancing dendrites. These areas also favor entrapment of inclusions. This would tend to cause both the positive alloy segregation and the MnS inclusions to remain in a distinctly distributed pattern in the forging. The microstructure at the failure origin of the Gallatin rotor is unique in as much as it is the only large cross-sectional region examined which contained a positive alloy segregation pattern along with extensive MnS inclusions.

A description of the microstructure near the failure origin site is presented below to aid in the understanding of the sequence of events which led to the ultimate failure of the rotor. First, a highly duplexed grain size existed in the bands of positive alloy inverse "V" segregation. The fine grained portions of this microstructure was significantly smaller than an ASTM 8 grain size. Many grain boundaries contained large $M_{23}C_6$ carbides. Other carbide species were absent between triple points causing a carbide denuded zone adjacent to the grain boundaries. Electron microscopy of extraction replicas definitely revealed these fine grains to be associated with ferritic carbides. Fractography of the Gallatin origin revealed predominant intergranular cracking between the type II (platelets) MnS inclusions. It is assumed that the intergranular cracking is a result of creep damage.[2.1, 2.2]

If it is also believed that a creep-fatigue mechanism is responsible for the initiation and growth of cracks from the MnS inclusions; thus, it is possible that a critical size flaw could develop as the result of the linkup between aligned MnS inclusions.

After a critical size flaw was developed from the link up process, the following cold start resulted in a fast cleavage fracture to a radial extent of approximately 14 inches. The crack arrested at this point as a result of the lower thermal stresses and higher toughness associated with the higher temperature at this location.[2.2] The final unstable crack propagation took place during the subsequent cold start causing a catastrophic failure of the rotor on June 19, 1974 after 17 years of service.

2.2 Metallurgical Testing of the Gallatin Rotor Material

In order to investigate the extent of the features microstructural found near the failure origin area, etched macro slabs were arranged to represent an axial-radial slice through the IP portion of the rotor.[2.1] The steady state isotherms and the isostress lines were obtained by using a finite element computer program[2.2] and were directly plotted on the etched surface, as shown in Figure 2.4. Metallographic specimens M1, M2 and M3 were taken along the 800°F (427°C) isotherm at intersections of the 20 ksi, 28 ksi, and 40 ksi isostress lines. Specimens M4, M5 and M6 were taken along the 44 ksi isostress line at intersections of the 725°F, 700°F and 675°F isotherms. These specific locations were chosen to evaluate the variation in microstructure with both service temperature and stress. A sulfur print was taken from each specimen along with a macroetch of the surface using ammonium persulfate. The specimens were then sectioned in order to establish the grain size and general microstructure. A sodium tradecyl benzene sulfonate etchant (STBS) was used.

Metallography [2.1] was conducted on specimens M1, M2 and M3 to determine if the Gallatin origin microstructure was stress dependent. While the macroetch and sulfur print do show segregation bands, they tend to be more dispersed and contain less intense MnS clusters than

previously noted at the primary failure origin. The grain size in the banded area appeared to be smaller by about 1 ASTM number than in the non-segregated area. Generally, MnS aspect ratios were approximately unity; however, specimen M3 (near bore material) did contain some ellipsoidal sulfides. No cracking of any kind was noted in any specimen including the specimen M2 which did contain somewhat more proeutectoid in the non banded area than was found in the banded area. SEM metallography did not show anything significant beyond the optical techniques. TEM thinfoils of M1 exhibited the normal Fe_3C platelets and carbides right up to the grain boundaries (Figure 2.5).

The microstructural characteristics associated with the 44 ksi isostress line are shown in specimens M4 to M6. The macro etched and sulfur printed surfaces of these specimens did not look significantly different from those taken from the 800°F isothermal line (M1, M2, and M3). It was found that the metallography was similar at both banded and non banded locations. However some banded grain boundaries do not seem to respond to the STBS etchant. Within those banded areas which did respond to the STBS etchant no grain boundary cracking or high aspect ratio MnS inclusions could be found. Slight amounts of cavitation and massive $M_{23}C_6$ grain boundary carbides were noted by SEM, but not nearly as predominate as those found at the fracture origin site.

The only significant variation in microstructure within the segregated bands were found by transmission electron microscope (TEM) thin foil metallography of specimens M1 and M5 (periphery verses near bore material). From the thin foil TEM metallography of specimen M5, a ferrite-ferrite grain boundary with massive $M_{23}C_6$ carbides along with an almost carbide free ferrite grain boundary is shown in Figure 2.6. The Fe_3C platelets and the denuded bainitic grains are shown in Figure 2.7. Again the $M_{23}C_6$ carbides are present but to a less degree than at the failure origin site. It should be noted that the material used in these TEM micrographs, taken from specimen M5, is similar in microstructure to the material adjacent to the Gallatin #2 primary and secondary failure origins. The detailed metallographic examination described above clearly

indicate that the microstructure at the failure origin was different from the material immediately adjacent to the origin.

2.3 Residual Gas Concentration Analysis of Segregated Areas

As a means of determining the environment that an internal flaw would encounter, a residual gas analysis was made on segregated material taken from points midway between the bore and the periphery of the Gallatin rotor. The concentrations of both oxygen and hydrogen were determined by the LECO technique. The concentration of nitrogen was determined by the Kjedahl technique. The results of the gas analysis on material taken from four axial locations; cold end (shaft), row 8, row 6 and hot end, are presented in Table 2.1. As can be seen, the oxygen, nitrogen and hydrogen contents are highest at the cold end of the rotor decreasing towards the hot end.

A previous metallographic analysis of the Gallatin shaft material did not reveal oxides, silicate inclusions or any other sources of oxygen which could possibly be entrapped within the structure. No evidence was found of gross entrappment of nitrogen or its compounds. The 3.6 ppm hydrogen concentration in the rotor shaft may be considered as rather high when compared to present day rotors; however, it would not be considered as abnormal for a similar sized 1950 vintage air-cast CrMoV rotor.[2.3] Even with this rather high hydrogen content, no excessively low room temperature tensile ductilities (see Section 3.1) or hydrogen flaking was found in this rotor. From the above results it can be concluded that the residual gas concentrations are not abnormal for this vintage rotor steel.

2.4 Scanning Auger Analysis

Lead contamination from electric furnace melting stock has been known to cause elevated temperature grain boundary liquidation problems in aircraft gas turbine disk forgings. Although this problem has not been encountered by the electrical industry, Scanning Auger Analysis was performed on the Gallatin rotor material to evaluate the possibility of lead contamination. Since both primary and secondary

fracture origin surfaces were immediately contaminated during the burst as well as subsequent handling, no useful Scanning Auger Analysis could be made on these surfaces. Therefore specimens removed from the material near the failure origin were broken in the scanning auger unit (high vacuum) at liquid nitrogen temperatures. This procedure gives enough intergranularity on the uncontaminated fracture surface to develop a good grain boundary segregate profile. The resultant spectra, as shown in Figure 2.8, shows no trace of lead. Figure 2.8, however, did reveal phosphorous and tin elements known to produce temper embrittlement of alloy steel. These elements disappeared, as shown in Figure 2.9, after sputtering of the grain facets for three minutes indicating low concentration levels. The Auger analysis did not reveal any significant observations regarding the influence of trace elements on subsequent fracture behavior.

2.5 REFERENCES

2.1 Kramer, L. D. and Randolph, D. D., in the 1976 ASME-MPC Symposium on Creep-Fatigue Interaction, R. M. Curran, Ed., ASME, New York, 1976, pp. 1-24.

2.2 Weisz, D. A., in 1976 ASME-MPC Symposium on Creep-Fatigue Interaction, R. M. Curran, Ed., ASME, New York, 1976 pp. 25-40.

2.3 J. H. Stoll, "Vacuum Pouring of Ingots for Heavy Forgings," Presented to the AISI, May 21, 1958.

TABLE 2.1

RESIDUAL GAS ANALYSIS OF SELECTED LOCATIONS FROM THE GALLATIN #2 ROTOR

Element and Method	Location V1 (cold end)	Location V2 (row 8)	Location V3 (row 6)	Location V4 (hot end)
Total Oxygen (LECO)	35 ppm	34 ppm	23 ppm	30 ppm
Total Nitrogen (Kjedahl)	37 ppm	18 ppm	15 ppm	13 ppm
Total Hydrogen (LECO)	3.6 ppm	1.3 ppm	2.7 ppm	2.2 ppm

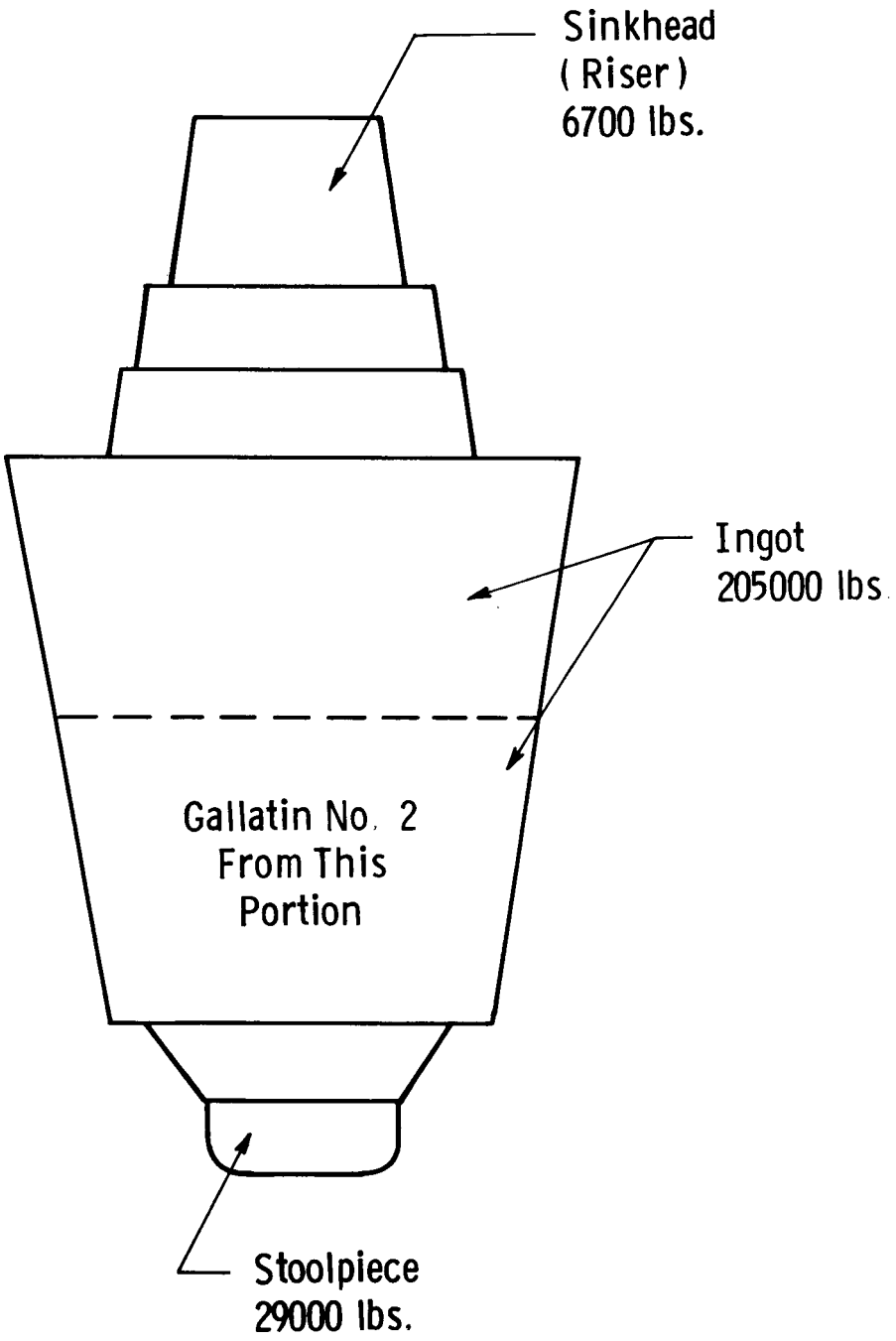

Fig. 2.1—Sketch of ingot used for the Gallatin rotor

Fig. 2.2 – 2.5X Ammonium persulfate macroetch showing segregation pattern in the Gallatin forging

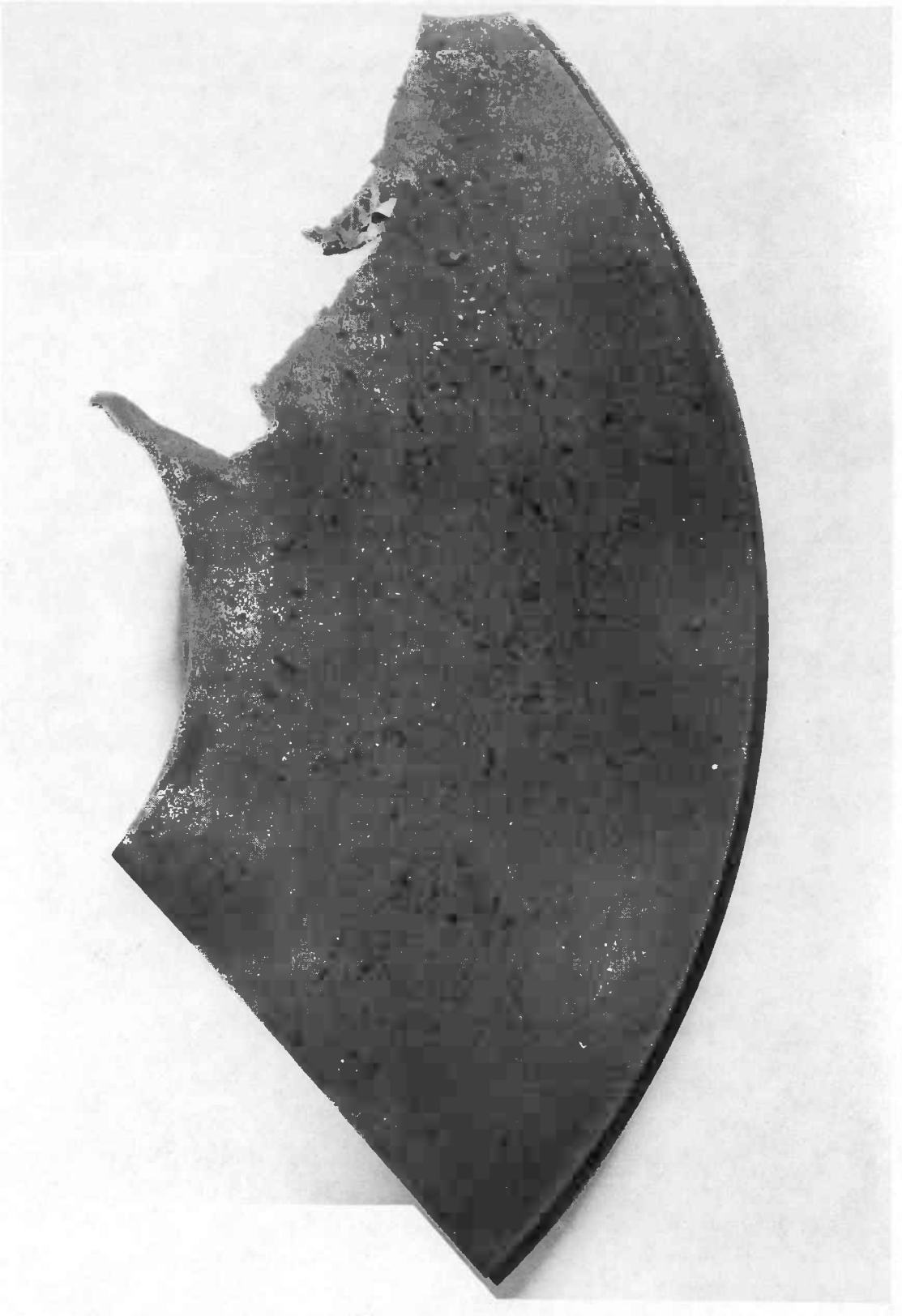

Fig. 2.3 – 2.5X Ammonium persulfate transverse macroetch of section shown in Fig. 1.2

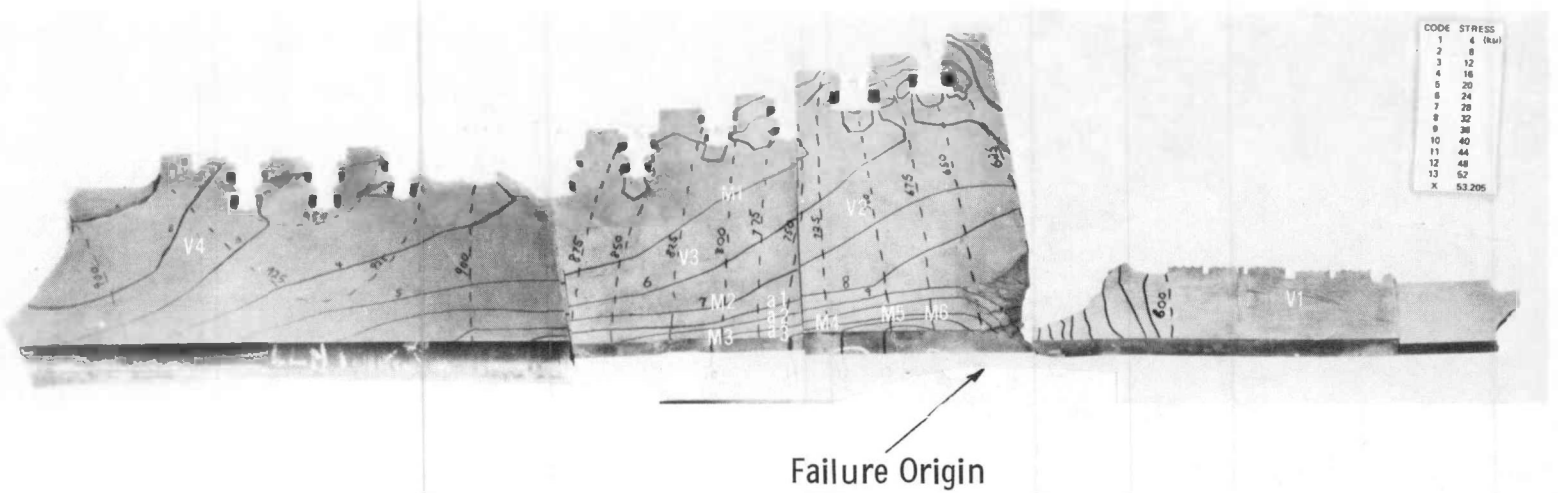

Fig. 2.4 – Ammonia persulfate etch. An overall view of the Task 1 microstructural characterization specimens. The identification code is as follows:

M ( ) – Re-macroetch, sulfur print, optical metallography, SEM
V ( ) – Residual gas analysis
a ( ) – Scanning auger analysis

Specimens M1 and M5 had additional TEM thin foil work. All specimens were removed from large macro etched bands

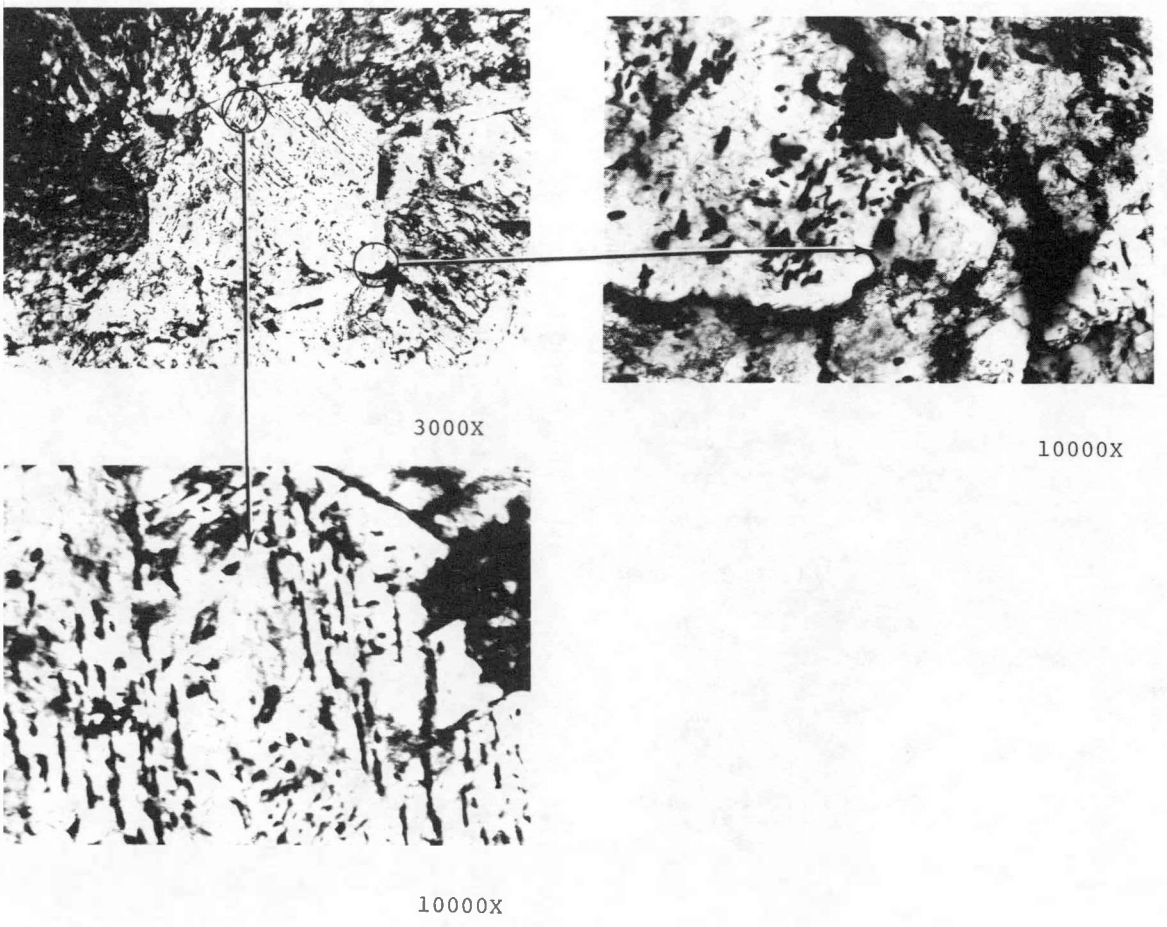

Fig. 2.5 — Magnifications as noted. Typical TEM thin foil of a bainitic area in M1 showing well defined Fe_3C platelets at 70° nominal orientations and lack of denudation (i.e. carbides up to grain boundaries)

Fig. 2.6 – 20000X. TEM thin foil from M5 showing massive grain boundary $M_{23}C_6$ and adjacent fine grained ferrite. Ferritic 'H' carbides are extremely agglomerated with Mo_3C carbides decorating the grain boundaries and denuding the adjacent area

Mag: 25,000X

Fig. 2.7 – 25000X. Denudation along a bainitic grain in M5. Note the Fe_3C spherordization compared to Figure 12

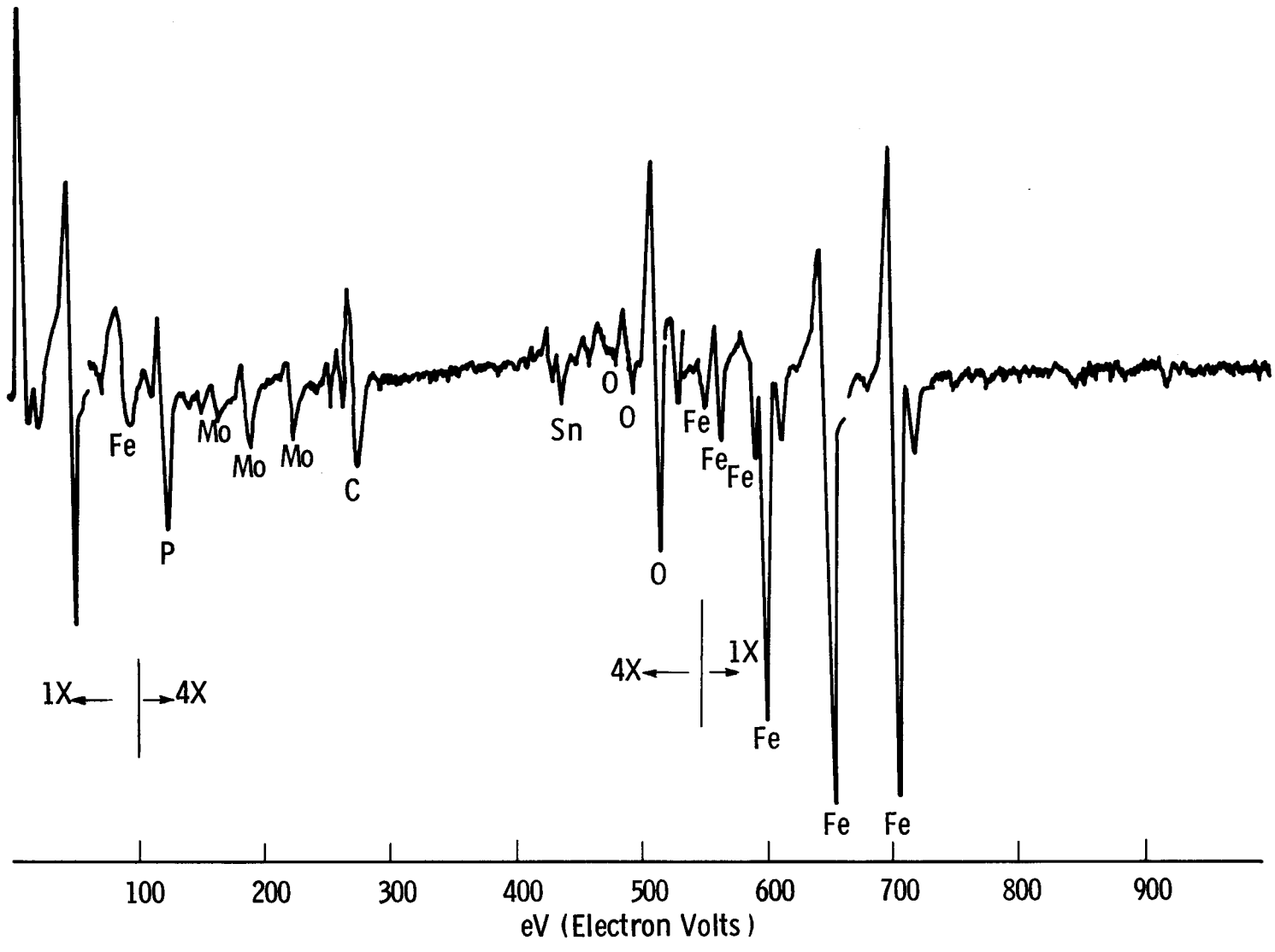

Fig. 2.8 — Auger spectra of sample A3- no sputtering

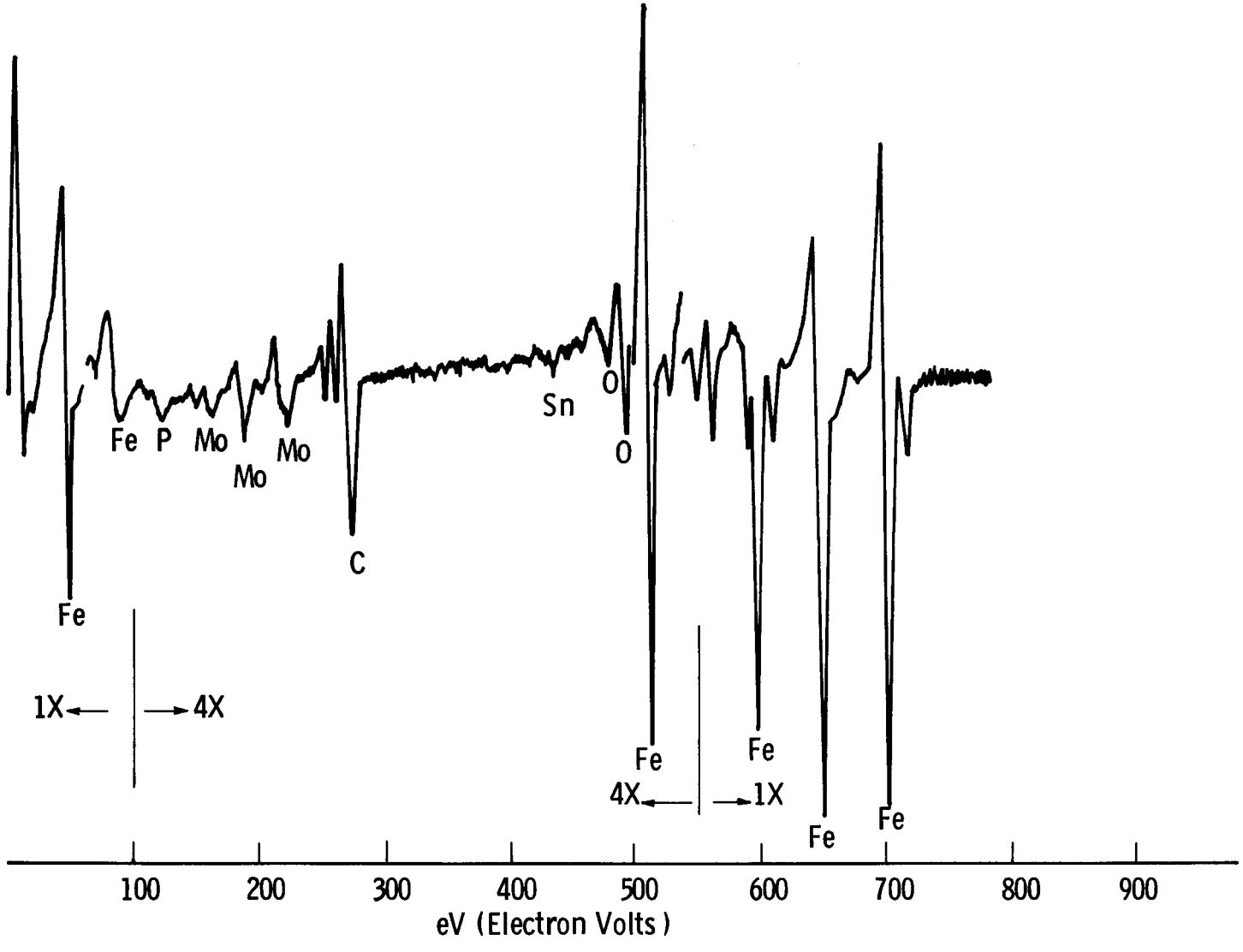

Fig. 2.9 — Auger spectra of sample A3-after 3 minutes of sputtering

3. MECHANICAL TESTING OF GALLATIN MATERIAL

Extensive mechanical testing of the Gallatin rotor material was conducted in order to substantiate the existence of a creep-fatigue interaction mechanism at the stress, load history and temperature encountered in the Gallatin rotor during service. These tests included conventional tensile, Charpy impact, creep, low cycle axial fatigue (LCAF), fracture toughness and fatigue crack growth rate tests. In addition, since the conventional uniaxial low cycle fatigue tests do not account for the possible effect of the biaxial state of stress normally found near the bore of the rotor at a temperature of 800°F, fatigue tests were conducted on blunt notch compact specimens. Detailed fractographic examinations were conducted on both the creep and uniaxial low cycle fatigue specimens. The experimental procedures and results of the above tests are presented separately in the following sections.

3.1 Tensile Testing

Standard 0.505 inch diameter plain bar specimens, oriented in various directions, were used for tensile studies. Test procedures as per ASTM A370 and E21 were used for room temperature and elevated temperature tests, respectively. A composite plot of ultimate tensile and 0.2% offset yield strengths as a function of temperature is presented in Figure 3.1. The data indicate that no significant difference exists as a function of specimen orientation or specimen location at various temperatures. Figure 3.2 is a composite plot of reduction of area and elongation as a function of temperature. In this case, a great deal more variability was noted in the results. At room temperature, the reduction of area ranges from 36% to 55% while the elongation varies from 10% to 20%. The greatest variation in ductility appears to be associated with specimens tested at 700°F (371°C) and 800°F (427°C). It should be noted that while the room temperature tensile properties

were mostly within current ASTM A470 guideline,several tension specimens had room temperature ductilities lower than the radial prolongation requirements of ASTM A470, class 8 material (38% R.A. Minimum). It was also noted that material containing a high concentration of inclusions, showed lower ductility values than did the inclusion free material.

A section of the Gallatin rotor was sent to UCLA for futher mechanical testing. However, the material was reheat treated prior to mechanical testing. Therefore, no correlation between the data generated at UCLA and the data generated at Westinghouse should be expected. As part of an earlier study on older rotors, tensile data was generated on two retired rotors, originally manufactured by Westinghouse. The tensile properties of these two retired rotors are included in Figures 3.1 and 3.2 for comparison with the Gallatin material. The results indicate that the tensile properties of the Gallatin rotor material are similar to the two retired Westinghouse rotors.

3.2 Impact Testing

The results of the Charpy impact tests are displayed as a scatterband in energy and percent fiberous fracture in Figure 3.3. A variation in the 50% fracture appearance transition temperature (FATT) from 175°F (79°C) to 290°F (143°C) was noted for the air cast CrMoV material. These FATT values are not significantly higher than the vacuum degassed CrMoV material which is shown to be approximately 100°F (38°C). After reheat treating the Gallatin material back to the final temper received during the rotor manufacturing process, a maximum FATT shift of 25°F (13.9°C) was noted. SEM fractography on selected impact specimen fractures revealed less than 2% intergranular failure. Taken together these data eliminates temper embrittlement as a probable cause of the Gallatin failure.

SEM fractography was also conducted to determine if segregated material taken from the bore region versus nonsegregated material taken from the periphery region had differences in upper and lower shelf fracture features; however, with the exception of the greater MnS inclusion concentrations in the bore material, no fractographic difference were observed as shown in Figure 3.4.

3.3 Creep Testing

All stress rupture tests were performed as per ASTM E139 by using a standard 0.357 in. diameter plain bar-notch bar specimen. By using this specimen, the life and rupture ductility of the plain bar can be determined. Concurrently, the notch sensitivity can be evaluated by observing the propensity to break in the notch bar region of the specimen. Results of the creep rupture tests are presented in Figure 3.5 as a standard Larson-Miller Parameter (LMP) plot. Although notch sensitivity has been known to occur in this grade of material with an austenization temperature above 1750°F (954°C), no notch bar break occurred prior to plain bar break irrespective of specimen location and orientation.[3.3, 3.4, 3.5] Therefore, for the same specimens, notch break consistently exhibited higher LMP values than plain bar break. Note that equal numbers of notch bar and plain bar point are not present since some notch bar tests were discontinued prior to rupture. The scatterband from prior data generated on 1950's CrMoV material is superimposed over the data from the present study. No gross deviation from the expected values was observed, although some points were below the lower scatter band values. Also, the plain bar rupture ductility of Gallatin material was found to be consistent with the expected values of early 1950's CrMoV material.[3.4,3.5]

To further the understanding of the effects of segregation and specimen location on creep performance, several specimens were selected for investigation by SEM fractography and conventional metallography. Test information for these selected specimens is given in Table 3.1. The first two specimens (CT8A and CT12A) were bore material and periphery material, respectively, and were tested at 1100°F with a stress of 32 ksi. Specimens CT13A and CR4A were tested at 800°F with a stress of 70 ksi. Specimen CT13A was oriented in a tangential direction and was taken from the bore region while specimen CR4A was oriented in a radial direction and was taken from the periphery. Specimens CT7A and CT15A, were 50 ksi minimum creep rate specimens tested at 800°F, where specimen location (bore versus periphery) was considered the only variable.

Figure 3.6 shows the condition of bore specimen CT3A where the reduction of area for the plain bar is readily observable. The plain bar fracture denotes the preferred segregate band location across the specimen as a valley. Similar incipient cracks (presumably the interaction of the segregate with the surface) can also be seen at the same circumferential location above and below the primary break. These cracks are marked by arrowheads in Figure 3.6. Because of the anisotropy induced by the band, the plain bar break can be classified as primarily a shear failure. The topography of the plain bar break within the band at area X in Figure 3.6, was found to be completely dimple rupture (Figure 3.7). In the area of high inclusion density, cracks initiated at the large microvoids. The ligaments between the MnS inclusions failed by shear in a microvoid sheet mechanism.[3.6] No intergranular fracture was noted - even along the ligaments where intergranularity was always seen at the Gallatin failure origin.

Figure 3.8 shows the metallographic development of microvoid formation in specimen CT3A. The specimen was axially sectioned through area X (Figure 3.6) to demonstrate that the high MnS concentration on the fracture corresponded to segregated locations. The development of shear dimples between inclusions is also readily observed. Figure 3.9 indicates that even small banded areas show gross grain size reductions surrounding the MnS. This location was remote from the plain bar failure and only shows matrix decohesion of the MnS inclusions.

The notch breaks of specimen CT3A was conical, as shown in Figure 3.6, and did not show segregate orientation on the fracture surface. The fractography of the notch bar break showed fewer MnS concentrations than the plain bar fracture. The notch bar portion of this specimen was sectioned axially in a direction to the plain bar section to observe the bore banding on an axial transverse plane (Figure 3.10). The fracture surface showed no effect of segregation banding; however, significant inclusion decohesion was observed in banded material below the notch. The metallography was identical to the plain bar material except that no microvoids were initiated from inclusions.

To evaluate the effect of specimen location (in a tangential direction) under identical test conditions, periphery specimen CT12A was investigated (Figure 3.11). Specimen CT12A had the greatest plain bar reduction of area seen in any creep specimens tested. A slight amount of surface cracking was observed adjacent to the plain bar fracture probably due to segregate; however, the actual break was a 'cup and cone' type. The notch bar break was a completely flat fracture. Neither break indicated that the inclusions were directionally oriented. Figure 3.12 indicates that in the center of the plain bar fracture the failure mode equiaxed microvoid coalescence while the notch bar fracture had smaller and fewer initiation sites (Fig. 3.13). The macroetched axial-transverse section of plain bar showed extremely diffuse bands with large voids present in the necked area (Figure 3.14). Again, microvoids initiated from the larger inclusions and were 'linked up' in a transgranular mode. The banded microstructure over the length of the specimen on an axial-transverse plane did not show significant duplexing.

Similar metallographic and fractographic analyses of specimen CT13A were conducted. The results were essentially identical to CT12A. Plain bar radial creep specimen CR4A had significant necking (reduction of area) and a 'cup and cone' break. The fractography of the center section of the specimen revealed significant MnS clusters linked by microvoid coalescence. No intergranularity was observed. The macro-etched axial section revealed that the non shear lip fracture surfaces were associated with segregate banding. The etched microstructure showed adjacent inclusions to have transgranular ligament tearing.

To further compare creep crack initiation with bore and periphery banding, minimum creep rate specimens (which had no visible cracks), CT7A and CT15A, were sectioned on axial-radial and axial-transverse planes. The significant finding is that bore segregated banding was present along the entire gage length of CT7A; however, microstructural and magnetic particle inspection could not detect incipient cracking. Significant banding was not observed in the CT15A

gage length. In short, therefore, bore material banding was intense while periphery banding was diffuse.

From the above data it is shown that the material is not notch sensitive as evidenced by the absence of any notch bar breaks prior to the plain bar breaks. The creep properties of this material are essentially unaffected by the location and orientation of the specimens taken from the rotor. In addition the properties were found to be similar to data generated from other 1950 vintage rotors. The fractographic evaluation of the broken specimens revealed that cracking initiated from the larger MnS inclusions and propagated in a transgranular mode. No intergranular cracking was observed in any creep specimens.

3.4 Fracture Toughness

Compact type specimens of various sizes were removed from the IP main body between the second reaction row and the governor end shaft. Specimens, oriented in the CR-direction, were tested at various temperatures according to procedures required by ASTM E399-74. The results of the tests conducted with different size specimens at various temperatures are presented in Figure 3.15. As expected, fracture toughness increases with increasing temperature. The narrow scatterband of these data indicates that the large variation in ingot segregation throughout the IP end did not affect the fracture toughness. (Careful optical observations on the fracture surface did reveal the presence of MnS concentrations.) It should be noted that, with specimens as large as 3 in. thick, valid K_{Ic} tests could not be achieved at temperatures above 225°F (107°C). However, these invalid data points (per ASTM E399-74) still fit into the extrapolation of the valid data.

Dynamic toughness tests conducted by Combustion Engineering[3.7] using instrumented Charpy impact specimens are also shown in Figure 3.15. These data are generally lower than the plain strain fracture toughness data, K_{Ic}, for temperatures higher than 200°F (93°C). This difference in the data is most likely due to the inadequacy of the small sized specimens to develop plain strain values.

The results of the toughness tests reveal properties equivalent to other 1950 vintage rotor material.

3.5 Small Specimen Uniaxial Low Cycle Fatigue Tests

Following the Westinghouse failure analysis of the Gallatin rotor, a low cycle fatigue testing program was undertaken to simulate the type of strain cycle seen by inclusions in near bore material. Accordingly, 0.3 in. diameter specimens were cycled from zero to a elected maximum strain at either 700°F or 800°F (bracketing the temperature found at the failure origin during steady state conditions). However, since the maximum thermal stress at the origin location during a cold start occurs when the temperature at that location is 230°F, several tests were run at this temperature also. Because failure could not be induced in practical time at the strain ranges calculated to exist in the rotor bore, most testings were done at considerable (8-10 times) higher strain ranges. All test parameters are noted in Tables 3.2 and 3.3 Typical strain cycles are presented in Figure 3.16.

All low cycle fatigue life plots are presented in Figures 3.17 and 3.18. Figure 3.17 is a summation of all continuous cycle results utilizing temperature, cycling rate, and location of specimen material as the appropriate test variables. The significant observations in data are the narrow scatterband and the insensitivity of the material to test temperatures up to 800°F (427°C). This observation is particularly surprising since the 230°F (110°C) data fall within the higher temperature scatterband. Ordinarily, a material which follows a "universal slopes" behavior would have a longer life presumeably due to higher tensile ductility at lower temperatures. Furthermore, the 230°F (110°C) periphery data and possibly the 700°F (371°C) periphery data in Figure 3.17 show shorter fatigue lives than those encountered by the bore material; however, the few data points are so closely grouped that they may not represent a sufficient statistical difference. On the other hand, both the universal slopes deviation and this latter observation may be explainable on the basis of a difference in the ductilities of the banded and unbanded areas within the specimen gage lengths. Such microstructural effects on ductility (for example, grain size, amount of ferrite, etc.) have been observed in the failed rotor.[3.8]

Since typical rotor applications involve significant hold time periods as part of the cyclic loading, a rational evaluation of fatigue performance requires the consideration of hold time effects. To this end, a limited number of LCF tests were performed with hold times (peak load) ranging from one hour to 23 hours. Figure 3.18 is a plot of a summation of all hold time points for three temperatures (700°F (371°C), 800°F (427°C), and 900°F (482°C)). For comparison, the scatterband for continuous cycling from Figure 3.17 is superimposed over the hold time data. Three specimens which were terminated at 20% or less of the predicted failure lives are shown as triangular points. Two significant points are evident from the hold time data shown in Figure 3.18. First, with the exception of a single four hour hold time point, the hold time data does not show a significant decrease in life over the continuous cycling data. Thus, any creep damage introduced by the hold time at temperatures between 700°F (371°C) and 900°F (482°C) did not appreciably shorten the fatigue life. Secondly, within the hold time scatterband, distinct trends in the data are not obvious. Details of selected microstructures will be discussed later.

3.5.1 Effect of Strain Range (Continuous Cycling) on Fracture Mode

For brevity, since the continuous cycling tests showed the same basic fractographic features irrespective of temperature, location of material, and cycling rate, only the bore specimens at the minimum and maximum strain ranges at 800°F (427°C) will be discussed. The fractography of the specimen subjected to the lowest strain range (ε_t = 0.6%, N_f = 7500 cycles) is shown in Figure 3.19. Surface crack initiation was visually observed around 90% of the gage circumference; however, subsurface crack initiation as well as internal crack initiation occurred at the MnS inclusion sites. The topography of the initiation sites were highly striated. Surface oxide spiking was not observed. A metallographic section along a subsurface inclusion revealed transgranular initiation with a slight amount of branching at the crack tip. Similar behavior was observed at secondary cracks along the gage length below the main fracture surface.

An evaluation of the specimens subjected to the maximum strain range (ε_t = 4.3%, N_f = 41 cycles) at 800°F (427°C), showed that cracks initiated internally at MnS inclusions. Figure 3.20 shows the multiple level fracture surface with each level corresponding to a MnS concentration. Since these inclusions were known to be concentrated in inverse 'V' segregation,[3.7] it is not surprising that parallel macro planes are observed at each cluster concentration. SEM fractography indicates that each major inclusion or cluster of minor inclusions has a small path of transgranular fatigue from each discrete inclusion on a plane normal to the applied stress axis. Once growth proceeds sufficiently to linkup adjacent stringers, shearing occurs between these planar fatigue cracks. As expected, a relatively small fraction of final topography is fatigue with the bulk being shear dimples. The surface of the gage length was perforated with oxide spikes; however, this phenomenon was not observed to affect either initiation location nor propagation direction. Metallography revealed transgranular fracture propagation; however, secondary cracking was significantly more branched than at lower strain ranges. In summary, at the minimum strain range the cracks initiated at the surface of the specimens while at the highest strain range, cracks initiated internally at MnS inclusions. No intergranularity was observed at either of these strain ranges.

3.5.2 Effect of Hold Time (Constant Strain Range) on Fracture Mode

In order to evaluate the effect of increasing hold time at approximately constant strain range, three near bore specimens were tested with various hold times at 800°F (427°C) to failure. The initial one hour hold time test involved a strain range of 3.2% (N_f = 106 cycles). Hold time tests of 4 and 23 hours were also conducted at a total strain range of 2.85% and 2.98%, respectively. Details of the cycle ramp rates and hold times are given in Table 3.3.

A cross section of a one hour hold time specimen is presented in Figure 3.21 and appears to have similar planar shearing observed in the non hold time specimens. Unfortunately, the fracture topography was grossly obliterated by oxidation. The gage section was uniformly

penetrated with oxide spikes up to 1.2mm deep. Metallography revealed transgranular cracking with various degrees of branching.

Detailed fractography of the 4 hour hold time specimen (N_f = 71 cycles) is presented in Figure 3.22. This specimen had definite internal initiation sites at discrete MnS inclusions with a transgranular striated fatigue linkup between these inclusions. Metallography revealed all cracking to be branched but transgranular.

The topography of the 23 hour hold time specimen tested at 2.98% strain range (N_f = 76 cycles) is shown in Figure 3.23. The primary fracture surface was oxidized since it was open to the air for at least 20 cycles during testing. An axial metallographic section (Figure 3.24) through this specimen gage section revealed numerous intergranular secondary cracks below the primary plane of fracture. Each crack corresponded exactly to a dark etching band of positive segregation in a similar manner to cracking at the Gallatin No. 2 origin.[3.7] The more intensely etched areas had longer linkup distances. This statement is corroborated by comparing Areas 1 and 2 in Figure 3.24. Detailed metallography of Area 1 (Figure 3.24) shows what appears to be inclusion decohesion and branched intergranular cracking similar to that observed in the Gallatin rotor failure. The same microstructure was observed in an identical test terminated after only 12 cycles as shown in Figure 3.25.

In order to evaluate the effects of hold time on the topography of specimens taken from various locations (bore versus periphery), specimens which were not tested to failure were sectioned to determine variations in microstructural appearance. Figures 3.26 and 3.27 are periphery material micrographs of the 1 hour hold time (ε_t = 1.74%) and 23 hour (ε_t = 2.98%) hold time specimens after 60 cycles (20% of N_f) and 7 cycles (9% of N_f), respectively. In comparing these microstructures with those associated with the bore material (Figures 3.24 and 3.25) it can be seen that the periphery material was much less segregated than the corresponding bore material. Hence, the mean free distance of the MnS inclusions was larger than that observed at the bore. Slight inclusion matrix decohesion as well as transgranular linkup between a few adjacent

inclusions was observed. No duplication of the Gallatin fracture morphology was observed in the periphery material. The near bore region 23 hour hold time uniaxial fatigue tests (2.98% strain, 800°F) produce the only evidence of intergranular cracking encountered with the Gallatin material. All other LCF tests at various strain ranges, frequencies, and temperatures produced transgranular cracking.

3.6 Effect of Biaxial Stress State on Cracking Initiation

Fatigue initiation data generated under uniaxial conditions were not able to fully explain the Gallatin #2 failure.[3.7] However, it has been shown by Manjoine[3.9] that in the creep regime, a multiaxial stress, similar to that found near to the rotor bore, has an effect on the crack initiation. In order to evaluate this possibility, work was initiated to determine the effect of a biaxial stress state on crack initiation at 800°F (427°C). The biaxial stress state was generated by using blunt notched compact specimens with a root radius of 0.100 in. as shown in Figure 3.28. Four specimens Gal-B1, B2, B3, B4 with notch depth of 1.000, 1.200, 1.260, and 1.300 in. respectively, were used such that various strain levels could be created while these specimens were subjected to the same load. During loading (between 450 lb and 4500 lb), the cyclic strain ranges at the notch root were measured using Micro-Measurement precision strain gages of 0.062 in. gage length, at 75°F (24°C). 150°F (71°C), and 200°F (93°C). By extrapolation, Figure 3.29, the cyclic strains ranges at 800°F were estimated to be 0.76%, 0.66%, 0.57% and 0.41% for specimens with notch depth of 1.300 in., 1.2600 in., 1.200 in. and 1.000 in., respectively.

These four blunt notch compact specimens were then cyclically loaded between 450 lb and 4500 lb at a temperature of 800°F (427°C). In order to simulate the service conditions as closely as practical, load cycles were applied once every hour (1 min. loading and unloading ramp with a 55 min. dwell at peak load). A travelling microscope was used to inspect the notch root periodically for crack initiation. After 1200 cycles elapsed, visual inspection indicated that crack initiation had occurred on specimens Gal B4 (a_N = 1.300 in.) and Gal B3 (a_N = 1.260 in.).

These two specimens were then pulled apart at liquid nitrogen temperature. The oxidation area on fracture surface of Gal B4 clearly indicated that a crack had initiated at 1200 cycles. No oxidation was observed on the fracture surface of specimen Gal B3. This result indicates that cracking had not initiated on this specimen at 1200 cycles. At this time, the cyclic frequency was changed to 1 cycle per minute such that a crack could be initiated on specimen Gal B1 and Gal B2 before the expiration of this contract. It was found that crack initiation occurred at approximately 13,000 cycles for specimen Gal B1 and 25,000 cycles for Gal B2.

These results were plotted with the low cycle uniaxial fatigue test results of Gallatin #2 material, Figure 3.30. The data clearly show that at 800°F (427°C), the biaxial stress state has little effect on crack initiation. Fractography also indicates that there was no intergranular cracking in the biaxial test (Figures 3.31 and 3.32). The absence of creep damage at this temperature may account for the lack of the effect of biaxial stress state on crack initiation at 800°F (427°C).

3.7 Large Low Cycle Fatigue Tests on Gallatin Rotor Material

In order to evaluate the crack initiation performance of material with a high density of MnS inclusions two large low cycle fatigue specimens were tested to simulate the near bore stress and temperature conditions of the Gallatin rotor. Three inch diameter specimens with a gage length of 19 inches were taken from the periphery of the low pressure section of the rotor in the tangential direction. This material was expected to have a large number of dispersed MnS inclusions. Previous estimates of the steady state conditions for the Gallatin rotor was a temperature of 775°F (413°C) and a stress of 48,000 psi. This information was used as a guide for the subsequent fatigue tests. In an attempt to reduce the required hold time, stress relaxation data developed on material similar to Gallatin was used to show that an equivalent amount of stress relaxation at a shorter time could be obtained by increasing the temperature. Consequently, a

15 minute hold time at 880°F (471°C) was used to simulate a hold time of 24 hours at a temperature of 745°C (394°C). An additional test was conducted at 800°F (427°C).

Prior to testing, each specimen was inspected by ultrasonic methods and found to be free of significant ultrasonic indications. The specimens were then cyclically loaded between 10,000 lbs and 388,800 lbs (corresponding to a minimum stress of 1.5 ksi and a maximum stress of 55 ksi) while deflection over a gage length of 15 in. was measured using an LVDT. One specimen was tested at 800°F (427°C) for 990 cycles, with no noticeable unrecoverable deflections. Also, no indication of cracking was found throughout the length of the specimen by ultrasonic or magnetic particle inspection. This specimen was held for possible future testing.

A second specimen was loaded to the same stress level at a temperature of 880°F (471°C). At the end of 800 cycles and 2000 cycles, the specimen was inspected by both ultrasonic and magnetic particle techniques with no crack indications found. The specimen was then cyclically loaded between 70,000 psi and 1.500 psi for an additional 440 cycles. Although the load displacement records remained linear, it became increasingly obvious that large amounts of unrecoverable displacements (approximately 0.5 in.) were being imparted to the specimen. Upon reinspection of the specimen, a severely necked region of 0.2 in. reduction in the diameter was found. Again no indication of cracking was found by ultrasonic or magnetic particle inspection.

The specimen was then sliced axially to perform a microscopic examination of the manganese sulfides in order to determine if cracks had formed from the sulfides. Slices were also taken perpendicular to the loading axis in the severely necked region. In both planes no cracks could be found emanating from the MnS inclusions, Figure 3.33. It should be noted, however, that debonding between the inclusions and the matrix occurred at many sites.

Sulfur prints taken from the axial slice and the cross section of the large low cycle fatigue specimens are shown in Figures 3.34 and 3.35, respectively. Note the extent and nature of the MnS inclusions. The difference between the sulfide distribution shown and that found near the fracture origin site is that at the failure origin. The sulfides appear to follow a directional stringer pattern[3.9] formed by the inverse V segregation during the ingot solidification.

The results of the large low cycle fatigue tests of the Gallatin material clearly demonstrate that extensive MnS inclusions have little effect on crack initiation performance under conditions expected to simulate service loading. In particular, no cracking occurred at temperatures, stress, and loading cycles in excess of that encountered by the Gallatin rotor. Of course, very long term exposure simulating operating condition could not be tested.

3.8 Fatigue Crack Growth Data

The following sections describe the fatigue crack growth rate testing performed on this Gallatin rotor material.

3.8.1 Fatigue Crack Growth in Air at Room Temperature

Because a conventional fatigue crack growth (FCG) mechanism is always possible in rotating machinery, a series of tests were conducted on Gallatin material from various locations in the forgings. These data were then compared with FCG data on two retired 1950 vintage CrMoV rotors [3.10] as well as FCG data generated at UCLA[3.2] on piece of the Gallatin rotor. A composite plot of all these data, Figure 3.36, shows no significant differences in the fatigue crack growth rate behavior of the various materials.

3.8.2 Effect of Microstructure on Fatigue Crack Growth Behavior [Air environment, 275°F (135°C)]

Examination of the broken fatigue crack growth rate tests specimens revealed the presence of a distinct variation in the appearance of the fracture surface. Specifically, several coarse bands were noted along the fatigue crack plane. These markings appeared to correspond to preexisting segregate bands. Figure 3.37 shows the bands on a specimen tested at 275°F (135°C) in air. Figures 3.38 and 3.39 show

macrographs (12X) and SEM fractographs (1000X) at the centerline thickness location of the three banded regions highlighted in Figure 3.37. The crack length as well as the corresponding stress intensity range (ΔK) levels associated with the three bands are also noted. In each case, the topography was extremely smooth before and after the crack front encountered the banded area. In addition, the SEM fractographs confirm the suspicion that the bands are in fact made up of areas of high MnS concentrations. Scanning electron microscopy did not reveal any intergranular cracking associated with the bands. Transgranular fatigue propagation was observed in most areas examined. It can be seen in the SEM fractographs (Figure 3.39), that higher values of ΔK result in progressively greater inclusion-matrix decohesion.

In order to evaluate the influence of the segregation bands on the fatigue crack growth rate of the Gallatin near bore material, the raw crack length versus time curves were evaluated in detail. Figure 3.40 shows the plot of crack length versus elapse time for a 2T WOL specimen tested at 275°F (135°C). These data were collected using a travelling ultrasonic beam technique which monitors the crack length in the center of the specimen. The test results clearly indicate localized areas of accelerated crack growth. However, due to the orientation of the segregate bands with regards to the crack front, it was not possible to correlate band location and localized accelerated growth. Note however, that the overall curve of crack length versus elapsed time was not affected by these localized bands of segregate. Consequently, we can conclude that the concentrated segregates found in the Gallatin rotor material would not have a significant effect on the average fatigue crack growth rate performance.

3.8.3 Environmental Effects on Fatigue Crack Growth of Gallatin Rotor Material

One problem in trying to estimate the life of a component is the absence of data concerning the fatigue crack growth rate of cracks imbedded in the material. Specifically, fatigue crack growth rate data can usually be generated in the service environment of interest; however, an internal flaw may grow in an entirely different environment. In

order to estimate the type of environment that an imbedded flaw in the Gallatin rotor was likely to see, the residual gas analysis of the rotor material was examined. As discussed in Section 2.2,the results did not reveal any abnormal values for material of this type. It was assumed therefore, that if a crack was growing within the body of the rotor it would be growing in an inert environment. In order to evaluate this situation, crack growth rate data were generated in an inert environment.

The fatigue crack growth rate tests were conducted with compact specimens taken from two locations in the Gallatin rotor selected to represent material with high concentrations of ultrasonic indications and material relatively free of ultrasonic indications. All tests were conducted at 800°F (427°C). Two specimens, one each with and without ultrasonic indications were tested in air and argon environment. The test frequency was maintained at a constant one cycle per second. The results of these tests are shown in Figure 3.41. Note that the rate of crack growth in argon is less than that in laboratory air. However this difference in behavior is not considered to be of practical concern since the argon data essentially fall within the typical air-data scatterband for CrMoV materials. In addition, for design purposes, the air data provide a rational upper bound.

The data summarized in Figure 3.41 also show that the presence of small ultrasonic indication have essentially no effect on the rate of fatigue crack growth in either an air or argon environment.

3.8.4 24 Hour Hold Time Fatigue Crack Growth Tests

The effects of temperature and frequency on the kinetics of fatigue crack growh have been studied and are described in Section 4. It is sufficient to state at this point that at elevated temperatures, crack growth rate increases with decreasing frequency or increasing hold time due to possible creep and/or oxidation damage at the crack tip. However, it is both costly and impractical to perform fatigue crack growth tests at frequencies similar to the start-stop operations of a

steam-turbine rotor. Extensive extrapolation is therefore required to determine the rate of crack growth at frequencies in the order of one cycle per month from the data generated in the range of one cycle per minute. In order to reduce the extent of data extrapolation, 24 hour (22-2/3 hr dwell at peak load) fatigue crack growth tests were initiated using specimens taken from the same axial location as the origin site of the Gallatin rotor failure.

Because of the very long time required, the conventional method of fatigue crack growth rate testing could not be applied over a wide range of stress intensities and cycles. Therefore, a test method similar to the one described by Brothers [3.12] was employed. A small number of constant load amplitude cycles were applied to a precracked specimen at a given temperature and frequency. Upon the completion of these cycles, the specimen was broken apart at a temperature that would insure cleavage. The amount of fatigue crack growth was determined from the difference in fracture surface appearance (beach marks) measured by microscopic techniques. The fatigue crack growth rate was obtained simply by dividing the average band width by the total number of cycles. The stress intensity factor range, ΔK, was calculated for the average of the initial and final crack lengths. This method only allows the determination of one point per specimen on the crack growth rate vs. ΔK curve. Therefore, a number of specimens are required in order to adequately describe the crack growth rate vs. ΔK curve completely.

In order to reduce the number of testing machines needed to complete these tests within a practical time period, a series of four compact specimens were loaded in tandam as shown in Figure 3.42. While each specimen was subjected to the same cyclic load, different levels of stress intensity factor range were achieved by providing different initial crack lengths in each specimen. To approximate a hot-start typical of the Gallatin rotor, tests were conducted at 800°F (427°C) with a ramp time to peak load of 1¼ hours. The maximum load, 4500 lbs in this test, was held for 22-2/3 hours, and then lowered to 450 lbs over a period of 5 minutes. This test was run continuously for 24 hours per day, 7 days per week, by using a continuous drive DATA-TRAC drum to control a stress relaxation machine.

In order to generate additional data points on the crack growth rate vs. ΔK curve, the two specimens with the shorter crack lengths were removed after 160 cycles of loading and precracked an additional amount. Unfortunately, one of the specimen was broken during precracking. The remaining specimens plus the two original long crack specimens were then loaded for an additional 50 cycles and then broken at a lower temperature.

Due to the extreme amount of oxidation on the fracture surface, as shown in Figure 3.43, it was necessary to remove the oxidation layer before a fractographic evaluation of the fatigue crack growth band could be made. A technique involving the reduction of the oxide in hydrogen at 1200°F (649°C) for 48 hours was used to remove this oxide layer. The success of this technique is clearly illustrated in Figure 3.43 and enabled us to determine the crack growth band without the fear that artifacts due to oxidation would distort the measurements. The fatigue band width for each specimen along with the number of elapsed cycles as well as the ΔK range involved are shown in Figures 3.44 through 3.47. The rates of crack growth versus ΔK are tabulated in Table 3.4 and plotted in Figure 3.48 along with data generated at 800°F (427°C) with a rapid load ramp and 15 minute hold. The general trend is that, at 800°F (427°C), the rate of crack growth increases with decreasing frequency. The amount of growth rate increase is of the order of three times faster than the 15 minute hold time data. The difference in fatigue crack growth rate generated with a hold time of 15 minutes and that with a hold time of 22-2/3 hours in air appears to be similar in magnitude to the difference in the data generated at 1 Hz frequency in air and argon. This observation suggests that the increased rate of crack growth for the 22-2/3 hour hold time test may be attributed to the increased oxidation damage at the crack tip rather than creep damage. This point of view is supported by the fact that no intergranular cracking indicative of creep was observed on the fatigue surface of any of the specimens.

3.9 REFERENCES

3.1 Clarke, G. A., Kramer, L. D., Tu, L. K., "Reliability of Steam Turbine Rotors — First Semi Annual Report," EPRI Contract No. RP502-4, July 1976.

3.2 Roman, I., "A Study of Crack Growth Under Operational Conditions in Turbine Steel: Phase 1," U.C.L.A. Report, 1976.

3.3 Krempl, E. and Walker, C. D., in Fatigue at High Temperature, STP 459, L. F. Coffin, Ed., ASTM, Philadelphia, 1969, pp. 75-99.

3.4 Conrad, J. D. and Mochel, N. L., "Operating Experience with High Temperature Steam Turbine Rotors and Design Improvements in Rotor Blade Fastening," ASME Power Division Paper 57-PWR-10, October 21, 1957.

3.5 Goldhoff, R. M. and Beattie, H. J., "The Correlation of High Temperature Properties and Structures in 1Cr-Mo-V Forging Steels," Trans. AIME, Vol. 233, pp. 1743-1756, September 1965.

3.6 Thompson, R. M., "A Material Scientists' View of Fracture," Presented at the 1976 Winter Annual Meeting of ASME.

3.7 Argo, H. C. and Seth, B. B., "Fracture Mechanics Analysis of Ultra-Sonic Indications in CrMoV Alloy Steel Turbine Rotors," Presented at Symposium on "Case Studies in Fracture Mechanics", June 1977.

3.8 Kramer, L. D. and Randolph, D. D. in the 1976 ASME-MPC Symposium on Creep-Fatigue Interaction, R. M. Curran, Ed., ASME, New York, 1976, pp. 1-24.

3.9 Manjoine, M. J., "Ductility Indices at Elevated Temperature," Presented at Winter Annual Meeting of ASME, October 1974.

3.10 Kramer, L. D., Unpublished Westinghouse Data.

3.11 Clarke, G. A., Shih, T. T. and Kramer, L. D., "Reliability of Steam Turbine Rotors — Third Semi Annual Report," EPRI Contract No. RP502-4, October 1977.

3.12 Brothers, A. J., "Fatigue Crack Growth in Nuclear Reactor Piping Steels," Research and Development Report GEAP-5067, U.S. Atomic Energy Commission, March 1968.

TABLE 3.1

CREEP SPECIMEN SELECTED FOR FRACTOGRAPHY AND METALLOGRAPHY EVALUATION

Specimen Identification	Specimen Location	Temperature (°F)	Stress (ksi)	Plain Bar Fracture				Notch Bar Fracture
				Time to Rupture (hours)	Elongation (%)	Reduction in Area (%)	LMP	Time to Rupture
CT3A	Bore	1100°F	32	130.5	26.4	26.4	34.6	1151
CT12A	Periphery	1100°F	32	278.3	24.2	70.6	35.0	1075
CT13A	Periphery	800°F	70	2176	18.1	55.7	29.4	>2176
CR4A*	Bore	800°F	70	2798	14.9	51.8	29.6	>2798
CT7A	Bore	800°F	50	MCR+	--	--	--	--
CT15A	Periphery	800°F	50	MCR+	--	--	--	--

*Specimen oriented in radial direction;all others in tangential direction.

+MCR - Minimum creep rate specimen, test stopped once stable second stage creep established.

TABLE 3.2

A SUMMARY OF CONTINUOUS CYCLE TESTING CONDUCTED ON GALLATIN NO. 2 INTEREMDIATE PRESSURE END MATERIAL *

Specimen Location	Test Temperature (°F)	Cycle Rate (CPM)	Total Strain Range (%)	Life to Failure N_f	Comments
Bore	230°	1	2.25	206	
Bore		1	1.12	1080	
Bore		1	0.63	5827	
Periphery		1	2.29	145	
Periphery		1	1.13	692	
Periphery		1	0.64	3964	
Bore	700°	1	4.80	23	
Bore		1	2.10	319	
Bore		1	1.00	1015	(a)
Bore		1	0.72	2473	
Periphery		1	4.80	3	
Periphery		1	2.10	162	
Periphery		1	1.00	669	(a)
Periphery		1	0.72	1617	
Bore	800°	1	4.30	41	
Bore		1	1.90	335	
Bore		1	0.95	1495	(a)
Bore		1	0.60	3285	
Periphery		1	3.05	73	
Periphery		1	1.43	340	
Periphery		1	0.75	1239	(a)
Periphery		1	0.56	2359	
Bore		100	1.83	205	
Bore		100	0.81	1545	
Bore		100	0.48	6080	(a)
Bore		100	0.33	40876	

(a) Symmetric loop tests

* 0.30 in. diameter uniaxial specimens

TABLE 3.3

A SUMMARY OF HOLD TIME TESTING CONDUCTED ON
GALLATIN NO. 2 INTERMEDIATE PRESSURE END MATERIAL*

Specimen Location	Test Temperature (°C)	Total Cycle Time (hrs.)	Hold Time (hrs.)	Total Up & Down Ramp Time (hrs.)	Total Strain Range (%)	Life to Failure (N_f)	Estimated Life at Termination
Periphery	371	1	59/60	1/60	1.82	192	
Periphery	371	1	59/60	1/60	1.00	2337	
Bore	427	1	59/60	1/60	3.23	106	
Bore	427	1	59/60	1/60	1.91	304	
Periphery	427	1	59/60	1/60	1.74	(60)	20% N_f
Bore	427	1	59/60	1/60	0.78	1800	
Bore	427	4	3 59/60	1/60	2.85	69	
Bore	427	4	3 59/60	1/60	1.59	145	
Bore	427	24	23	1	2.98	76	
Bore	427	24	23	1	2.98	(12)	16% N_f
Periphery	427	24	23	1	2.98	(7)	9% N_f
Periphery	482	1	59/60	1/60	1.30	712	
Periphery	482	1	59/60	1/60	2.90	97	

( ) denotes test terminated prior to failure

*0.30 in. diameter uniaxial specimens

TABLE 3.4

FATIGUE CRACK GROWTH DATA FOR SPECIMEN TESTED AT 800°F (427°C) WITH A FREQUENCY OF 1 CYCLE PER 24 HOURS*

Specimen ID	No. of Cycles	Width of Fatigue Band	Average da/dN in./cycle	Average Crack Length in.	ΔK ksi$\sqrt{\text{in.}}$
FRIA 2	160	.001"	6.25×10^{-6}	0.845	18.0
FRIA 1A	160	.00165	1.03×10^{-5}	1.157	25.6
FRIA 3	210	.012"	5.7×10^{-5}	1.327	30.5
FRIA 4	210	.014"	6.66×10^{-5}	1.507	38.2
FRIA 1B	50	.023	4.6×10^{-4}	1.742	55.3

*22-2/3 hour dwell at peak load.

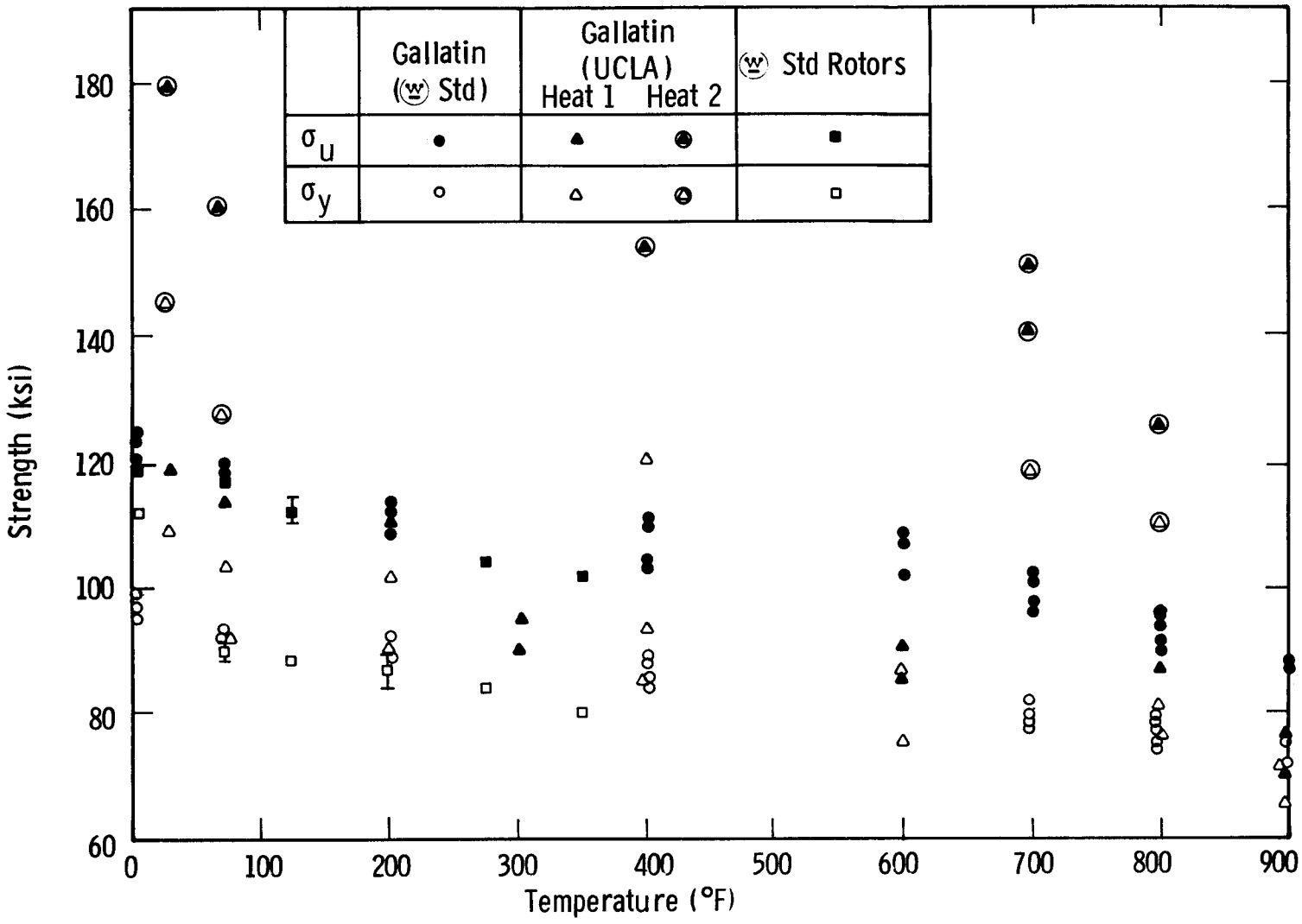

Fig. 3.1 – Strength vs. temperature for Gallatin No. 2 rotor and Ⓦ 1950 vintage rotors

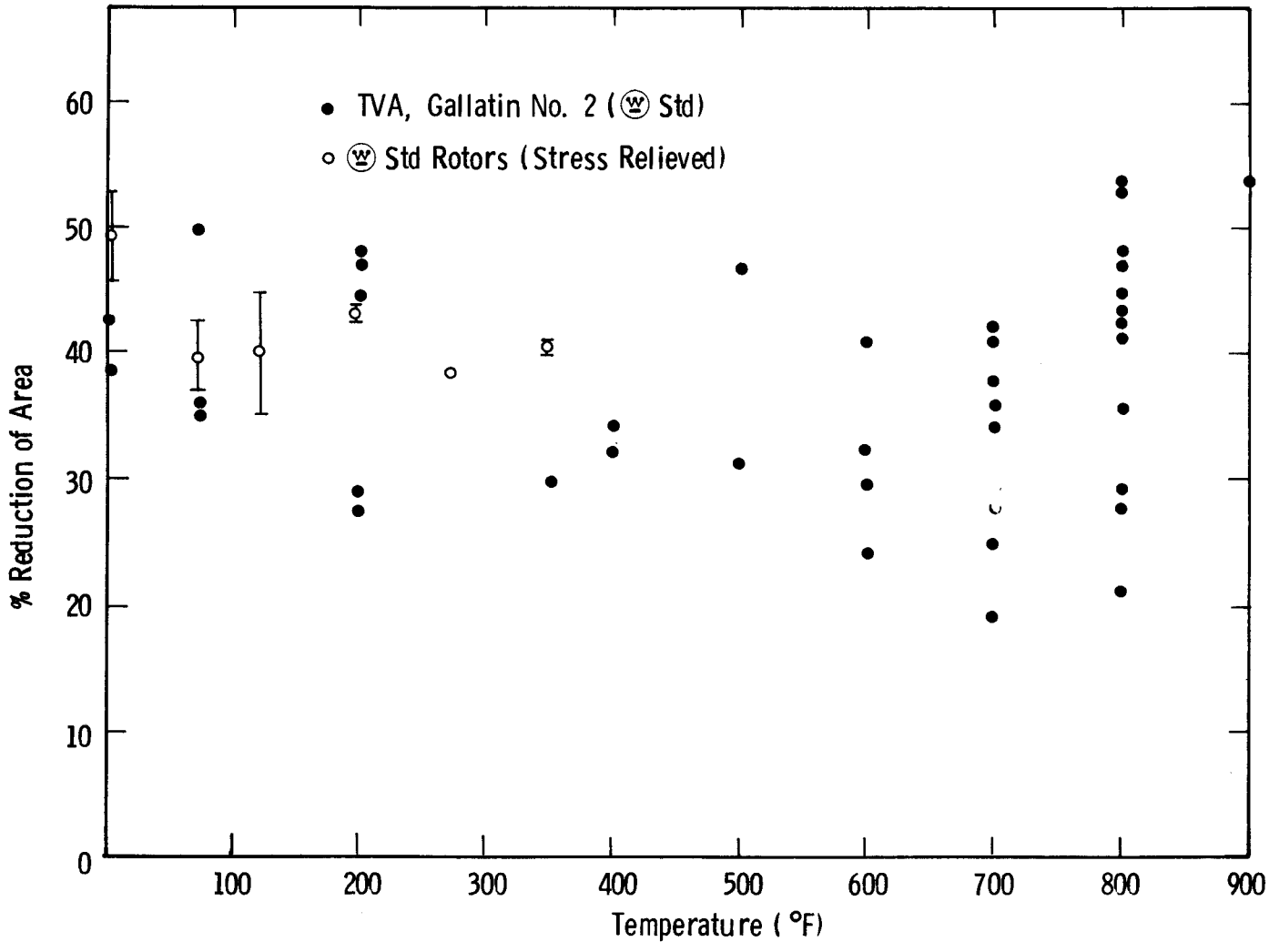

Fig. 3.2a — Reduction of area vs. temperature for Gallatin No. 2 and Ⓦ 1950 vintage rotors

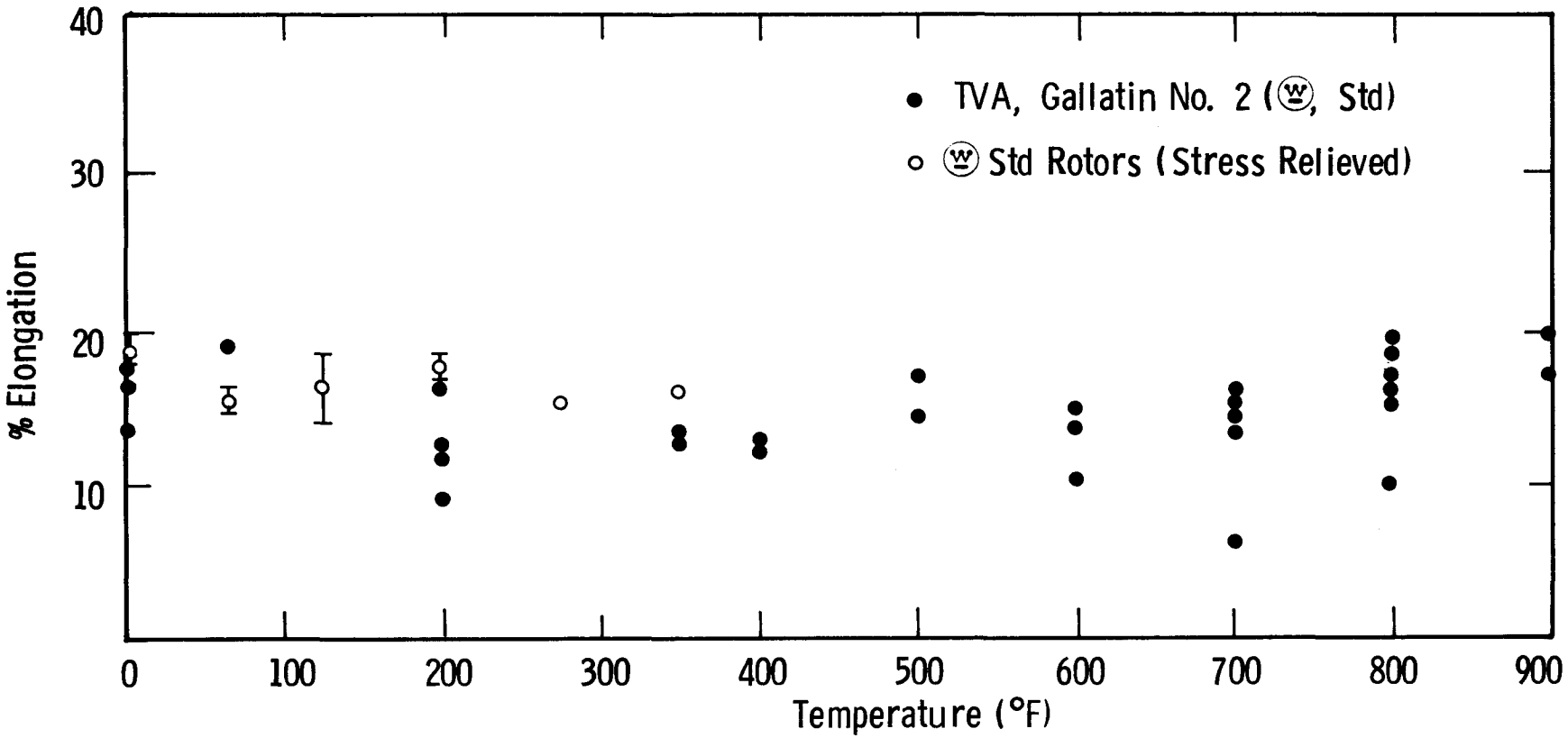

Fig. 3.2b– Percent elongation vs. temperature for Gallatin No. 2 rotor and Ⓦ 1950 vintage rotors

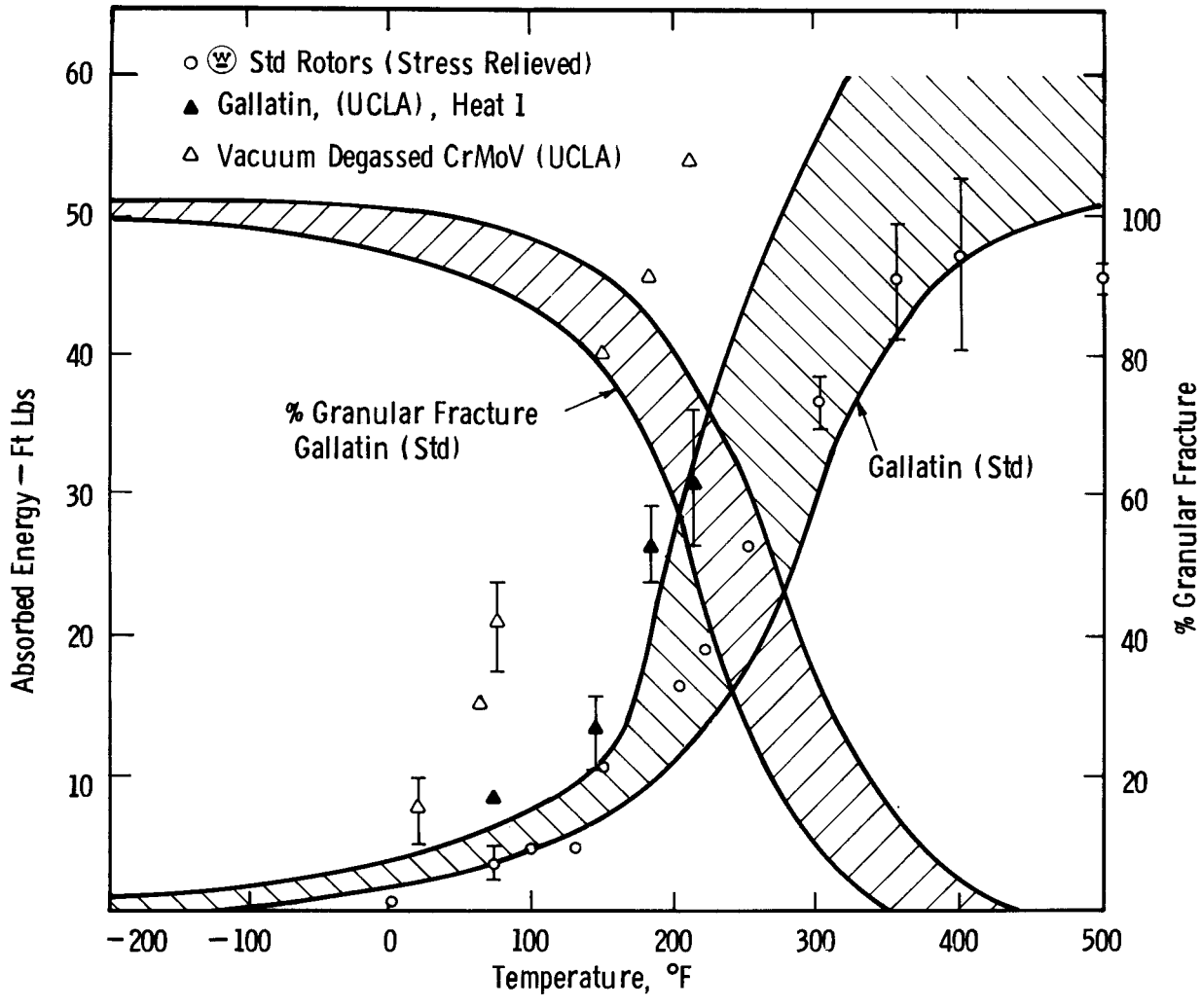

Fig. 3.3 – Impact energy and % granular fracture vs temperature

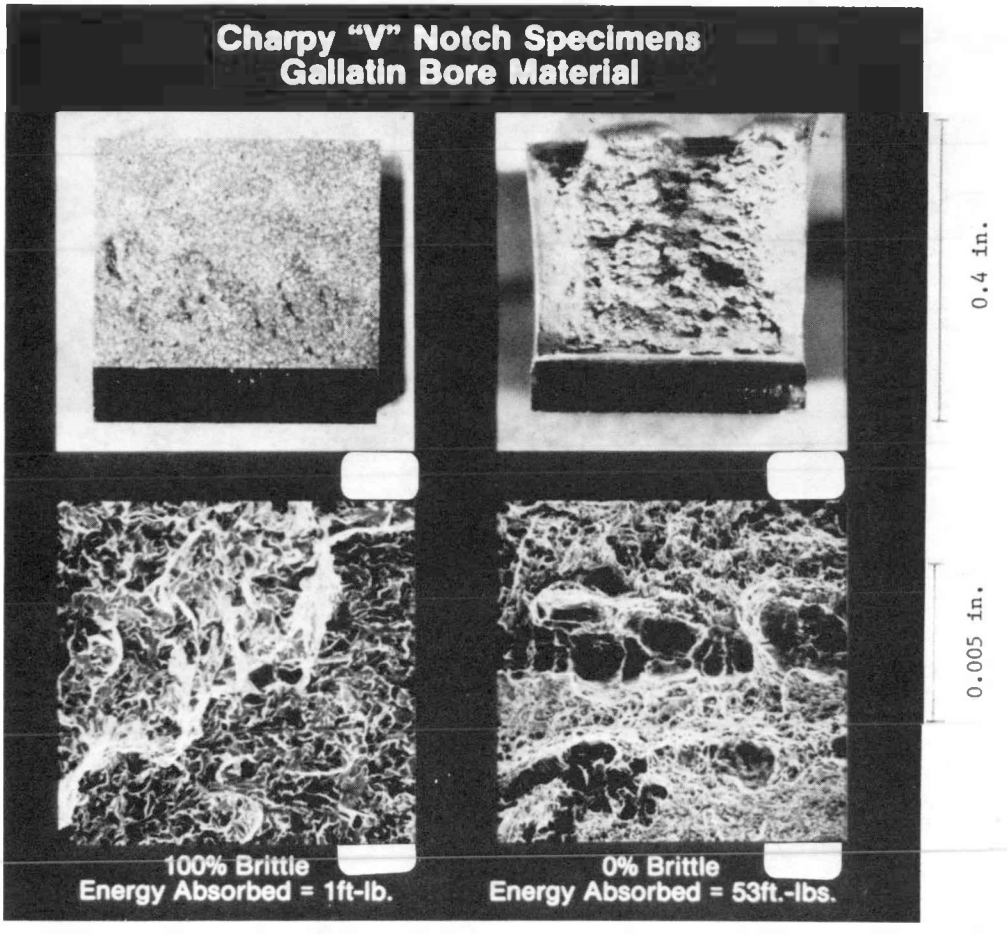

Fig. 3.4a – Fractographic features of Charpy impact specimens taken from the bore of the Gallatin rotor

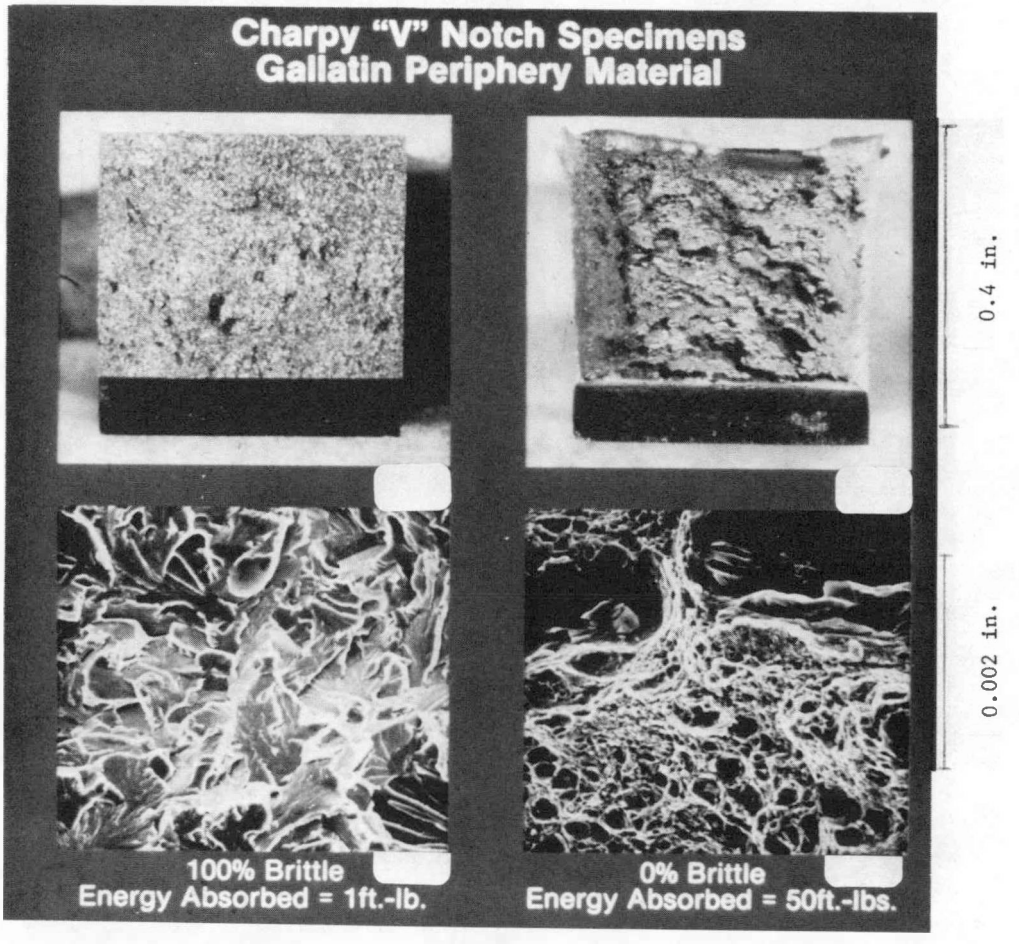

Fig. 3.4b – Fractographic features of Charpy impact specimens taken from the periphery of the Gallatin rotor

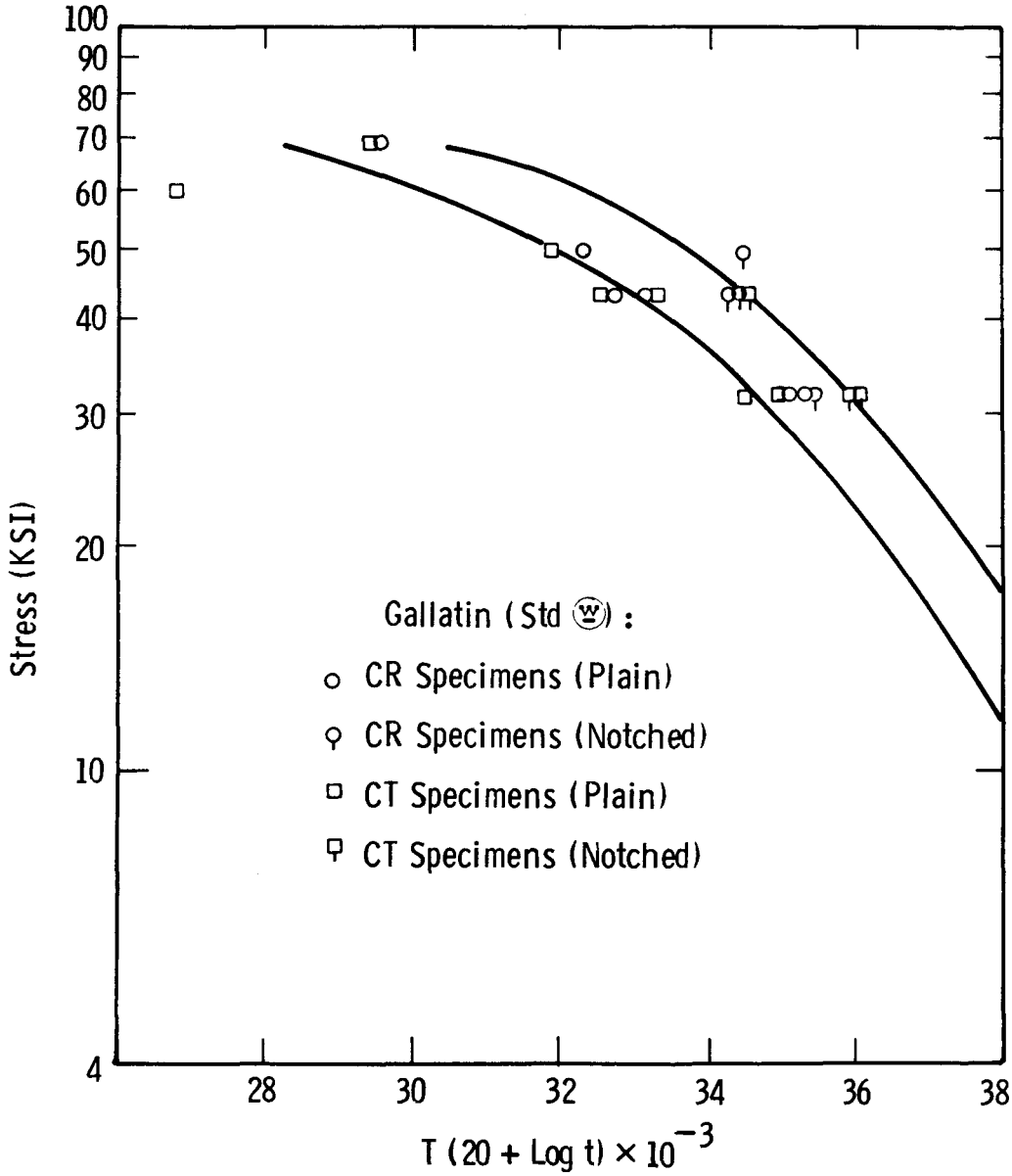

Fig. 3.5– Stress rupture data for Gallatin material

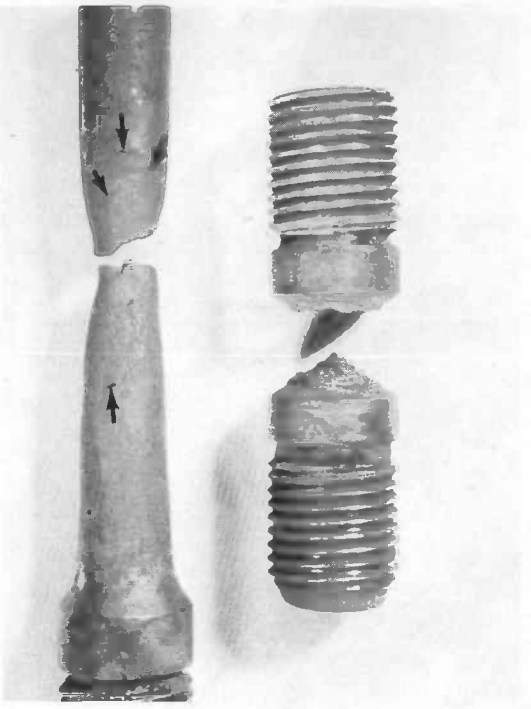

1.7X

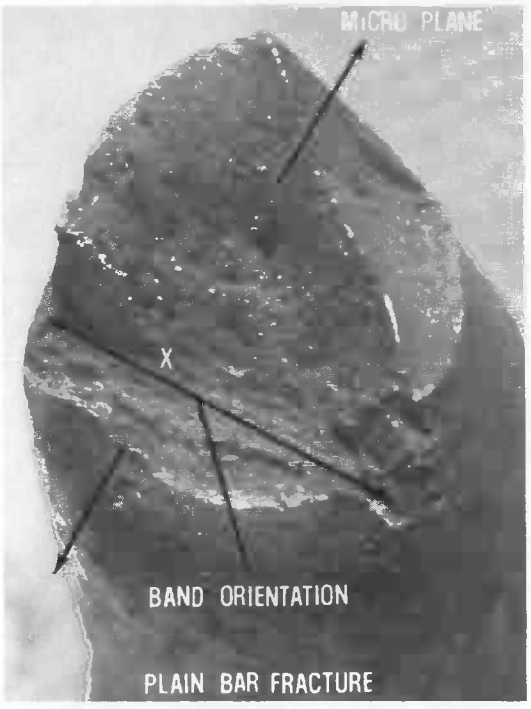

12X

8X

Fig. 3.6 — Fractographic features of both the plane bar and the notch bar fracture surface of the stress rupture specimen CT3A

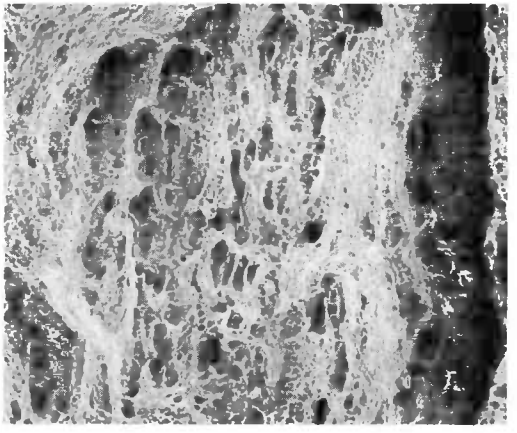

55X

1000X

Fig. 3.7 — SEM fractography of the plane bar fracture surface of specimen CT3A as designated by area X in Fig. 3.6

8.25X

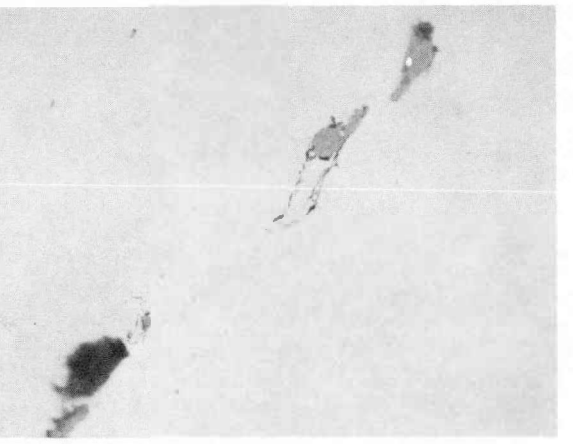

500X

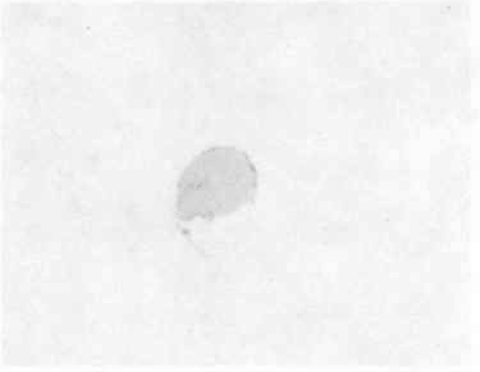

1000X

1000X

Fig. 3.8 — View of a section taken axially through the area designated by X in Fig. 3.6

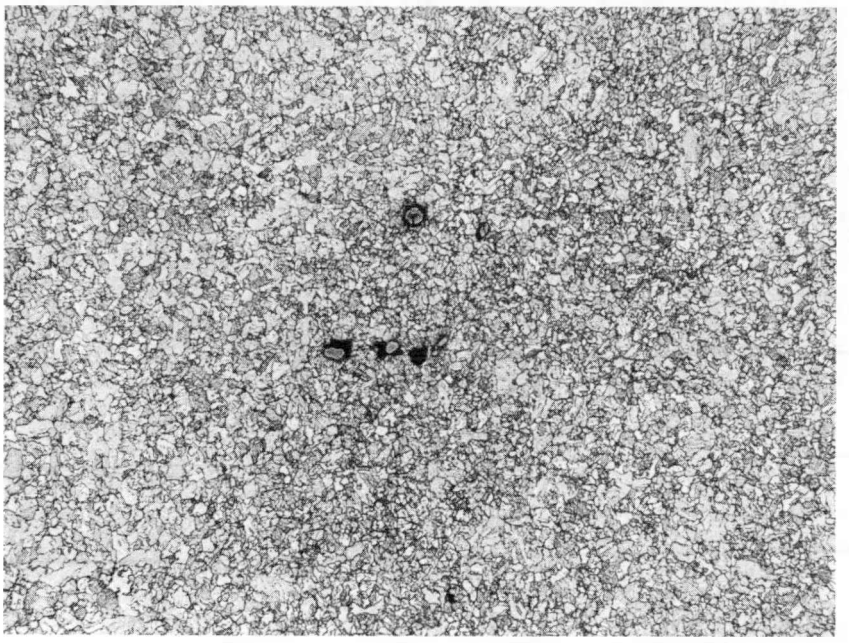

100X

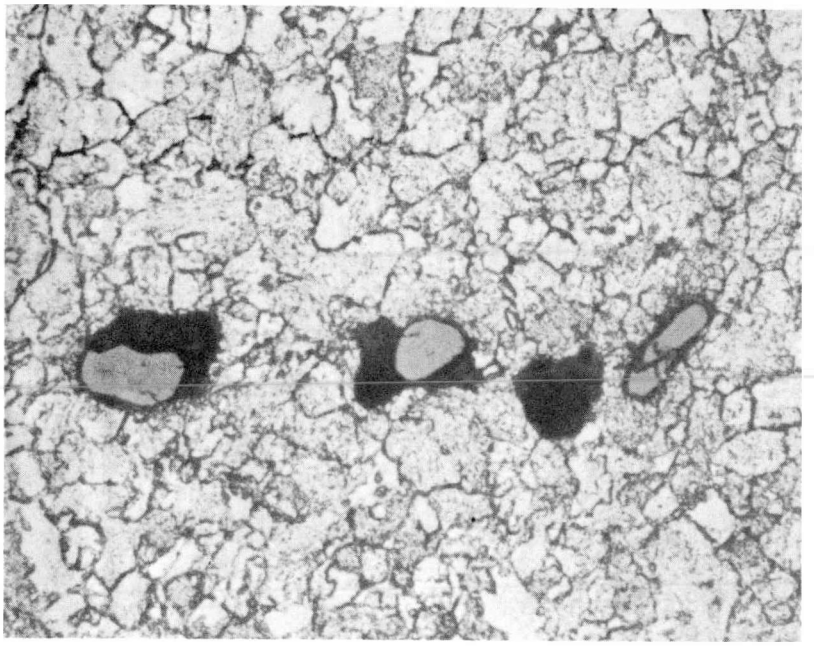

500X

Fig. 3.9 — Two micrographs showing the change of grain size when approaching a cluster of MnS inclusions

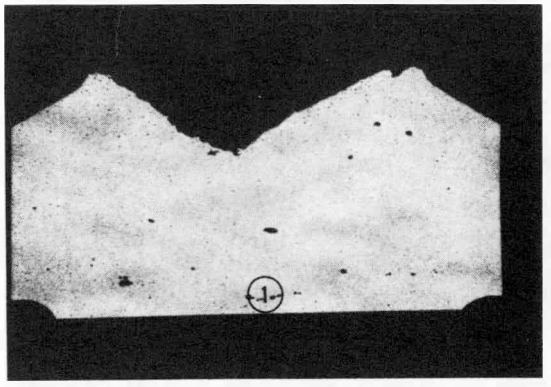

8X

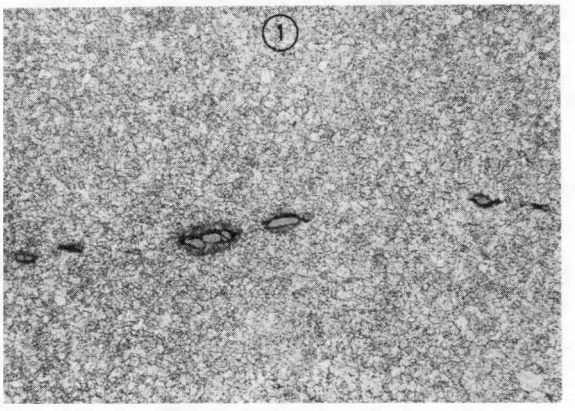

100X

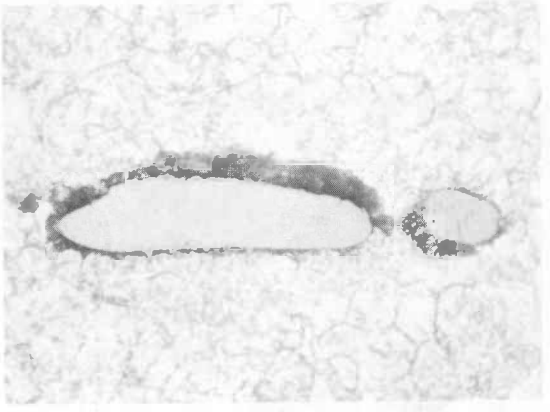

1000X

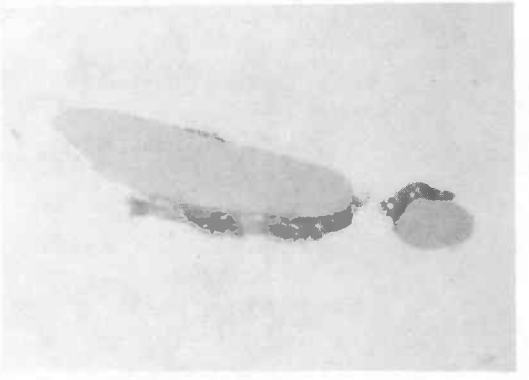

1000X

Fig. 3.10 — Fractographic features of a section taken through the notch of the stress rupture specimen CT3A

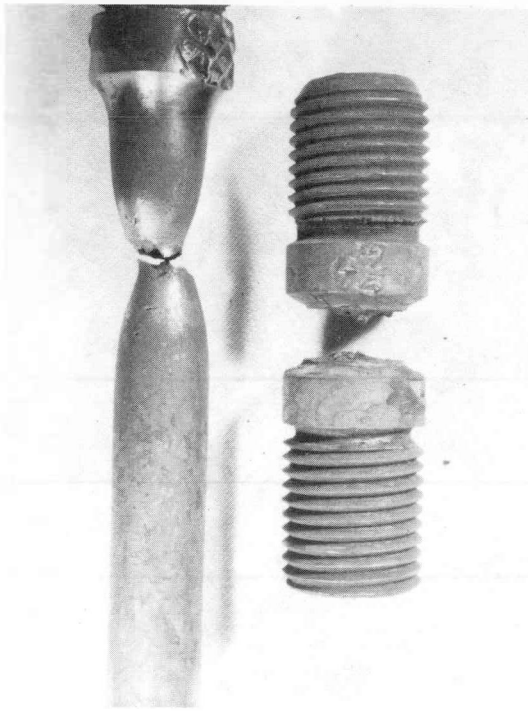

1. 1X

8. 8X

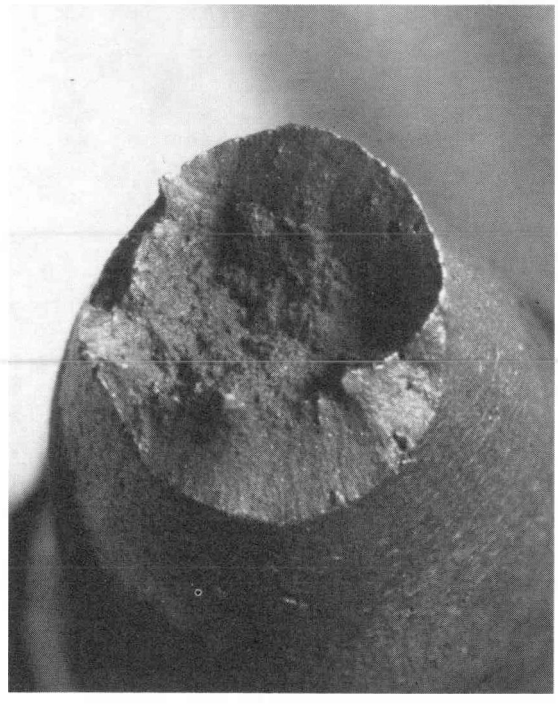

12X

Fig. 3.11 — Fractographic features of both the plane bar and notch bar fracture surfaces of the stress rupture specimen CT12A

55X

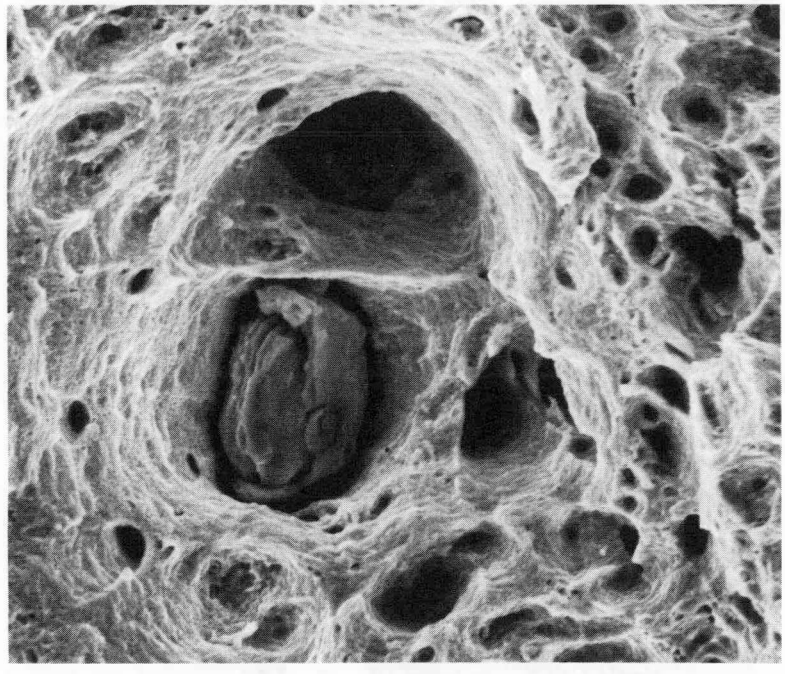

1000X

Fig. 3.12 — SEM fractography of the plane bar fracture surface of specimen CT12A

55X

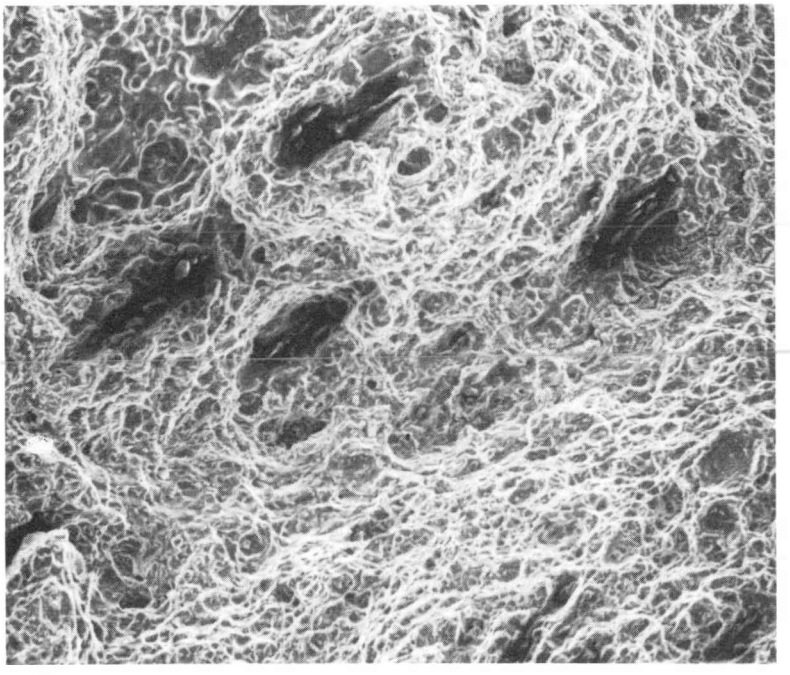

300X

Fig. 3.13 — Fractographic features of the notch bar fracture surface of specimen CT12A

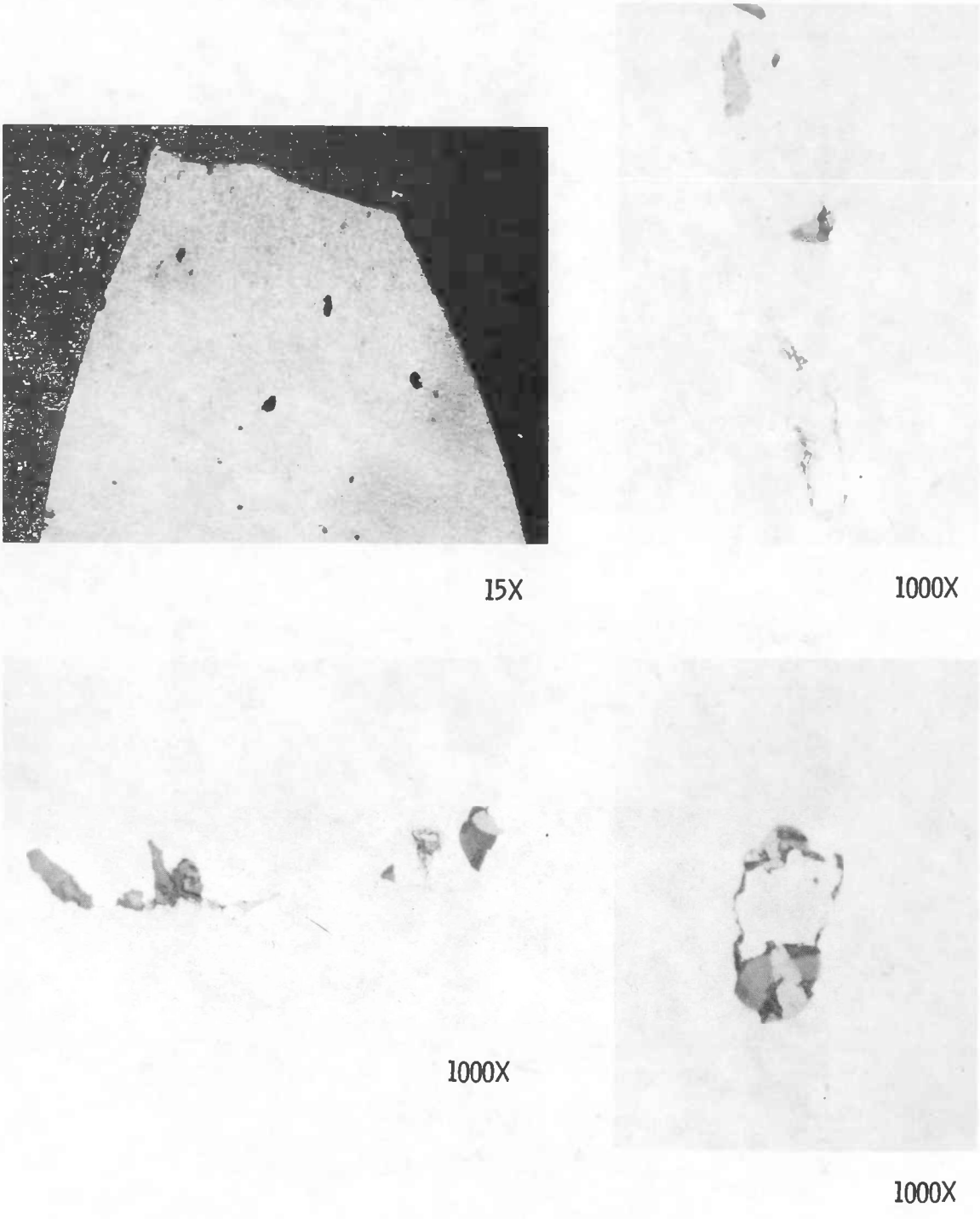

Fig. 3.14 — Micrographs of an axial section taken through the plane bar fracture surface of specimen CT12A

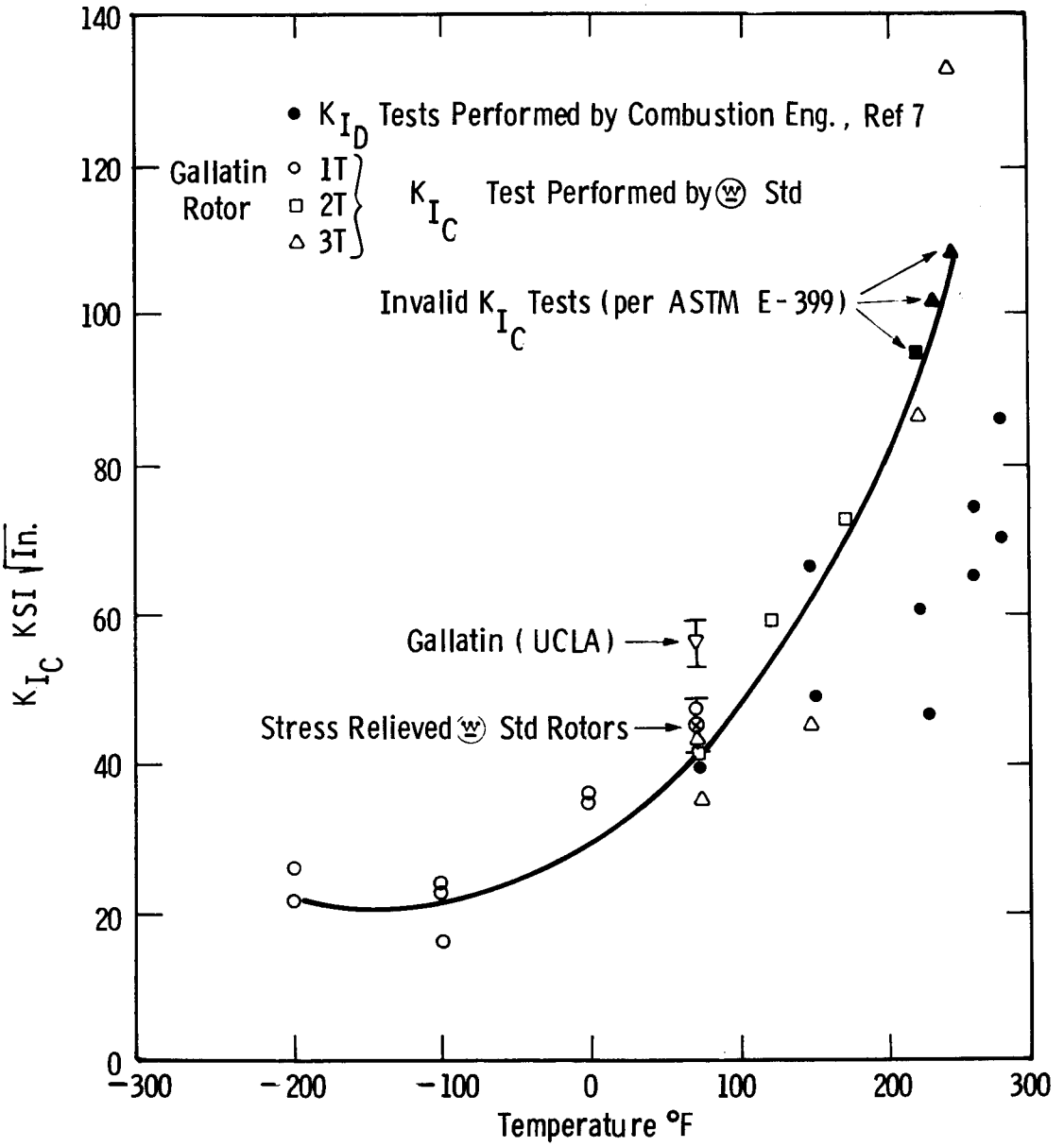

Fig. 3.15 – Fracture toughness of 1950 vintage rotor material

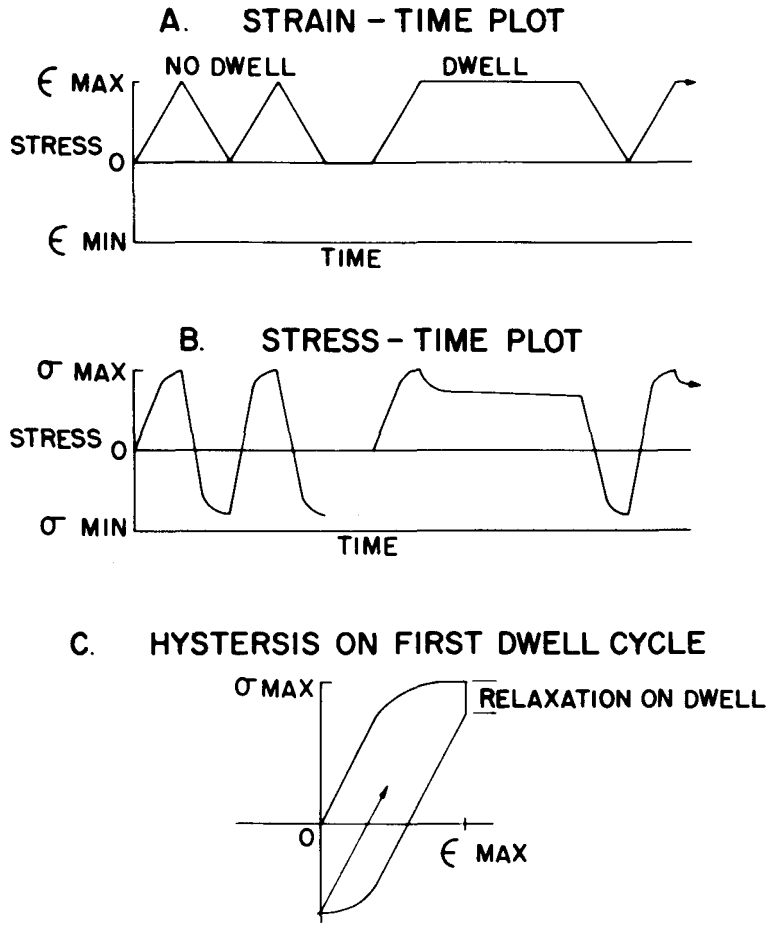

Fig. 3.16 – Schematic diagrams for both continuous cycling and hold time tests showing the strain pattern imposed on the specimen, the resultant stress profile, and a typical initial hold time hysteresis loop

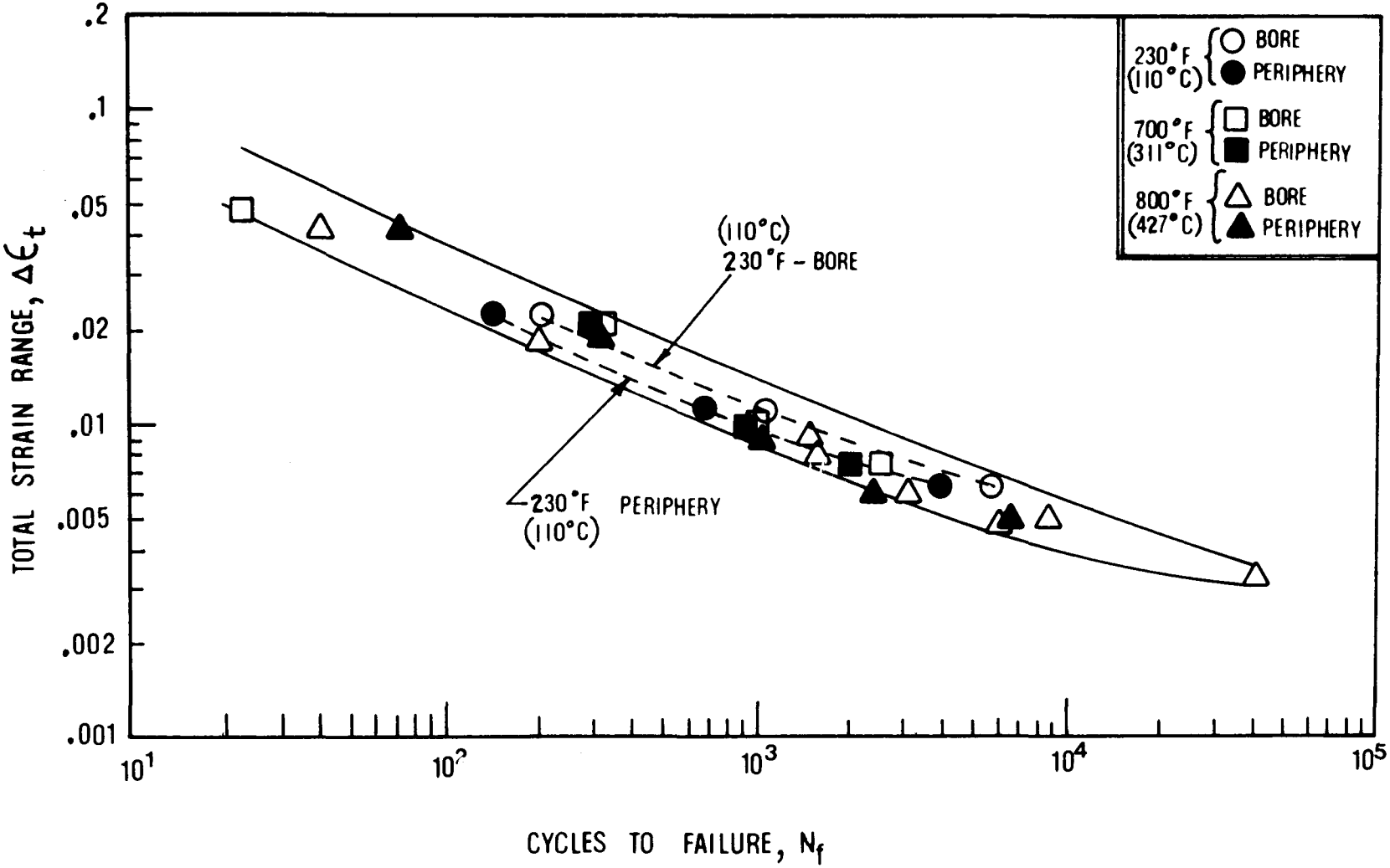

Fig. 3.17 – A summary of all continuous cycling axial fatigue results

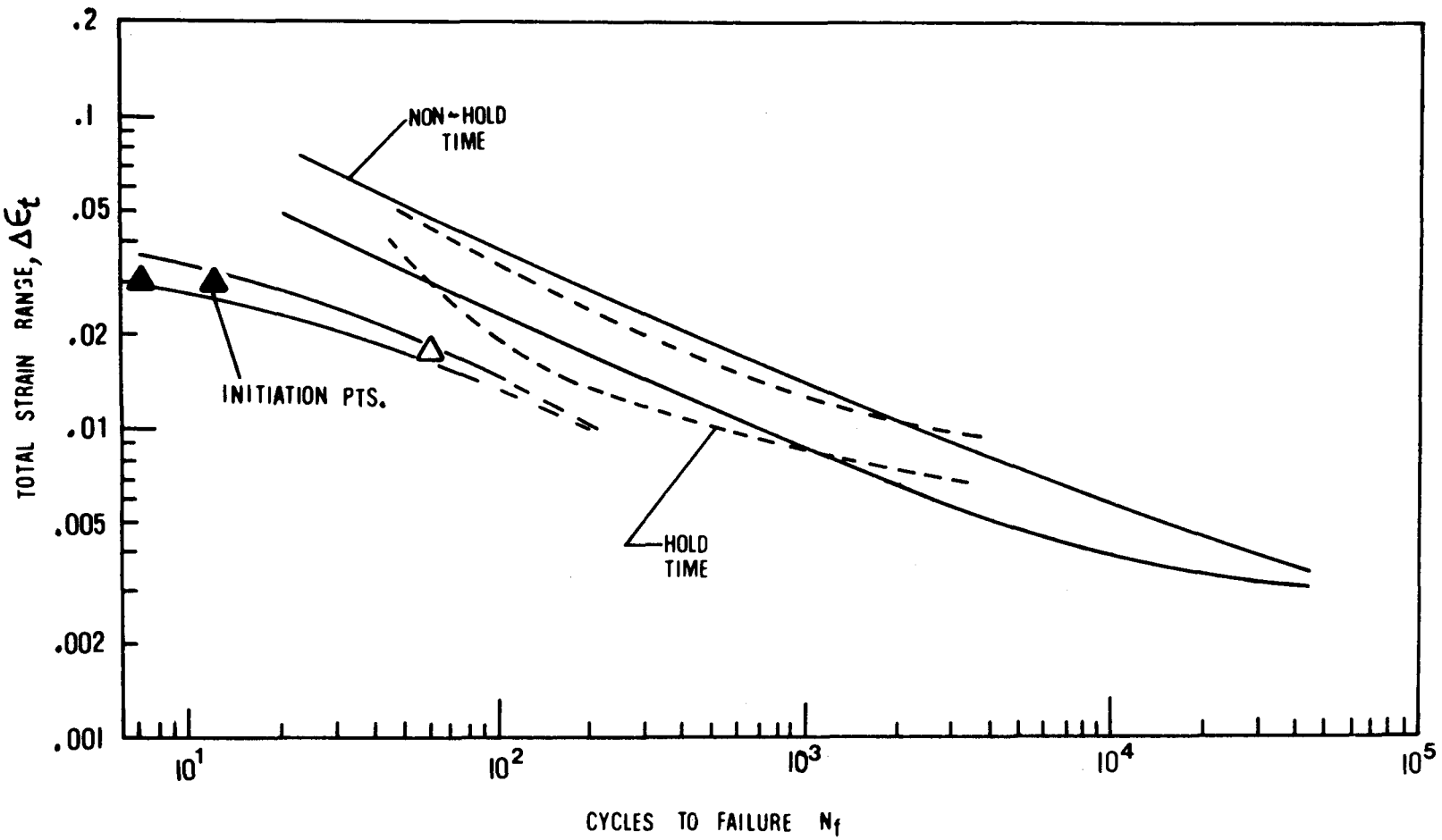

Fig. 3.18 — A summary of all hold time axial fatigue results with superposition of the continuous cycling scatterband

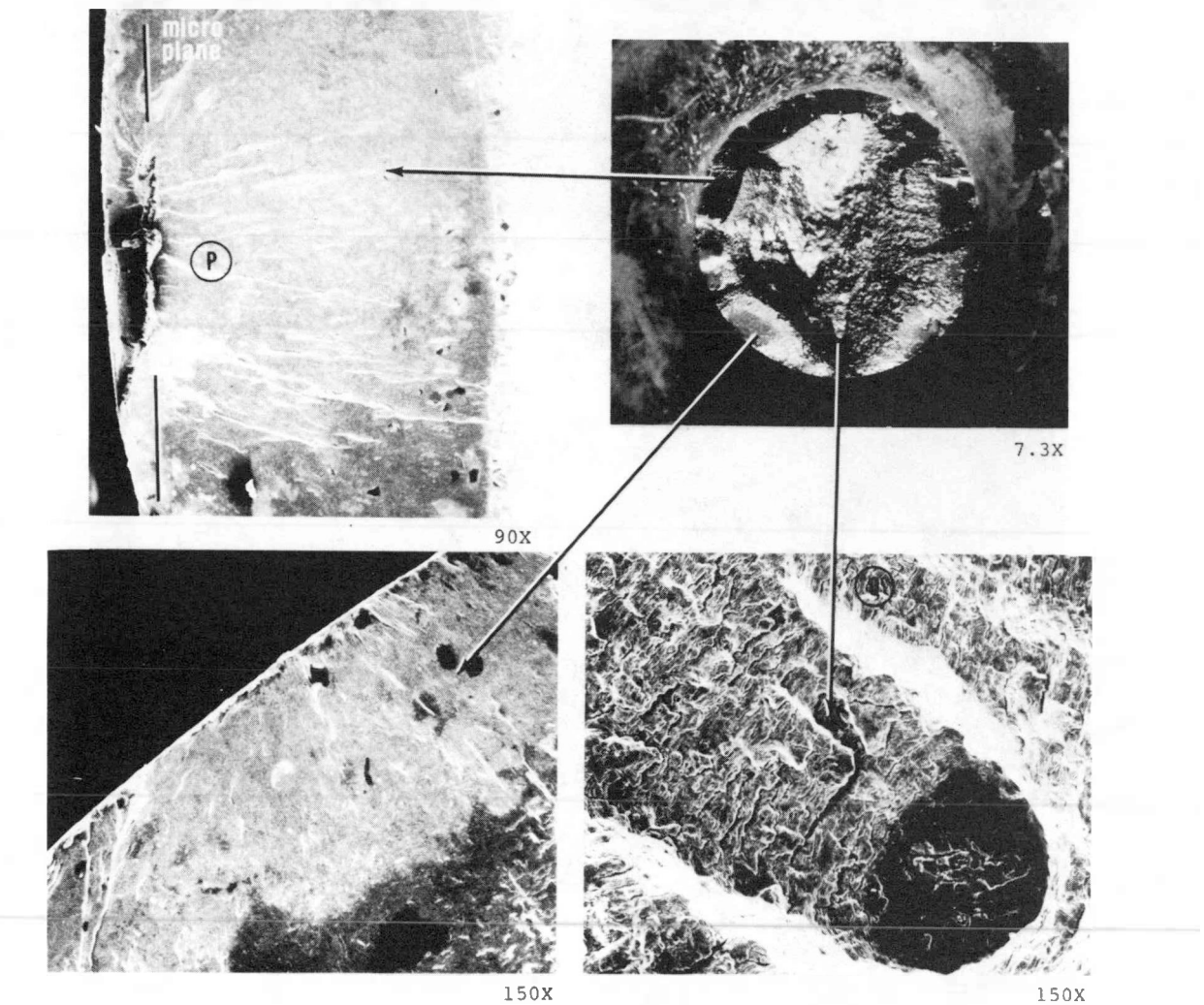

Fig. 3.19 — Fracture surface topography of a LCF specimen tested at a strain range of 0.6% at 800° F

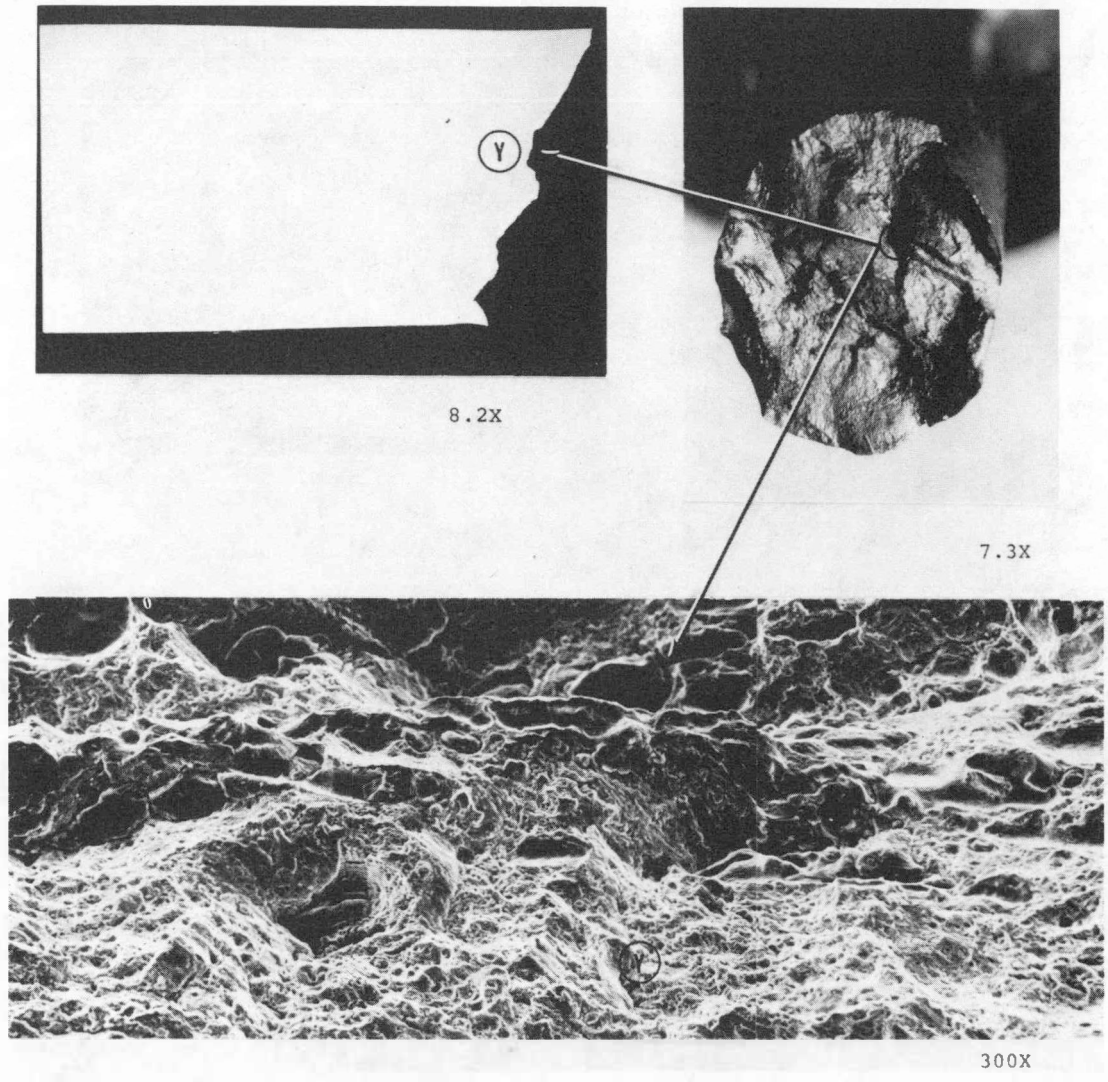

Fig. 3.20 — Fracture surface topography of a LCF specimen taken from the bore region of the rotor and tested at a strain range of 4.3% at 800°F

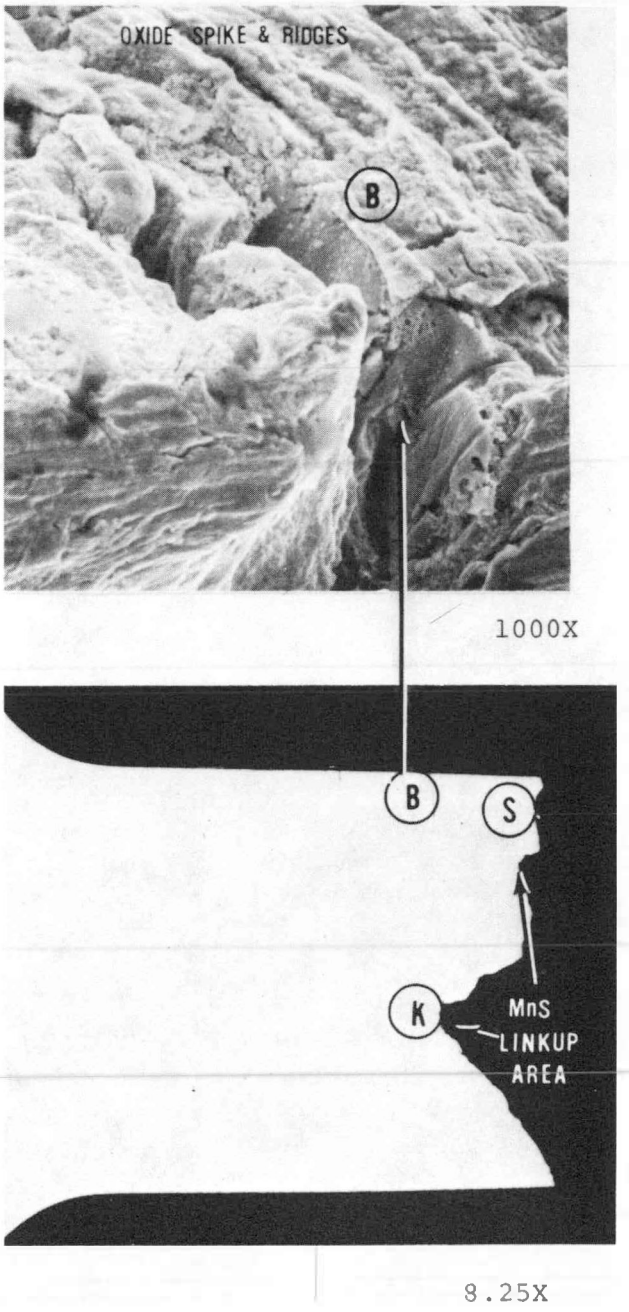

Fig. 3.21 – Metallographic features of a one hour hold time LCF specimen taken from the bore region of the rotor and tested at a strain range of 3.23% at 800°F

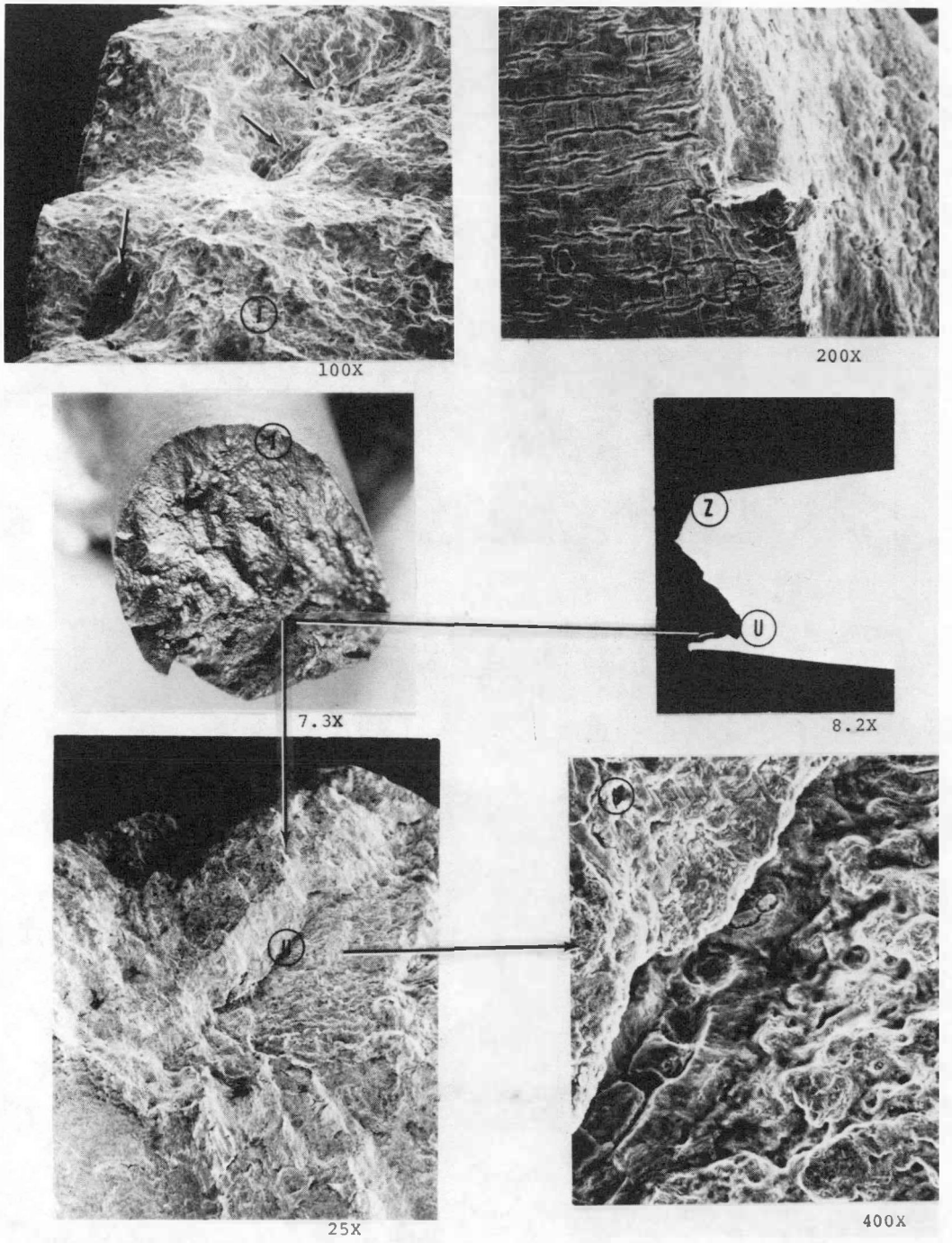

Fig. 3.22 — Fractographic features of a four hour hold time LCF specimen taken from the bore region of the rotor and tested at a strain range of 2.85% at 800°F

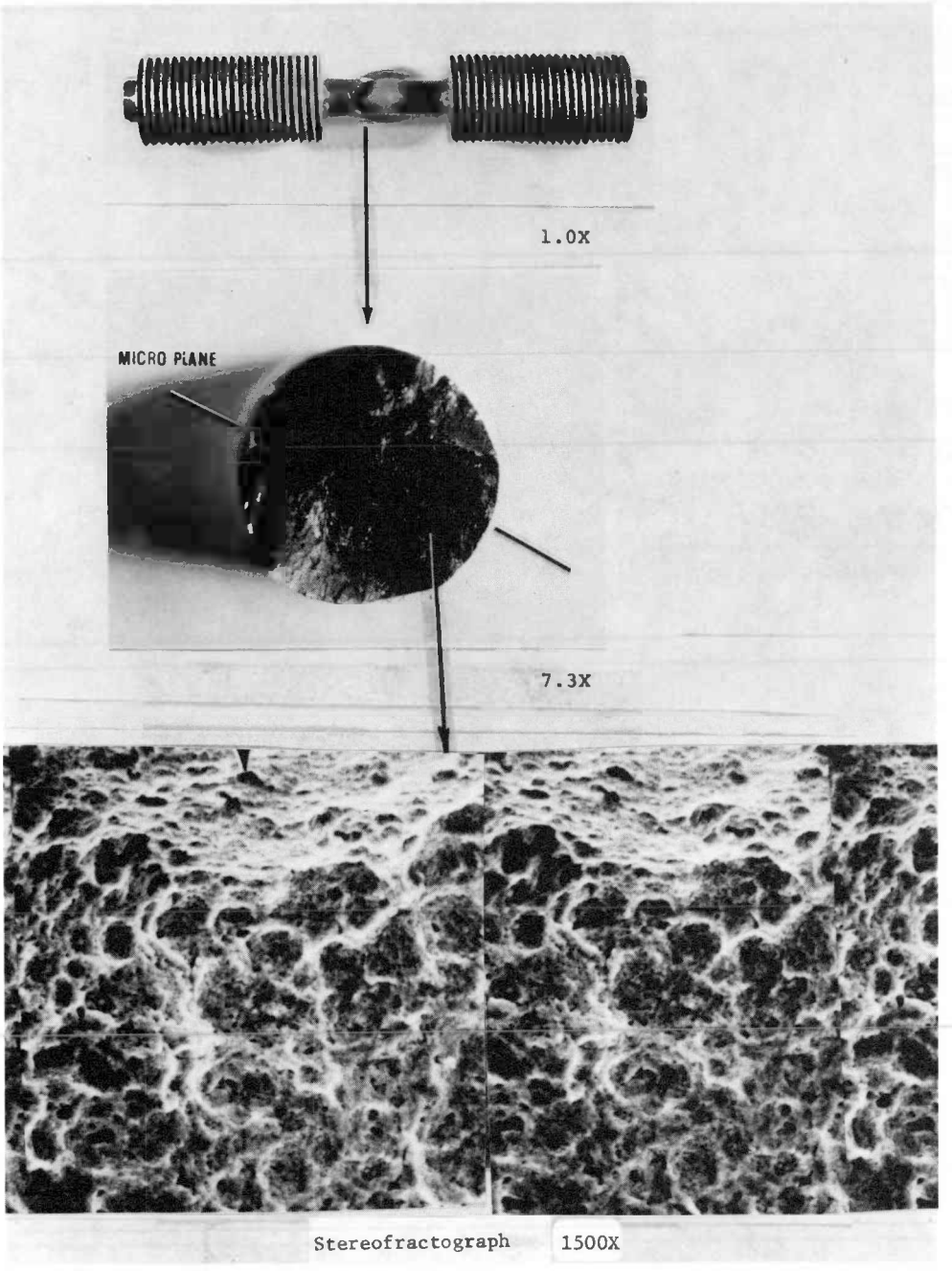

Fig. 3.23 — Stereofractograph of a 23 hour hold time LCF specimen taken from the bore region of the rotor and tested at a strain range of 2.98% at 800° F

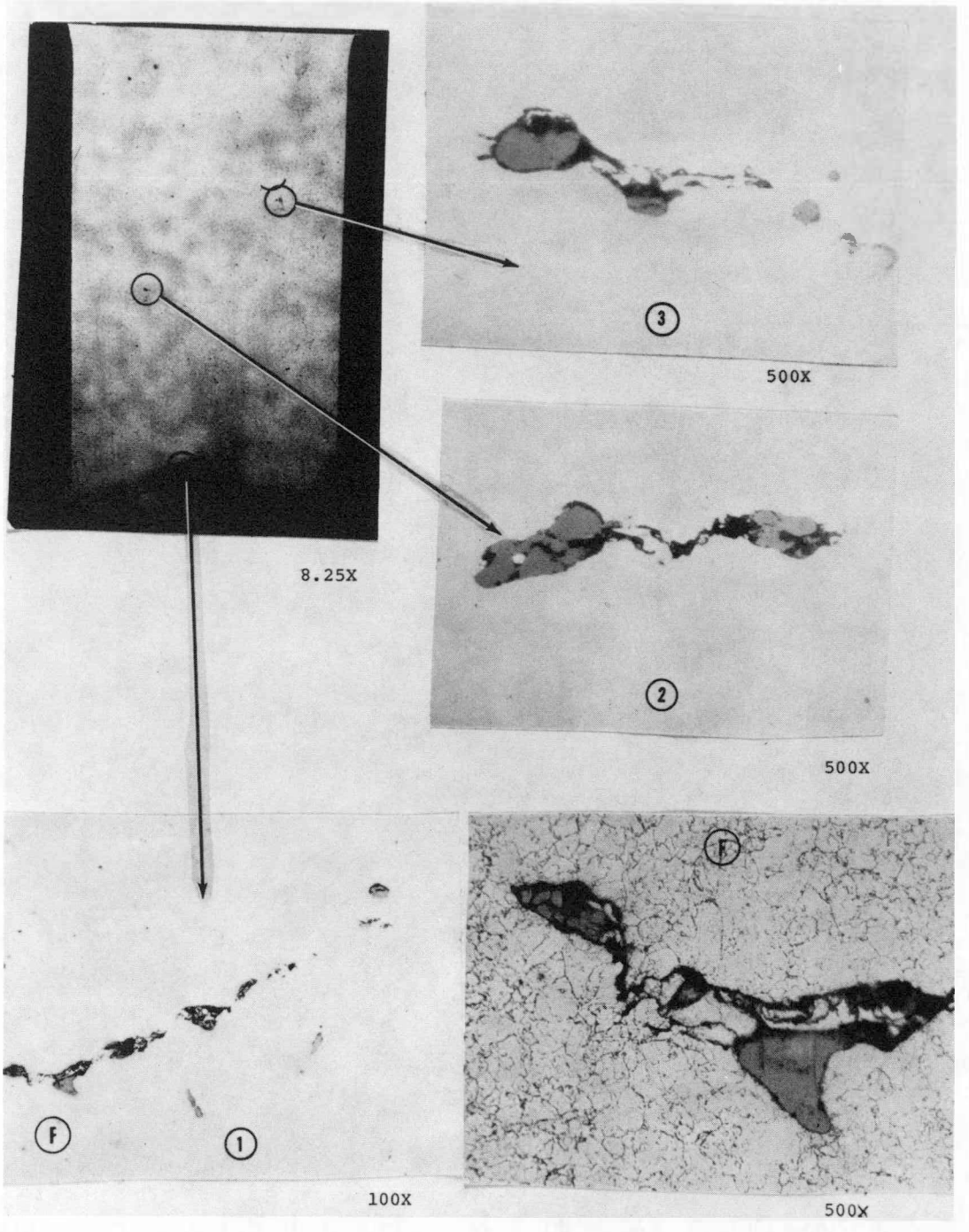

Fig. 3.24 — Metallographic features of the 23 hour hold time specimen, as shown in Figure 3.23 (2.98% strain, 800°F)

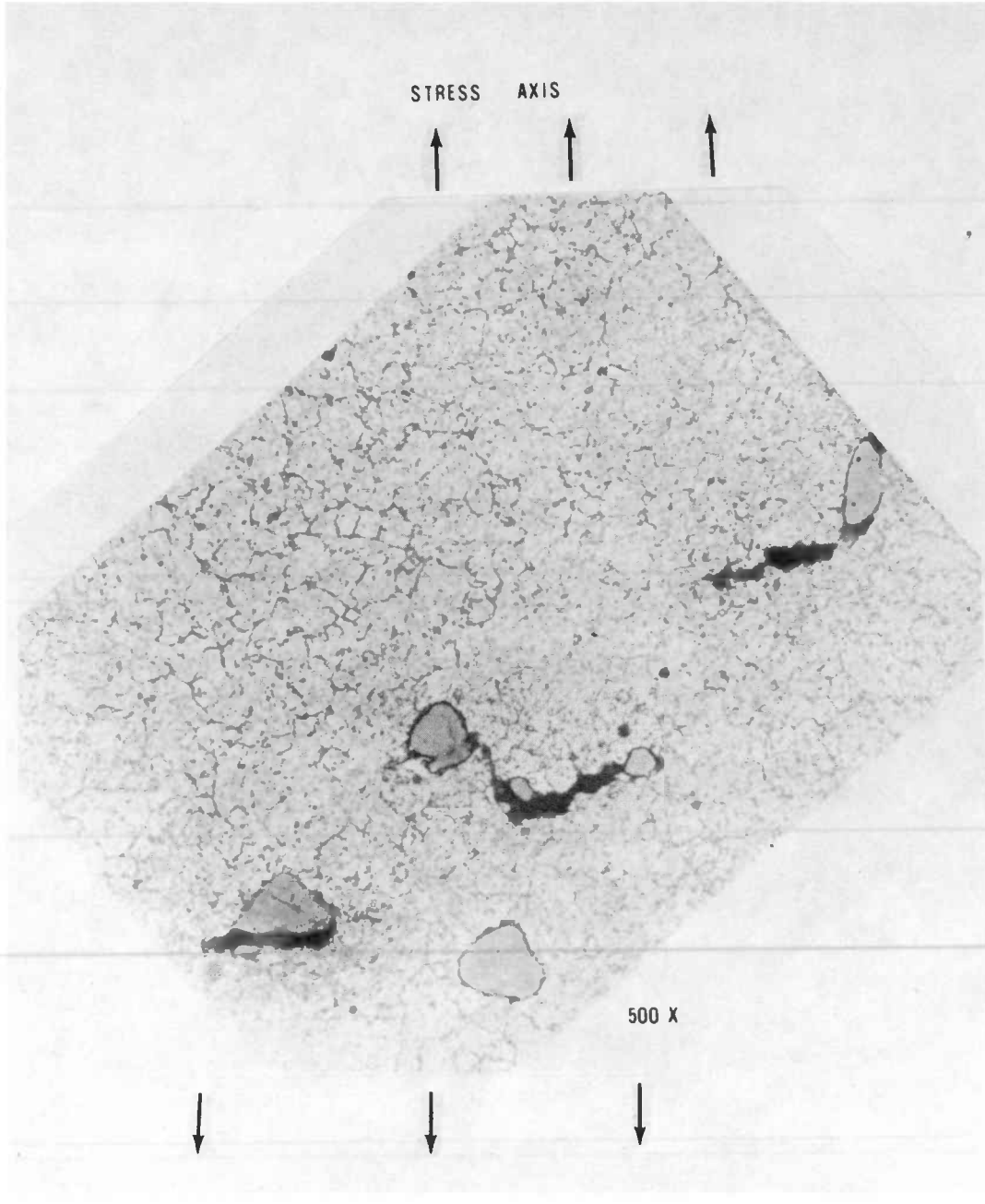

Fig. 3.25 – A view of integranular cracking between MnS inclusions in a 24 hour hold time LCF specimen tested at a strain range of 2.98% at 800°F (12 loading cycles)

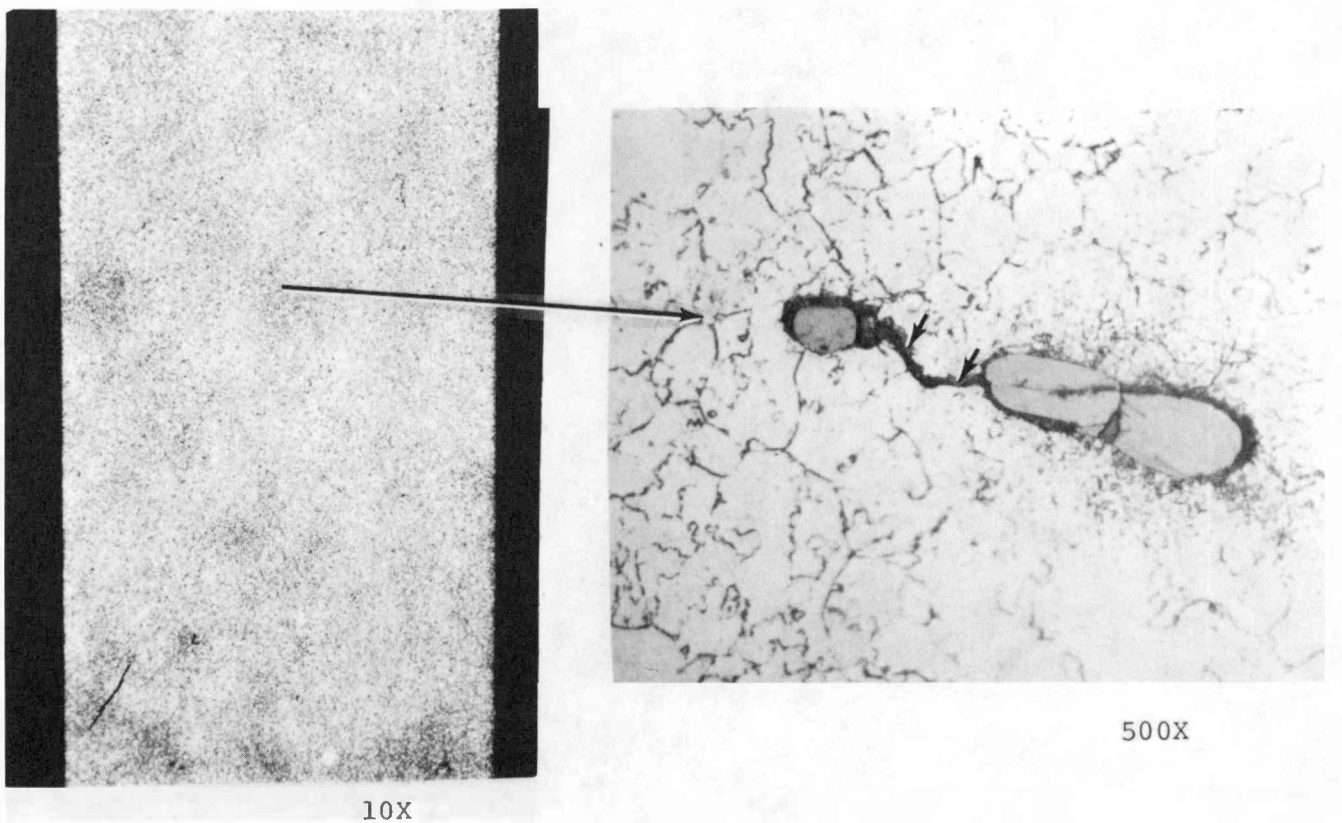

Fig. 3.26 — A view of transgranular cracking between MnS inclusions from a specimen taken from the periphery of the rotor tested with a one hour hold time, at a strain range of 1.75% at 800°F

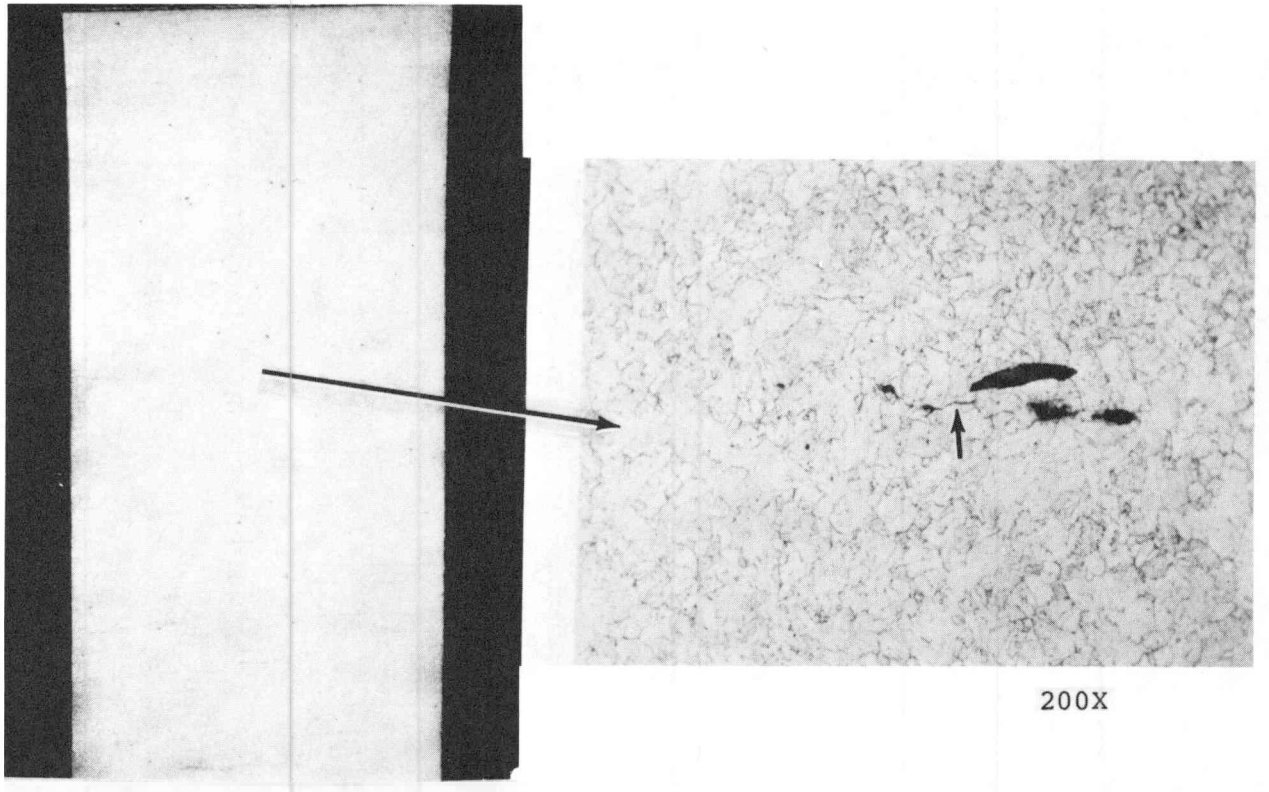

Fig. 3.27 — A view of transgranular cracking between MnS inclusions from a specimen taken from the periphery of the rotor tested with a 24 hour hold time, at a strain range of 1.75% at 800° F

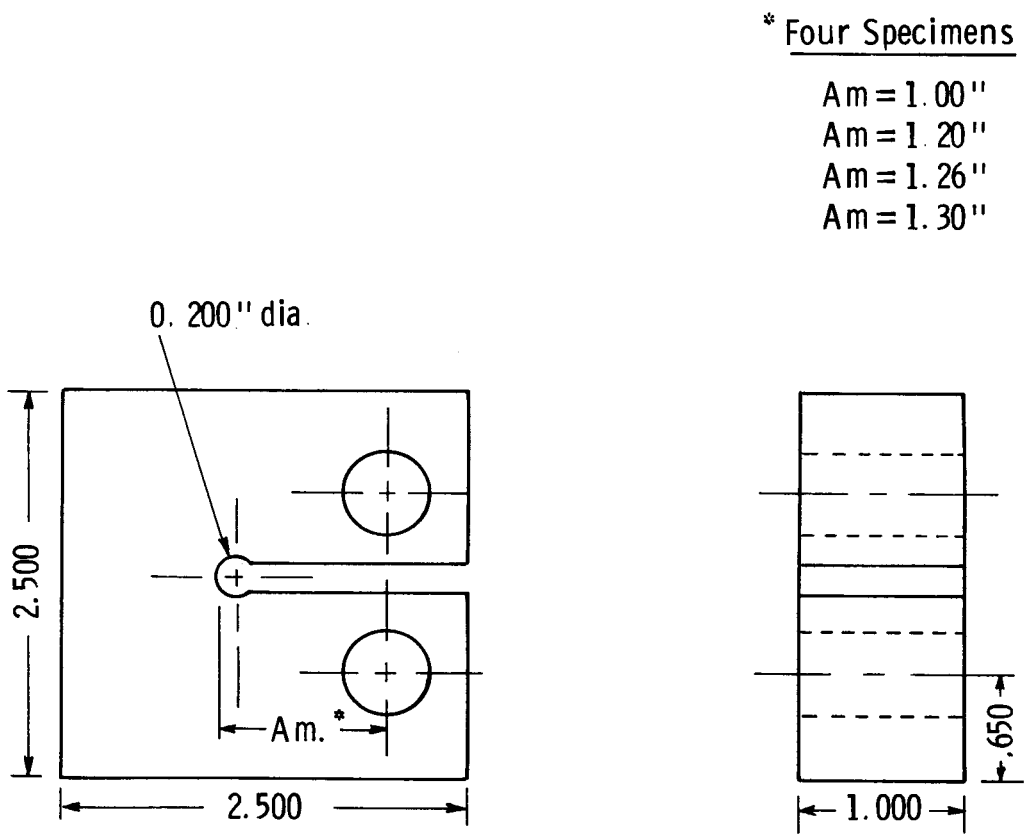

Fig. 3.28—Keyhole type blunt notch compact specimen used in biaxial low cycle fatigue testing

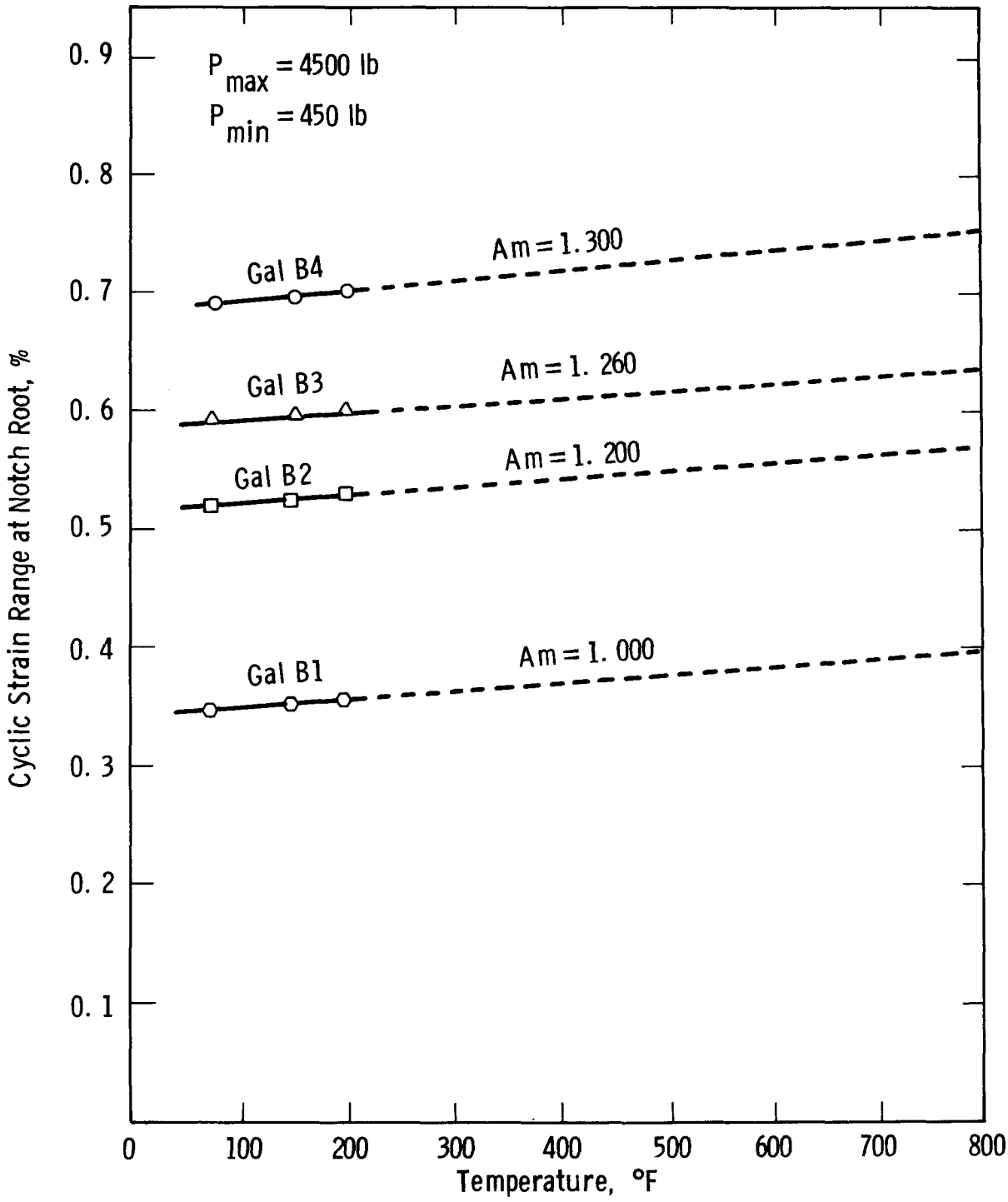

Fig. 3. 29—Cyclic strain range at notch root versus temperature for blunt notched specimen subjected to cyclic load between 450 lb. and 4500 lb

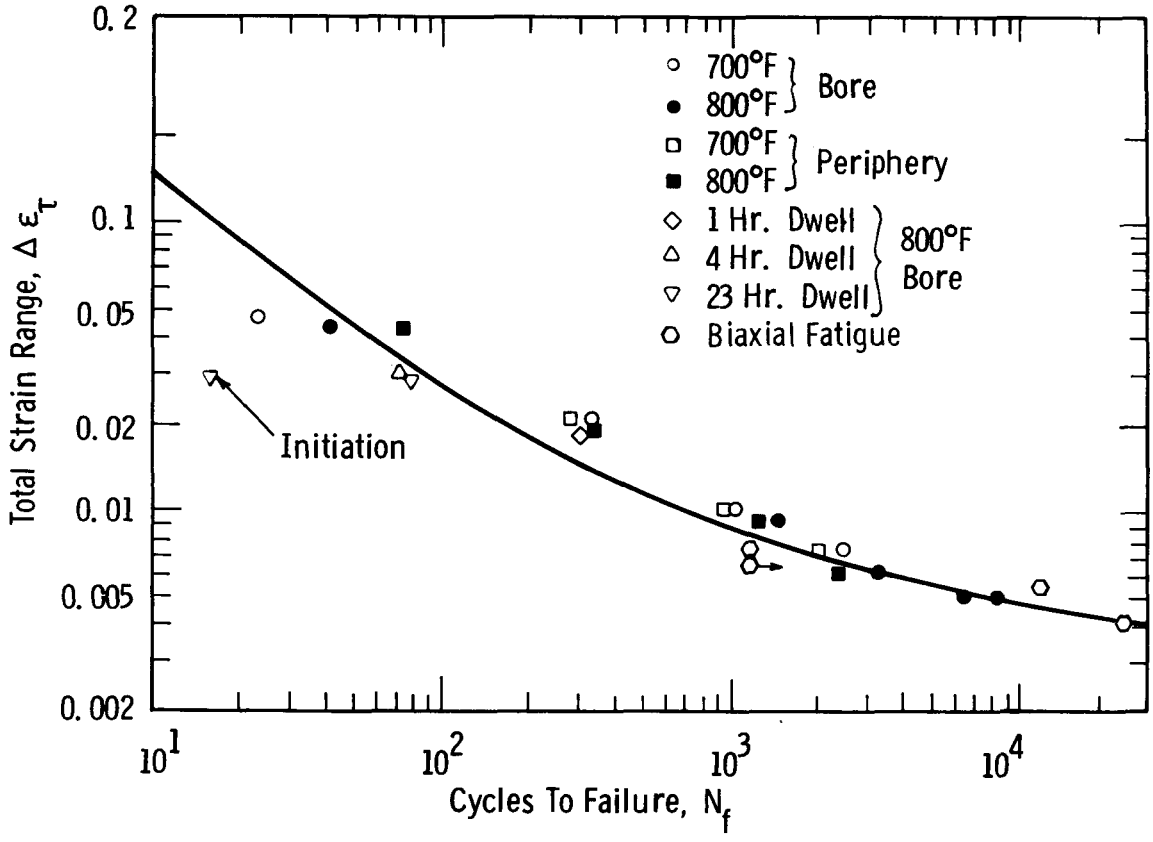

Fig. 3.30—A summary of LCAF tests including dwell times for both uniaxial and biaxial states of stress (Gallatin material)

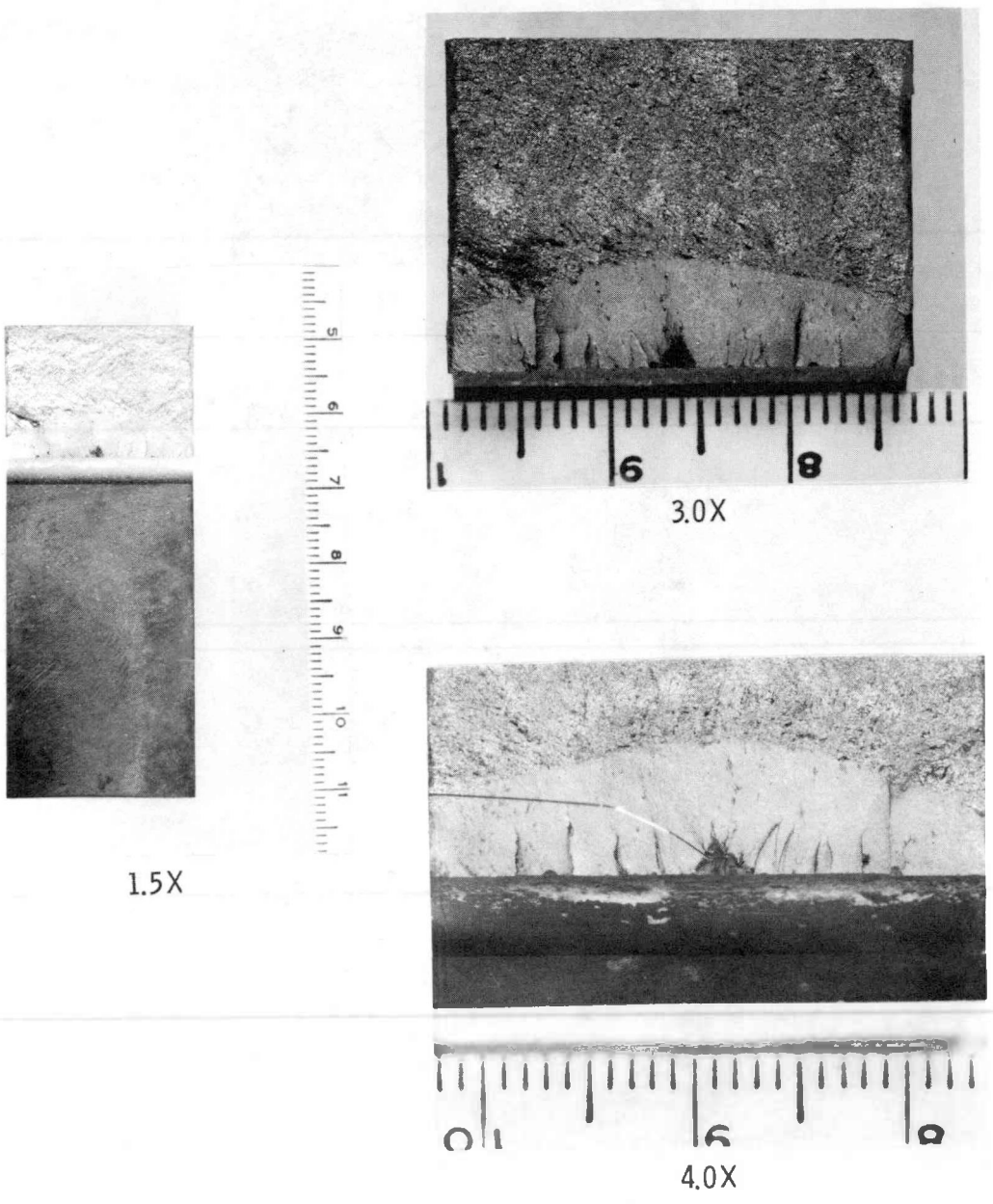

Fig. 3.31—View of triangular initiation point of 1 hour hold time low cycle fatigue test on blunt notch compact specimen (Gallatin material) at 800° F (427° C)

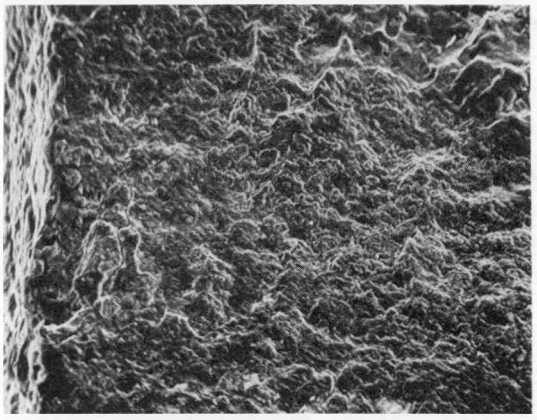

200X

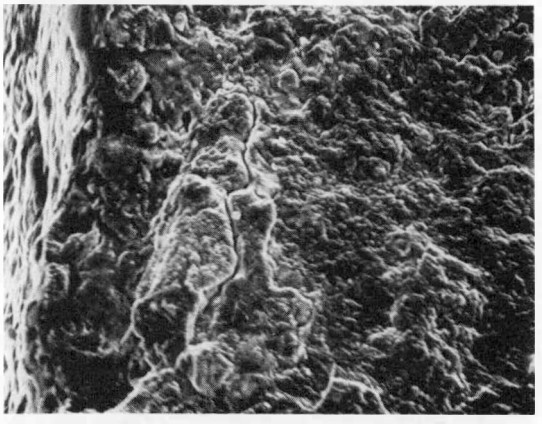

500X

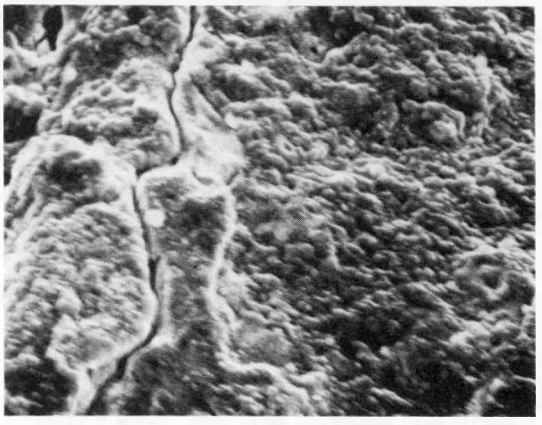

1000X

Fig. 3.32 — High magnification view of triangular crack initiation area (see Fig. 3.31) showing typical fatigue morphology

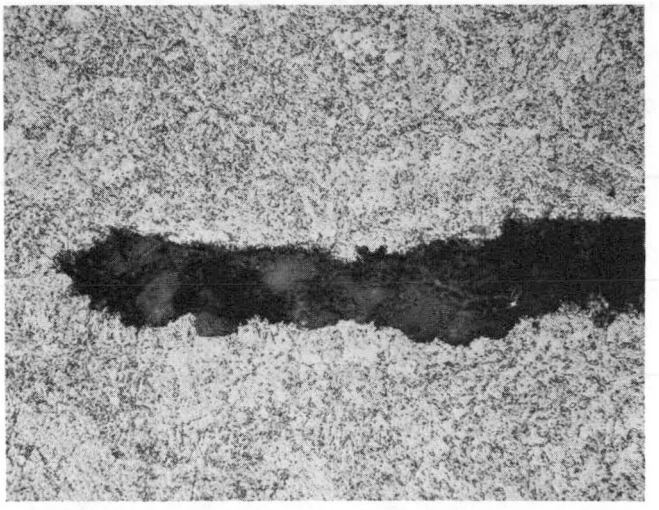

500X

A

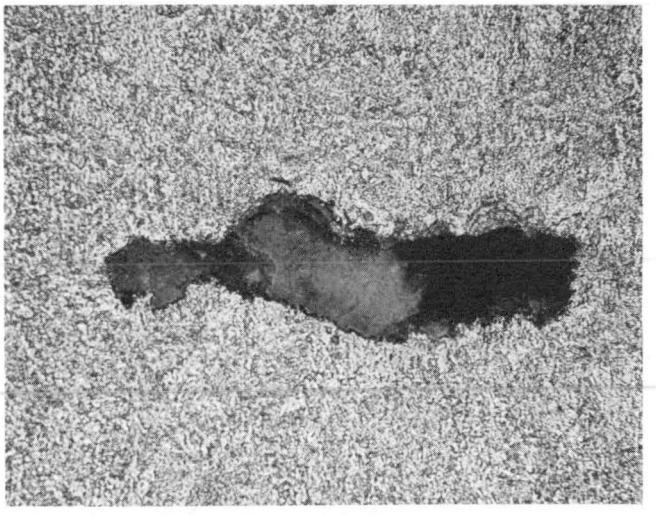

500X

B

Fig. 3.33 — The mangenese sulfide inclusions in LCF specimen of Gallatin material (A) in the transverse plane (B) in the longitudinal plane

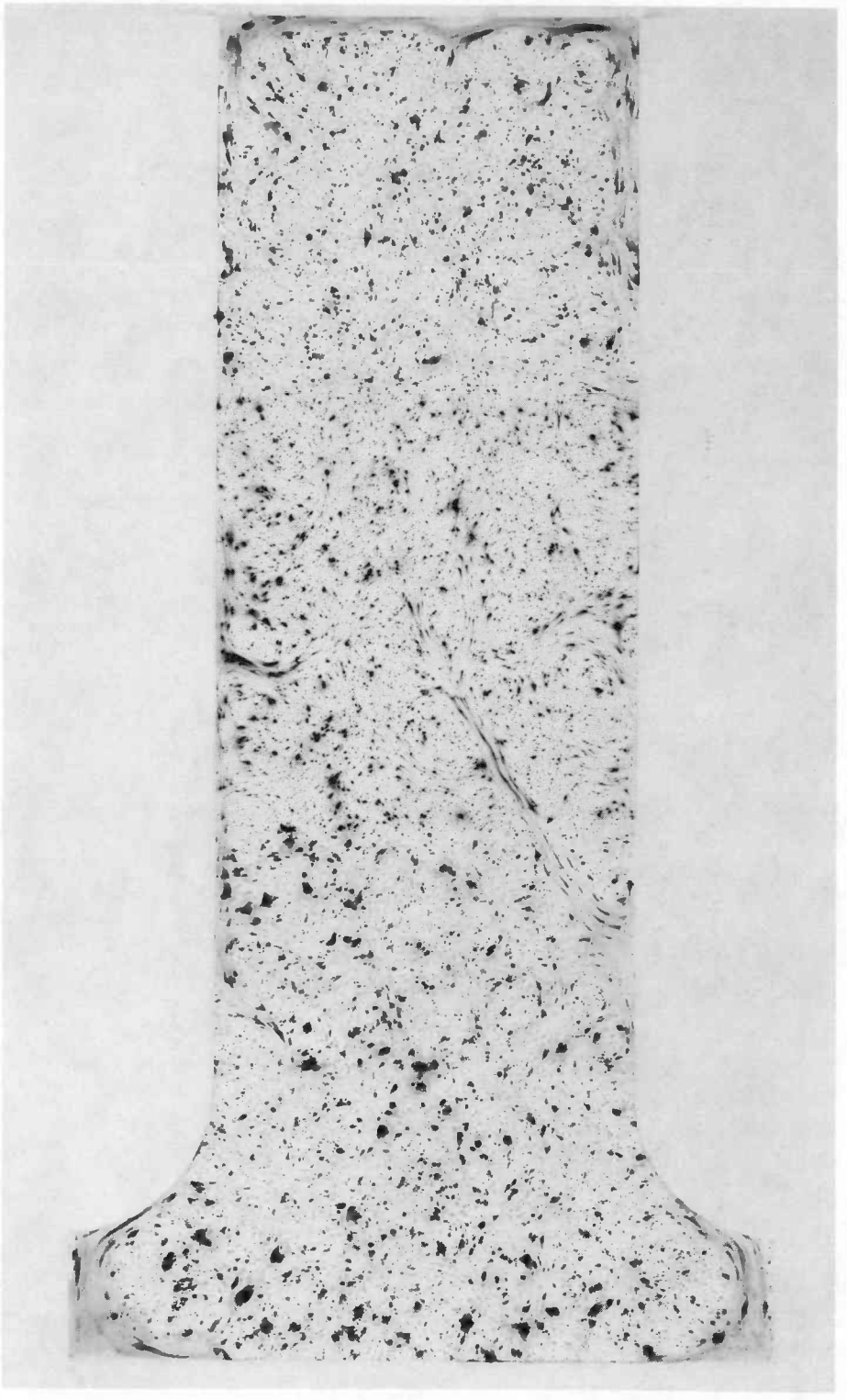

Fig. 3.34 — Sulfur print of axial slice of a large low cycle fatigue specimen taken from the periphery of the Gallatin rotor

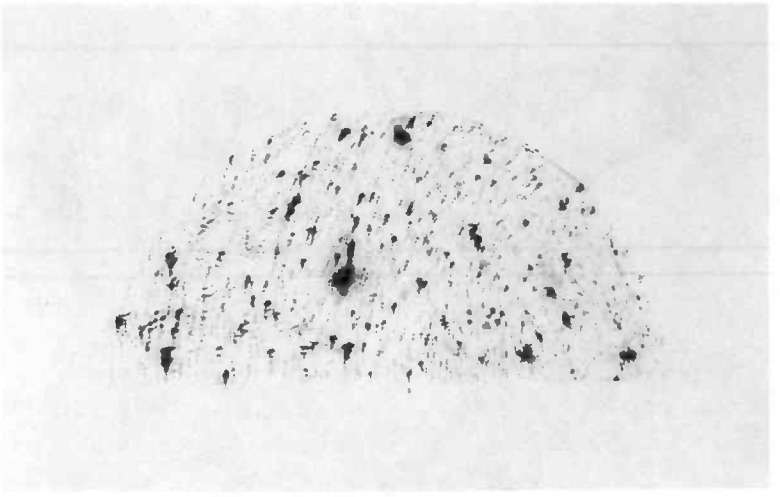

Fig. 3.35 — Sulfur print of the cross-section of a large low cycle fatigue specimen taken from the periphery of the Gallatin rotor

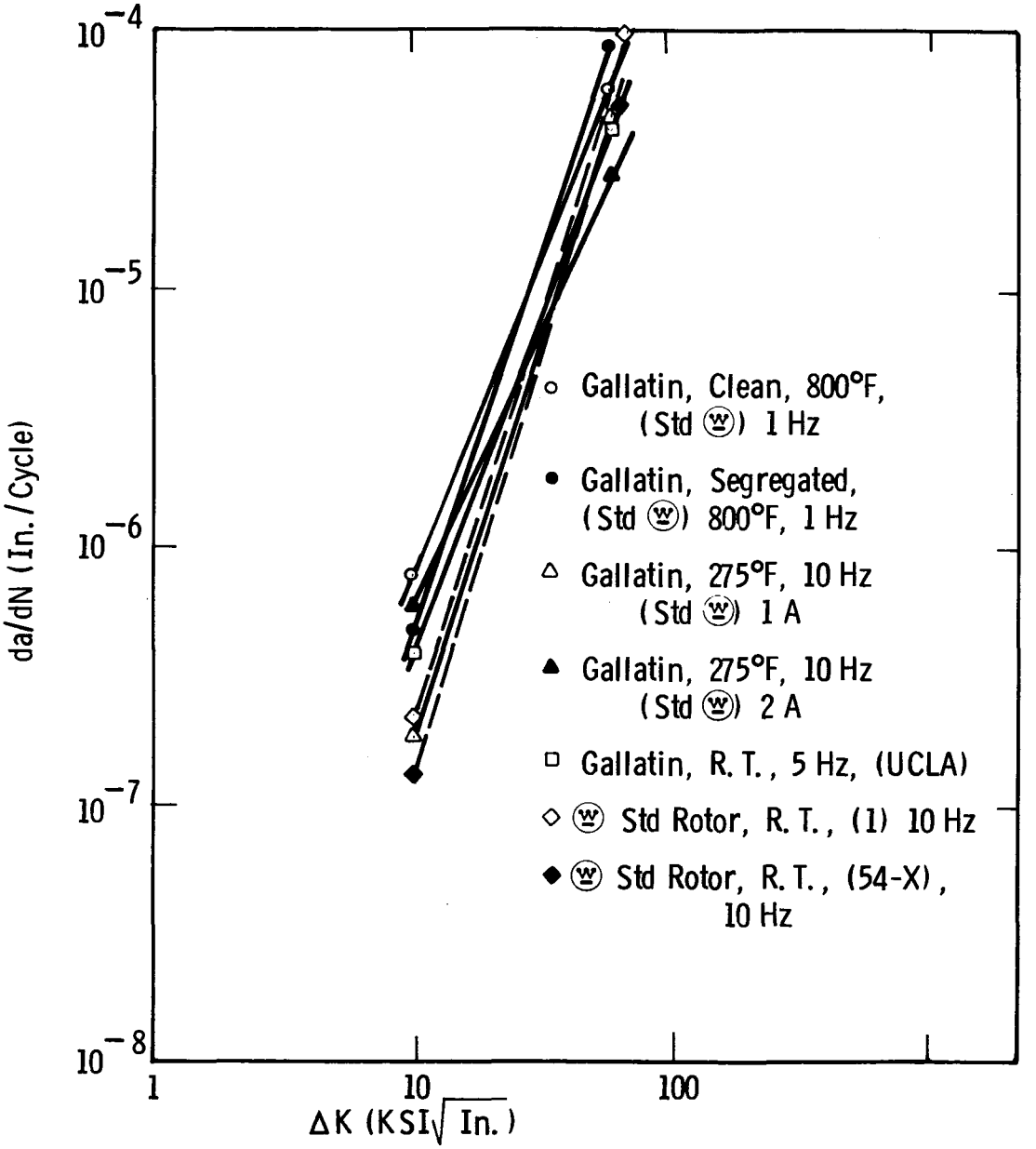

Fig. 3.36 – Summary of da/dN vs. ΔK data from various sources

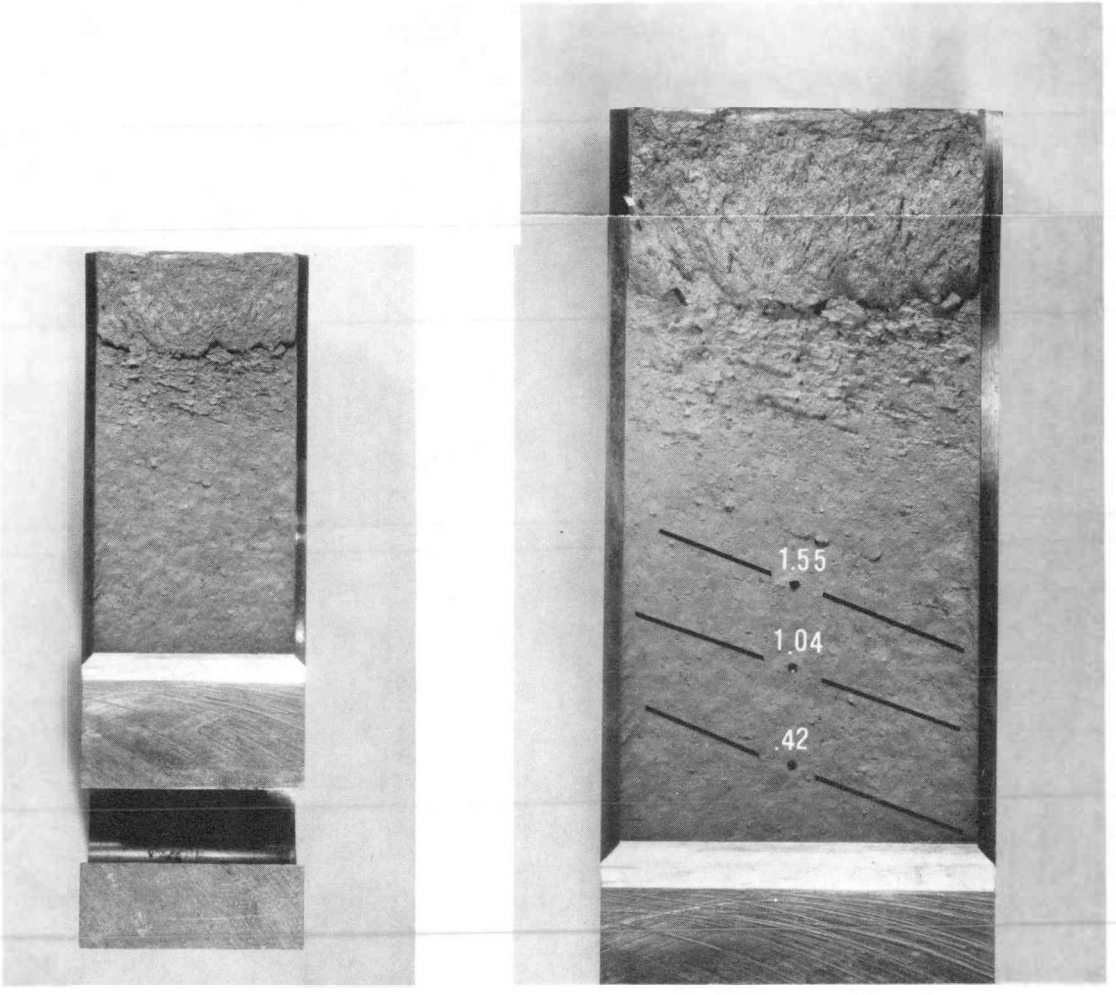

1X 0.65X

Fig. 3.37 — Dark lines denote band orientations on fatigue surface of specimen 1A (2T-WOL) taken from the Gallatin rotor

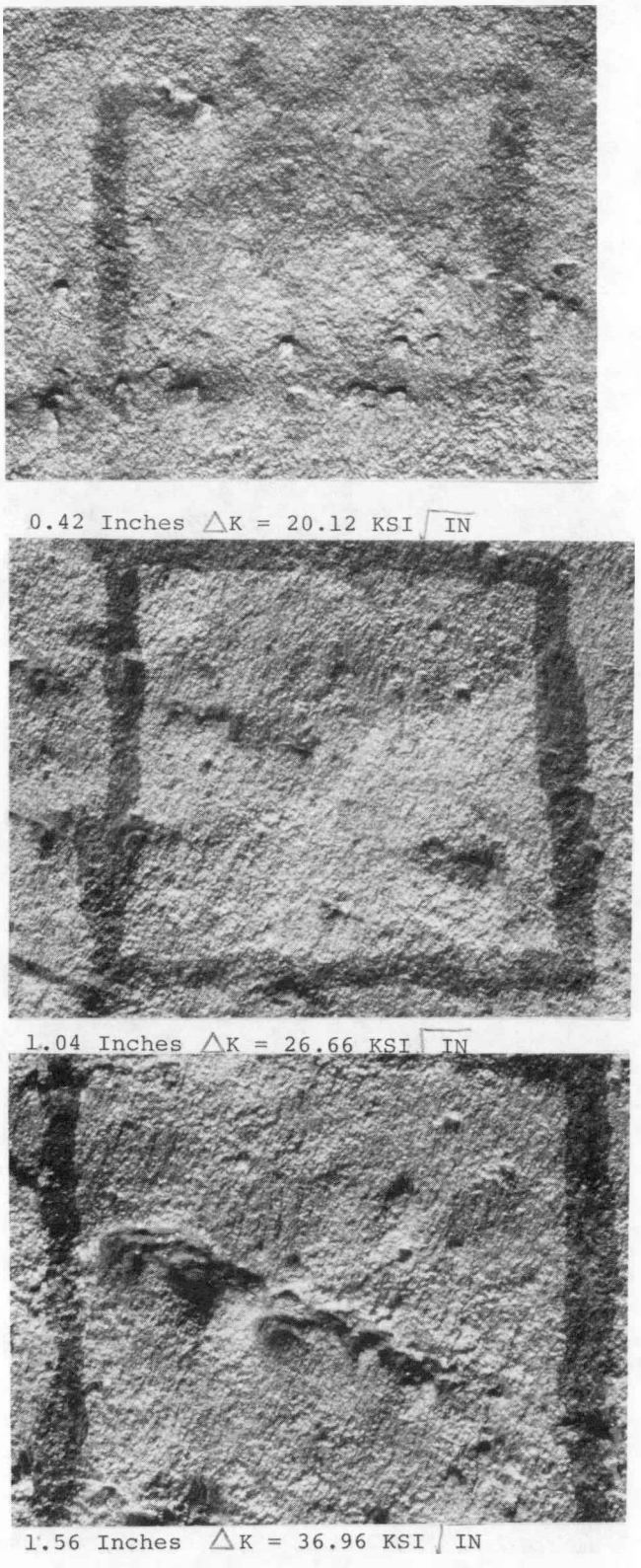

Fig. 3.38 – 12X. Optical macrographs of the 0.42, 1.04 and 1.55 inch locations on specimen 1A

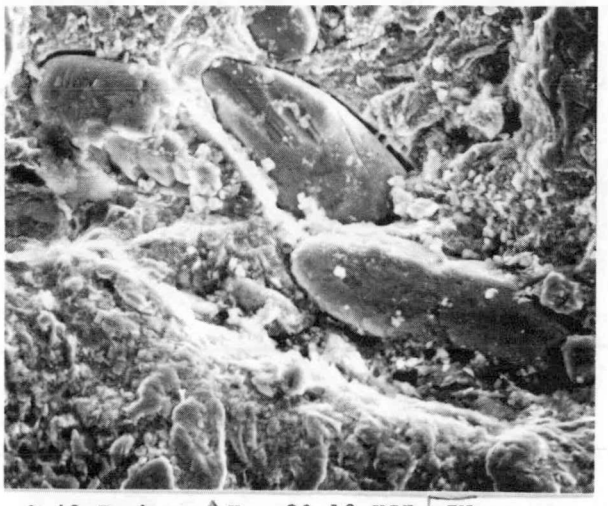

0.42 Inches ΔK = 20.12 KSI $\sqrt{IN}$

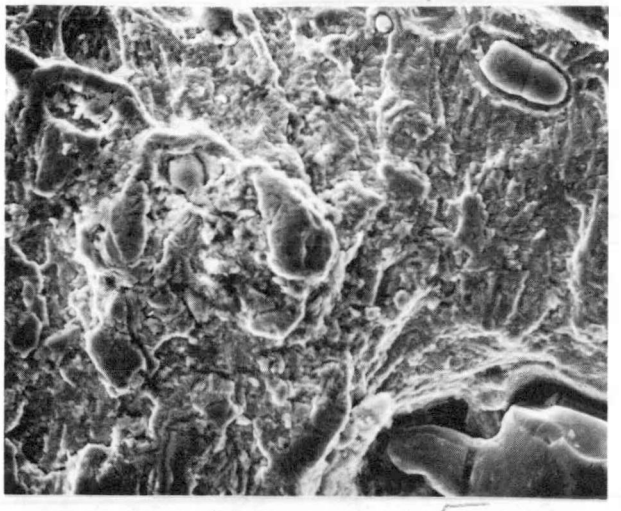

1.04 Inches ΔK = 26.66 KSI $\sqrt{IN}$

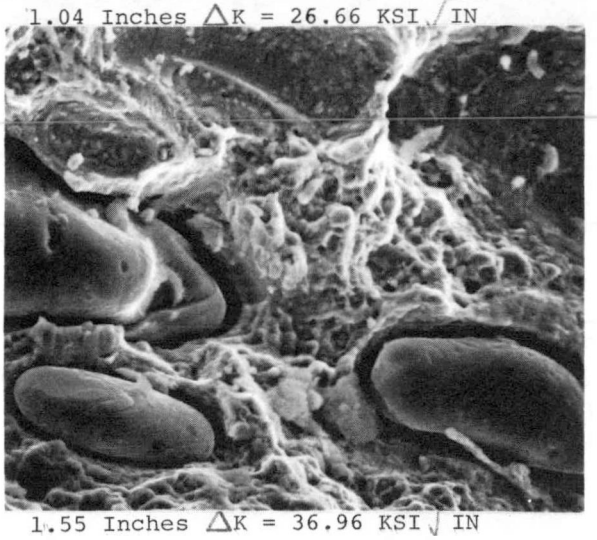

1.55 Inches ΔK = 36.96 KSI $\sqrt{IN}$

Fig. 3.39 – 1000X. SEM topography at the 0.42, 1.04 and 1.55 inch locations on specimen 1A

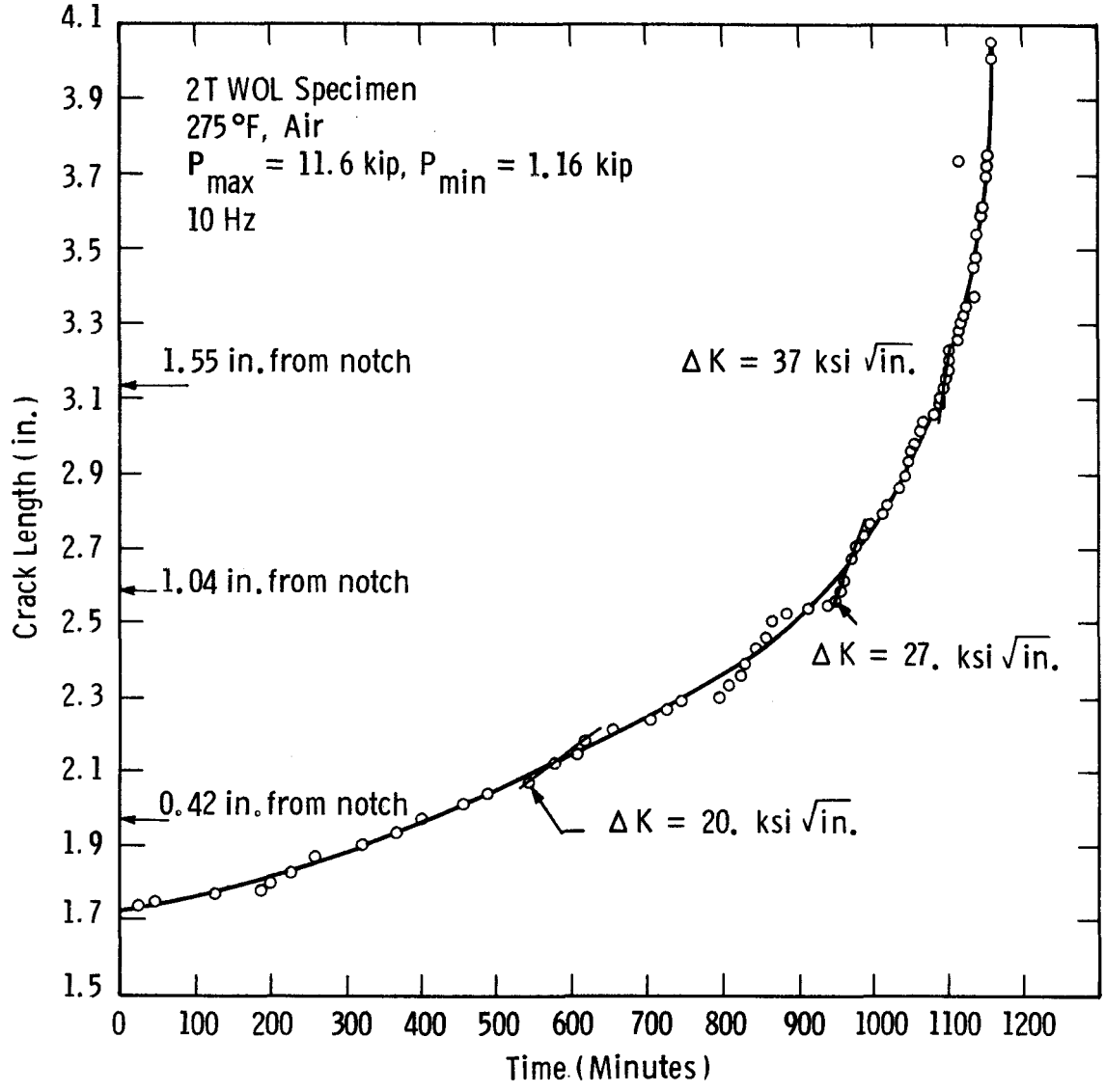

Fig. 3.40 – Crack length versus time for Gallatin material showing periods of accelerated crack growth rate in specimen WOL 1A

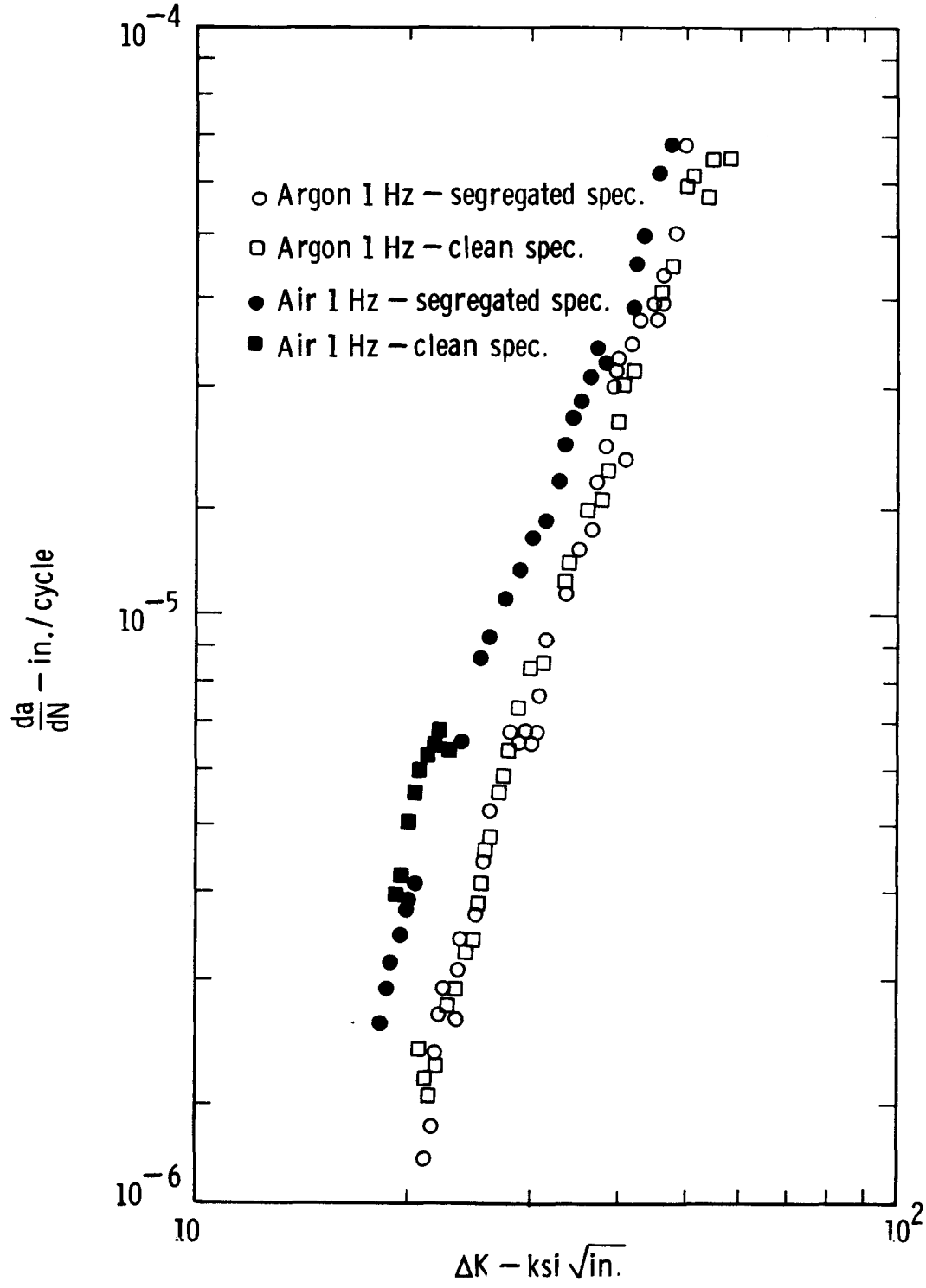

Fig. 3.41 –Fatigue crack growth data for CrMoV (Gallatin) at 800.°F

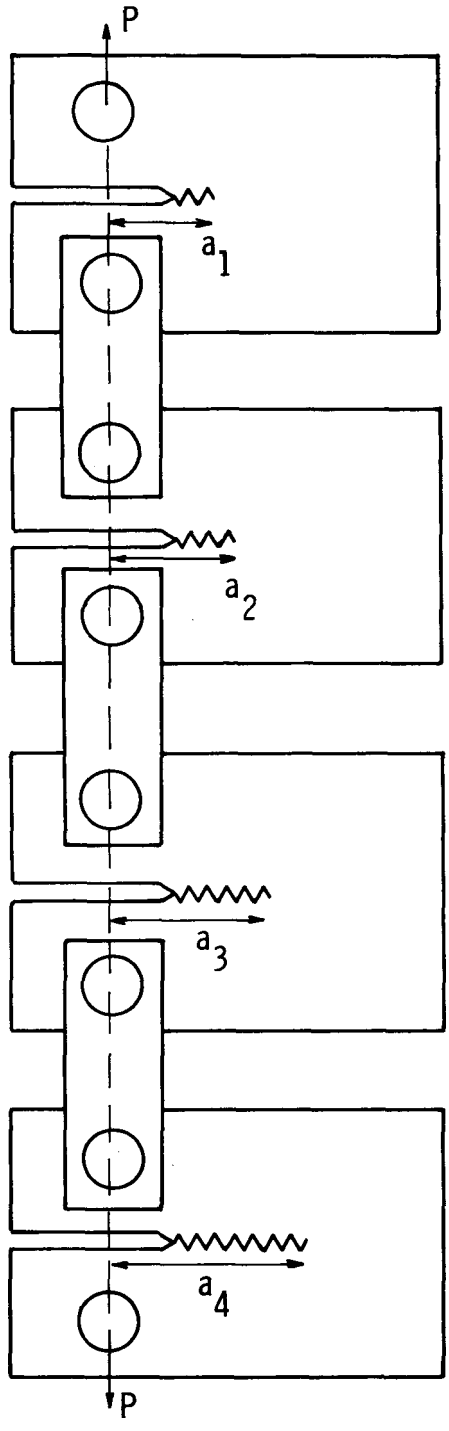

Fig. 3.42—Schematic of test method used to perform 24 hour hold time fatigue crack growth rate test using 4 specimens in a single testing machine

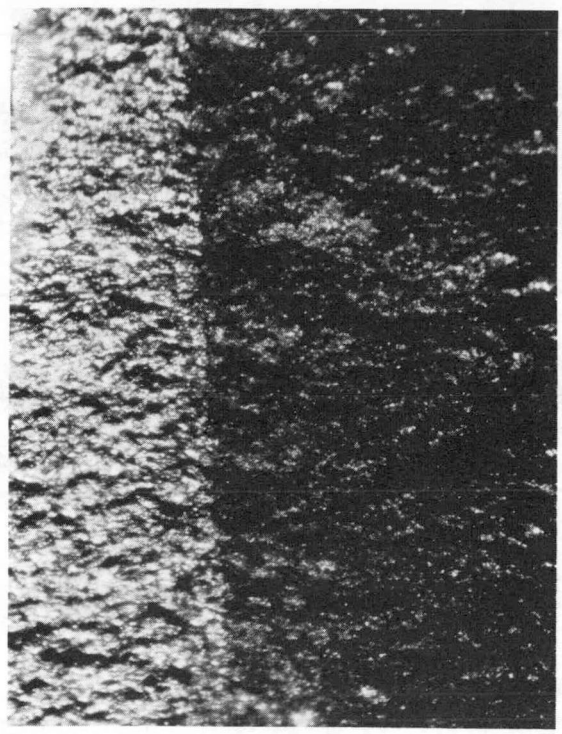

A

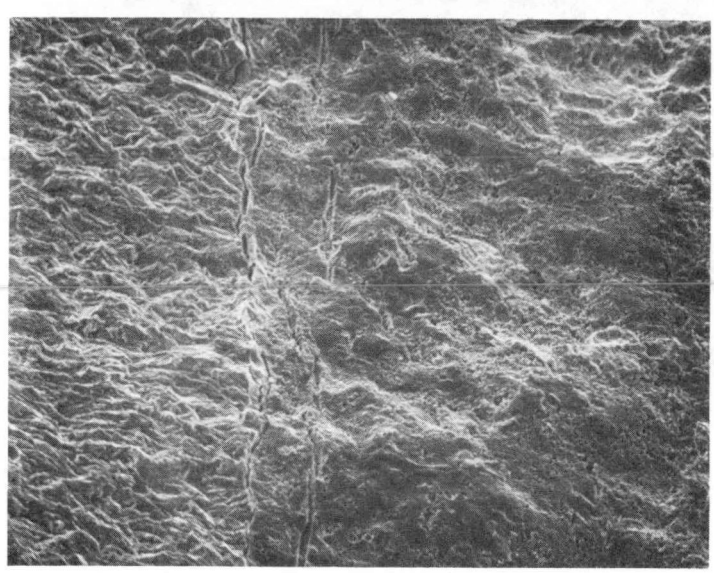

B

Fig. 3.43 – Effect of hydrogen reduction on the surface oxide. (A) as tested surface, (B) reduced surface

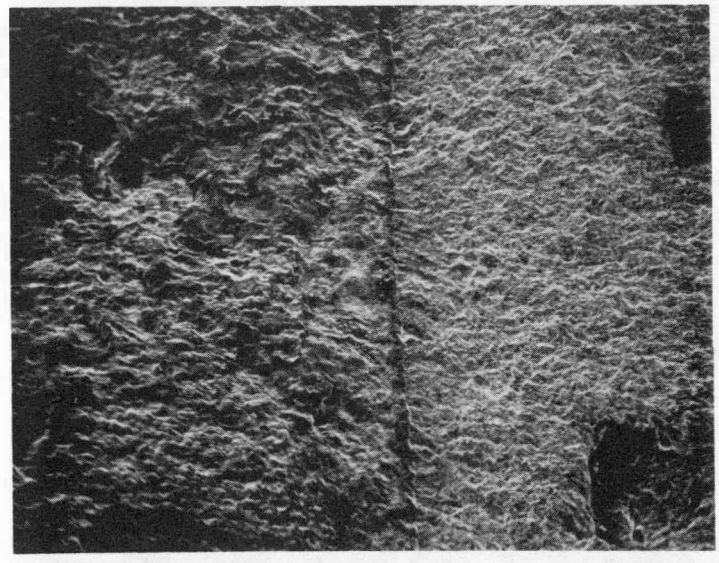

50X

A

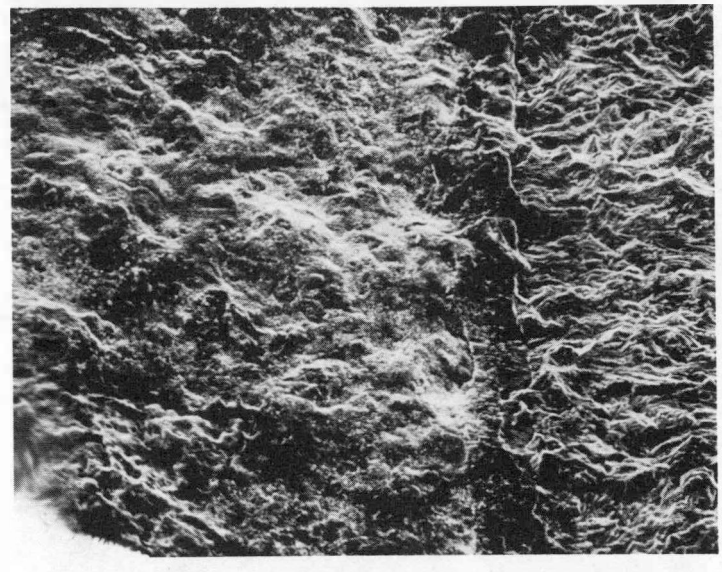

200X

B

Fig. 3.44 — Fatigue band widths for 160 cycles at $\Delta K = 18$ ksi $\sqrt{\text{in.}}$ magnified to (A) 50X and (B) 200X for specimen number FRIA2 tested at 800°F (427°C) at a frequency of 1 cycle per 24 hrs

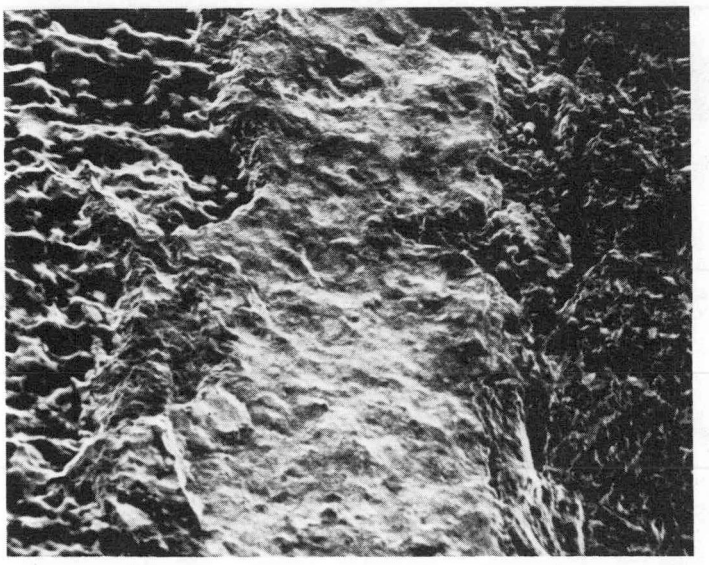

100X

A

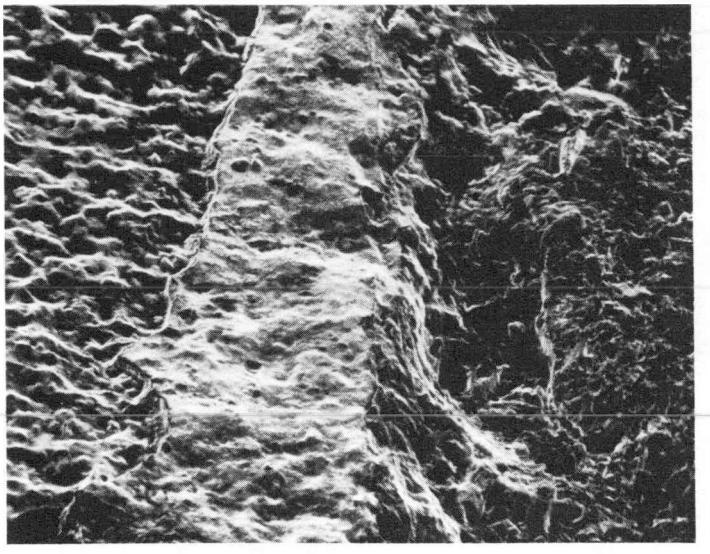

100X

B

Fig. 3.45 — Fatigue band widths in specimen number FRIA3 for 210 cycles at a $\Delta K = 20.5$ ksi $\sqrt{in.}$ magnified to 100X at (A) the center of the specimen and (B) at 1/4" from the edge of the specimen

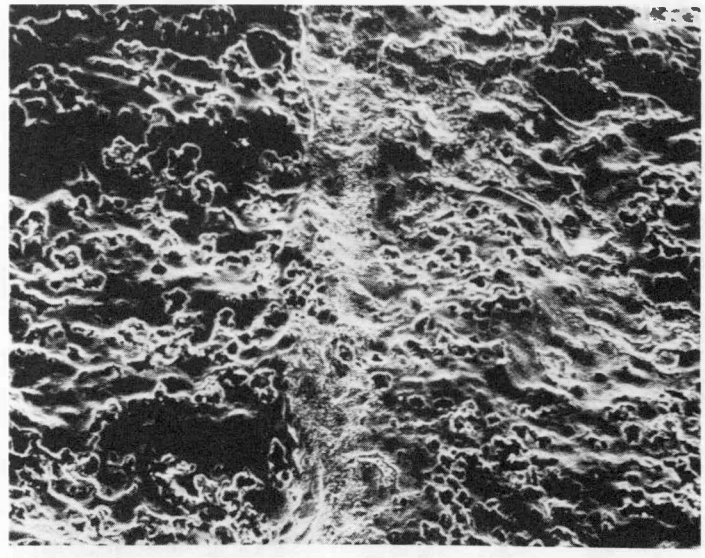

200X

A

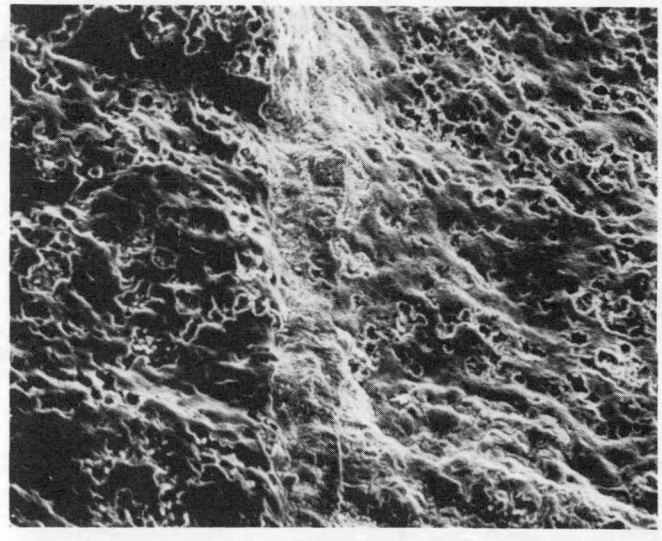

200X

B

Fig. 3.46 – Fatigue band widths in specimen FRIA1 at 200X for two separate fatigue periods. (A) at a $\Delta K = 25.6$ ksi $\sqrt{\text{in.}}$ for 160 cycles and (B) at $\Delta K = 55.28$ for 50 cycles tested at 800° F (427° C) with a frequency of 1 cycle per 24 hrs

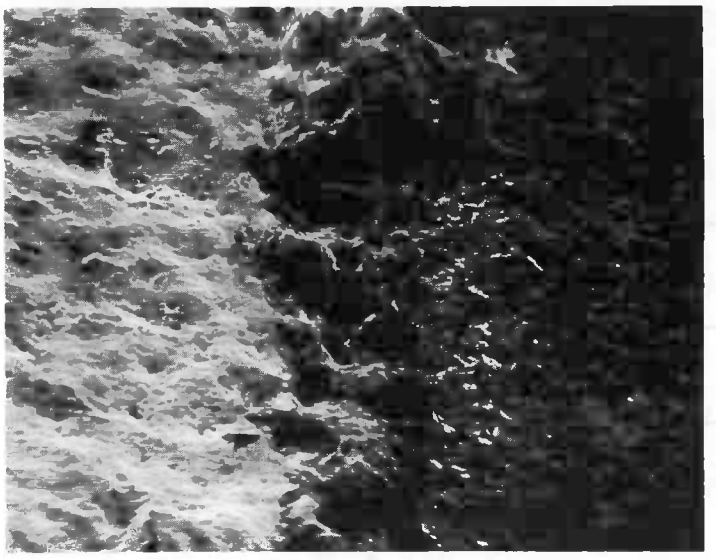

50X

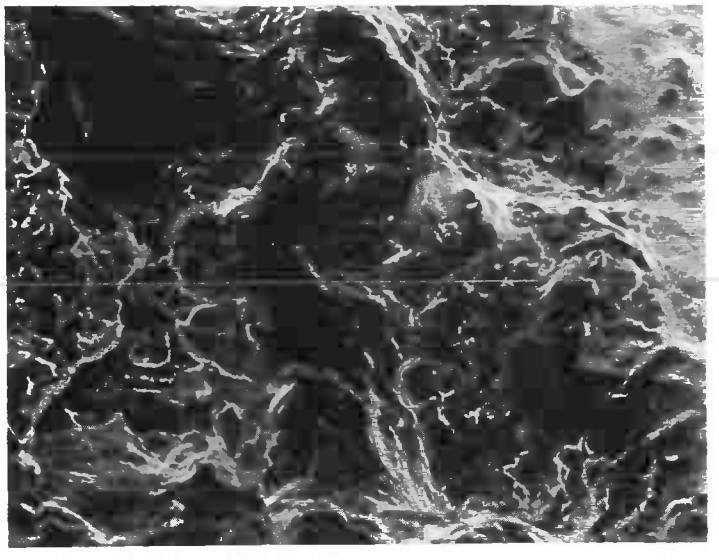

200X

Fig. 3.47 — Fatigue band widths in specimen FRIA4 after 210 cycles at a $\Delta K = 38$ ksi $\sqrt{in.}$ tested at 800° F (427° C)

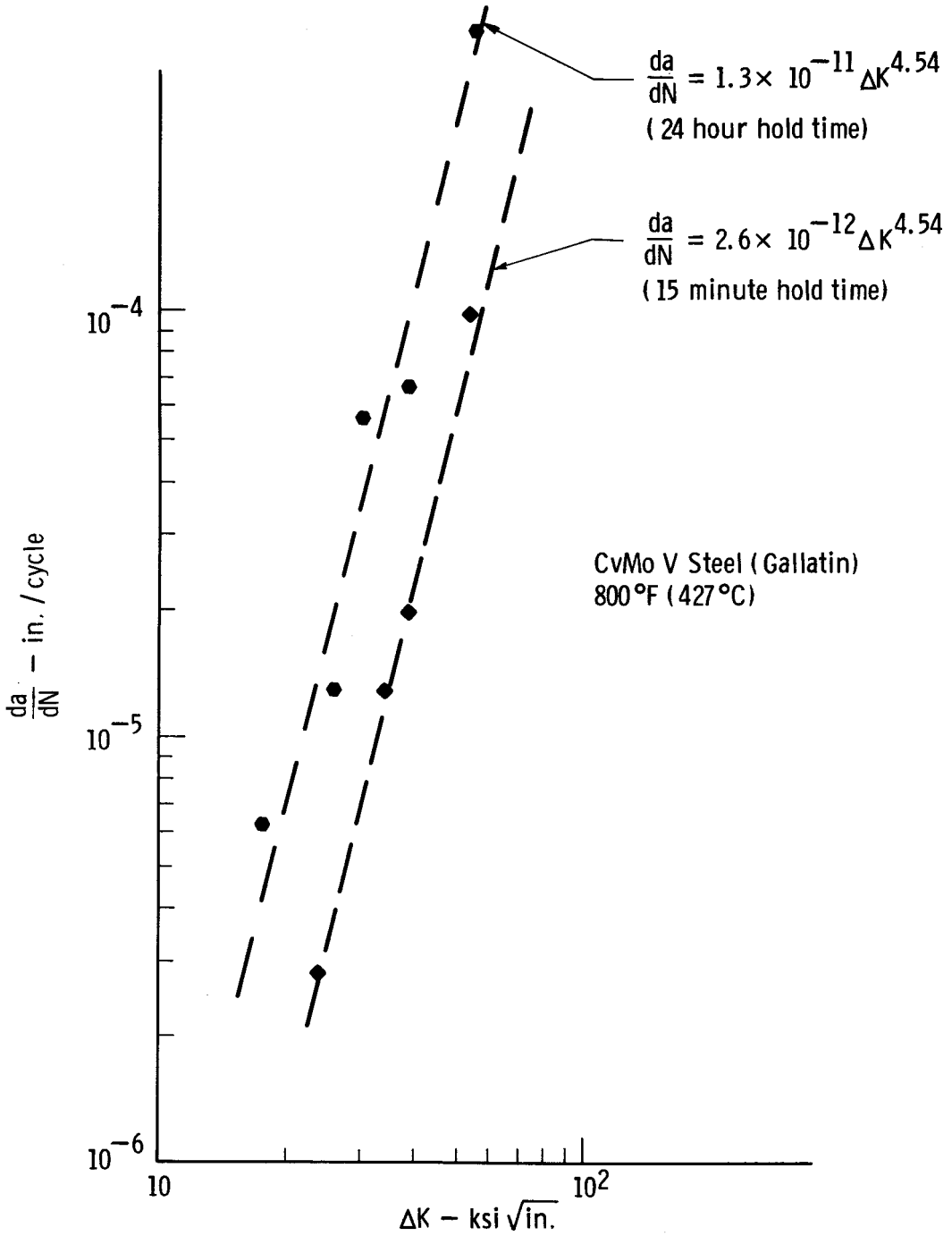

Fig. 3.48 —Fatigue crack growth rate of CrMoV at 800°F (427°C) with 24 hour hold time and 15 minute hold time

4. MECHANICAL PROPERTIES OF JOPPA NO. 3

An important aspect of the RP502 program, "Reliability of Steam Turbine Rotors", is its focus on developing consistent mechanical property data for a single group of turbine rotors. The 1950 vintage air cast CrMoV rotors were selected due to the availability of retired rotors, the high likelihood of defect observations, and the current interest in predictions of remaining life in these rotors. One of the first rotors tested was the No. 3 IP-LP rotor retired from the Joppa Station of Electric Energy Inc. The chemical composition of this 1950 vintage air cast CrMoV rotor is presented in Table 4.1 along with the chemical compositions of Gallatin No. 2 and a third retired rotor, Buck No. 6.* It can be seen that, except for the sulphur content, there is very little difference between these rotors and the analysis is equivalent to that expected of an air cast 1950 vintage CrMoV rotor.

The mechanical properties evaluated on Joppa #3 include tensile properties, Charpy impact properties, fracture toughness, fatigue crack growth rate, and low cycle fatigue performance. Test results are presented separately in the following sections. The rotor was sectioned into a series of discs as shown in Figure 4.1. Specimens were selected from various locations to examine the possible effect of service history (temperature and stress range) and discontinuities (as indicated by ultrasonic inspection records) on the mechanical properties of the rotor. The orientation of the tensile, Charpy impact, compact specimens is shown in Figure 4.2.

4.1 Tensile Tests

In order to characterize the mechanical properties of the Joppa rotor, tensile tests were performed on material taken from various locations in the rotor. Tests were performed over a range of temperatures from room temperatures to 1000°F (583°C).

*Buck No. 6 is a retired rotor from Duke Power Co., Charlotte, NC.

A summation of the tensile test results are presented in Table 4.2. The results of the tensile tests performed at room temperature with specimens taken from Sections 3A and 2A, are presented in Figures 4.3 and 4.4, respectively. These data show that there is little variation in tensile properties with radial position in the rotor. Limited data, as shown in Figure 4.3, also suggest that there is little variation of tensile properties with angular position. Figure 4.3 and 4.4 show that at room temperature, the reduction of area and percent elongation of this rotor are approximately 21% and 12%, respectively. The average 0.2% yield strength and ultimate strength of the material taken from Section 3A is 97 ksi and 120 ksi, respectively. These values are slightly higher than those exhibited by specimens taken from Section 2A, that is, 94 ksi and 114 ksi, for 0.2% yield and ultimate strength, respectively. However, this variation of strength with axial position is negligible.

The results of the tensile tests performed at temperatures ranging from room temperature to 1000°F (538°C) are presented in Figure 4.5. It can be seen that there is no difference in tensile properties of specimens taken from Section 3A and Section 4C over the whole range of temperature studied. Figure 4.5 also shows that both 0.2% yield strength and ultimate tensile strength decrease with increasing temperature while the percent elongation and reduction in area remain essentially the same. Note however, that the data scatter associated with elongation and reduction in area is much larger than that of the 0.2% yield and ultimate tensile strengths.

The relationship between temperature and flow stress, which is arbitrarily defined as the average of the ultimate strength and yield strength, can be represented by the following equation:

$$\sigma_f(T) = 109.7 - 0.0329T \qquad (4.1)$$

where T is temperature in degrees Fahrenheit and flow stress, σ_f is given in ksi. This equation will be used later in combination with Charpy test results to determine a toughness-temperature curve.

4.2 Charpy Energy and Fracture Appearance Transition Temperature

In order to further characterize the Joppa material, standard Charpy impact tests were conducted with specimens taken from various locations along the axis of the rotor. Tests were conducted to determine both the room temperature Charpy energy and the Charpy energy on the upper-shelf of the fracture transition curve. The 50% fracture appearance transition temperature (FATT) was also determined.

The variation of impact properties at different radial positions was initially studied by using specimens taken from Section 3A. This variation is important in as much as all "in service" FATT specimens are taken from a position near to or at the periphery of the rotor. In order to use such information to estimate near bore properties, a correlation between periphery and bore properties is required. Test results, as shown in Figure 4.6a indicate that there is no variation in impact properties between specimens taken from the bore and periphery of this rotor. However, the extrapolation of such findings to other rotors must be made very carefully, since marked differences in FATT values between the bore and the periphery can sometimes occur.

Charpy impact results of specimens taken from Sections 3A, 1B, 5A, and 6B are presented in Figures 4.6a, b, c and d, respectively. These results are summarized in terms of room temperature Charpy energy, upper shelf Charpy energy and FATT in Figure 4.7 and Table 4.3. These results show that the room temperature Charpy energy does not vary along the axial length of the rotor. However, a rather definite trend of increasing upper shelf energy is noted when the specimen location tends toward the lower temperature end of the rotor. A similar shift in the FATT would give rise to the suspicion that some embrittlement had taken place. However, Figure 4.7 shows that the FATT did not vary with axial location which suggests that this rotor saw little if any in-service material degradation. FATT values between 310°F (154°C) and 370°F (188°C) are rather high compared to present day rotor properties. However, such values are not considered abnormal for 1950 vintage CrMoV steel. The room temperature Charpy energy values of this rotor material,

2 ft-lb, is considerably lower than those found in present day vacuum cast CrMoV rotors. Again, this is not an unusual value for this vintage CrMoV.

4.3 Fracture Toughness

In order to evaluate the fracture toughness properties of the Joppa material, 1 in. to 3 in. thick compact specimens were tested at temperatures ranging from room temperature to 800°F (427°C). These tests were conducted using an electrohydraulic MTS testing machine operated in displacement control. A displacement versus load curve was autographically recorded during the test. The precracking procedure, total crack length and loading rate were kept within the specifications of ASTM standard E399-74. A typical displacement versus load curve for a 1 in. thick specimen tested at 250°F (121°C) is shown in Figure 4.8. This record shows that the specimen had unstable crack growth in the form of a "pop-in" before any stable crack growth could occur. Therefore, the value of K_Q was calculated based on the maximum load, P_{max}. The plane strain fracture toughness, K_{Ic}, of this rotor material at room temperature was found to be 42 ksi$\sqrt{in.}$ (46.2 MN/m$^{-3/2}$). At 250°F (121°C), the size requirement for a valid K_{Ic} test, as per ASTM standard E399-74, could not be met with a 1 in. thick specimen. Therefore, plane strain fracture toughness tests were carried out on 2T and 3T compact specimens. The K_{Ic} values obtained from the 2T-CT and 3T-CT specimens are 78 ksi$\sqrt{in.}$ (85.8 MN/m$^{-3/2}$) and 68 ksi$\sqrt{in.}$ (74.8 MN/m$^{-3/2}$), respectively.

Since the fracture toughness tends to increase with increasing temperature and yield strength tends to decrease with increasing temperature, extraordinarily large specimens are needed to obtain valid K_{Ic} values above 250°F (121°C). Therefore, in order to develop a toughness versus temperature curve for temperatures up to 800°F (427°C) with this rotor material, the J-integral testing technique was employed.[4.2] The plane strain fracture toughness, K_{Ic}, was established from J_{Ic} results using the following formula:[4.1]

$$K_{Ic} = \sqrt{\frac{JE}{(1-\nu^2)}} \qquad (4.2)$$

A single specimen unloading compliance technique was used to determine the J_{Ic} value. This technique has been described in reference 2. It requires a periodic partial unloading during the test as illustrated in Figure 4.9. Actual crack extension, Δa, at each J level is determined by the measurement of the elastic unloading compliance. The J-integral at each unloading point is calculated from the area under the load displacement curve using the approximation given by Rice, et al.[4.3]

$$J = \frac{2A}{Bb} \tag{4.3}$$

where A is the area under the load displacement curve

B is the specimen thickness

b is the remaining ligament, that is, W-a

By knowing both the J value and the amount of crack extension at intermittant points along the load displacement curve, a plot of J vs. crack extension can be completed. The J-resistance curves of specimens tested at 350°F (177°C), 400°F (204°C), 500°F (260°C), 550°F (288°C), 650°F (343°C), 750°F (399°C) and 800°F (427°C) are shown in Figures 4.10a, b,c,d,e,f, and g, respectively. The J_{Ic} values at various temperatures were obtained from these J-resistance curves as per the recommended J_{Ic} testing procedure.[4.4] These results were then converted to K_{Ic} values.

The fracture toughness versus temperature curve is presented in Figure 4.11. These results shows that: (1) There is essentially no difference in fracture toughness between specimens taken from the near bore region and from the periphery region. (2) Fracture toughness peaks at 500°F (260°C), (the temperature where zero percent brittle fracture first occurred in the Charpy impact tests), and then decreases slightly.

As fracture toughness values were not available in the early 1950's, nor for that matter are they taken on a routine basis today, it become necessary to utilize Charpy energy as a toughness monitor. Therefore, a number of Charpy impact vs. K_{Ic} correlation techniques[4.5-4.7] were evaluated as part of this program. It was found that the Begley-Logsdon method appears to be the best method for such purposes. While

this method of estimating fracture toughness is purely empirical, it is in most cases the only way in which toughness can be evaluated from existing data for 1950 vintage rotor materials. This method of estimating K_{Ic} versus temperature from conventional Charpy and tensile data is briefly described below:

1. Perform the Charpy test over a range of temperatures and obtain the full transition curves of impact energy and fracture appearance.
2. Obtain tensile properties corresponding to both the upper and lower Charpy shelves.
3. At the 100% brittle fracture temperature set, $K_{Ic} = .45\ \sigma_{yp}\sqrt{in.}$ (4.4)
4. At the 100% ductile fracture temperature, the upper shelf toughness is calculated from; $(K_{Ic}/\sigma_{yp})^2 = 5\ (CVN/\sigma_{yp} - .05)$. (4.5)
5. At the 50% FATT (Fracture Appearance Transition Temperature) place K_{Ic} at one half the sum of the upper and lower shelf toughness values.
6. At -320°F (-196°C), set K_{Ic} equal to 25 ksi$\sqrt{in.}$
7. To form an estimated K_{Ic} versus temperature curve, join the above K_{Ic} points with a segmented straight line.
8. On the upper shelf, set the relationship between toughness and temperature equal to that of flow stress, σ_f, and temperature. As an example of the upper shelf K_{Ic} correlation with temperature, the use of Equation (4.1) for the flow stress at temperature would define

$$K_{Ic(T)} = K_{Ic500} - 0.0329\ (T-500) \qquad (4.6)$$

where $K_{Ic(T)}$ is the K_{Ic} at any temperature above the upper shelf temperature, K_{Ic500} is the K_{Ic} at 500°F (the 100% ductile temperature), as calculated from Equation (4.5). The Begley-Logsdon toughness estimate for the Joppa material is shown as a solid line in Figure 4.11. Note that of temperatures up to 500°F (260°C) excellent agreement exists between the estimate and actual data points. At temperatures above 500°F (260°C),the difference between the estimate and the toughness from J_{Ic} tests is explained as follows. The value of J_{Ic} is determined from the onset of stable crack growth, whereas the K_{Ic} value is determined at 2% crack extension. Therefore, the valid K_{Ic} value should be somewhat higher than that found by J_{Ic} testing.

To determine if there is any variation in fracture toughness between material with and without ultrasonic indications, extensive J_{Ic} tests were performed with 1T-CT specimens at 250°F (121°C). Test results, as shown in Figure 4.12, indicate that there is essentially no difference in toughness between these materials. As reported previously, at 250°F (121°C) all the specimens had unstable crack growth in the form of a "pop-in" before any stable crack growth could be measured. Therefore, a J_{Ic} test at this temperature is essentially a K_{Ic} test. The toughness data were plotted with the results of K_{Ic} tests at 75°F (24°C) and 250°F (121°C) along with the results of J_{Ic} tests at 350°F (177°C) to 800°F (427°F), as shown in Figure 4.11.

In summary, a complete fracture toughness versus temperature characterization was developed for the Joppa material using both K_{Ic} and J_{Ic} techniques. In addition, a good correlation was found between the Begley-Logsdon estimate (from Charpy data) and actual toughness data. The results also show that there was no significant difference between either bore or periphery specimens or material with and without ultrasonic indications.

4.4 Fatigue Crack Growth Rate Testing

In order to evaluate the effect of frequency and temperature on the fatigue crack growth rate behavior of the Joppa rotor material, the test matrix shown in Table 4.4 was developed. All the tests were carried out in laboratory air under tension-tension (triangular wave) loading in a MTS closed-loop electrohydraulic testing machine operated in load control. Load was controlled within an accuracy of $\pm$ 1%. The desired temperature was achieved by using electrical resistance heating tapes. The temperature was continuously monitored during the tests by means of thermocouples. Temperature stability was kept better than $\pm$ 5°F ($\pm$ 3°C) during the test by using fiberglass insulation.

All fatigue crack growth rate testing was conducted with one inch (25.4 mm) thick compact tension (1C-CT) specimens with H/W = 0.486, as shown in Figure 4.13. Grooves 0.05 in. (1.27 mm) deep were machined on each side of the specimen to insure crack propagation along a plane perpendicular to the loading direction. The specimens were oriented

in the C-R direction, that is, so that the crack propagated in the radial direction of the original rotor forging. All the specimens were fatigue precracked at a stress ratio R of 0.1 (R = minimum load/maximum load) through a sequence of loads that reduced the maximum stress intensity, K_{max}, to a level that was equal to or less than the selected starting K_{max} level for the actual experiments. Fatigue cracks of at least 0.08 in. (2 mm) in length from the end of the starter notch were provided to insure that subsequent crack growth would be through material that had not been altered by the notch preparation procedures and would be unaffected by the starter notch geometry.

The stress intensity factor, K_I, for this compact tension specimen was computed from Equation (4.7).[4.8]

$$K_I = \frac{P(2 + a/w)}{(BB_N)^{1/2} W^{1/2} (1 - a/w)^{3/2}} \{0.8072 + 8.858\ (a/w) - 30.23\ (a/w)^2 + 41.088\ (a/w)^3 - 24.15\ (a/w)^4 + 4.951\ (a/w)^{1/5}\} \quad (4.7)$$

where P = applied load
B = specimen thickness
B_N = net thickness at groove
W = specimen width, and
a = crack length.

Both specimen width and crack length were measured from the line of loading, as shown in Figure 4.13. The term $(BB_N)^{1/2}$ is used here to account for the effect of side grooves.[4.9]

All tests with the exception of those run at 0.0017 Hz, were accomplished by constant load-amplitude fatigue cycling with a stress ratio R = 0.1. Visual crack length measurements were made without interrupting the test by using a 10X traveling microscope. The number

of cycles were recorded for approximately each 0.025 in. (0.6 mm) crack extension. A seven point polynomial technique[4.10] was used to obtain the crack growth rate from the raw "a" versus N data; while the stress intensity range was calculated by using Equation (4.7) with ΔP replacing P.

For the 0.0017 Hz tests, a test method similar to the method used by Brothers[4.11] and Ohmura, et al.[4.12] was used to reduce the testing time and is described as follows. For tests conducted at 800°F (427°C) and 500°F (260°C), a given number of test cycles were applied to the specimen at the desired temperature and ΔK level, after which, the frequency was increased to 10 Hz and the temperature decreased to 250°F (121°C). Once a predetermined amount of crack extension was obtained at this frequency and temperature, the original frequency and temperature were resumed and testing continued. This procedure of alternating test frequency and temperature was repeated several times during the test and resulted in a well defined change in the macroscopic appearance of the fatigue fracture surfaces, as shown in Figures 4.14 and 4.15. The fatigue crack growth rate was determined simply by dividing the width of the crack growth band by the number of cycle elapsed. This test method was modified slightly to accommodate the test conducted at 250°F (121°C). Under this circumstance, crack growth marks were produced by alternating testing frequency along with stress ratio instead of temperature. To ensure that fatigue crack growth marks were produced, a periodic heat tint at 800°F (427°C) was made prior to the application of the testing cycles.

Fatigue crack growth rate data generated in this program are presented, in terms of log da/dN versus log ΔK, in Figures 4.16 thru 4.20. For the crack growth rate range studied, the rotor steel generally exhibits a linear relationship between log da/dN versus log ΔK. Consequently, these data can readily be expressed in terms of the Paris equation, $da/dN = A(\Delta K)^n$.[4.13] Here n is the slope of the log da/dN versus log ΔK curve and A is the value of da/dN at $\Delta K = 1$ ksi$\sqrt{\text{in}}$. It was found that a slope of 2.7 is appropriate for most of the data generated in this program. The Paris equation with appropriate empirical constants are noted on the respective crack growth curves.

The effect of small discontinuities on the fatigue crack growth rate of rotor material was also an integral part of this study. This was accomplished by comparing the rate of fatigue crack growth through "defect free" material and material with a high concentration of ultrasonic indication.

Figure 4.16 presents room temperature laboratory air fatigue crack growth data generated at 20 Hz from an ultrasonically clean specimens and from a specimen with reported ultrasonic indications, the cross sectional area of the largest discontinuity is 0.0064 $in.^2$ (4.19 mm^2). These data clearly show that dispersed small discontinuities, as reported by ultraonic procedures, have little effect on fatigue crack growth rates. This is consistent with the report on a T1 steel[4.14] and with the report on Gallatin No. 2 rotor steel.[4.15] On the other hand, inclusion segregates were found to locally accelerate the crack growth rate on NiCrV rotor steel.[4.16] This discrepancy could be attributed to the difference in the morphology and distribution of discontinuities in the various material studied.

The effect of frequency on fatigue crack growth rates at various temperatures is presented from Figures 4.17 to 4.20. Figure 4.17 shows that, at room temperature in air, the rate of fatigue crack growth increases with decreasing frequency. Fatigue crack growth rates at 0.017 Hz are approximately two times faster than that encountered at 1 Hz. On the other hand, Figure 4.18 shows that at 250°F (121°C), the testing frequency has little effect on fatigue crack growth rates. At 500°F (260°C) and 800°F (427°C), fatigue crack growth rates were again found to increase with decreasing frequency, as shown in Figures 4.19 and 4.20, respectively. Fatigue crack growth rates at 0.0017 Hz are approximately 3.5 times and 4.5 times faster than those encountered at 1.0 Hz for 500°F (260°C) and 800°F (427°C), respectively.

To show the effect of temperature on fatigue crack growth rates at different frequencies, the fatigue crack growth data presented from Figures 4.17 to 4.20 were cross plotted and are presented in Figures 4.21 to 4.24. Figure 4.21 shows that at a cyclic frequency of 1 Hz, there

is barely any change in fatigue crack growth rates for this rotor steel as the temperature was raised from 75°F (24°C) to 250°F (121°C). As the temperature was further increased to 500°F (260°C), fatigue crack growth rates were found to decrease slightly. Fatigue crack growth rates, however, were increased by a factor of two as temperature was raised from 500°F (260°C) to 800°F (427°C). At a cyclic frequency of 0.1 Hz, Figure 4.22, fatigue crack growth rates decrease slightly as temperature increased from 75°F (24°C) to 250°F (121°C) and remained similar as temperature is further increased to 500°F (260°C). Figure 4.22 shows that fatigue crack growth rates at 800°F (427°C) are two times faster than that encountered at 250°F (121°C) and 500°F (260°C). Figure 4.23 shows that, at a cyclic frequency of 0.017 Hz, fatigue crack growth rates increases in the following order of temperature: 250°F (121°C), 500°F (260°C), 75°F (24°C) and 800°F (427°C). At this frequency, fatigue crack growth rates at 800°F (427°C) are approximately three times faster than those encountered at 250°F (121°C). At a cyclic frequency of 0.0017 Hz, Figure 4.24 shows that fatigue crack growth rates increase monotonically with increasing temperature from 250°F (121°C) up to 800°F (427°C). Fatigue crack growth rates at 800°F (427°C) are approximately four times higher than those encountered at 250°F (121°C).

A summary of results from the fatigue crack growth rate evaluation indicates that dispersed discontinuities have little effect on room temperature fatigue crack growth rates. At room temperature, crack growth rates were found to increase with decreasing frequency, while crack growth rates are frequency independent at 250°F. It was also noted that at 500°F (260°C) and 800°F (427°C), crack growth rates increase with decreasing frequency. This frequency effect on crack growth rate is more significant at 800°F (427°C) than at 500°F (260°C). At a given cyclic frequency, crack growth rates initially decrease before increasing at higher temperatures. This anomalous behavior of initially decreasing crack growth rates with increasing temperature can be attributed to the decrease in humidity with increasing temperatures. The temperature dependence of crack growth rate was also found to be more significant at lower frequencies.

The results of this investigation clearly demonstrate that fatigue crack growth rate does not necessarily increase with increasing temperature. Consequently, attempts to interpolate the interaction of temperature and frequency such as that described by Carden[4.17] are not adequate when environmental effects are involved.

4.5 Low Cycle Fatigue Tests

Three uniaxial tension specimens were taken from the Joppa No. 3 for low cycle fatigue testing. The goal of these tests was three fold:

1. To determine if a normal pitch-catch ultrasonic test could detect the presence of a growing crack.
2. To determine if it is possible to relate the ultrasonic test results to the subsequent fractographic features of the failure.
3. To characterize the failure mechanisms operating during the life of the specimen.

These low cycle fatigue specimens, shown in Figure 4.26, were machined such that one side is in fact the bore of the rotor. However, this surface was further machined to insure symmetry of the surface on both sides of the specimen. The axial and radial position of these specimens are presented in Table 4.5. The specimen locations were selected such that a high concentration of discontinuities would be present in each specimen. Initially, three specimens were to be taken from a section of the rotor approximately 116 in. from the coupling face of the generator end of the rotor. This section of rotor was identified by the original ultrasonic record, Table 4.6, to have many discontinuities. However, only two specimens, LCF1 and LCF2 could be manufactured as a result of an error made during the machining process. Therefore, the third specimen, LCF3, had to be taken from the hot end of the rotor. These specimens were ultrasonically examined by a hand held transducer. The position of the ultrasonic indications within the specimens and the amplitude of the sweep to peak readings are presented in Figure 4.27 and TAble 4.7, respectively. As can be seen, while specimen LCF2 did not show any significant indications, LCF1 and LCF3 did show reportable indications. The results of a C-scan ultrasonic inspection of the specimens are shown in Figure 4.28. While

a considerable amount of further data is required to determine the absolute size within the C-scan record, it is obvious that specimen LCF3 has by far a higher concentration of defects than LCF1. All ultrasonic testing was conducted at 2.25 MHz using a 1/16 inch dia. flat bottom hole reference block.

To ensure that brittle failure would not end the test prematurely, the fatigue tests were carried out at 250°F (121°C) where the toughness of the material is higher than that at room temperature. All specimen were fatigued between an axial strain of 0.6% and zero. This was accomplished by using a diametral extensometer to continuously measure the diametral strain during the test. The axial strain value was converted from diametral strain measurements using the following equation.[4.18]

$$\varepsilon_a = \frac{-\hat{\varepsilon_d}}{\hat{\nu_p}} + \frac{\sigma}{E}\left(1 - \frac{\hat{\nu_e}}{\hat{\nu_e}}\right) \tag{4.8}$$

where ε_a is the axial strain, $\hat{\varepsilon_d}$ is the diametral strain and $\hat{\nu_e}$ is the elastic Poisson's ratio and $\hat{\nu_p}$ is the plastic Poisson's ratio.

Each specimen was evaluated by UT methods prior to actual testing. The ulrasonic evaluation was completed at both zero load and at 1/2 of the estimated maximum load. No evidence of increased ultrasonic amplitude due to this preloading was reported for any of the specimens tested.

Using a straight beam pitch-catch system, ultrasonic testing was performed on specimen LCF3 at the end of 1000 cycles and 2000 cycles. Again, UT tests were performed at zero load and at 1/2 of the maximum load. No evidence of significant crack growth was observed. However, the specimen failed after a further 29 cycles; that is, it failed at 2029 cycles. An examination of the fracture surface of LCF3, Figures 4.29a and b shows two large thumbnail cracks, one is approximately 1.13 in. long by 0.61 in. deep and the other approximately 0.51 in. long by 0.24 in. deep.

A process known as selective oxidation was used to aid in the fractographic study. This was accomplished by heating the specimen and watching carefully the various oxidation colors on the fracture surface. A stereo pair, high contrast photo was taken from the area of the large thumbnail crack as shown in Figure 4.30. The white islands within these pictures was identified as shrinkage porosity. Results of an energy dispersion analyses by X-ray indicate that these shrinkage porosities are composed mainly of alumina and silica, as shown in Figure 4.31, rather than the mangenese sulfide found in the Gallatin rotor.[4.19] It is proposed that several large shrinkage pores near the edge of the specimen linked up to form a large crack at an early stage in the life of the specimen. This crack then propagated outward towards the surface of the specimen. The partial thickness semi-elliptical crack then propagated toward the center of the specimen. This fatigue crack growth is represented by the blue area, as substantiated by the striations found in this region, Figure 4.32. A shear, when out-of-plane, or dimple rupture process occurred when the overall fatigue crack front linked up with the local fatigue crack growth around the shrinkage porosity as denoted by the light brown area. This fatigue crack growth and defect linkup was not confined to a single plane but rather sought out its nearest neighbor. This three dimensional nature of the link up process can be seen in Figure 4.30, since the picture is a stereo pair. As this part-through elliptical crack reached a depth of approximately 0.61 in., the stress intensity factor reached the K_{Ic} value of this material and caused cleavage fracture, as indicated by the brown area. A simple calculation given below tends to support this hypothesis.

Assuming the thumbnail crack was represented by a partial thickness semielliptical defect, the stress intensity factor can be calculated by using Equation (4.9).[4.20]

$$K_I = 1.12\sigma\sqrt{\frac{\pi a}{Q}} \qquad (4.9)$$

where Q is the shape factor. The specimen failed at a load of 176,000 lbs, or at a net section stress of 70.4 ksi. The shape factor Q of a flaw with a depth to length ratio of 0.54 at a relative stress ratio (σ/σ_{ys})

of 0.66 was found to be approximately 2.25.[4.20] The corresponding stress intensity factor is computed as follows

$$K_I = 1.12 \times 70.4 \times \sqrt{\frac{\pi \times 0.61}{2.25}} = 72.7 \text{ ksi}\sqrt{\text{in.}} \qquad (4.10)$$

A stress intensity factor of 72.7 ksi$\sqrt{\text{in.}}$ is enough to cause this rotor material to fail in cleavage at 250°F (121°C) since a K_{Ic} value of 69 ksi$\sqrt{\text{in.}}$ was observed at this temperature.

Similar findings were also noted for specimen LCF1 and LCF2. However, the concentration of shrinkage cavities in those two specimens are much less than those found in specimen LCF3. As a result, 230,000 lbs were required for specimens LCF1 and LCF2 to reach an axial strain of 0.6%, instead of the 200,000 lb required for LCF3.

A significant observation from the fractographic results is that a linkup process occurred between a number of closely spaced shrinkage pores in the early stages of fatigue life. It was also noted that the crack front followed a three dimensional pattern with the crack searching out the nearest discontinuity. The pitch-catch ultrasonic test was not able to detect the growth of the internal crack. This may well be due to the orientation of the transducer with respect to the growing flaw, (i.e., the sound wave is parallel to the plane of the fatigue crack).

While the volume fraction of defects to matrix was found to be less than 2% for the Joppa No. 3 material by Task 3, it should be noted that a two dimensional projection of the thumbnail region as shown in Fig. 4.30 gave an area fraction of approximately 20% of defects to matrix. While this is not a fair comparison of the defect area fractions, it does illustrate the three dimensional nature of the crack front. A two dimensional projection of the cleavage region of the fracture surface gave an area fraction of defects of approximately 10%.

4.1 REFERENCES

4.1 J. A. Begley and J. D. Landes, "The J Integral as a Fracture Criterion," in ASTM STP 514, Fracture Toughness, 1972.

4.2 G. A. Clarke, W. R. Andrews, P. C. Paris and D. W. Schmidt, "Single Specimen Tests for J_{Ic} Determination," ASTM STP 590, Mechanics of Crack Growth, 1976.

4.3 J. A. Rice, P. C. Paris, and J. G. Merkle, "Some Further Results on J-Integral Analysis and Estimates," in ASTM STP 536, Progress in Flaw Growth and Fracture Toughness Testing, 1973.

4.4 G. A. Clarke, "Recommended Procedure for J_{Ic} Determination," Presented at the ASTM E24.01.09 Task Group Meeting, Norfolk, March 1977.

4.5 H. T. Corten and P. H. Sailors, "Relationship Between Materials Fracture Toughness Using Fracture Mechanics and Transition Temperature Tests," ASTM STP 514, Fracture Toughness, 1972.

4.6 B. Marandet and G. Sanz, "Evaluation of the Toughness of Thick Medium Strength Steels by Using LEFM and Correlations Between K_{Ic} and CVN," ASTM STP 631, Flaw Growth and Fracture, 1977.

4.7 J. A. Begley and W. A. Logsdon, "Correlation of Fracture Toughness and Charpy Properties for Rotor Steels," Presented at the Fifth National Symposium on Fracture Mechanics, Pittsburgh, PA, August 1971.

4.8 A. Saxena and S. J. Hudak, Jr., "Review and Extension of Compliance Information for Common Crack Growth Specimens," Westinghouse Scientific Paper 77-9E7-AFCGR-P1, May 1977.

4.9 C. N. Freed and J. M. Kraft, "Effect of Side Grooving on Measurements of Plane-Strain Fracture Toughness," Journal of Materials, Vol. 1, No. 4, 1966.

4.10 W. G. Clark, Jr. and S. J. Hudak, Jr., "Variability in Fatigue Crack Growth Rate Testing," Journal of Testing and Evaluation, Vol. 3, No. 6, 1975.

4.11 A. J. Brothers, "Fatigue Crack Growth in Nuclear Reactor Piping Steels," Research and Development Report GEAP-5067, U.S. Atomic Energy Commission, March 1968.

4.12 T. Ohmura, R. M. Pelloux, and N. J. Grant, "High Temperature Fatigue Crack Growth in a Cobalt Based Superalloy," Engineering Fracture Mechanics, Vol. 5, No. 4, 1973.

4.13 P. C. Paris, "The Fracture Mechanics Approach to Fatigue," Proceedings 10th Sagamore Army Materials Research Conference, August 1963, Syracuse University Press, 1964.

4.14 R. J. Bucci, W. G. Clark, Jr., and P.C. Paris, "Fatigue Crack Propagation Growth Rate Under a Wide Variation of ΔK for an ASTM A517 Grade F (T1) Steel," Stress Analysis and Growth of Cracks, ASTM STP 513, 1972.

4.15 G. A. Clarke, "Reliability of Steam Turbine Rotors - Material Mechanical Property Measurements," Eleventh through Fourteenth Monthly Letter Report, Westinghouse Contract No. RP502-4.

4.16 A. J. Brothers and S. Yukuwa, "Fatigue Crack Propagation in Low-Alloy Heat-Treated Steels," Journal of Basic Engineering, March 1967.

4.17 A. E. Cardon, "Parametric Analysis of Fatigue Crack Growth," Int. Conf. on Creep and Fatigue in Elevated Temperature Application, Philadelphia, PA, 1973.

4.18 J. B. Conway, R. H. Stentz, and J. T. Berling, "Fatigue, Tensile, and Relaxation Behavior of Stainless Steel," 1975. Available through Technical Information Center, United States Atomic Energy Commission.

4.19 L. D. Kramer and D. Randolph, "Analysis of the Tennessee Valley Authority Gallatin No. 2 Unit Turbine Rotor Burst Part I - Metallurgical Considerations," Symposium on Creep-Fatigue Interactions, New York, NY, December 6-10, 1976.

4.20 W. G. Clark, Jr., "Fracture Mechanics and Nondestructive Testing of Brittle Materials," Journal of Engineering for Industry, February 1972.

TABLE 4.1

CHEMICAL PROPERTIES OF THREE 1950 VINTAGE AIR CAST CrMoV ROTORS

	Cr	Mo	V	C	Mn	Si	P	S
Gallatin No. 2	1.1	1.43	.25	.34	.97	.27	.016	.019
Joppa No. 3	.99	1.1	.25	.26	.75	.30	.017	.004
Buck No. 6	.99	1.1	.25	.26	.74	.28	.019	.0102

TABLE 4.2

TENSILE PROPERTIES OF JOPPA NO. 3

Specimen Number	Axial† Location	Radial Location	Angular Position	Test Temperature	Ultimate Strength ksi	0.2% Yield Strength ksi	% Elongation	% Reduction in Area
2A TB 1	134.5	Bore	166°	75°F (24°C)	115.2	96.8	10.8	25.6
2A TB 2	135.8	Bore	166°	75°F (24°C)	112.4	92.9	10.9	21.3
2A TM 1	134.5	Midwall	166°	75°F (24°C)	113.1	94.4	11.5	25.0
2A TM 2	135.8	Midwall	166°	75°F (24°C)	112.0	93.1	12.3	27.0
2A TP 1	134.5	Periphery	166°	75°F (24°C)	115.6	97.0	8.4	13.7
2A TP 2	135.8	Periphery	166°	75°F (24°C)	115.8	97.1	11.9	27.4
3A TB 1	103.5	Bore	0°	75°F (24°C)	117.4	96.0	13.8	31.1
3A TB 2	104.6	Bore	0°	200°F (93°C)	113.0	92.1	12.1	27.5
3A TB 3	105.8	Bore	0°	75°F (24°C)	119.8	98.0	8.9	12.0
3A TB 4	107.0	Bore	0°	300°F (149°C)	112.3	92.4	9.9	21.3
3A TB 5	108.5	Bore	0°	75°F (24°C)	118.5	97.2	13.2	29.2
3A TM 6	103.5	Midwall	0°	400°F (204°C)	108.1	88.5	13.0	30.4
3A TM 7	104.6	Midwall	0°	75°F (24°C)	119.4	97.2	11.1	19.0
3A TM 8	105.6	Midwall	0°	600°F (316°C)	107.8	88.5	10.1	22.0
3A TM 9	107.0	Midwall	0°	75°F (24°C)	119.8	98.5	12.7	26.0
3A TP 10	103.5	Periphery	0°	600°F (316°C)	106.9	86.7	9.3	13.8
3A TP 11	104.6	Periphery	0°	75°F (24°C)	120.3	98.3	11.3	19.5
3A TP 12	105.8	Periphery	0°	700°F (371°C)	103.1	85.4	11.3	23.6
3A TP 13	107.0	Periphery	0°	75°F (24°C)	121.5	99.0	9.8	16.0
3A TP 14	108.5	Periphery	0°	800°F (427°C)	97.1	68.9	9.9	25.8
4C TB 1	93.0	Bore	246°	200°F (93°C)	110.1	89.2	12.5	31.2
4C TB 2	93.0	Bore	246°	200°F (93°C)	110.4	90.2	14.0	35.1
4C TB 3	93.0	Bore	246°	400°F (204°C)	107.3	86.1	10.9	19.9
4C TB 4	93.0	Bore	246°	400°F (204°C)	108.1	85.9	12.2	23.1
4C TB 5	93.0	Bore	246°	600°F (316°C)	107.1	86.1	8.8	15.2
*4C TB 6	93.0	Bore	0.0°	600°F (316°C)	105.8	85.2	7.5	9.7
*4C TB 7	93.0	Bore	0.0°	800°F (427°C)	94.1	78.4	10.5	18.8
*4C TB 8	93.0	Bore	0.0°	800°F (427°C)	92.9	77.4	12.5	30.2
*4C TB 9	93.0	Bore	0.0°	1000°F (538°C)	76.6	69.2	15.9	45.3
**4C TB 10	93.0	Bore	0.0°	1000°F (538°C)	80.6	53.9	16.7	50.9

*Numerous small indications recorded by ultrasonics

**Temperature over shot to 1400°F, test conducted at 1000°F (538°C).

†Distance from generator coupling, in.

TABLE 4.3

CHARPY IMPACT RESULTS FOR JOPPA NO. 3

Specimen Number	Axial* Location	Radial Location	Room Temperature Charpy Energy ft-lbs	Upper Shelf Charpy Energy ft-lbs	50% Brittle Appearance Transition Temperature
1B CB	152	Bore	2.0	49.0	+300°F
3A CB	105	Bore	3.0	41.0	+356°F
3A CM	105	Midwall	2.0	41.0	+360°F
3A CP	105	Periphery	2.5	43.5	+350°F
5A CB	87.5	Bore	2.0	41.0	+320°F
6B CB	58	Bore	4.0	35.0	+310°F

* Distance from generator coupling, in.

TABLE 4.4

TEST MATRIX OF FATIGUE CRACK GROWTH RATE STUDY

Temperature / Frequency	75°F (24°C)	250°F (121°C)	500°F (260°C)	800°F (427°C)
1 Hz (1 cps)	X	X	X	X
0.1 Hz (0.1 cps)	X	X	X	X
0.017 Hz (1cpm)	X	X	X	X
0.0017 Hz (0.1 cpm)		X	X	X

TABLE 4. 5
LOCATION AND ORIENTATION OF LARGE LOW CYCLE FATIGUE SPECIMENS

Specimen	LCF1	LCF2	LCF3
Z*	115	119	149
θ	315	130	35

*In. from the coupling face of generator end of rotor.

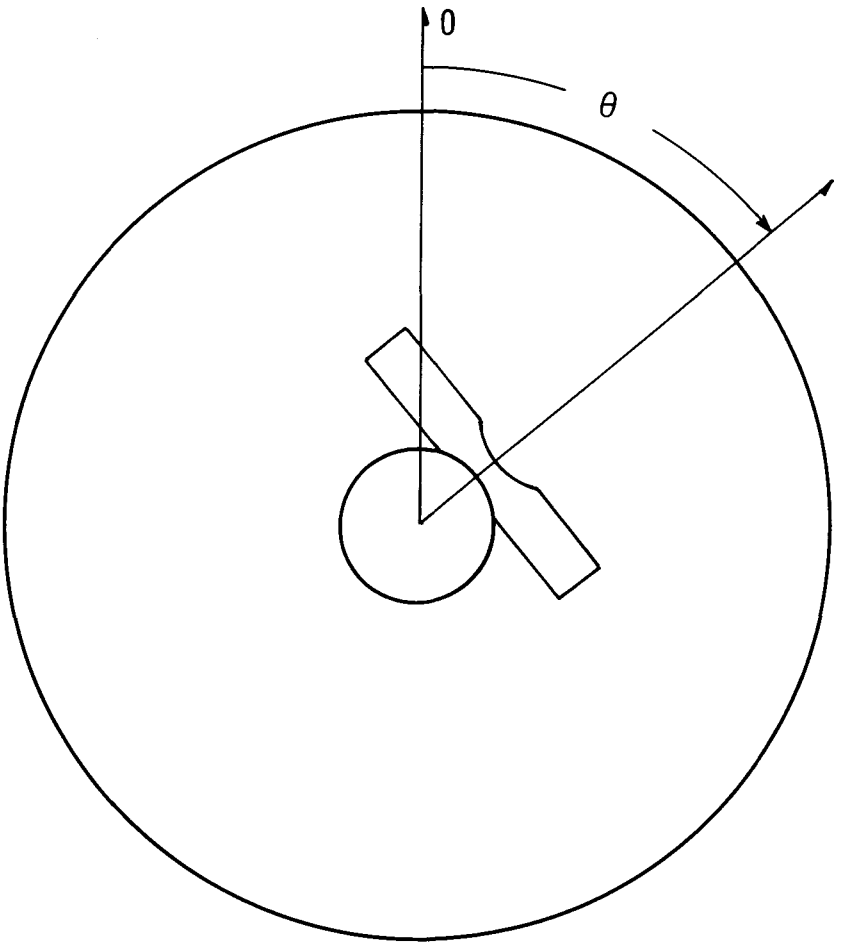

TABLE 4.6a

BORSONIC TESTING RESULTS FROM BATTELLE MEMORIAL INSTITUTE

Z (in.)	θ (degree)	R (in.)	Amp. % DAC*	
115	190-200	0.12	30	
115	225	0.85	20	
115	310-330	0.80	50	
115	320	0.40	23	
115	320	0.9	50	
115	330	1.7	60	
116	130-160	0.4	23	
116	330-360	0.2-1.8	10-25	very dirty
117	75	0.5	50	
117	90	0.9	20	
117	225	0.2	28	
117	225	0.6	20	
117	290-300	0.1-1.5	18-10	
117	290-300	0.2-0.8	30	
118	75	0.6	75-80	
118	80	0.5	45	
118	210	0.3	25	
118	210	1.2	30	
119	45	0.6	30	
119	60	0.9	35	

*DAC was established from 1/16 in. FBH.

TABLE 4.6b

ULTRASONIC TESTING RECROD FROM WESTINGHOUSE

Z (in.)	R (in.)	θ (degree)	Cal. Reflect Eq. Area (10^{-4}-in.^{2})
114	1-3/8	311	18.36
114	1-1/2	316	21.46
114	1-1/8	317	38.56
114	3/4	326	23.86
114	1-1/8	315	34.27
114	7/18	317	23.03
114.2	1-1/8	320	49.56
114.2	1-3/8	314	18.36
114.2	1	312	21.92
114.2	9/16	308	23.86
114.2	1/8	308	15.3
114.2	1-1/8	320	49.92
114.5	1-1/16	317	27.76
114.5	1-1/4	314	24.48
114.5	3/4	314	21.42
114.5	1-1/4	314	21.42
114.5	1-1/4	315	18.97
114.7	1	313	27.54
114.7	1-1/16	310	34.27
115	1/2	316	22.95
115.2	1/2	311	21.42
115.2	1/4	309	21.42
115.5	1/2	313	29.98
115.5	1/2	323	20.8
115.5	5/8	328	20.19
115.7	3/8	309	24.48
116	1/2	318	22.03
116	3/8	314	19.89
116	1/2	318	21.72
116.3	4/16	322	21.72
117.4	5/8	313	27.54
117.4	3/16	314	17.74
117.6	9/16	315	18.66
118.4	1/2	126	34.27
119.1	5/8	130	34.27
119.3	1/2	129	30.29
119.3	3/8	140	30.84
119.5	1/2	120	30.60
119.5	7/16	116	34.27
120	3/8	120	19.89
121.2	1/2	137	29.07

TABLE 4.7

ULTRASONIC TESTING RESULTS OF LARGE LOW CYCLE FATIGUE SPECIMEN
(see Fig. 4.36)

LCF1

Indication No.	"S/P	Depth	X	Y	Remarks
A1	0.9	3/8	1-22/32	24/32	
A2	0.4	1-1/8	17/32	1-12/32	
A3	0.4	7/8	2-6/32	17/32	
B1	0.3	1	1-31/32	1	
C1	0.2	7/8	1-5/32	10/32	
C2	0.4	1-1/4	1-24/32	28/32	

LCF2

No significant signals present from any of the surfaces.

LCF3

Indication No.	"S/P	Depth	X	Y	Remarks
A1	0.3	9/16	1-24/32	6/32	
A2	0.3	3/8	12/32	1-7/32	Double signal
B1	0.4	3/4	1-1/16	5/8	
B2	0.55	7/8	15/32	19/32	
B3	0.4	1.0	21/32	16/32	
B4	0.4	7/16	25/32	1-11/16	
B5	0.4	3/4	25/32	1-5/16	
B6	0.5	1	27/32	1-9/32	Possible double signal
B7	0.7	3/4	1-1/32	24/32	
B8	0.4	3/4	1-16/32	17/32	
B9	0.6	3/4	1-23/32	30/32	
B10	0.9	1/2	1-20/32	1-13/32	
B11	0.5	7/8	1-1/4	30/32	
C1	0.4	1/2	4/32	1-15/32	
C2	0.8	7/16	1-15/32	28/32	
C3	0.3	3/4	1-4/32	1	
D1	0.4	7/8	16/32	22/32	
D2	0.6	3/8	31/32	25/32	
D3	0.6	15/16	30/32	22/32	
D4	0.4	3/4	25/32	1-6/32	
D5	0.35	5/16	28/32	1-6/32	
D6	0.45	3/8	26/32	1-11/32	
D7	0.5	1-3/16	1-1/32	1-12/32	
D8	0.6	3/4	29/32	1-17/32	
D9	0.45	3/4	19/32	13/32	
D10	0.4	7/16	1-20/32	19/32	

TABLE 4.7 (Continued)

Indication No.	"S/P	Depth	X	Y	Remarks
D11	0.6	3/4	1-21/32	1-7/32	
D12	0.7	3/4	1-23/32	1-14/32	
D13	0.45	13/16	1-26/32	1-14/32	
D14	0.4	11/16	2	1-10/32	
D15	0.4	13/16	2	1-4/32	
D16	0.4	7/8	1-13/32	1-1/32	

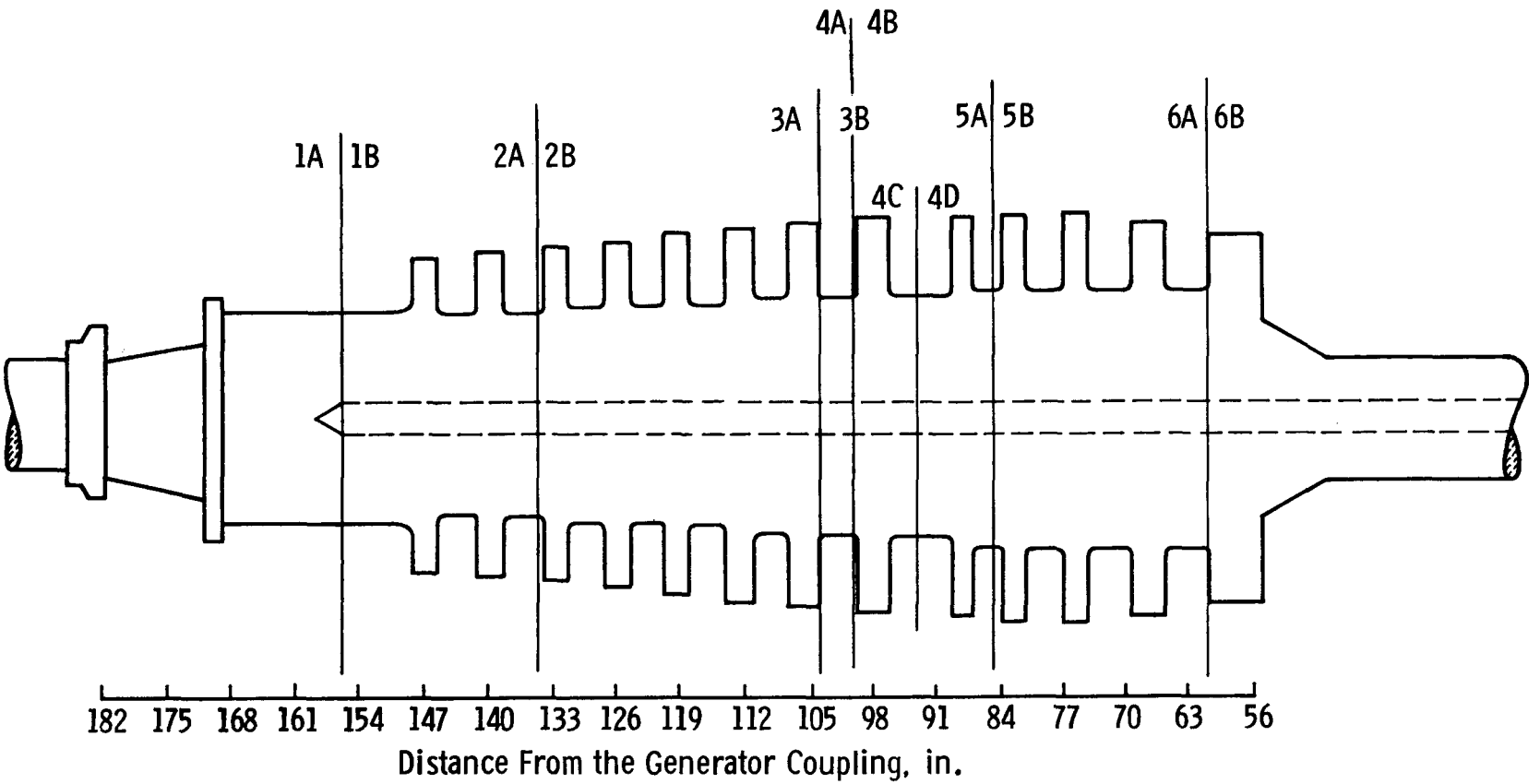

Fig. 4.1 – Schematic of Joppa #3 showing positions of saw cuts and numbering for each saw cut face

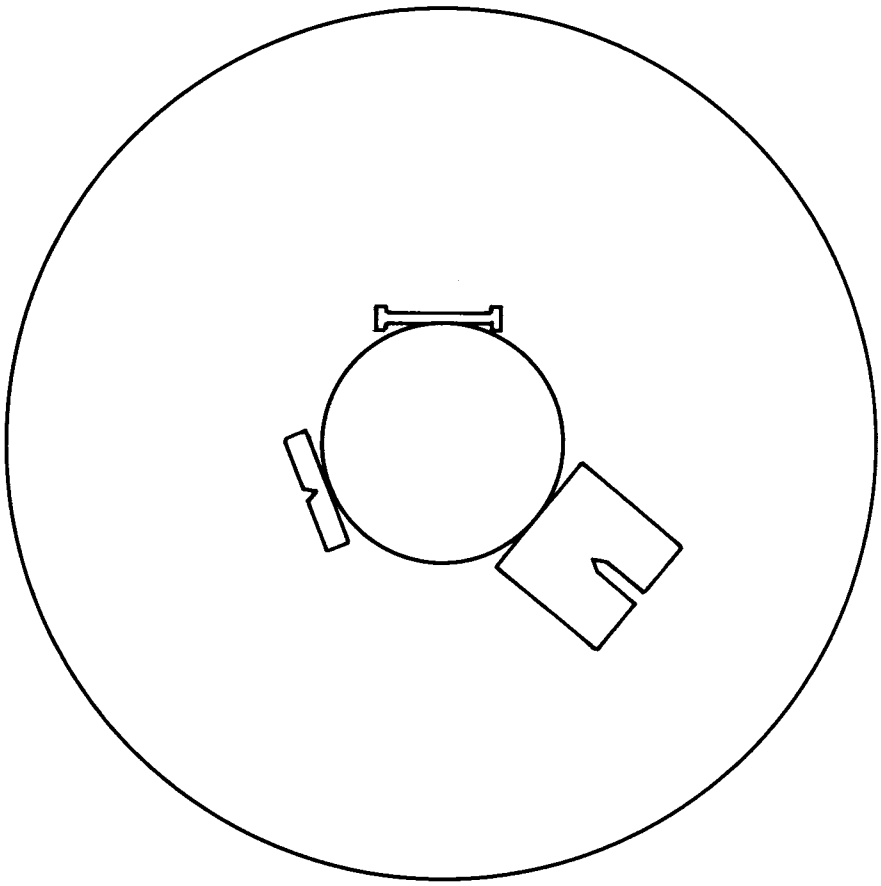

Fig. 4. 2—Orientation of the specimens tested in this program

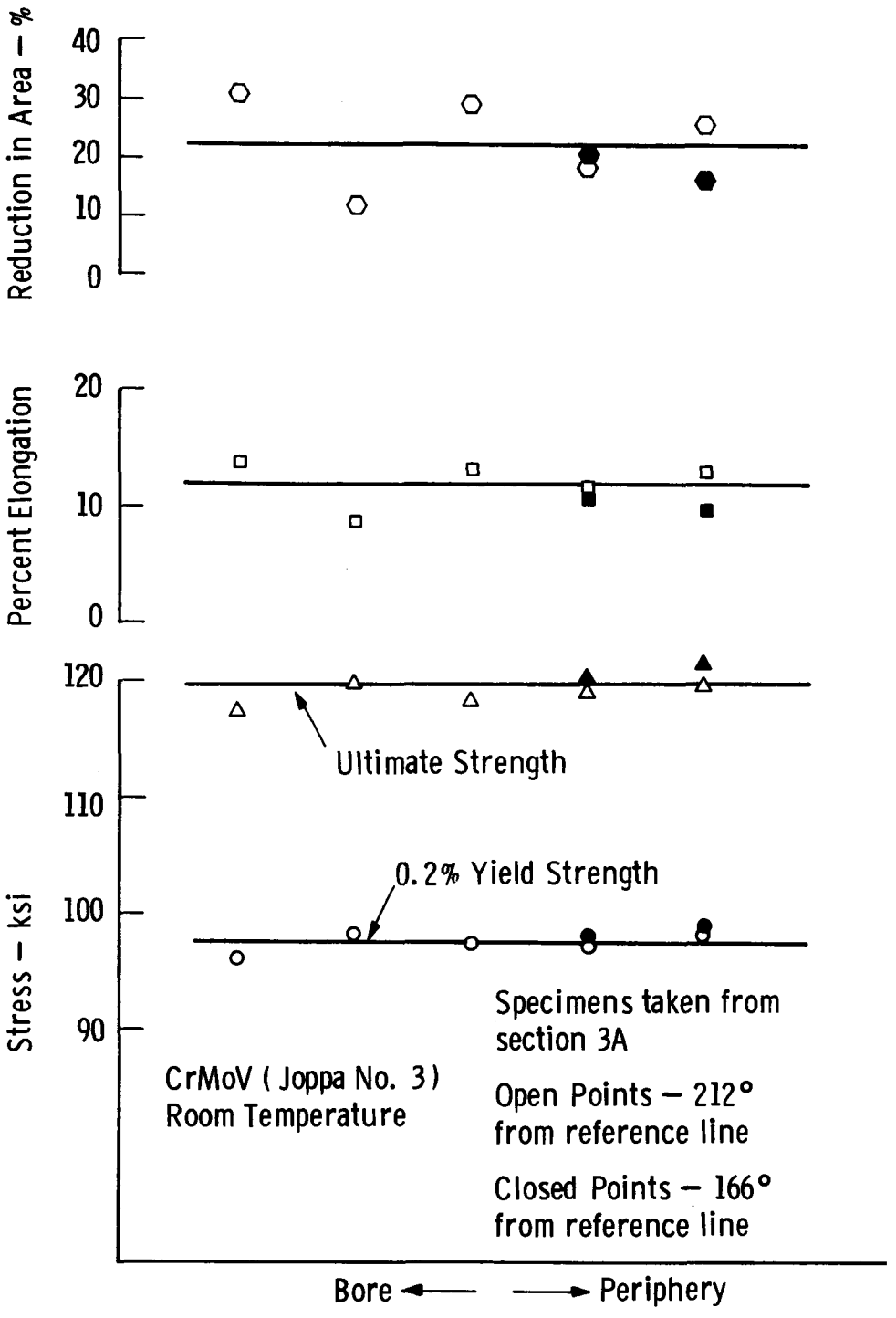

Fig. 4.3-Room temperature tensile properties of CrMoV taken from section 3A at various radial and angular location

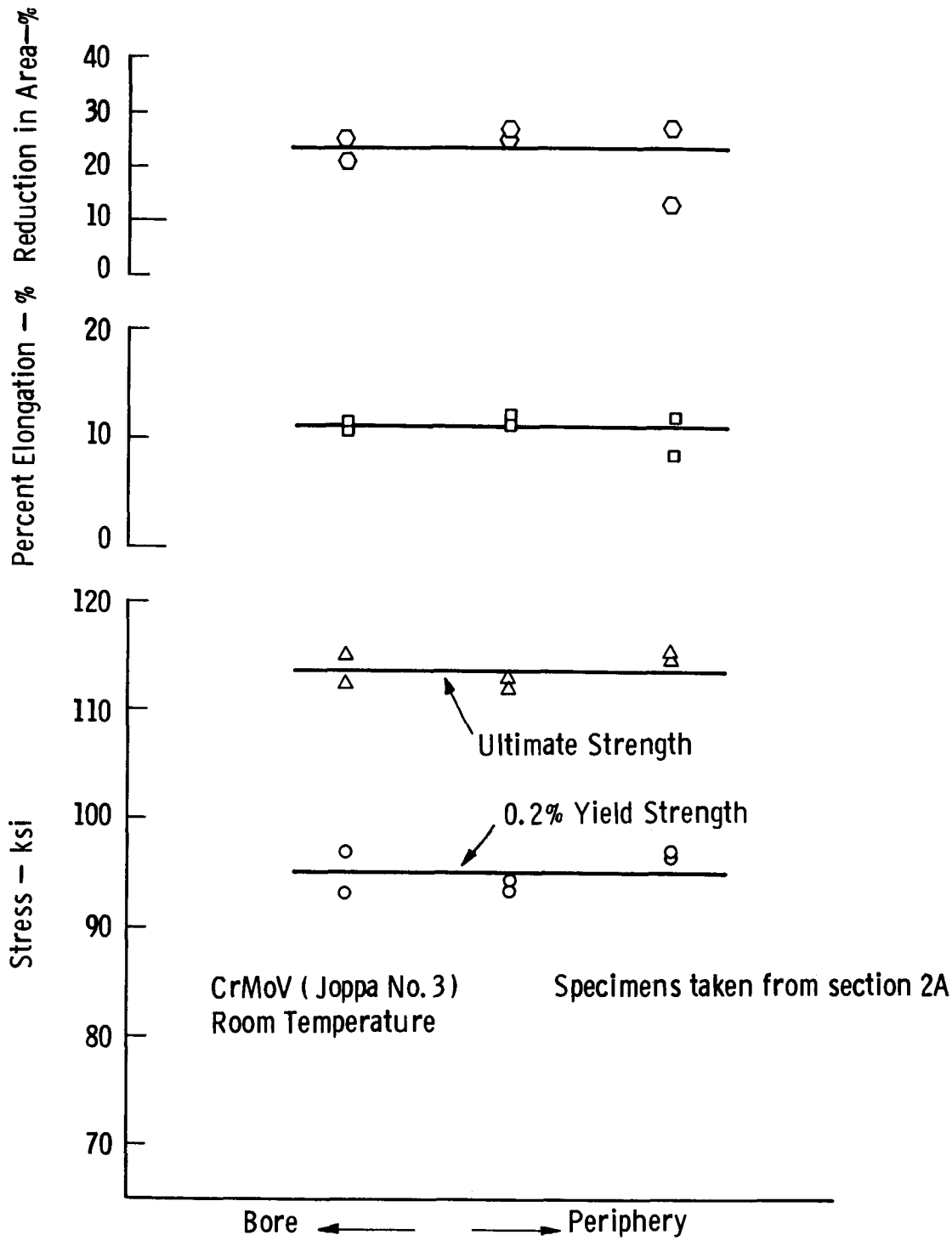

Fig. 4.4– Room temperature tensile properties of CrMoV taken from section 2A at various radial location

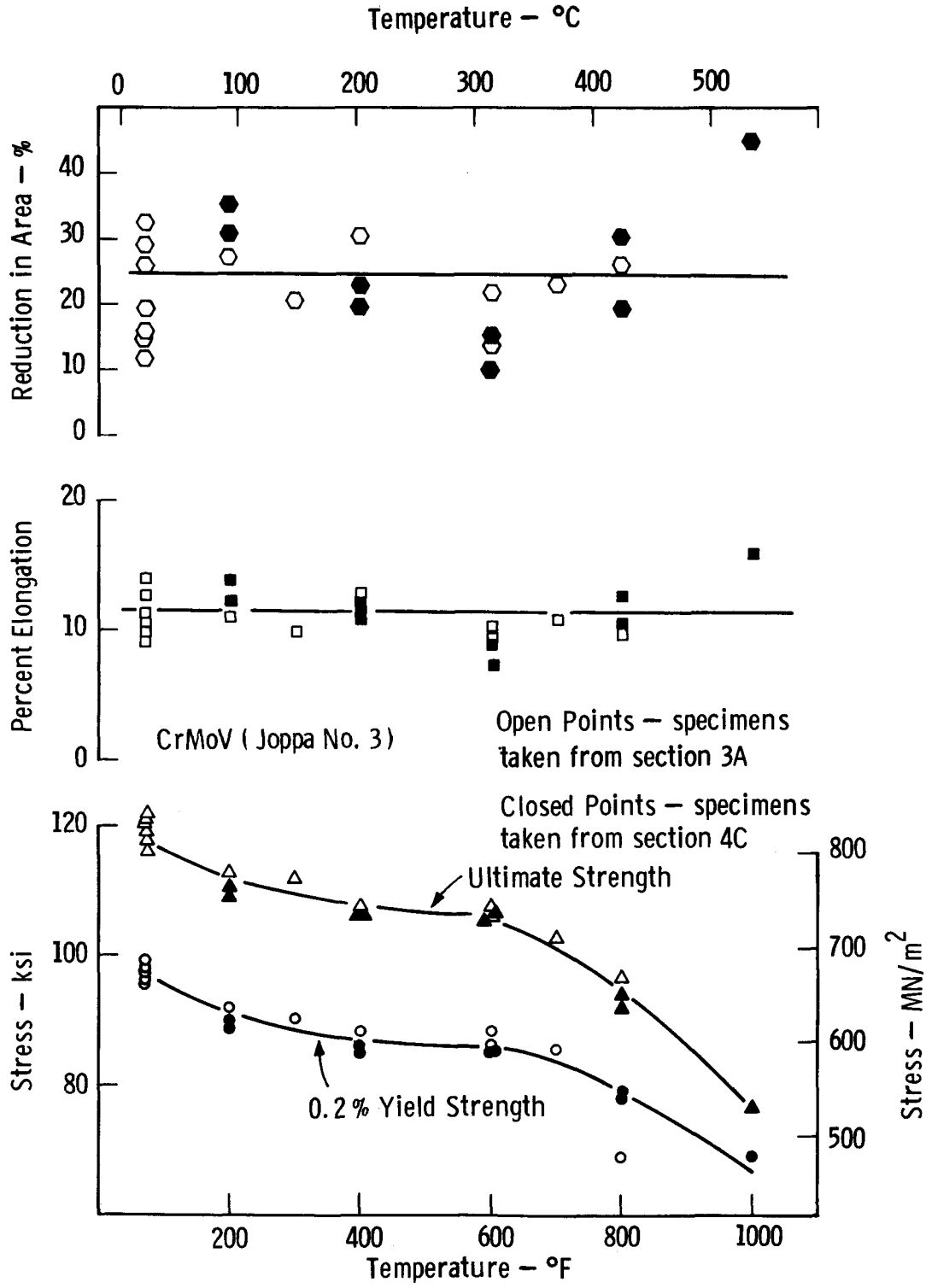

Fig. 4.5 – Tensile properties of CrMoV taken from sections 3A and 4C at various temperatures

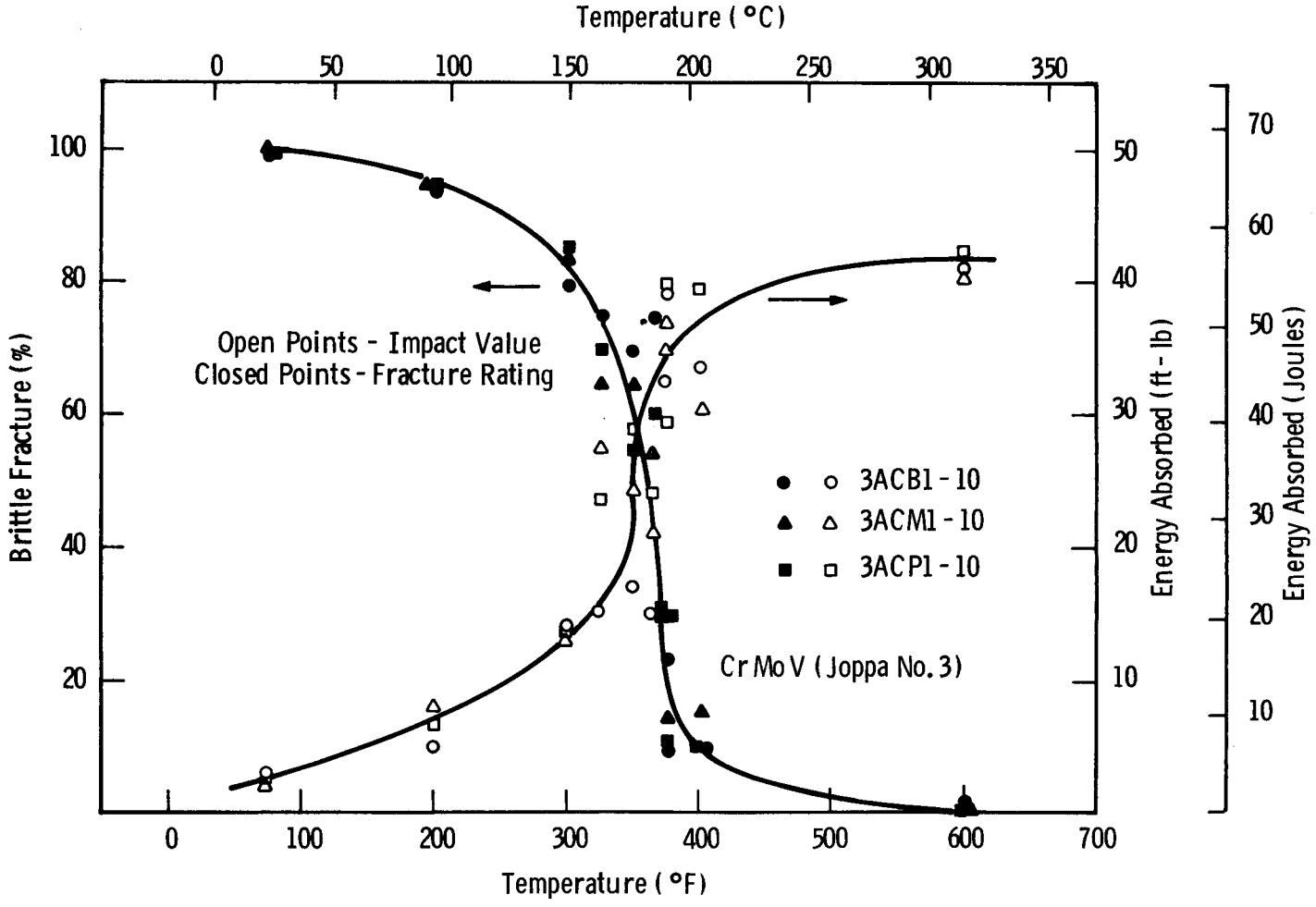

Fig. 4.6a — Charpy V-notch impact properties of Cr Mo V steel taken from Joppa No. 3

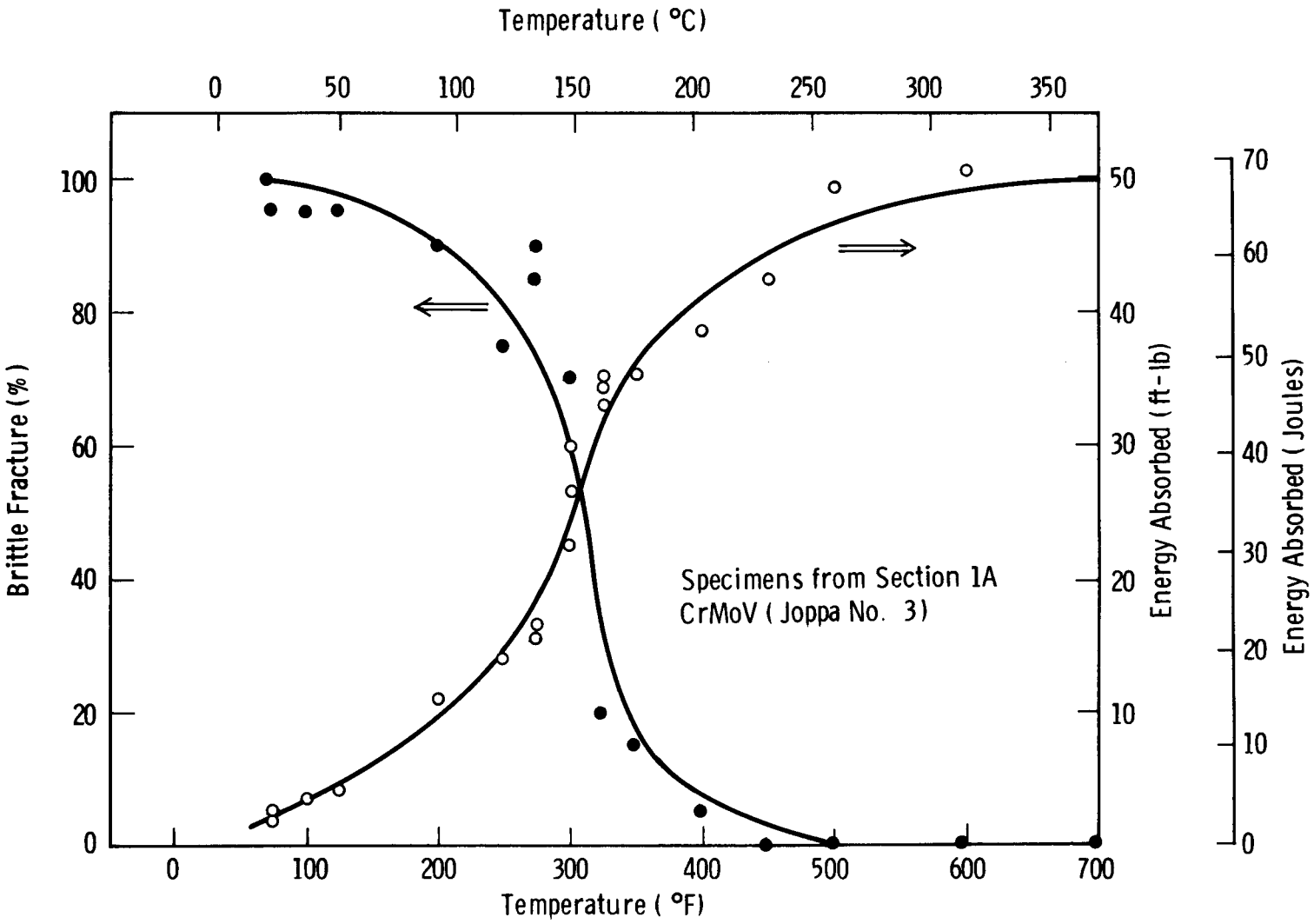

Fig. 4.6b -Charpy V-notch impact properties of CrMoV steel of Joppa no. 3 taken from section 1A

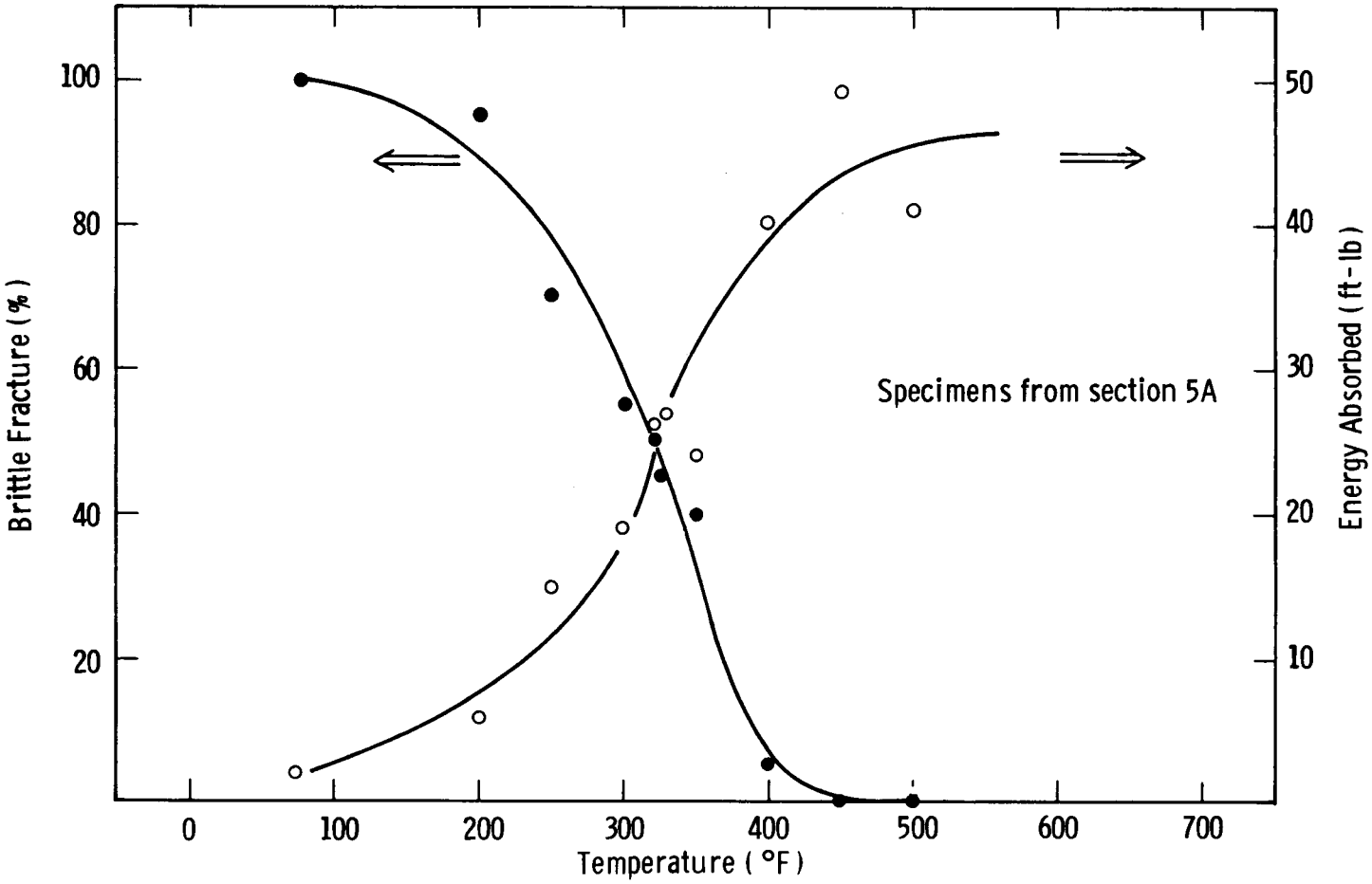

Fig. 4.6c —Charpy V-notch impact properties of CrMoV steel of Joppa No. 3 taken from section 3A

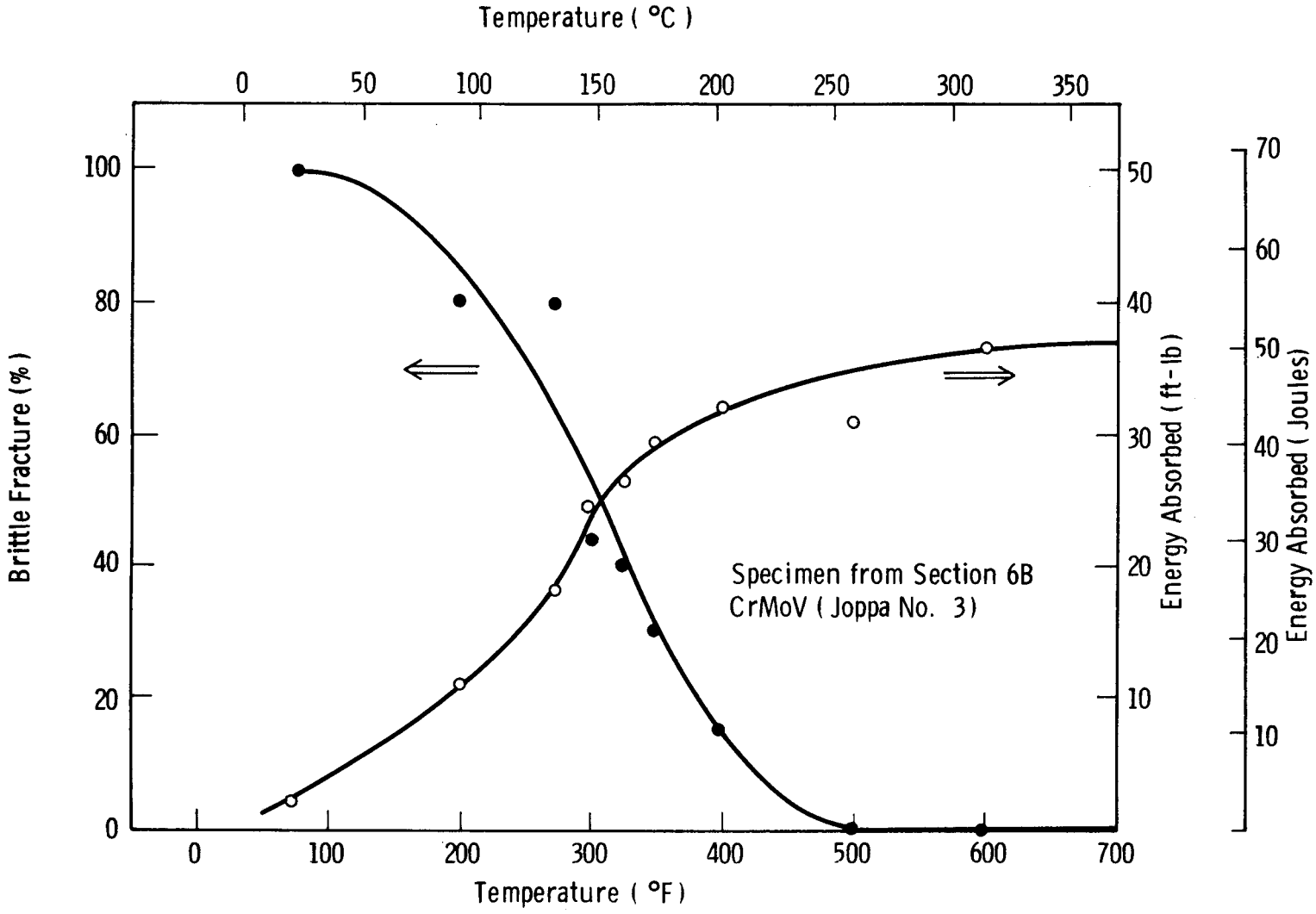

Fig. 4.6d —Charpy V-notch impact properties of CrMoV steel of Joppa no. 3 taken from section 6B

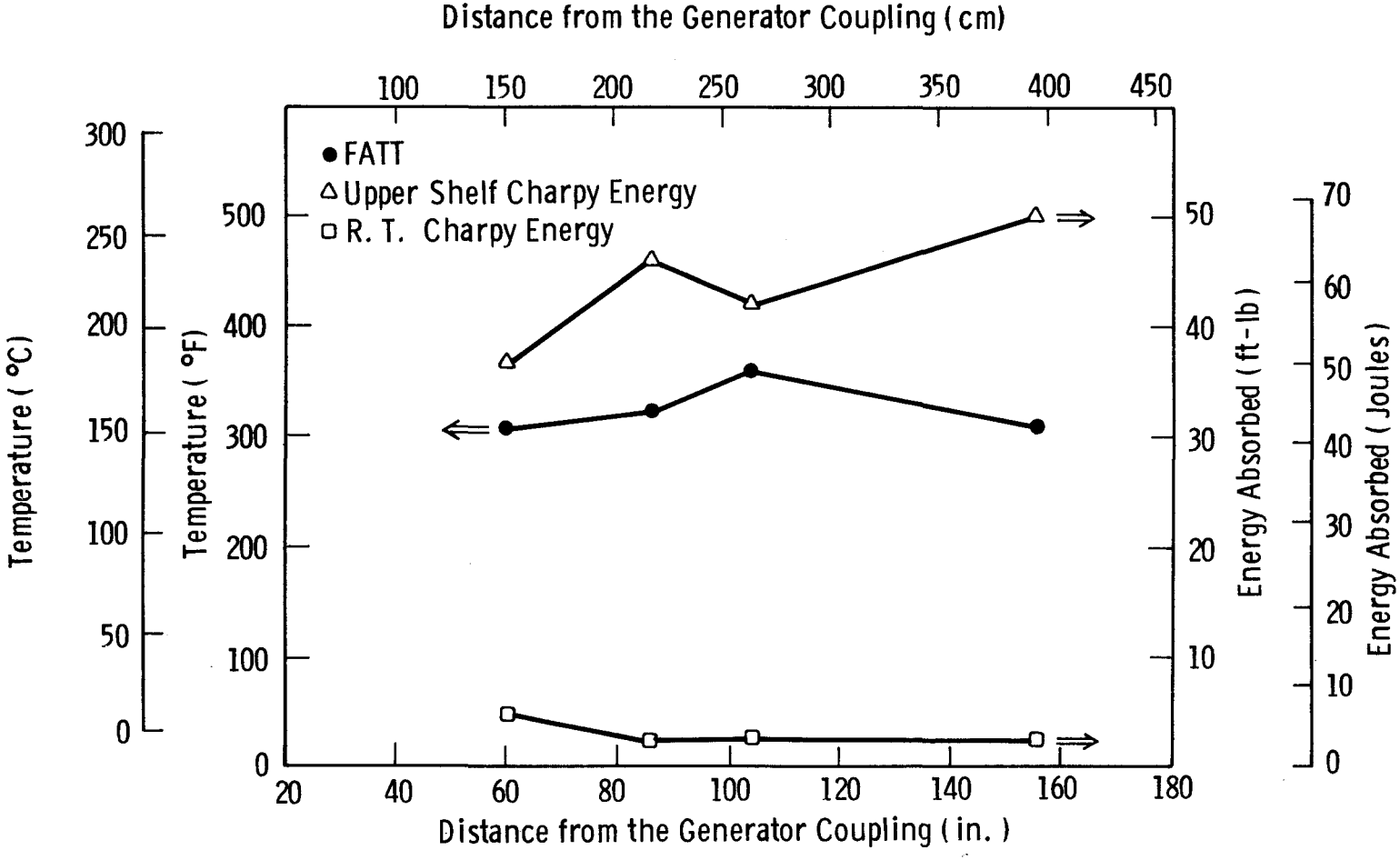

Fig. 4. 7—Charpy V-notch impact properties of CvMoV steel as a function of axial position in Joppa No. 3

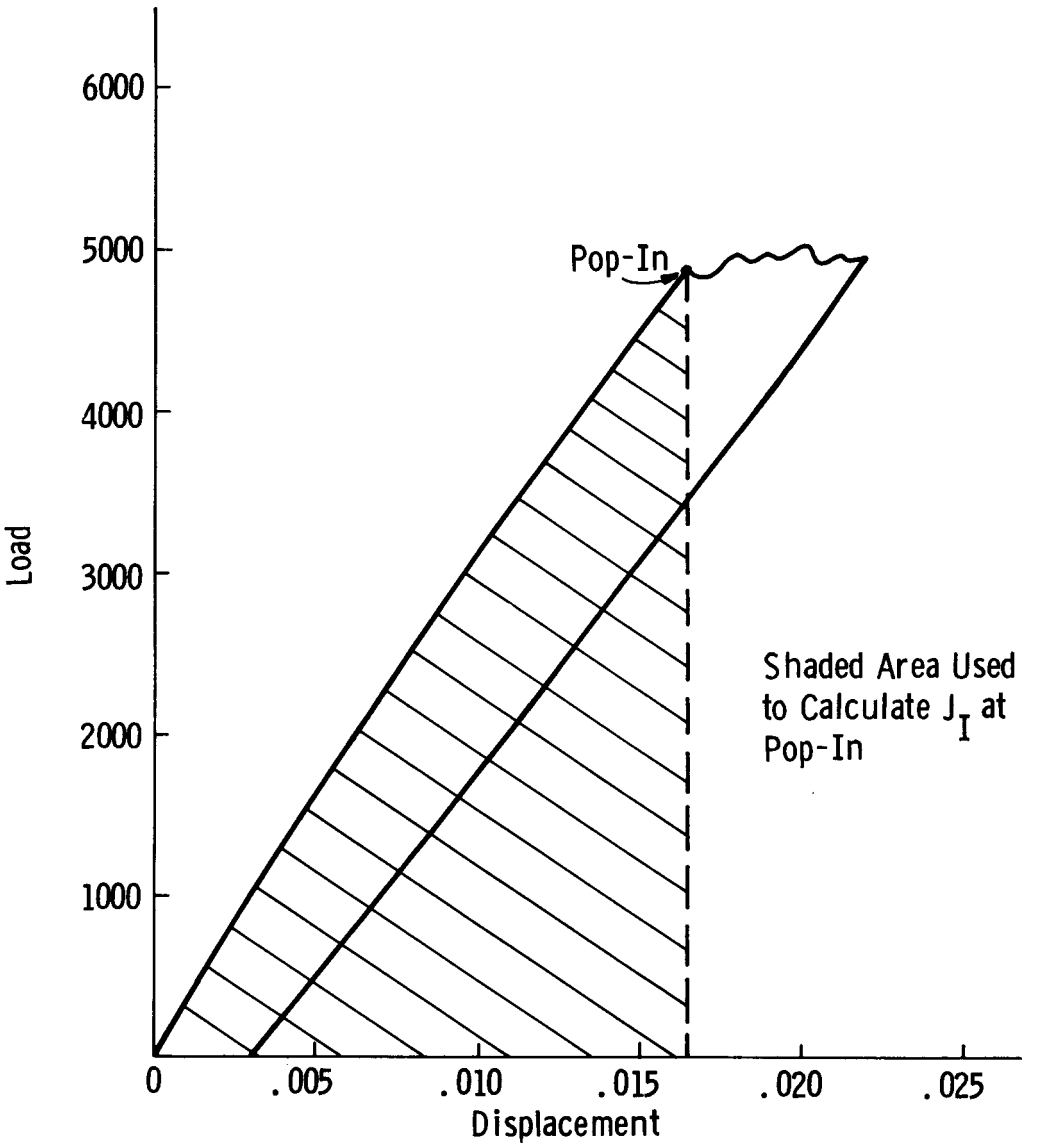

Fig. 4.8 —Load vs. load line displacement for a 1T-CT specimen tested at 250°F

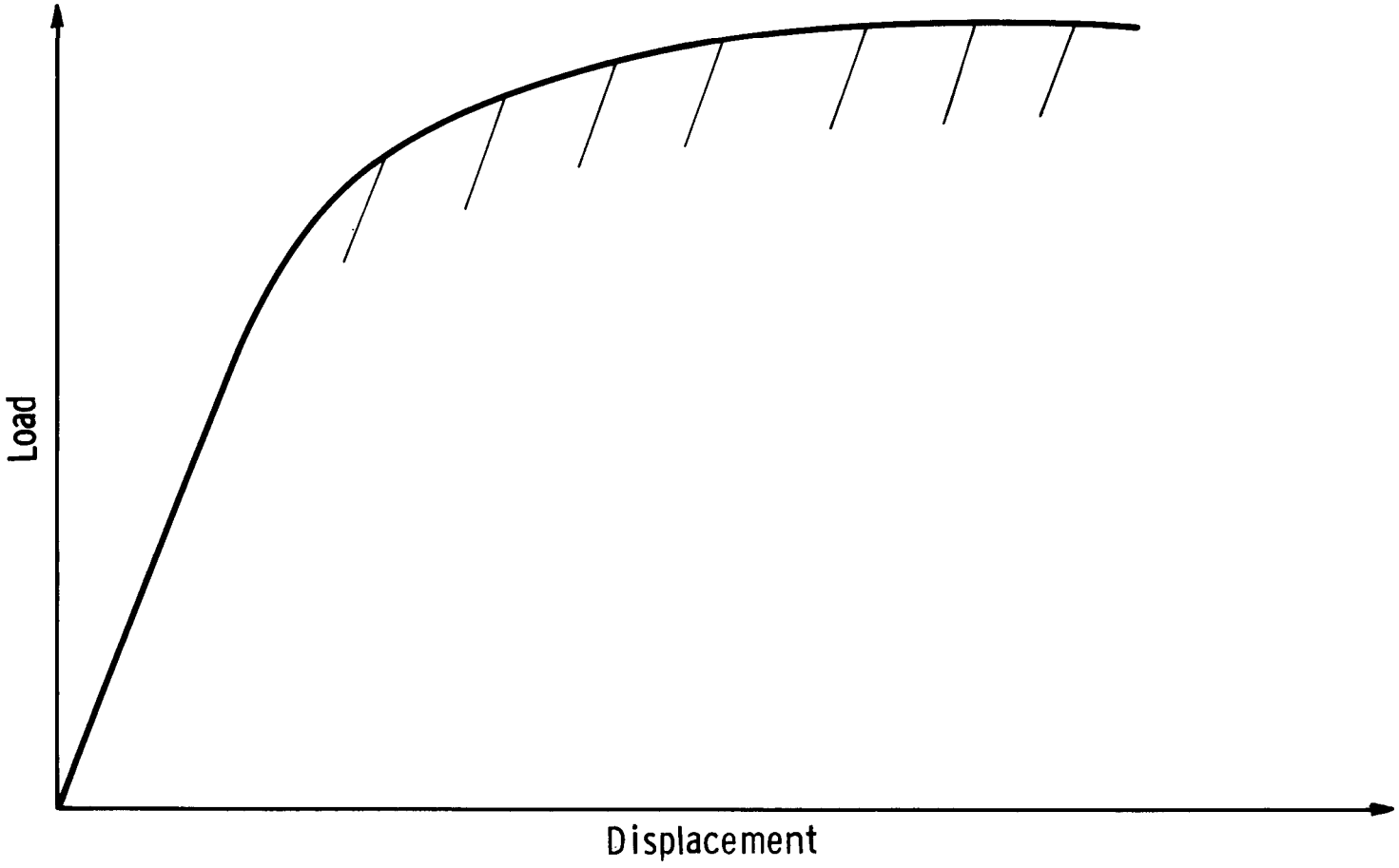

Fig. 4.9 —Schematic representation of the unloading compliance technique for J resistance curve determination

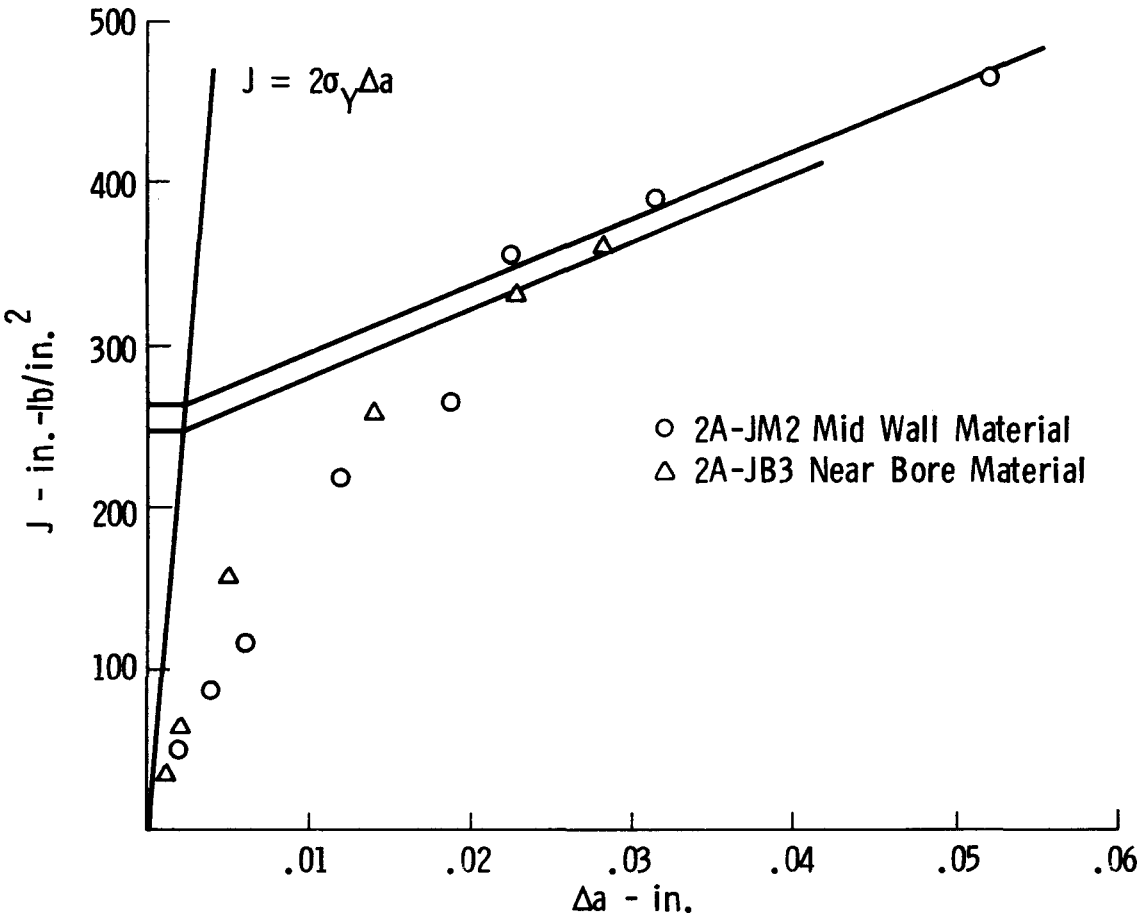

Fig. 4.10a – J vs Δa R-curve for Joppa #3 CrMoV at 350° F

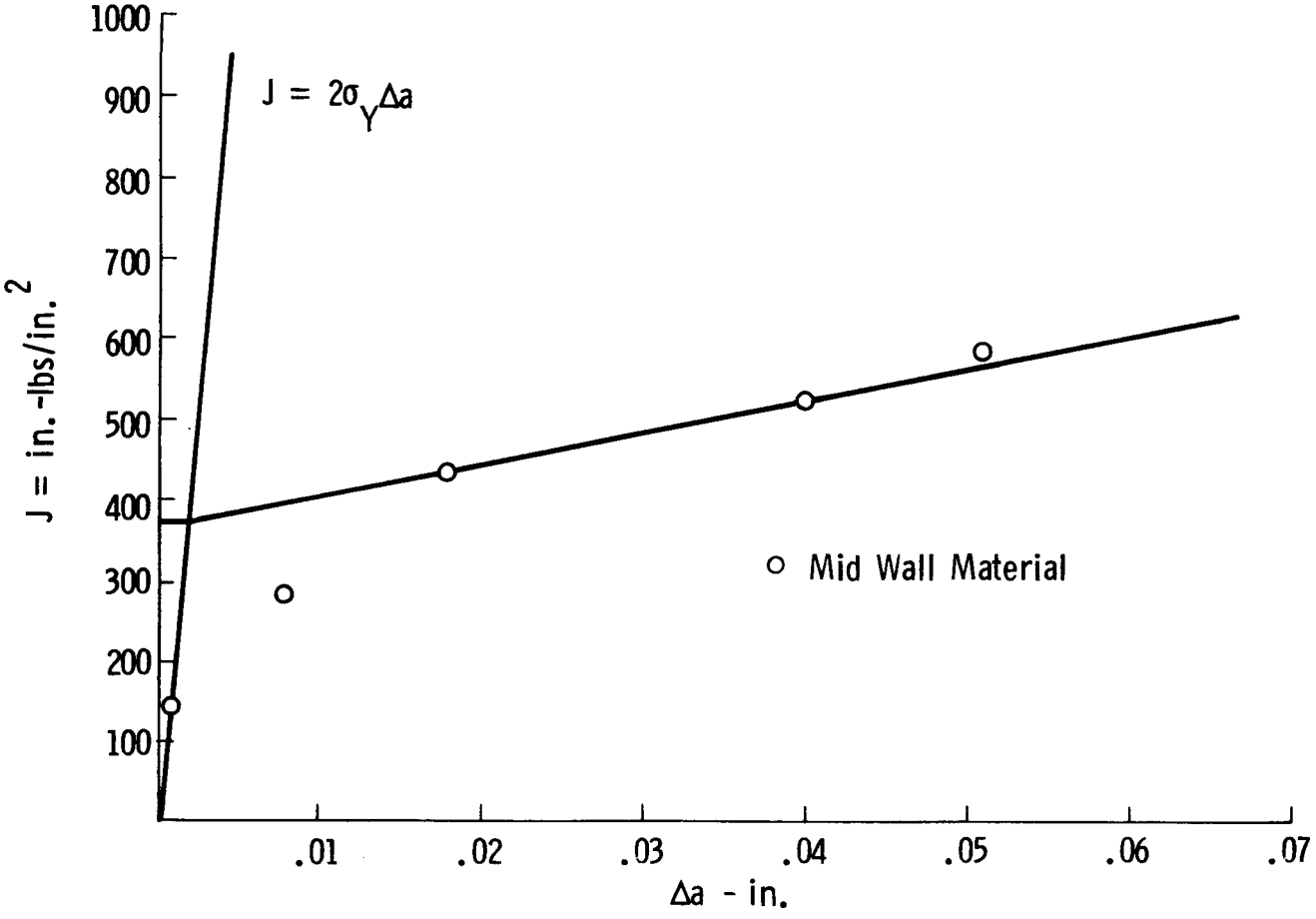

Fig. 4.10b – J vs Δa R-curve for Joppa #3 rotor CrMoV at 400° F

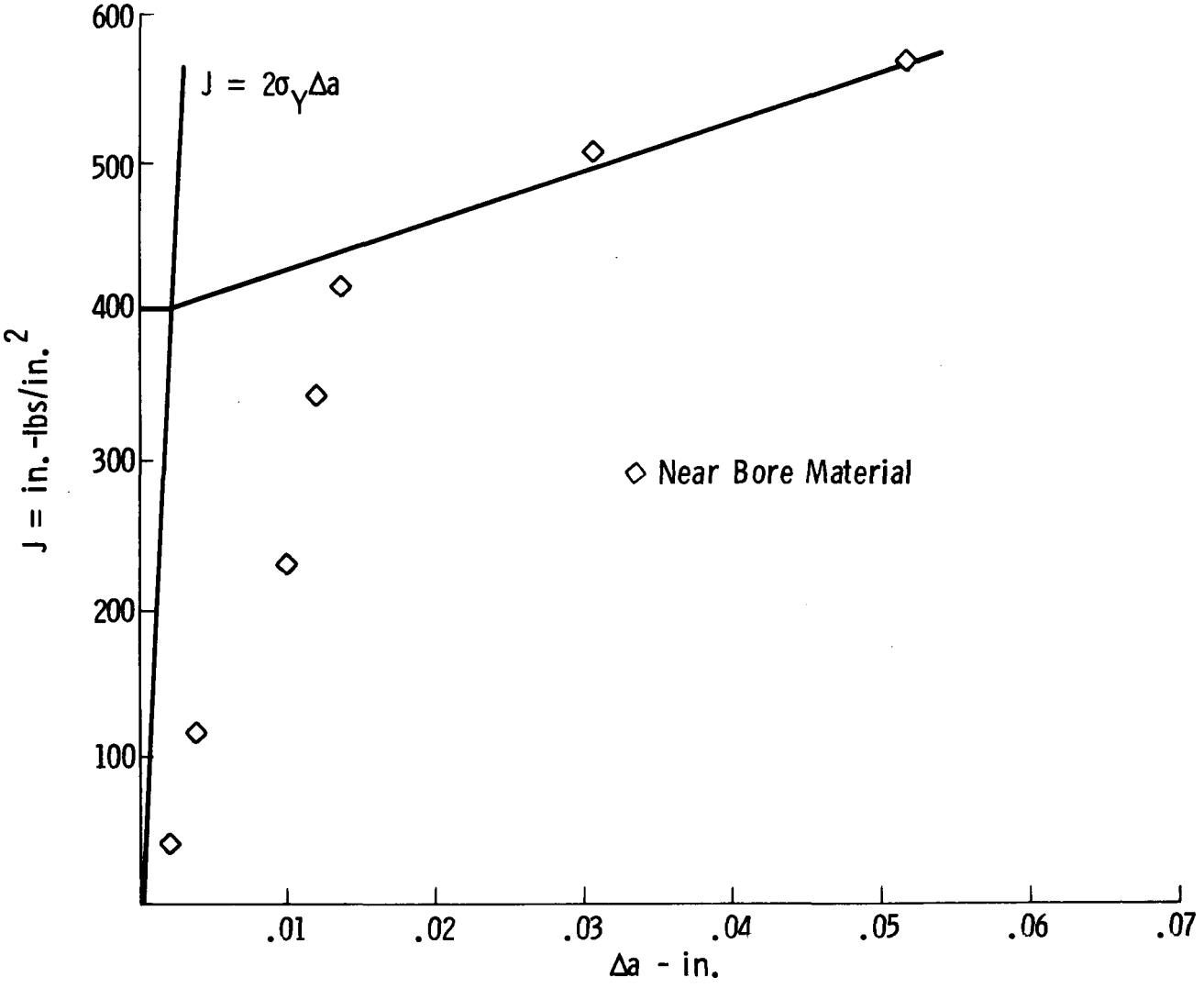

Fig. 4.10c – vs Δa R-curve for Joppa #3 rotor CrMoV at 500° F

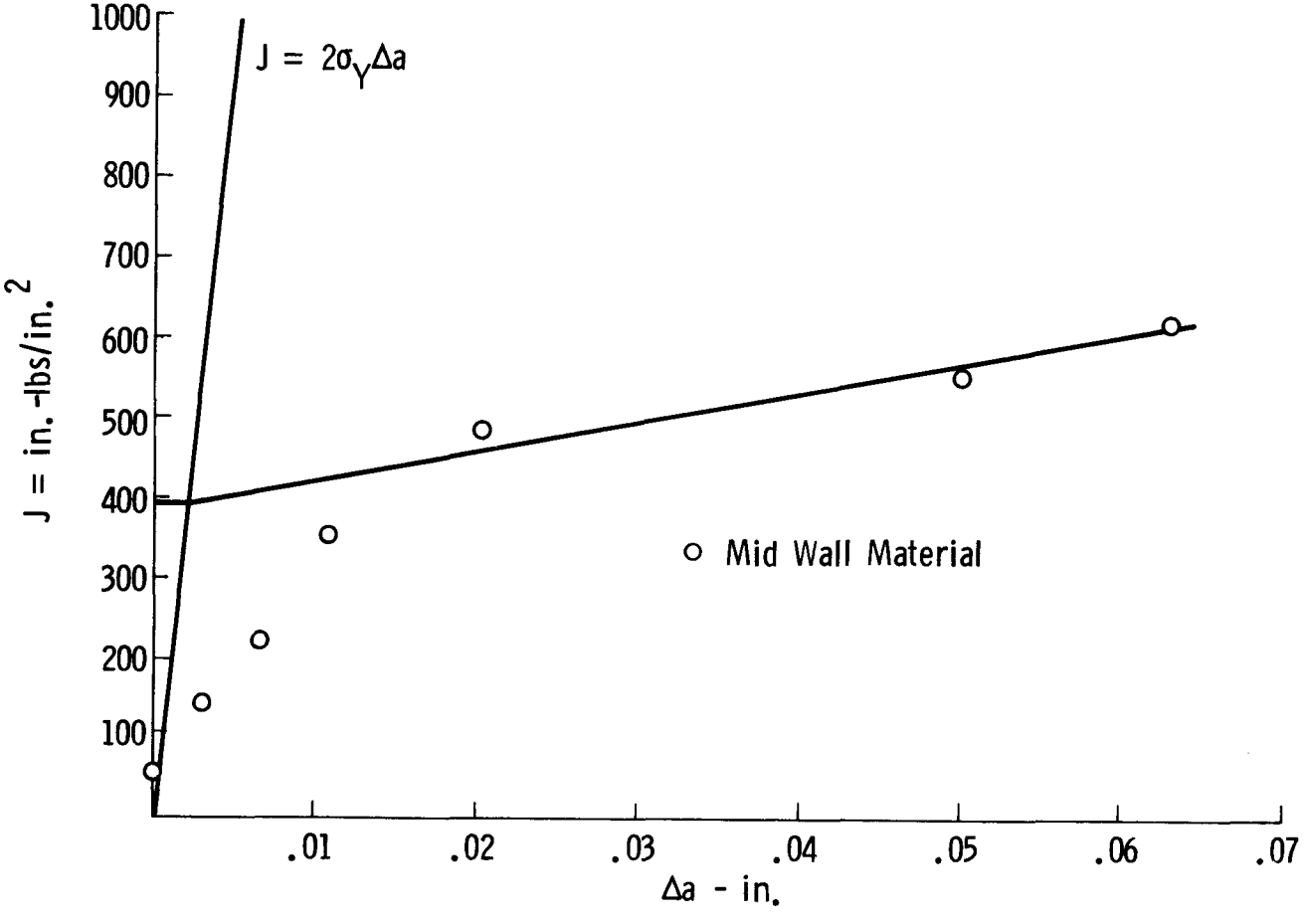

Fig. 4.10d – J vs Δa R-curve for Joppa #3 rotor at 550° F

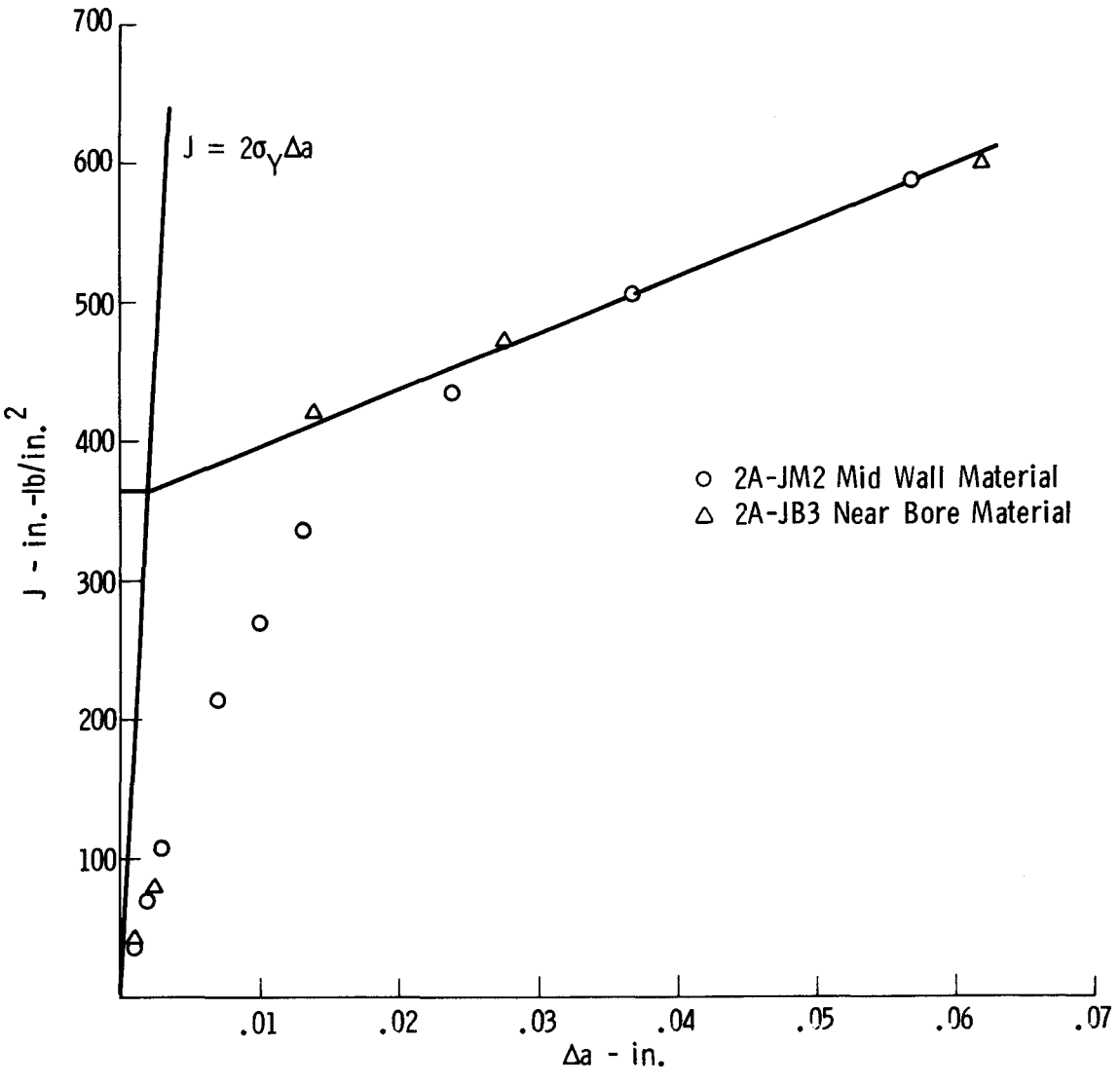

Fig. 4.10e – J vs Δa R-curve for Joppa #3 CrMoV at 650° F

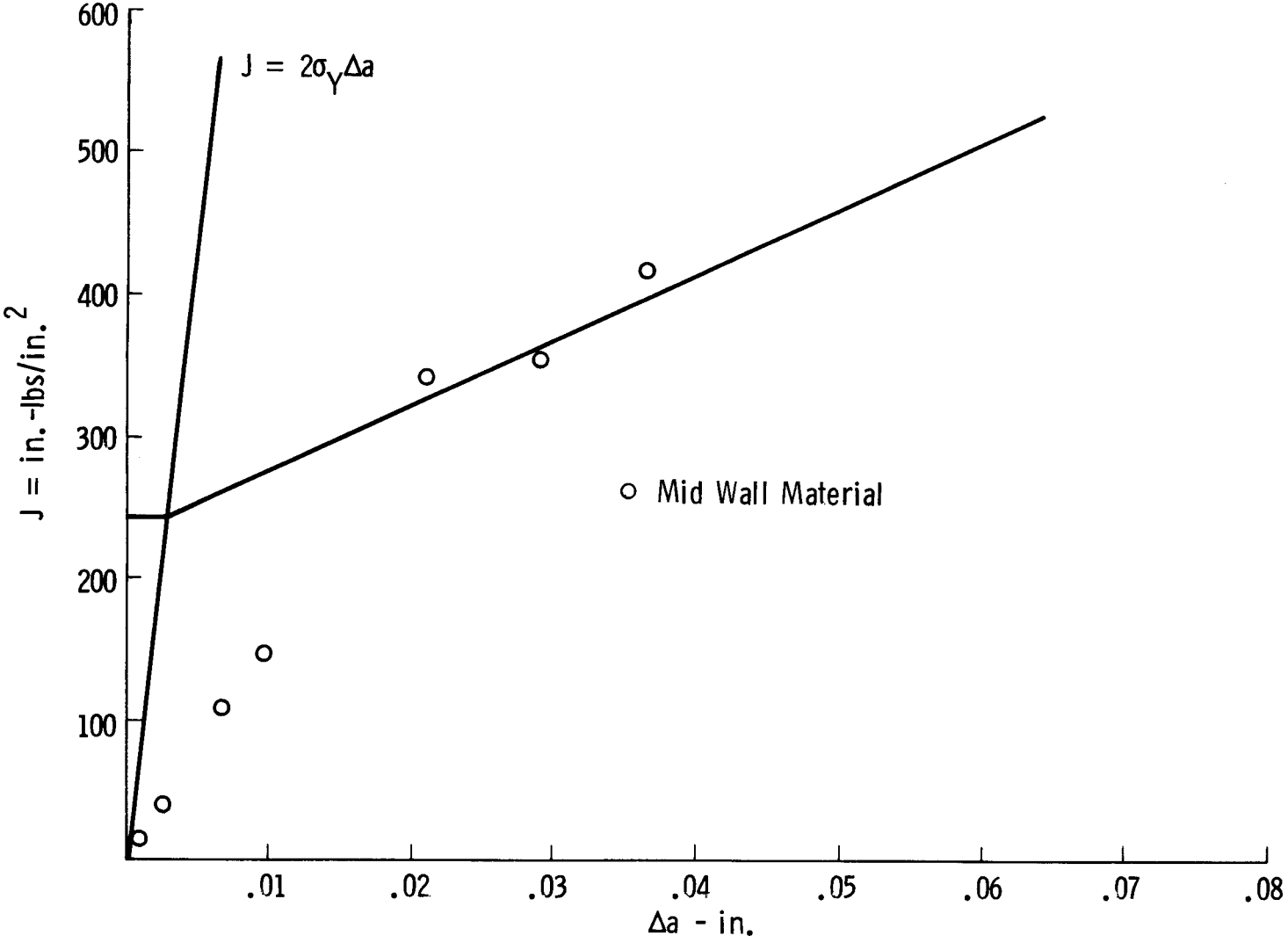

Fig. 4.10 f – J vs Δa R-curve for Joppa #3 rotor CrMoV at 750° F

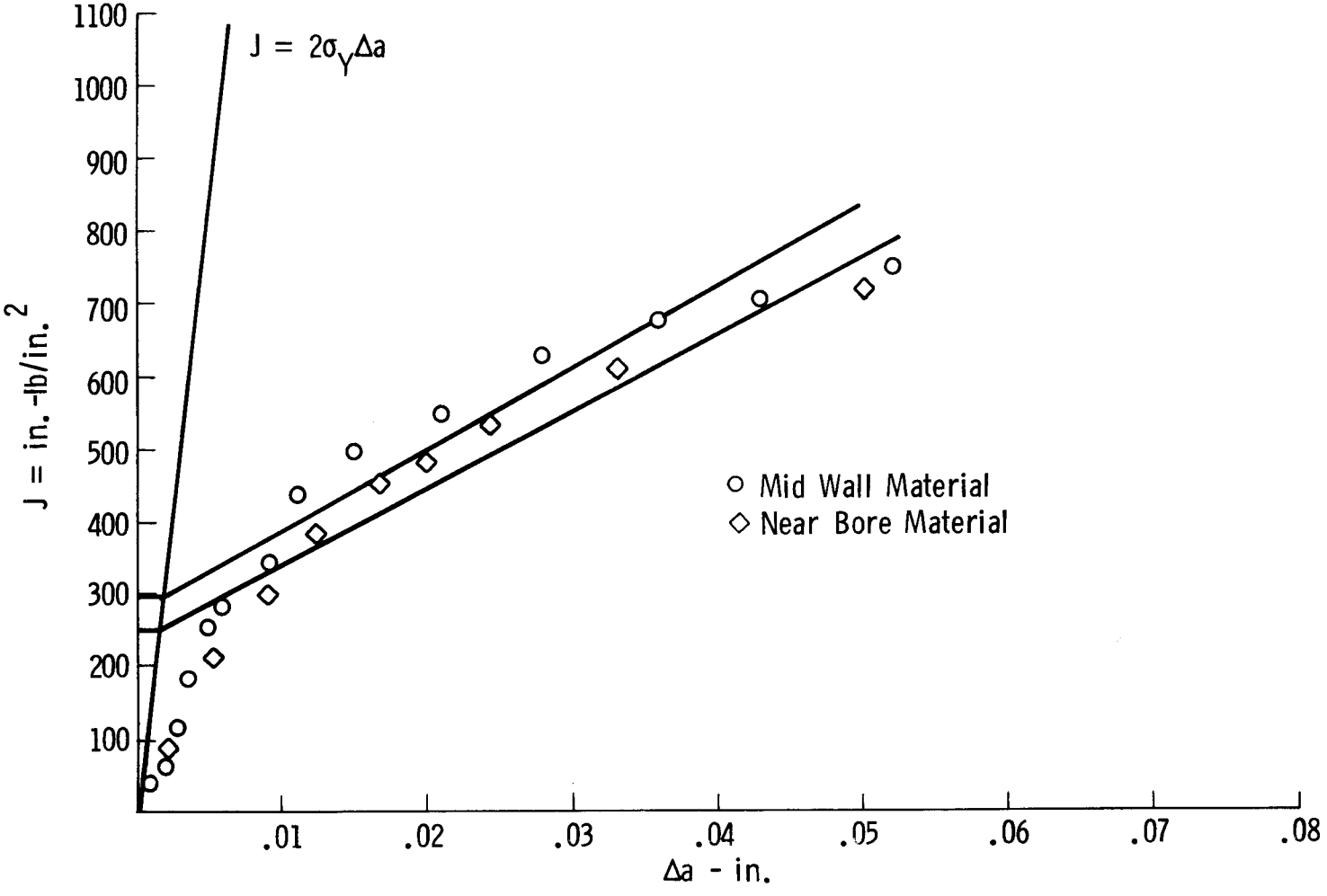

Fig. 4.10g – J vs Δa R-curve for Joppa #3 rotor CrMoV at 800° F

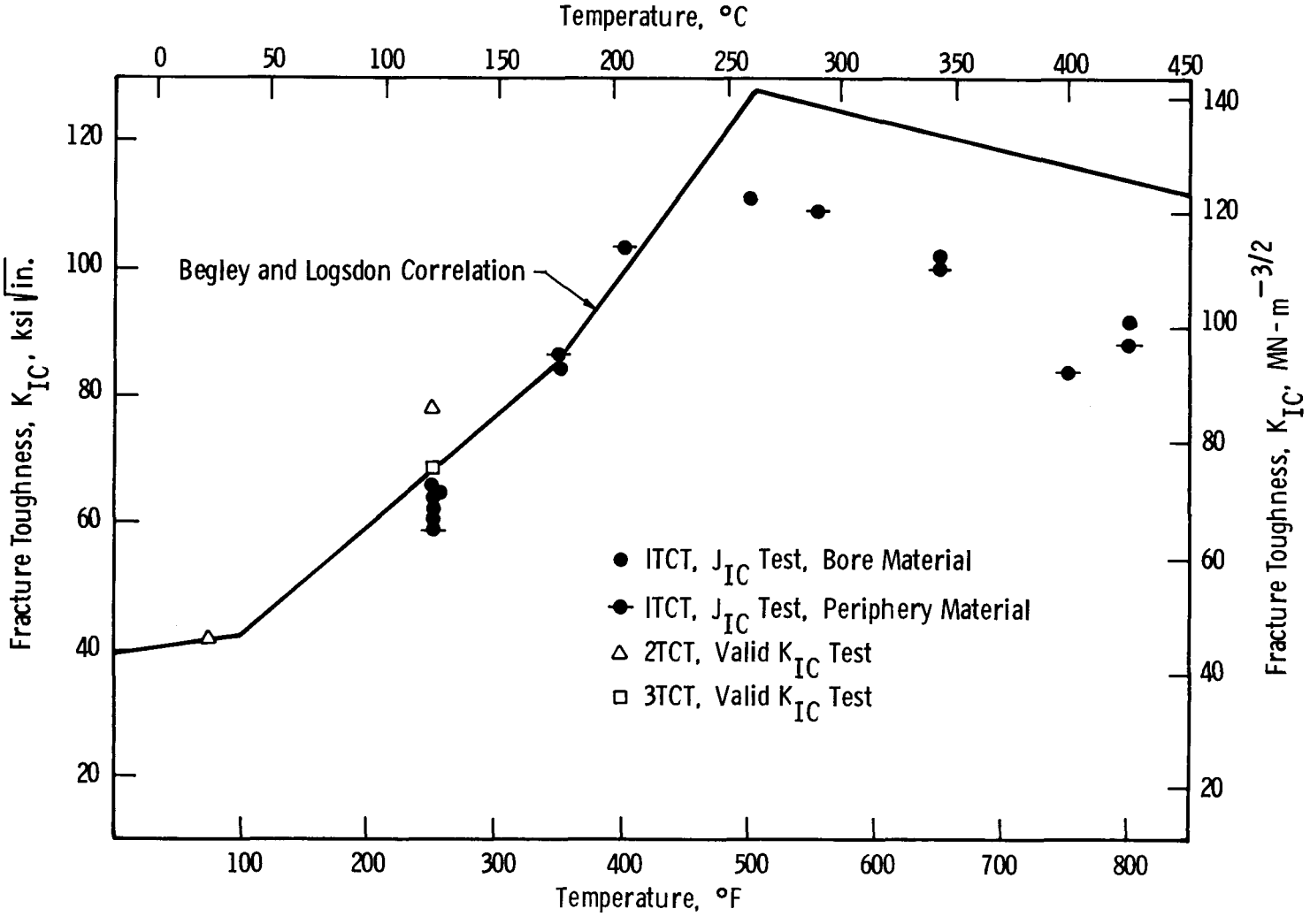

Fig. 4.11 – Fracture toughness properties of CrMoV taken from Joppa No. 3

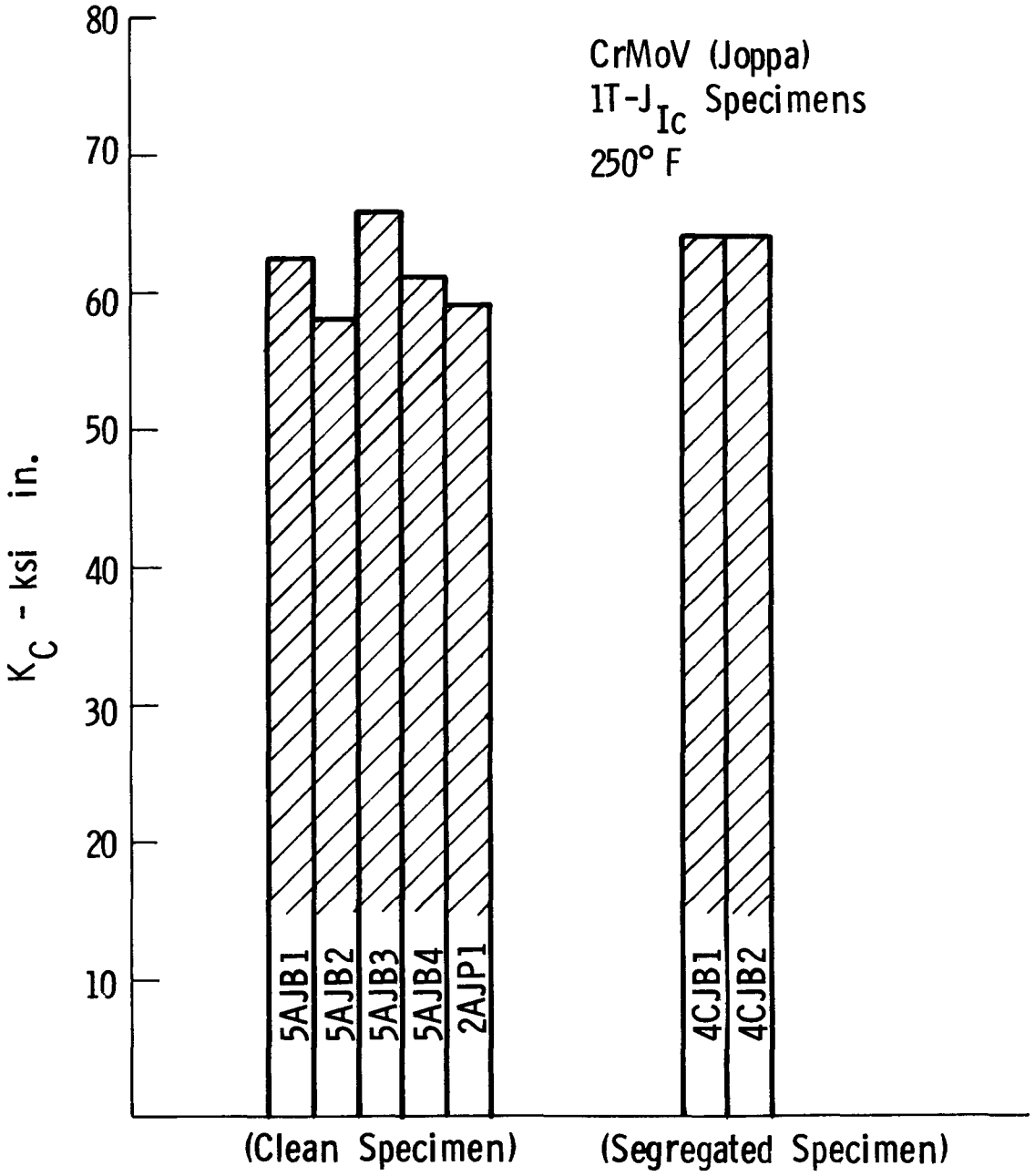

Fig. 4.12 – Results of J_{Ic} tests at 250° F show the lack of effect of discontinuities on fracture toughness

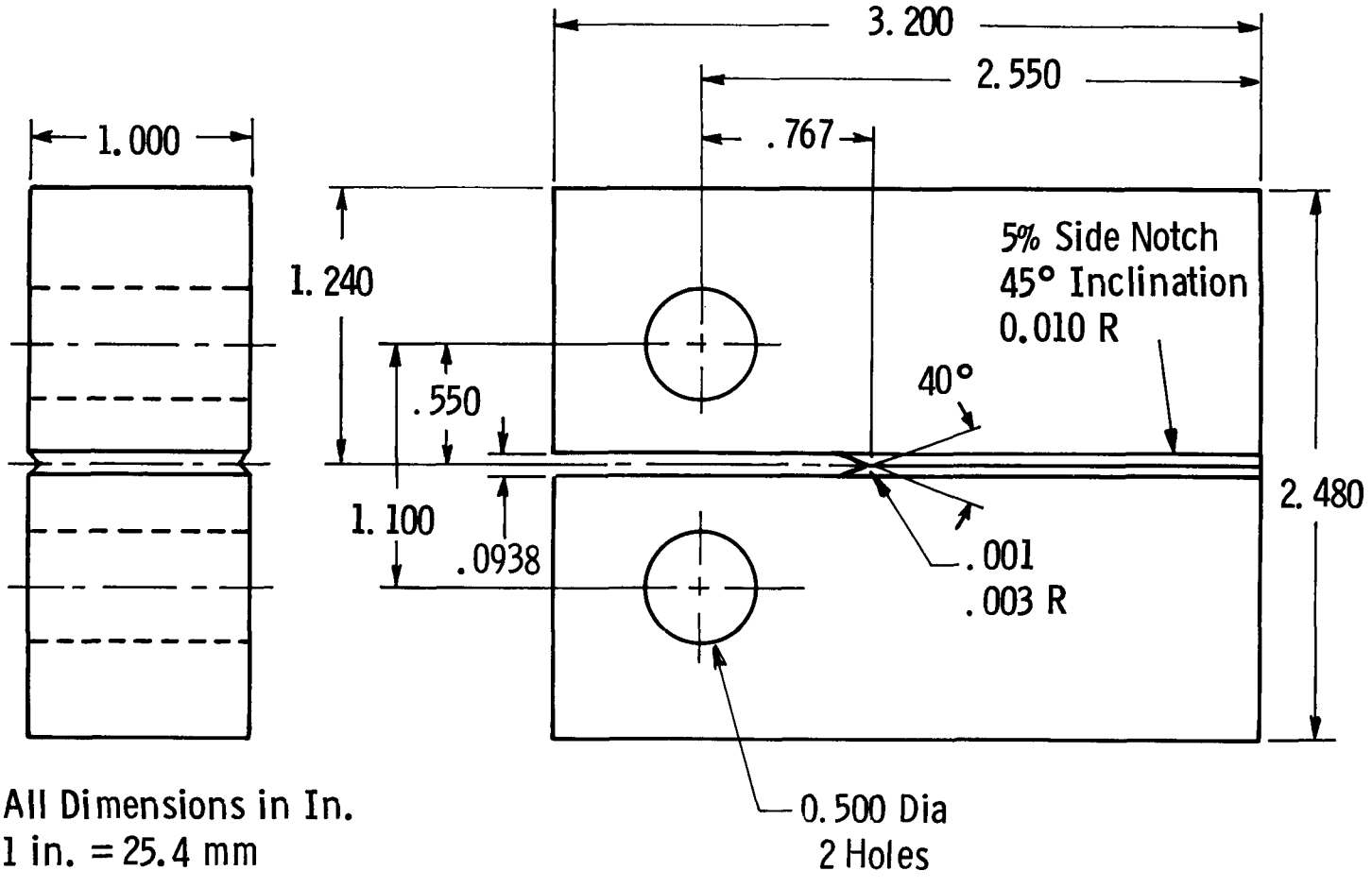

Fig. 4.13 – Compact tension fatigue crack growth specimen

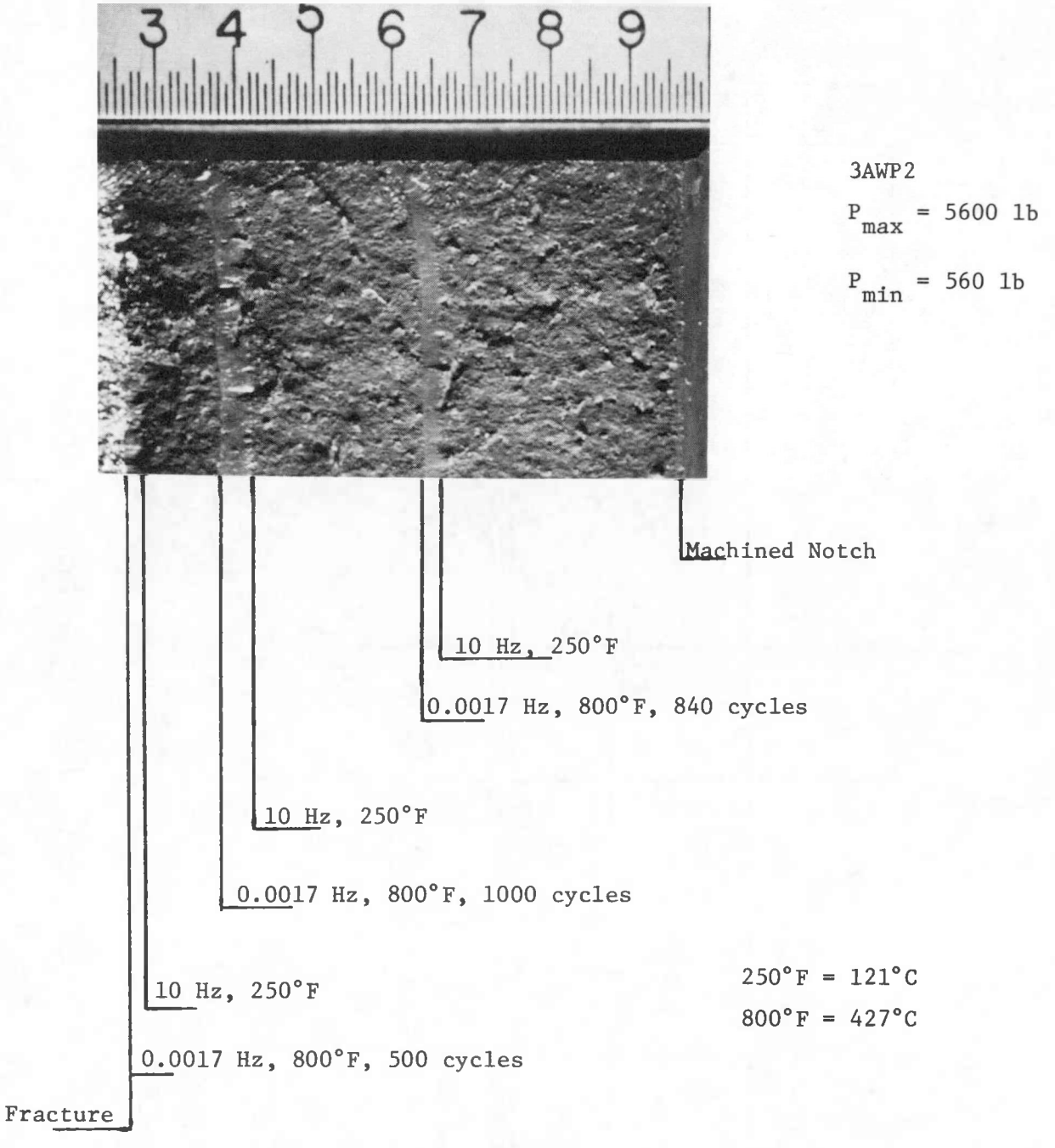

Fig. 4.14 — Macroscopic fractograph of a test specimen subjected to alternating temperature and frequency loading

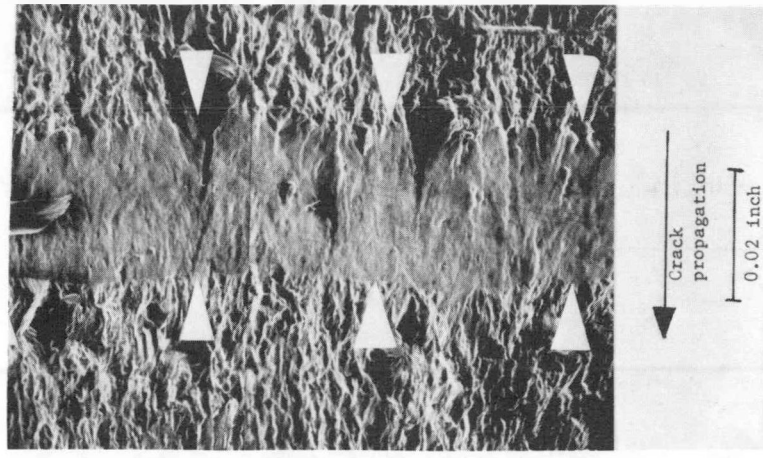

(A)

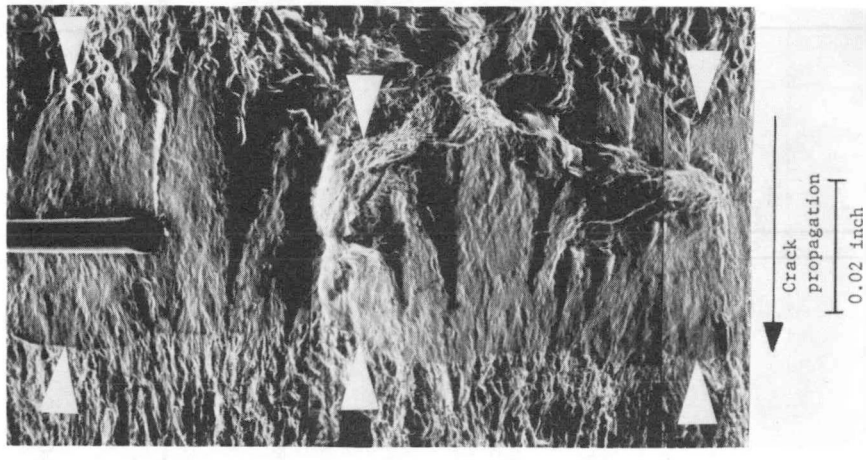

(B)

(C)

Fig. 4.15 – SEM of fracture surface at 50X showing fatigue crack growth band for CrMoV at 800°F, 0.0017 Hz: A. 840 cycles at $\Delta K = 29.5$ ksi $\sqrt{in.}$ (32 MN/m$^{3/2}$); B. 1010 cycles at $\Delta K = 37.5$ ksi $\sqrt{in.}$ (41 MN/m$^{-3/2}$); C. 500 cycles at $\Delta K = 44.0$ ksi $\sqrt{in.}$ (48 MN/m$^{-3/2}$)

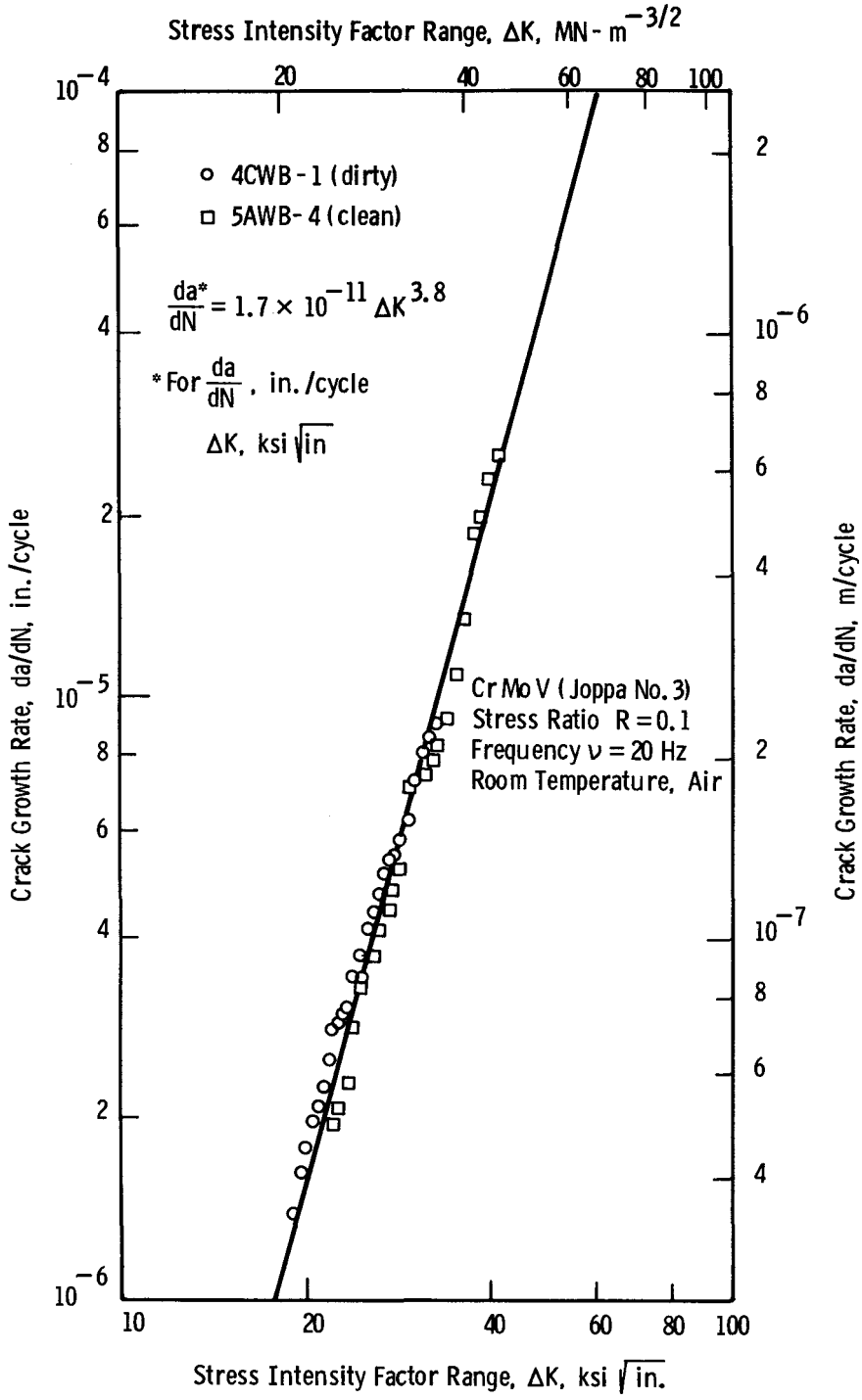

Fig. 4.16 — Room temperature fatigue crack growth rate of CrMoV steel tested at 20 Hz

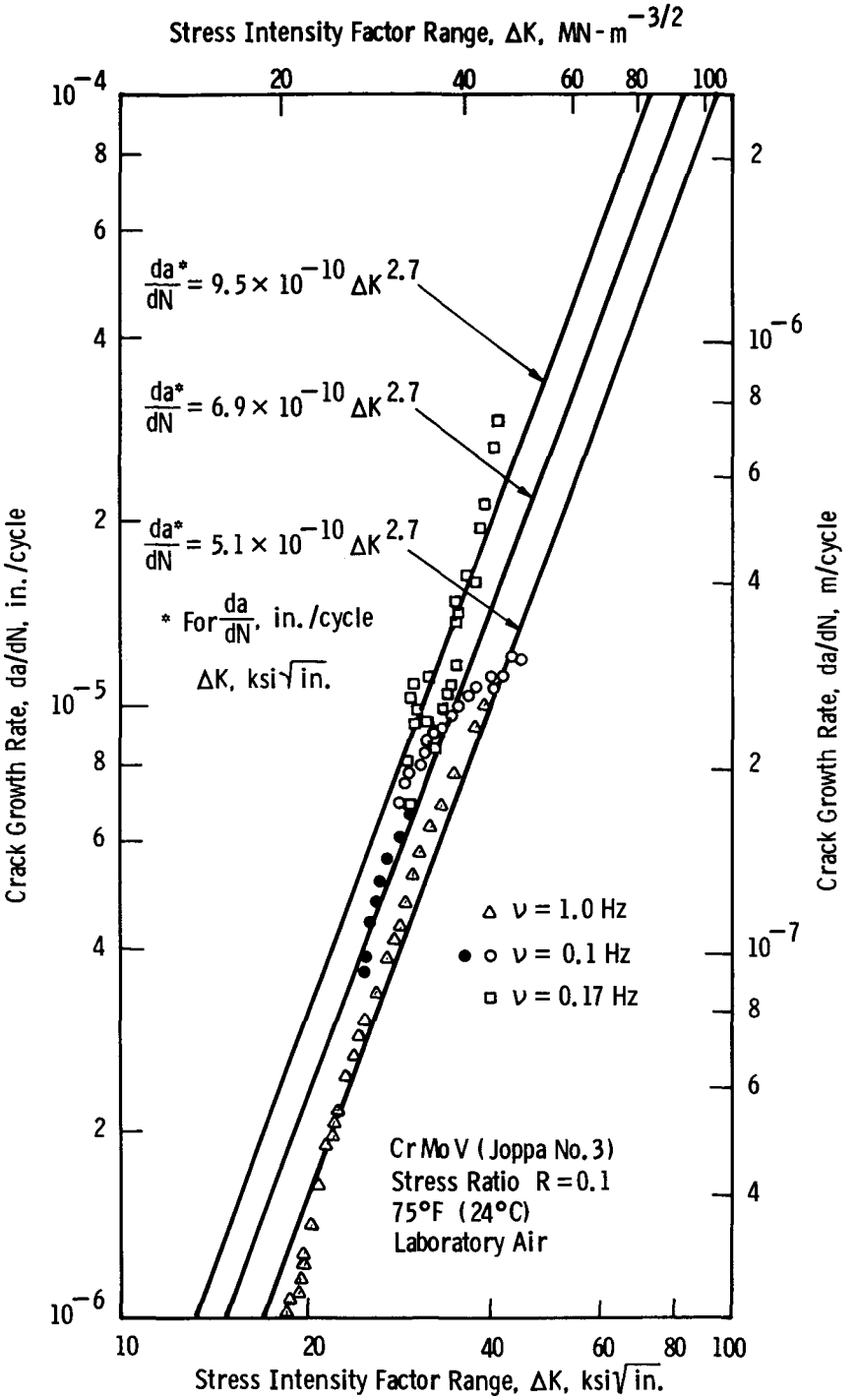

Fig. 4.17 – Effect of frequency on fatigue crack growth rate of CrMoV steel tested at 75°F (24°C)

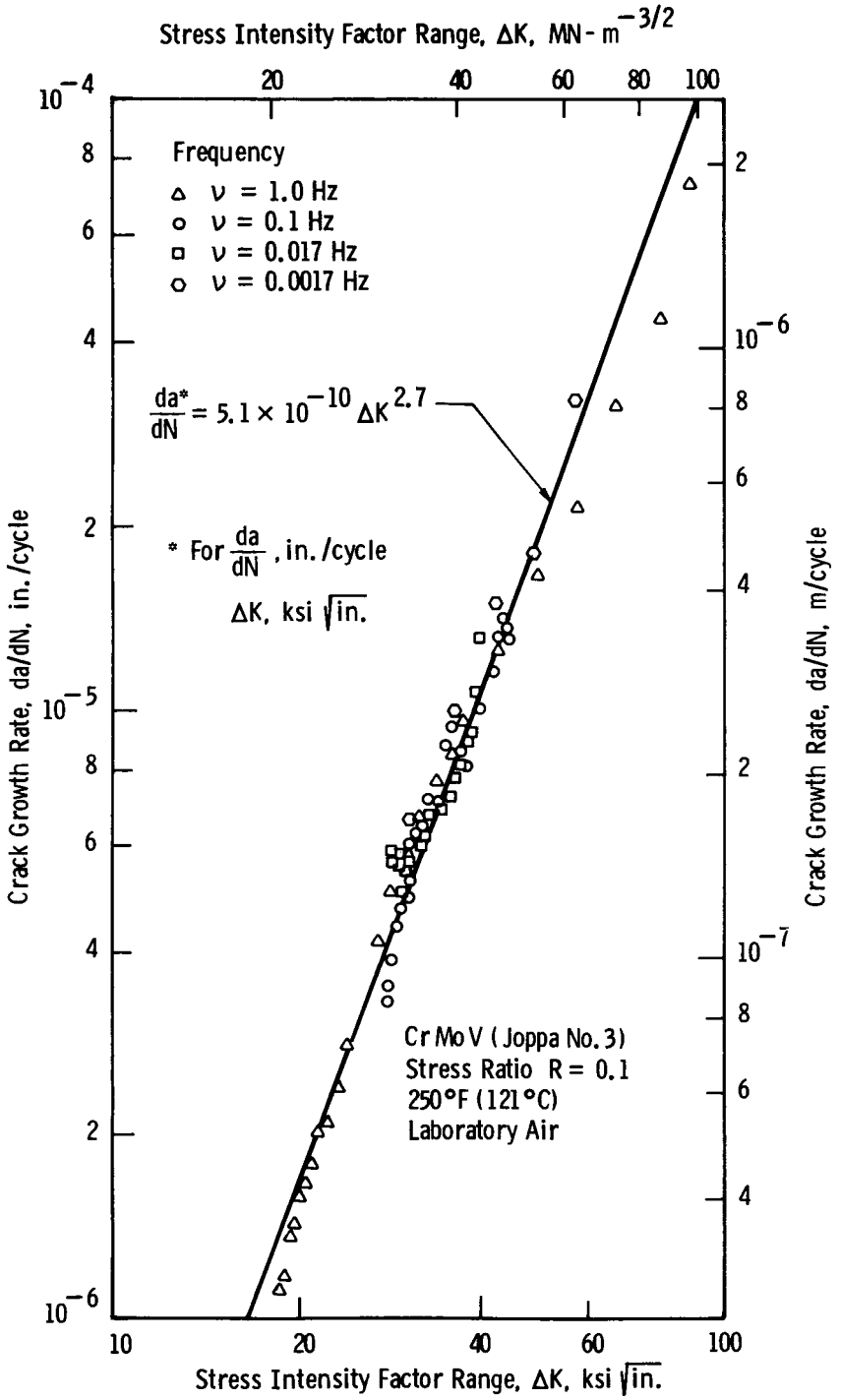

Fig. 4.18 – Effect of frequency on fatigue crack growth rate of Cr Mo V steel tested at 250°F (121°C)

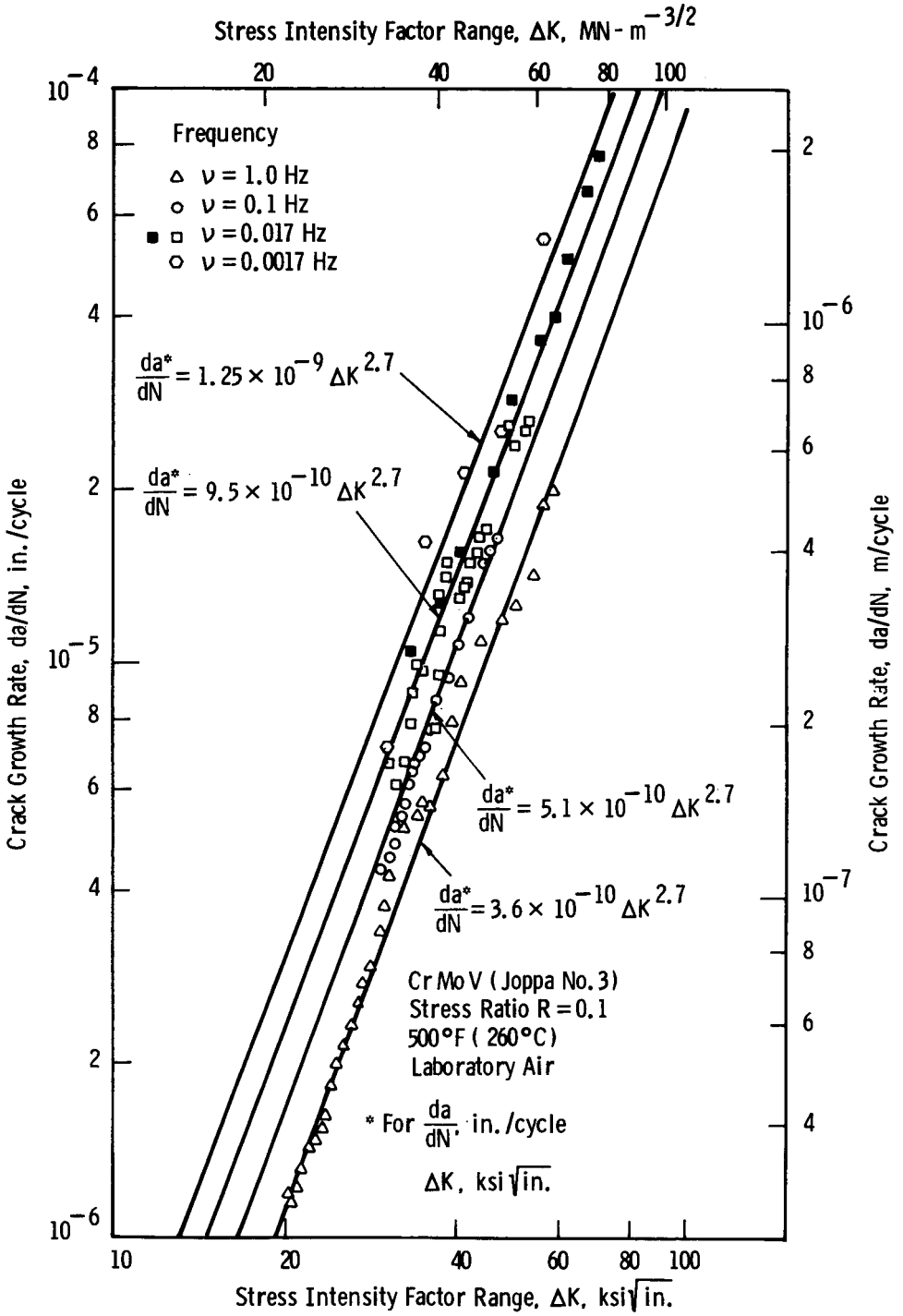

Fig. 4.19 – Effect of frequency on fatigue crack growth rate of Cr Mo V steel tested at 500°F (260°C)

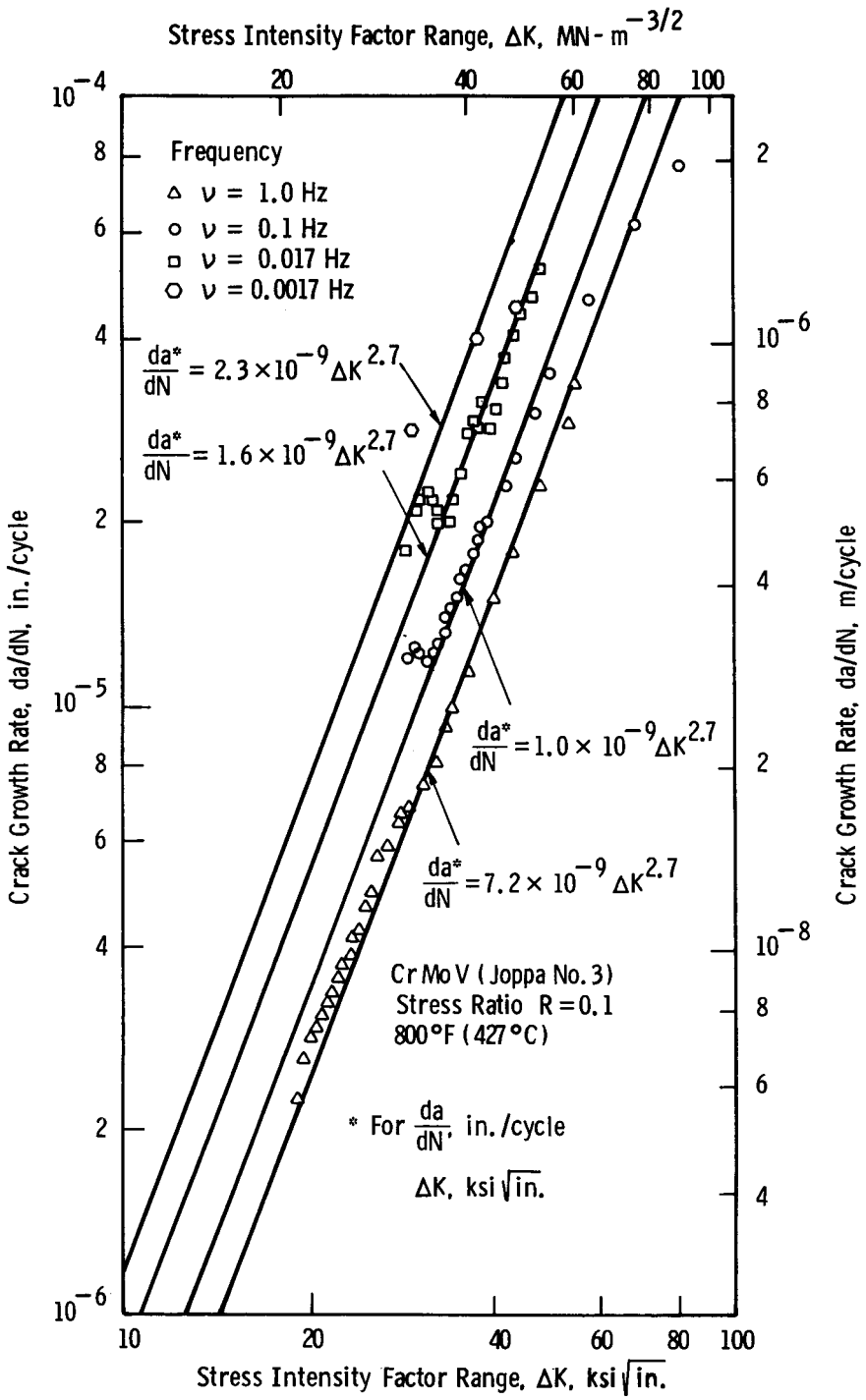

Fig. 4.20 – Effect of frequency on fatigue crack growth rate of Cr Mo V steel tested at 800°F (427°C)

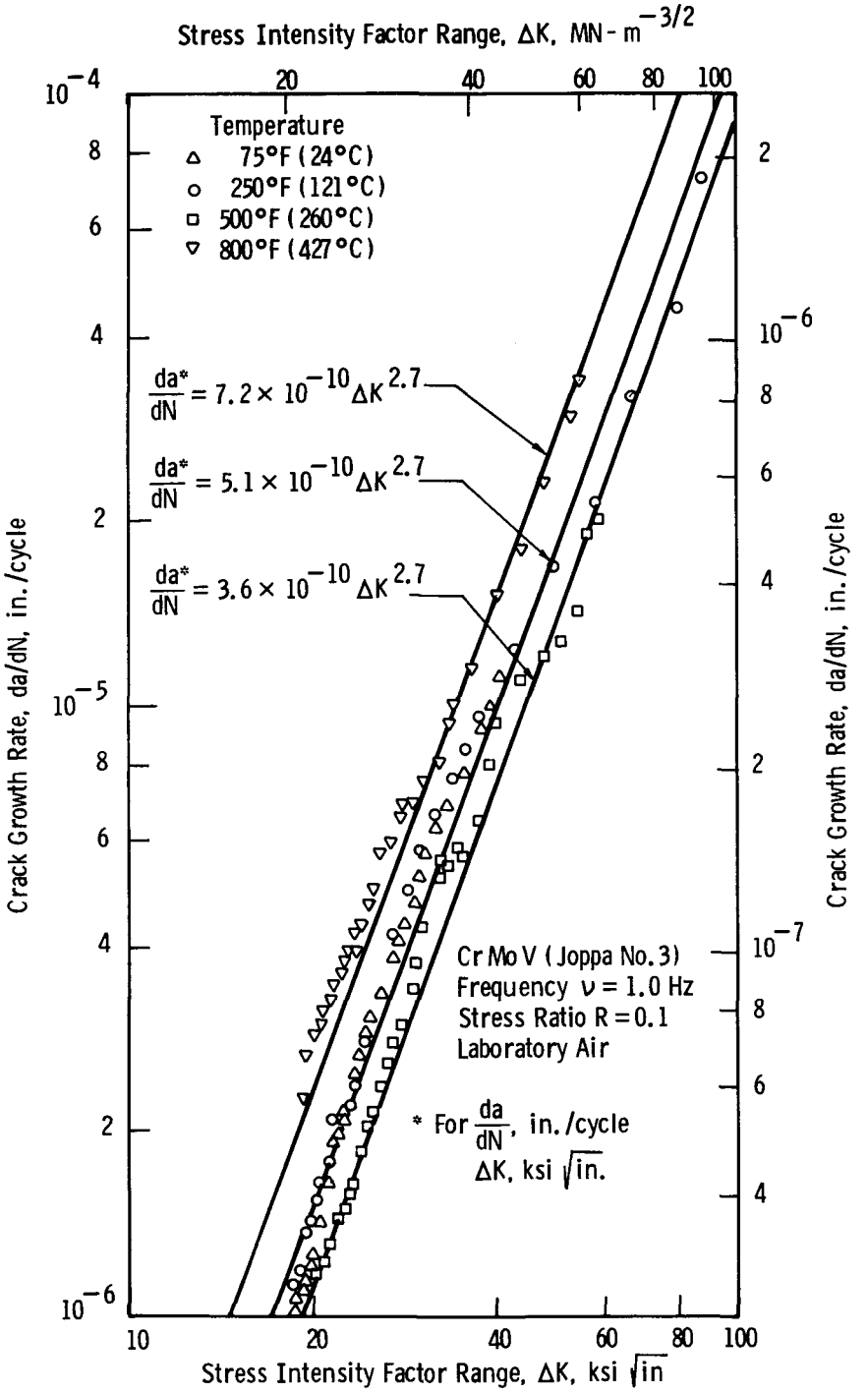

Fig. 4.21 – Effect of temperature on fatigue crack growth rate of Cr Mo V steel tested at 1.0 Hz

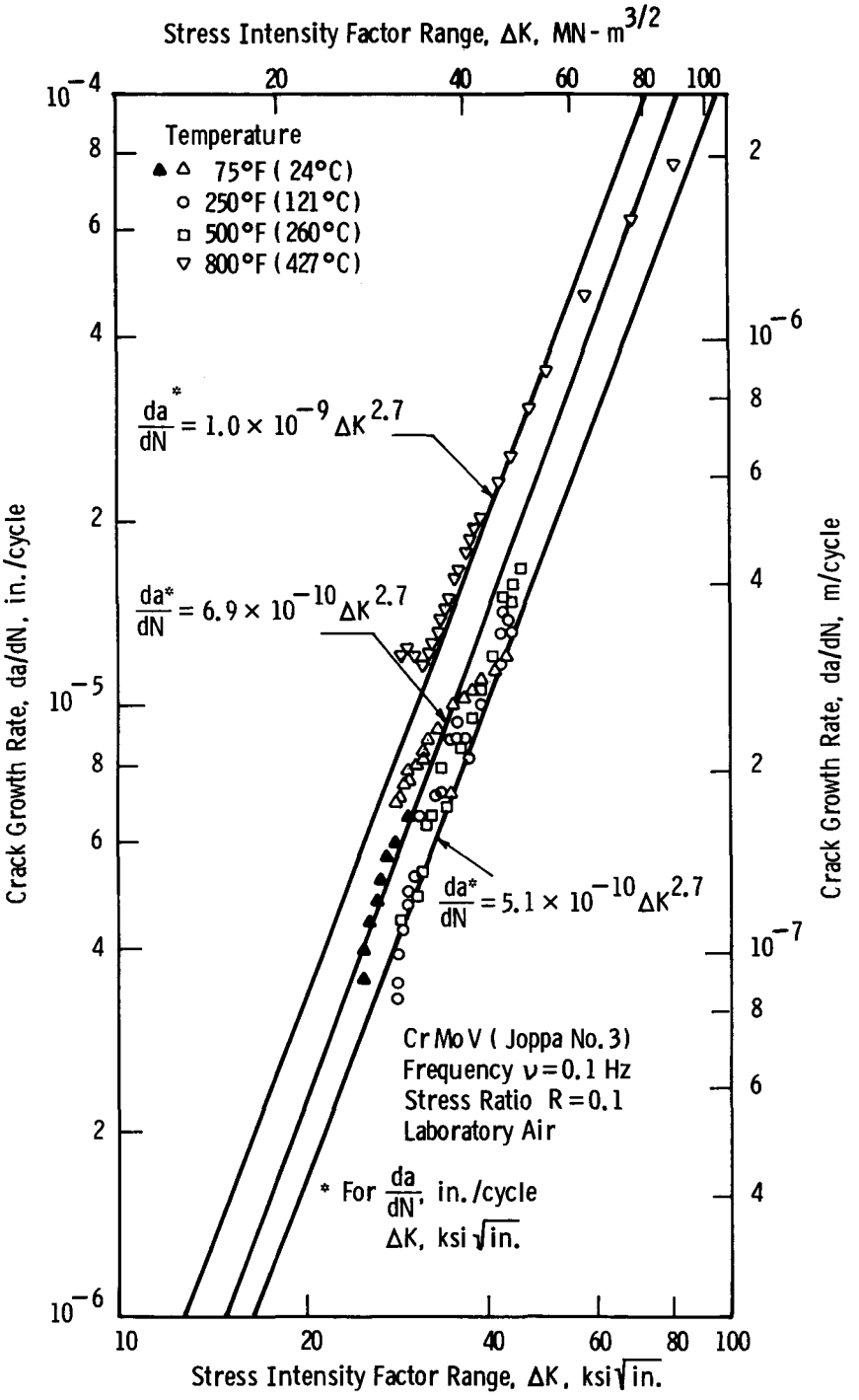

Fig. 4.22 – Effect of temperature on fatigue crack growth rate of Cr Mo V steel tested at 0.1 Hz

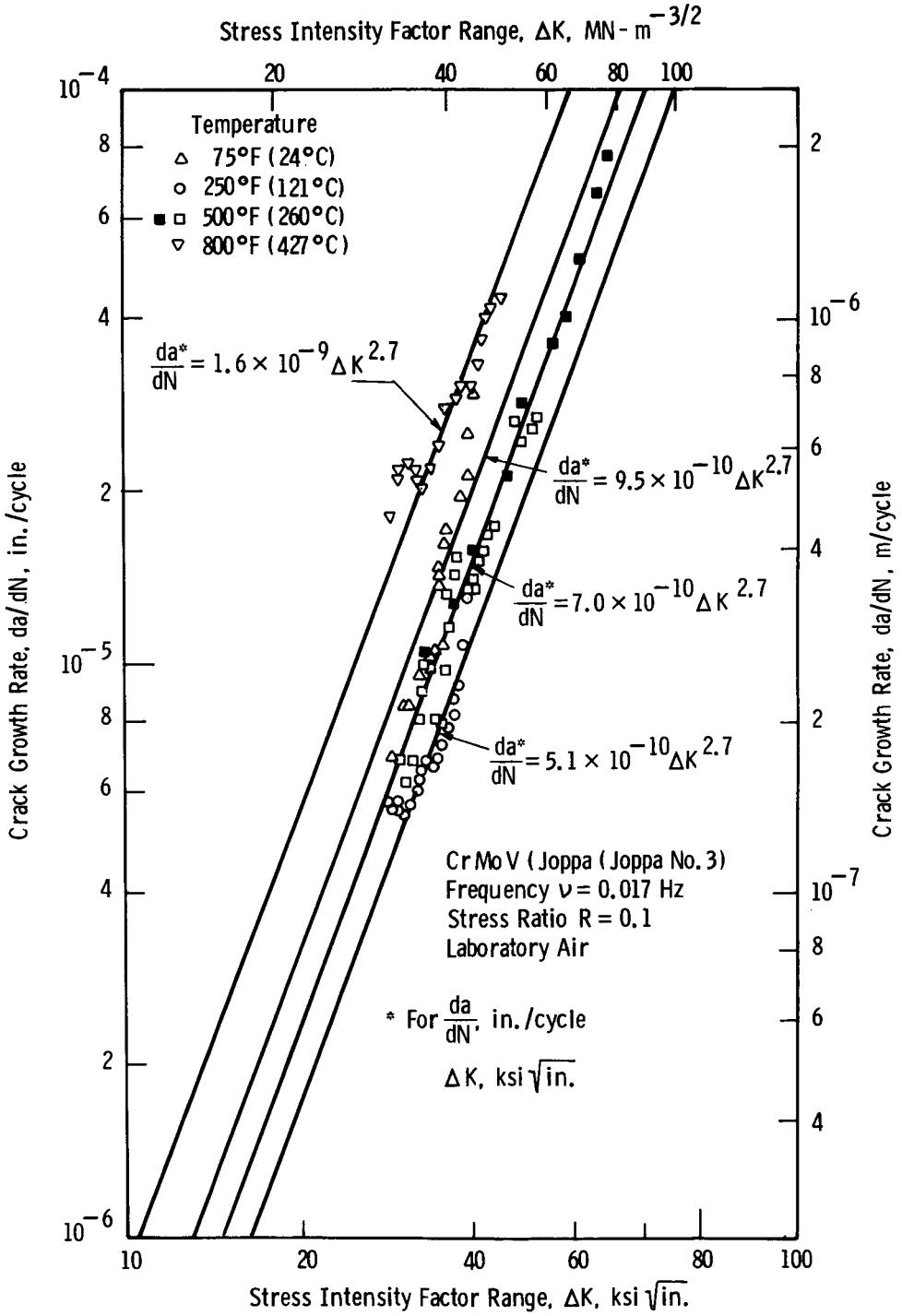

Fig. 4.23 — Effect of temperature on fatigue crack growth rate of CrMoV steel tested at 0.017 Hz.

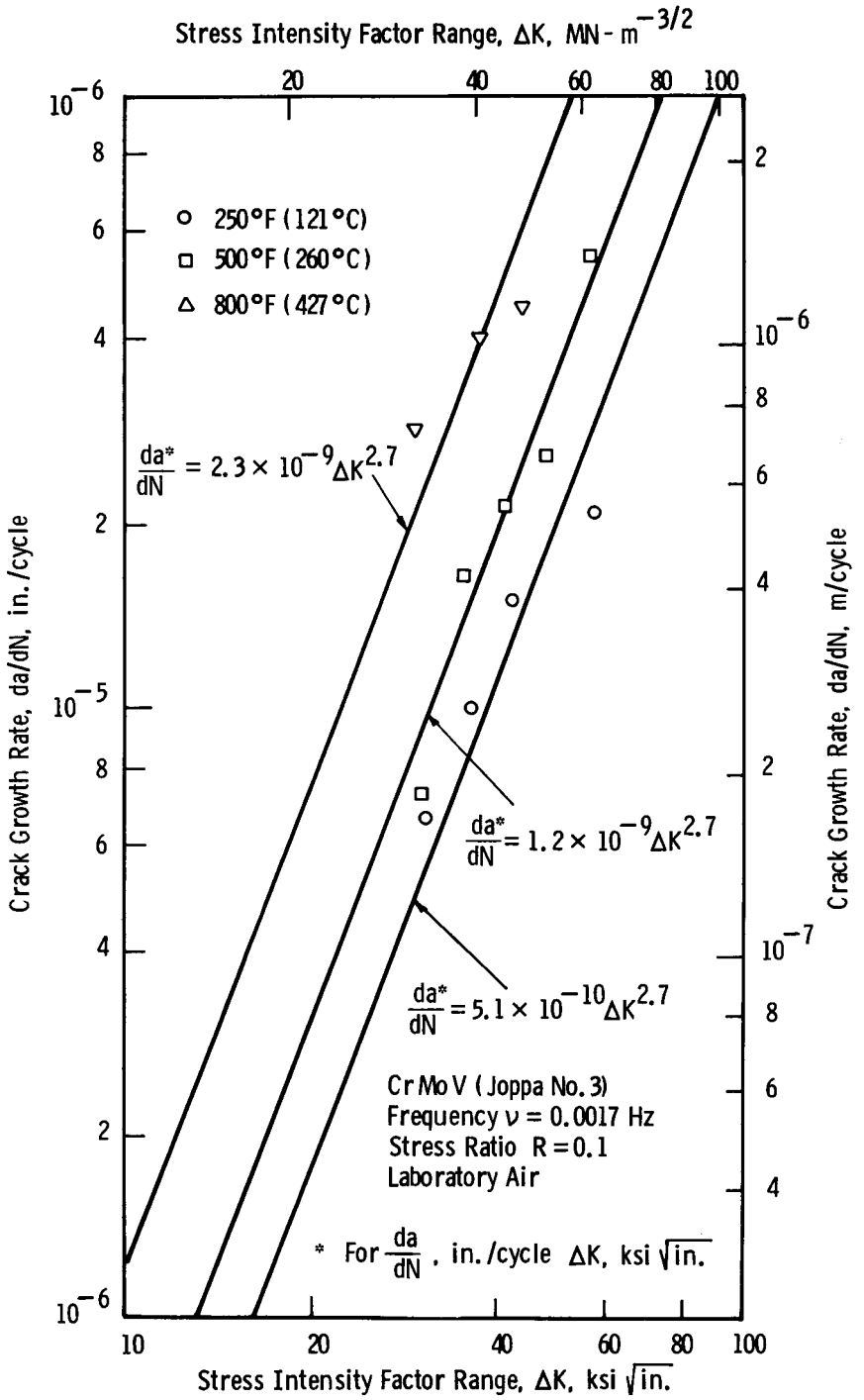

Fig. 4.24 – Effect of temperature on fatigue crack growth of Cr Mo V steel tested at 0.0017 Hz

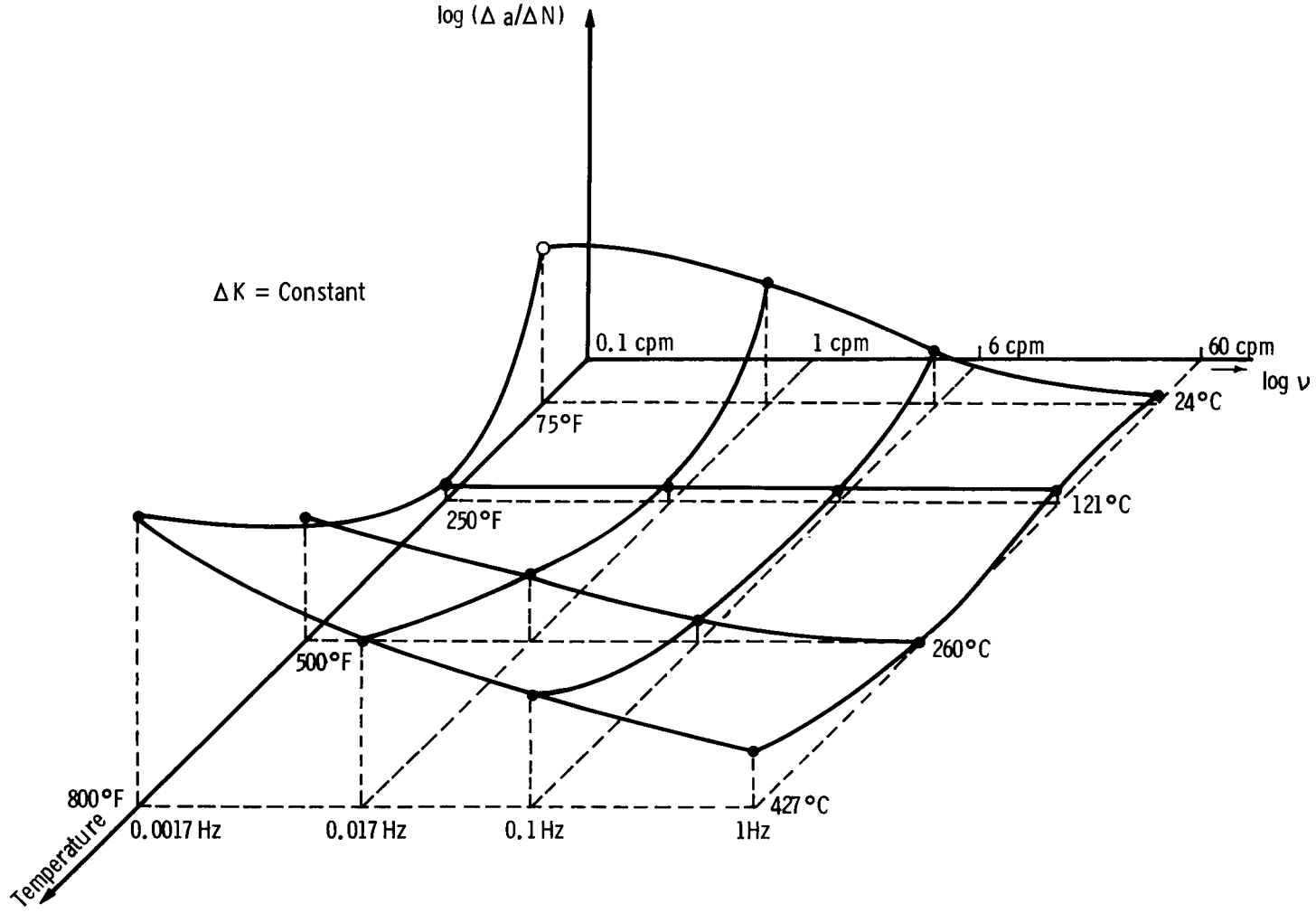

Fig. 4.25 – Three dimensional representation of effects of frequency and temperature on fatigue crack growth rate in air

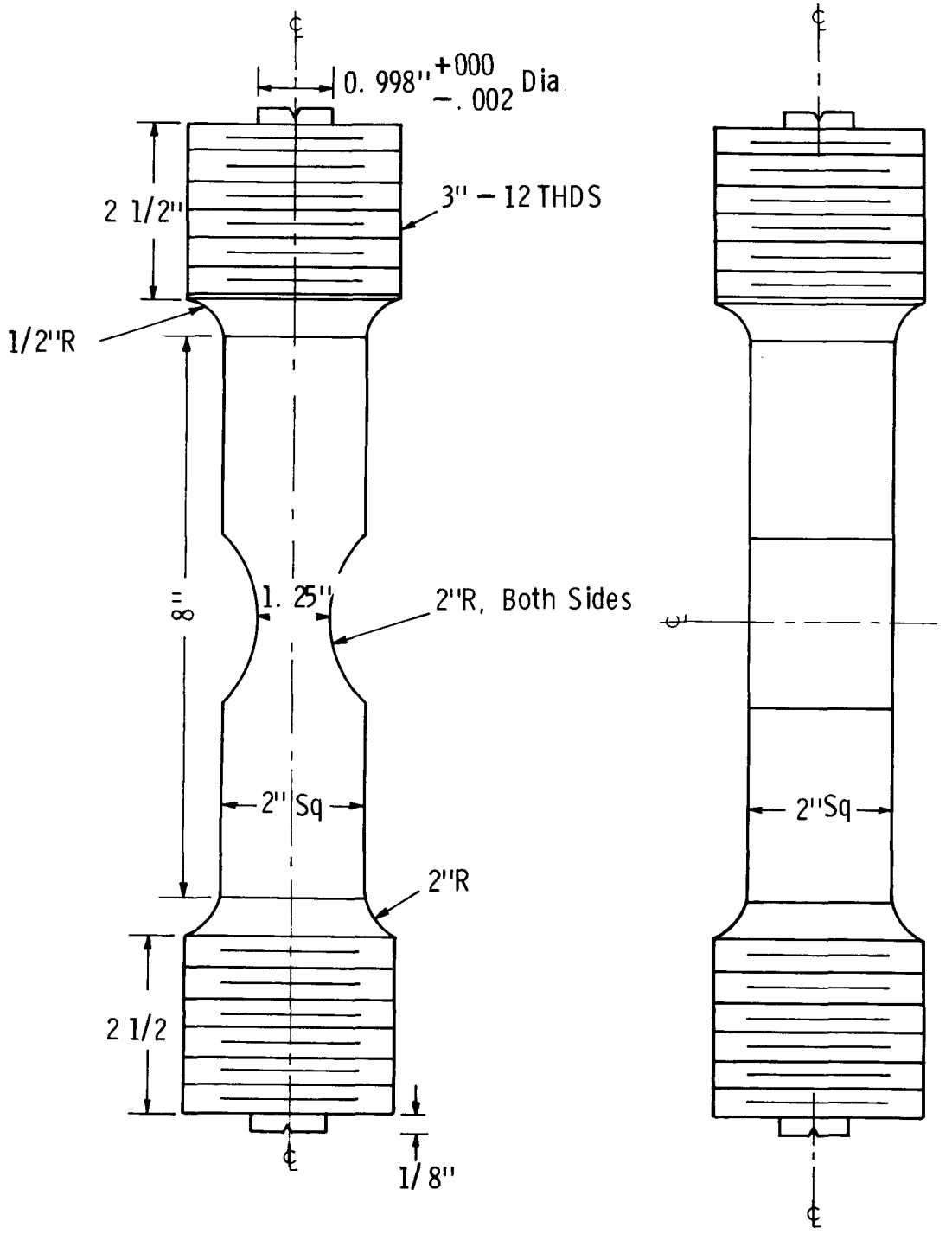

Fig. 4.26 —Dimensions of low cycle fatigue specimen

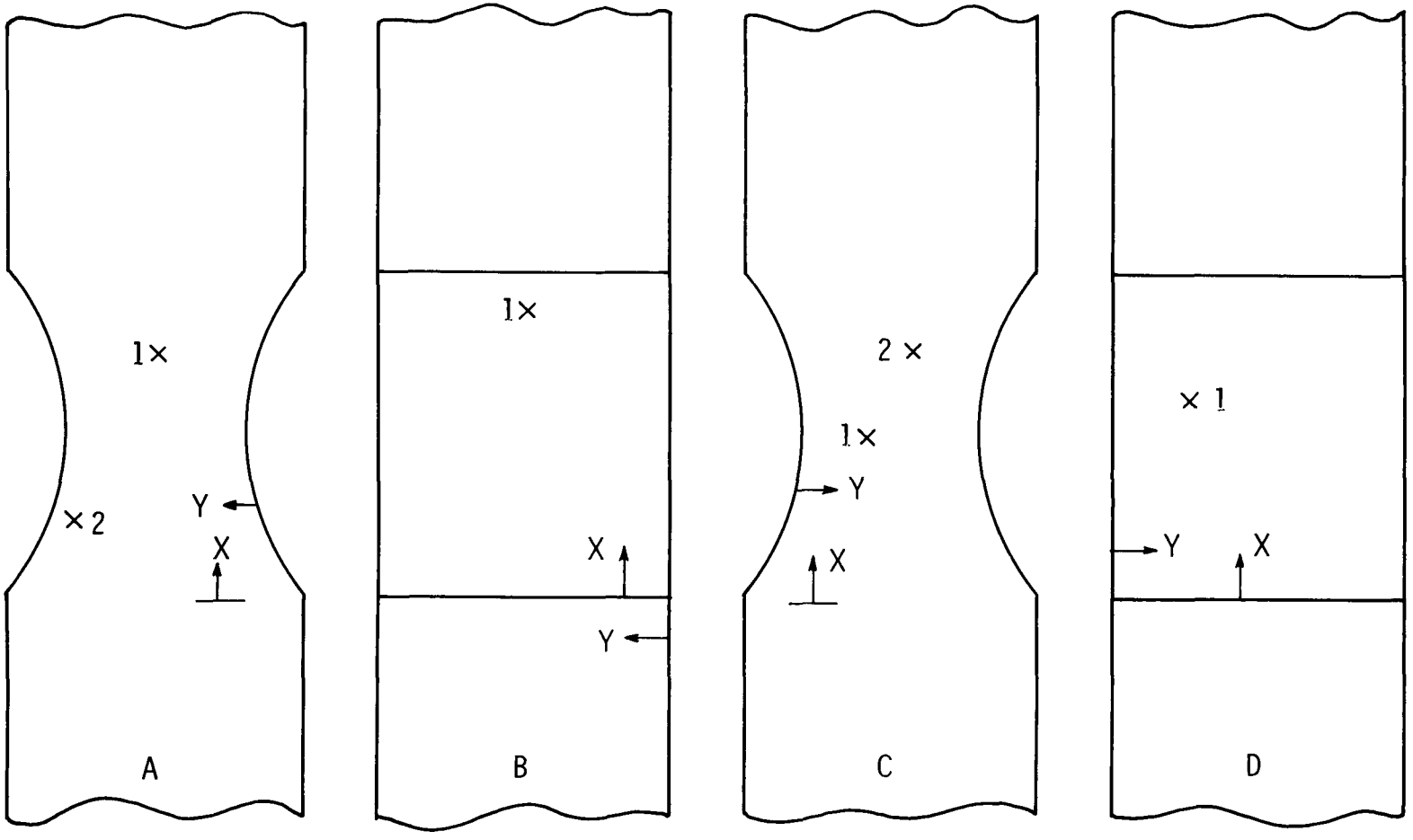

Fig. 4.27a —Ultrasonic indications of specimen LCF1 (see Table 4. 7)

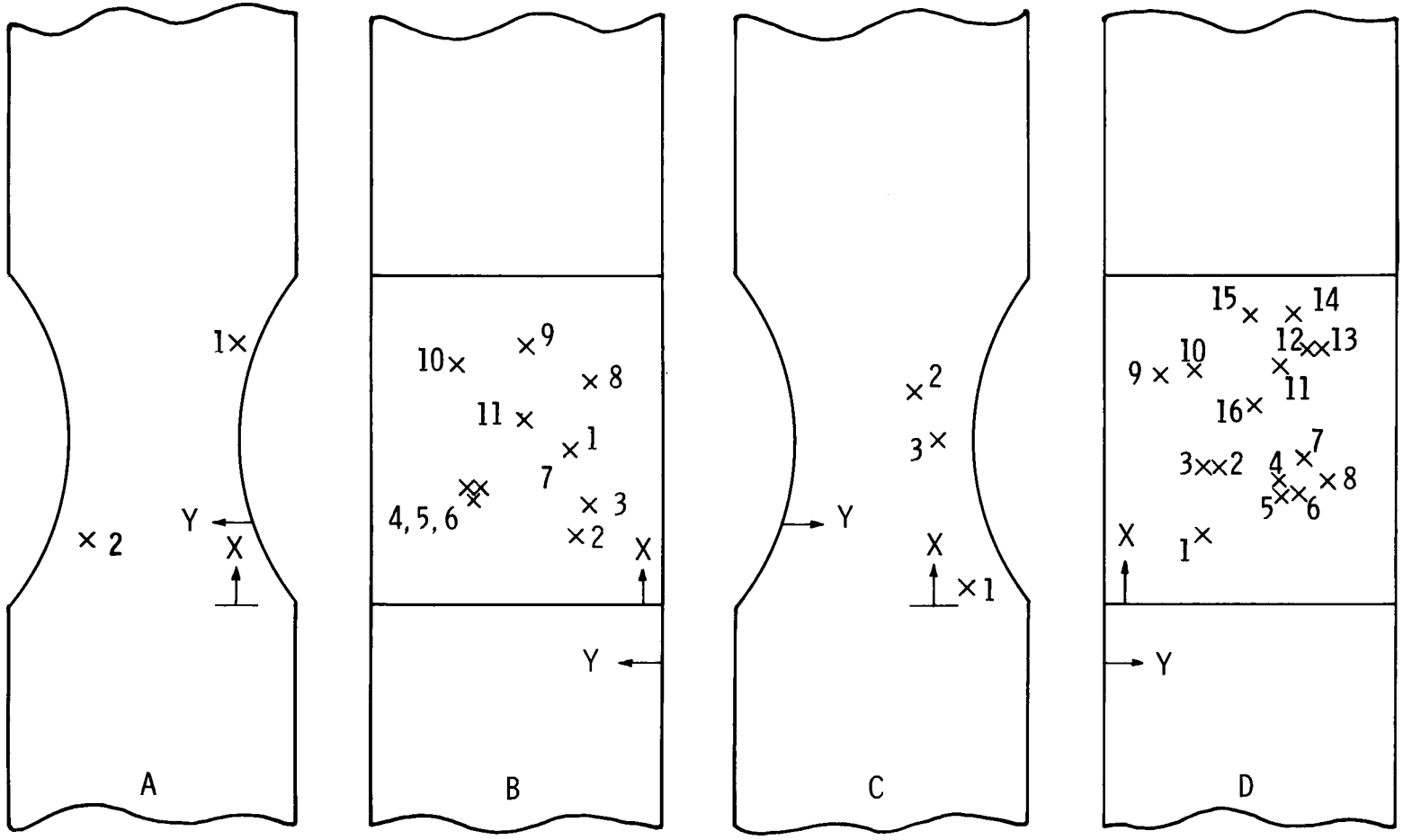

Fig. 4.27 B —Ultrasonic indications of specimen LCF3 (see Table 4. 7)

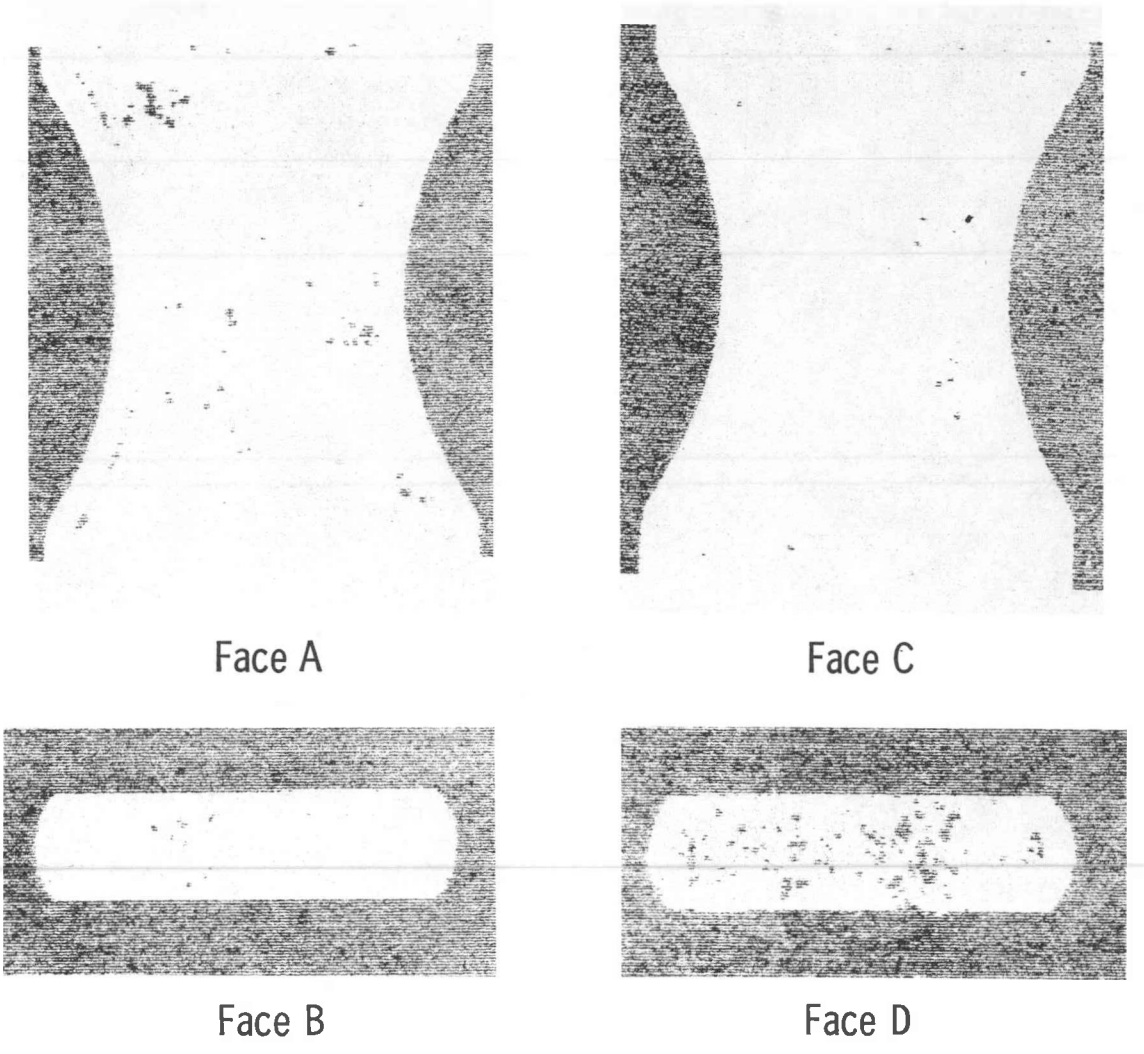

Fig. 4.28a – C scan of specimen LCF1

Face A

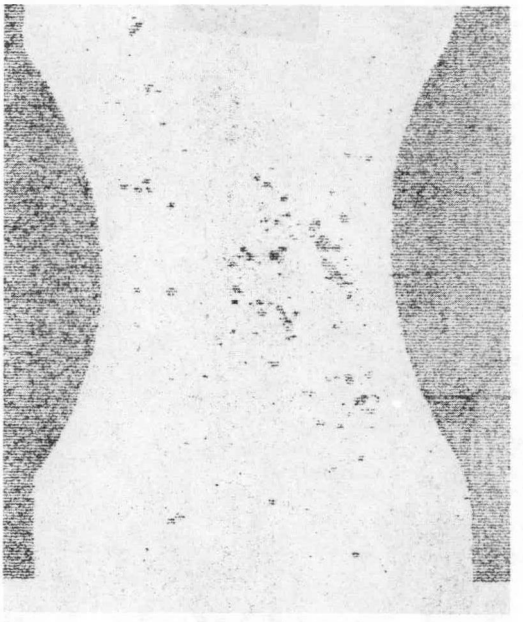

Face C

Face B

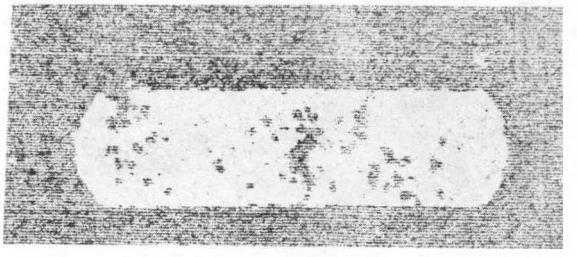

Face D

Fig. 4.28b — C scan of specimen LCF2

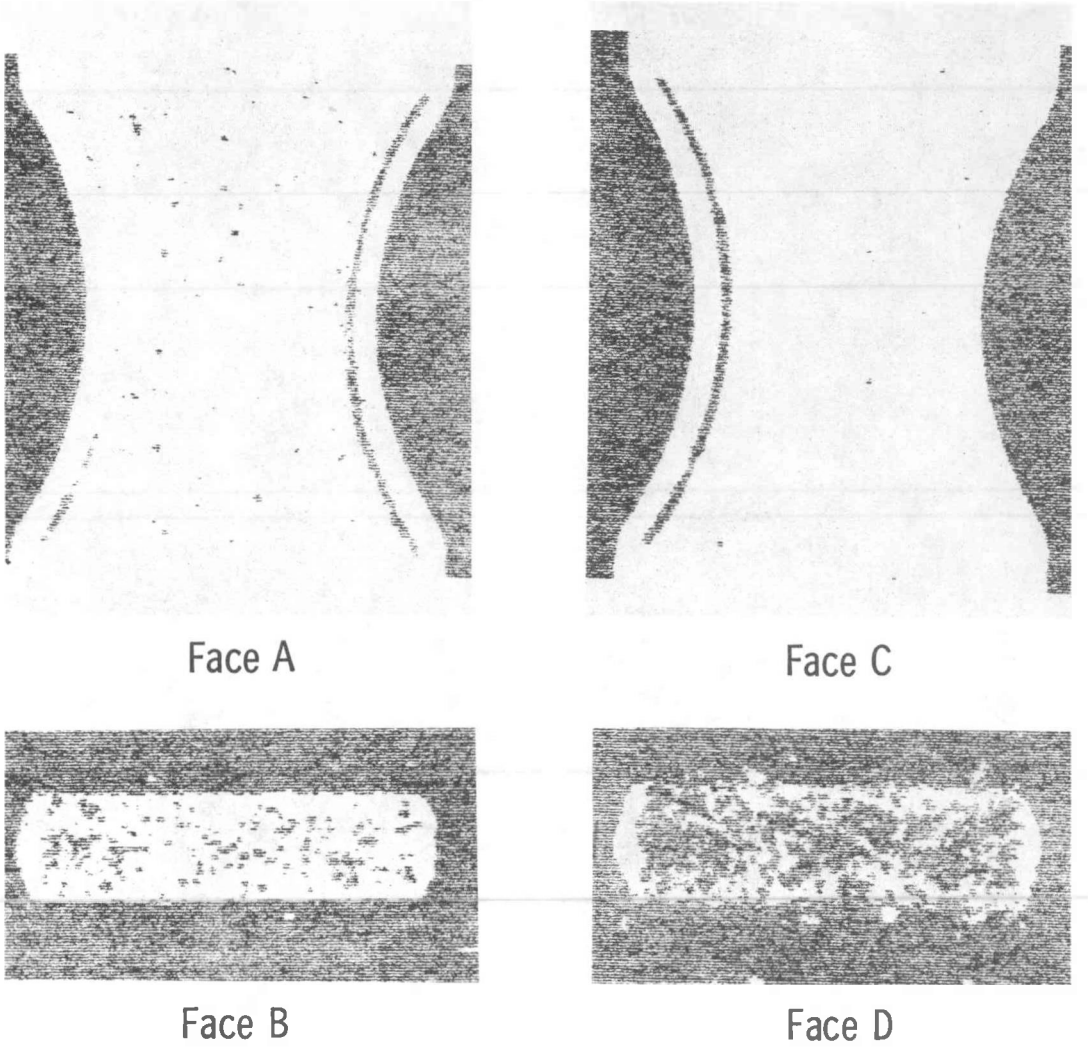

Fig. 4.28c – C scan of specimen LCF3

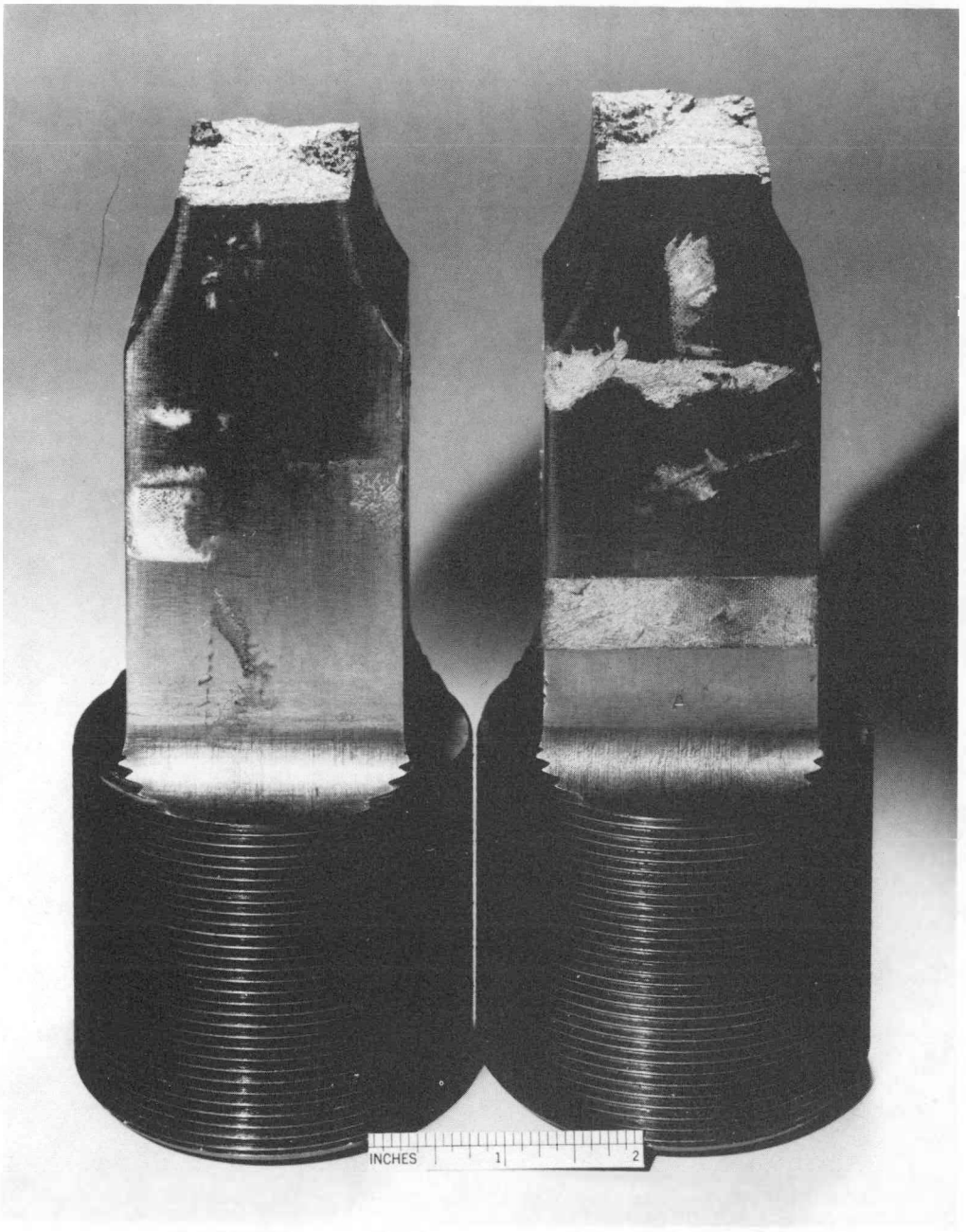

Fig. 4.29a – Broken halves of specimen LFC3

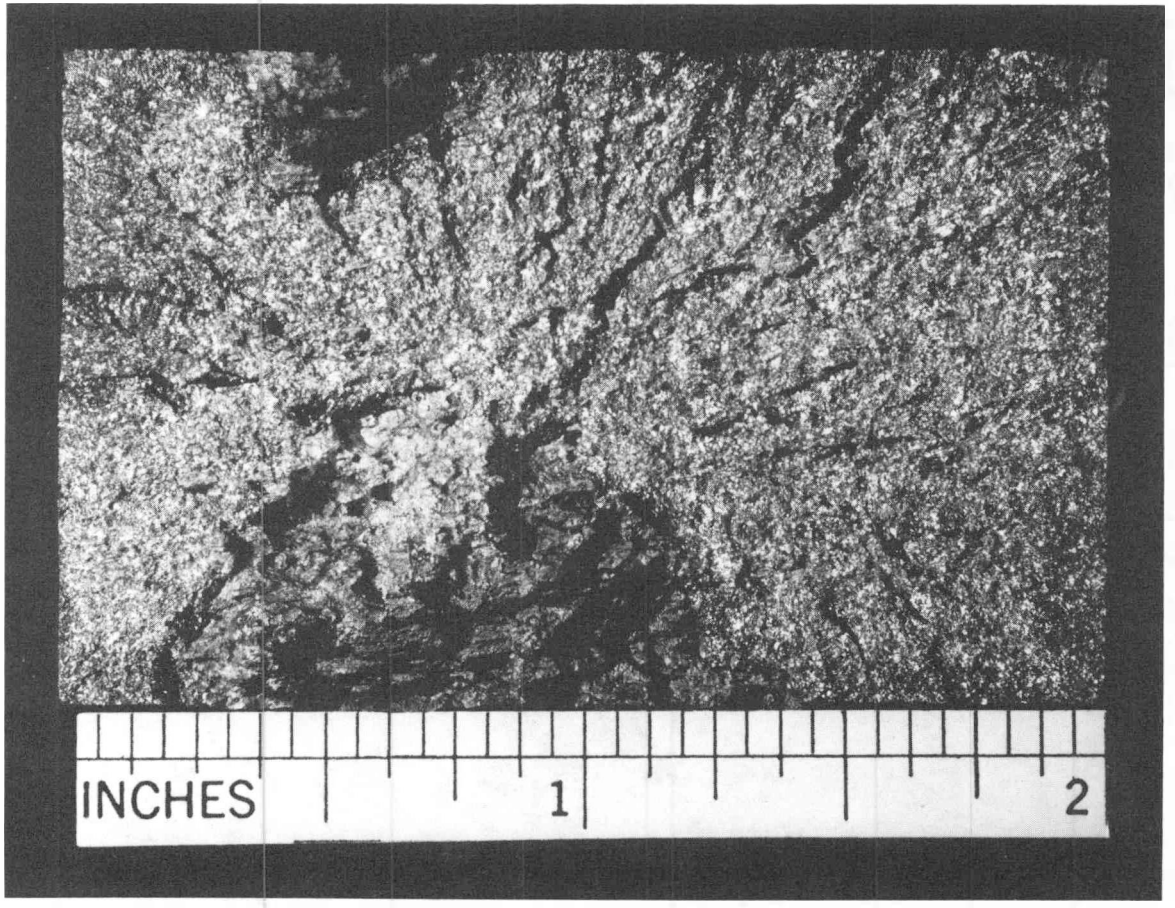

Fig. 4. 29b – Fracture surface of specimen LCF3

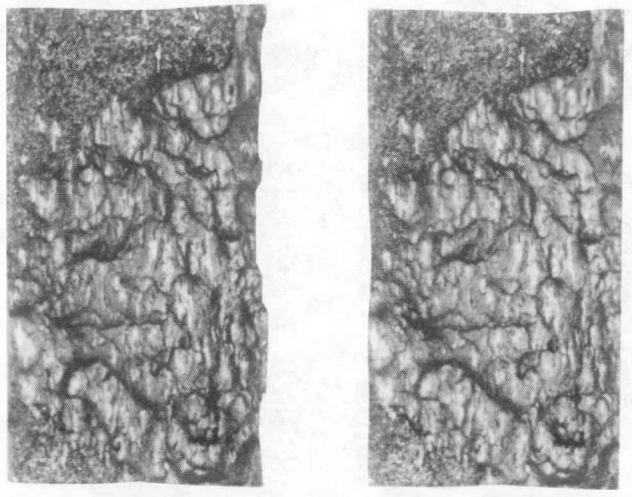

Direction of Crack Propagation

Fig. 4.30 – Stereo pair of selectively oxidized thumbnail crack in large low cycle fatigue specimen with the blue color being the fatigue crack progation region and the light brown, surrounding the white shrinkage porosity, being a region of rapid crack growth

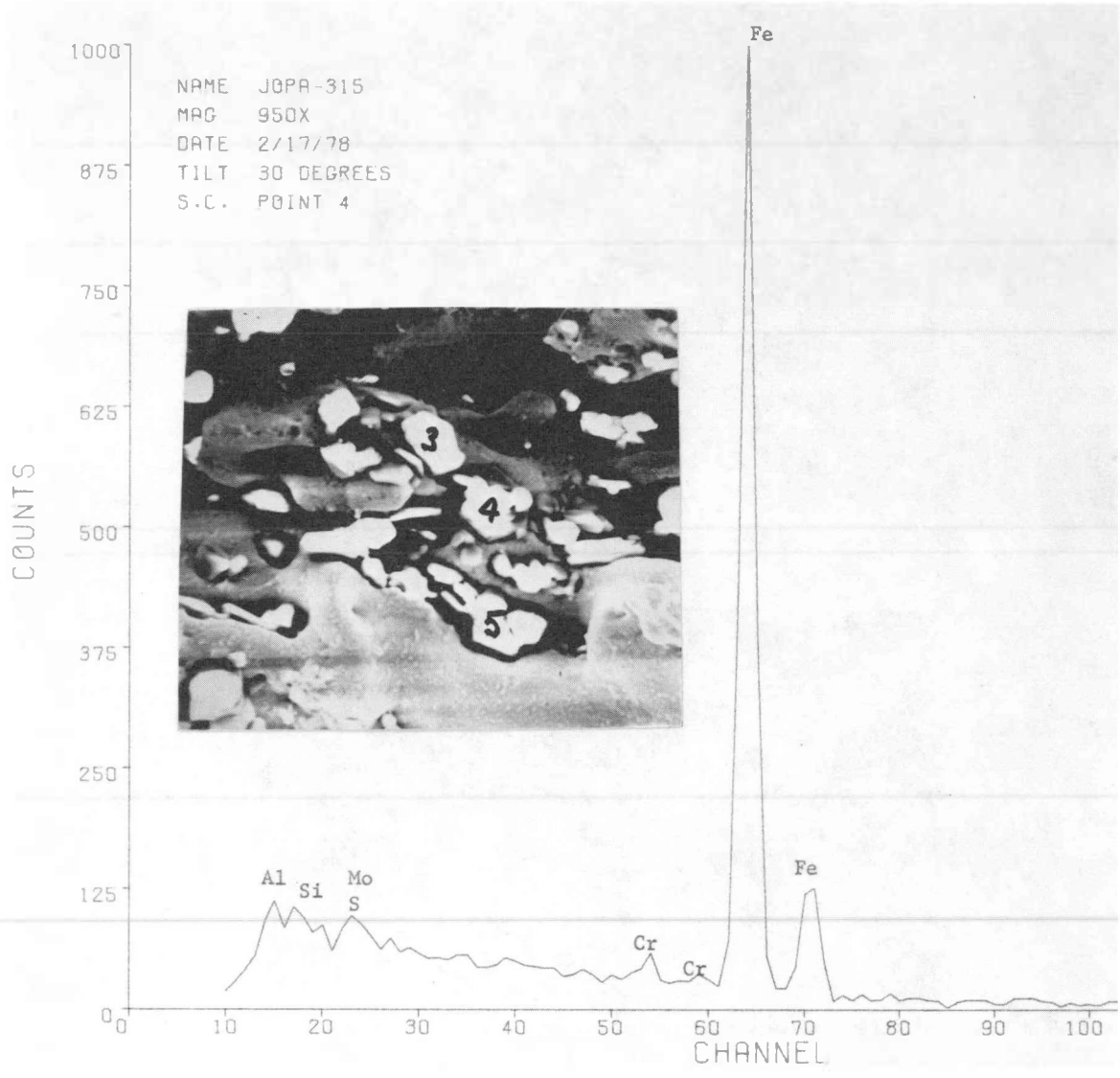

Fig. 4.31—Results of energy dispersion analysis by X-ray indicate shrinkage porosity consists of alumina and silica

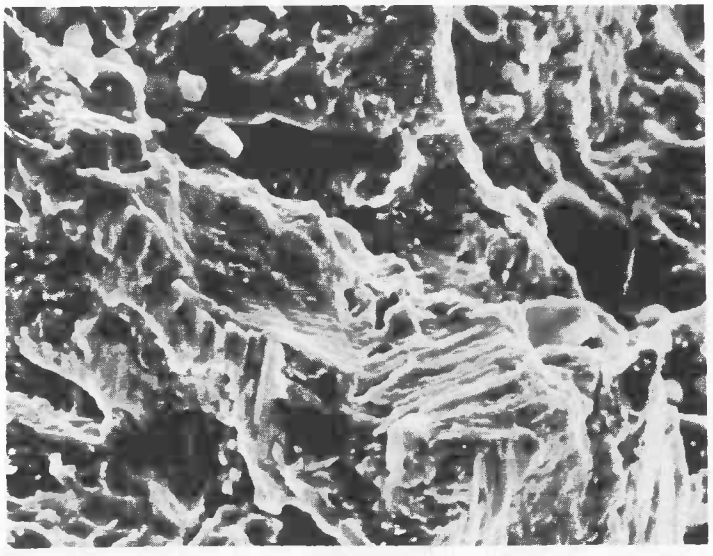

1000 X

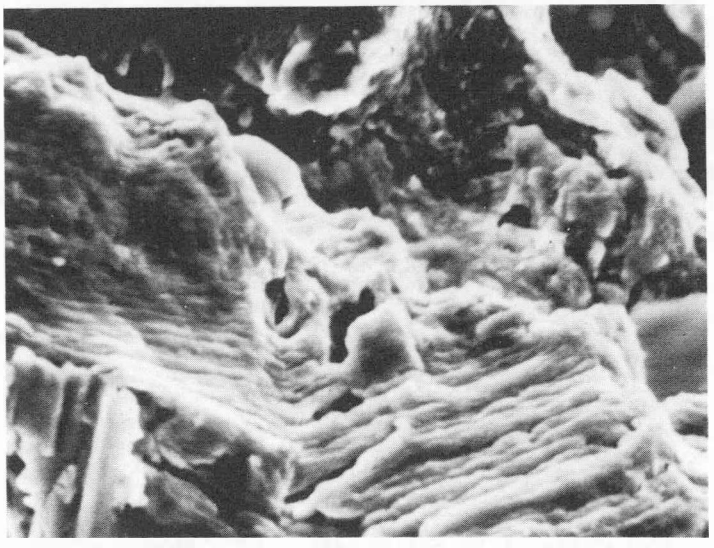

2000 X

Fig. 4.32 – Fatigue striations found in the region of blue color (see Fig. 4.30)

5. DISCUSSION AND CONCLUSIONS

The detailed evaluation of the reliability of a large steam turbine rotor is indeed a complex process. Even if other parts of the problem are ignored (i.e., obtaining the actual service cycle history, NDT uncertainties, finite element model boundary conditions, etc.), understanding the metallurgy and potential fracture mechanisms within a single rotor is also frought with difficulties. The TVA Gallatin No. 2 rotor burst demonstrated that large forgings can be highly segregated in axial and radial extents. If this segregation is present at a critical position in the rotor, unit reliability and possibly safety may be affected. From the failure analysis of the Gallatin rotor burst by Kramer, et al.[5.1], intergranular cracking was found on the fracture surface of the failure origin. It was assumed that the intergranularity was caused by a creep-fatigue interaction mechanism. It was suspected, however, that the microstructure at the failure origin was particularly susceptible to this creep-fatigue interaction mechanism.

It is obvious that we cannot ignore the possibilities of a creep-fatigue mechanism being responsible for a possible future failure. Therefore, before a routine testing program began, (to develop data as input to the life prediction program), a detailed reassessment of the conditions responsible for the Gallatin rotor burst was completed. As part of this ressessment, an analysis of the microstructure of the material adjacent to the failure origin was performed. Mechanical testing was also completed in an attempt to reproduce the failure conditions and fracture mode experienced by the Gallatin rotor. Following is a list of conclusions from the tests performed on the Gallatin rotor material.

1) The microstructure at the failure origin was different from the material adjacent to the failure origin.

2) A residual gas analysis clearly shows that the concentrations of hydrogen, nitrogen and oxygen are not abnormal in the segregated regions when compared to other 1950 vintage CrMoV air cast material.

3) An Auger analysis did not reveal lead at the grain boundaries. The amount of tin and phosphorous (normally associated with temper embrittlement) was found to be insignificant at the grain boundaries.

4) The tensile and Charpy impact properties were found to be typical for this vintage CrMoV. In particular, the tensile ductilities were found to be normal (low tensile ductilities are indicative of temper embrittlement) for this material.

5) The stress rupture specimens were found to be notch strengthening as evidenced by the fact that no break occurred in the notch bar region of the specimen, prior to a break in the plain bar region.

6) The creep properties of this material were found to be within normal scatterbands for 1950 vintage air cast CrMoV. It was also noted that all cracking in the creep specimens was found to be transgranular.

7) The only evidence of intergranular cracking was found in an uniaxial low cycle fatigue specimen which was tested at 800°F (427°C) with a strain range of 2.98% and a dwell period of 23 hours. This material was taken from the bore region of the rotor. All other specimens, tested at various dwell times and strain ranges displayed transgranular fracture.

8) No effect of a biaxial stress state on fatigue crack initiation was found for test conducted at 800°F (427°C) with a dwell time of one hour. Again no intergranular cracking was found at the crack initiation site.

9) The fracture toughness of this material was found to be similar to other 1950 vintage CrMoV rotors.

10. The fatigue crack growth rate of the Gallatin rotor material was found to be similar to other CrMoV rotors of this vintage. The segregation banding found in the Gallatin rotor did not significantly affect the average fatigue crack growth rate. The fatigue crack growth rate determined at 800°F with a dwell time of 22-2/3 hours, increased by a factor of 3 when compared to the data generated with a 15 minute dwell period at 800°F (427°C). Again, it was noted that no intergranular cracking occurred in any of the fatigue crack growth rate tests.

From the results of this investigation, temper embrittlement was ruled out as a possible cause of failure. In addition, the mechanical properties are well within the scatterbands of a 1950 vintage CrMoV rotor material. It is also noted, that the failure analysis of the Gallatin rotor burst showed[5.1] that the linear summation of both creep and fatigue damage cannot account for this failure. Therefore, from the evidence of the intergranular cracking found at the failure origin site, it was assumed that the failure of the Gallatin rotor was due to the interaction of creep and fatigue. However, the fracture mode of the Gallatin burst was not reproduced in any of the mechanical tests performed in this program with the possible exception of a low cycle fatigue test at 800°F (427°C) with a dwell period of 23 hours tested at an extremely high strain range (2.98%).

It is increasingly apparent that the creep-fatigue interaction would not have lead to failure if the microstructure, observed at the Gallatin failure origin, behaved normally at the specific strain range and temperature found within the rotor. Therefore unless this microstructure is suspected to exist, the creep-fatigue interaction mechanism may not be a major concern to reliability.

The results of the large, low cycle fatigue tests conducted with the Joppa material indicate that shrinkage porosity can indeed linkup at an early stage of life if the strain range is large enough. A fracture mechanics approach to the "Reliability of Steam Turbine Rotors" is therefore appropriate in such cases. The fatigue crack growth rate and

fracture toughness data generated in this program can be used to calculate the propagation life of a flaw to a critical size. Using these data as input to the life prediction computer program, the service life of a 1950 vintage steam turbine rotor can be evaluated provided that adequate ultrasonic inspection results are available.

Similar fracture toughness and fatigue crack growth rate properties were found between the Gallatin rotor and the Joppa rotor. It was also noted that the mechanical properties of both the Joppa and Gallatin rotors were similar to two retired Westinghouse rotors. Based on this information it is suggested that the data generated on this program can be used for the life prediction analysis of 1950 vintage steam turbine rotors. However, due to the limited data base, it is recommended that further testing on other rotors be conducted.

The highlights of the results generated on the two rotors investigated on this program are presented below.

1. The mechanical properties of the Joppa rotor are extremely uniform throughout the axial and radial extent of the rotor. Small ultrasonic indications appear to have no effect on the tensile properties of this rotor.

2. The Charpy FATT values and the fracture toughness values are similar in both the Joppa and Gallatin rotor.

3. A good correlation exists between the fracture toughness and the FATT values when the Begley-Logsdon correlation technique is employed.

4. The Carden method for the interpolation of the temperature-frequency interaction for fatigue crack growth is inappropriate for data generated in this program at temperatures between room temperature and 800°F (427°C).

5. The large low cycle fatigue specimens from the Joppa rotor displayed a classic example of fatigue crack propagation and linkup between

shrinkage pores. The crack front followed a three dimensional pattern searching out the nearest defect during the linkup process. The results of the sectioning of the Joppa rotor by task III of this program showed a volumetric fraction of flaws to matrix to be of the order of 0.01. However, a two dimensional projection of the shrinkage pores found in the stable propagation region of the low cycle fatigue specimen showed an area fraction of flaws to matrix to be approximately 0.21. While a direct comparison cannot be made between a two dimensional projection and a volumetric average of the flaw to matrix fraction, obvious discrepancies still exists between these two results. Further evaluations are required to explain this anomaly.

5.1 REFERENCES

5.1 Kramer, L. D. and Randolph, D. D., in the 1976 ASME-MPC Symposium on Creep-Fatigue Interaction, R. M. Curran, Ed., ASME, New York, 1976, pp. 1-24.

6. RECOMMENDATIONS

As a result of this investigation, a fracture mechanics approach to determining the Reliability of Steam Turbine Rotors is shown to be appropriate. The success of such a method is, however, based on the availability of accurate ultrasonic test results. While the importance of a good characterization of a rotor by ultrasonic methods is obvious, continued evaluations of fracture mechanics and analysis are equally desirous. Below is a list of recommendations for continued testing and analysis resulting from the test program completed by Task group IV.

1. Defect Interactions with Other Defects and the Bore Surface

While most of the fracture analysis of a steam turbine rotor is concerned with linear elastic fracture, the process of defect linkup and defect interaction with the bore surface is most certainly an elastic-plastic problem. Approximation techniques have been used in an attempt to utilize experimental properties of materials to determine when a defect might "pop" through to a bore. These techniques are rather approximate and require further evaluation to determine their applicability to steam turbines. It might well prove fruitful if an artifical defect program was developed to determine the effect of loss of constraint for an imbedded flaw near a free surface. The possibility of using known geometry ceramic flaws in a powdered metal material may well answer many of these questions. A similar approach could be used for defect to defect interaction studies.

2. Correlation of Ultrasonic Indications with Fracture Surface Topography

It is of extreme importance to evaluate the performance of defects (as defined by ultrasonic indications) under cyclic loading conditions. While a model may be used to evaluate the propagation rate of a known defect, it is important to remember that a defect can only be characterized by ultrasonic techniques. Therefore, a

correlation of the fracture behavior of an ultrasonic indication to a given model is required. This may well be accomplished by further testing and periodic inpsection of material with various levels of ultrasonic indications in a manner similar to the large low cycle specimens already tested.

3. Growing of an Embedded Flaw at a Frequency of One Cycle Every 24 Hour

In order to determine the growth rate of an internal defect at a frequency similar to that found during normal duty, it may be necessary to perform tests similar to the long hold time tests already completed but utilizing an inert atmosphere. This would have the added advantage of deciding whether or not the increased crack growth rate already noted for the 24 hour hold time tests was due to oxidation damage or a creep phenomena.

4. Parametrization of the Fatigue Crack Growth Equation

If it is indeed necessary for a single parametric equation to be inserted in the life prediction computer program it may well prove valuable to perform a further series of tests at temperatures above 250°F (121°C). This would remove the possibility of an environmental interaction at room temperature.

For the development of the Carden equation, four frequencies and temperatures are required to develop the required constants. This must be tested in a single environment. The room temperature tests were not exactly the same as those tested at temperatures above 250°F (121°C) due to the presence of humidity. While the Carden approach is only interpolative, it may be of interest to see how well it would predict the 24 hour hold time tests.

5. Biaxial Fatigue Testing of Tubular Specimens

A test method developed and used by The Japan Steel Works may well prove valuable in any further studies on the interaction of creep and fatigue. The principal advantage of this method is

that the correct state of stress may be imposed on the material under consideration. The single disadvantage of this test method is that it utilizes a thin wall tube which may not give the required plane strain conditions. The tube is loaded both axially, by a push pull load train, and radially by using internal pressure. Initial results by The Japan Steel Works are very encouraging and shows promise.